frontiers | Research Topics

iSensor and iMedicine for human health

Edited by
Yan Zhang, Dejin Zang, Chengchao Chu, Huanshun Yin
and Laurent Ruhlmann

Published in
Frontiers in Chemistry

ISSN 1664-8714
ISBN 978-2-83251-013-1
DOI 10.3389/978-2-83251-013-1

About Frontiers

Frontiers is more than just an open access publisher of scholarly articles: it is a pioneering approach to the world of academia, radically improving the way scholarly research is managed. The grand vision of Frontiers is a world where all people have an equal opportunity to seek, share and generate knowledge. Frontiers provides immediate and permanent online open access to all its publications, but this alone is not enough to realize our grand goals.

Frontiers journal series

The Frontiers journal series is a multi-tier and interdisciplinary set of open-access, online journals, promising a paradigm shift from the current review, selection and dissemination processes in academic publishing. All Frontiers journals are driven by researchers for researchers; therefore, they constitute a service to the scholarly community. At the same time, the *Frontiers journal series* operates on a revolutionary invention, the tiered publishing system, initially addressing specific communities of scholars, and gradually climbing up to broader public understanding, thus serving the interests of the lay society, too.

Dedication to quality

Each Frontiers article is a landmark of the highest quality, thanks to genuinely collaborative interactions between authors and review editors, who include some of the world's best academicians. Research must be certified by peers before entering a stream of knowledge that may eventually reach the public - and shape society; therefore, Frontiers only applies the most rigorous and unbiased reviews. Frontiers revolutionizes research publishing by freely delivering the most outstanding research, evaluated with no bias from both the academic and social point of view. By applying the most advanced information technologies, Frontiers is catapulting scholarly publishing into a new generation.

What are Frontiers Research Topics?

Frontiers Research Topics are very popular trademarks of the *Frontiers journals series*: they are collections of at least ten articles, all centered on a particular subject. With their unique mix of varied contributions from Original Research to Review Articles, Frontiers Research Topics unify the most influential researchers, the latest key findings and historical advances in a hot research area.

Find out more on how to host your own Frontiers Research Topic or contribute to one as an author by contacting the Frontiers editorial office: frontiersin.org/about/contact

iSensor and iMedicine for human health

Topic editors
Yan Zhang — University of Jinan, China
Dejin Zang — Tsinghua University, China
Chengchao Chu — Xiamen University, China
Huanshun Yin — Shandong Agricultural University, China
Laurent Ruhlmann — Université de Strasbourg, France

Citation
Zhang, Y., Zang, D., Chu, C., Yin, H., Ruhlmann, L., eds. (2022). *iSensor and iMedicine for human health*. Lausanne: Frontiers Media SA.
doi: 10.3389/978-2-83251-013-1

Table of contents

frontiers | Frontiers in Chemistry

TYPE Editorial
PUBLISHED 01 December 2022
DOI 10.3389/fchem.2022.1107145

Editorial: iSensor and iMedicine for human health

Chengchao Chu[1] and Yan Zhang[2,3]*

[1]School of Medicine, Xiamen University, Xiamen, China, [2]School of Chemistry and Chemical Engineering, University of Jinan, Jinan, China, [3]Key Laboratory of Optic-Electric Sensing and Analytical Chemistry for Life Science, MOE, Qingdao University of Science and Technology, Qingdao, China

KEYWORDS

sensor, wearable devices, electrochemistry, electroluminescence, *in vitro*, *in vivo*

Editorial on the Research Topic
iSensor and iMedicine for human health

OPEN ACCESS

EDITED AND REVIEWED BY
Jin-Wen Liu,
Guangxi Medical University, China

*CORRESPONDENCE
Yan Zhang,
chm_zhangyan@hotmail.com

SPECIALTY SECTION
This article was submitted to Analytical Chemistry, a section of the journal Frontiers in Chemistry

RECEIVED 24 November 2022
ACCEPTED 25 November 2022
PUBLISHED 01 December 2022

CITATION
Chu C and Zhang Y (2022), Editorial: iSensor and iMedicine for human health. *Front. Chem.* 10:1107145.
doi: 10.3389/fchem.2022.1107145

Up to now, precise diagnosis and treatment of diseases have always been the hot Research Topic in the fields of analytical chemistry, biology and medicine (Nie et al., 2021; Hou et al., 2022). In order to serve public health and obtain a better understanding of diseases, in-depth researches have been carried out, with much more attention attached to the occurrence, mechanism, prevention and diagnosis of diseases, as well as safe and effective treatments, which play a critical role in disease events. Thus, iSensor (intelligentized sensor) and iMedicine (intelligentized medicine) were proposed to satisfy the high requirements for the recent medical environment.

Diagnosis of disease can be divided into *in vitro* diagnosis and *in vivo* diagnosis. *In vivo* diagnosis can be further divided into two methods, wearable diagnosis (Zhu et al.) and *in vivo* imaging, both of which are already involved in important clinical practice. In addition, *in vitro* diagnosis refers to the diagnosis of diseases through the analysis of blood, urine, saliva, tears and even breath gas collected in the body, and combined with the analysis of active ingredients, and thus understand the disease by sensors. Among various *in vitro* diagnostic strategy, electrochemical immunosensor has received more and more attention due to its convenient and rapid detection. To increase the sensitivity of electrochemical sensor, methylene blue (MB) modified MWCNT (MWCNT-MB) was coated on the surface of glassy carbon electrode (GCE) to increase the electron transfer property (Zhang et al.). Then, polydopamine was synthesized on MWCNT to connect the anti- carcinoembryonic antigen (CEA) antibody (Ab). With the addition of CEA, the redox signal of MWCNT-MB decreased due to the reduction of electron transfer efficiency. Thus, the immunosensor was applied to the detection of CEA with a low limit of detection (LOD). Similarly, chitosan-reduced graphene oxide composite and gold nanoparticles were modified on the surface of GCE to increase the electrochemical signal (Chang et al.). After the modification of Ab, bone gamma-carboxyglutamate protein was immobilized on GCE, reducing the electrochemical signal of added electrochemical probe ($[Fe(CN)_6]^{3-/4-}$).

Furthermore, electroluminescence (ECL) was another research hotspot for its low background, fast detection speed and high detection sensitivity (Fereja et al., 2020; Liu et al., 2022). In this Research Topic, the vertically ordered mesoporous silica-nanochannel film (VMSF) was coated on the surface of ITO electrode, in which positively charged $Ru(bpy)_3^{2+}$enriched inner the nanochannel (Ma et al.). In a further step, prostate-specific antigen (PSA) Ab was modified on the surface of VMSF/ITO electrode. In addition, the PSA could specifically bind with Ab and thus resisting the physical absorption of $Ru(bpy)_3^{2+}$ into the nanochannel, resulting in the decrease of ECL signal. Finally, the constructed ECL sensor was applied to the detection of PSA, and the immunosensor possessed a low LOD. Meanwhile, Wei et al. coated polyethylene terephthalate (PET) on ITO electrode, and further modified with VMSF. The clindamycin was confirmed to enhance the ECL of $Ru(bpy)_3^{2+}$, and the VMSF/PET-ITO sensor could detect clindamycin, using $Ru(bpy)_3^{2+}$ as ECL luminophores. In a further study, Gong et al. constructed a three-dimensional (3D) ECL platform using VMSF modified macroporous 3D graphene electrode. Unlike traditional electrode, 3D graphene showed high diffusion/mass transfer efficiency, benefiting for the ECL detection. The $Ru(bpy)_3^{2+}$/tri-n-propylamine (TPrA) was applied to the detection of 4-chlorophenol using the ECL sensor, in which the ECL signal of $Ru(bpy)_3^{2+}$/TPrA was quenched by 4-chlorophenol. Moreover, chlorpheniramine could promote the ECL signal of $Ru(bpy)_3^{2+}$, and the chlorpheniramine could be detected using the ECL sensor, with a LOD of 430 nM. Therefore, the proposed VMSF modification is an effective strategy to increase the sensitivity of ECL sensors.

Other than the traditional single-mode sensor, dual-mode or multi-mode sensor could improve detection rate and reduce the background influence (Zhang et al. 2020). For example, Tan et al. constructed a colorimetric/fluorescent dual-mode sensor using Co_3O_4 nanozymes, which was then applied in the detection of H_2O_2 and glucose with high sensitivity; Wan et al. constructed a colorimetric/fluorescent dual-mode sensor using nitrogen-doped graphene quantum dot and applied in the detection of H_2O_2, ascorbic acid and acid phosphatase with high sensitivity. In addition, researchers modified multi-biosensor on one chip for simultaneous detection of multi-biomarker, enabling fast quantification of the multi-biomarker associated disease. (Meng et al. 2022)

In recent years, the intelligent method has also been applied in drug development. Cheng et al. synthesized a non-alcoholic steatohepatitis treated compound YWS01125. To evaluate the pharmacokinetics of YWS01125, an ultraperformance liquid chromatography-tandem mass spectrometry (UPLC-MS/MS) strategy was applied. The pharmacokinetics studies indicated that YWS01125 could be an advanced drug to treat with non-alcoholic steatohepatitis. Furthermore, with the continuous development of nano/micro-medicine, the use of nano/micro-materials for drug delivery or nano-therapy arose (Shi et al.; Wang et al.). All in all, it could be concluded that the future of iSensor and iMedicine depends on three key factors: 1) new types of *in vitro* and *in vivo* diagnostic equipment; 2) advanced diagnostic probes, imaging probes, and smart medicines; 3) effective data integration and analysis.

Author contributions

CC was a Guest Editor of the Research Topic and wrote the paper text. YZ was a Guest Editor of the Research Topic and edited the text.

Funding

This work was financially supported by the NSFC (32271447 and 21904047), Taishan Scholars Program (tsqn202103082), the Excellent Youth Innovation Team in Universities of Shandong (2021KJ021), and the Open Fund of Key Laboratory of Optic-electric Sensing and Analytical Chemistry for Life Science, MOE, Qingdao University of Science and Technology (M2023-5).

Acknowledgments

We thank authors of the papers published in this Research Topic for their valuable contributions and the referees for their rigorous review.

Conflict of interest

The authors declare that the research was conducted in the absence of any commercial or financial relationships that could be construed as a potential conflict of interest.

Publisher's note

References

Fereja, T. H., Du, F., Wang, C., Snizhko, D., Guan, Y., and Xu, G. (2020). Electrochemiluminescence imaging techniques for analysis and visualizing. *J. Anal. Test.* 4, 76–91. doi:10.1007/s41664-020-00128-x

Hou, Y., Lv, C.-C., Guo, Y.-L., Ma, X.-H., Liu, W., Jin, Y., et al. (2022). Recent advances and applications in paper-based devices for point-of-care testing. *J. Anal. Test.* 6, 247–273. doi:10.1007/s41664-021-00204-w

Liu, F.-Y., Zhang, T.-K., Zhao, Y.-L., Ning, H.-X., and Li, F.-S. (2022). Electrochemiluminescence of 1, 8-naphthalimide-modified carbon nitride for Cu^{2+} detection. *J. Anal. Test.* 6, 296–307. doi:10.1007/s41664-021-00203-x

Meng, F., Zhang, L., Lian, J., Huo, W., Shi, X., and Gao, Y. (2022). One-shot full range quantification of multi biomarkers with different abundance by a tandem giant magnetoresistance assay. *Front. Chem.* 10, 911795. doi:10.3389/fchem.2022.911795

Nie, Y., Liang, Z., Wang, P., Ma, Q., and Su, X. (2021). MXene-derived quantum dot@gold nanobones heterostructure based electrochemiluminescence sensor for triple-negative breast cancer diagnosis. *Anal. Chem.* 93, 17086–17093. doi:10.1021/acs.analchem.1c04184

Zhang, Y., Xu, J., Zhou, S., Zhu, L., Lv, X., Zhang, J., et al. (2020). DNAzyme-triggered visual and ratiometric electrochemiluminescence dual-readout assay for Pb(II) based on an assembled paper device. *Anal. Chem.* 92, 3874–3881. doi:10.1021/acs.analchem.9b05343

frontiers in Chemistry

ORIGINAL RESEARCH
published: 17 November 2021
doi: 10.3389/fchem.2021.774486

Colorimetric and Fluorescent Dual-Modality Sensing Platform Based on Fluorescent Nanozyme

Yejian Wan[1†], Jingwen Zhao[2†], Xiaochun Deng[2], Jie Chen[1], Fengna Xi[2*] and Xiaobo Wang[1*]

[1]Guangxi Medical University Cancer Hospital, Guangxi Medical University, Nanning, China, [2]Department of Chemistry, Zhejiang Sci-Tech University, Hangzhou, China

Compared with natural enzymes, nanozymes based on carbonaceous nanomaterials are advantages due to high stability, good biocompatibility, and the possibility of multifunctionalities through materials engineering at an atomic level. Herein, we present a sensing platform using a nitrogen-doped graphene quantum dot (NGQD) as a highly efficient fluorescent peroxidase mimic, which enables a colorimetric/fluorescent dual-modality platform for detection of hydrogen peroxide (H_2O_2) and biomolecules (ascorbic acid-AA, acid phosphatase-ACP) with high sensitivity. NGQD is synthesized using a simple hydrothermal process, which has advantages of high production yield and potential for large-scale preparation. NGQD with uniform size (3.0 ± 0.6 nm) and a single-layer graphene structure exhibits bright and stable fluorescence. N-doping and ultrasmall size endow NGQD with high peroxidase-mimicking activity with an obviously reduced Michaelis–Menten constant (K_m) in comparison with natural horseradish peroxidase. Taking advantages of both high nanozyme activity and unique fluorescence property of NGQD, a colorimetric and fluorescent dual-modality platform capable of detecting H_2O_2 and biomolecules (AA, ACP) with high sensitivity is developed as the proof-of-concept demonstration. Furthermore, the mechanisms underlying the nanozyme activity and biosensing are investigated.

Keywords: dual-modality sensing, colorimetric detection, fluorescent detection, nanozyme, graphene quantum dots

Edited by:
Yan Zhang,
University of Jinan, China

Reviewed by:
Chuanxia Chen,
University of Jinan, China
Xiangheng Niu,
Jiangsu University, China

***Correspondence:**
Fengna Xi
fengnaxi@zstu.edu.cn
Xiaobo Wang
wangxiaobo@stu.gxmu.edu.cn

[†]*These authors have contributed equally to this work*

Specialty section:
This article was submitted to Analytical Chemistry, a section of the journal Frontiers in Chemistry

Received: 12 September 2021
Accepted: 26 October 2021
Published: 17 November 2021

Citation:
Wan Y, Zhao J, Deng X, Chen J, Xi F and Wang X (2021) Colorimetric and Fluorescent Dual-Modality Sensing Platform Based on Fluorescent Nanozyme. Front. Chem. 9:774486. doi: 10.3389/fchem.2021.774486

INTRODUCTION

Nanozymes are artificial nanomaterials with enzyme-mimicking properties (Gao et al., 2007; Ju et al., 2016; Sun et al., 2018; Yan, 2020). They promise a wide range of applications (e.g., sensing, catalysis) by overcoming the drawbacks of natural enzymes, including high cost and poor stability (Ding et al., 2019; Xu et al., 2019; Jiao et al., 2020; Liu et al., 2020; Wang et al., 2020; Wang and Wei, 2020; Zhang et al., 2020). In addition, the unique and tunable physicochemical properties of nanomaterials can not only endow nanozymes with multiple functionalities (e.g., optical or magnetic properties), but also provide vast possibilities for rational design for tailored properties (Liu et al., 2019a; Liu et al., 2019b; Jin et al., 2019). In comparison with noble or transition metal–based nanozymes, carbon-based nanozymes are attractive because of their high biocompatibility and chemical stability (Garg et al., 2015; Sun et al., 2015; Garg and Bisht, 2016; Wen et al., 2017; Zeng et al., 2017; Lu et al., 2018; Yang et al., 2020; Li et al., 2022).

Graphene quantum dots (GQDs) or 0D graphene materials, which are atomically thin and nanometer-wide planar carbon structures, are promising for a spectrum of novel applications [e.g.,

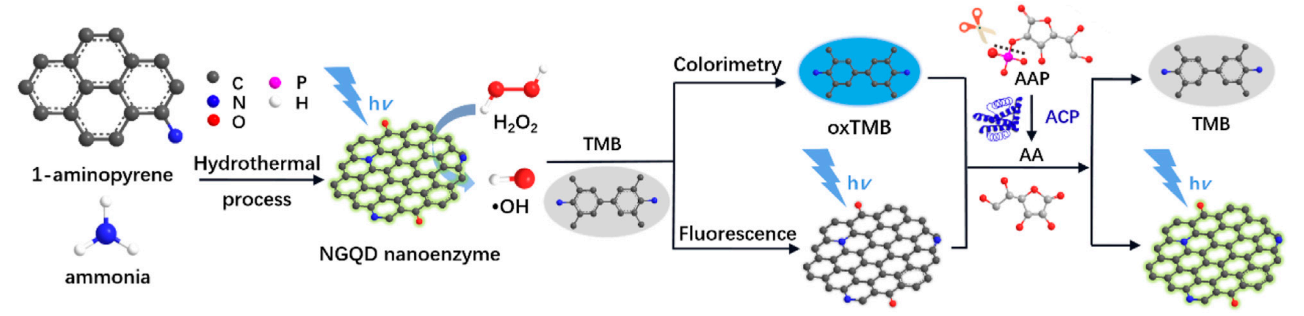

FIGURE 1 | Schematic illustration for the one-step preparation of NGQD nanozymes and the colorimetric/fluorescent dual-modality sensing of H_2O_2, AA, and ACP.

sensing (Bian et al., 2017; Shen et al., 2017; Haque et al., 2018), imaging (Chen et al., 2018; Yan et al., 2019), display (Zhao et al., 2020), anticounterfeiting (Li et al., 2018), catalysis (Li et al., 2015; Tian et al., 2018; Yan et al., 2018; Yan et al., 2020), and energy storage and conversion (Xi et al., 2019)] owing to their molecular size, quantum-confinement-induced bandgap opening, fluorescence, good dispersibility, highly tunable chemicophyscial properties, high chemical and photostability, and good biocompatibility (Wang et al., 2014; Lin et al., 2015). Studies also show that GQDs with functional groups and heteroatom dopants can exhibit nanozyme properties (Ju et al., 2016). However, the current GQD nanozymes are usually synthesized from expensive precursors (e.g., carbon nanotube) using environmentally unfriendly, time-consuming processes (e.g., oxidative cutting in hot concentrated nitric acid).

Sensitive detection of important small molecules or biomolecules using simple and low-cost assays is of great significance in health-related monitoring, diagnosis, and treatment. Hydrogen peroxide (H_2O_2) implicates in many biological processes. It is a product of various enzymatic reactions, an important signal molecule, and an indicator of oxidative stress in biological systems (Han et al., 2020). For example, any substrates of oxidoreductases (e.g., glucose, cholesterol, lactate) can be detected because the corresponding enzymatic reactions produce H_2O_2. Thus, detection of H_2O_2 provides a universal strategy for the detection of a variety of biomarkers and biological states (Wang et al., 2018). Ascorbic acid (AA) is a reducing bioactive molecule, and its antioxidant properties help to prevent cancer development, enhance immunity, and protect cholesterol from oxidative damage. Detection of AA is important because its imbalance in the body is associated with a series of diseases. For macromolecules, acid phosphatase (ACP, EC 3.1.3.2) is a phosphatase ubiquitous in the human body. Abnormally elevated ACP levels indicate prostate or kidney diseases. In comparison with the current detection methods (e.g., electrochemical detection, high-performance liquid chromatography, etc.), optical sensing based on colorimetric and fluorescence detection has the unique advantages of simple and fast operation, high sensitivity, potential of real time, and direct visual monitoring. In contrast to detection using a single readout, a sensing assay based on multisignals is attractive because it simultaneously provides more than one mode of signal output, leading to high diversity and good accuracy. Thus, exploration of a new colorimetric and fluorescence dual-mode sensing platform with simplicity in operation, high sensitivity, and efficiency for detection of small molecules or biomolecules is highly desired.

In this work, we demonstrate a colorimetric and fluorescent dual-modality platform based on a nitrogen-doped graphene quantum dot (NGQD) fluorescent nanozyme, which is able to detect a spectrum of analytes (**Figure 1**). In this platform, NGQD, that is, facile and one-step synthesized with gram-scalable production, serves as peroxidase mimics with high activity. In addition to nanozyme-catalyzed colorimetric sensing, the fluorescent property of NGQD also enable simultaneous fluorescent sensing. As the proof-of-concept demonstrations, this technique is employed to detect H_2O_2 and biomolecules (AA, ACP) with high sensitivity. In comparison with other nanozymes, the NGQD nanozyme has the advantages of simple and scalable synthesis, high activity, and potential of mass production. The dual-mode sensing based on these multifunctional nanozymes further extend the applications of carbonaceous nanozymes.

MATERIALS AND METHODS

Chemicals and Materials

3,3′, 5,5′-tetramethylbenzidine, 5,5-dimethyl-1-pyrroline-n-oxide, AA, ACP, and L-ascorbic acid-2-phosphate (AAP) were obtained from Sigma-Aldrich (United States). 1-aminopyrene, riboflavin, methionine, nitrotetrazolium chloride blue, terephthalic acid, ethylenediamine tetraacetic acid disodium salt, alanine (Ala), tryptophan (Trp), aspartate (Asp), phenylalanine (Phe), tyrosine (Tyr), threonine (Thr), leucine (Leu), glutamic (Glu), arginine (Arg), histidine (His), ethanol, and ammonia were purchased from Aladdin (China). All chemicals were of analytical grade. Ultrapure water (18.2 MΩ cm) was used to prepare aqueous solution throughout the work.

Synthesis of NGQD

Using 1-aminopyrene as the precursor and ammonia (0.4 M) as the medium, NGQDs were synthesized hydrothermally. After reaction at 200°C for 6 h, a reddish brown solution is resulted without any solid precipitation. Unreacted molecules were removed through dialysis for 2 days using a dialysis bag with cutoff molecular weight of 1000 Da. The dialysate was filtered through a microporous membrane (0.22 μm) and freeze-dried to obtain NGQD powder. Undoped GQDs were prepared using the same protocol but without adding ammonia.

Characterization

Transmission electron microscopy (TEM) images were obtained at 200 kV from a transmission electron microscope (JEM-2100; JEOL, Japan). Freshly peeled mica was used as the substrate to deposit NGQDs for atomic force microscopy (AFM) measurement. Tapping mode was employed to obtain AFM images on a Bruker Multimode 8 (Bruker, United States). X-ray photoelectron spectroscopy (XPS) was obtained with Mg Ká radiation (250 W, 14 kV) on an electron spectrometer (PHI5300; Perkin-Elmer, United States). The ultraviolet-visible (UV-Vis) absorption and fluorescence spectra were taken by a UV-Vis spectrometer (UV-2450; Shimadzu, Japan) and a fluorescence spectrometer (RF-5301PC; Shimadzu), respectively. The fluorescence emission spectrum was obtained when excited at 465 nm, and the fluorescence excitation spectrum was measured using an emission wavelength of 520 nm. The absolute photoluminescence (PL) quantum yield was determined by a fluorescence spectrometer (FL 3C-11; Hariba Scientific, United States). Electron paramagnetic resonance (EPR) spectrum was recorded on an EMX-10/12 spectrometer (Bruker, Germany).

Assays for Nanozyme Activity

The catalyzed reduction of H_2O_2 into radicals and the subsequent oxidization of 3,3′,5,5′-tetramethylbenzidine (TMB) was used to determine the peroxidase-like activity of NGQDs (Hu et al., 2018). Specifically, NGQDs (10 μg/ml) were added in the mixture of H_2O_2 (6.6 mM) and TMB (0.5 mM) dissolved in HAc-NaAc (0.1 M, pH 4). The UV-vis absorption spectrum and absorbance at 652 nm were obtained after reaction for 10 min. Terephthalic acid (TA, 0.5 mM) was applied to capture •OH radicals upon decomposition of hydrogen peroxide (50 mM) catalyzed by NGQDs (10 μg/ml). The reaction was performed at 37°C for 12 h. Then, the fluorescence spectrum was recorded with an excitation wavelength of 315 nm. For EPR measurement, HAc-NaAc buffer (0.1 M, pH 4.0) containing dimethyl pyridine N-oxide (DMPO) (20 mM) and H_2O_2 (20 mM) was applied as the supporting solution. The spectra before and after addition of NGQDs (10 μg/ml) were measured.

The possible oxidase, catalase, or superoxide dismutase (SOD)-mimicking activities of NGQDs were measured according to the literature (Chen et al., 2019a). The activity of oxidase was obtained by measuring the absorbance of TMB solution (0.5 mM in HAc-NaAc buffer, pH = 4.0) after it was directly oxidized by NGQDs (10 μg/ml). The assay of catalase-mimicking activity is based on the decrease of characteristic UV absorption of H_2O_2 (10 μM) at 240 nm after its decomposition catalyzed by NGQDs (10 μg/ml). The activity of superoxide dismutase was determined by the improved tetrazolium blue method (Chen et al., 2019a). Briefly, riboflavin was reduced under light conditions, and the reduction product produced $\bullet O_2^-$ in the presence of O_2, which could further reduce nitrotetrazolium blue (NBT) to blue methylhydrazone with characteristic absorption at 560 nm. Materials with SOD activity can eliminate $\bullet O_2^-$ and inhibit the formation of methylhydrazone. Specially, the absorbance of the mixture solution (in 0.2 M phosphate buffered saline, pH = 7.4) containing riboflavin (85 μM), NBT (1 mM), methionine (5 mM), and EDTA (2.5 mM) at 560 nm with or without NGQDs (10 μg/ml) was measured.

Detection of H_2O_2, AA, and ACP

The mixture of NGQDs (10 μg/ml) and TMB (0.5 mM) in HAc-NaAc buffer (0.1 M, pH 4) was used as the medium. To detect H_2O_2, different concentrations of H_2O_2 were introduced into the medium at 37°C for 10 min, followed by colorimetric or fluorescence detection. The reduction of oxidated TMB (oxTMB) reports the presence of AA. Specifically, oxTMB was first generated by adding H_2O_2 (6.6 mM) in the medium for 30 min reaction at 37°C. Then, different concentrations of AA were added to the oxTMB solution and incubated at 37°C for 10 min, followed by measurement of UV-vis absorption or fluorescence spectrum (excited at 465 nm). The same method was used to determine ACP, for which AA was first generated by preincubating different concentrations of ACP with L-ascorbic acid-2-phosphate (AAP, 20 μM) at 37°C for 30 min (Fan et al., 2018).

RESULTS AND DISCUSSION

Facile and Scalable Synthesis of NGQDs

A nitrogen (N) atom in the catalytic center of natural enzymes often plays a key role owing to its electron-rich nature (large electronegativity of 3.04 on the Pauling scale) and high catalytic activity toward oxygen reduction or evolution reactions (Fan et al., 2016; Pillar-Little et al., 2018). Thus, an N dopant may endow nanomaterials, such as GQDs, with enzyme-like activity. Wang et al. demonstrates a bottom-up synthesis of GQDs in alkaline solutions using 1,3,6-trinitropyrene as the precursor. However, the synthesis involves nitration of pyrene using hot HNO_3 (refluxing at 80°C for 12 h) and total removal of N through nucleophilic substitution reactions between NO_2 groups and alkaline species (e.g., OH groups) (Lin et al., 2015).

As illustrated in **Figure 1**, NGQDs were synthesized in this work through one-step, bottom-up molecular fusion in hydrothermal conditions using 1-aminopyrene as the precursor, which possesses a honeycomb carbon structure like graphene and amino groups. Ammonia solution (NH_4OH) is employed as the dopant source of nitrogen owing to its high reactivity with the defect sites of GQDs under hydrothermal conditions. To achieve gram-scale synthesis, a large-volume (500 ml; 40% actual usage for pressure safety) autoclave is used (**Figure 2A,B**), which is much larger than the commonly used reactor for GQDs (50 or 100 ml). Reddish brown powder (0.22 g) was obtained with a production yield of 55.0% after the hydrothermal treatment, purification by dialysis, and freeze-

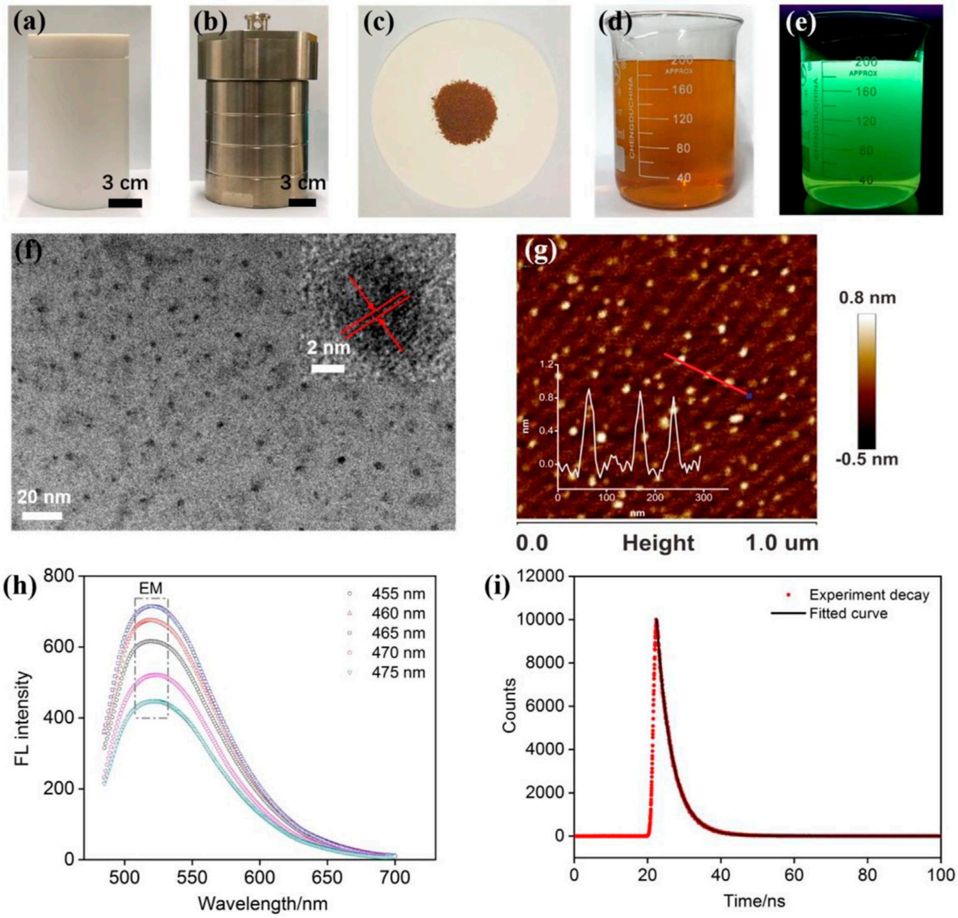

FIGURE 2 | (A,B) Photographs of internal Teflon reactor **(A)** and stainless steel housing **(B)** of an autoclave for the preparation of NGQDs. **(C)** Powder of NGQDs obtained by one-pot synthesis. **(D,E)** Photographs of NGQD solution (2 mg/ml) under visible **(D)** or 365 nm UV lights **(E)**. **(F)** TEM image. Insets are HRTEM image **(top)** and size distribution of NGQDs. **(G)** AFM image. Inset shows the height profile along the red line. **(H)** Fluorescence emission spectra obtained at different excitation wavelengths. **(I)** Fluorescence lifetime spectrum.

drying (**Figure 2C**). In comparison with the "top-down" synthesis of GQDs that relies on cutting large graphitized carbon materials (e.g., graphene sheets, carbon nanotubes, or carbon black) using different strategies (e.g., oxidative cutting by strong acids), this "bottom-up" synthesis is green, easy, and of high yield. The as-prepared NGQDs disperse well in water (2 mg/ml) and remain stable for months without precipitation (**Figure 2D**). NGQDs emit bright green fluorescence under UV irradiation (365 nm, **Figure 2E**).

Characterizations of NGQDs

As revealed by TEM (**Figure 2F**), NGQDs have narrowly distributed sizes with an average diameter of 3.0 ± 0.6 nm (103 samples). The lattice spacing of 0.28 nm can be clearly resolved in high-resolution TEM (HRTEM) images, which corresponds to the [100] facet of graphene. Their thickness is ~0.8 nm as characterized by AFM (**Figure 2G**), indicating the single-layered graphene structure. As shown in **Figure 2H**, the PL emission peaks at 520 nm are independent of excitation wavelength and reach the maximum intensity under 465 nm excitation, suggesting that NGQDs are rather homogeneous in size and surface states. The maximum emission wavelength is 465 nm (**Supplementary Figure S1** in SI). The absolute PL quantum yield of NGQDs is as high as 13.5% with a fluorescent lifetime of 4.3 ns (**Figure 2I**). The undoped GQDs that were prepared using the same protocol but without adding ammonia have an absolute PL quantum yield of 9.8%. Thus, the introduction of ammonia as a nitrogen source leads to the improved fluorescence efficiency of the obtained NGQDs. When NGQDs are continuously irradiated by UV light (365 nm, 40 W) for 3 h, the fluorescence intensity remains at 98.8% of the original intensity, indicating good stability against photobleaching. In addition, NGQDs are stored in an indoor environment for 30 days. The remaining fluorescence intensity is 99.5% of the original intensity, suggesting high long-term storage stability. Even in the presence of high concentrations of salt (NaCl, up to 0.5 M), the fluorescence intensity can still remain at 99.5% of the original intensity. Taken together, NGQDs have high stability.

XPS is used for chemical and elemental analysis of NGQDs. Three characteristic peaks corresponding to C1s, O1s, and N1s are identified in the survey spectrum, revealing the atomic

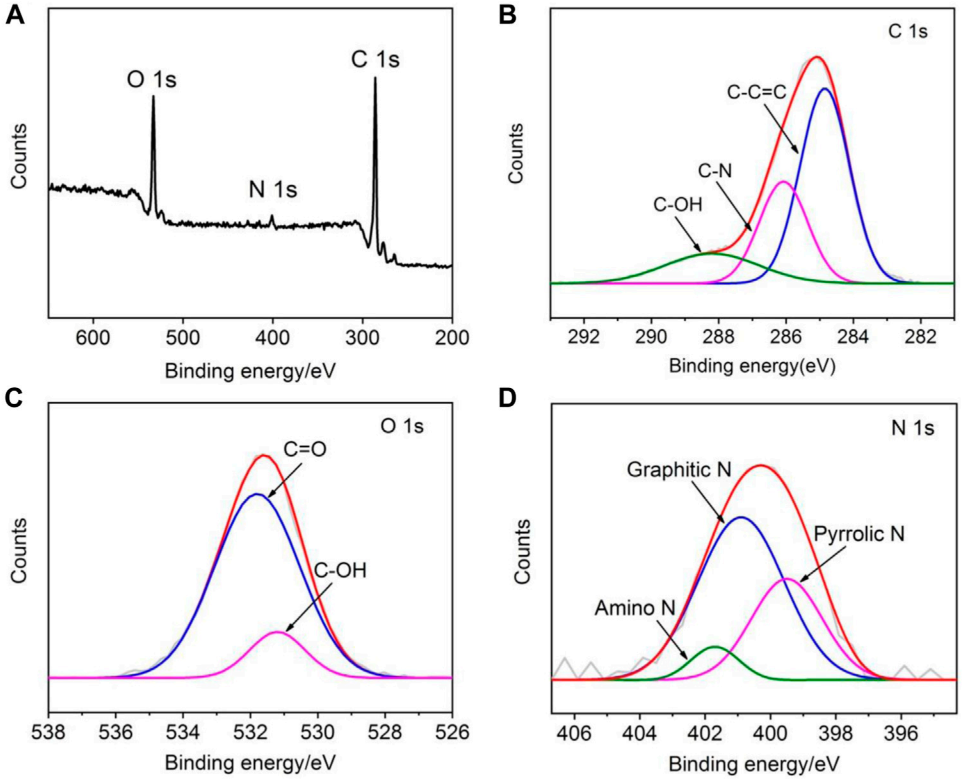

FIGURE 3 | XPS survey spectrum **(A)** and high-resolution C1s **(B)**, O1s **(C)**, and N1s **(D)** spectra of NGQDs.

concentrations of C, O, and N in NGQDs of about 76.2%, 20.6%, and 3.2%, respectively (**Figure 3A**). The peak at a binding energy of 285.9 eV in the high-resolution C1s spectrum confirms the graphitic structure (C-C=C), and the two peaks at 286.3 and 288.5 eV are, respectively, attributed to sp (Ju et al., 2016) C in C-N and C-O bonds, indicating oxygenated and N-containing groups in NGQDs (**Figure 3B**). The–OH and C=O groups are revealed in the high-resolution O1s spectrum (**Figure 3C**). The characteristic peaks of amino N, graphitic N, pyrrolic N, and pyridinc N are identified by deconvolving the high-resolution N1s spectrum, confirming that nitrogen is doped in the framework of NGQDs (**Figure 3D**) (Pillar-Little et al., 2018). Except amino N inherited from the precursor (1-aminopyrene), other N species might be produced through a reaction of NH_4OH with the defect sites of GQDs under hydrothermal conditions (Tang et al., 2014; Yang et al., 2017).

The Nanozyme Activity of NGQD and Catalytic Mechanisms

Peroxidase represents a large family of oxidoreductases that catalyze various biological oxidation reactions. Nanozymes with peroxidase-mimicking activities offer a wide range of applications [immunoassays (Zheng et al., 2013), biosensors (Cheng et al., 2019; Zhang et al., 2019), etc.]. Unlike natural enzymes, however, the catalytic activity and specificity of nanozymes are often moderate. Thus, improvement based on nanomaterials engineering is crucial. Heteroatom doping can endow nanomaterials with various new or improved chemico-physical properties. Here, we demonstrate that N-doping confers GQDs with high peroxidase activity.

The peroxidase activity of NGQDs is reported by the catalyzed reduction of H_2O_2 into radicals and subsequent oxidization of TMB into blue colored oxTMB (**Figure 1**). Based on the change of absorbance at 652 nm determined by a UV-vis spectrometer, this biocatalytic reaction can be monitored in a time-dependent manner. As shown in **Figure 4A,B**, GQDs alone cannot oxidize TMB. In comparison with the weak reaction in the mixture of H_2O_2 and TMB, the ternary system containing NGQDs, H_2O_2, and TMB gives an obvious color change, demonstrating the intrinsic peroxidase-like activity of NGQDs. In contrast, undoped GQDs that were synthesized under the same conditions but without the addition of NH_4OH only show very low peroxidase-mimicking activity (**Supplementary Figure S2** in SI). Under the same conditions, the absorbance at 652 nm of the undoped GQD system (ternary solution containing GQDs, H_2O_2, and TMB) is only about 20% of that of the NGQD system. Thus, N doping shall be responsible for the improved nanozyme activity of NGQDs. The peroxidase-mimicking activity of NGQDs was also measured when NGQDs (0.2 mg/ml) were stored at pH 4 (0.1 M HAc-NaAc) or at room temperature or with a high concentration of salt (NaCl, 0.5 M) for 7 days. The obtained three NGQDs were then applied to react with H_2O_2 and TMB. The absorbance of the mixture at 652 nm is 97.0%,

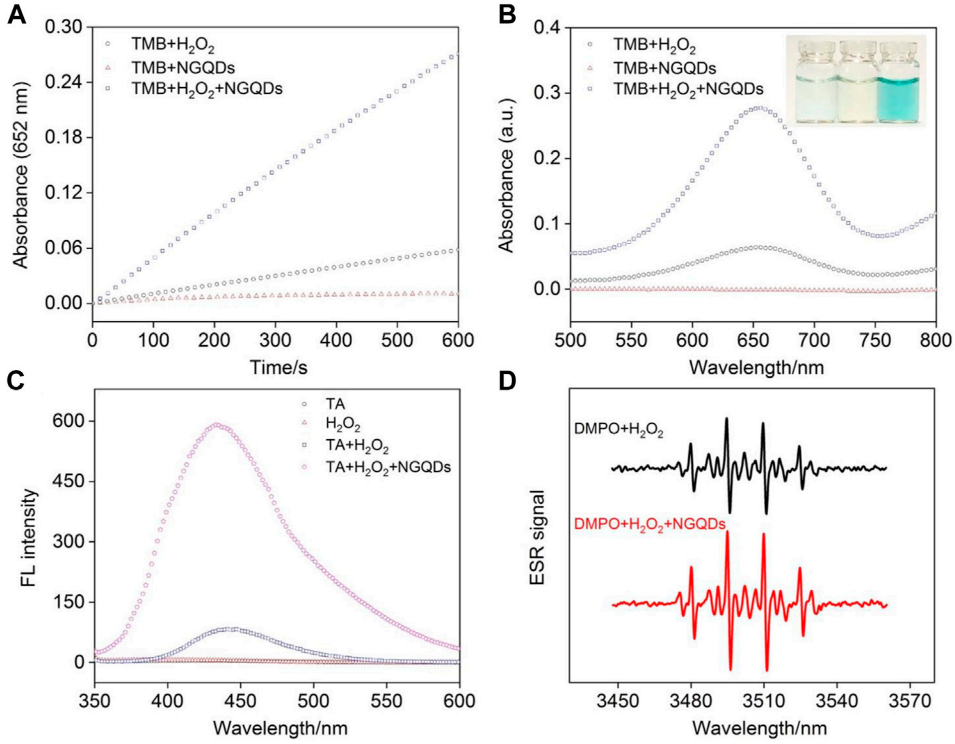

FIGURE 4 | (A) Time-dependent change of absorbance at 652 nm and **(B)** absorbance spectra of different mixture solutions of NGQDs, H_2O_2, and TMB after 10 min reaction. Inset in b are photographs of TMB solution in the presence of NGQDs **(left)**, H_2O_2 **(middle)**, and NGQDs + H_2O_2 **(left)**. **(C)** Fluorescence spectra obtained in TA, H_2O_2, TA + H_2O_2, and TA + H_2O_2+NGQDs solutions. **(D)** EPR spectra obtained in the mixture of DMPO and H_2O_2 in absence or presence of NGQDs.

99.1%, and 98.9% of that obtained using the original NGQDs, indicating negligible changes in nanozyme activity. These phenomena might be ascribed to the high stability of NGQDs. In comparison with natural bioenzymes that commonly need to be refrigerated under neutral pH, NGQD nanozymes exhibit good tolerance to harsh environments.

TA and DMPO were applied as indicators for the generated hydroxyl radical (•OH). The mixture containing TA, H_2O_2, and NGQDs exhibited high fluorescence intensity, demonstrating that •OH was produced from the catalytic reaction (**Figure 4C**). EPR spectra obtained in the presence of DMPO also confirms the production of •OH (**Figure 4D**) (Song et al., 2010). We speculate that the mechanism for the generation of •OH radicals is due to the presence of C=O groups and C/N heterostructures by N doping. The C=O groups act as the catalytic active centers, and heterostructures improve the electron transfer process, facilitating the formation of •OH radicals through cleavage of O-O bond of H_2O_2 (Sun et al., 2015).

We speculate that N dopants in NGQDs can selectively activate H_2O_2 by trapping the oxygen atoms of H_2O_2 to promote the formation of oxygen radicals, which subsequently oxidize TMB. This similarly explains the peroxidase-mimicking activity of previously reported N-doped carbon nanoparticles (Fan et al., 2018), N-doped reduced graphene oxide (rGO), or mesoporous carbon (Zheng et al., 2013). This catalytic mechanism is also consistent with that for natural enzymes, that is, the iron in the catalytic active center of heme in natural horseradish peroxidase (HRP) promotes the adsorption of O atoms on H_2O_2 (Fan et al., 2018). The possibility that NGQD may also mimic other enzymes similar to peroxidase, including oxidase (direct oxidation of TMB by NGQD), catalase (production of O_2 from NGQD-catalyzed decomposition of H_2O_2), and SOD (elimination of $•O_2^-$ by NGQD) were also investigated. As shown (**Supplementary Figure S3** in SI), NGQD exhibits negligible oxidase- and SOD-mimicking activities and very low catalase-mimicking activity, indicating that the NGQD nanozyme is highly specific to peroxidase-mimicking activity.

As with other nanozymes or natural enzymes, the peroxidase-like activity of NGQDs is also pH- and temperature-dependent (**Supplementary Figure S4** in SI). Similar to a natural peroxidase, the activity of NGQDs maximizes at pH 4, but NGQD exhibits higher thermal stability than natural enzymes. Specifically, NGQD retains 65% of its activity at 50°C compared to 42% for HRP (Sun et al., 2018). In comparison with other representative carbon-based nanozymes, NGQD exhibits higher peroxidase-like activity at a low concentration (10 μg/ml) under similar experimental conditions (Wang et al., 2011; Hu et al., 2018; Yadav et al., 2018). The high enzymatic activity is ascribed to the unique set of merits, including catalytically active N dopants, molecular size, and high dispersibility.

The Michaelis–Menten model was employed to analyze the kinetic parameters of the NGQD nanozyme (Hu et al., 2018). As

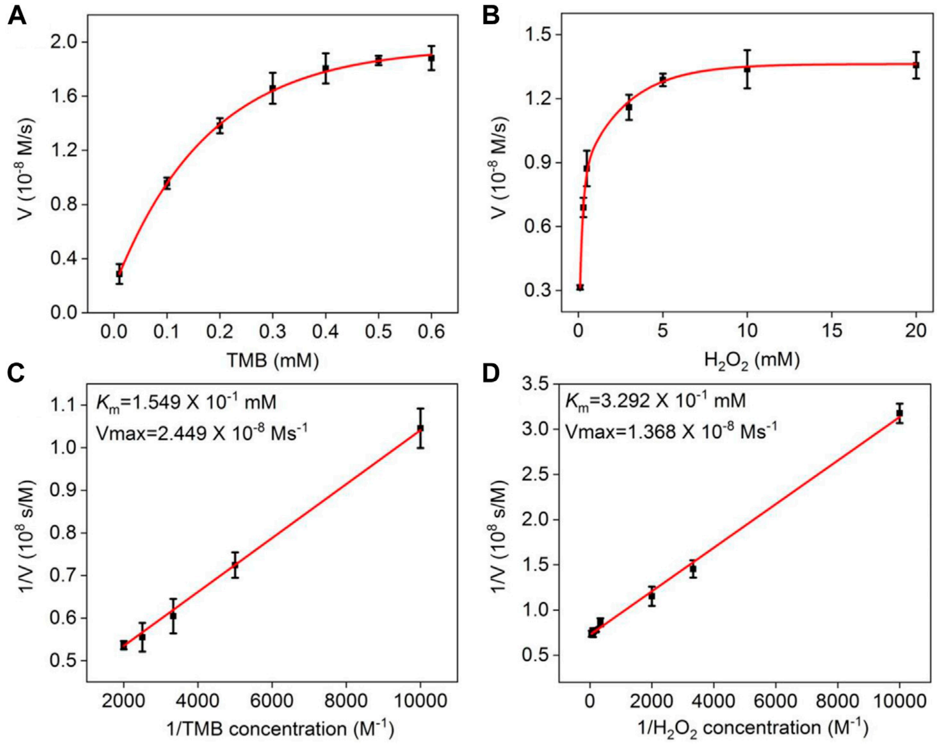

FIGURE 5 | (A,B) Steady-state kinetic assay of NGQDs, in which the reaction velocity is determined through oxidation of TMB based on absorption at 652 nm with varying concentrations of **(A)** TMB or **(B)** H_2O_2. **(C,D)** Double-reciprocal plots of NGQD activity obtained using Michaelis–Menten model at a fixed concentration of H_2O_2 (c, 6.6 mM) or TMB (d, 0.5 mM) versus various concentrations of TMB **(C)** or H_2O_2 **(D)**.

shown in **Figure 5**, the Michaelis–Menten constant (K_m) and maximum initial velocity (V_{max}) are obtained from a Lineweaver–Burk plot. The former reflects the binding affinity between the enzyme and substrate, and the latter reveals the maximum rate achieved at the saturating substrate concentration. Using TMB as the substrate, K_m and V_{max} of NGQD nanozyme are 0.1549 mM and 2.449×10^{-8} M/s, respectively (**Figure 5A,B**). The K_m value is the lowest as compared with that of natural HRP and other carbon-based nanozymes (Li et al., 2016; Bano et al., 2018; Singh et al., 2018; Sun et al., 2018; Hu et al., 2018; Chandra et al., 2019). Using H_2O_2 as the substrate, K_m and V_{max} of the NGQD nanozyme are 0.3292 mM and 1.380×10^{-8} M/s, respectively (**Figure 5C,D**). The K_m value is an order of magnitude lower than the natural enzyme and is lower than that of carboxylated graphene oxide (COOH-GO) (Wang et al., 2011), carbon nanoparticles (Wang et al., 2018), and N-doped carbon dots (N-CDs) (Bano et al., 2018). The obviously reduced K_m is attributable to the abundant N-dopants on ultrasmall GQDs, which act as the binding sites for H_2O_2.

Colorimetric and Fluorescent Detection of H_2O_2

In the presence of NGQDs and TMB, the absorbance of oxTMB at 652 nm increases with increasing concentration of H_2O_2 along with the change from colorless to blue (**Figure 6A**). Good linearity is obtained from this colorimetric detection in the concentration range of 0.1–25 μM with a limit of detection (LOD) of 60 nM at a signal-to-noise ratio (S/N) of 3 (**Figure 6B**).

Owing to the highly tunable fluorescence properties and high photostability, GQDs show great potential in fluorescence-based sensing. Here, we for the first time combine the nanozyme and fluorescence property for biosensing. As shown in **Figure 6C**, TMB does not quench the fluorescence of NGQDs. In the presence of H_2O_2, the fluorescence of NGQDs also remains unchanged despite the generation of hydroxyl radicals, whereas the fluorescence of NGQDs is significantly quenched while having both TMB and H_2O_2. Thus, the fluorescence quenching of NGQDs is caused by oxTMB. The lifetime of NGQDs in the presence of oxTMB and H_2O_2 remain the same (4.3 ns), suggesting static quenching without electron transfer (**Supplementary Figure S5** in SI) (Chen et al., 2018; Yan et al., 2019). In addition, as revealed by TEM, florescence quenching is not caused by aggregation of NGQDs (**Supplementary Figure S6** in SI). As shown in **Figure 6D**, the fluorescence spectra of NGQD and the absorption spectrum of oxTMB overlap in the wavelength range of 500–700 nm. Thus, the fluorescent emission from NGQDs can be adsorbed by oxTMB, leading to fluorescence quenching.

Taken together, it is conceivable that a sensing platform based on the fluorescence and nanozyme properties may be constructed. **Figure 6E** shows detection of H_2O_2 based on

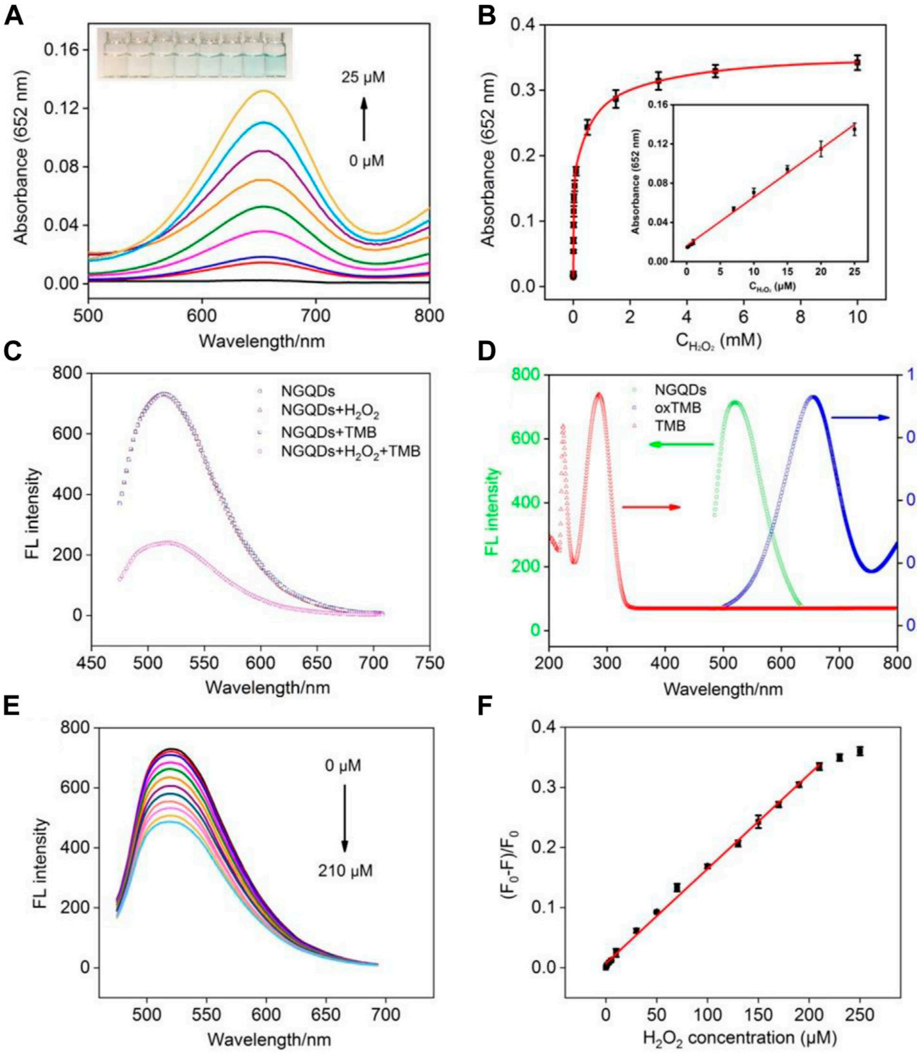

FIGURE 6 | (A) Absorbance spectra and photographs (inset) obtained from the mixture of NGQDs and TMB in the presence of different concentrations of H_2O_2. **(B)** Change in absorbance at 652 nm with the increasing H_2O_2 concentration. Inset is the linear calibration plot for colorimetric detection of H_2O_2. **(C)** The fluorescence spectra of NGQDs in the absence or presence of H_2O_2, TMB, H_2O_2, or their combination. **(D)** Fluorescence spectrum of NGQDs and absorbance spectra of TMB or oxTMB. **(E)** Fluorescence spectra of NGQDs in TMB solution containing different concentrations of H_2O_2 (0–210 μM). **(F)** The linear calibration plot for fluorescent detection of H_2O_2.

fluorescence quenching using NGQDs as both peroxidase-mimicking nanozyme and fluorescent reporters. Good linear correlation is found between the ratio of fluorescence quenching and the concentration of H_2O_2 from 0.5 to 210 μM (**Figure 6F**). The LOD is 120 nM at a S/N of 3. As demonstrated, detection of H_2O_2 can be realized using both colorimetric and fluorescent methods based on NGQDs.

Dual-Modality Detection of AA and ACP

The sensitive response of NGQDs toward H_2O_2 provides a universal strategy to detect a variety of molecules. In addition, molecules that can decrease the concentration of H_2O_2 or react with oxTMB can also be detected. When AA (50 μM) is added in the solution containing NGQDs, TMB and H_2O_2, the blue color from the produced oxTMB gradually fades away because AA reduces oxTMB back to TMB (inset in **Supplementary Figure S7** in SI). AA can be sensitively detected using both colorimetric (**Supplementary Figure S7** in SI, linear range of 10~90 μM with LOD of 4.1 μM) and fluorescence (**Supplementary Figure S8** in SI, linear range of 5~70 μM with LOD of 3.6 μM) modes. The selectivity for AA detection is investigated by testing the fluorescence quenching ratio obtained in the mixture of NGQDs and TMB in presence of uric acid (UA), dopamine (DA), different types of amino acids, or reducing agents (**Supplementary Figure S9** in SI). As seen, UA and DA that usually coexist with AA and significantly interfere with the determination of AA in electrochemical sensing have a negligible effect on AA detection. The tested amino acids other than cysteine (Cys) also have no significant interference with the detection. When Cys, glutathione (GSH), or

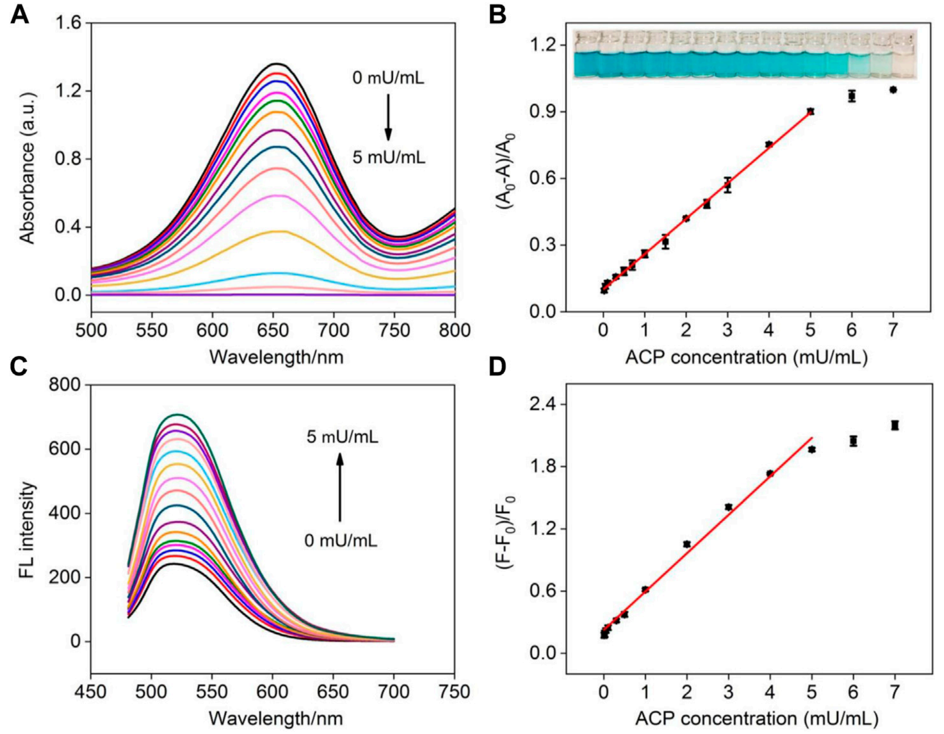

FIGURE 7 | (A) Absorbance spectra obtained in the mixture of NGQDs + H_2O_2 + TMB in the presence of different concentrations of ACP (0–5 mU/ml). **(B)** Linear calibration plot for colorimetric detection of ACP. Insets are photographs of the corresponding solutions (from low to high concentrations of ACP). **(C)** The fluorescence spectra of NGQDs obtained in the mixture of NGQDs + H_2O_2 + TMB in the presence of different concentrations of ACP (0–5 mU/ml). **(D)** The linear calibration plot for ACP detection in fluorescent detection.

homocysteine (Hcy) with reducibility are tested, reduced fluorescence of NGQDs can be found, indicating the reaction with oxTMB. However, AA results in the highest reduction of fluorescence, suggesting the highest activity. The influence of coexisting reducing substances can be eliminated by establishing a standard curve for detection using the sample matrix as the supporting medium. On the other hand, the accurate concentration of AA can also be obtained using linear extrapolation in a standard recovery method.

As illustrated in **Figure 1**, AA is the specific hydrolysis product of AAP in the present of ACP. Therefore, ACP can also be detected by the NGQD nanozyme in the presence of TMB and H_2O_2 after being incubated with AAP to produce AA. As depicted in **Figure 7A**, the blue solution colored by oxTMB gradually fades away with the increase of ACP concentration. Good linearity is obtained using colorimetric detection in the concentration range of 20~5 mU/ml with an LOD of 14 μU/ml (S/N = 3) (**Figure 7B**). Comparison between determination of ACP using different electrodes is demonstrated in **Supplementary Table S1** (SI) (Hu et al., 2016; Deng et al., 2017; Chen et al., 2019b; Lin et al., 2020; Zhang et al., 2021). The LOD is lower than that obtained from palladium square nanoplates on reduced graphene oxide (PdSP@rGO) (Chen et al., 2019b), chitosan modified platinum nanoparticles (Ch-PtNPs) (Deng et al., 2017), and acridone derivative 10-benzyl-2-amino-acridone (Zhang et al., 2021). The started concentration in the detection linear range is lower than that obtained using bathocuproinedisulfonate complex and molybdenum oxide nanoparticles (MoO_3 NPs) (Hu et al., 2016; Lin et al., 2020). For the detection using a fluorescence signal channel, a linear detection range of 10~5 mU/ml with an LOD of 4.6 μU/ml (S/N = 3) is obtained. The LOD is lower than that obtained using N-CDs, N-CDs-MnO_2 nanocomposites, or Eu^{3+}-coordination polymer (**Supplementary Table S1** in SI) (Zhu et al., 2018; Zhu et al., 2019; Li et al., 2021). To investigate the specificity of ACP detection, the detection system was, respectively, treated with ACP, bovine serum albumin, trypsin, glucose oxidase, pepsin, or lysozyme. As shown in **Supplementary Figure S10** (SI), the fluorescence signal dramatically changed in the presence of ACP, and the other enzymes or proteins exhibit negligible effects, indicating high specificity of detection.

The practicability and reliability of the developed dual-modality detection are assessed by detecting ACP in serum (diluted by a factor of 10). As shown in **Supplementary Table S2** (SI), the recoveries of colorimetric determination of ACP range from 98.9% to 106.6% and the relative standard deviation values are no more than 3.8%. For fluorescent detection (**Supplementary Table S3** in SI), satisfactory recoveries between 100.8% and 104.2% are obtained. In addition, the results obtained using colorimetric and fluorescent determination is close, indicating high accuracy of the dual-modality detection. Compared with the commonly used ACP detection methods (e.g., electrochemistry, colorimetry, fluorescence, potentiometric immunoassay, surface-enhanced Raman spectroscopy, and chromatography), our nanozyme-based detection is simple, convenient, fast, and sensitive.

CONCLUSION

In summary, we develop a colorimetric/fluorescence dual-modality sensing platform based on the NGQD nanozyme. NGQD is synthesized using a one-step, bottom-up method in aqueous solution, which is simple, green, of low-cost, and easily scalable. The obtained NGQD exhibits high peroxidase-mimicking activity as well as a bright and stable fluorescence property. Such a novel fluorescent nanozyme may be employed for various applications, such as sensing, photo-catalysis, chemical synthesis, antimicrobial agents, and flexible devices. In comparison with other nanozymes, our NGQD is synthesized by a high-yield, convenient, one-pot, scalable, and low-cost method, and it is catalytically efficient and selective. As the proof-of-concept demonstration, NGQD is utilized here for a colorimetric/fluorescence dual-modality sensing platform that can be used to sensitively detect a variety of chemicals, biomolecules, and physiological states. In comparison with other nanozymes, our NGQD possesses the advantage of convenient and low-cost synthesis and high catalytical efficiency. Owing to highly tunable chemico-physical properties through materials engineering at an atomic level, the multifunctional GQD nanozyme, therefore, allows vast opportunities for dual-mode sensing in combination with diverse nanozyme substrates.

DATA AVAILABILITY STATEMENT

The original contributions presented in the study are included in the article/**Supplementary Material**, further inquiries can be directed to the corresponding authors.

AUTHOR CONTRIBUTIONS

YW: Data curation, JZ: Data curation, XD: Data curation, JC: Writing-Reviewing and Editing, XW: Writing-Reviewing and Editing, FX: Supervision, Writing-Original draft preparation.

FUNDING

We acknowledge the financial support from the National Natural Science Foundation of China (No. 81860512), the Guangxi Natural Science Foundation (2018GXNSFAA138006), Guangxi Medical University Training Program for Distinguished Young Scholars, Guangxi medical high-level backbone talents “139” program training project, and the Fundamental Research Funds of Zhejiang Sci-Tech University ZSTU (2019Q044).

SUPPLEMENTARY MATERIAL

The Supplementary Material for this article can be found online at: https://www.frontiersin.org/articles/10.3389/fchem.2021.774486/full#supplementary-material

REFERENCES

Bano, D., Kumar, V., Singh, V. K., Chandra, S., Singh, D. K., Yadav, P. K., et al. (2018). A Facile and Simple Strategy for the Synthesis of Label Free Carbon Quantum Dots from the Latex of euphorbia Milii and its Peroxidase-Mimic Activity for the Naked Eye Detection of Glutathione in a Human Blood Serum. *ACS Sustain. Chem. Eng.* 7, 1923–1932. doi:10.1021/acssuschemeng.8b04067

Bian, S., Shen, C., Qian, Y., Liu, J., Xi, F., and Dong, X. (2017). Facile Synthesis of Sulfur-Doped Graphene Quantum Dots as Fluorescent Sensing Probes for Ag+ Ions Detection. *Sensors Actuators B: Chem.* 242, 231–237. doi:10.1016/j.snb.2016.11.044

Chandra, S., Singh, V. K., Yadav, P. K., Bano, D., Kumar, V., Pandey, V. K., et al. (2019). Mustard Seeds Derived Fluorescent Carbon Quantum Dots and Their Peroxidase-like Activity for Colorimetric Detection of H2O2 and Ascorbic Acid in a Real Sample. *Analytica Chim. Acta* 1054, 145–156. doi:10.1016/j.aca.2018.12.024

Chen, C., Liu, W., Ni, P., Jiang, Y., Zhang, C., Wang, B., et al. (2019). Engineering Two-Dimensional Pd Nanoplates with Exposed Highly Active {100} Facets toward Colorimetric Acid Phosphatase Detection. *ACS Appl. Mater. Inter.* 11, 47564–47570. doi:10.1021/acsami.9b16279

Chen, C., Liu, W., Ni, P., Jiang, Y., Zhang, C., Wang, B., et al. (2019). Engineering Two-Dimensional Pd Nanoplates with Exposed Highly Active {100} Facets toward Colorimetric Acid Phosphatase Detection. *ACS Appl. Mater. Inter.* 11 (50), 47564–47570. doi:10.1021/acsami.9b16279

Chen, W., Lv, G., Hu, W., Li, D., Chen, S., and Dai, Z. (2018). Synthesis and Applications of Graphene Quantum Dots: a Review. *Nanotechnol. Rev.* 7, 157–185. doi:10.1515/ntrev-2017-0199

Cheng, N., Li, J. C., Liu, D., Lin, Y., and Du, D. (2019). Single-Atom Nanozyme Based on Nanoengineered Fe-N-C Catalyst with Superior Peroxidase-Like Activity for Ultrasensitive Bioassays. *Small* 15, 1901485. doi:10.1002/smll.201901485

Deng, H.-H., Lin, X.-L., Liu, Y.-H., Li, K.-L., Zhuang, Q.-Q., Peng, H.-P., et al. (2017). Chitosan-stabilized Platinum Nanoparticles as Effective Oxidase Mimics for Colorimetric Detection of Acid Phosphatase. *Nanoscale* 9, 10292–10300. doi:10.1039/c7nr03399k

Ding, H., Cai, Y., Gao, L., Liang, M., Miao, B., Wu, H., et al. (2019). Exosome-like Nanozyme Vesicles for H2O2-Responsive Catalytic Photoacoustic Imaging of Xenograft Nasopharyngeal Carcinoma. *Nano Lett.* 19, 203–209. doi:10.1021/acs.nanolett.8b03709

Fan, K., Wang, H., Xi, J., Liu, Q., Meng, X., Duan, D., et al. (2016). Optimization of Fe3O4 Nanozyme Activity via Single Amino Acid Modification Mimicking an Enzyme Active Site. *Chem. Commun. (Camb)* 53, 424–427. doi:10.1039/c6cc08542c

Fan, K., Xi, J., Fan, L., Wang, P., Zhu, C., Tang, Y., et al. (2018). *In Vivo* guiding Nitrogen-Doped Carbon Nanozyme for Tumor Catalytic Therapy. *Nat. Commun.* 9, 1440–1451. doi:10.1038/s41467-018-03903-8

Gao, L., Zhuang, J., Nie, L., Zhang, J., Zhang, Y., Gu, N., et al. (2007). Intrinsic Peroxidase-like Activity of Ferromagnetic Nanoparticles. *Nat. Nanotech* 2, 577–583. doi:10.1038/nnano.2007.260

Garg, B., and Bisht, T. (2016). Carbon Nanodots as Peroxidase Nanozymes for Biosensing. *Molecules* 21, 1653–1669. doi:10.3390/molecules21121653

Garg, B., Bisht, T., and Ling, Y.-C. (2015). Graphene-based Nanomaterials as Efficient Peroxidase Mimetic Catalysts for Biosensing Applications: an Overview. *Molecules* 20, 14155–14190. doi:10.3390/molecules200814155

Han, Y., Quan, K., Chen, J., and Qiu, H. (2020). Advances and Prospects on Acid Phosphatase Biosensor. *Biosens. Bioelectron.* 170, 112671. doi:10.1016/j.bios.2020.112671

Haque, E., Kim, J., Malgras, V., Reddy, K. R., Ward, A. C., You, J., et al. (2018). Recent Advances in Graphene Quantum Dots: Synthesis, Properties, and Applications. *Small Methods* 2, 1800050. doi:10.1002/smtd.201800050

Hu, Q., Zhou, B., Li, F., Kong, J., and Zhang, X. (2016). Turn-on Colorimetric Platform for Dual Activity Detection of Acid and Alkaline Phosphatase in Human Whole Blood. *Chem. Asian J.* 11 (21), 3040–3045. doi:10.1002/asia.201601006

Hu, Y., Gao, X. J., Zhu, Y., Muhammad, F., Tan, S., Cao, W., et al. (2018). Nitrogen-doped Carbon Nanomaterials as Highly Active and Specific Peroxidase Mimics. *Chem. Mater.* 30, 6431–6439. doi:10.1021/acs.chemmater.8b02726

Jiao, L., Yan, H., Wu, Y., Gu, W., Zhu, C., Du, D., et al. (2020). When Nanozymes Meet Single-Atom Catalysis. *Angew. Chem. Int. Ed.* 59, 2565–2576. doi:10.1002/anie.201905645

Jin, S., Wu, C., Ye, Z., and Ying, Y. (2019). Designed Inorganic Nanomaterials for Intrinsic Peroxidase Mimics: a Review. *Sensors Actuators B: Chem.* 283, 18–34. doi:10.1016/j.snb.2018.10.040

Ju, E., Dong, K., Chen, Z., Liu, Z., Liu, C., Huang, Y., et al. (2016). Copper(II)-graphitic Carbon Nitride Triggered Synergy: Improved ROS Generation and Reduced Glutathione Levels for Enhanced Photodynamic Therapy. *Angew. Chem. Int. Ed.* 55, 11467–11471. doi:10.1002/anie.201605509

Li, K., Chen, J., Yan, Y., Min, Y., Li, H., Xi, F., et al. (2018). Quasi-homogeneous Carbocatalysis for One-Pot Selective Conversion of Carbohydrates to 5-hydroxymethylfurfural Using Sulfonated Graphene Quantum Dots. *Carbon* 136, 224–233. doi:10.1016/j.carbon.2018.04.087

Li, N., Than, A., Wang, X., Xu, S., Sun, L., Duan, H., et al. (2016). Ultrasensitive Profiling of Metabolites Using Tyramine-Functionalized Graphene Quantum Dots. *ACS Nano* 10, 3622–3629. doi:10.1021/acsnano.5b08103

Li, S., Fu, G., Wang, Y., Xiang, Y., Mu, S., Xu, Y., et al. (2021). A Dual-Signal Fluorescent Probe for Detection of Acid Phosphatase. *Anal. Bioanal. Chem.* 413, 3925–3932. doi:10.1007/s00216-021-03343-2

Li, X., Rui, M., Song, J., Shen, Z., and Zeng, H. (2015). Carbon and Graphene Quantum Dots for Optoelectronic and Energy Devices: a Review. *Adv. Funct. Mater.* 25, 4929–4947. doi:10.1002/adfm.201501250

Li, Z., Liu, W., Ni, P., Zhang, C., Wang, B., Duan, G., et al. (2022). Carbon Dots Confined in N-Doped Carbon as Peroxidase-like Nanozyme for Detection of Gastric Cancer Relevant D-Amino Acids. *Chem. Eng. J.* 428, 131396. doi:10.1016/j.cej.2021.131396

Lin, L., Song, X., Chen, Y., Rong, M., Zhao, T., Wang, Y., et al. (2015). Intrinsic Peroxidase-like Catalytic Activity of Nitrogen-Doped Graphene Quantum Dots and Their Application in the Colorimetric Detection of H2O2 and Glucose. *Analytica Chim. Acta* 869, 89–95. doi:10.1016/j.aca.2015.02.024

Lin, Z., Zhang, X., Liu, S., Zheng, L., Bu, Y., Deng, H., et al. (2020). Colorimetric Acid Phosphatase Sensor Based on MoO3 Nanozyme. *Analytica Chim. Acta* 1105, 162–168. doi:10.1016/j.aca.2020.01.035

Liu, X., Yan, Z., Zhang, Y., Liu, Z., Sun, Y., Ren, J., et al. (2019). Two-Dimensional Metal-Organic Framework/Enzyme Hybrid Nanocatalyst as a Benign and Self-Activated Cascade Reagent for *In Vivo* Wound Healing. *ACS Nano* 13, 5222–5230. doi:10.1021/acsnano.8b09501

Liu, Y., Wang, X., and Wei, H. (2020). Light-responsive Nanozymes for Biosensing. *Analyst* 145, 4388–4397. doi:10.1039/d0an00389a

Liu, Y., Zhou, M., Cao, W., Wang, X., Wang, Q., Li, S., et al. (2019). Light-Responsive Metal-Organic Framework as an Oxidase Mimic for Cellular Glutathione Detection. *Anal. Chem.* 91, 8170–8175. doi:10.1021/acs.analchem.9b00512

Lu, L., Zhou, L., Chen, J., Yan, F., Liu, J., Dong, X., et al. (2018). Nanochannel-confined Graphene Quantum Dots for Ultrasensitive Electrochemical Analysis of Complex Samples. *ACS Nano* 12, 12673–12681. doi:10.1021/acsnano.8b07564

Pillar-Little, T. J., Wanninayake, N., Nease, L., Heidary, D. K., Glazer, E. C., and Kim, D. Y. (2018). Superior Photodynamic Effect of Carbon Quantum Dots through Both Type I and Type II Pathways: Detailed Comparison Study of Top-Down-Synthesized and Bottom-Up-Synthesized Carbon Quantum Dots. *Carbon* 140, 616–623. doi:10.1016/j.carbon.2018.09.004

Shen, C., Ge, S., Pang, Y., Xi, F., Liu, J., Dong, X., et al. (2017). Facile and Scalable Preparation of Highly Luminescent N,S Co-doped Graphene Quantum Dots and Their Application for Parallel Detection of Multiple Metal Ions. *J. Mater. Chem. B* 5, 6593–6600. doi:10.1039/c7tb00506g

Singh, V. K., Yadav, P. K., Chandra, S., Bano, D., Talat, M., and Hasan, S. H. (2018). Peroxidase Mimetic Activity of Fluorescent NS-Carbon Quantum Dots and Their Application in Colorimetric Detection of H2O2 and Glutathione in Human Blood Serum. *J. Mater. Chem. B* 6, 5256–5268. doi:10.1039/c8tb01286e

Song, Y., Qu, K., Zhao, C., Ren, J., and Qu, X. (2010). Graphene Oxide: Intrinsic Peroxidase Catalytic Activity and its Application to Glucose Detection. *Adv. Mater.* 22, 2206–2210. doi:10.1002/adma.200903783

Sun, H., Zhao, A., Gao, N., Li, K., Ren, J., and Qu, X. (2015). Deciphering a Nanocarbon-Based Artificial Peroxidase: Chemical Identification of the Catalytically Active and Substrate-Binding Sites on Graphene Quantum Dots. *Angew. Chem. Int. Ed.* 54, 7176–7180. doi:10.1002/anie.201500626

Sun, H., Zhou, Y., Ren, J., and Qu, X. (2018). Carbon Nanozymes: Enzymatic Properties, Catalytic Mechanism, and Applications. *Angew. Chem. Int. Ed.* 57, 9224–9237. doi:10.1002/anie.201712469

Tang, L., Ji, R., Li, X., Bai, G., Liu, C. P., Hao, J., et al. (2014). Deep Ultraviolet to Near-Infrared Emission and Photoresponse in Layered N-Doped Graphene Quantum Dots. *ACS Nano* 8, 6312–6320. doi:10.1021/nn501796r

Tian, J., Chen, J., Liu, J., Tian, Q., and Chen, P. (2018). Graphene Quantum Dot Engineered Nickel-Cobalt Phosphide as Highly Efficient Bifunctional Catalyst for Overall Water Splitting. *Nano Energy* 48, 284–291. doi:10.1016/j.nanoen.2018.03.063

Wang, H., Liu, C., Liu, Z., Ren, J., and Qu, X. (2018). Specific Oxygenated Groups Enriched Graphene Quantum Dots as Highly Efficient Enzyme Mimics. *Small* 14, 1703710. doi:10.1002/smll.201703710

Wang, L., Wang, Y., Xu, T., Liao, H., Yao, C., Liu, Y., et al. (2014). Gram-scale Synthesis of Single-Crystalline Graphene Quantum Dots with superior Optical Properties. *Nat. Commun.* 5, 5357–5366. doi:10.1038/ncomms6357

Wang, X., Qu, K., Xu, B., Ren, J., and Qu, X. (2011). Multicolor Luminescent Carbon Nanoparticles: Synthesis, Supramolecular Assembly with Porphyrin, Intrinsic Peroxidase-like Catalytic Activity and Applications. *Nano Res.* 4, 908–920. doi:10.1007/s12274-011-0147-4

Wang, X., and Wei, H. (2020). Peroxidase-like Nanozyme Sensing Arrays for Versatile Analytes. *J. Nanopart. Res.* 22, 22. doi:10.1007/s11051-019-4738-4

Wang, Z., Zhang, R., Yan, X., and Fan, K. (2020). Structure and Activity of Nanozymes: Inspirations for De Novo Design of Nanozymes. *Mater. Today* 41, 81–119. doi:10.1016/j.mattod.2020.08.020

Wen, Y., Yan, L., and Ling, Y.-C. (2017). The Designing Strategies of Graphene-Based Peroxidase Mimetic Materials. *Sci. China Chem.* 61, 266–275. doi:10.1007/s11426-017-9127-y

Xi, F., Zhao, J., Shen, C., He, J., Chen, J., Yan, Y., et al. (2019). Amphiphilic Graphene Quantum Dots as a New Class of Surfactants. *Carbon* 153, 127–135. doi:10.1016/j.carbon.2019.07.014

Xu, B., Wang, H., Wang, W., Gao, L., Li, S., Pan, X., et al. (2019). A Single-Atom Nanozyme for Wound Disinfection Applications. *Angew. Chem. Int. Ed.* 58, 4911–4916. doi:10.1002/anie.201813994

Yadav, P. K., Singh, V. K., Chandra, S., Bano, D., Kumar, V., Talat, M., et al. (2018). Green Synthesis of Fluorescent Carbon Quantum Dots from Azadirachta Indica Leaves and Their Peroxidase-Mimetic Activity for the Detection of H2O2 and Ascorbic Acid in Common Fresh Fruits. *ACS Biomater. Sci. Eng.* 5, 623–632. doi:10.1021/acsbiomaterials.8b01528

Yan, X. (2020). *Nanozymology Connecting Biology and Nanotechnology*. Berlin, Germany: Springer, 1571–5744.

Yan, Y., Chen, J., Li, N., Tian, J., Li, K., Jiang, J., et al. (2018). Systematic Bandgap Engineering of Graphene Quantum Dots and Applications for Photocatalytic Water Splitting and CO2 Reduction. *ACS Nano* 12, 3523–3532. doi:10.1021/acsnano.8b00498

Yan, Y., Gong, J., Chen, J., Zeng, Z., Huang, W., Pu, K., et al. (2019). Recent Advances on Graphene Quantum Dots: from Chemistry and Physics to Applications. *Adv. Mater.* 31, 1808283. doi:10.1002/adma.201808283

Yan, Y., Zhai, D., Liu, Y., Gong, J., Chen, J., Zan, P., et al. (2020). van der Waals Heterojunction between a Bottom-Up Grown Doped Graphene Quantum Dot and Graphene for Photoelectrochemical Water Splitting. *ACS Nano* 14, 1185–1195. doi:10.1021/acsnano.9b09554

Yang, W., Huang, T., Zhao, M., Luo, F., Weng, W., Wei, Q., et al. (2017). High Peroxidase-like Activity of Iron and Nitrogen Co-doped Carbon Dots and its Application in Immunosorbent Assay. *Talanta* 164, 1–6. doi:10.1016/j.talanta.2016.10.099

Yang, Y., Zhu, D., Liu, Y., Jiang, B., Jiang, W., Yan, X., et al. (2020). Platinum-carbon-integrated Nanozymes for Enhanced Tumor Photodynamic and Photothermal Therapy. *Nanoscale* 12, 13548–13557. doi:10.1039/d0nr02800b

Zeng, Y., Miao, F., Zhao, Z., Zhu, Y., Liu, T., Chen, R., et al. (2017). Low-cost Nanocarbon-Based Peroxidases from Graphite and Carbon Fibers. *Appl. Sci.* 7, 924–935. doi:10.3390/app7090924

Zhang, J., Wu, S., Lu, X., Wu, P., and Liu, J. (2019). Lanthanide-Boosted Singlet Oxygen from Diverse Photosensitizers along with Potent Photocatalytic Oxidation. *ACS Nano* 13, 14152–14161. doi:10.1021/acsnano.9b06840

Zhang, R., Fan, K., and Yan, X. (2020). Nanozymes: Created by Learning from Nature. *Sci. China Life Sci.* 63, 1183–1200. doi:10.1007/s11427-019-1570-7

Zhang, T., He, W., Song, X., Wu, D., Xia, Y., Liu, Y., et al. (2021). A Colorimetric Sensor for Acid Phosphatase Activity Detection Based on Acridone Derivative as Visible-Light-Stimulated Oxidase Mimic. *Analytica Chim. Acta* 1155, 338357. doi:10.1016/j.aca.2021.338357

Zhao, J., Zheng, Y., Pang, Y., Chen, J., Zhang, Z., Xi, F., et al. (2020). Graphene Quantum Dots as Full-Color and Stimulus Responsive Fluorescence Ink for Information Encryption. *J. Colloid Interf. Sci.* 579, 307–314. doi:10.1016/j.jcis.2020.06.077

Zheng, A.-X., Cong, Z.-X., Wang, J.-R., Li, J., Yang, H.-H., and Chen, G.-N. (2013). Highly-efficient Peroxidase-like Catalytic Activity of Graphene Dots for Biosensing. *Biosens. Bioelectron.* 49, 519–524. doi:10.1016/j.bios.2013.05.038

Zhu, Z., Lin, X., Wu, L., Zhao, C., Li, S., Liu, A., et al. (2019). Nitrogen-doped Carbon Dots as a Ratiometric Fluorescent Probe for Determination of the Activity of Acid Phosphatase, for Inhibitor Screening, and for Intracellular Imaging. *Microchim. Acta* 186, 558. doi:10.1007/s00604-019-3600-9

Zhu, Z., Lin, X., Wu, L., Zhao, C., Zheng, Y., Liu, A., et al. (2018). "Switch-On" Fluorescent Nanosensor Based on Nitrogen-Doped Carbon Dots-MnO2 Nanocomposites for Probing the Activity of Acid Phosphatase. *Sensors Actuators B: Chem.* 274, 609–615. doi:10.1016/j.snb.2018.08.011

Conflict of Interest: The authors declare that the research was conducted in the absence of any commercial or financial relationships that could be construed as a potential conflict of interest.

frontiers in Chemistry

ORIGINAL RESEARCH
published: 22 November 2021
doi: 10.3389/fchem.2021.770512

Vertically Ordered Mesoporous Silica-Nanochannel Film-Equipped Three-Dimensional Macroporous Graphene as Sensitive Electrochemiluminescence Platform

Jiawei Gong[1†], Hongliang Tang[2†], Xuan Luo[1], Huaxu Zhou[1], Xueting Lin[3], Kailong Wang[4]*, Fei Yan[1], Fengna Xi[1] and Jiyang Liu[1]*

[1]Department of Chemistry, Key Laboratory of Surface and Interface Science of Polymer Materials of Zhejiang Province, Zhejiang Sci-Tech University, Hangzhou, China, [2]Affiliated Fangchenggang Hospital, Guangxi University of Chinese Medicine, Fangchenggang, China, [3]The First Clinical Faculty of Guangxi University of Chinese Medicine, Nanning, China, [4]The First Affiliated Hospital of Guangxi University of Chinese Medicine, Nanning, China

OPEN ACCESS

Edited by:
Huanshun Yin,
Shandong Agricultural University,
China

Reviewed by:
Yue Cao,
Nanjing University, China
Xinya Jiang,
Yangtze Normal University, China

***Correspondence:**
Kailong Wang
wangkl2010@gxtcmu.edu.cn
Jiyang Liu
liujyxx@126.com

†These authors have contributed equally to this work

Specialty section:
This article was submitted to Analytical Chemistry, a section of the journal Frontiers in Chemistry

Received: 03 September 2021
Accepted: 06 October 2021
Published: 22 November 2021

Citation:
Gong J, Tang H, Luo X, Zhou H, Lin X, Wang K, Yan F, Xi F and Liu J (2021) Vertically Ordered Mesoporous Silica-Nanochannel Film-Equipped Three-Dimensional Macroporous Graphene as Sensitive Electrochemiluminescence Platform. Front. Chem. 9:770512. doi: 10.3389/fchem.2021.770512

Three-dimensional (3D) electrochemiluminescence (ECL) platform with high sensitivity and good anti-fouling is highly desirable for direct and sensitive analysis of complex samples. Herein, a novel ECL-sensing platform is demonstrated based on the equipment of vertically ordered mesoporous silica-nanochannel films (VMSF) on monolithic and macroporous 3D graphene (3DG). Through electrografting of 3-aminopropyltriethoxysilane (APTES) onto 3DG as molecular glue, VMSF grown by electrochemically assisted self-assembly (EASA) method fully covers 3DG surface and displays high stability. The developed VMSF/APTES/3DG sensor exhibits highly sensitized ECL response of tris(2,2′-bipyridyl) ruthenium (Ru(bpy)$_3^{2+}$) taking advantages of the unique characteristics of 3DG (high active area and conductivity) and VMSF nanochannels (strong electrostatic enrichment). The VMSF/APTES/3DG sensor is applied to sensitively detect an important environmental pollutant (4-chlorophenol, with limit of detection or LOD of 30.3 nM) in term of its quenching effect (ECL signal-off mode) toward ECL of Ru (bpy)$_3^{2+}$/tri-n-propylamine (TPrA). The VMSF/APTES/3DG sensor can also sensitively detect the most effective antihistamines chlorpheniramine (with LOD of 430 nM) using ECL signal-on mode because it acts as co-reactant to promote the ECL of Ru (bpy)$_3^{2+}$. Combined with the excellent antifouling ability of VMSF, the sensor can also realize the analysis of actual environmental (lake water) and pharmaceutical (pharmacy tablet) samples. The proposed 3D ECL sensor may open new avenues to develop highly sensitive ECL-sensing platform.

Keywords: three-dimensional graphene, electrochemiluminescence sensor, vertically ordered mesoporous silica-nanochannel film, 4-chlorophenol, chlorpheniramine

INTRODUCTION

Solid-state nanofilms have recently been widely used in the fields of molecular sieves, energy conversion, nanofluidics, and biosensing owing to their adjustable nanopores, intelligent control of molecular transport, and high device integration capabilities (Huang et al., 2016; Dong et al., 2020; Garbayo et al., 2021). The vertically ordered mesoporous silica-nanochannel thin film (VMSF) has attracted extensive attentions because of its unique characteristics (Nasir et al., 2016; Chen et al., 2019; Ullah et al., 2020; Wang et al., 2020). In general, VMSF has well-ordered (regular hexagonal packing) and vertically aligned nanochannel arrays with uniform diameter (usually 2–3 nm), high density (more than 10^{12} pores/cm^2), and adjustable thickness (usually 50–200 nm) (Yan et al., 2016; Wang et al., 2017; Ding et al., 2020a; Zhou et al., 2020a; Ding et al., 2020b; Ullah et al., 2021). In addition to the high specific surface area, chemical and mechanical stability of mesoporous materials, VMSF also exhibits high selectivity for molecular size and charge. On the one hand, derived from its silanol groups (pK_a ~ 2), VMSF usually has an anionic nature under normal pH conditions. This charge characteristic accelerates the transfer of positively charged molecules to the electrode surface, thereby improving the detection sensitivity. In addition, VMSF shows good anti-fouling ability because the ultrasmall nanochannels can effectively inhibit the interference of co-existing large substances (e.g., proteins), leading to good signal stability in analysis of complex samples (e.g., whole blood, biological fluids, environmental, or food samples) (Yan and Su, 2016; Zhou et al., 2018; Duan et al., 2021; Gamero-Quijano et al., 2021). Thus, electrode equipped with VMSF shows great potential in direct and sensitive detection of complex samples owing to significant anti-fouling and signal amplification abilities of VMSF.

Electroluminescence (ECL) is the luminescence caused by the electron transfer of reactants at an electrode surface under the excitation of electrochemistry (Cheng et al., 2020; Gu et al., 2020; Ma et al., 2020). Compared with luminescence technologies such as fluorescence and chemiluminescence, ECL does not need excitation light and, therefore, has the advantages of low background and high signal-to-noise ratio. At the same time, the luminescence reaction of ECL is strictly controlled by electrochemical excitation and occurs in the diffusion layer adjacent to the electrode surface, leading to controllable reaction and high sensitivity. Up to now, ECL has become a powerful tool for immunoassay, DNA or cell analysis, environmental analysis, etc. (Liu et al., 2015; Li et al., 2017; Zhang et al., 2019). Among a large number of organic or inorganic ECL luminophores, tris(2,2′-bipyridine) ruthenium (Ru $(bpy)_3^{2+}$) is the most extensively used in scientific research and commercial applications because of its good chemical stability, high electrochemiluminescence quantum yield, and water solubility (Ding et al., 2020b; Duan et al., 2021). Owing to the strong electrostatic attraction and accelerated mass transfer of the negatively charged VMSF nanochannel arrays to positively charged Ru $(bpy)_3^{2+}$, VMSF-modified electrodes promise great potential in highly sensitive ECL detection.

Until now, most VMSF-based sensors are mainly using indium tin oxide (ITO) as the supporting electrodes, essentially because the hydroxyl groups on ITO surface ensure good mechanical stability of VMSF through the formation of Si–O covalent bond between VMSF and the electrode surface. For carbon or gold electrodes that have poor adhesion with VMSF, organosilane or specific nanomaterials are needed as molecular glue or adhesive layer to pre-modify the electrode surface to improve the stability of VMSF. For instance, the Walcarius group proposed to improve the adhesion of VMSF on glassy carbon electrode by electrografting 3-aminopropyltriethoxysilane (APTES) on the electrode (Nasir et al., 2016). They also assembled 3-mercaptopropyl (trimethoxysilane) on gold electrode as a molecular glue to grow stable VMSF (Ullah et al., 2020). Our group demonstrated the use of reduced graphene oxide (rGO) sheets as conductive adhesive and electroactive layer for growing stable VMSF on GCE (Xi et al., 2019). In addition to electrode materials, electrode structure is also critical to the performance of electroanalysis. Compared with the traditional 2D planar electrode, three-dimensional (3D) porous electrode has high surface area and excellent diffusion/mass transfer, which can effectively improve the detection sensitivity (Huang et al., 2020; Beluomini et al., 2021; He et al., 2021). Up to now, however, a stable equipment of VMSF on 3D porous electrode for the development of highly sensitive ECL sensor has not been reported.

In this work, we present a novel 3D ECL sensing platform based on the equipment of VMSF on porous 3D graphene foam electrode (3DG). The 3DG is grown by chemical vapor deposition (CVD) using Ni foam as template and, therefore, has monolithic and macroporous structure. Through the electrografting of APTES onto the surface of 3DG as molecular glue, stable VMSF is conveniently grown on the 3D electrode using electrochemically assisted self-assembly (EASA) method (**Figure 1**). The feasibility and universality of the ECL sensor (VMSF/APTES/3DG) is validated by the detection of an important environmental pollutant (4-chlorophenol) and a common antihistamine drug (chlorpheniramine) as the proof-of-concept demonstrations. A signal-off ECL mode is developed to detect 4-chlorophenol based on its quenching effect on the ECL system of Ru $(bpy)_3^{2+}$/TPrA. On the contrary, the chlorpheniramine can act as a co-reactant to enhance the ECL of Ru $(bpy)_3^{2+}$, so it can be detected in a signal-on ECL mode. Owing to the good conductivity and high active surface of 3DG, and the significant enrichment effect of VMSF nanochannels on the ECL probe of Ru $(bpy)_3^{2+}$, VMSF/APTES/3DG sensor exhibits high sensitivity and low detection limits. Thanks to the excellent anti-fouling ability of VMSF, VMSF/APTES/3DG sensors that worked well in the analysis of real environmental or pharmaceutical samples.

MATERIALS AND METHODS

Chemicals and Materials

Tetraethoxysilane (TEOS), tris(2,2-bipyridyl) dichlororuthenium (II) hexahydrate (Ru $(bpy)_3Cl_2$ $6H_2O$), cetyltrimethylammonium bromide (CTAB), and hexaammineruthenium (III) chloride ($Ru(NH_3)_6Cl_3$) were purchased from Sigma-Aldrich (USA). Tripropylamine (TPrA), 4-chlorophenol (4-CP), potassium ferricyanide ($_{K3}$ [$Fe(CN)_6$]), (3-aminopropyl) trimethoxysilane (APTES), tetrabutylammonium tetrafluoroborate ($Bu_4N^+BF_4^-$), and acetonitrile were obtained from Aladdin (China). Lake water sample was obtained from the campus lake of Zhejiang Sci-Tech University (Hangzhou, China). Chlorphenamine maleate tablets

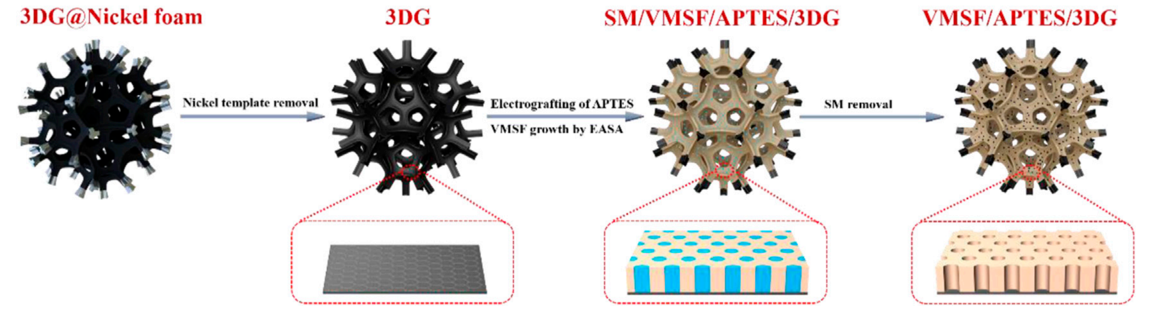

FIGURE 1 | Schematic illustration for the preparation of vertically ordered mesoporous silica-nanochannel films (VMSFs)/(3-aminopropyl) trimethoxysilane (APTES)/ three-dimensional grapheme (3DG).

were purchased from Tianjin Lisheng Pharmaceutical Co., Ltd (China). All other chemicals were of analytical grade. Ultrapure water (18.2 MΩ cm) was used throughout the work.

Preparation of Three-Dimensional Graphene Electrode

As previously reported (Xi et al., 2013), 3DG was synthesized by CVD using nickel foam as the template and ethanol as the precursor. Subsequently, the nickel substrate was etched away with 3 M HCl solution overnight at 80°C to obtain the free-standing 3DG. To prepare electrode, 3DG (3 × 8 mm, 1-mm thick) was fixed onto a glass slide. Electrode wire was made by connection copper wire and 3DG by silver glue. Then, copper wire and silver glue were insulated with silicone rubber.

Fabrication of Vertically Ordered Mesoporous Silica-Nanochannel Films /(3-Aminopropyl) Trimethoxysilane /3D Grapheme Sensor

The fabrication of VMSF/APTES/3DG sensor included three steps. First, APTES is electrografted onto the surface of 3DG as a molecular glue to improve the mechanical stability of VMSF according to a published procedure (Nasir et al., 2016). Briefly, 3DG electrode was placed in an acetonitrile solution containing APTES (1.0 mM) and tetrabutylammonium tetrafluoroborate ($Bu_4N^+BF_4^-$, 0.1 M). The electrografting of APTES was achieved through electrochemical oxidation of aliphatic amines by 5-circle scan using cyclic voltammetry (CV, scan rate was 100 mV/s, potential range was 0.7–2.0 V). The obtained APTES/3DG was then thoroughly rinsed with acetone. Second, EASA method was used to prepare surfactant-containing VMSF/APTES/3DG using surfactant micelles (SM) as a template (Nasir et al., 2016). Typically, $NaNO_3$ solution (0.1 M, pH = 2.6) and ethanol was mixed at a ratio of 1:1 (v/v) before CTAB (32 mM) and TEOS (100 mM) were added. The resulting precursor solution was pre-hydrolyzed under stirring at room temperature for 2.5 h. Then, the APTES/3DG was immersed in the above electrodeposition medium and a current density of −0.74 mA/cm^2 was applied for 10 s for the growth of VMSF. The resulting electrode was quickly taken out followed with thorough rinse with water and drying with N_2 stream, respectively. After being aged at 80°C overnight to cross-link the silica network, VSMF modified electrode with SM in nanochannels was obtained and designated as SMs@VMSF/APTES/3DG. Finally, SM was removed by incubating the electrode in a mixture of HCl (0.1 M) and ethanol solution (1/1, v/v) under stirring for 5 min, leading to the final VMSF/APTES/3DG electrode with open nanochannels. For comparison, VMSF modified GCE electrode (VMSF/APTES/GCE) was prepared using the same procedure with GCE as the supporting electrode.

Measurements and Instrumentations

Transmission electron microscopy (TEM) images were obtained on copper grid at 100 kV using a HT7700 microscope (Hitachi, Japan). The morphology of the bare or modified 3D electrodes and the chemical composition at the sample surface were characterized by field emission scanning electron microscopy (SEM, HT7700, Hitachi, Japan) equipped with an energy dispersive spectrometer (EDS, Bruker Nano Xflash610-H, Germany). Electrochemical measurements were carried out on an Autolab PGSTAT302N potentiostat (Metrohm, Switzerland). A conventional three-electrode system was adopted. Briefly, bare or modified 3DG or GCE was the working electrode. Ag/AgCl electrode (saturated with KCl) was used as the reference electrode and Pt sheet (1 × 1 cm) was the counter electrode. ECL intensity measurements were performed on the MPI-E ECL analytical system (Remex Analysis Instrument, Xi'an, China). The photomultiplier tube (PMT) biased at 600 V.

Electroluminescence Determination of 4-Chlorophenol

To detect 4-chlorophenol, phosphate buffered saline (PBS, 0.01 M, pH 7.4) containing Ru $(bpy)_3^{2+}$ (10 μM) and TPrA (3 mM) was used as the supporting solution. After different concentrations of 4-chlorophenol was added, the VMSF/APTES/3DG electrode was scanned using CV method (potential range: 0–1.5 V, scan rate: 100 mV/s). The corresponding ECL signal generated during CV scan was recorded. For real sample analysis, the standard addition method was used to evaluate the reliability of the developed ECL sensor. The lake water was filtered using Nylon

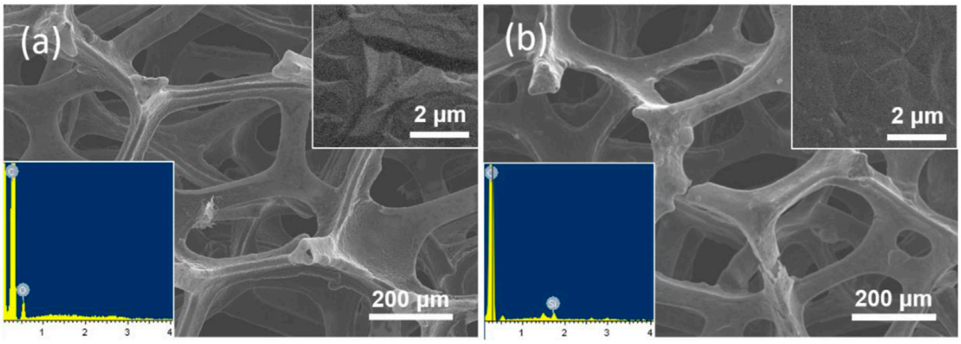

FIGURE 2 | SEM images of **(A)** bare 3DG and **(B)** VMSF/APTES/3DG at different magnifications. Inset in (a) and (b) is the corresponding energy dispersive spectrometer (EDS) spectrum.

microfiltration membrane (0.22 μm) and then diluted by a factor of 20 with PBS (0.01 M, pH 7.4). ECL detection was carried out after adding a certain amount of 4-chlorophenol.

Electroluminescence Determination of Chlorpheniramine

For the detection of chlorpheniramine, PBS (0.01 M, pH 7.4) containing10 μM $Ru (bpy)_3^{2+}$ was applied as the medium. After different concentrations of chlorpheniramine were added, ECL signal of the solution was measured under CV scanning (potential range: 0–1.5 V, scan rate: 100 mV/s). To analyze chlorpheniramine in pharmacy tablets, the tablets were grinded and dissolved in PBS (0.01 M, pH 7.4). The resulting solution was centrifuged at 7,000 rpm for 5 min to remove insoluble starch and the supernatant was analyzed using VMSF/APTES/3DG sensor.

RESULTS AND DISCUSSION

Convenient Equipment of Vertically Ordered Mesoporous Silica-Nanochemical Films on Three-Dimensional Grapheme Electrode

In present work, the equipment of VMSF on 3D electrode is first demonstrated. The 3D monolithic graphene foam (3DG) served as the supporting electrode. **Figure 1** illustrates the convenient growth of VMSF after electrografting APTES on 3DG. **Figure 2A** shows SEM images of 3DG grown by CVD under different magnifications. As shown, bare 3DG presents a monolithic structure with well-defined macropores. The surface of the graphene skeleton is smooth, and the wrinkled structure of graphene can be obviously observed. The energy dispersive spectrometer (EDS) characterization shows high content of C atoms (inset in **Figure 2A**, the O signals result from oxygen in macropores of 3DG). Compared with other porous 3D graphene assembled from rGO sheets, 3DG has interconnected skeleton comprised of defect-free graphene, allowing rapid charge and mass transfer. In addition to the high conductivity of CVD-grown graphene, 3DG electrode also exhibits large active area and unhindered substance diffusion in comparison with 2D planar electrodes (Li et al., 2019). However, the high hydrophobicity of graphene foam brings difficulties to its functionalization and application.

After the direct growth of VMSF on 3DG, the resulted VMSF/3DG electrode presents uneven white areas visible to the naked eye, indicating that the electrode surface was not completely covered by VMSF. This was attributed to the poor wettability of 3DG in film forming solutions caused by its high hydrophobicity during the film growth process. In addition, the white areas disappeared after rinsing with water, suggesting the poor adhesion of VMSF to the unmodified 3DG substrate. Thus, electrografting APTES on the surface of 3DG as hydrophilic molecular glue is used to overcome these two problems. On the one hand, the electrografting medium contains organic solvent acetonitrile, which can ensure the spread of the solution on the surface of 3DG. On the other hand, APTES could be electrografted to carbon surface by forming C-N covalent bond through oxidizing its amine groups. At the same time, three silane groups of APTES are able to anchor VMSF (Nasir et al., 2016; Nasir et al., 2018; Jiokeng et al., 2019; Nasir et al., 2019; Zhou et al., 2020b; Nasir et al., 2020). Therefore, APTES can function as an effective molecular glue to improve the adhesion of VMSF to the surface of 3DG.

VMSF can be quickly and conveniently deposited onto APTES/3DG electrode by electrochemically assisted self-assembly (EASA) method. Through applying a cathode potential to the APTES/3DG electrode, the reduction of protons on the electrode causes a local increase in the pH value adjacent to the electrode surface. The generated hydroxyl ions (OH^-) at the electrode/solution interface could serve as catalysts to induce the condensation of TEOS around SM by self-assembly, leading to concomitant growth of VMSF on the electrode.

SEM images of VMSF/APTES/3DG electrode at different magnification are shown in **Figure 2B**. As revealed, the morphology of 3DG hardly changed after modification with APTES owing to the characteristic of molecular glue. After VMSF was subsequently equipped, there was still no significant change in morphology of 3DG because of the

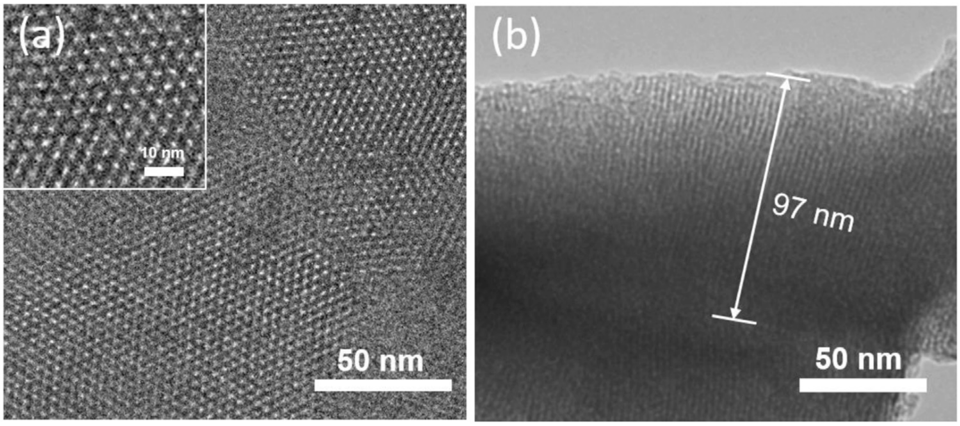

FIGURE 3 | (A) Top view of transmission electron microscopy (TEM) images of VMSF. **(B)** Cross-section view of TEM image of VMSF. Inset in (a) shows the magnified view.

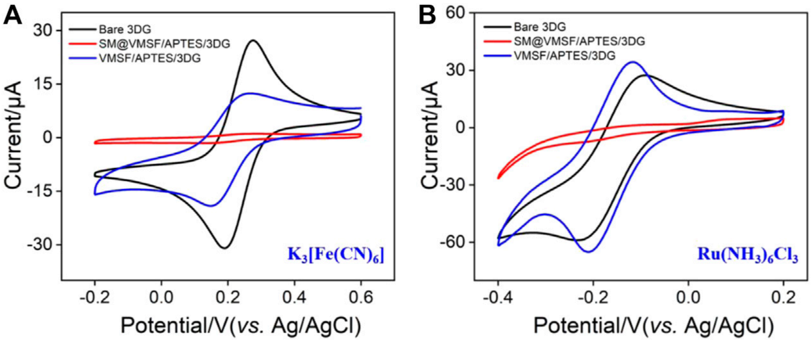

FIGURE 4 | CV curves obtained at bare 3DG, SM@VMSF/APTES/3DG, and VMSF/APTES/3DG in 0.05 M KHP solution containing 0.5 mM K_3 [Fe(CN)$_6$] **(A)** and 0.5 mM hexaammineruthenium III chloride (Ru(NH$_3$)$_6$Cl$_{3)}$ **(B)**. The scan rate was 50 mV s^{-1}.

nanofilm structure. However, EDS characterization shows that Si groups appear on the surface of VMSF/APTES/3DG electrode, indicating the effective combination of VMSF (inset in **Figure 2B**).

Characterization of Vertically Ordered Mesoporous Silica-Nanochannel Film and Vertically Ordered Mesoporous Silica-Nanochannel Film/(3-Aminopropyl) Trimethoxysilane/Three-Dimensional Graphene Electrode

The structure and morphology of the prepared VMSF were characterized by TEM. **Figure 3** shows TEM images of VMSF detached from APTES/3DG electrode. The top view (**Figure 3A**) reveals the hexagonal compact arrangement of mesopores with an aperture of approximately 2.2 nm (inset in **Figure 3A**). In addition, the film is uniform over a wide area. The cross section (**Figure 3B**) demonstrates the mesopore nanochannels possess long-range ordered structure with an average length of around 97 nm.

The integrity, permeability, and charge permselectivity of VMSF/APTES/3DG were investigated by cyclic voltammetry (CV). For comparison, bare 3DG and SM@3DG/APTES/3DG were also examined. **Figure 4** shows the CV curves of standard redox probes including anionic Fe(CN)$_6^{3-}$ and Ru(NH$_3$)$_6^{3+}$ at the three types of electrodes. Bare 3DG exhibits well-defined redox peaks owing to the high conductivity of graphene. Due to the presence of templated SM inside the nanochannels of VMSF, the SM@VMSF/APTES/3DG electrode shows almost no electrochemical responses toward the two redox molecules, indicating that the SM inside the nanochannels prevents the charged probes from contacting the substrate electrode. This phenomenon also proves the good adhesion and full coverage of VMSF on the APTES/3DG electrode without cracks. In contrast, SM@VMSF/3DG electrode that was prepared without APTES displayed an obvious redox peak, proving low adhesion of VMSF on 3DG (**Supplementary Figure S1** in **Supplementary material**). After removal of the SM template from the nanochannels, the obtained VMSF/APTES/3DG electrode exhibits definite electrochemical signals, indicating the efficient diffusion of the redox probes through the

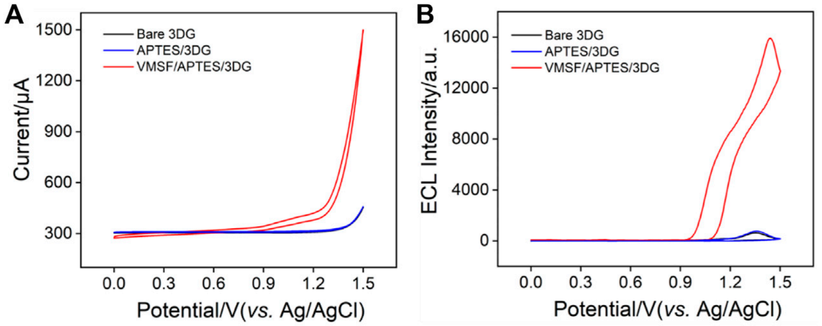

FIGURE 5 | (A) CV or **(B)** electroluminescence (ECL) curves obtained at bare 3DG, APTES/3DG, and VMSF/APTES/3DG in phosphate buffered saline (PBS) (0.01 M, pH 7.4) containing tris(2,2′-bipyridine) ruthenium (Ru $(bpy)_3^{2+)}$ (10 μM) and tripropylamine (TPrA) (3 mM). The scan rate was 100 mV s^{-1}.

nanochannels and the electron transfer with the supporting electrode.

Owing to the negatively charged nanochannels (the pK_a of silica is ~2), VMSF exhibits strong effect on the mass transfer of the charged molecules through electrostatic interactions. On the one hand, the signal of $Fe(CN)_6^{3-}$ at VMSF/APTES/3DG is lower than that at bare 3DG due to the electrostatic repelling of VMSF nanochannels. In case of $Ru(NH_3)_6^{3+}$, on the other hand, the response on VMSF/APTES/3DG is even higher than that on bare 3DG, suggesting that negatively charged VMSF is quite beneficial to enrich the positive probes.

Enhanced Electrochemiluminescence of tris(2,2'-Bipyridine Ruthenium by Vertically Ordered Mesoporous Silica-Nanochannel Film

Owing to the negatively charged nanochannels surface, VMSF can significantly enrich positively charged species and facilitate their mass transport *via* strong electrostatic interactions (Zhou et al., 2015; Liu et al., 2016; Guo et al., 2016; Xiao et al., 2017). Thus, the enhanced electrochemiluminescence (ECL) of Ru $(bpy)_3^{2+}$ on VMSF/APTES/3DG during CV scan was investigated using TPrA as the co-reactant. For comparison, the ECL signals on bare 3DG or APTES/3DG were also measured. As shown in **Figure 5**, 3DG and APTES/3DG exhibit very close CV and ECL signals, indicating that APTES modification did not significantly change the electrode performance of 3DG. In addition to modifying 3DG with APTES to improve its hydrophilicity and promote VMSF adhesion, we also tried to treat 3DG with oxygen plasma to achieve the same purpose. The obtained electrode is designated as pl-3DG. As known, oxygen plasma treatment of carbon materials can introduce oxygen-containing groups (e.g., −OH groups) and improve their hydrophilicity. The generated oxygen-containing groups are also conducive to the stable adhesion with VMSF. However, we found that the ECL signal of pl-3DG was 50% lower than that of bare 3DG due to the quench effect of the surface oxygen-containing groups on the excited luminophore Ru $(bpy)_3^{2+*}$ (Zu and Bard, 2000; Qin et al., 2020). Thus, modification of 3DG with APTES is quite suitable to integrate VMSF for further construction of the 3D ECL sensor.

In the case of VMSF/APTES/3DG, a remarkable anodic current wave is revealed at potentials more positive than 0.9 V (**Figure 5A**). At the same time, the corresponding ECL signal is significantly enhanced (**Figure 5B**). The ECL intensity is about 25 times higher than that of bare 3DG. The remarkably sensitized ECL signal is attributed to the strong enrichment effect by the negatively charged nanochannel of VMSF on the cationic Ru $(bpy)_3^{2+}$. To further confirm the sensitization effect of VMSF matrix on the ECL signal of Ru $(bpy)_3^{2+}$, we used the same method to modify the traditional 2D planar electrode, glassy carbon electrode (GCE). Compared with bare GCE, the obtained VMSF/APTES/GCE shows a remarkably improved ECL signal, confirming the universality of VMSF-sensitized ECL signal (**Supplementary Figure S2** in **Supplementary material**). In addition, VMSF/APTES/3DG shows a significantly higher ECL signal than VMSF/APTES/GCE, indicating that 3DG electrode with larger active electrode area can effectively enhance ECL signal. Thus, a high ECL signal can be obtained at a low Ru $(bpy)_3^{2+}$ concentration (10 μM). This can significantly reduce the cost of ECL analysis because Ru $(bpy)_3^{2+}$ is expensive. In addition, VMSF/APTES/3DG has great potential in the fabrication of ECL platform with high sensitivity.

The Stability, Reproducibility and Anti-Fouling Abilities of Vertically Ordered Mesoporous Silica-Nanochannel Film/(3-Aminopropyl) Trimethoxysilane/Three-Dimensional Graphene Electrode

To evaluate the ECL stability, time-dependent ECL signals of VMSF/APTES/3DG electrode in Ru $(bpy)_3^{2+}$/TPrA solution during successive CV scans were investigated. As shown in **Supplementary Figure S3** (**Supplementary material**), a relative standard deviation (RSD) of 1.6% was observed for 11th measurements, indicating high ECL stability. The reproducibility of the electrode was studied by preparing five electrodes in parallel under the same conditions. The RSD of the ECL signal was 2.5%, confirming high reproducibility. After the three VMSF/APTES/3DG electrodes were stored in the refrigerator (4°C) for 2 weeks, the RSD of 2.7% was observed. Thus, VMSF/APTES/3DG electrode has good operational stability and reproducibility.

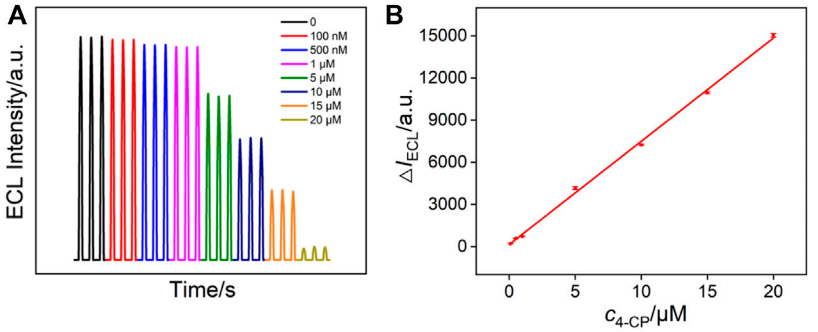

FIGURE 6 | (A) ECL intensity of Ru $(bpy)_3^{2+}$/TPrA system in the presence of different concentrations of 4-chlorophenol. **(B)** The linear dependence between the reduced ECL intensity (ΔI_{ECL}) and the concentration of 4-chlorophenol.

The anti-fouling ability of the electrode is very important because electrode fouling leads to low accuracy and sensitivity. To evaluate the anti-fouling ability of VMSF/APTES/3DG, starch and humic acid, that are abundant in medical tablets or environmental water sample, are chosen as the investigated matrices. The ECL intensity of Ru $(bpy)_3^{2+}$/TPrA at VMSF/APTES/3DG in the presence of starch or humic acid was compared with that at bare 3DG electrode (**Supplementary Figure S4** in **Supplementary material**). As shown, the ECL intensity on bare 3DG electrode is significantly reduced in the presence of starch or humic acid. On the contrary, no remarkable change in ECL intensity is observed for VMSF/APTES/3DG, indicating high anti-fouling ability.

Electrochemiluminescence Determination of 4-Chlorophenol Using Signal-off Mode

Through monitoring the quenching effects of analytes on the ECL system, ECL signal-off detection mode can be realized. As a proof-of-concept demonstration, ECL generated by the ECL system of Ru $(bpy)_3^{2+}$/TPrA on VMSF/APTES/3DG was employed to detect 4-chlorophenol (4-CP) in term of its quenching effect (Li et al., 2015; Qi et al., 2017). Generally, 4-chlorophenol is released into the environment as a by-product of paper bleaching, drinking water disinfection, petroleum industry, and other industries, causing serious pollution in aquatic and terrestrial ecosystems. As 4-chlorophenol itself is relatively stable to photodegradation, so its environmental residence time is relatively long. Therefore, both the US Environmental Protection Agency (EPA) and the European Union (EU) have marked 4-chlorophenol as a priority pollutant. Therefore, sensitive detection of 4-chlorophenol is of great significance. **Figure 6A** shows the ECL signals of Ru $(bpy)_3^{2+}$/TPrA in the presence of different concentrations of 4-chlorophenol. A linear dependence between the reduced ECL intensity (ΔI_{ECL}) and the concentration of 4-chlorophenol ($c_{4\text{-}CP}$) is obtained with a range from 0.1 to 20 μM ($\Delta I_{ECL} = 734.9c_{4\text{-}CP} + 43.2$, $R^2 = 0.9982$, **Figure 6B**). The limit of detection (LOD) is calculated to be 30 nM ($S/N = 3$). In addition, the ECL signal is quite stable. The relative standard deviation of ECL intensity for three consecutive detections is less than 2.5%. Owing to the high active area of 3DG electrode, the sensitivity on VMSF/APTES/3DG is four times higher than that of the corresponding system on the planar electrode (VMSF/APTES/GCE). The selectivity of the sensor was evaluated by comparing the ECL intensity in the presence of 5 orders of magnitude higher concentrations of ions (Na^+, K^+, Cl^-, NO_3^-) or bioactive molecules (e.g., glucose, urea). The ECL intensity remained more than 98%, indicating no remarkable interference and high selectivity.

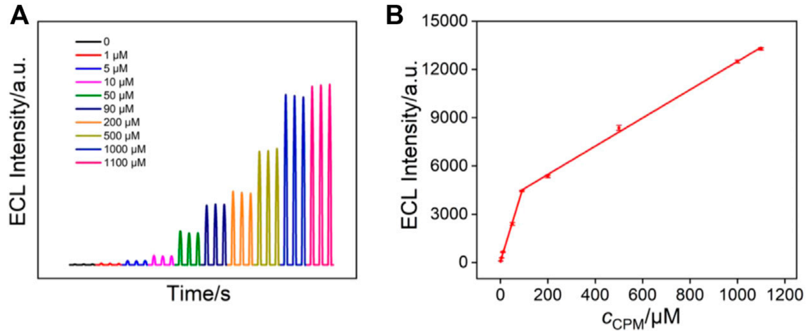

FIGURE 7 | (A) ECL intensity of 10 μM Ru $(bpy)_3^{2+}$ in the presence of different concentrations of chlorpheniramine. **(B)** The linear dependence between the ECL intensity and the concentration of chlorpheniramine.

Electroluminescence Determination of Chlorpheniramine Using Signal-on Mode

The ECL response of Ru $(bpy)_3^{2+}$ can be significantly enhanced in the presence of a co-reactant. Therefore, it is also possible to construct a signal-on ECL mode to detect co-reactants of Ru $(bpy)_3^{2+}$ (Liu and Zhou, 2006; Al-Hinaai et al., 2015). As a proof-of-concept demonstration, chlorpheniramine (CPM), which is one of the most effective antihistamines for the treatment of allergic and vasomotor rhinitis, allergic conjunctivitis, mild urticaria, angioedema, and anaphylactic shock, was detected by the VMSF/APTES/3DG sensor. **Figure 7A** shows the ECL signals of Ru $(bpy)_3^{2+}$ in the presence of different concentrations of chlorpheniramine. As seen, the ECL intensity of Ru $(bpy)_3^{2+}$ gradually increases with increasing the concentration of chlorpheniramine. A good linear correlation is found between the ECL intensity (I_{ECL}) and the concentration of chlorpheniramine (c_{CPM}) in the range of 1.0–90.0 μM ($I_{ECL} = 48.15c_{CPM} + 78.54$, $R^2 = 0.9981$, **Figure 7B**) and 90.0–1,100.0 μM ($I_{ECL} = 8.78c_{CPM} + 3{,}714$, $R^2 = 0.9986$). The LOD was calculated to be 430 nM (S/N = 3).

Analysis of Real Samples

The application of VMSF/APTES/3DG in the detection of 4-chlorophenol in real environmental samples (lake water) was investigated (**Supplementary Table S1** in **Supplementary material**). Since 4-chlorophenol was not detected in the lake water samples, the standard addition recovery method was used to evaluate the accuracy and reliability of the method. As seen, satisfactory recoveries (99.0–103%) and low RSD (<2.7%) for parallel detections were achieved, proving the high accuracy and reliability of detection in lake water. VMSF/APTES/3DG sensor was also applied to detect the content of chlorpheniramine in tablets. It is worth noting that the sensitivity in the tablet matrix is consistent with that obtained in the buffer (**Supplementary Figure S5** in **Supplementary material**), indicating good anti-fouling characteristics of the sensor resulted from the VMSF nanochannels. The content of diphenhydramine in the tablets was determined to be 57.92 mg/g by the developed ECL sensor using linear extrapolation, which was quite similar with that (58.57 mg/g) obtained by standard high-performance liquid chromatography (HPLC) method.

CONCLUSION

In summary, we have developed a novel 3D electrochemiluminescence platform based on monolithic and macroporous 3DG equipped with VMSF. In order to overcome the high hydrophobicity of 3DG and realize stable adhesion of VMSF, 3-aminopropyltriethoxysilane (APTES) is simply electrografted on 3DG as a hydrophilic molecular glue. The construction of the VMSF/APTES/3DG sensor is simple and convenient. Owing to the high conductivity and high active area of 3DG as well as the strong enrichment effect of VMSF on the ECL probe of Ru $(bpy)_3^{2+}$, VMSF/APTES/3DG exhibits significantly sensitized ECL signals. Using ECL signal-off and signal-on detection mode, 4-chlorophenol and chlorpheniramine can be sensitively detected as the proof-of-concept demonstrations. VMSF-modified 3DG might open a new way for the fabrication of 3D ECL sensors with high sensitivity and good anti-fouling performance.

DATA AVAILABILITY STATEMENT

The original contributions presented in the study are included in the article/**Supplementary Material**. Further inquiries can be directed to the corresponding authors.

AUTHOR CONTRIBUTIONS

FX prepared and wrote the original draft. JG, XLu, HZ, Xli, and FY conducted the data curation. HT and KW were in charge of reviewing, editing, and writing the manuscript. JL handled the supervision, reviewing, editing, and writing of the manuscript.

FUNDING

We acknowledge the financial support from the National Natural Science Foundation of China (21904117) and the Zhejiang Provincial Natural Science Foundation of China (LY20B050007and LY21B050003).

SUPPLEMENTARY MATERIAL

The Supplementary Material for this article can be found online at: https://www.frontiersin.org/articles/10.3389/fchem.2021.770512/full#supplementary-material

REFERENCES

Al-Hinaai, M., Khudaish, E. A., Al-Harthy, S., and Suliman, F. O. (2015). A Solid-State Electrochemiluminescence Composite Modified Electrode Based on Ru(bpy)32+/PAHNSA: Characterization and Pharmaceutical Applications. *Electrochim. Acta* 176, 179–187. doi:10.1016/j.electacta.2015.06.148

Beluomini, M. A., Stradiotto, N. R., and Boldrin, M. V. (2021). Electrosynthesis of Three-Dimensional Nanoporous Nickel on Screen-Printed Electrode Used for the Determination of Narirutin in Citrus Wastewater. *Food Chem.* 353, 129427. doi:10.1016/j.foodchem.2021.129427

Chen, K., Yao, L., and Su, B. (2019). Bionic Thermoelectric Response with Nanochannels. *J. Am. Chem. Soc.* 141, 8608–8615. doi:10.1021/jacs.9b03569

Cheng, S., Liu, H., Zhang, H., Chu, G., Guo, Y., and Sun, X. (2020). Ultrasensitive Electrochemiluminescence Aptasensor for Kanamycin Detection Based on Silver Nanoparticle-Catalyzed Chemiluminescent Reaction between Luminol and Hydrogen Peroxide. *Sens. Actuators B: Chem.* 304, 127367. doi:10.1016/j.snb.2019.127367

Ding, H., Guo, W., and Su, B. (2020). Imaging Cell-Matrix Adhesions and Collective Migration of Living Cells by Electrochemiluminescence Microscopy. *Angew. Chem. Int. Ed.* 59, 449–456. doi:10.1002/anie.201911190

Ding, H., Guo, W., Zhou, P., and Su, B. (2020). Nanocage-confined Electrochemiluminescence for the Detection of Dopamine Released from Living Cells. *Chem. Commun.* 56, 8249–8252. doi:10.1039/d0cc03370g

Dong, L., Wei, G., Cheng, T., Tang, J., Ye, X., Hong, M., et al. (2020). Thermal Conductivity, Electrical Resistivity, and Microstructure of Cu/W Multilayered Nanofilms. *ACS Appl. Mater. Inter.* 12, 8886–8896. doi:10.1021/acsami.9b21182

Duan, S., Peng, J., Cheng, H., Li, W., Jia, R., Liu, J., et al. (2021). A Label-free and Homogenous Electrochemical Assay for Matrix Metalloproteinase 2 Activity Monitoring in Complex Samples Based on Electrodes Modified with Orderly Distributed Mesoporous Silica Films. *Talanta* 231, 122418. doi:10.1016/j.talanta.2021.122418

Gamero-Quijano, A., Dossot, M., Walcarius, A., Scanlon, M. D., and Herzog, G. (2021). Electrogeneration of a Free-Standing Cytochrome C-Silica Matrix at a Soft Electrified Interface. *Langmuir* 37, 4033–4041. doi:10.1021/acs.langmuir.1c00409

Garbayo, I., Santiago, A., Judez, X., de Buruaga, A. S., Castillo, J., and Muñoz-Márquez, M. A. (2021). Alumina Nanofilms as Active Barriers for Polysulfides in High-Performance All-Solid-State Lithium-Sulfur Batteries. *ACS Appl. Energ. Mater.* 4, 2463–2470. doi:10.1021/acsaem.0c03032

Gu, W., Wang, H., Jiao, L., Wu, Y., Chen, Y., Hu, L., et al. (2020). Single-Atom Iron Boosts Electrochemiluminescence. *Angew. Chem.* 132, 3562–3566. doi:10.1002/ange.201914643

Guo, W., Lin, X., Yan, F., and Su, B. (2016). Vertically Ordered Silica Mesochannel Modified Bipolar Electrode for Electrochemiluminescence Imaging Analysis. *ChemElectroChem* 3, 480–486. doi:10.1002/celc.201500329

He, M., Cao, L., Li, W., Chang, X., and Ren, Z. (2021). α-MnO2 Nanotube@ δ-MnO2 Nanoflake Hierarchical Structure on Three-Dimensional Graphene Foam as a Lightweight and Free-Standing Supercapacitor Electrode. *J. Alloys Comp.* 865, 158934. doi:10.1016/j.jallcom.2021.158934

Huang, X., Xie, L., Lin, X., and Su, B. (2016). Permselective Ion Transport across the Nanoscopic Liquid/liquid Interface Array. *Anal. Chem.* 88, 6563–6569. doi:10.1021/acs.analchem.6b01383

Huang, H., Xia, L., Zhao, Y., Zhang, H., Cong, T., Wang, J., et al. (2020). Three-dimensional Porous Reduced Graphene oxide/PEDOT:PSS Aerogel: Facile Preparation and High Performance for Supercapacitor Electrodes. *Electrochim. Acta* 364, 137297. doi:10.1016/j.electacta.2020.137297

Jiokeng, S. L. Z., Tonle, I. K., and Walcarius, A. (2019). Amino-attapulgite/mesoporous Silica Composite Films Generated by Electro-Assisted Self-Assembly for the Voltammetric Determination of Diclofenac. *Sens. Actuators B: Chem.* 287, 296–305. doi:10.1016/j.snb.2019.02.038

Li, L., Yu, B., Zhang, X., and You, T. (2015). A Novel Electrochemiluminescence Sensor Based on Ru(bpy)32+/N-Doped Carbon Nanodots System for the Detection of Bisphenol A. *Anal. Chim. Acta* 895, 104–111. doi:10.1016/j.aca.2015.08.055

Li, L., Chen, Y., and Zhu, J.-J. (2017). Recent Advances in Electrochemiluminescence Analysis. *Anal. Chem.* 89, 358–371. doi:10.1021/acs.analchem.6b04675

Li, G., Huang, B., Pan, Z., Su, X., Shao, Z., and An, L. (2019). Advances in Three-Dimensional Graphene-Based Materials: Configurations, Preparation and Application in Secondary Metal (Li, Na, K, Mg, Al)-Ion Batteries. *Energy Environ. Sci.* 12, 2030–2053. doi:10.1039/c8ee03014f

Liu, Y., and Zhou, W. (2006). Determination of Chlorpheniramine and its Binding with Human Serum Albumin by Capillary Electrophoresis with Tris(2,2'-bipyridyl)Ruthenium(II) Electrochemiluminescence Detection. *Anal. Sci.* 22, 999–1003. doi:10.2116/analsci.22.999

Liu, Z., Qi, W., and Xu, G. (2015). Recent Advances in Electrochemiluminescence. *Chem. Soc. Rev.* 44, 3117–3142. doi:10.1039/c5cs00086f

Liu, J., He, D., Liu, Q., He, X., Wang, K., Yang, X., et al. (2016). Vertically Ordered Mesoporous Silica Film-Assisted Label-free and Universal Electrochemiluminescence Aptasensor Platform. *Anal. Chem.* 88, 11707–11713. doi:10.1021/acs.analchem.6b03317

Ma, C., Cao, Y., Gou, X., and Zhu, J.-J. (2020). Recent Progress in Electrochemiluminescence Sensing and Imaging. *Anal. Chem.* 92, 431–454. doi:10.1021/acs.analchem.9b04947

Nasir, T., Zhang, L., Vilà, N., Herzog, G., and Walcarius, A. (2016). Electrografting of 3-aminopropyltriethoxysilane on a Glassy Carbon Electrode for the Improved Adhesion of Vertically Oriented Mesoporous Silica Thin Films. *Langmuir* 32, 4323–4332. doi:10.1021/acs.langmuir.6b00798

Nasir, T., Herzog, G., Hébrant, M., Despas, C., Liu, L., and Walcarius, A. (2018). Mesoporous Silica Thin Films for Improved Electrochemical Detection of Paraquat. *ACS Sens.* 3, 484–493. doi:10.1021/acssensors.7b00920

Nasir, T., Vodolazkaya, N. A., Herzog, G., and Walcarius, A. (2019). Critical Effect of Film Thickness on Preconcentration Electroanalysis with Oriented Mesoporous Silica Modified Electrodes. *Electroanalysis* 31, 202–207. doi:10.1002/elan.201800533

Nasir, T., Gamero-Quijano, A., Despas, C., Dossot, M., Herzog, G., and Walcarius, A. (2020). Signal Amplification by Electro-Oligomerisation for Improved Isoproturon Detection. *Talanta* 220, 121347. doi:10.1016/j.talanta.2020.121347

Qi, B.-P., Zhang, X., Shang, B.-B., Xiang, D., Qu, W., and Zhang, S. (2017). A Facile Method to Sensitively Monitor Chlorinated Phenols Based on Ru(bpy)32+ Electrochemiluminescent System Using Graphene Quantum Dots as Coreactants. *Carbon* 121, 72–78. doi:10.1016/j.carbon.2017.05.045

Qin, Y., Wang, Z., Xu, J., Han, F., Zhao, X., Han, D., et al. (2020). Carbon Nitride Quantum Dots Enhancing the Anodic Electrochemiluminescence of Ruthenium(II) Tris(2,2′-Bipyridyl) via Inhibiting the Oxygen Evolution Reaction. *Anal. Chem.* 92, 15352–15360. doi:10.1021/acs.analchem.0c02568

Ullah, W., Herzog, G., Vilà, N., Brites Helú, M., and Walcarius, A. (2020). Electrochemically Assisted Deposition of Nanoporous Silica Membranes on Gold Electrodes: Effect of 3-Mercaptopropyl(trimethoxysilane) "Molecular Glue" on Film Formation, Permeability and Metal Underpotential Deposition. *ChemElectroChem* 8, 142–150. doi:10.1002/celc.202001347

Ullah, W., Herzog, G., Vilà, N., and Walcarius, A. (2021). Electrografting and Electropolymerization of Nanoarrays of Pani Filaments through Silica Mesochannels. *Electrochemistry Commun.* 122, 106896. doi:10.1016/j.elecom.2020.106896

Wang, Z.-M., Peng, W., Takenaka, Y., Yoshizawa, N., Kosuge, K., Wang, W., et al. (2017). Sandwich-type Nanocomposite of Reduced Graphene Oxide and Periodic Mesoporous Silica with Vertically Aligned Mesochannels of Tunable Pore Depth and Size. *Adv. Funct. Mater.* 27, 1704066. doi:10.1002/adfm.201704066

Wang, Y., Guo, W., Yang, Q., and Su, B. (2020). Electrochemiluminescence Self-Interference Spectroscopy with Vertical Nanoscale Resolution. *J. Am. Chem. Soc.* 142, 1222–1226. doi:10.1021/jacs.9b12833

Xi, F., Zhao, D., Wang, X., and Chen, P. (2013). Non-enzymatic Detection of Hydrogen Peroxide Using a Functionalized Three-Dimensional Graphene Electrode. *Electrochem. Commun.* 26, 81–84. doi:10.1016/j.elecom.2012.10.017

Xi, F., Xuan, L., Lu, L., Huang, J., Yan, F., Liu, J., et al. (2019). Improved Adhesion and Performance of Vertically-Aligned Mesoporous Silica-Nanochannel Film on Reduced Graphene Oxide for Direct Electrochemical Analysis of Human Serum. *Sens. Actuators B: Chem.* 288, 133–140. doi:10.1016/j.snb.2019.02.115

Xiao, Y., Xu, L., Li, P., Tang, X.-C., and Qi, L.-W. (2017). A Simple Microdroplet Chip Consisting of Silica Nanochannel-Assisted Electrode and Paper Cover for Highly Sensitive Electrochemiluminescent Detection of Drugs in Human Serum. *Anal. Chim. Acta* 983, 96–102. doi:10.1016/j.aca.2017.06.014

Yan, F., and Su, B. (2016). Tailoring Molecular Permeability of Nanochannel-Micelle Membranes for Electrochemical Analysis of Antioxidants in Fruit Juices without Sample Treatment. *Anal. Chem.* 88, 11001–11006. doi:10.1021/acs.analchem.6b02823

Yan, F., Lin, X., and Su, B. (2016). Vertically Ordered Silica Mesochannel Films: Electrochemistry and Analytical Applications. *Analyst* 141, 3482–3495. doi:10.1039/c6an00146g

Zhang, J., Jin, R., Jiang, D., and Chen, H.-Y. (2019). Electrochemiluminescence-based Capacitance Microscopy for Label-free Imaging of Antigens on the Cellular Plasma Membrane. *J. Am. Chem. Soc.* 141, 10294–10299. doi:10.1021/jacs.9b03007

Zhou, Z., Guo, W., Xu, L., Yang, Q., and Su, B. (2015). Two Orders-Of-Magnitude Enhancement in the Electrochemiluminescence of Ru(bpy)32+ by Vertically Ordered Silica Mesochannels. *Anal. Chim. Acta* 886, 48–55. doi:10.1016/j.aca.2015.06.005

Zhou, L., Ding, H., Yan, F., Guo, W., and Su, B. (2018). Electrochemical Detection of Alzheimer's Disease Related Substances in Biofluids by Silica Nanochannel Membrane Modified Glassy Carbon Electrodes. *Analyst* 143, 4756–4763. doi:10.1039/c8an01457d

Zhou, P., Yao, L., Chen, K., and Su, B. (2020). Silica Nanochannel Membranes for Electrochemical Analysis and Molecular Sieving: a Comprehensive Review. *Crit. Rev. Anal. Chem.* 50, 424–444. doi:10.1080/10408347.2019.1642735

Zhou, P., Yao, L., and Su, B. (2020). Fabrication, Characterization, and Analytical Application of Silica Nanopore Array-Modified Platinum Electrode. *ACS Appl. Mater. Inter.* 12, 4143–4149. doi:10.1021/acsami.9b20165

Zu, Y., and Bard, A. J. (2000). Electrogenerated Chemiluminescence. 66. The Role of Direct Coreactant Oxidation in the Ruthenium Tris(2,2')bipyridyl/Tripropylamine System and the Effect of Halide Ions on the Emission Intensity. *Anal. Chem.* 72, 3223–3232. doi:10.1021/ac000199y

Conflict of Interest: The authors declare that the research was conducted in the absence of any commercial or financial relationships that could be construed as a potential conflict of interest.

frontiers
in Chemistry

ORIGINAL RESEARCH
published: 10 December 2021
doi: 10.3389/fchem.2021.810861

ZIF-8/PI Nanofibrous Membranes With High-Temperature Resistance for Highly Efficient $PM_{0.3}$ Air Filtration and Oil-Water Separation

Yu Li, Dan Wang, Guanchen Xu, Li Qiao, Yong Li, Hongyu Gong, Lei Shi, Dongwei Li, Meng Gao, Guoran Liu, Jingjing Zhang, Wenhui Wei, Xingshuang Zhang* and Xiu Liang*

Shandong Provincial Key Laboratory of High Strength Lightweight Metallic Materials, Advanced Materials Institute, Qilu University of Technology (Shandong Academy of Sciences), Jinan, China

Edited by:
Dejin Zang,
Tsinghua University, China

Reviewed by:
Deng-Guang Yu,
University of Shanghai for Science and Technology, China
Kok Keong Lau,
University of Technology Petronas, Malaysia
Fengyun Guo,
Zhejiang Sci-Tech University, China
Zhichao Yu,
Taiyuan University of Technology, China

****Correspondence:***
Xingshuang Zhang
xszhang@qlu.edu.cn
Xiu Liang
xliang@sdas.org

Specialty section:
This article was submitted to Analytical Chemistry, a section of the journal Frontiers in Chemistry

Received: *08 November 2021*
Accepted: *29 November 2021*
Published: *10 December 2021*

Citation:
Li Y, Wang D, Xu G, Qiao L, Li Y, Gong H, Shi L, Li D, Gao M, Liu G, Zhang J, Wei W, Zhang X and Liang X (2021) ZIF-8/PI Nanofibrous Membranes With High-Temperature Resistance for Highly Efficient $PM_{0.3}$ Air Filtration and Oil-Water Separation. Front. Chem. 9:810861. doi: 10.3389/fchem.2021.810861

Air and water pollution poses a serious threat to public health and the ecological environment worldwide. Particulate matter (PM) is the major air pollutant, and its primary sources are processes that require high temperatures, such as fossil fuel combustion and vehicle exhaust. $PM_{0.3}$ can penetrate and seriously harm the bronchi of the lungs, but it is difficult to remove $PM_{0.3}$ due to its small size. Therefore, $PM_{0.3}$ air filters that are highly efficient and resistant to high temperatures must be developed. Polyimide (PI) is an excellent polymer with a high temperature resistance and a good mechanical property. Air filters made from PI nanofibers have a high PM removal efficiency and a low air flow resistance. Herein, zeolitic imidazolate framework-8 (ZIF-8) was used to modify PI nanofibers to fabricate air filters with a high specific surface area and filtration efficiency. Compared with traditional PI membranes, the ZIF-8/PI multifunction nanofiber membranes achieved super-high filtration efficiency for ultrafine particles ($PM_{0.3}$, 100%), and the pressure drop was only 63 Pa. The filtration mechanism of performance improvement caused by the introduction of ZIF-8/PI nanofiber membrane is explored. Moreover, the ZIF-8/PI nanofiber membranes exhibited excellent thermal stability (300 C) and efficient water–oil separation ability (99.85%).

Keywords: polyimide, ZIF-8, nanofibers, high-temperature resistance, air filtration, oil-water separation

1 INTRODUCTION

Air and water pollution due to rapid industrialization and urbanization poses a serious threat to the ecological environmental and human health (Wang B et al., 2015; Lv et al., 2019). Air pollution mainly refers to the presence of airborne particulate matter (PM), which mostly comes from combustion reactions, such as combustion of fossil fuel, biomass, and garbage (Liang et al., 2019). PM pollutants with an aerodynamic diameter of less than or equal to 2.5 μm ($PM_{2.5}$) are the major hazardous substances because they can block the alveoli and damage the lungs (Li and Yin, 2019). In particular, $PM_{0.3}$, owing to its smaller particle size than other PM, it can cause greater harm that may lead to cardiovascular diseases, respiratory disease, diabetes, and lung cancer (Mosanenzadeh et al., 2020; Wang Z et al., 2020; Zhang et al., 2020). PM has a complex composition and may carry as many as 791 bacterial genera, which can cause allergy and infection (Gao et al., 2019; Zhang et al., 2020). Aside from air pollution, the presence of oil in wastewater and the water pollution caused by spillage of oil–organic solvents also seriously threaten public health (Zhang W et al., 2013; Wang B et al., 2015; Li et al., 2019) Therefore, filter membrane materials that can used for PM air filtration and oil–water separation must be developed.

Nanofiber filter materials have a small fiber diameter, a high porosity, and a large specific surface area, which are characteristics that compensate for the shortcomings of conventional filter materials that cannot absorb $PM_{0.3}$ with a small particle size (Li D et al., 2020; Zhang et al., 2020). Electrospinning technology is a simple method for obtaining continuous, uniform, and controllable nanofibers with various polymers (Doimoto and Greiner, 2018). Electrospinning, on one hand, is fast developing from a single-fluid process (Zhang et al., 2021) to coaxial (Ning et al., 2021), tri-axial (Wang et al., 2020a), side-by-side (Wang et al., 2020b), and other complicated processes (Aidana et al., 2021). On the other hand, more and more active components are encapsulated into electrospun nanofibers through chemical or physical methods to take advantages of the physical properties of electrospun nanofiber mats. As a high-performance engineering polymer, polyimide (PI) has been extensively explored (Liu et al., 2015). Owing to its excellent mechanical properties, thermal stability, low dielectric constants, and insulation, it can be used in various applications, such as gas separation, oil-water separation, and cell separation (Miao et al., 2013; Zhang R et al., 2016; Chen et al., 2017; Bai et al., 2019). Metal-organic frameworks (MOFs) are composed of metal ions or ion clusters connected by organic ligands (Ma et al., 2019), which are widely used in gas separation (Dai et al., 2018), filtration (Lai et al., 2016), catalysis (Wang et al., 2015a), and sensing (Wang et al., 2015b) because of their high specific surface area, high porosity, and adjustablility (Li T. T et al., 2020). Zeolitic imidazolate framework-8 (ZIF-8) is one of the most widely used MOFs. Owing to its special tetrahedral skeleton structure, ZIF-8 not only has a high specific surface area and porosity but also has excellent thermal stability and chemical stability (Dai et al., 2018). The application of ZIF-8 in powder form in filtration is limited. Therefore, PI nanofibers doped with ZIF-8 nanoparticles can harness this MOF's special open metal position, functional group, and surface charge to achieve highly efficient air filtration (Hao et al., 2019). Moreover, the introduction of ZIF-8 can change its hydrophobicity for oil-water separation.

Three methods for loading ZIF-8 on nanofiber membranes are currently available, namely, *in-situ* growth method (Xu et al., 2018; Wang et al., 2019), impregnation method (Tao et al., 2013; Ren et al., 2019), and co-spinning method (Dai et al., 2016; Zheng et al., 2020). In *in-situ* growth method, the ZnO seed layer is deposited on the fiber surface, and then ZnO is converted into ZIF-8 by *in-situ* solvothermal growth. Li et al. (Xu et al., 2018) prepared a ZIF-8 seed on PVDF/ZnO membranes by activation step and then expanded it in the growth step to separate water from oil solution. However, this method involves numerous steps, which compromise the repeatability and stability of experiments (An et al., 2016). Impregnation method involves a simple preparation process, but controlling the size and distribution of ZIF-8 grains via this method is difficult (Bechelany et al., 2015). Co-spinning method has the unique ability to make ZIF-8 nanoparticles evenly disperse in nanofibers, and load contents are easy to control via this method. The most important advantage of co-spinning method is that one-step electrospinning is easy to operate, controllable, and repeatable (Ostermann et al., 2011). In addition, the most significant advantage is that ZIF-8 is directly doped in PAA precursor solution. The semi embedded structure makes ZIF-8 stably load the interior and surface of PI nanofiber membrane. Hao et al. (2019) prepared soluble PI/ZIF-8 nanofiber membranes for air filtration *via* electrospinning. By contrast, a previous work (Dai et al., 2016) prepared PI nanofiber membranes by using the electrospinning precursor polyamide acid (PAA) solution on the gate receiver. This innovation has lowered the cost of PI synthesis, broaden its application range, and increased its filtration efficiency (the maximum filtration efficiency of $PM_{0.3}$ was 100%).

Here, we developed a low-cost and a highly efficient material for filtering PM, which can be applied to high-temperature industrial waste filtration without affecting the structure and morphology of filtration materials. The unit price of polyimide powder required for the preparation of PI nanofibers by one-step method is as high as 17.2 yuan/g, while the average unit price of PMDA and ODA used in this study is only 1.08 yuan/g, which shows that the material cost developed in this study is low. The nanofiber diameter, porosity, filtration, and separation performance of the PI nanofibers membrane can be controlled by the loading contents of ZIF-8 nanoparticles (Lin et al., 2016; Ji et al., 2019; Dou et al., 2020; Wu et al., 2021). To address the attendant problems in air filtration and oil–water separation, we prepared herein highly efficient ZIF-8/PI nanofiber membranes via a simple co-spinning method. Moreover, the PI nanofiber membranes could be modified into superhydrophobic and superlipophilic membranes, a property that is not only conducive to the filtration of PM particles but can also be applied to oil-water separation. The filter membranes can be used for oil-water separation because the positive charge carried by ZIF-8 can interact with the negative charge carried by the oil drop to enhance its lipophilicity, and its superhigh specific surface area leads to hydrophobic interactions, thereby improving filtration efficiency.

2 EXPERIMENTAL SECTION

2.1 Materials

Pyromellitic dianhydride (PMDA), 4,4-oxidianiline (ODA), N,N-dimethylacetamide (DMAc), petroleum ether (C_5H_{12}), n-hexane (C_6H_{14}), oil red O ($C_{26}H_{24}N_4O$), methylene blue (MB, $C_{16}H_{18}C_lN_3S$), and sodium chloride (NaCl) were purchased from Shanghai Macklin Biochemical Co., Ltd., Zinc nitrate hexahydrate [$Zn(CH_3COO)_2$] and 2-methylimidazole were bought from Aladdin (Shanghai, China). Dichloroethane ($C_2H_4Cl_2$) and toluene ($C_6H_5CH_3$) were procured from Sinopharm Chemical Reagent (Shanghai, China). All of these chemicals were used as received. All solutions were prepared with ultrapure water supplied by a water-purifying device in our laboratory.

2.2 Synthesis of ZIF-8

$Zn(CH_3COO)_2$ (175 mg) and 2-methylimidazole (263 mg) were dissolved in methanol (40 ml) by stirring at room temperature for 5 min and standing for 24 h. The white solid powder was centrifuged three times with methanol and dried at 120°C. The Raman spectra of the prepared powder samples (**Supplementary Figure S1**) were the same as those of known structural data, indicating that the powder obtained was ZIF-8. As shown in **Supplementary Figure S2A**, the synthesized ZIF-8 particles had a uniform dodecahedral structure. The particle size of the ZIF-8 precursor was approximately 280 nm (**Supplementary Figure S2B**).

2.3 Preparation of PI Nanofiber Membranes

PI nanofibers were synthesized *via* a two-step method (**Supplementary Figure S3**). ODA and PMDA were weighed in equal molar ratio and dissolved in DMAC to form 20wt% PAA precursor solution. When preparing the solution, ODA was first dissolved in DMAC, and then PMDA was added into the flask 8–10 times after complete dissolution. At the end of feeding, the solution was continuously and quickly stirred for 1 h to ensure that the monomer definitively indicated the formation of PAA. At the end of the reaction, the solution was allowed to stand for 12 h.

The prepared solution was electrospun on a metal mesh fixed on the surface of the drum shaped receiver. The voltage was set at 20 kV, the rotation speed was 200 r/min, and the steady flow rate was 0.95 ml/h. The material was extruded from an 18 G needle tip. After electrospinning, PAA was imidized into PI nanofibers by annealing at 350°C in an air muffle furnace (**Supplementary Figure S4**, FT-IR spectroscopy showed imidization).

2.4 Preparation of ZIF-8/PI Nanofiber Membranes

The precursor solution of ZIF-8/PAA was prepared via electrospinning. First, ZIF-8 was dissolved in DMAC, and the same experimental steps outlined in the previous section were followed. By controlling the mass ratio of ZIF-8 to PMDA, ODA, which was the precursor solution with doping amounts of 0, 1, 2, and 3%, was prepared. The same parameters of electrospinning and annealing mentioned in the preceding section were used.

2.5 Air Filtration Performance

The filtration efficiency and pressure drop of the nanofiber membranes were measured using a comprehensive performance test instrument for filter materials (**Supplementary Figure S5**). This instrument was connected to the PM particle emission source, and it regulated the air flow velocity through an air pump. PM particles with diameters ranging from 300 nm to 10 μm were supplied by neutral monodispersed solid sodium chloride aerosol, and filtration efficiency was calculated by a particle counter connected at both sides before and after filtration. The test was conducted at a steady flow rate of 4–14 L/min, and the effective area of the air inlet of the filter was 200.9 cm^2.

2.6 Oil-Water Separation Tests

The oil–water separation performance of the membranes was tested using a simple oil–water separator. The prepared membranes were fixed between two sealable and linkable glass devices, and a conical bottle was placed at the bottom as a receiving container. When the mixture of water and oil (1/1 volume ratio) was directly poured into the upper glass container, the oil passed through the membrane and the water remained.

2.7 Characterizations

The morphology of the nanofiber membranes was examined via SEM. The structure of PI and the imidization process of PAA were analyzed via Fourier Transform Infrared (FTIR) spectroscopy. The composition of the ZIF-8/PI nanofiber membranes was analyzed *via* X-ray Photoelectron Spectroscopy (XPS) and Raman spectroscopy. The thermal stability of the membranes was tested via Thermogravimetric Analysis (TGA) at the heating rate of 5°C/min. The mechanical properties of the membranes were tested using a tensile tester. The porosity and specific surface area of the membranes were measured *via* Brunauer-Emmett-Teller (BET) analysis. The filtration efficiency and pressure drop of the membranes were tested by a mask tester (G506). The device used for the oil-water separation experiment was self-assembled.

3 RESULTS AND DISCUSSION

3.1 Characterization of the ZIF-8/PI Nanofiber Membranes

Figure 1A shows the method for preparing the ZIF-8/PI nanofiber membranes and their application. The ZIF-8/PI nanofiber membranes were obtained by electrospinning the ZIF-8/PAA nanofiber membranes and via thermal imidization (**Figure 1A**). Owing to the doping of ZIF-8 nanoparticles, the specific surface area and porosity of ZIF-8/PI nanofiber membranes increased, improving the air filtration and oil-water separation properties (**Figures 1B,C**). ZIF-8-1/PI, ZIF-8-2/PI, and ZIF-8-3/PI were used to represent the loading content of 1, 2, and 3%, respectively, to distinguish the samples with different loading contents of ZIF-8. As shown in **Figure 2A**, the diameter of the as-prepared PI nanofibers was approximately 340 nm and their nanogrid pores were large. The surface morphology of ZIF-8 nanoparticles only marginally changed and was slightly rough. As shown in **Figure 2B**, the ZIF-8/PI nanofiber diameter substantially decreased to about 300 nm, and the nanogrid structure was more compact. The X-Ray Diffraction (XRD) patterns of the ZIF-8-3/PI nanofiber membranes were similar to those of pure PI nanofiber membranes, but the peaks of the ZIF-8/PI nanofiber membranes at 12.75° and 19.53° were enhanced, which corresponded to the position of the characteristic peak of ZIF-8 (Wang et al., 2015a). Furthermore, the element distribution of the full elements of C, N, O, and Zn of the ZIF-8/PI nanofibers (**Figure 2C**) indicated that ZIF-8 nanoparticles were evenly distributed in the PI nanofibers. The XRD patterns of the ZIF-8-3/PI nanofiber membranes contained the characteristics of both ZIF-8 and pure PI, indicating that

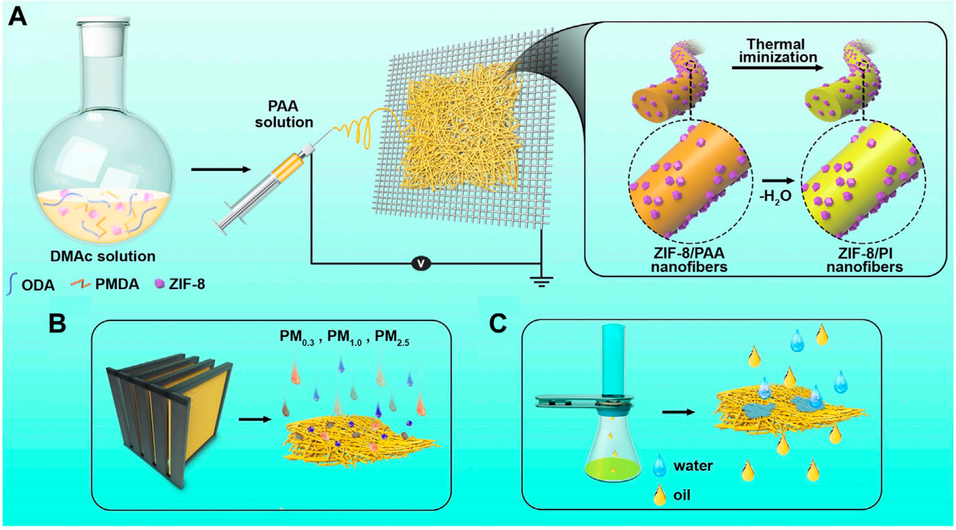

FIGURE 1 | Schematic of the procedure for preparing ZIF-8/PI electrospun nanofiber membranes and their applications. **(A)** Schematic of the membranes prepared by the two-step electrospinning method. **(B)** Air filtration of the membranes. **(C)** Water–oil separation.

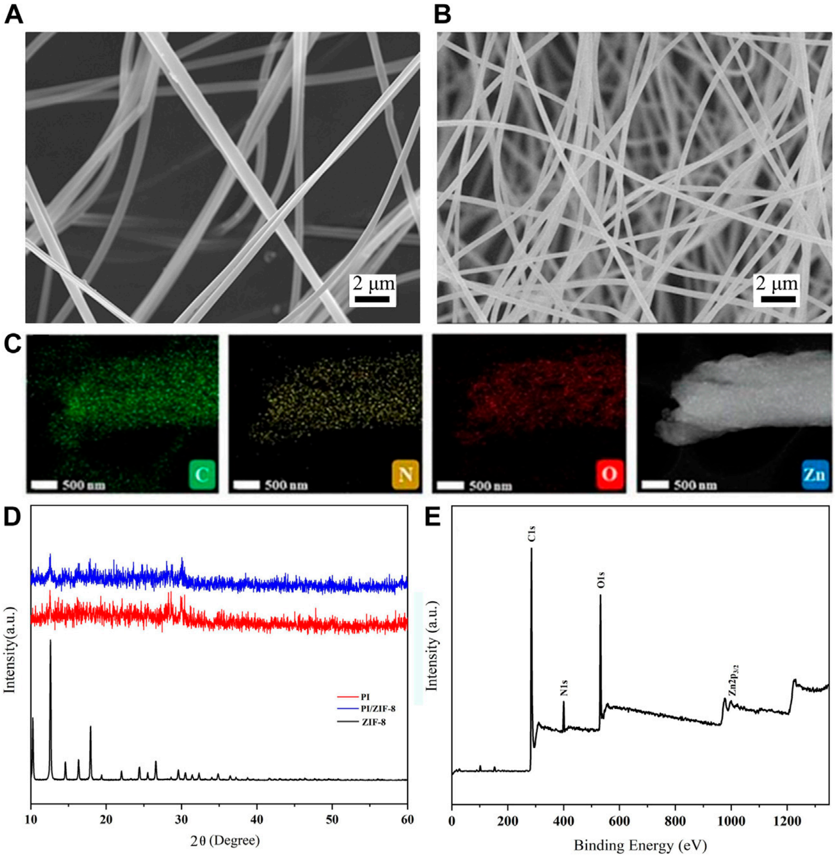

FIGURE 2 | Scanning electron micrographs of the PI-ZIF nanofibers **(A)** PI and **(B)** ZIF-8-3/PI. **(C)** C, N, O, and Zn element distribution of ZIF-8/PI nanofibers. **(D)** X-ray diffraction patterns of the ZIF-8, PI, and ZIF-8-3/PI nanofiber membranes. **(E)** X-ray photoelectron spectroscopy images of the ZIF-8-3/PI nanofiber membranes.

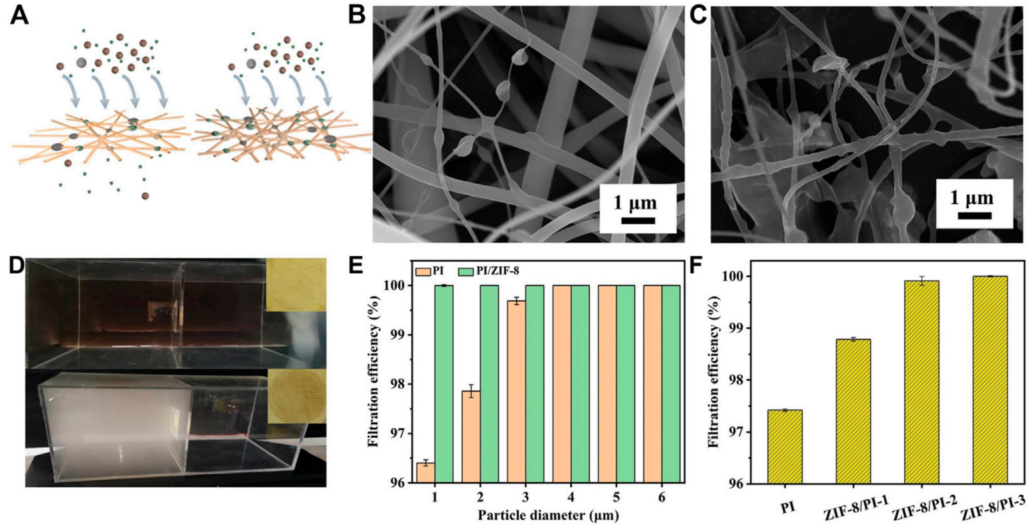

FIGURE 3 | (A) Diagram of different fiber membranes before and after filtration. **(B)** Scanning electron micrograph (SEM) of the PI fiber membranes after filtration. **(C)** SEM of the ZIF-8-3/PI fiber membranes after filtration. **(D)** Digital image of the nanofiber filter membrane before and after filtering in the filtering device. **(E)** Comparison of the filtration efficiency of the PI and ZIF-8/PI-3 fiber membranes for $PM_{0.3}$ filtration at the air flow rate of 6 L/min). **(F)** Effects of the PI nanofiber membranes with different ZIF-8 loadings on $PM_{0.3}$ filtration efficiency.

ZIF-8 nanoparticles were successfully embedded into the PI nanofiber membranes (**Figure 2D**). The XPS spectra (**Figure 2E**; **Supplementary Figure S6**) indicated that ZIF-8 nanoparticles were introduced in the PI nanofibers successfully.

3.2 $PM_{0.3}$ Filtration Performance of the PI Nanofiber Membranes

Figure 3A shows the process of membrane filtration of PM particles. To obtain a large amount of filtered PM membranes, the device shown in **Figure 3D** was used for continuous long-term filtration, and incense was ignited in the left acrylic box to provide PM source. After adsorbing PM particles, the PI nanofiber membranes changed from light yellow to brown (**Figure 3D**, inset). Within the same filtration time, the filtration capacity of PM particles on PI and the ZIF-8-3/PI nanofiber membranes was obviously different. The dense grid structure of the ZIF-8-3/PI nanofibers was conducive to the filtration of PM particles. As shown in **Figures 3B,C**, the major PM particles were adsorbed on the fiber nodes, while the smaller porosity (**Supplementary Figure S7**), the more nodes (Zhang et al., 2019). Moreover, the introduction of ZIF-8 increased the specific surface area of the membranes, thus providing more filtration points for PM filtration (Hao et al., 2019). **Figure 3E** also directly shows that the introduction of ZIF-8 substantially improved the filtration efficiency of the membranes. The filtration efficiency of the PI nanofiber membranes for $PM_{0.3}$ was only 96.38%, whereas that of the doped ZIF-8/PI nanofiber membranes could reach 100% (6 L/min). Furthermore, the smaller the diameter of PM particles was, the higher the filtration efficiency was. According to the comparative report, compared with the non-woven PI membrane in the previous research (Li et al., 2017), the filtration efficiency of ZIF-8/PI nanofiber membrane PI nanofiber membrane prepared in this study is considerably higher than that formed by multi-layer fiber composite, and it also has significant advantages in pressure drop (Wang et al., 2016). A comparison of the filtration efficiency of the different loading contents of ZIF-8 in the PI nanofiber membranes (**Figure 3F**), it can be seen that when the loading amount of ZIF-8 was lower than 3 wt%, the filtration efficiency of the PI nanofiber membranes gradually increased with the increase in ZIF-8 doping amount. However, excessive doping of ZIF-8 affected the conductivity of the precursor solution, which was not conducive to electrospinning. Therefore, the optimal doping ratio was 3 wt%.

As the base weight of the ZIF-8-3/PI nanofiber membranes increased, the filtration efficiency of $PM_{0.3}$ considerably improved (**Figure 4A**) because the increase in base weight increased the thickness of the nanofiber membranes, thereby prolonging the contact time between PM and the fibers and enhancing the filtration efficiency. By contrast, the increase in air velocity reduced the contact time, which was not conducive to PM filtration. However, the increase in both base weight and air velocity also increased the pressure drop, which was not conducive to the service life of the membranes. The best base weight of the membranes was determined to be 7.32 g/m^2. Moreover, the pressure drop was only 63 Pa at 14 L/min, which was considerably lower than that of traditional commercial filters (data). Furthermore, the filtration efficiency was as high as 99.9375%. When air velocity was reduced to 6 L/min at this weight, the filtration efficiency of $PM_{0.3}$ could reach 100% (**Figure 4B**). Quality factor (Q_F) was used to evaluate the comprehensive performance of the filter materials, which is defined as follows (1):

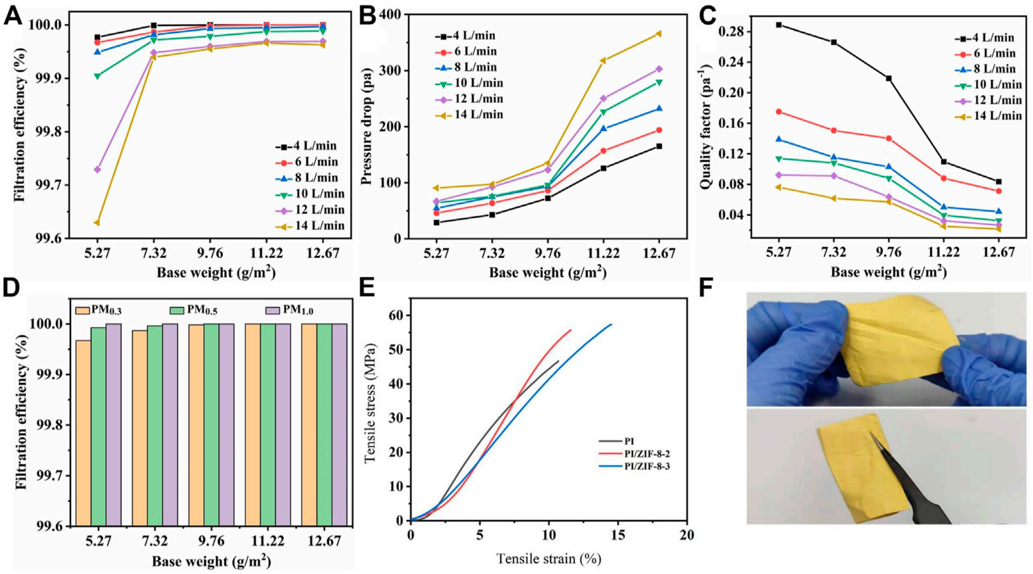

FIGURE 4 | The filtration efficiency **(A)**, pressure drop **(B)**, and quality factor **(C)** of the ZIF-8-3/PI membranes varied with base weight and air flow rate. **(D)** Effects of different base weights of the ZIF-8/PI nanofiber membranes on the filtration efficiency of PM$_{0.3}$, PM$_{0.5}$, and PM$_{1.0}$. **(E)** Stress–strain curves. **(F)** Rigidity and flexibility of the ZIF-8/PI nanofiber membranes.

$$Q_F = \frac{-\ln(1-\eta)}{\Delta P}, \tag{1}$$

where η is filtration efficiency, and ΔP is pressure drop. According to **Eq. 1**, pressure drop is an important factor affecting Q_F. The lowest pressure drop was at 4 L/min. When the base weight was 5.27, 7.32, 9.76, 11.22, and 12.67 g/m^2, the values of Q_F were 0.2888, 0.2661, 0.2189, 0.1096, and 0.0837, respectively (**Figure 4C**). A high Q_F value also indicated a high PM interception performance. The ZIF-8/PI nanofiber membranes had a very high filtration efficiency (>99.9%) for all PM particles (PM$_{0.3-10}$), even when the base weight was only 5.27 g/m^2 (**Figure 4D**). With the introduction of ZIF-8, the tensile strength and elongation of the membrane increased slightly. With the increase of ZIF-8 content, it is directly proportional to the improvement of mechanical properties (**Figure 4E**). Aside from their high tensile strength, the ZIF-8-3/PI nanofiber membranes also had a good flexibility and could be bent at will (**Figure 4F**).

Apart from physical filtration, the air filtration mechanism of ZIF-8/PI nanofiber membrane include: 1) The positive charge on the surface of ZIF-8 nanoparticles can polarize the surface of PM particles, making it easier to interact with nanofibers, thus improving the ability of the membrane to capture PM particles (Ma et al., 2019; Dou et al., 2020; Wu et al., 2021). 2) The high specific surface area of ZIF-8 nanoparticles will improve the specific surface area of the PI nanofiber membrane, which is helpful to improve the surface energy of the membrane and increase the adsorption efficiency (Lin et al., 2016). 3) The essence of adhesion is that when air flows around nanofibers, a certain force should be responsible for fixing the tiny particles in the air (Gong et al., 2015). The results show that although the adhesion effect is widespread in nanofibers, the fiber diameter has a significant effect on the adsorbability (Zhang Y et al., 2016). After the introduction of ZIF-8 nanoparticles, the diameter of PI nanofibers reduced, and the slightly rough surface morphology provides more adsorption sites for PM particles, resulting in a higher adhesion to PM particles (Miao et al., 2013; Liu et al., 2015; Ji et al., 2019).

3.3 Thermal Stability of the ZIF-8/PI Nanofiber Membranes

Among the advantages of the PI nanofiber membranes was the fact that they could be used in high-temperature gas filtration. The resistance of the ZIF-8-3/PI nanofiber membranes to high temperatures was tested *via* TGA. As shown in **Figure 5A**, the change trend of the two membranes was roughly the same from room temperature up to 800°C. The pyrolysis of the ZIF-8/PI nanofiber membranes begun at 450°C because the pyrolysis temperature of ZIF-8 was near that temperature. By comparison, the pyrolysis of the PI nanofiber membranes begun at 500°C (Yang et al., 2020). Although the introduction of ZIF-8 reduced the initial pyrolysis temperature of the membranes, they remained suitable for high-temperature gas filtration (300°C). In practical filtration applications, the membranes were heat-treated at 100°C, 200°C, and 300°C for 2 h, and then their filtration efficiency was tested. Results showed that the filtration efficiency of both the PI nanofiber membranes and the ZIF-8/PI nanofiber membranes for PM$_{0.3}$ did not change after heat treatment (**Figure 5B**). The morphology of the ZIF-8/PI nanofiber membranes did not change after heat treatment at 300°C (**Figures 5C,D**), also

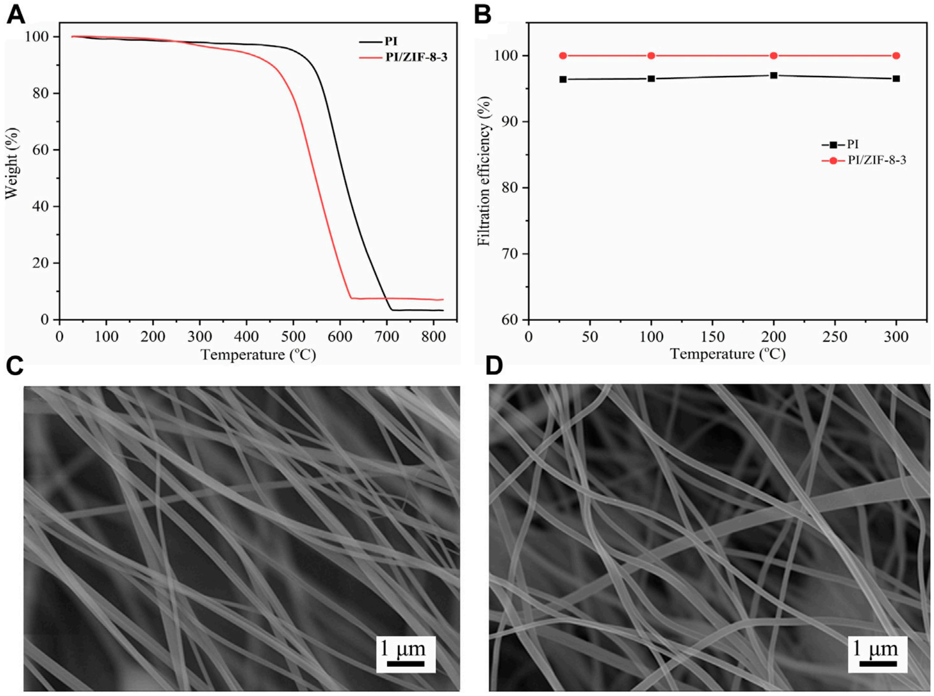

FIGURE 5 | (A) Thermogravimetric curves of PI and the ZIF-8-3/PI membranes. **(B)** Filtration efficiency of the PI nanofiber membranes and the ZIF-8-3/PI nanofiber membrane to $PM_{0.3}$ after being treated at different temperatures for 2 h. Scanning electron micrographs of the ZIF-8/PI nanofiber membranes before **(C)** and after **(D)** heat treatment (300°C).

proving that the ZIF-8/PI nanofiber membranes were the thermally stable.

3.4 Oil–Water Separation Performance of the PI/ZIF-8 Nanofiber Membranes

The wettability of membranes to water and oil is an important prerequisite for their application to oil–water separation. It can be seen from capillary utility that the lipophilic membrane will become more lipophilic with the increase of surface roughness (Cai et al., 2017). At the same time, the introduction of ZIF-8 will significantly reduce the pore size of the membrane (**Supplementary Figure S7**), and the smaller pore size is also conducive to improve the oil-water separation efficiency (Xu et al., 2018; Wu et al., 2021). The PI/ZIF-8 nanofiber membranes had a high surface roughness because of the introduction of ZIF-8, which changed the hydrophobicity of the PI nanofiber membranes (Zhang F et al., 2013). The original PI membrane was transformed into a hydrophobic PI membrane, and the contact angle was changed from 87° to 107° (**Figure 6C**). This is also due to the hydrophobicity of ZIF-8. The water droplets on the surface of the PI/ZIF-8 nanofiber membranes were spherical and could last for 60 s (**Figure 6A**). The PI/ZIF-8 nanofiber membranes had good self-cleaning performance because they had a great contact angle to all kinds of common liquids in daily life, such as milk, water, brine, and tea (**Figure 6B**).

An experimental separation device (**Figure 6E**) was designed to evaluate the oil–water separation performance of the membranes. Separation performance was calculated by **Eq. 2** as follows:

$$\eta = \frac{M_1}{M_0} \times 100\%, \tag{2}$$

where M_1 and M_o represent the quality of oil before and after separation, respectively. Owing to the superlipophilic property of the ZIF-8/PI nanofiber membranes, they could achieve highly efficient separation for various oily reagents. Separate 10 ml water oil mixed solution of oily reagents Petroleum ether, N-hexane, petroleum ether carrene and toluene respectively. According to **Figure 6D**, the filtration efficiency of dichloromethane can be as high as 99.85%, while that of other oily reagents can also be as high as 91.66, 93.71, 88.56%. As shown in **Figure 6F**, taking carrene as the filtration object, with the increase of ZIF-8 doping, the filtration efficiency is significantly improved, from 56.54% of pure PI to 99.85% of ZIF-8/PI. The different filtration efficiency may be due to the different viscosity of different oily reagents and the different blockage degree of fiber pores. Reflected in the oil flux is that the oil flux is positively correlated with the filtration efficiency. In order to study the fouling of oil on the membrane, the circulating performance of ZIF-8/PI membrane was tested, and it was found that its circulating filtration performance needs to be improved. Compared with the oil flux data in **Figure 6H**, with the increase of test times, the oil flux decreases, which also directly reflects the reduction of

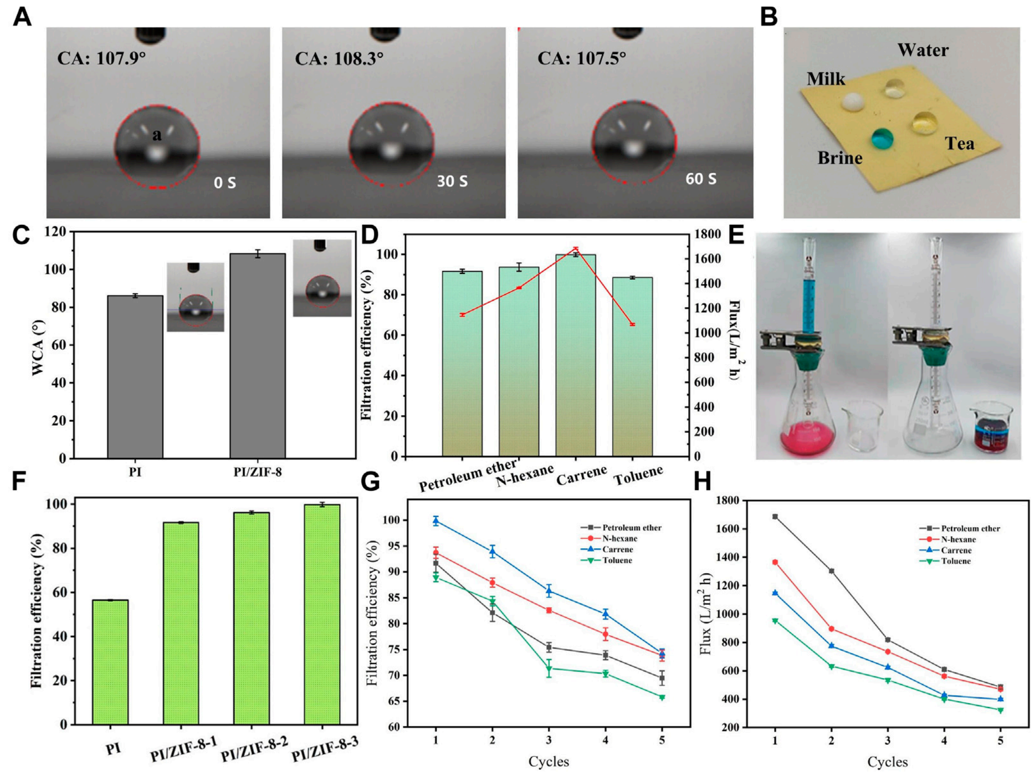

FIGURE 6 | (A) Contact angles of hydrophobic ZIF-8/PI nanofiber membranes. **(B)** Droplets of different pollution levels can be kept spherical. **(C)** The water-contact angles of both the PI nanofiber membranes and the PI/ZIF-8 nanofiber membranes were measured. **(D)** Water–oil separation efficiency. **(E)** Filter unit diagram. **(F)** The filtration efficiency of dichloromethane by PI membrane with different doping amount of ZIF-8. **(G)** Circulating filtration efficiency. **(H)** Circulating filtered oil flux.

filtration efficiency, as shown in **Figure 6G**. Therefore, it is necessary to further improve the recoverability and circulating filtration performance of the membrane in the follow-up research. Therefore, the ZIF-8/PI nanofiber membranes can be widely used in the separation of light oil–water mixture ($\rho_{oil} < \rho_{water}$).

4 CONCLUSION

PI/ZIF-8 nanofiber membranes for air filtration and oil–water separation were developed in this work, and its filtration mechanism was studied. The ZIF-8/PI nanofiber membranes obtained *via* doping and the co-spinning method exhibited excellent synergistic properties. Owing to the versatility of ZIF-8, the membranes could achieve super highly efficient filtration ($PM_{0.3}$, 100%; 6 L/min) and highly efficient oil-water separation (99.85%). In addition, it's a new developing idea to electrospin the ZIF-8 precursor on the polymer nanofibers using a coaxial process to surficializate the functional particles. The excellent comprehensive properties of the ZIF-8/PI nanofiber membranes, including their super highly efficient low-pressure air filtration, oil-water separation, and thermodynamic stability, indicate that they have broad industrial application prospects.

DATA AVAILABILITY STATEMENT

The original contributions presented in the study are included in the article/**Supplementary Material**, further inquiries can be directed to the corresponding authors.

AUTHOR CONTRIBUTIONS

YL: Data curation, Formal analysis, Investigation, Methodology, Project administration, Writing—original draft. DW, GX, LQ, YL, HG, LS, DL, MG, GL, JZ, and WW: Investigation and measurement. XZ and XL: Conceptualization, Funding acquisition, Resources, Supervision, Validation, Project administration, Writing—review and editing.

FUNDING

This work was supported by the National Natural Science Foundation of China (Nos. 51808328, 21801157, 61903235, and 22005160), the National Key Research and Development Program of China (No. 2019YFC1604600), and Shandong Provincial Natural Science Foundation (No. ZR2020QB069), the Major Scientific and Technological Innovation Project of Shandong (Nos. 2019JZZY020309, 2019JZZY010457), Qilu

University of Technology (Shandong Academy of Sciences) Science, Education and Industry integration innovation pilot Project (2020KJC-ZD07, 2020KJC-ZD19, and 2020KJC-CG04), Production education and research projects (2020-CXY36).

SUPPLEMENTARY MATERIAL

The Supplementary Material for this article can be found online at: https://www.frontiersin.org/articles/10.3389/fchem.2021.810861/full#supplementary-material

REFERENCES

Aidana, Y., Wang, Y., Li, J., Chang, S., Wang, K., and Yu, D.-G. (2021). *Curr. Drug Deliv.* 18, 1. doi:10.2174/1567201818666210215110359

An, S., Lee, J. S., Joshi, B. N., Jo, H. S., Titov, K., Chang, J.-S., et al. (2016). Freestanding Fiber Mats of Zeolitic Imidazolate Framework 7 via One-step, Scalable Electrospinning. *J. Appl. Polym. Sci.* 133, 43788. doi:10.1002/app.43788

Bai, W., Xu, J., Guan, M., He, Y., Xu, Y., and Lin, J. (2019). Preparation of Superhydrophobic Polyimide Microstructural Layer on Copper Mesh for Oil/water Separation. *J. Taiwan Inst. Chem. Eng.* 95, 71–77. doi:10.1016/j.jtice.2018.10.001

Bechelany, M., Drobek, M., Vallicari, C., Abou Chaaya, A., Julbe, A., and Miele, P. (2015). Highly Crystalline MOF-Based Materials Grown on Electrospun Nanofibers. *Nanoscale* 7, 5794–5802. doi:10.1039/c4nr06640e

Cai, Y., Chen, D., Li, N., Xu, Q., Li, H., He, J., et al. (2017). Nanofibrous Metal-Organic Framework Composite Membrane for Selective Efficient Oil/water Emulsion Separation. *J. Membr. Sci.* 543, 10–17. doi:10.1016/j.memsci.2017.08.047

Chen, F., Lu, Y., Liu, X., Song, J., He, G., Tiwari, M. K., et al. (2017). Table Salt as a Template to Prepare Reusable Porous PVDF-MWCNT Foam for Separation of Immiscible Oils/Organic Solvents and Corrosive Aqueous Solutions. *Adv. Funct. Mater.* 27, 1702926. doi:10.1002/adfm.201702926

Dai, X., Cao, Y., Shi, X., and Wang, X. (2016). The PLA/ZIF-8 Nanocomposite Membranes: The Diameter and Surface Roughness Adjustment by ZIF-8 Nanoparticles, High Wettability, Improved Mechanical Property, and Efficient Oil/Water Separation. *Adv. Mater. Inter.* 3, 1600725. doi:10.1002/admi.201600725

Dai, X., Li, X., and Wang, X. (2018). Morphology Controlled Porous Poly(lactic Acid)/zeolitic Imidazolate Framework-8 Fibrous Membranes with superior PM2.5 Capture Capacity. *Chem. Eng. J.* 338, 82–91. doi:10.1016/j.cej.2018.01.025

Doimoto, M., and Greiner, A. (2018). Sustainable Approach to Superhydrophobic Surfaces Based on Water-Born Electrospinning. *Macromol. Mater. Eng.* 303, 1700621. doi:10.1002/mame.201700621

Dou, Y., Zhang, W., and Kaiser, A. (2020). Electrospinning of Metal-Organic Frameworks for Energy and Environmental Applications. *Adv. Sci.* 7, 1902590. doi:10.1002/advs.201902590

Gao, X., Li, Z.-K., Xue, J., Qian, Y., Zhang, L.-Z., Caro, J., et al. (2019). Titanium Carbide Ti3C2Tx (MXene) Enhanced PAN Nanofiber Membrane for Air Purification. *J. Membr. Sci.* 586, 162–169. doi:10.1016/j.memsci.2019.05.058

Gong, G., Zhou, C., Wu, J., Jin, X., and Jiang, L. (2015). Nanofibrous Adhesion: The Twin of Gecko Adhesion. *ACS Nano* 9, 3721–3727. doi:10.1021/nn5063112

Hao, Z., Wu, J., Wang, C., and Liu, J. (2019). Electrospun Polyimide/Metal-Organic Framework Nanofibrous Membrane with Superior Thermal Stability for Efficient PM2.5 Capture. *ACS Appl. Mater. Inter.* 11, 11904–11909. doi:10.1021/acsami.8b22415

Ji, D., Fan, L., Li, L., Peng, S., Yu, D., Song, J., et al. (2019). Atomically Transition Metals on Self-Supported Porous Carbon Flake Arrays as Binder-free Air Cathode for Wearable Zinc-Air Batteries. *Adv. Mater.* 31, e1808267. doi:10.1002/adma.201808267

Lai, Q., Zhao, Y., Liang, Y., He, J., and Chen, J. (2016). *In Situ* Confinement Pyrolysis Transformation of ZIF-8 to Nitrogen-Enriched Meso-Microporous Carbon Frameworks for Oxygen Reduction. *Adv. Funct. Mater.* 26, 8334–8344. doi:10.1002/adfm.201603607

Li, D., Liu, H., Shen, Y., Wu, H., Liu, F., Wang, L., et al. (2020). Preparation of PI/PTFE-PAI Composite Nanofiber Aerogels with Hierarchical Structure and High-Filtration Efficiency. *Nanomaterials* 10, 1806. doi:10.3390/nano10091806

Li, L., Shang, L., Li, Y., and Yang, C. (2017). Three-layer Composite Filter media Containing Electrospun Polyimide Nanofibers for the Removal of fine Particles. *Fibers Polym.* 18, 749–757. doi:10.1007/s12221-017-1094-9

Li, M., Chen, F., Liu, C., Qian, J., Wu, Z., and Chen, Z. (2019). Electrospun Fibrous PTFE Supported ZnO for Oil-Water Separation. *J. Inorg. Organomet. Polym.* 29, 1738–1745. doi:10.1007/s10904-019-01135-x

Li, T.-T., Cen, X., Ren, H.-T., Wu, L., Peng, H.-K., Wang, W., et al. (2020). Zeolitic Imidazolate Framework-8/Polypropylene-Polycarbonate Barklike Meltblown Fibrous Membranes by a Facile *In Situ* Growth Method for Efficient PM2.5 Capture. *ACS Appl. Mater. Inter.* 12, 8730–8739. doi:10.1021/acsami.9b21340

Li, Y., Yin, X., Yu, J., and Ding, B. (2019). Electrospun Nanofibers for High-Performance Air Filtration. *Composites Commun.* 15, 6–19. doi:10.1016/j.coco.2019.06.003

Liang, W., Xu, Y., Li, X., Wang, X.-X., Zhang, H.-D., Yu, M., et al. (2019). Transparent Polyurethane Nanofiber Air Filter for High-Efficiency PM2.5 Capture. *Nanoscale Res. Lett.* 14, 361. doi:10.1186/s11671-019-3199-0

Lin, K.-Y. A., Chen, Y.-C., and Phattarapattamawong, S. (2016). Efficient Demulsification of Oil-In-Water Emulsions Using a Zeolitic Imidazolate Framework: Adsorptive Removal of Oil Droplets from Water. *J. Colloid Interf. Sci.* 478, 97–106. doi:10.1016/j.jcis.2016.05.057

Liu, C., Hsu, P.-C., Lee, H.-W., Ye, M., Zheng, G., Liu, N., et al. (2015). Transparent Air Filter for High-Efficiency PM2.5 Capture. *Nat. Commun.* 6, 6205. doi:10.1038/ncomms7205

Lv, D., Wang, R., Tang, G., Mou, Z., Lei, J., Han, J., et al. (2019). Ecofriendly Electrospun Membranes Loaded with Visible-Light-Responding Nanoparticles for Multifunctional Usages: Highly Efficient Air Filtration, Dye Scavenging, and Bactericidal Activity. *ACS Appl. Mater. Inter.* 11, 12880–12889. doi:10.1021/acsami.9b01508

Ma, S., Zhang, M., Nie, J., Tan, J., Song, S., and Luo, Y. (2019). Lightweight and Porous Cellulose-Based Foams with High Loadings of Zeolitic Imidazolate Frameworks-8 for Adsorption Applications. *Carbohydr. Polym.* 208, 328–335. doi:10.1016/j.carbpol.2018.12.081

Miao, Y.-E., Zhu, G.-N., Hou, H., Xia, Y.-Y., and Liu, T. (2013). Electrospun Polyimide Nanofiber-Based Nonwoven Separators for Lithium-Ion Batteries. *J. Power Sourc.* 226, 82–86. doi:10.1016/j.jpowsour.2012.10.027

Mosanenzadeh, S. G., Karamikamkar, S., Saadatnia, Z., Park, C. B., and Naguib, H. E. (2020). PPDA-PMDA Polyimide Aerogels with Tailored Nanostructure Assembly for Air Filtering Applications. *Separation Purif. Technology* 250, 117279. doi:10.1016/j.seppur.2020.117279

Ning, T., Zhou, Y., Xu, H., Guo, S., Wang, K., and Yu, D.-G. (2021). Orodispersible Membranes from a Modified Coaxial Electrospinning for Fast Dissolution of Diclofenac Sodium. *Membranes* 11, 802. doi:10.3390/membranes11110802

Ostermann, R., Cravillon, J., Weidmann, C., Wiebcke, M., and Smarsly, B. M. (2011). Metal-organic Framework Nanofibers Viaelectrospinning. *Chem. Commun.* 47, 442–444. doi:10.1039/c0cc02271c

Ren, L., Yu, Y., Yang, Y., Zhang, Q., Xiao, X., Liu, R., et al. (2019). Efficient Removal of Formaldehyde with ZIF-8 Growth on TiO2-Coated Activated Carbon Fiber Felts Prepared via Atomic Layer Deposition. *J. Mater. Sci.* 55, 3167–3180. doi:10.1007/s10853-019-04142-y

Tao, K., Cao, L., Lin, Y., Kong, C., and Chen, L. (2013). A Hollow Ceramic Fiber Supported ZIF-8 Membrane with Enhanced Gas Separation Performance Prepared by Hot Dip-Coating Seeding. *J. Mater. Chem. A.* 1, 13046–13049. doi:10.1039/c3ta13371k

Wang, B., Liang, W., Guo, Z., and Liu, W. (2015). Biomimetic Super-lyophobic and Super-lyophilic Materials Applied for Oil/water Separation: a New Strategy beyond Nature. *Chem. Soc. Rev.* 44, 336–361. doi:10.1039/c4cs00220b

Wang, L., Fang, M., Liu, J., He, J., Deng, L., Li, J., et al. (2015). The Influence of Dispersed Phases on polyamide/ZIF-8 Nanofiltration Membranes for Dye Removal from Water. *RSC Adv.* 5, 50942–50954. doi:10.1039/c5ra06185g

Wang, L., Feng, X., Ren, L., Piao, Q., Zhong, J., Wang, Y., et al. (2015). Flexible Solid-State Supercapacitor Based on a Metal-Organic Framework Interwoven by Electrochemically-Deposited PANI. *J. Am. Chem. Soc.* 137, 4920–4923. doi:10.1021/jacs.5b01613

Wang, M., Hou, J., Yu, D.-G., Li, S., Zhu, J., and Chen, Z. (2020). Electrospun Tri-layer Nanodepots for Sustained Release of Acyclovir. *J. Alloys Compounds* 846, 156471. doi:10.1016/j.jallcom.2020.156471

Wang, M., Li, D., Li, J., Li, S., Chen, Z., Yu, D.-G., et al. (2020). Electrospun Janus Zein-PVP Nanofibers Provide a Two-Stage Controlled Release of Poorly Water-Soluble Drugs. *Mater. Des.* 196, 109075. doi:10.1016/j.matdes.2020.109075

Wang, Q., Bai, Y., Xie, J., Jiang, Q., and Qiu, Y. (2016). Synthesis and Filtration Properties of Polyimide Nanofiber Membrane/carbon Woven Fabric Sandwiched Hot Gas Filters for Removal of PM 2.5 Particles. *Powder Technology* 292, 54–63. doi:10.1016/j.powtec.2016.01.008

Wang, Y., Zhang, H., Wang, X., Zou, C., Meng, B., and Tan, X. (2019). Growth of ZIF-8 Membranes on Ceramic Hollow Fibers by Conversion of Zinc Oxide Particles. *Ind. Eng. Chem. Res.* 58, 19511–19518. doi:10.1021/acs.iecr.9b04464

Wang, Z., Zhang, Y., Ma, X. Y. D., Ang, J., Zeng, Z., Ng, B. F., et al. (2020). Polymer/MOF-derived Multilayer Fibrous Membranes for Moisture-Wicking and Efficient Capturing Both fine and Ultrafine Airborne Particles. *Separation Purif. Technology* 235, 116183. doi:10.1016/j.seppur.2019.116183

Wu, M., Zhai, M., and Li, X. (2021). Adsorptive Removal of Oil Drops from ASP Flooding-Produced Water by Polyether Polysiloxane-Grafted ZIF-8. *Powder Technology* 378, 76–84. doi:10.1016/j.powtec.2020.09.068

Xu, S., Ren, L.-F., Zhou, Q., Bai, H., Li, J., and Shao, J. (2018). Facile ZIF-8 Functionalized Hierarchical Micronanofiber Membrane for High-Efficiency Separation of Water-In-Oil Emulsions. *J. Appl. Polym. Sci.* 135, t46462. doi:10.1002/app.46462

Yang, B., Ding, X., Zhang, M., Wang, L., and Huang, X. (2020). A Flexible, strong, Heat- and Water-Resistant Zeolitic Imidazolate Framework-8 (ZIF-8)/Aramid Nanofibers (ANFs) Composite Nanopaper. *Composites Commun.* 17, 192–196. doi:10.1016/j.coco.2019.12.008

Zhang, C., Yao, L., Yang, Z., Kong, E. S.-W., Zhu, X., and Zhang, Y. (2019). Graphene Oxide-Modified Polyacrylonitrile Nanofibrous Membranes for Efficient Air Filtration. *ACS Appl. Nano Mater.* 2, 3916–3924. doi:10.1021/acsanm.9b00806

Zhang, F., Zhang, W. B., Shi, Z., Wang, D., Jin, J., and Jiang, L. (2013). Nanowire-Haired Inorganic Membranes with Superhydrophilicity and Underwater Ultralow Adhesive Superoleophobicity for High-Efficiency Oil/Water Separation. *Adv. Mater.* 25, 4192–4198. doi:10.1002/adma.201301480

Zhang, L., Li, L., Wang, L., Nie, J., and Ma, G. (2020). Multilayer Electrospun Nanofibrous Membranes with Antibacterial Property for Air Filtration. *Appl. Surf. Sci.* 515, 145962. doi:10.1016/j.apsusc.2020.145962

Zhang R, R., Liu, C., Hsu, P.-C., Zhang, C., Liu, N., Zhang, J., et al. (2016). Nanofiber Air Filters with High-Temperature Stability for Efficient PM2.5 Removal from the Pollution Sources. *Nano Lett.* 16, 3642–3649. doi:10.1021/acs.nanolett.6b00771

Zhang, W., Shi, Z., Zhang, F., Liu, X., Jin, J., and Jiang, L. (2013). Superhydrophobic and Superoleophilic PVDF Membranes for Effective Separation of Water-In-Oil Emulsions with High Flux. *Adv. Mater.* 25, 2071–2076. doi:10.1002/adma.201204520

Zhang, X., Guo, S., Qin, Y., and Li, C. (2021). Functional Electrospun Nanocomposites for Efficient Oxygen Reduction Reaction. *Chem. Res. Chin. Univ.* 37, 379–393. doi:10.1007/s40242-021-1123-5

Zhang Y, Y., Yuan, S., Feng, X., Li, H., Zhou, J., and Wang, B. (2016). Preparation of Nanofibrous Metal-Organic Framework Filters for Efficient Air Pollution Control. *J. Am. Chem. Soc.* 138, 5785–5788. doi:10.1021/jacs.6b02553

Zheng, X., Zhang, Y., Zou, L., Wang, Y., Zhou, X., Yao, L., et al. (2020). Robust ZIF-8/alginate Fibers for the Durable and Highly Effective Antibacterial Textiles. *Colloids Surf. B: Biointerfaces* 193, 111127. doi:10.1016/j.colsurfb.2020.111127

Conflict of Interest: The authors declare that the research was conducted in the absence of any commercial or financial relationships that could be construed as a potential conflict of interest.

frontiers in Chemistry

PERSPECTIVE
published: 16 February 2022
doi: 10.3389/fchem.2022.854045

Degradation and Detection of Endocrine Disruptors by Laccase-Mimetic Polyoxometalates

Kun Chen[1,2]*, *Shengqiu Liu*[1,2] *and Qiongyu Zhang*[1,2]

[1]*South China Advanced Institute for Soft Matter Science and Technology, School of Molecular Science and Engineering, South China University of Technology, Guangzhou, China,* [2]*State Key Laboratory of Luminescent Materials and Devices and Guangdong Provincial Key Laboratory of Functional and Intelligent Hybrid Materials and Devices, South China University of Technology, Guangzhou, China*

Endocrine disruptors are newly identified water contaminants and immediately caught worldwide concern. An effort has been made to degrade endocrine disruptors in the water body by relying on laccase-assisted approaches, including laccase-mediated catalytic systems, immobilized laccase catalytic systems, and nano-catalytic systems based on atypical protein enzymes. Analogous to laccases, polyoxometalates (POMs) have a similar size as these enzymes. They are also capable of using oxygen as an electron acceptor, which could assist the removal of endocrine disruptors in water. This perspective begins with a brief introduction to endocrine disruptors and laccases, summarizes current approaches employing laccases, and focuses on the nano-catalytic systems that mimic the function of laccases. Among the inorganic nanoparticles, POMs meet the design requirements and are easy for large-scale production. The catalytic performance of POMs in water treatment is highlighted, and an example of using polyoxovanadates for endocrine disruptor degradation is given at the end of this perspective. Exploring laccase-mimetic POMs will give key insights into the degradation of emergent water contaminants.

Keywords: endocrine disruptors, polyoxometalates (POMs), water contaminants, laccase-mimetic degradation, nanozymes

Edited by:
Dejin Zang,
Tsinghua University, China

Reviewed by:
Zonghai Sheng,
Chinese Academy of Sciences (CAS), China
Jiahui Chen,
Argonne National Laboratory (DOE), United States

***Correspondence:**
Kun Chen
mschenk@scut.edu.cn

Specialty section:
This article was submitted to Analytical Chemistry, a section of the journal Frontiers in Chemistry

Received: *13 January 2022*
Accepted: *31 January 2022*
Published: *16 February 2022*

Citation:
Chen K, Liu S and Zhang Q (2022) Degradation and Detection of Endocrine Disruptors by Laccase-Mimetic Polyoxometalates. Front. Chem. 10:854045. doi: 10.3389/fchem.2022.854045

INTRODUCTION

Endocrine disruptors are emergent water contaminants which frequently found in every aspect of human life, including some plastic bottles and containers, fungicides, disinfectants, anti-viral agents, pharmaceutical drugs for oral analgesic and mild anesthetic, and cosmetics and skin care products (**Figure 1A**) (Bilal et al., 2019a). Some of the endocrine disruptors are phenol products that are analogous to natural hormones due to their capability of acting like natural hormones and disrupting the endocrine system (Barrios-Estrada et al., 2018). Endocrine disruptors receive more attention than other phenols because of their appearance in various sources and unique interferences with natural hormones in interaction with corresponding receptors that result in an altered cellular signal and subsequent a failure in the body. The persistence of endocrine disruptors in water bodies has raised particular concern because of the widespread and continuing sewage discharge.

Enzymatic degradation approaches have been developed for addressing this growing issue (Bilal et al., 2019b). Laccase catalyzed reaction effectively removes many kinds of trace pollutants, which are difficult to degrade in wastewater, especially some phenolic endocrine disruptors (Mate and Alcalde, 2017; Janusz et al., 2020). Laccases catalyze one-electron oxidation of a broad range of these

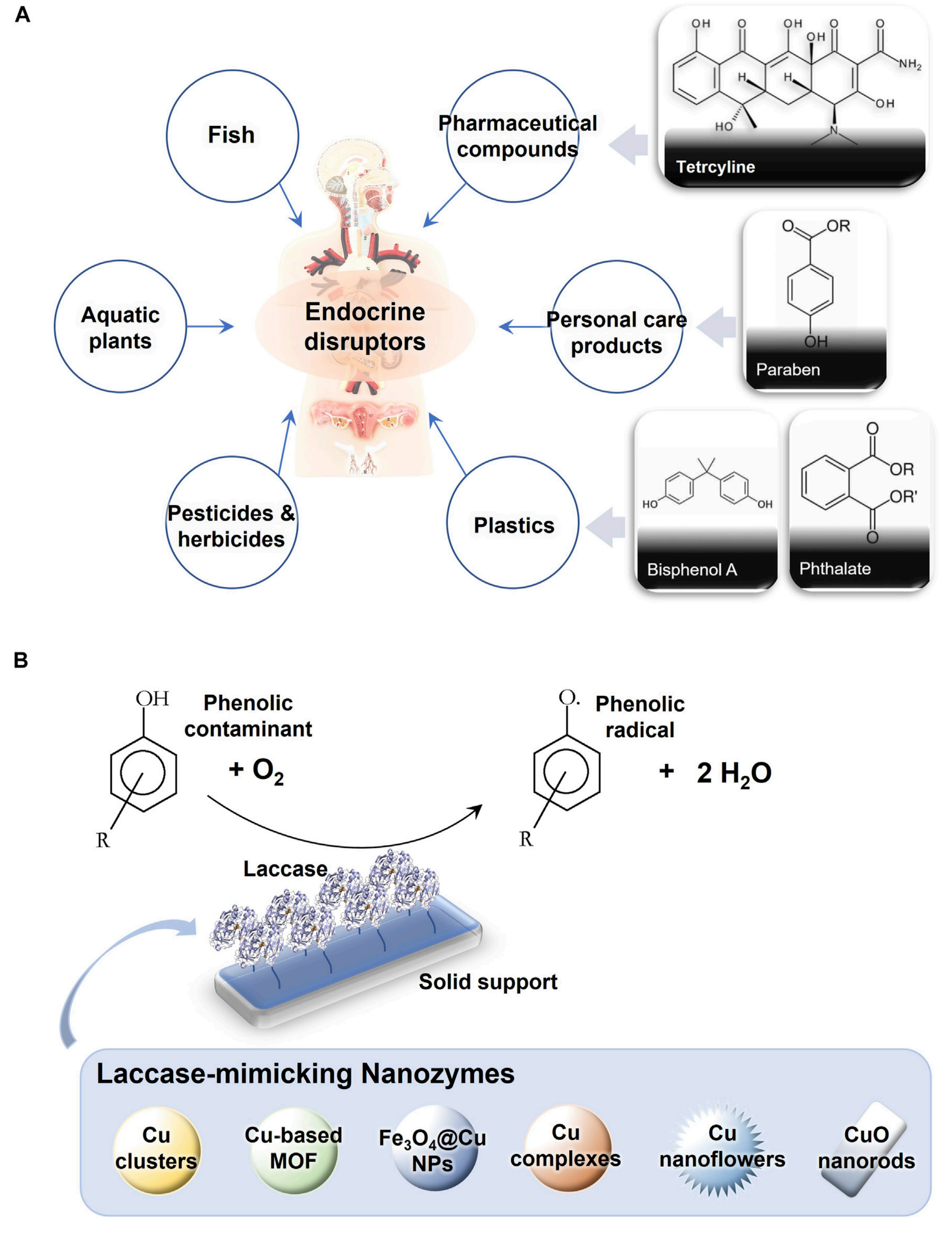

FIGURE 1 | (A) Common sources and typical structures of endocrine disruptors in water environment. **(B)** Scheme of immobilized laccase-assisted degradation of phenolic contaminants and the representative nanozymes that have been reported the catalytic activities of mimicking laccase.

phenol substrates and release water as the by-product (**Figure 1B**). As an eco-friendly and versatile biocatalyst, laccases have been applied in enzymatic bioremediation of the water bodies (Sharma et al., 2018; Morsi et al., 2020). To extend the using range in the harsh environment, a set of nanosystems, mostly nanozymes, are designed to mimic the function of laccases in wastewater treatment (Zhou et al., 2017). Polyoxometalates (POMs) are nanosized soluble molecular metal-oxo clusters with well-defined structures. Each metal-oxo cluster comprises an array of corner-sharing and edge-sharing pseudo-octahedral MO_6 (M = Mo, W, V, Nb, etc.) units (Gumerova and Rompel, 2018). POMs have demonstrated promising catalytic activities over a wide range of catalysis fields (Anyushin et al., 2018). POMs for constructing the nanocatalytic system can be directly used to catalyze the same substrates as laccases. Meanwhile, POMs are much more cost-effective for production and robust for working at high temperature, high pressure, and extreme pH conditions (Liu et al., 2020). In this perspective, the current development in this field is briefly summarized, and the scientific and technological challenges are outlined. Exploring laccase-mimetic POMs would spark future research interest in advancing the technic for the removal of emergent water contaminants.

Endocrine Disruptors in Water

Environmental endocrine disruptors, a type of pollutant in water, are a classification of exotic chemicals that alter or interact with the endocrine systems of vertebrates and invertebrates (**Figure 1A**). Endocrine disruptors belong to the endocrine organic chemicals, but differ from natural phytoestrogens in that they mimic, block, or alter the actions of normal hormones (Landrigan et al., 2018). Endocrine disruptors have shown the potential to interact with biological systems, such as the hormonal system and nervous system, and cause various complications, such as neurodevelopmental toxicity and Parkinson's disease (Barrios-Estrada et al., 2018). Endocrine disruptors have a variety of mechanisms of action. One pathway is through the direct interaction with a given estrogen receptor, which may interfere with or regulate downstream gene expression. For example, most endocrine disruptor-related reproductive and developmental defects are thought to be due to endocrine disruptors interfering with the function of estrogen receptors and androgen receptors, thereby interfering with the regular activity of estrogen and androgen ligands (Barrios-Estrada et al., 2018). In addition to sex steroid receptors, the estrogen receptor superfamily includes transcription factors that play a key role in integrating complex metabolic homeostasis and development. The ability of endocrine disruptors to interact with these estrogen receptors is supported and explained by metabolic disorders in experimental and epidemiological studies (Barrios-Estrada et al., 2018). During early development, the exposure of even extremely low doses of endocrine disruptors will likely lead to permanent impairments in fetus organ function and increase their disease risk. In addition, many endocrine disruptors are also developmental neurotoxicants and can be stored in animal and human fats for years (Schug et al., 2011). These chemicals include bisphenol A, phthalates, and dioxins.

Water pollution has become a pressing issue as populations grow and industrial production expands. This growing problem is often linked to poor wastewater management, outdated infrastructure, factories, and limited treatment strategies. Most endocrine disruptors come from products used to combat unfavorable wildlife and agricultural threats, such as pesticides and fungicides, as well as various synthetic products used in the plastics industry (bisphenol A or phthalates), insulation materials (polychlorinated biphenyls), and brominated flame retardants (Bilal et al., 2019a). These chemicals are manufactured in the high output of millions of kilograms per year and have caused substantial impacts on our daily life. They are everywhere around people, in consumer products such as perfumes, shampoos, soaps, plastics, and food containers. Another problem associated with such chemicals is that they degrade very slowly or are not photodegradable (Bilal et al., 2019b). Therefore, endocrine disruptors have become a significant public health problem globally due to their high stability, low degradation, high toxicity, and persistence in the environment. Biological technics for the degradation of these pollutants using oxidoreductases are a promising area of research (Cabana et al., 2007a; Cabana et al., 2007b; Torres-Duarte et al., 2012).

Laccase-Assisted Detection and Degradation

Laccase is a group of enzymes with a wide taxonomic distribution that belongs to the copper oxidases (MCOs) superfamily (Mate and Alcalde, 2017; Janusz et al., 2020). MCOs reduce oxygen molecules to water without releasing harmful substances, including those species often generated during oxygen reduction (**Figure 1B**), such as the partially reduced products of O_2, reactive oxygen species (ROS). Laccases are widely distributed in nature. Higher plants, bacteria, lichens, sponges, and fungi, especially white rot fungi, can produce laccases with different biological functions and substrate diversity (Mate and Alcalde, 2017). Aromatic compounds (e.g., catechol and hydroquinone, methoxy substituted phenols, diamines, and phenylthiols), organometals ($[Fe(EDTA)]^{2-}$ and $[W(CN)_8]^{4-}$), and metal ions are all the substrates of laccases.

The remarkable broad substrate specificity of laccase aroused the attention of those who are worried about the environment. Over the past few decades, laccases have been used as a biocatalyst to detect and reduce pollutants by removing electrons from these organic substrates and blocking the entry of these contaminants into the water bodies. The laccase-involving enzymolysis approach has been used in different industrial applications to replace traditional chemical processes in the paper, textile, cosmetics, paint, pulp, furniture, and pharmaceutical factories (Sharma et al., 2018; Morsi et al., 2020). To develop a robust laccase-based biocatalytic platform, the enzymes are normally immobilized on a support matrix to address the limitations related to enzyme reusability and recycling (Lassouane et al., 2019; Zhou et al., 2021). The stability and resistance of laccase (e.g., isolated from the basidiomycete *Trametes versicolor*) to protease is increased by the immobilization on a solid carrier (Sharma et al., 2018). Several methods for immobilizing enzymes have been developed, such as covalently attaching to solid carriers, solid carrier adsorption methods, embedding in polymeric gels, cross-linking with biofunctional reagents, and embedding in solid carriers (Bilal et al., 2017; Shakerian et al., 2020). Laccase immobilization is a promising water purification technology. Compared with free laccase, the reusability of immobilized laccase makes it more advantageous in the practical application of water purification (Lassouane et al., 2019; Lou et al., 2020; Masjoudi et al., 2021).

In recent years, nanocarriers have been engineered to immobilize and support enzymes, which greatly advanced traditional enzyme-immobilization methods. Many enzyme systems based on nanostructures are designed and used to detect a variety of organic pollutants and degrade them efficiently into harmless smaller intermediates (Alarcón-Payán et al., 2017; Chen C. et al., 2018; Masjoudi et al., 2021; Qiu et al., 2021). Furthermore, the attachment of laccase to its nanocarrier not only reduces its mobilization, but also increases activity and stability of the enzyme (Koyani and Vazquez-Duhalt, 2016; Costa et al., 2019). It was reported that the electrode modified with laccase-immobilizing polyaniline/magnetic graphene exhibited superior electrical properties, high detection sensitivity to hydroquinone, low detection limit, and wide linear range (Lou et al., 2020). Many carrier nanomaterials for laccase immobilization have been engineered. Co-immobilization of laccase and 2,2-binamine-di-3-ethylbenzothiazolin-6-sulfonic acid (ABTS) onto amino-functionalized ionic liquid-modified magnetic chitosan nanoparticles improves the capability of biocatalyst for the pollutant removal of bisphenol A, indole, and anthracene (Qiu et al., 2021). Functionalized multi-walled carbon nanotubes (CNTs) are used as nanocarriers for laccase immobilization to enhance the biocatalytic sustainability of laccase (Costa et al., 2019). In another work, laccase was also cross-linked onto hollow mesoporous carbon spheres (HMCs) for antibiotic degradation and removal from the aqueous phase (Shao et al., 2019). A biomimetic dynamic membrane (BDM) fabricated by using carbon nanotubes (CNTs) and laccases (Chen et al., 2019; Bilal et al., 2021), was proved to be very effective for wastewater treatment (Shao et al., 2019). Quite a few reviews have summarized the progress in nanoengineered laccases-advanced biotechnology (Bilal et al., 2021).

The support nanomaterials used for enzyme-immobilization are expected to be low cost and have a large enough surface area to avoid diffusion limitations of substrates and products of enzyme reaction. Meanwhile, the catalytic efficiency of the enzyme is anticipated to be improved by the immobilization to a solid surface. In general, enzymes are immobilized in various ways: binding to affinity labels, adsorption on substrates, and covalently anchoring to carriers (Shakerian et al., 2020). The immobilization model of laccase with its carriers greatly impacts on the properties of the enzyme (Bilal et al., 2017). At least, immobilization should not affect the conformation and activity of the enzyme, and the activity of immobilized enzymes should be retained for a longer time than that of free enzymes. The degradation of foreign biological compounds using immobilized enzymes may prove economical because of their enhanced stability and reusability. However, the immobilized enzyme cannot be recycled and reused too many times. Sometimes, intracellular enzymes do not work well in cell-free systems. Therefore, a group of nanomaterials was engineered to mimic the function of protein enzymes (Chen et al., 2019; Bilal et al., 2021), a relatively new strategy we are going to discuss in the next part.

Laccase-Mimicking Nanozymes

Nanozymes are a class of nanomaterials that mimic and achieve the function of natural enzymes (**Figure 1B**) (Zhou et al., 2017). Nanozyme-based water treatment methods have many advantages over protein enzymes (Tian et al., 2020). Nanozymes are able to operate both at high and low pollutant concentrations, which reduces sludge generation. In addition, nanozymes can work catalytically to a wide range of pollutants with low energy inputs. Although protein enzyme has many advantages, it should be pointed out that it also has some challenges, such as the high catalyst cost, low reusability, and tendence to deactivation. Compared with protein enzymes, nanozymes are attractive for both applied and fundamental research. A nanomaterial based on guanosine monophosphate coordinated copper mimics the activity of laccase and converts a diverse range of phenol-containing substrates as laccase, including catechol, hydroquinone, epinephrine, and naphthol (Liang et al., 2017). While the cost of this nanomaterial is about 2400-fold lower than that of laccase, its stability is overwhelming. Normally, these laccase mimics are nanozymes formed by copper and biological molecules, such as guanosine monophosphate, dipeptide, guanine-rich ssDNA, and proteins (Wang et al., 2019; Rashtbari and Dehghan, 2021; Tran et al., 2021; Xu et al., 2021). In the last two years, inorganic nanozymes appeared in the form of Cu-base metal-organic framework (MOF) (Shams et al., 2019; Hu et al., 2021) or CuO nanorods (Alizadeh et al., 2020) for efficient dye detection and phenolic pollutant degradation. Apparently, inorganic nanozymes are more robust than the ones involving biomolecules. They are abiotic and much stable at high salt, high temperature, and extreme pH and could be stored for a very long time.

Enzyme-Mimicking POMs and POMs in Water Treatment

Polyoxometalates (POMs) are a kind of inorganic molecular materials with well-defined structures and mono-dispersity (**Figure 2A**). These nano-scaled clusters are composed of up to hundreds of face-, edge-, and/or angular shared bonds of metal-oxo polyhedral units. Most POMs can undergo reversible multi-electron redox reactions without structural change, which is a fantastic property in catalysis. Structures of POMs are rich and varying in morphisms and are versatile for co-assembly with other building blocks to construct diverse catalytic platforms. Some of them have nanopore or nanochannel structures with strong and/or selective affinity for guest molecules and/or ions, which makes them advantageous for size-selective catalysis. At the same time, POM surfaces are rich in oxygen, hydroxyl, and/or water ligands, suggesting that POM-based materials are excellent candidates for biomimetic applications. Over the last decades, POMs have demonstrated their promising biological activities, such as antitumoral (Bijelic et al., 2019), antimicrobial (Xu et al., 2020; Chen et al., 2021; Chen et al., 2022), insulin-sensitizing (Chen et al., 2020), immune-enhancing activities (Li et al., 2021; Li et al., 2022). In virtue of their structural diversity and physicochemical properties, POM-based nanomaterials exert oxidoreductase-mimicking activities, including oxidase,

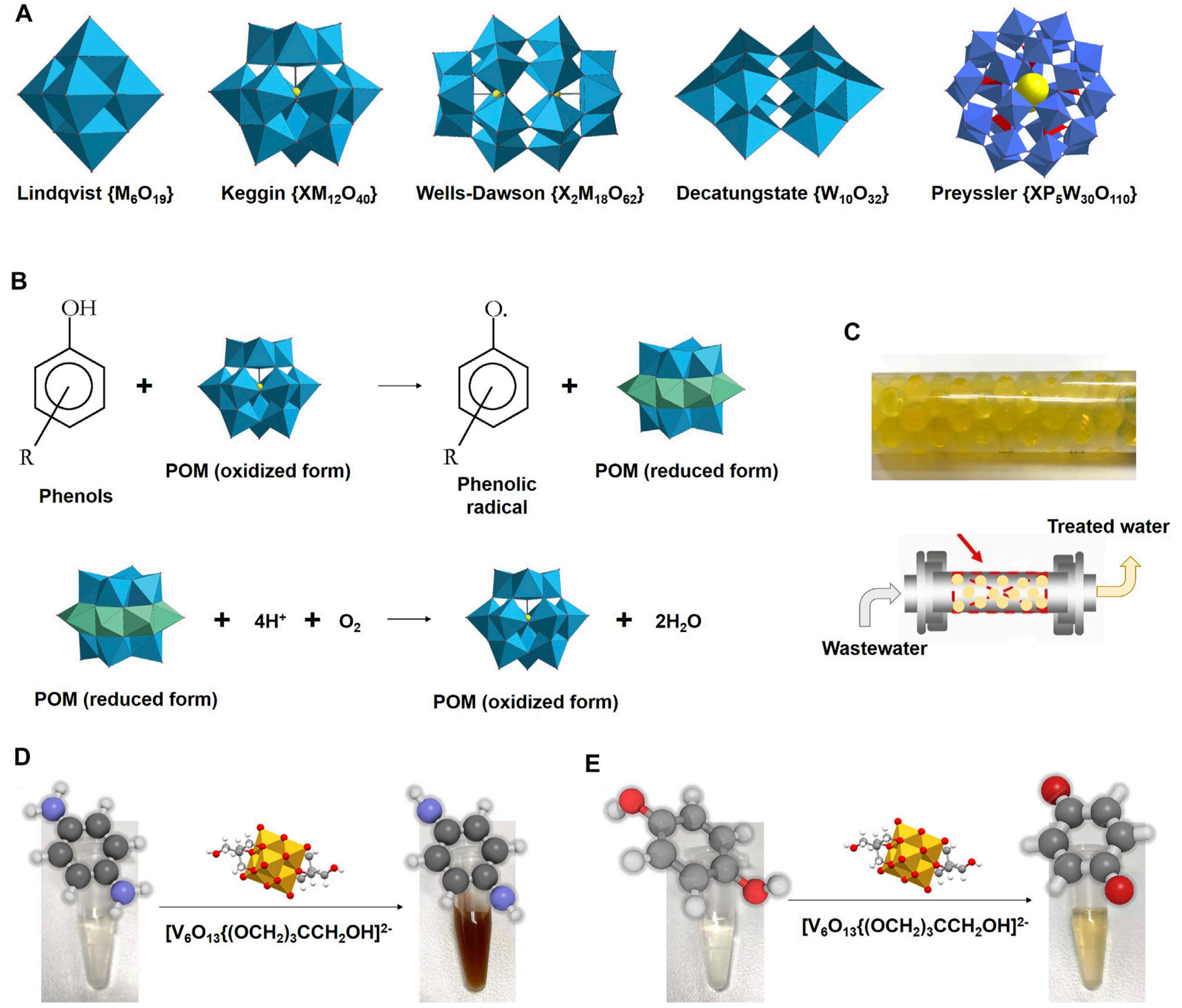

FIGURE 2 | (A) Conventional types of polyoxometalates (M = Mo, W, V, Nb; X = heteroatom). **(B)** Scheme of degradation of phenolic contaminants by laccase-mimicking POMs. **(C)** Scheme of a batch reactor with POV hybrid as a quasi-homogeneous catalyst for degradation of emergent water contaminants. Scheme of laccase-like catalytic activity of POV hybrids for oxidating *p*-phenylenediamine **(D)** and hydroquinone **(E)**.

peroxidase (Chen K. et al., 2018; Jia et al., 2019), and catalase (Yadav and Singh, 2021). Compared with other nanomaterials, POMs are advantageous in their well-defined composition and molecular structure, as well as their economical production costs and mass production.

In addition, POM-based nanomaterials have been successfully applied in wastewater treatment. An electrocatalyst was prepared with polyoxometalate (POM) as a molecular platform on a large scale by a one-step pyrolysis method and showed its prospects in directly usage in seawater (Ma et al., 2017). A series of Ln/Cu-POMs were used for wastewater treatment with rapid adsorption and excellent selective separation of cationic dyes from aqueous solutions (Yi et al., 2015). Efficient heterogeneous photocatalytic materials, nanosized and bimodal porous polyoxotungstate-anatase TiO_2 composites, were prepared and exhibited visible-light photocatalytic activities in degrading organophosphorus pesticides in aqueous solution (Li et al., 2005). POM-based hybrid materials showed great potential for the removal of contaminants, such as phthalates and bisphenol A (**Figure 2B**), from wastewater (Zou et al., 2021; Huo et al., 2022). These POM-based hybrid materials showed high stability and long duration in either continuous or separated modes for effective water remediation (Galiano et al., 2021; Lai et al., 2021). In addition, a voltametric sensor was prepared with the aid of POMs for the determination of simazine in wastewater samples (Ertan et al., 2016). Such hybrid materials combined with POMs offer new insights for designing functional materials with low cost and high efficiency for wastewater treatment.

Challenges and Perspective

In recent years, POM has played a salient role in catalysis and showed its successful application in industrial catalysis, especially in the catalytic degradation of emerging contaminants in wastewater treatment. Structural diversity and excellent redox properties make POMs a vast treasure trove of active catalysts with intrinsic enzyme mimicking activities. The recent development of POM-based nanomaterials has created a new way for the development of artificial enzymes with high catalytic activity. Yet, people need to realize that nanozymes, including POMs, have not reached the catalytic activity as high as natural enzymes. There are several scientific and technologic challenges faced by POMs in catalytic degradation of endocrine disruptors. Since catalytic reactions involving nanozymes take place on the surface of the nanomaterials, surface modification represents an effective way to improve nanozyme activity. POMs are highly tailorable. Specifically, the capacity for POMs will be enlarged by the covalent or non-covalent interaction of POMs with a limitless range of organic moieties (Jia et al., 2017; Jia et al., 2018). POM organic derivatives have been shown to be able to assemble into a variety of hierarchical nanostructures applicable to different needs while maintaining their catalytic properties (Chen K. et al., 2018). Companied with low activity, the lack of reaction-specificity is another concern related to nanozymes, including POMs. POMs are able to catalyze the oxidation of a wide range of substrates and act as enzymes. However, the catalytic reactions involving nanozyme systems are typically more complex than natural enzymes. Laccase catalyzes substrate oxidation coupled to the four-electron reduction of molecular oxygen to water without releasing these partially reduced O_2 products ROS. While the oxidation catalyzed by POMs may be coupled to the oxygen reduction to produce superoxides, $\bullet O_2^-$ anions (Lai et al., 2021), in the real and complicated water environment. POMs are suitable for facile post-functionalization with other organic or inorganic molecules, which is an effective approach to design advanced catalytic materials. With rationale functionalization, POMs are expected to gain novel and improved physicochemical properties relevant to the development of novel catalysts for wastewater treatment in the near future.

DISCUSSION

Polyoxovanadates (POVs) are a subclass of POMs and have been described as bioinorganic drugs (Aureliano et al., 2021). POVs have shown different bioactivities not observed for monovanadate alone. Hybrid-type hexavanadate is one of the earliest organometallic POV derivatives that has been attracting research attention since its isolation. POV derivatives $[V_6{}^{V}O_{13}\{(OCH_2)_3CCH_2OH\}_2]^{2-}$ are redox stable and have been applied in homogeneous catalysis, materials science, and energy storage (Anyushin et al., 2020). Hybrid-type hexavanadates could be obtained through a simple, nontoxic, and one-pot method and showed favorable enzyme-like catalytic activity for oxidating phenylenediamine and hydroquinone (**Figure 2**). This oxidation could be conducted in a batch reactor with POV hybrid as a quasi-homogeneous catalyst (**Figure 2C**). $[V_6{}^{V}O_{13}\{(OCH_2)_3CCH_2OH\}_2]^{2-}$ is a versatile platform that can undergo DMAP-catalyzed esterification reactions with acid anhydrides to generate functional hybrid materials in catalysis. Following the etherate method for preparation and separation, solution stable POV hybrids were obtained and showed intrinsic laccase-like activities for catalyzing the oxidation of laccase substrate endocrine-disrupting *p*-phenylenediamine and hydroquinone to produce typical color changes (**Figures 2D,E**). These features POM-based hybrid catalysis as a potentially cost-effective approach for degradation of emergent water contaminants.

DATA AVAILABILITY STATEMENT

The original contributions presented in the study are included in the article, further inquiries can be directed to the corresponding author.

AUTHOR CONTRIBUTIONS

KC and SL participated in the preparation of the original draft. KC and QZ participated in revision and editing. All authors listed have made a substantial, direct, and intellectual contribution to the work and approved it for publication.

FUNDING

The work is supported financially by the National Natural Science Foundation of China (22101086) and the Natural Science Foundation of Guangdong Province (2021A1515010271).

REFERENCES

Alarcón-Payán, D. A., Koyani, R. D., and Vazquez-Duhalt, R. (2017). Chitosan-based Biocatalytic Nanoparticles for Pollutant Removal from Wastewater. *Enzyme Microb. Tech.* 100, 71–78. doi:10.1016/j.enzmictec.2017.02.008

Alizadeh, N., Ghasemi, S., Salimi, A., Sham, T.-K., and Hallaj, R. (2020). CuO Nanorods as a Laccase Mimicking Enzyme for Highly Sensitive Colorimetric and Electrochemical Dual Biosensor: Application in Living Cell Epinephrine Analysis. *Colloids Surf. B: Biointerfaces* 195, 111228. doi:10.1016/j.colsurfb.2020.111228

Anyushin, A. V., Sap, A., Quanten, T., Proost, P., and Parac-Vogt, T. N. (2018). Selective Hydrolysis of Ovalbumin Promoted by Hf(IV)-Substituted Wells-Dawson-Type Polyoxometalate. *Front. Chem.* 6, 614. doi:10.3389/fchem.2018.00614

Anyushin, A. V., Kondinski, A., and Parac-Vogt, T. N. (2020). Hybrid Polyoxometalates as Post-Functionalization Platforms: From Fundamentals to Emerging Applications. *Chem. Soc. Rev.* 49, 382–432. doi:10.1039/C8CS00854J

Aureliano, M., Gumerova, N. I., Sciortino, G., Garribba, E., Rompel, A., and Crans, D. C. (2021). Polyoxovanadates with Emerging Biomedical Activities. *Coord. Chem. Rev.* 447, 214143. doi:10.1016/j.ccr.2021.214143

Barrios-Estrada, C., de Jesús Rostro-Alanis, M., Muñoz-Gutiérrez, B. D., Iqbal, H. M. N., Kannan, S., and Parra-Saldívar, R. (2018). Emergent Contaminants: Endocrine Disruptors and Their Laccase-Assisted Degradation - A Review. *Sci. Total Environ.* 612, 1516–1531. doi:10.1016/j.scitotenv.2017.09.013

Bijelic, A., Aureliano, M., and Rompel, A. (2019). Polyoxometalates as Potential Next-Generation Metallodrugs in the Combat against Cancer. *Angew. Chem. Int. Ed.* 58 (10), 2980–2999. doi:10.1002/anie.201803868

Bilal, M., Asgher, M., Parra-Saldivar, R., Hu, H., Wang, W., Zhang, X., et al. (2017). Immobilized Ligninolytic Enzymes: An Innovative and Environmental Responsive Technology to Tackle Dye-Based Industrial Pollutants - A Review. *Sci. Total Environ.* 576, 646–659. doi:10.1016/j.scitotenv.2016.10.137

Bilal, M., Adeel, M., Rasheed, T., Zhao, Y., and Iqbal, H. M. N. (2019a). Emerging Contaminants of High Concern and Their Enzyme-Assisted Biodegradation - A Review. *Environ. Int.* 124, 336–353. doi:10.1016/j.envint.2019.01.011

Bilal, M., Rasheed, T., Nabeel, F., Iqbal, H. M. N., and Zhao, Y. (2019b). Hazardous Contaminants in the Environment and Their Laccase-Assisted Degradation - A Review. *J. Environ. Manage.* 234, 253–264. doi:10.1016/j.jenvman.2019.01.001

Bilal, M., Ashraf, S. S., Cui, J., Lou, W.-Y., Franco, M., Mulla, S. I., et al. (2021). Harnessing the Biocatalytic Attributes and Applied Perspectives of Nanoengineered Laccases-A Review. *Int. J. Biol. Macromolecules* 166, 352–373. doi:10.1016/j.ijbiomac.2020.10.195

Cabana, H., Jiwan, J.-L. H., Rozenberg, R., ElisashviliPenninckx, V. M., Penninckx, M., Agathos, S. N., et al. (2007a). Elimination of Endocrine Disrupting Chemicals Nonylphenol and Bisphenol A and Personal Care Product Ingredient Triclosan Using Enzyme Preparation from the White Rot Fungus *Coriolopsis Polyzona*. *Chemosphere* 67, 770–778. doi:10.1016/j.chemosphere.2006.10.037

Cabana, H., Jones, J. P., and Agathos, S. N. (2007b). Preparation and Characterization of Cross-Linked Laccase Aggregates and Their Application to the Elimination of Endocrine Disrupting Chemicals. *J. Biotechnol.* 132, 23–31. doi:10.1016/j.jbiotec.2007.07.948

Chen, C., Sun, W., Lv, H., Li, H., Wang, Y., and Wang, P. (2018). Spacer Arm-Facilitated Tethering of Laccase on Magnetic Polydopamine Nanoparticles for Efficient Biocatalytic Water Treatment. *Chem. Eng. J.* 350, 949–959. doi:10.1016/j.cej.2018.06.008

Chen, W., Mo, J., Du, X., Zhang, Z., and Zhang, W. (2019). Biomimetic Dynamic Membrane for Aquatic Dye Removal. *Water Res.* 151, 243–251. doi:10.1016/j.watres.2018.11.078

Chen, K., Bayaguud, A., Li, H., Chu, Y., Zhang, H., Jia, H., et al. (2018). Improved Peroxidase-Mimic Property: Sustainable, High-Efficiency Interfacial Catalysis with H2O2 on the Surface of Vesicles of Hexavanadate-Organic Hybrid Surfactants. *Nano Res.* 11 (3), 1313–1321. doi:10.1007/s12274-017-1746-5

Chen, K., Jia, H., Liu, Y., Yin, P., and Wei, Y. (2020). Insulin-Sensitizing Activity of Sub-Nanoscaled Polyalkoxyvanadate Clusters. *Adv. Biosys.* 4 (5), 1900281. doi:10.1002/adbi.201900281

Chen, K., Yu, Q., Liu, Y., and Yin, P. (2021). Bacterial Hyperpolarization Modulated by Polyoxometalates for Solutions of Antibiotic Resistance. *J. Inorg. Biochem.* 220, 111463. doi:10.1016/j.jinorgbio.2021.111463

Chen, K., Liu, Y., Li, M., Liu, L., Yu, Q., and Wu, L. (2022). Amelioration of Enteric Dysbiosis by Polyoxotungstates in Mice Gut. *J. Inorg. Biochem.* 226, 111654. doi:10.1016/j.jinorgbio.2021.111654

Costa, J. B., Lima, M. J., Sampaio, M. J., Neves, M. C., Faria, J. L., Morales-Torres, S., et al. (2019). Enhanced Biocatalytic Sustainability of Laccase by Immobilization on Functionalized Carbon Nanotubes/Polysulfone Membranes. *Chem. Eng. J.* 355, 974–985. doi:10.1016/j.cej.2018.08.178

Ertan, B., Eren, T., Ermiş, İ., Saral, H., Atar, N., and Yola, M. L. (2016). Sensitive Analysis of Simazine Based on Platinum Nanoparticles on Polyoxometalate/Multi-Walled Carbon Nanotubes. *J. Colloid Interf. Sci.* 470, 14–21. doi:10.1016/j.jcis.2016.02.036

Galiano, F., Mancuso, R., Carraro, M., Bundschuh, J., Hoinkis, J., Bonchio, M., et al. (2021). A Polyoxometalate-Based Self-Cleaning Smart Material with Oxygenic Activity for Water Remediation with Membrane Technology. *Appl. Mater. Today* 23, 101002. doi:10.1016/j.apmt.2021.101002

Gumerova, N. I., and Rompel, A. (2018). Synthesis, Structures and Applications of Electron-Rich Polyoxometalates. *Nat. Rev. Chem.* 2 (2), 0112. doi:10.1038/s41570-018-0112

Hu, C. Y., Jiang, Z. W., Huang, C. Z., and Li, Y. F. (2021). Cu2+-modified MOF as Laccase-Mimicking Material for Colorimetric Determination and Discrimination of Phenolic Compounds with 4-aminoantipyrine. *Microchim. Acta* 188 (8), 272. doi:10.1007/s00604-021-04944-5

Huo, Y., Zhang, D., Wu, J., Wang, X., Wang, X., Shao, C., et al. (2022). Oxidation of Phthalate Acid Esters Using Hydrogen Peroxide and Polyoxometalate/Graphene Hybrids. *J. Hazard. Mater.* 422, 126867. doi:10.1016/j.jhazmat.2021.126867

Janusz, G., Pawlik, A., Świderska-Burek, U., Polak, J., Sulej, J., Jarosz-Wilkołazka, A., et al. (2020). Laccase Properties, Physiological Functions, and Evolution. *Ijms* 21 (3), 966. doi:10.3390/ijms21030966

Jia, H., Li, Q., Bayaguud, A., She, S., Huang, Y., Chen, K., et al. (2017). Tosylation of Alcohols: An Effective Strategy for the Functional Group Transformation of Organic Derivatives of Polyoxometalates. *Sci. Rep.* 7 (1), 12523. doi:10.1038/s41598-017-12633-8

Jia, H., Li, Q., Bayaguud, A., Huang, Y., She, S., Chen, K., et al. (2018). Diversified Polyoxovanadate Derivatives Obtained by Copper(I)-Catalysed Azide-Alkyne Cycloaddition Reaction: Their Synthesis and Structural Characterization. *Dalton Trans.* 47 (2), 577–584. doi:10.1039/c7dt03822d

Jia, Y., Sun, S., Cui, X., Wang, X., and Yang, L. (2019). Enzyme-like Catalysis of Polyoxometalates for Chemiluminescence: Application in Ultrasensitive Detection of H2O2 and Blood Glucose. *Talanta* 205, 120139. doi:10.1016/j.talanta.2019.120139

Koyani, R. D., and Vazquez-Duhalt, R. (2016). Laccase Encapsulation in Chitosan Nanoparticles Enhances the Protein Stability against Microbial Degradation. *Environ. Sci. Pollut. Res.* 23 (18), 18850–18857. doi:10.1007/s11356-016-7072-8

Lai, S. Y., Ng, K. H., Cheng, C. K., Nur, H., Nurhadi, M., and Arumugam, M. (2021). Photocatalytic Remediation of Organic Waste over Keggin-Based Polyoxometalate Materials: A Review. *Chemosphere* 263, 128244. doi:10.1016/j.chemosphere.2020.128244

Landrigan, P. J., Fuller, R., Acosta, N. J. R., Adeyi, O., Arnold, R., Basu, N., et al. (2018). The Lancet Commission on Pollution and Health. *The Lancet* 391 (10119), 462–512. doi:10.1016/s0140-6736(17)32345-0

Lassouane, F., Aït-Amar, H., Amrani, S., and Rodriguez-Couto, S. (2019). A Promising Laccase Immobilization Approach for Bisphenol A Removal from Aqueous Solutions. *Bioresour. Tech.* 271, 360–367. doi:10.1016/j.biortech.2018.09.129

Li, L., Wu, Q.-Y., Guo, Y.-H., and Hu, C.-W. (2005). Nanosize and Bimodal Porous Polyoxotungstate-Anatase TiO2 Composites: Preparation and Photocatalytic Degradation of Organophosphorus Pesticide Using Visible-Light Excitation. *Microporous Mesoporous Mater.* 87 (1), 1–9. doi:10.1016/j.micromeso.2005.07.035

Li, X., He, X., He, D., Liu, Y., Chen, K., and Yin, P. (2021). A Polymeric Co-assembly of Subunit Vaccine with Polyoxometalates Induces Enhanced Immune Responses. *Nano Res.* 15, 1–6. doi:10.1007/s12274-021-4004-9

Li, X., Liu, S., Yin, P., and Chen, K. (2022). Enhanced Immune Responses by Virus-Mimetic Polymeric Nanostructures Against Infectious Diseases. *Front. Immunol.* 12, 804416. doi:10.3389/fimmu.2021.804416

Liang, H., Lin, F., Zhang, Z., Liu, B., Jiang, S., Yuan, Q., et al. (2017). Multicopper Laccase Mimicking Nanozymes with Nucleotides as Ligands. *ACS Appl. Mater. Inter.* 9 (2), 1352–1360. doi:10.1021/acsami.6b15124

Liu, J.-X., Zhang, X.-B., Li, Y.-L., Huang, S.-L., and Yang, G.-Y. (2020). Polyoxometalate Functionalized Architectures. *Coord. Chem. Rev.* 414, 213260. doi:10.1016/j.ccr.2020.213260

Lou, C., Jing, T., Zhou, J., Tian, J., Zheng, Y., Wang, C., et al. (2020). Laccase Immobilized Polyaniline/Magnetic Graphene Composite Electrode for Detecting Hydroquinone. *Int. J. Biol. Macromolecules* 149, 1130–1138. doi:10.1016/j.ijbiomac.2020.01.248

Ma, Y.-Y., Wu, C.-X., Feng, X.-J., Tan, H.-Q., Yan, L.-K., Liu, Y., et al. (2017). Highly Efficient Hydrogen Evolution from Seawater by A Low-Cost and Stable CoMoP@C Electrocatalyst Superior to Pt/C. *Energy Environ. Sci.* 10 (3), 788–798. doi:10.1039/c6ee03768b

Masjoudi, M., Golgoli, M., Ghobadi Nejad, Z., Sadeghzadeh, S., and Borghei, S. M. (2021). Pharmaceuticals Removal by Immobilized Laccase on Polyvinylidene Fluoride Nanocomposite with Multi-Walled Carbon Nanotubes. *Chemosphere* 263, 128043. doi:10.1016/j.chemosphere.2020.128043

Mate, D. M., and Alcalde, M. (2017). Laccase: a Multi-purpose Biocatalyst at the Forefront of Biotechnology. *Microb. Biotechnol.* 10 (6), 1457–1467. doi:10.1111/1751-7915.12422

Morsi, R., Bilal, M., Iqbal, H. M. N., and Ashraf, S. S. (2020). Laccases and Peroxidases: The Smart, Greener and Futuristic Biocatalytic Tools to Mitigate Recalcitrant Emerging Pollutants. *Sci. Total Environ.* 714, 136572. doi:10.1016/j.scitotenv.2020.136572

Qiu, X., Wang, S., Miao, S., Suo, H., Xu, H., and Hu, Y. (2021). Co-immobilization of Laccase and ABTS onto Amino-Functionalized Ionic Liquid-Modified Magnetic Chitosan Nanoparticles for Pollutants Removal. *J. Hazard. Mater.* 401, 123353. doi:10.1016/j.jhazmat.2020.123353

Rashtbari, S., and Dehghan, G. (2021). Biodegradation of Malachite Green by a Novel Laccase-Mimicking Multicopper BSA-Cu Complex: Performance Optimization, Intermediates Identification and Artificial Neural Network Modeling. *J. Hazard. Mater.* 406, 124340. doi:10.1016/j.jhazmat.2020.124340

Schug, T. T., Janesick, A., Blumberg, B., and Heindel, J. J. (2011). Endocrine Disrupting Chemicals and Disease Susceptibility. *J. Steroid Biochem. Mol. Biol.* 127 (3–5), 204–215. doi:10.1016/j.jsbmb.2011.08.007

Shakerian, F., Zhao, J., and Li, S.-P. (2020). Recent Development in the Application of Immobilized Oxidative Enzymes for Bioremediation of Hazardous Micropollutants - A Review. *Chemosphere* 239, 124716. doi:10.1016/j.chemosphere.2019.124716

Shams, S., Ahmad, W., Memon, A. H., Wei, Y., Yuan, Q., and Liang, H. (2019). Facile Synthesis of Laccase Mimic Cu/H3BTC MOF for Efficient Dye Degradation and Detection of Phenolic Pollutants. *RSC Adv.* 9 (70), 40845–40854. doi:10.1039/c9ra07473b

Shao, B., Liu, Z., Zeng, G., Liu, Y., Yang, X., Zhou, C., et al. (2019). Immobilization of Laccase on Hollow Mesoporous Carbon Nanospheres: Noteworthy Immobilization, Excellent Stability and Efficacious for Antibiotic Contaminants Removal. *J. Hazard. Mater.* 362, 318–326. doi:10.1016/j.jhazmat.2018.08.069

Sharma, B., Dangi, A. K., and Shukla, P. (2018). Contemporary Enzyme Based Technologies for Bioremediation: A Review. *J. Environ. Manage.* 210, 10–22. doi:10.1016/j.jenvman.2017.12.075

Tian, R., Xu, J., Luo, Q., Hou, C., and Liu, J. (2020). Rational Design and Biological Application of Antioxidant Nanozymes. *Front. Chem.* 8, 831. doi:10.3389/fchem.2020.00831

Torres-Duarte, C., Viana, M. T., Viana, M. T., and Vazquez-Duhalt, R. (2012). Laccase-mediated Transformations of Endocrine Disrupting Chemicals Abolish Binding Affinities to Estrogen Receptors and Their Estrogenic Activity in Zebrafish. *Appl. Biochem. Biotechnol.* 168 (4), 864–876. doi:10.1007/s12010-012-9825-2

Tran, T. D., Nguyen, P. T., Le, T. N., and Kim, M. I. (2021). DNA-copper Hybrid Nanoflowers as Efficient Laccase Mimics for Colorimetric Detection of Phenolic Compounds in Paper Microfluidic Devices. *Biosens. Bioelectron.* 182, 113187. doi:10.1016/j.bios.2021.113187

Wang, J., Huang, R., Qi, W., Su, R., Binks, B. P., and He, Z. (2019). Construction of a Bioinspired Laccase-Mimicking Nanozyme for the Degradation and Detection of Phenolic Pollutants. *Appl. Catal. B: Environ.* 254, 452–462. doi:10.1016/j.apcatb.2019.05.012

Xu, Z., Chen, K., Li, M., Hu, C., and Yin, P. (2020). Sustained Release of Ag+ Confined inside Polyoxometalates for Long-Lasting Bacterial Resistance. *Chem. Commun.* 56 (39), 5287–5290. doi:10.1039/d0cc01676d

Xu, X., Wang, J., Huang, R., Qi, W., Su, R., and He, Z. (2021). Preparation of Laccase Mimicking Nanozymes and Their Catalytic Oxidation of Phenolic Pollutants. *Catal. Sci. Technol.* 11 (10), 3402–3410. doi:10.1039/d1cy00074h

Yadav, N., and Singh, S. (2021). Polyoxometalate-Mediated Vacancy-Engineered Cerium Oxide Nanoparticles Exhibiting Controlled Biological Enzyme-Mimicking Activities. *Inorg. Chem.* 60 (10), 7475–7489. doi:10.1021/acs.inorgchem.1c00766

Yi, F.-Y., Zhu, W., Dang, S., Li, J.-P., Wu, D., Li, Y.-H., et al. (2015). Polyoxometalates-Based Heterometallic Organic-Inorganic Hybrid Materials for Rapid Adsorption and Selective Separation of Methylene Blue from Aqueous Solutions. *Chem. Commun.* 51 (16), 3336–3339. doi:10.1039/c4cc09569c

Zhou, Y., Liu, B., Yang, R., and Liu, J. (2017). Filling in the Gaps between Nanozymes and Enzymes: Challenges and Opportunities. *Bioconjug. Chem.* 28 (12), 2903–2909. doi:10.1021/acs.bioconjchem.7b00673

Zhou, W., Zhang, W., and Cai, Y. (2021). Laccase Immobilization for Water Purification: A Comprehensive Review. *Chem. Eng. J.* 403, 126272. doi:10.1016/j.cej.2020.126272

Zou, X., Shi, R., Zhang, Z., Fu, G., Li, L., Yu, L., et al. (2021). Calcined ZnTi-Layered Double Hydroxide Intercalated with H 3 PW 12 O 40 with Efficiently Photocatalytic and Adsorption Performances. *Chem. Eur. J.* 27 (67), 16670–16681. doi:10.1002/chem.202102762

Conflict of Interest: The authors declare that the research was conducted in the absence of any commercial or financial relationships that could be construed as a potential conflict of interest.

ORIGINAL RESEARCH
published: 03 March 2022
doi: 10.3389/fchem.2022.851178

Ultrasensitive Immunosensor for Prostate-Specific Antigen Based on Enhanced Electrochemiluminescence by Vertically Ordered Mesoporous Silica-Nanochannel Film

Kai Ma[1,2], Yanyan Zheng[3], Lizhe An[1,2] and Jiyang Liu[3]*

[1]Urology and Lithotripsy Center, Peking University People's Hospital, Beijing, China, [2]Peking University Applied Lithotripsy Institute, Peking University, Beijing, China, [3]Key Laboratory of Surface and Interface Science of Polymer Materials of Zhejiang Province, Department of Chemistry, Zhejiang Sci-Tech University, Hangzhou, China

Edited by:
Huanshun Yin,
Shandong Agricultural University,
China

Reviewed by:
Weiliang Guo,
Nanjing Normal University, China
Xiaomei Chen,
Jimei University, China

***Correspondence:**
Jiyang Liu
liujyxx@126.com
liujy@zstu.edu.cn

Specialty section:
This article was submitted to
Analytical Chemistry,
a section of the journal
Frontiers in Chemistry

Received: 09 January 2022
Accepted: 08 February 2022
Published: 03 March 2022

Citation:
Ma K, Zheng Y, An L and Liu J (2022)
Ultrasensitive Immunosensor for
Prostate-Specific Antigen Based on
Enhanced Electrochemiluminescence
by Vertically Ordered Mesoporous
Silica-Nanochannel Film.
Front. Chem. 10:851178.
doi: 10.3389/fchem.2022.851178

Ultrasensitive and specific detection of prostate-specific antigen (PSA) in complex biological samples is crucial for early diagnosis and treatment of prostate-related diseases. Immunoassay with a simple sensing interface and ultrahigh sensitivity is highly desirable. Herein, a novel electroluminescence (ECL) immunosensing platform is demonstrated based on the equipment of vertically ordered mesoporous silica-nanochannel films (VMSFs) with PSA antibody, which is able to realize ultrasensitive detection of PSA in human serum. Through the electrochemically assisted self-assembly (EASA) method, the VMSF is easily grown on an indium tin oxide (ITO) electrode in a few seconds. Owing to a large surface area and the negatively charged surface, VMSF nanochannels display strong electrostatic attraction to the positively charged ECL luminophores (tris(2,2-bipyridyl) dichlororuthenium (II), $(Ru(bpy)_3^{2+})$, leading to two orders-of-magnitude enhancement of ECL emission compared with that of the bare ITO electrode. The outer surface of the VMSF is functionalized with reactive epoxy groups, which further allows covalent attachment of PSA antibody (Ab) on the entry of nanochannels. As the combination of PSA with Ab decreases the ECL signal by hindering the mass transfer of ECL luminophores and coreactant, the developed immunosensor can achieve ultrasensitive detection of PSA ranging from 1 pg ml^{-1} to 100 ng ml^{-1} with a limit of detection (LOD) of 0.1 pg ml^{-1}. Considering the antifouling ability of the VMSF, sensitive detection of PSA in human serum is also realized. The proposed nanochannel-based immunosensor may open up a new way for the facile development of the universal immunosensing platform for rapid and ultrasensitive detection of disease markers.

Keywords: immunosensor, electrochemiluminescence, ultrasensitive detection, prostate-specific antigen, vertically ordered mesoporous silica-nanochannel film

1 INTRODUCTION

Detection of disease-related biomarkers in complex biological samples is of great significance for the early diagnosis and treatment of diseases. (Li et al., 2015; Wang and Kan, 2021; Xu et al., 2021) For instance, prostate-specific antigen (PSA) is considered to be the most effective biomarker for clinical diagnosis of prostate-related diseases (e.g. rostatitis, enlarged prostate, nephritis, prostate polyps, and prostate cancer) because it can specifically reflect the condition of the prostate. (Liu et al., 2017; Yang et al., 2017; Yang et al., 2020) PSA is a single-chain polypeptide comprising 237 amino acid residues belonging to the human kallikrein family. As known, the concentration of PSA in the blood of a normal man is usually low (less than 4 ng/ml), but the PSA concentration in patients with prostate-related diseases is abnormally elevated. (Ma et al., 2016; Cao et al., 2018; Khoshfetrat et al., 2021) In the past few decades, various traditional techniques have been used for PSA detection, including enzyme-linked immunosorbent assay (ELISA), colorimetry, fluorescence, electrochemistry, chemiluminescence, and surface-enhanced Raman scattering (SERS). (Deng et al., 2015; Zhu et al., 2018; Hou et al., 2020) However, ultrasensitive detection of PSA in blood serum through a specific immunoassay platform with a simple sensing interface and high sensitivity is still a challenge.

Electroluminescence (ECL), which is generated with the electrochemical redox reaction of luminophores on the electrode surface, is an important and powerful analytical technology in bioassay owing to its fast detection, low background, high potential and spatial controllability, and wide dynamic response range. (Liu et al., 2015; Li et al., 2017; Zhang et al., 2019; Ma et al., 2020) In addition, the electrochemical excitation and simplified optical devices make ECL possible to be miniaturized in portable point-of-care testing (POCT). For instance, ECL of tris(2,2-bipyridyl) dichlororuthenium (II) ($Ru(bpy)_3^{2+}$) with tripropylamine (TPrA) as a coreactant has been widely used in most ECL systems to detect various samples. (Liu et al., 2015; Gu et al., 2020) In recent years, the rapid development of nanotechnology has greatly benefited ECL technology by further improving its sensitivity and universality. On the one hand, some nanomaterials (e.g. graphene quantum dots, gold nanoclusters, etc.) have been directly used as ECL emitters due to their high stability, good biocompatibility, and excellent luminescent characteristics. (Li et al., 2017; Zhang et al., 2019; Ma et al., 2020) On the other hand, nanomaterials with high surface area and porous structure promise great potential in the fabrication of an ultrasensitive ECL detection platform by loading a large number of luminophores.

Solid nanofilms (SNFs) have recently attracted extensive attention and displayed great potential in the fields of nanofluids, molecular sieves, nanoreactors, and biosensing because of their advantages of low cost, high stability, adjustable nanopores, and intelligent control of molecular transmission. (Huang et al., 2016; Cui et al., 2020; Cui et al., 2021; Duan et al., 2021; Garbayo et al., 2021) As an important class of SNFs, the vertically ordered mesoporous silica-nanochannel film (VMSF) is of particular interest because of its ordered and vertically arranged nanochannels, uniform and adjustable pore size distribution (usually 2–3 nm), controllable nanoscale thickness (ranging from 50 to 150 nm), excellent permeability property, and easy modification. (Nasir et al., 2016; Chen et al., 2019; Wang et al., 2020; Zhu et al., 2022) Owing to the capability of sieving molecules on the nanoscale, the VMSF-modified electrodes possess excellent antifouling ability in complex real samples and allow direct detection of analytes without complicated sample pre-treatment processes (e.g. separation). (Yan et al., 2016; Ding et al., 2020a; Ding et al., 2020b) It is also noteworthy that the VMSF offers great advantages for the fabrication of a universal ECL biosensor with ultrahigh sensitivity. On the one hand, open silica-nanochannels with high packing density ($>10^{12}$ pores/cm^2) endow the VMSF with high surface area and a large number of silanol groups (pK_a of ~2). The abundant negatively charged sites on the surface of VMSF nanochannels favor accelerated mass transfer and enrichment of the positively charged luminophore (e.g., $Ru(bpy)_3^{2+}$) through strong electrostatic attraction, leading to significantly improved ECL sensitivity. (Zhou et al., 2015; Guo et al., 2016; Liu et al., 2016) On the other hand, silanol groups at the outer surface of the VMSF (also the entry of nanochannels) offer easy modification with silane-coupling reagents containing reactive groups (e.g., epoxy or amino group), allowing further immobilization of biomacromolecules with recognitive properties. Thus, it is highly encouraged to adopt VMSF-modified electrodes to fabricate the ECL immunosensor with ultrahigh sensitivity.

In this study, we present a novel immunosensor for ultrasensitive detection of PSA based on enhanced ECL by the VMSF nanochannel. As illustrated in **Figure 1**, the VMSF is fast and easily grown on an indium tin oxide (ITO) electrode through an electrochemically assisted self-assembly (EASA) method. Owing to the significant enrichment of the positively charged luminophores ($Ru(bpy)_3^{2+}$) by VMSF nanochannels, the VMSF/ITO electrode displays a significantly enhanced ECL signal, which is 100 times higher than that of the bare ITO electrode. To fabricate a specifically recognitive interface, the outer surface of the VMSF is modified with reactive epoxy groups to further allow covalent attachment of PSA antibody (Ab). The feasibility of the developed immunosensor is validated by ECL detection of PSA based on the decrease in the mass transfer of $Ru(bpy)_3^{2+}$ luminophore after the specific binding of PSA and Ab. Combined with the excellent antifouling performance of the VMSF, the immunosensor can also be used for the ultrasensitive and selective detection of PSA in serum.

2 MATERIALS AND METHODS

2.1 Chemicals and Materials

Prostate-specific antigen (PSA) and mouse anti-human PSA monoclonal antibody (Ab) were purchased from Beijing KEY-BIO Biotech Co., Ltd. (China). Tris(2,2-bipyridyl) dichlororuthenium (II) hexahydrate ($Ru(bpy)_3Cl_2 \cdot 6H_2O$) and hexaammineruthenium (III) chloride ($Ru(NH_3)_6Cl_3$) were

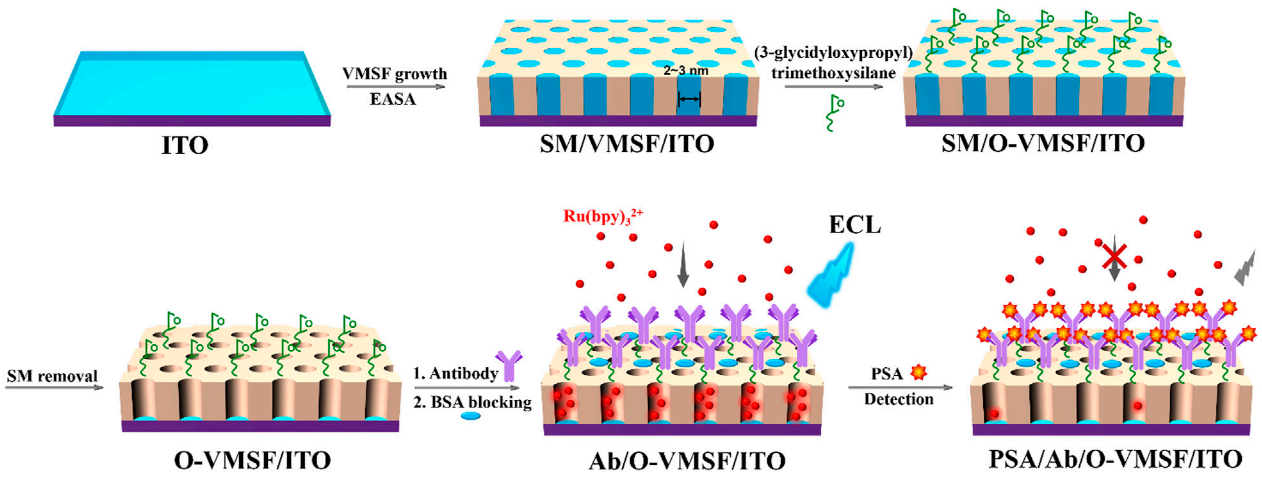

FIGURE 1 | Schematic illustration for the fabrication of the immunosensing interface on the VMSF-modified electrode and the following label-free ECL detection of PSA.

obtained from Sigma-Aldrich (United States). Tetraethoxysilane (TEOS), cetyltrimethylammonium bromide (CTAB), potassium ferricyanide ($K_3[Fe(CN)_6]$), bovine serum albumin (BSA), (3-glycidyloxypropyl) trimethoxysilane, and NaOH were obtained from Aladdin (China). Phosphate-buffered saline (PBS, 0.01 M, pH 7.4) was prepared by mixing NaH_2PO_4 and Na_2HPO_4 in a certain ratio. Human blood serum (healthy man) for real sample analysis was provided by Hangzhou Institute of Occupational Diseases (Hangzhou, China). ITO glass (<17Ω/square, thickness: 100 ± 20 nm) was obtained from Zhuhai Kaivo Optoelectronic Technology (China). To obtain a clean and negatively charged surface, the ITO glass was cleaned by NaOH solution (1 M) and then ultrasonically treated in acetone, ethanol, and deionized water. All other chemicals were of analytical grade. Ultrapure water (18.2 MΩ cm) was used throughout the study.

2.2 Measurements and Instrumentations

Scanning electron microscopy (SEM) images were collected on a SU8100 microscope (Hitachi, Japan) at an acceleration voltage of 5 kV. Transmission electron microscope (TEM) investigation was performed on a JEM-2100 microscope (JEOL Ltd., Japan) using an acceleration voltage of 200 kV. Electrochemical investigations including electrochemical impedance spectroscopy (EIS) and cyclic voltammetry (CV) were carried out on an Autolab electrochemical workstation (PGSTAT302N, Metrohm, Switzerland). Electrochemiluminescence (ECL) measurements were performed in a quartz cell using an MPI A multifunctional ECL analyzer (Xi'an Remax Electronic Science and Technology Co. Ltd.). The voltage of the photomultiplier tube was set at 400 V. A conventional three-electrode system was used for both electrochemical and ECL measurements. Briefly, a bare or modified ITO electrode was applied as the working electrode. A platinum disk (1 cm × 1 cm) was used as the counter electrode, and an Ag/AgCl electrode (saturated with KCl) was used as the reference electrode.

2.3 Preparation of Vertically Ordered Mesoporous Silica-Nanochannel Film–Modified Indium Tin Oxide Electrode

As previously reported, (Zhu et al., 2022) the VMSF-modified ITO electrode was prepared by growing the VMSF on the conducting ITO electrode by an electrochemically assisted self-assembly (EASA) method. Briefly, the precursor solution was prepared by adding TEOS (13.6 mM) and CTAB (4.35 mM) in the mixture (v:v = 1:1) of ethanol and $NaNO_3$ solution (0.1 M). After adjusting the pH value to 3.0 with hydrochloric acid (HCl, 6 M), the solution was aged for 2.5 h under stirring. A cleaned ITO was then immersed into the precursor solution, and a constant current (−350 μA) was applied for 10 s. After that, the electrode was quickly taken out and thoroughly washed with ultrapure water. After drying with nitrogen (N_2), the obtained electrode was aged at 120°C overnight. As the CTAB surfactant micelle (SM) still existed in the VMSF channel, the obtained electrode was recorded as SM@VMSF/ITO. The SM could be removed by stirring in 0.1 M HCl/ethanol solution for 5 min.

2.4 Fabrication of the Immunosensor

The fabrication of the immuno-recognitive interface on the VMSF-modified ITO electrode included three steps. First, reactive epoxy groups were introduced on the outer surface of the VMSF. To avoid modification of the interior surface of VMSF nanochannels, the SM@VMSF/ITO with SM-blocked nanochannels was immersed in (3-glycidyloxypropyl) trimethoxysilane (2.26 mM in ethanol) for 1 h to introduce epoxy groups on the outer surface of the VMSF. The electrodes were then thoroughly washed with ultrapure water. Second, the SM in the VMSF was removed to obtain open nanochannels, and the obtained electrode is named O-VMSF/ITO. Third, PSA antibody (Ab) was covalently immobilized through incubation with Ab (10 μg/ml) at 37°C for 90 min

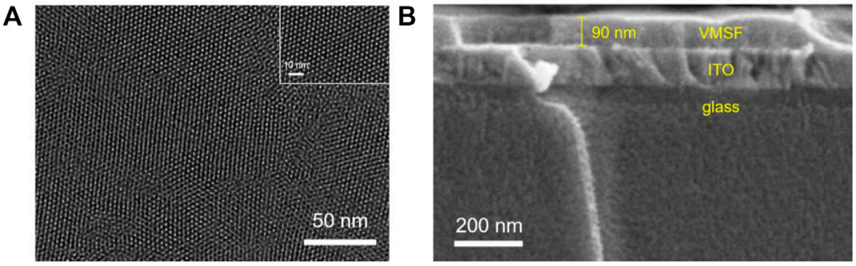

FIGURE 2 | (A) Top-view TEM images of the VMSF separated from the ITO electrode at different magnification. **(B)** Cross-sectional SEM image of the VMSF/ITO.

followed by thorough rinsing with PBS (0.01 M, pH 7.4). Then, the electrode was incubated with BSA solution (1%, w/w) for 90 min to block the nonspecific binding sites to produce a PSA immunosensor, which was denoted as Ab/O-VMSF/ITO.

2.5 Electroluminescence Determination of Prostate-Specific Antigen

The Ab/O-VMSF/ITO sensor was incubated with different concentrations of PSA (antigen) at 37°C for 45 min. The ECL intensity of the immunosensor before and after PSA binding was measured. Briefly, Ab/O-VMSF/ITO or PSA/Ab/O-VMSF/ITO electrodes were immersed in $Ru(bpy)_3^{2+}$ solution (10 μM, in 0.01 M PBS, pH = 7.4) containing TPrA (3 mM) for 30 min to enrich the ECL luminophores. Then, ECL signals of the electrodes were recorded when continuous potential scanning between 0 to 1.25 V was applied at a scanning rate of 100 mV/s. For real sample analysis, human serum (healthy male) was diluted 50 times with PBS (0.01 M, pH 7.4) and directly determined using the developed immunosensor.

3 RESULTS AND DISCUSSION

3.1 Facile Preparation of Vertically Ordered Mesoporous Silica-Nanochannel Film–Modified Electrode and the Significantly Enhanced Electroluminescence Signal

Figure 1 illustrates the fabrication of the immunosensing interface on the VMSF modified electrode and the following label-free electrochemiluminescence (ECL) detection of prostate-specific antigen (PSA). The first step for the construction of an immunosensor is to rapidly grow vertically ordered mesoporous silica-nanochannel films (VMSFs) on an ITO by the electrochemically assisted self-assembly (EASA) method. EASA allows quick deposition of the VMSF (within 10 s) under kinetic control at room temperature. When the cathode potential is applied to the ITO electrode, the protons and water molecules are reduced, causing a local increase in the pH at the electrode/solution interface. It is beneficial to the condensation of the siloxane precursor (tetraethoxysilane, TEOS) around the surfactant (cetyltrimethylammonium bromide, CTAB) micelle (SM) template. After the VMSF grows, the SM is found in the electrode (SM@VMSF/ITO), and it can be easily removed by soaking in hydrochloric acid–ethanol to obtain the VMSF-modified electrode (VMSF/ITO) with open nanochannels.

Scanning electron microscopy (SEM) and transmission electron microscopy (TEM) are used to confirm that the VMSF could be successfully modified on the ITO electrode. As shown in **Figure 2A**, the VMSF separated from the ITO electrode has highly uniform and ordered nanopores with a diameter of about 2–3 nm. The pore density is ~$7.4 \times 10^{12}/cm^2$, which corresponds to porosity of ~38%. The cross-sectional SEM image of the VMSF/ITO shows a three-layer structure, corresponding to VMSF, ITO, and glass (**Figure 2B**). In addition, the VMSF is a uniform film with a thickness of about 90 nm.

To prove the integrity and permeability of the VMSF, the electrochemical behaviors of the standard redox probes on different electrodes are investigated (**Figures 3A,B**). As shown, almost no electrochemical signals of both cationic ($Ru(NH_3)_6^{3+}$) and anionic ($Fe(CN)_6^{3-}$) probes are observed on the electrode containing the micelle (SM@VMSF/ITO). Thus, the full coverage of SM blocks nanochannels and inhibits the electron transfer between the probe and the electrode substrate. This phenomenon proves that the grown VMSF is intact with almost no defects. When the micelles in the nanochannel are removed, the electrochemical signals of the two probes can be detected on the VMSF/ITO, indicating the entrance of the redox probe into the nanochannel. Compared with the bare ITO electrode, the VMSF/ITO displays a suppressed signal of anionic $Fe(CN)_6^{3-}$. On the contrary, a significantly higher current of cationic $Ru(NH_3)_6^{3+}$ is observed, indicating a remarkable enrichment effect. This charge-selective permeability of the VMSF is attributed to the anionic nature of the silica walls generated by the abundant silanol groups ($pK_a \sim 2$). Owing to the large surface-to-volume ratio of the VMSF and high load capacity, the VMSF offers accelerated mass transport and significant amplification characteristics toward cationic probes.

Among the developed ECL emitters, tris(2,2-bipyridyl) dichlororuthenium (II) ($Ru(bpy)_3^{2+}$) is the most extensively investigated and commercially used owing to its good chemical stability, high ECL quantum yield, and water solubility. The electrochemical and ECL signals of $Ru(bpy)_3^{2+}$ on the bare ITO or VMSF/ITO are compared with those of tripropylamine (TPrA) as the coreactant. As shown in **Figure 3C**, a significant anodic current wave is observed on the VMSF/ITO at potentials more positive than 0.9 V. In comparison with the bare

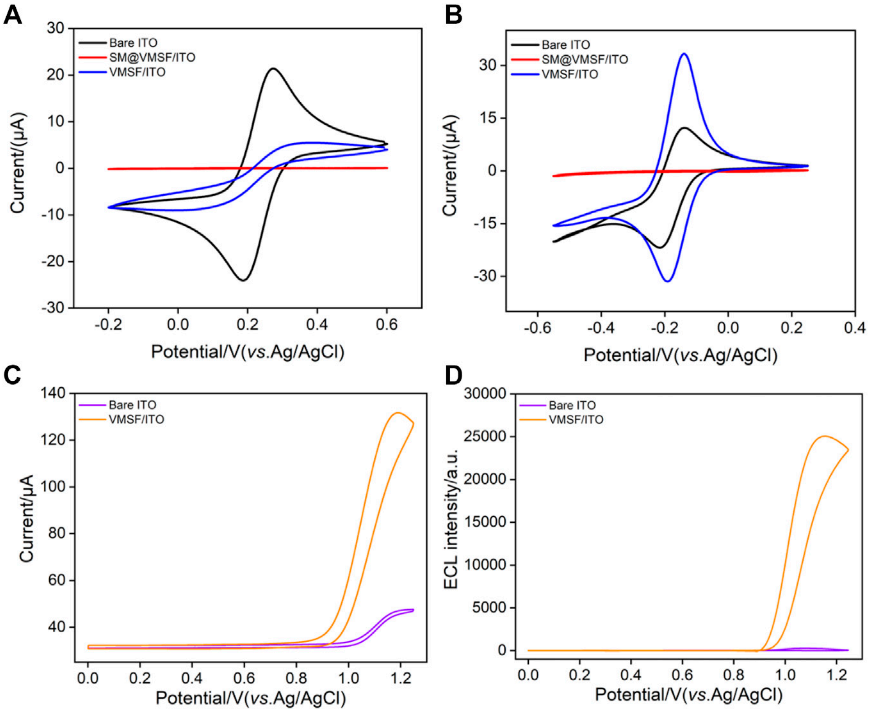

FIGURE 3 | Cyclic voltammetric curves of **(A)** $K_3[Fe(CN)_6]$ (0.5 mM) or **(B)** $Ru(NH_3)_6Cl_3$ (0.5 mM) on the bare ITO, SM@VMSF/ITO, and VMSF/ITO electrodes in KHP solution (0.05 M, pH = 7.4). The scan rate is 50 mV s^{-1}.Cyclic voltammetric curves **(C)** and ECL intensity-potential curves **(D)** obtained at the bare ITO or VMSF/ITO in 0.1 M PBS (pH 7) containing $Ru(bpy)_3^{2+}$ (10 μM) and TPrA (3 mM).

ITO, the VMSF/ITO displays higher current and lower electrochemical oxidation potential, indicating the facilitated charge transfer of $Ru(bpy)_3^{2+}$ on the underlying electrode. The corresponding ECL signal can be observed in **Figure 3D**. Even at low voltage of the photomultiplier tube (400 V), the ECL signal on the VMSF/ITO electrode is two orders-of-magnitude (100 times) higher than that of the bare ITO electrode, indicating significant enhancement of ECL emission. Owing to the ultrasmall diameter (2–3 nm) and the negatively charged surface, the VMSF displays a strong electrostatic attraction to the positively charged $Ru(bpy)_3^{2+}$, which remarkably increases its concentration on the electrode surface, resulting in effective signal amplification.

3.2 Fabrication of the Immunosensing Interface on Vertically Ordered Mesoporous Silica-Nanochannel Films/Indium Tin Oxide Electrode

As a biosensing technology based on the specific recognition between antigen (Ag) and antibody (Ab), immunosensors have attracted wide attention due to their high specificity and sensitivity. With the recent development of bioengineering technology, antibodies toward various microorganisms, cell surface antigens, or protein antigens can be easily developed. This greatly expands the application of immunosensors in the fields of biological analysis, clinical diagnosis, etc. The VMSF itself is inert without biosensing capability. The facile method to fabricate the immunosensor by equipping the VMSF with antibody can greatly expand the application of nanochannel-based sensors. Although antibodies are too large to be introduced into the VMSF nanochannels, they could be easily immobilized on the outer surface of the VMSF, that is, entrances of the nanochannels. As illustrated in **Figure 1**, the antibody is immobilized at the nanochannel entry, giving rise to bio-recognitive function. The abundant hydroxyl groups at the VMSF surface favor the modification with the silane-coupling reagent with reactive groups. As shown, the VMSF is modified with (3-glycidyloxypropyl) trimethoxysilane to functionalize its surface with reactive epoxy groups, which further allows covalent attachment of the PSA antibody. In order to make the modification of epoxy groups only occur on the outer surface of the VMSF without changing the surface of nanochannels, SM@VMSF/ITO electrodes with nanochannels blocked with the SM are used for the modification. Then, the SM is removed to obtain an electrode with rich epoxy groups on the entry of nanochannels (O-VMSF/ITO). Compared with -COOH or $-NH_2$ groups, that could be used to covalently link antibodies with catalysis (e.g. 1-(3-dimethylaminopropyl)-3-ethylcarbodiimide hydrochloride/N-hydroxysuccimide, EDC/NHS) or further modification (e.g. glutaraldehyde linker for $-NH_2$ groups), epoxy

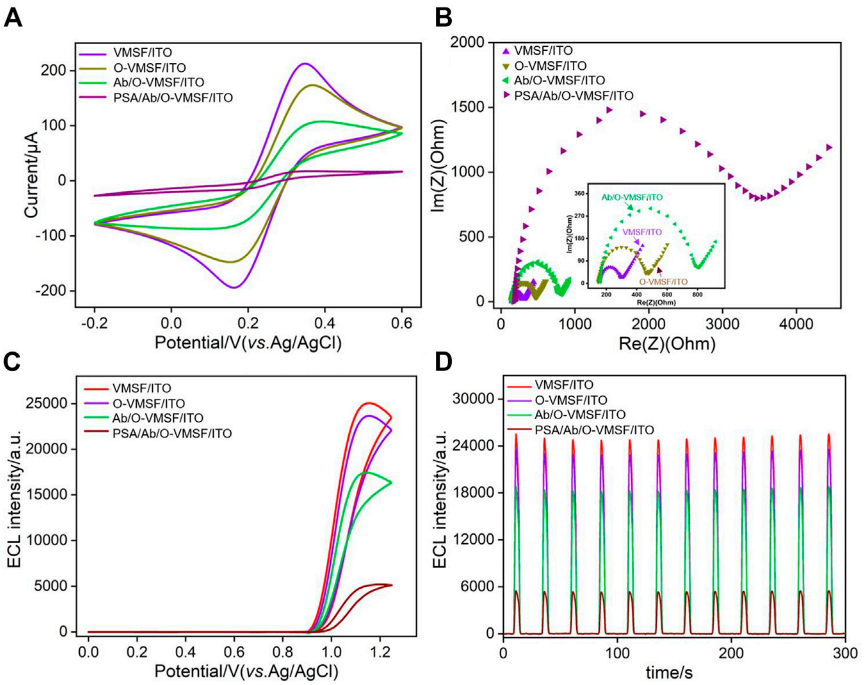

FIGURE 4 | Cyclic voltammetric curves **(A)** and Nyquist plots **(B)** recorded on different electrodes in 5 mM $K_3[Fe(CN)_6]/K_4[Fe(CN)_6]$ (1: 1) containing 0.1 M KCl. ECL intensity-potential curves **(C)** and ECL intensity-curves **(D)** obtained on different electrodes.

groups offer a simple process for the covalent immobilization of antibodies without additional catalysts or modification.

Cyclic voltammetry (CV) and electrochemical impedance spectroscopy (EIS) are used to investigate the changes occurring at the electrode surface during the fabrication of the immunosensor. As shown in **Figure 4A**, voltammograms recorded at the O-VMSF/ITO using $[Fe(CN)_6]^{4-/3-}$ as the redox probe is similar to that on the VMSF/ITO, indicating that the epoxy group modification does not significantly affect the properties of the nanochannels. When Ab is covalently immobilized and the nonspecific binding site is blocked by BSA, the redox current response of $[Fe(CN)_6]^{4-/3-}$ on the Ab/O-VMSF/ITO electrode is significantly reduced owing to the increased interface resistance generated by the nonconductive antibody. After incubation of the Ab/O-VMSF/ITO with PSA, the redox signal of the probe on the electrode is quite low, proving the formation of an antigen–antibody complex. Similar conclusions could be deduced from EIS measurements as illustrated in **Figure 4B**. As shown, the electron transfer resistance (R_{et}), which is related to the semicircle diameter of each curve, is similar before and after modification with epoxy groups. Consecutive increase of the impedance value is obtained due to immobilization of Ab and the following BSA blocking because the protein layer acts as the inert electron and hinders the electron transfer. A significant increase in impedance value is observed when the Ab/O-VMSF/ITO electrode is incubated with PSA, indicating the successful capture of the antigen at the immuno-recognitive interface.

In order to verify the application of the as-prepared immunosensor in ECL detection, the ECL intensity-potential and intensity-time curves of $Ru(bpy)_3^{2+}$ are also investigated in presence of the TPrA coreactant. As shown in **Figures 4C,D**, strong ECL responses with similar intensity are obtained on both VMSF/ITO and O-VMSF/ITO electrodes, further proving that the group modification of the outer surface of the VMSF does not significantly affect the enrichment of positively charged luminophores by nanochannels. After Ab immobilization and BSA blocking, the ECL intensity of the Ab/O-VMSF/ITO electrode decreases. Owing to the ultrasmall pore size and high pore density of the nanochannels, the surface area of the nanochannels is significantly higher than that of the outer surface of the VMSF. Thus, the change of surface charge upon the modifications of biochemical species is not remarkable. The decreased ECL signal is due to the hindrance of the diffusion of the ECL luminophores and the coreactant to the electrode surface. Subsequently, the combination of PSA and Ab leads to a significant decrease in ECL intensity because the diffusion of $Ru(bpy)_3^{2+}$ and TPrA is further blocked. In addition, the ECL intensity of each electrode under continuous scanning exhibits a low relative standard deviation (RSD, less than 4%), indicating excellent stability.

The optimal conditions for preparation of an immunosensor, including the incubation time for antibody immobilization and reaction time for antigen–antibody interaction, are determined. The ECL intensity on the O-VMSF/ITO electrode before and after incubation with Ab for different time is investigated. As shown in **Figure 5A**, the relative ECL signal reaches a plateau when the incubation time for antibody immobilization is 90 min. In addition, when the interaction between the antigen and antibody is less than 45 min, the ECL signal decreases

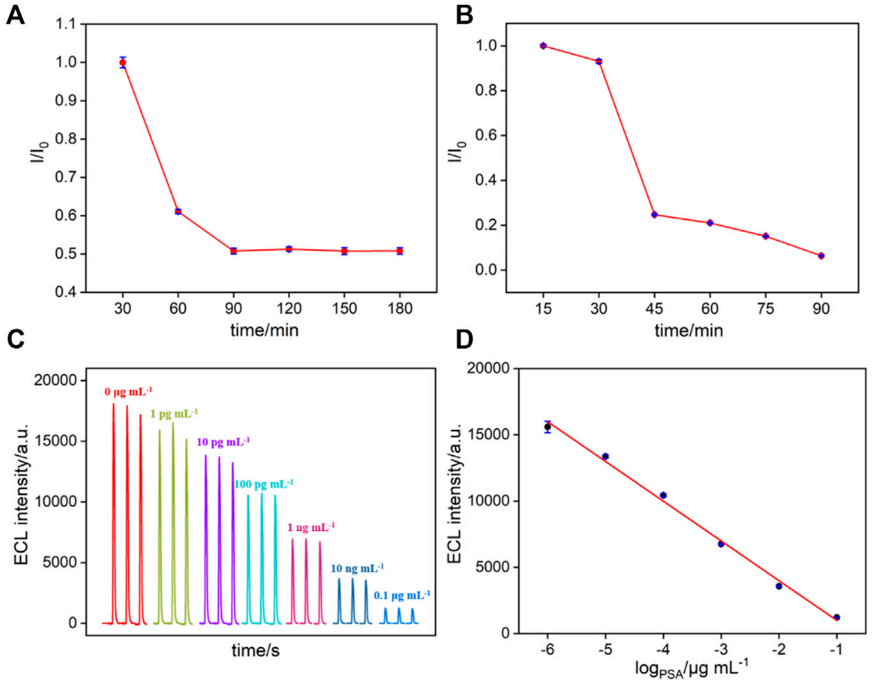

FIGURE 5 | (A–B) The effect of antibody immobilization **(A)** or **(B)** PSA incubation time **(B)** on relative ECL signal ratio. **(C)** ECL response of the immunosensor in the presence of different concentrations of PSA. **(D)** Calibration curve for the detection of PSA.

significantly with prolonged incubation time (**Figure 5B**). Thus, 90 min for antibody immobilization and 45 min for antigen–antibody interaction are chosen for further investigations.

3.3 Label-free Electroluminescence Determination of Prostate-Specific Antigen

The developed immunosensor is applied for label-free ECL determination of PSA based on the decrease in the mass transfer of the $Ru(bpy)_3^{2+}$ luminophore after specific binding of PSA and Ab (**Figure 1**). The analytical performance is evaluated by incubation with different concentrations of target PSA. As revealed in **Figure 5C**, the ECL intensity of the immunosensor gradually decreased with the increasing concentration of PSA. The calibration curve shows a good linear relationship between ECL intensity (I_{ECL}) and the logarithmic value of PSA concentration ($\log C_{PSA}$) ranging from 1 pg ml^{-1} to 100 ng ml^{-1} ($I_{ECL} = -2999 \log C_{PSA} + 411.2$, $R^2 = 0.995$, **Figure 5D**). The limit of detection (LOD) is calculated to be 0.1 pg ml^{-1} ($S/N = 3$). **Supplementary Table S1** shows the comparison of ECL detection of PSA using different modified electrodes (in *Supporting Information*, SI). The LOD is lower than that obtained from the gold nanoparticle–modified glassy carbon electrode (AuNPs/GCE) (Wang and Kan, 2021), potassium niobate-Au nanoparticles@ bismuth sulfide–modified GCE ($KNbO_3$-Au NPs@Bi_2S_3/GCE) (Li et al., 2015), ferrocene–graphene sheets and Au-CdS flower-like 3D assembly–modified GCE (Fc-GNs/Au-CdS flower-like 3D assemblies/GCE) (Yang et al., 2017), Au nanoparticle/graphene quantum dots-poly(etherimide)-graphene oxide–modified GCE (AuNP/GQDs-PEI-GO/GCE) (Yang et al., 2020), $EuPO_4$-modified GCE (Ma et al., 2016), gold nanorods functionalized graphene oxide multilabeled with glucose oxidase/electrodeposited gold–modified GCE (GO@AuNRs-GOD/DPAu) (Cao et al., 2018), AuNP-decorated MoS_2/SiO_2 nanoparticles labeled with glucose oxidase–modified GCE (MoS_2-AuNPs/SiO_2-GOD) (Hou et al., 2020), luminol loaded within the MIL-53(Fe)-NH_2/nitrogen-doped graphene-coated Cu foam/bipolar electrode (L@MIL-53(Fe)-NH_2/fCu/N-GN/RuNPs/BPE) (Khoshfetrat et al., 2019), and gold nanoprobe consisting of a peptide with a ruthenium(II)- and nafion-modified GCE (AuNP peptide-Ru1/nafion/GCE) (Zhe et al., 2019), but higher than that obtained on amino-modified multiwalled carbon nanotubes/nafion- and $Ru(bpy)_3^{2+}$-modified GCE (MWCNTs-NH_2@N/$Ru(bpy)_3^{2+}$/GCE). (Liu et al., 2017)

3.4 Selectivity, Reproducibility, and Stability of the Immunosensor

The specific recognition capacity of the developed immunosensor was studied by performing detection of PSA or other interfering tumor biomarkers, including carcinoembryonic antigen (CEA),

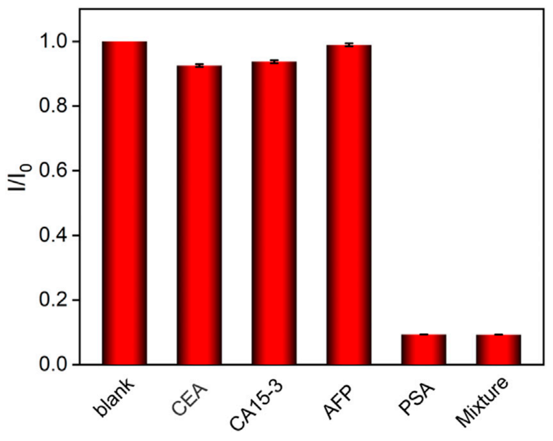

FIGURE 6 | Relative ratio of ECL intensity before (I_0) and after (I_0) incubation with buffer (blank), CEA (500 ng ml^{-1}), CA15-3 (500 ng ml^{-1}), AFP (500 ng ml^{-1}), PSA (0.1 ng ml^{-1}), or protein mixture (0.1 ng ml^{-1} PSA + 500 ng ml^{-1} other proteins).

carbohydrate antigen 15-3 (CA 15-3), and alphafetoprotein (AFP). Single tumor biomarker or their mixture is detected using the Ab/O-VMSF/ITO electrode. As shown in **Figure 6**, the obvious ECL decrease is only observed when the immunosensor is incubated with the PSA and the mixture. Other tumor biomarkers lead to no significant change in the ECL responses, indicating high selectivity for PSA detection. To evaluate the reproducibility of the immunosensor, five sensing electrodes are prepared in parallel, and their responses are investigated by measuring the ECL response toward 10 ng ml^{-1} PSA. All electrodes exhibit a similar analytical response, and a relative standard deviation of 3.2% is revealed, demonstrating high reproducibility. After 15 days of storage at 4°C, the analytical response of the immunosensor to 10 ng ml^{-1} PSA remained 97.2% of the initial signal, indicating high stability.

3.5 Real Sample Analysis

The feasibility of the developed immunosensor for practical application is evaluated by determining the concentration of the PSA in complex biological samples. A human serum sample of a healthy man is measured. The PSA concentration detected using the proposed immunosensor (1.48 ng ml^{-1}) is in acceptable agreement with that obtained by the ROCHE ELISA ECL analyzer (1.51 ng ml^{-1}). In addition, different concentrations of standard PSA solutions are artificially added into serum samples to simulate cancer patients with high PSA concentrations. Satisfactory recoveries of PSA ranging from 98.8% to 102.3% are obtained in this standard addition method, indicating good accuracy (**Supplementary Table S2** in SI). The results demonstrate the practicability of the immunosensor for potential clinical analysis of PSA.

4 CONCLUSION

In summary, we have developed a novel label-free immunosensor based on vertically ordered mesoporous silica-nanochannel films (VMSFs), which is able to perform ultrasensitive detection of prostate-specific antigen (PSA) with high selectivity. Owing to the ultrasmall diameter and negatively charged surface, the VMSF nanochannels display strong electrostatic attraction to the positively charged ECL luminophores, leading to two orders-of-magnitude enhancement of ECL emission. The outer surface of the VMSF is functionalized with reactive epoxy groups, which further allows covalent attachment of the PSA antibody on the entry of nanochannels. The combination of PSA with Ab hinders the mass transfer of the ECL luminophores and coreactant, resulting in ultrasensitive detection of PSA ranging from 1 pg ml^{-1} to 100 ng ml^{-1} with an LOD of 0.1 pg ml^{-1}. In combination with the antifouling ability of the VMSF, the developed immunosensor exhibits potential in PSA detection in complex biological samples. The VMSF-based immunosensor might open a new way for the facile fabrication of biosensing platforms with ultrahigh sensitivity and good antifouling performance.

DATA AVAILABILITY STATEMENT

The original contributions presented in the study are included in the article/**Supplementary Material**; further inquiries can be directed to the corresponding authors.

AUTHOR CONTRIBUTIONS

KM: data curation and writing—original draft preparation; YZ: data curation; LA: data curation; JL: supervision and writing—review and editing.

FUNDING

We acknowledge the financial support from the National Natural Science Foundation of China (21904117) and the Zhejiang Provincial Natural Science Foundation of China (LY20B050007).

SUPPLEMENTARY MATERIAL

The Supplementary Material for this article can be found online at: https://www.frontiersin.org/articles/10.3389/fchem.2022.851178/full#supplementary-material

REFERENCES

Cao, J.-T., Yang, J.-J., Zhao, L.-Z., Wang, Y.-L., Wang, H., Liu, Y.-M., et al. (2018). Graphene Oxide@gold Nanorods-Based Multiple-Assisted Electrochemiluminescence Signal Amplification Strategy for Sensitive Detection of Prostate Specific Antigen. *Biosens. Bioelectron.* 99, 92–98. doi:10.1016/j.bios.2017.07.050

Chen, K., Yao, L., and Su, B. (2019). Bionic Thermoelectric Response with Nanochannels. *J. Am. Chem. Soc.* 141, 8608–8615. doi:10.1021/jacs.9b03569

Cui, Y., Duan, W., Jin, Y., Wo, F., Xi, F., and Wu, J. (2020). Ratiometric Fluorescent Nanohybrid for Noninvasive and Visual Monitoring of Sweat Glucose. *ACS Sens.* 5, 2096–2105. doi:10.1021/acssensors.0c00718

Cui, Y., Duan, W., Jin, Y., Wo, F., Xi, F., and Wu, J. (2021). Graphene Quantum Dot-Decorated Luminescent Porous Silicon Dressing for Theranostics of Diabetic Wounds. *Acta Biomater.* 131, 544–554. doi:10.1016/j.actbio.2021.07.018

Deng, L., Chen, H.-Y., and Xu, J.-J. (2015). A Novel Electrochemiluminescence Resonance Energy Transfer System for Ultrasensitive Detection of Prostate-specific Antigen. *Electrochem. Commun.* 59, 56–59. doi:10.1016/j.elecom.2015.07.009

Ding, H., Guo, W., and Su, B. (2020a). Imaging Cell-Matrix Adhesions and Collective Migration of Living Cells by Electrochemiluminescence Microscopy. *Angew. Chem. Int. Ed.* 59, 449–456. doi:10.1002/anie.201911190

Ding, H., Guo, W., Zhou, P., and Su, B. (2020b). Nanocage-confined Electrochemiluminescence for the Detection of Dopamine Released from Living Cells. *Chem. Commun.* 56, 8249–8252. doi:10.1039/d0cc03370g

Duan, W., Jin, Y., Cui, Y., Xi, F., Liu, X., Wo, F., et al. (2021). A Co-delivery Platform for Synergistic Promotion of Angiogenesis Based on Biodegradable, Therapeutic and Self-Reporting Luminescent Porous Silicon Microparticles. *Biomaterials* 272, 120772. doi:10.1016/j.biomaterials.2021.120772

Garbayo, I., Santiago, A., Judez, X., de Buruaga, A. S., Castillo, J., and Muñoz-Márquez, M. A. (2021). Alumina Nanofilms as Active Barriers for Polysulfides in High-Performance All-Solid-State Lithium-Sulfur Batteries. *ACS Appl. Energ. Mater.* 4, 2463–2470. doi:10.1021/acsaem.0c03032

Gu, W., Wang, H., Jiao, L., Wu, Y., Chen, Y., Hu, L., et al. (2020). Single-Atom Iron Boosts Electrochemiluminescence. *Angew. Chem.* 132, 3562–3566. doi:10.1002/ange.201914643

Guo, W., Lin, X., Yan, F., and Su, B. (2016). Vertically Ordered Silica Mesochannel Modified Bipolar Electrode for Electrochemiluminescence Imaging Analysis. *ChemElectroChem* 3, 480–486. doi:10.1002/celc.201500329

Hou, F., Hu, X.-B., Ma, S.-H., Cao, J.-T., and Liu, Y.-M. (2020). Construction of Electrochemiluminescence Sensing Platform with *In Situ* Generated Coreactant Strategy for Sensitive Detection of Prostate Specific Antigen. *J. Electroanal. Chem.* 858, 113817. doi:10.1016/j.jelechem.2019.113817

Huang, X., Xie, L., Lin, X., and Su, B. (2016). Permselective Ion Transport across the Nanoscopic Liquid/liquid Interface Array. *Anal. Chem.* 88, 6563–6569. doi:10.1021/acs.analchem.6b01383

Khoshfetrat, S. M., Khoshsafar, H., Afkhami, A., Mehrgardi, M. A., and Bagheri, H. (2019). Enhanced Visual Wireless Electrochemiluminescence Immunosensing of Prostate-Specific Antigen Based on the Luminol Loaded into MIL-53(Fe)-NH_2 Accelerator and Hydrogen Evolution Reaction Mediation. *Anal. Chem.* 91, 6383–6390. doi:10.1021/acs.analchem.9b01506

Khoshfetrat, S. M., Hashemi, P., Afkhami, A., Hajian, A., and Bagheri, H. (2021). Cascade Electrochemiluminescence-Based Integrated Graphitic Carbon Nitride-Encapsulated Metal-Organic Framework Nanozyme for Prostate-specific Antigen Biosensing. *Sens. Actuators B: Chem.* 348, 130658. doi:10.1016/j.snb.2021.130658

Li, J., Ma, H., Wu, D., Li, X., Zhao, Y., Zhang, Y., et al. (2015). A Label-free Electrochemiluminescence Immunosensor Based on $KNbO_3$-Au nanoparticles@Bi_2S_3 for the Detection of Prostate Specific Antigen. *Biosens. Bioelectron.* 74, 104–112. doi:10.1016/j.bios.2015.06.027

Li, L., Chen, Y., and Zhu, J.-J. (2017). Recent Advances in Electrochemiluminescence Analysis. *Anal. Chem.* 89, 358–371. doi:10.1021/acs.analchem.6b04675

Liu, Z., Qi, W., and Xu, G. (2015). Recent Advances in Electrochemiluminescence. *Chem. Soc. Rev.* 44, 3117–3142. doi:10.1039/c5cs00086f

Liu, J., He, D., Liu, Q., He, X., Wang, K., Yang, X., et al. (2016). Vertically Ordered Mesoporous Silica Film-Assisted Label-free and Universal Electrochemiluminescence Aptasensor Platform. *Anal. Chem.* 88, 11707–11713. doi:10.1021/acs.analchem.6b03317

Liu, Y., Zhao, Y., Zhu, Z., Xing, Z., Ma, H., and Wei, Q. (2017). Ultrasensitive Immunosensor for Prostate Specific Antigen Using Biomimetic Polydopamine Nanospheres as an Electrochemiluminescence Superquencher and Antibody Carriers. *Anal. Chim. Acta* 963, 17–23. doi:10.1016/j.aca.2017.01.068

Ma, H., Zhou, J., Li, Y., Han, T., Zhang, Y., Hu, L., et al. (2016). A Label-Free Electrochemiluminescence Immunosensor Based on $EuPO_4$ Nanowire for the Ultrasensitive Detection of Prostate Specific Antigen. *Biosens. Bioelectron.* 80, 352–358. doi:10.1016/j.bios.2016.01.069

Ma, C., Cao, Y., Gou, X., and Zhu, J.-J. (2020). Recent Progress in Electrochemiluminescence Sensing and Imaging. *Anal. Chem.* 92, 431–454. doi:10.1021/acs.analchem.9b04947

Nasir, T., Zhang, L., Vilà, N., Herzog, G., and Walcarius, A. (2016). Electrografting of 3-Aminopropyltriethoxysilane on a Glassy Carbon Electrode for the Improved Adhesion of Vertically Oriented Mesoporous Silica Thin Films. *Langmuir* 32, 4323–4332. doi:10.1021/acs.langmuir.6b00798

Wang, Y., and Kan, X. (2021). Sensitive and Selective "Signal-Off" Electrochemiluminescence Sensing of Prostate-specific Antigen Based on an Aptamer and Molecularly Imprinted Polymer. *Analyst* 146, 7693–7701. doi:10.1039/d1an01645h

Wang, Y., Guo, W., Yang, Q., and Su, B. (2020). Electrochemiluminescence Self-Interference Spectroscopy with Vertical Nanoscale Resolution. *J. Am. Chem. Soc.* 142, 1222–1226. doi:10.1021/jacs.9b12833

Xu, C., Li, J., Kitte, S. A., Qi, G., Li, H., and Jin, Y. (2021). Light Scattering and Luminophore Enrichment-Enhanced Electrochemiluminescence by a 2D Porous Ru@SiO_2 Nanoparticle Membrane and its Application in Ultrasensitive Detection of Prostate-specific Antigen. *Anal. Chem.* 93, 11641–11647. doi:10.1021/acs.analchem.1c02708

Yan, F., Lin, X., and Su, B. (2016). Vertically Ordered Silica Mesochannel Films: Electrochemistry and Analytical Applications. *Analyst* 141, 3482–3495. doi:10.1039/c6an00146g

Yang, J.-J., Cao, J.-T., Wang, H., Liu, Y.-M., and Ren, S.-W. (2017). Ferrocene-graphene Sheets for High-Efficiency Quenching of Electrochemiluminescence from Au Nanoparticles Functionalized Cadmium Sulfide Flower-like Three Dimensional Assemblies and Sensitive Detection of Prostate Specific Antigen. *Talanta* 167, 325–332. doi:10.1016/j.talanta.2017.01.077

Yang, C., Guo, Q., Lu, Y., Zhang, B., and Nie, G. (2020). Ultrasensitive "Signal-On" Electrochemiluminescence Immunosensor for Prostate-specific Antigen Detection Based on Novel Nanoprobe and Poly(indole-6-Carboxylic Acid)/flower-like Au Nanocomposite. *Sens. Actuators B: Chem.* 303, 127246. doi:10.1016/j.snb.2019.127246

Zhang, J., Jin, R., Jiang, D., and Chen, H.-Y. (2019). Electrochemiluminescence-Based Capacitance Microscopy for Label-free Imaging of Antigens on the Cellular Plasma Membrane. *J. Am. Chem. Soc.* 141, 10294–10299. doi:10.1021/jacs.9b03007

Zhe, L., Cao, B., and Zhou, C. (2019). A Novel Gold Nanoprobe for a Simple Electrochemiluminescence Determination of a Prostate Specific Antigen Based on a Peptide Cleavage Reaction. *Anal. Sci.* 35, 195–199. doi:10.2116/analsci.18P377

Zhou, Z., Guo, W., Xu, L., Yang, Q., and Su, B. (2015). Two Orders-Of-Magnitude Enhancement in the Electrochemiluminescence of $Ru(bpy)_3{}^{2+}$ by Vertically Ordered Silica Mesochannels. *Anal. Chim. Acta* 886, 48–55. doi:10.1016/j.aca.2015.06.005

Zhu, W., Saddam Khan, M., Cao, W., Sun, X., Ma, H., Zhang, Y., et al. (2018). $Ni(OH)_2$/NGQDs-based Electrochemiluminescence Immunosensor for Prostate Specific Antigen Detection by Coupling Resonance Energy Transfer with Fe_3O_4@MnO_2 Composites. *Biosens. Bioelectron.* 99, 346–352. doi:10.1016/j.bios.2017.08.005

Zhu, X., Xuan, L., Gong, J., Liu, J., Wang, X., Xi, F., et al. (2022). Three-dimensional Macroscopic Graphene Supported Vertically-Ordered Mesoporous Silica-Nanochannel Film for Direct and Ultrasensitive Detection of Uric Acid in Serum. *Talanta* 238, 123027. doi:10.1016/j.talanta.2021.123027

Conflict of Interest: The authors declare that the research was conducted in the absence of any commercial or financial relationships that could be construed as a potential conflict of interest.

frontiers in Chemistry

ORIGINAL RESEARCH
published: 16 March 2022
doi: 10.3389/fchem.2022.870666

Fabrication of Curcumin@Ag Loaded Core/Shell Nanofiber Membrane and its Synergistic Antibacterial Properties

*Qiuxiang Wang†, Songlin Liu†, Wenjuan Lu and Pingping Zhang**

School of Pharmacy & Pharmaceutical Sciences, Shandong First Medical University & Shandong Academy of Medical Sciences, Jinan, China

The core/shell structure nanofiber membrane loaded with curcumin and silver nanoparticles was prepared by coaxial electrospinning technology, which is a high-efficiency combined antibacterial material composed of photodynamic antibacterial agent and metal nanoparticle. As a photosensitizer, curcumin could generate singlet oxygen under laser irradiation. Silver nanoparticles have antibacterial properties, and could also enhance the singlet oxygen production of curcumin due to the metal-enhanced singlet oxygen effect, thereby producing a synergistic antibacterial effect. Compared with the antibacterial rate of uniaxial curcumin fiber membrane (45.65%) and uniaxial silver nanoparticle-loaded fiber membrane (66.96%), the antibacterial rate of curcumin@Ag core/shell structure fiber membrane against *Staphylococcus aureus* is as high as 93.04%. In addition, the antibacterial experiments show that the core/shell fiber membrane also has excellent antibacterial effects on *Escherichia coli*.

Keywords: photodynamic antibacterial, curcumin, silver nanoparticles, electrospinning, core/shell fibers, synergistic antibacterial properties

Edited by:
Dejin Zang,
Tsinghua University, China

Reviewed by:
Qifang Lu,
Qilu University of Technology, China
Wei Li,
Qiannan Normal College for Nationalities, China
Mingrui Guo,
Qingdao University, China

***Correspondence:**
Pingping Zhang
pingpingzhang6087@163.com

†These authors have contributed equally to this work

Specialty section:
This article was submitted to Analytical Chemistry, a section of the journal Frontiers in Chemistry

Received: 07 February 2022
Accepted: 25 February 2022
Published: 16 March 2022

Citation:
Wang Q, Liu S, Lu W and Zhang P (2022) Fabrication of Curcumin@Ag Loaded Core/Shell Nanofiber Membrane and its Synergistic Antibacterial Properties. Front. Chem. 10:870666. doi: 10.3389/fchem.2022.870666

INTRODUCTION

The overuse of antibiotics has led to acquired resistance of bacteria to most antibiotics, so there is an urgency to find new antibacterial methods or alternative strategies (Farhat et al., 2020; Yu et al., 2021; Zhao et al., 2021). There are mainly two approaches among the new antibacterial strategies. One is photodynamic antibacterial therapy (Wu et al., 2021), and the other is the use of metal nanoparticles (Godoy-Gallardo et al., 2021) or antimicrobial peptides (Qiu et al., 2021) to replace antibiotics. Photodynamic antimicrobial chemotherapy (PACT) kills bacteria through the combined action of light and photosensitizers (Liu et al., 2020; Sun et al., 2021). The mechanism of PACT is that the chromophore of the photosensitizer generates singlet oxygen and other reactive oxygen species (ROS) under light irradiation (Im et al., 2021; Xiao et al., 2021). ROS chemically attacks bacteria, and while bacteria at one site are naturally resistant to ROS attack, another site may be susceptible to the attack (Lyutakov et al., 2014).

The photosensitizer is the core and the key factor affecting the antibacterial effect of PACT (Wu et al., 2020). Natural photosensitizers with low toxicity and side effects are the hotspot of PACT research. Curcumin is a natural polyphenol found in plant rhizomes, which possesses a wide range of biological activities such as antioxidant (Hou et al., 2022), anti-inflammatory (Pontes-Quero et al., 2021), antitumor (Chen et al., 2021), antibacterial (Barros et al., 2021), antiviral (Dourado et al., 2021), and photosensitizing activities (Li et al., 2020). As a natural photosensitizer, curcumin can be activated by light at 400–500 nm to generate singlet oxygen to exert antibacterial effects (Hu et al., 2018). Feng et al. obtained a tough and biodegradable polyurethane-curcumin (PU-Cur) hydrogel with strongly antioxidant properties by *in-situ* copolymerization of Cur and PU. Under laser irradiation, the PU-Cur degradation solution can improve the inhibition rate of *Staphylococcus aureus*, which can promote wound healing (Feng et al., 2021). However, the singlet oxygen quantum yield of curcumin is relatively low, which makes it difficult to achieve the desired antibacterial effect. Combining curcumin with metal nanoparticles can improve the photosensitizer quantum yield by triggering the metal-enhanced singlet oxygen generation (MEO) effect (Mooi and Heyne, 2014). Among metal nanoparticles, silver nanoparticles (Ag NPs) are considered potential antibacterial agents because they can disrupt bacterial wall integrity (Fu et al., 2021; Wu et al., 2022), interfere with DNA replication (Li et al., 2011; Dhanalekshmi and Meena, 2016), and block adenosine triphosphate (ATP) synthesis in bacteria (Wang et al., 2018; Tong et al., 2020). Cao et al. used plant extract lignin as a reducing agent to synthesize Ag NPs (L-Ag NPs) with uniform size distribution by using one-step method, and found that L-Ag NPs have good antibacterial properties against gram-positive Candida albicans and gram-negative *Escherichia coli* (Cao et al., 2021). Ag NPs can enter the interior of bacteria to destroy the bacterial structure and exert antibacterial effects (Khalandi et al., 2017). The particle size and concentration of Ag NPs are the key factors affecting their antibacterial properties. Within a certain concentration range, the higher the concentration of Ag NPs, the better the antibacterial effect (Chen et al., 2019). However, too high concentration will cause Ag NPs to agglomerate and reduce their antibacterial properties (Zhang et al., 2022). Achieving uniform dispersion of Ag NPs at high concentrations is the premise to ensure their high-efficiency antibacterial properties.

Electrospinning is a technique of spraying a solution into a nanofiber membrane under a high-voltage electric field (Sun et al., 2019). Among them, uniaxial electrospinning, which is more commonly used, refers to electrospinning the drug solution through a single nozzle. He et al successfully prepared ciprofloxacin-loaded fibrous mats composed of different ratios of poly-ε-caprolactone (PCL) and polyethylene glycol (PEG) for wound healing by uniaxial electrospinning. The drug release could be controlled by changing the PEG ratio and the fiber mat geometry. The antibacterial effect of different fiber mats on gram-positive *Staphylococcus aureus* and gram-negative *Escherichia coli* was tested by the agar diffusion method. The experimental results showed that when the proportion of PEG was 10%, the fiber mat consisting of grids with a spacing of 0.8 mm had obvious inhibition zone (He et al., 2019). Pisani et al. loaded gentamycin sulfate (GS) into polylactic acid-co-polycaprolactone (PLA-PCL) electrospinning nanofibers for local drug delivery. Controlled drug release could reduce the side effects of GS and prolong the treatment effect. *In-vitro* antibacterial experiments showed that GS-loaded fiber mats had good antibacterial effects on both *Staphylococcus aureus* and *Escherichia coli* (Pisani et al., 2019). Wang et al. successfully prepared Cur-loaded zein fibers (zein-Cur) with encapsulation efficiency close to 100% using uniaxial electrospinning technology. When the content of Cur is 40% based on the weight of zein, the antibacterial rate of fiber against *Staphylococcus aureus* and *Escherichia coli* can reach 90%, and the antibacterial activity of zein-Cur fiber against *Staphylococcus aureus* is better than that of *Escherichia coli* (Wang et al., 2017). Uniaxial electrospinning is used for drug loading with the advantages of various types of loaded drugs or active ingredients and easy adjustment of the fiber structure (Li et al., 2021). When using uniaxial electrospinning to prepare electrospun antibacterial fibers co-loaded with multiple drugs or active ingredients, it is necessary to homogeneously mix multiple drug solutions or active ingredient solutions, which has relatively high requirements for electrospinning system. Coaxial electrospinning, one of the electrospinning technologies, is a technology in which two electrospinning solutions are put into different syringes and sprayed through a concentric needle device to obtain nanofibers with a core/shell structure (Rathore and Schiffman, 2021). The multi-component could be easily co-loaded by coaxial electrospinning. The active pharmaceutical ingredients that are unstable, require sustained release, and have poor spinnability can be used as the fiber core layer, while the shielding effect established by the core/shell structure can act to protect the active pharmaceutical ingredient (Luraghi et al., 2021).

Here, curcumin@Ag (Cur@Ag) core/shell nanofibers co-loaded with curcumin and Ag NPs were fabricated by coaxial electrospinning using polycaprolactone (PCL) and polyvinylpyrrolidone (PVP) solutions containing curcumin as the core layer electrospinning solution, and the PVP solution of Ag NPs as the shell layer electrospinning solution. The prepared nanofibrous membrane can achieve uniform loading of curcumin and Ag NPs. The photosensitizer curcumin generates singlet oxygen under 405 nm light irradiation, and Ag NPs improve the singlet oxygen quantum yield of curcumin through the metal-enhanced singlet oxygen generation effect, combined with the antibacterial effect of Ag NPs, thereby achieving a synergistic antibacterial effect. The as-prepared core/shell structured fibrous membrane has good antibacterial effect against *Staphylococcus aureus*, *Escherichia coli*, and methicillin-resistant *Staphylococcus aureus*.

EXPERIMENTAL SECTION

Materials

Silver nitrate, sodium chloride, and N, N-dimethylformamide (DMF) were purchased from Sinopharm Chemical Reagent Co., Ltd. Curcumin (Cur), polycaprolactone (PCL, $Mw = 8\times10^4$), and polyvinylpyrrolidone K-90 (PVP, $Mw = 1.3\times10^6$) were obtained from Dalian Meilun Biological Co., Ltd. Chloroform ($CHCl_3$) was bought from Laiyang Kangde Chemical Co., Ltd., and ethanol (C_2H_5OH) was purchased from Tianjin Fuyu Fine Chemical Co., Ltd. Beef extract was obtained from Beijing Obosing Biotechnology Company. Tryptone was bought from OXOID, and agar powder was purchased from Solarbio. *Staphylococcus aureus* and *Escherichia coli* were obtained from Beijing Beina Chuanglian Institute of Biotechnology. Methicillin-resistant *Staphylococcus aureus* was purchased from Shanghai Biotechnology Center, and 2, 2, 6, 6-Tetramethylpiperidine (TEMP) was bought from Tongren Institute of Chemistry.

Preparation of PCL/PVP@Cur Electrospun Fiber Membranes

Briefly, PCL/PVP (w/w, 0.6 g:0.4 g) was added in the mixture solvent of $CHCl_3$/DMF (v/v, 8 ml:2 ml), and stirred at room temperature for 1.5 h until completely dissolved. Then, 0.15 g (15 wt% of the total polymer mass) curcumin was introduced and stirred at room temperature for 1 h in the dark to obtain a yellow homogeneous electrospinning solution C1. Similarly, 10 wt% of curcumin, 20 wt% of curcumin, and no curcumin were added to prepare electrospinning solutions C2, C3, and C4, according to the aforementioned method. Finally, the electrospinning solutions C1, C2, C3, and C4 were electrospun with a single nozzle by uniaxial electrospinning. The electrospinning process was performed at a constant flow rate of 0.2 mm/min under the conditions of 25°C temperature and 30% humidity by applying 20 kV voltage, and the nanofibers were collected on aluminum foil at a distance of 15 cm. The collected fiber membranes were dried at 50°C in the dark for 24 h to obtain electrospun fiber membranes CF1, CF2, and CF3 with single-loaded curcumin and a blank matrix fiber membrane CF4.

Preparation of PVP@Ag Electrospun Fiber Membranes

First, 1.5 g of PVP was dissolved in the mixture solvent of C_2H_5OH/DMF (v/v, 7 ml:3 ml), and stirred at room temperature to reach uniformity. Then, 0.12 g (8 wt% of PVP mass) silver nitrate was added and stirred at room temperature in the dark to obtain a light yellow and transparent electrospinning solution S1. Similarly, 6 wt% and 10 wt% of silver nitrate were added to prepare electrospinning solutions S2 and S3, respectively, according to the aforementioned method. Finally, the electrospinning solutions S1, S2, and S3 were electrospun with a single nozzle. The electrospinning process was performed at a constant flow rate of 0.2 mm/min under the conditions of 25°C temperature and 30% humidity by applying 20 kV voltage, and the collect distance was 15 cm. The deposited fiber membranes were cross-linked at 150°C for 3 h, and then irradiated under a 254 nm UV lamp for 1 h to obtain electrospun fiber membranes SF1, SF2, and SF3 single-loaded with Ag NPs.

Preparation of Cur@Ag Core/Shell Fiber Membranes

The electrospinning solutions C1 and S1 were used as core layer and shell layer electrospinning solutions, respectively, and coaxial electrospinning was conducted under the following electrospinning conditions: 20 kV positive pressure, 0.05 kV negative pressure, 25°C temperature, 30% humidity, the distance between the needle and the receiving plate was 15 cm, and the flow rate of electrospinning solution C1 and S1 was 0.2 mm/min and 0.4 mm/min, respectively. The deposited fiber membranes were cross-linked at 150°C for 3 h, and then irradiated under a 254 nm UV lamp for 1 h to obtain the electrospun fiber membrane CS co-loaded with Cur and Ag NPs.

Characterization

The morphologies of the fiber membranes were characterized by field emission scanning electron microscopy (FE-SEM, JSM-6700F). The distribution of Ag NPs in fiber membranes was characterized by transmission electron microscopy (TEM, JEM-1011). The distribution of curcumin in fibrous membranes PCL/PVP@Cur was characterized by fluorescence microscopy (OLYMPUS DP80). The fiber diameter distribution of fiber membranes and the size distribution of Ag NPs in PVP@Ag fibrous membranes were analyzed by Image J software. The Fourier transform infrared (FTIR) analysis was performed with a Fourier transform infrared spectrometer (PerkinElmer).

Electron paramagnetic resonance (EPR) spectrometer (Bruker EMX PLUS) was used to measure the EPR signal intensity of 2, 2, 6, 6-tetramethylpiperidine oxide (TEMPO), which was formed after singlet oxygen generated by fiber membrane CF1 and CS was captured by 2, 2, 6, 6-tetramethylpiperidine (TEMP). The 3 × 3 cm fiber membrane was dissolved in 4 ml of pure water and sonicated for 5 min to obtain the sample solution, and then 100 μL of the sample solution was mixed with 200 μL of the singlet oxygen capture agent TEMP. After 10 min of darkness or light, the singlet oxygen was measured of the mixtures. Test conditions: center field 3,502.00 G, sweep width 100.0 G, power 6.325 mW, power attenuation 15.0 dB, frequency mon 9.829482 GHz, sweep time 30.00 s, modulation amplitude 1.000 G, and modulation frequency 100.00 kHz. The light source was a mercury lamp (500 W) with a 400 nm filter.

Antibacterial Test

Antibacterial Experiment of Electrospun Fiber Membranes Against *Staphylococcus aureus*

In order to evaluate the antibacterial effect of PCL/PVP@Cur electrospun fiber membranes CF1, CF2, and CF3, the antibacterial study was carried out against gram-positive *Staphylococcus aureus* by using the colony counting method (Mahmud et al., 2020). First, a single colony of *Staphylococcus aureus* was inoculated into beef extract peptone liquid medium and placed in a shaker, which was cultured at 37°C and 220 rpm for 24 h to obtain the original bacterial solution. Then, the original bacterial solution was diluted to 1.0–3.0 × 10^7 CFU/ml with sterile pure water to obtain a diluent solution. The CF1, CF2, and CF3 fiber membranes were cut into discs with a diameter of 1 cm and placed in eppendorf (EP) tubes containing 1 ml of diluent solution. Subsequently, the EP tubes were irradiated under a 405 nm UV lamp for 10 min and allowed to stand for 30 min to obtain the treatment solution. The EP tube containing diluent solution without fiber membrane was used as the blank group. 100 μl of the treatment solution was diluted 10^5 times and spread evenly on a solid agar plate, and then incubated in the incubator at 37°C for 24 h. The number of viable colonies with samples was counted, and the antibacterial rates were calculated using the following formula:

$$\text{antibacterial rate} = \frac{N_b - N_t}{N_b} \times 100\% \tag{1}$$

where N_b = number of colonies without sample, and N_t = number of colonies with sample.

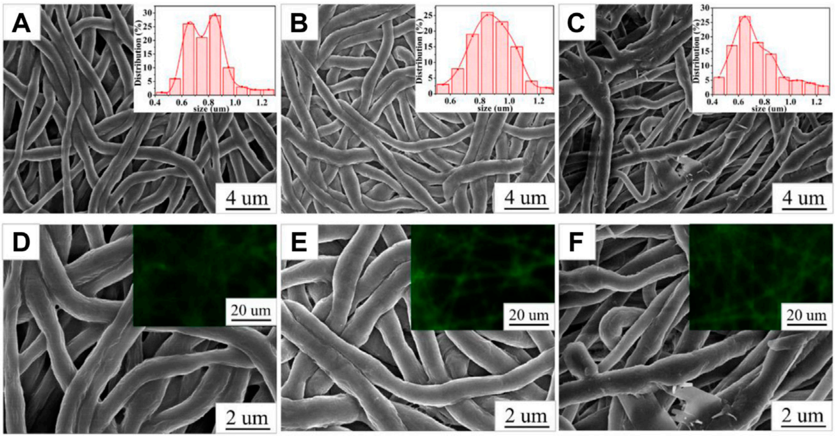

FIGURE 1 | SEM images of CF2 **(A,D)**, CF1 **(B,E)**, and CF3 **(C,F)**; the insets in **(A,B, and C)** are the fiber diameter distribution graphs of CF2, CF1, and CF3; the insets in **(D,E, and F)** are the fluorescence micrographs of CF2, CF1, and CF3.

The PVP@Ag fiber membranes SF1, SF2, and SF3 were cut into discs with a diameter of 1 cm and placed in EP tubes containing 1 ml of diluent solution, and then allowed to stand for 40 min to obtain the treatment solution. The EP tube containing diluent solution without fiber membrane was used as the blank group.

The Cur@Ag core/shell fiber membrane CS was cut into a disc with a diameter of 1 cm and placed in an EP tube containing 1 ml of diluent solution. Subsequently, the EP tube was irradiated under a 405 nm UV lamp for 10 min and allowed to stand for 30 min to obtain the treatment solution. The EP tube containing diluent solution without fiber membrane was used as the blank group.

According to the antibacterial experimental method of PCL/PVP@Cur, the antibacterial rates of PVP@Ag fiber membrane and Cur@Ag core/shell fiber membrane were calculated to characterize their antibacterial properties.

Antibacterial Experiment of Electrospun Fiber Membranes CF1, SF1, and CS Against *Escherichia coli* and Methicillin-Resistant *Staphylococcus aureus* (MRSA)

The CF1, SF1, and CS fiber membranes were cut into discs with a diameter of 1 cm and placed in EP tubes containing 1 ml of *Escherichia coli* or MRSA dilutions, respectively. Then, the CF1 and CS fiber membranes were allowed to stand for 30 min after being irradiated under a 405 nm UV lamp for 10 min to obtain treatment solutions, and SF1 was left to stand for 40 min to obtain a treatment solution. The EP tube containing diluent solution without fiber membrane was used as the blank group. 100 μL of the treatment solutions drawn from the four treatment solutions were diluted 10^5 times and spread evenly on solid agar plates, and then incubated in an incubator at 37°C for 24 h. The number of viable colonies with samples was counted, and the antibacterial rates of fiber membranes against *Escherichia coli* and MRSA, respectively, were calculated, according to **Formula (1)**.

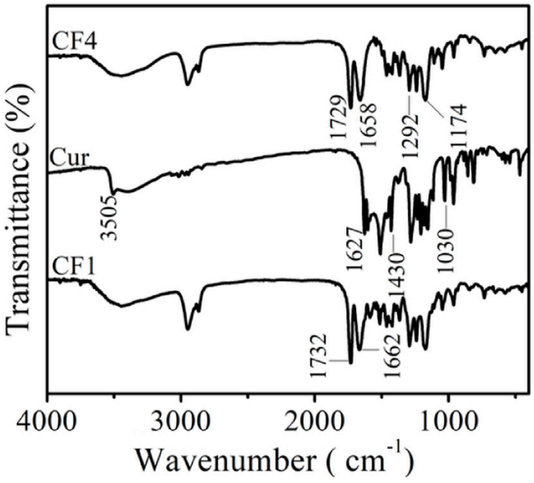

FIGURE 2 | FTIR spectra of CF4, Cur, and CF1.

RESULTS AND DISCUSSION

Characterization of PCL/PVP@Cur Fiber Membranes

The SEM images of PCL/PVP@Cur electrospun fiber membranes are shown in **Figure 1**, and it can be seen that the prepared nanofibers were continuous. The surface of the fiber membranes CF2 and CF1 prepared at a curcumin concentration of 10% and 15%, respectively, was smooth without obvious defects (**Figures 1A,B**). Differently, the fiber membrane CF3 prepared when the concentration of curcumin was 20% had local fiber adhesion phenomenon, and the local fiber thickness difference was obvious (**Figure 1C**). The diameter distribution of the PCL/PVP@Cur electrospun fiber membranes was analyzed with Image J software. As shown in the insets of **Figures 1A–C**, the mean diameters of the fiber membranes CF2, CF1, and CF3 were 0.78 ± 0.15 um, 0.88 ± 0.15 um, and 0.74 ± 0.19 um, respectively. That is, when

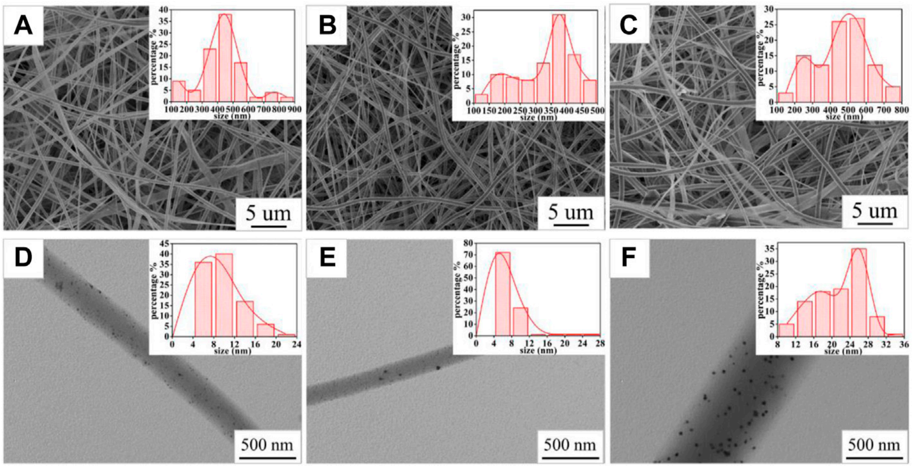

FIGURE 3 | SEM images of SF2 **(A)**, SF1 **(B)**, and SF3 **(C)**; TEM images of SF2 **(D)**, SF1 **(E)**, and SF3 **(F)**; the insets in **(A,B,C)** are the fiber diameter distribution graphs of SF2, SF1, and SF3; the insets in **(D,E,F)** are the Ag NP size distribution graphs of SF2, SF1, and SF3.

the curcumin concentration was 10% and 15%, the fiber diameter distribution was uniform and increased with the increase of curcumin concentration, whereas when the curcumin concentration increased to 20%, the fiber diameter distribution was uneven due to the existence of finer fibers, and the average diameter became smaller. Curcumin has fluorescent properties, so its distribution in the fibrous membrane can be observed by fluorescence microscopy. As shown in the insets of **Figures 1D–F**, a continuous strong fluorescence signal appeared throughout the fiber length, indicating that curcumin was uniformly distributed in the fibers (Tsekova et al., 2017).

The infrared spectra of blank matrix fiber membranes CF4 and Cur and fiber membrane CF1 are shown in **Figure 2**. The absorption peak of curcumin at 3,505 cm^{-1} is attributed to the stretching vibration of phenolic hydroxyl O-H, and the peak at 1,627 cm^{-1} is due to the C=O stretching vibration. The peak at 1,430 cm^{-1} corresponds to the bending vibration of = C-H, and the absorption peak at 1,030 cm^{-1} is ascribed to the C-O-C stretching vibration of aromatic hydrocarbons (Liu et al., 2021). The peaks at 1729 cm^{-1} and 1,658 cm^{-1} in the CF4 fiber membrane correspond to the C=O stretching vibrations in the polymer PCL and PVP, respectively. The absorption peaks at 1,292 cm^{-1} and 1,174 cm^{-1} are assigned to the stretching vibration of C-N in the polymer PVP and the stretching vibration of C-O in polymer PCL, respectively. With the disappearance of the peak (3,505 cm^{-1}) from the phenolic hydroxyl group of curcumin in the CF1 fiber membrane, the C=O stretching vibration peak in the PCL structure changed from 1729 cm^{-1} to 1732 cm^{-1}, and the C=O stretching vibration in the PVP structure also changed from 1,658 cm^{-1} to 1,662 cm^{-1} (Yakub et al., 2020). It is speculated that the redshift of the peaks are caused by the formation of hydrogen bonds between the -OH in curcumin and the C=O structure in PCL and PVP, indicating that curcumin was successfully loaded into the fibers (Tsekova et al., 2017).

Characterization of PVP@Ag Fiber Membranes

The SEM images (**Figures 3A–C**) of the PVP@Ag electrospun fiber membranes showed that the prepared nanofibers were all continuous. The surface of the fiber membranes SF2 and SF1 prepared with the silver nitrate concentration of 6–8% was smooth and there was no slag ball (**Figures 3A,B**). Differently, the fiber membrane SF3 prepared when the silver nitrate concentration was 10% appeared as slag balls and ribbon fibers (**Figure 3C**). The TEM images (**Figures 3D–F**) of SF2, SF1, and SF3 indicated that Ag NPs obtained by silver nitrate reduction were dispersed in the fibers. Image J software was used to determine the fiber diameter distribution of the fiber membranes SF2, SF1, and SF3 and the size distribution of Ag NPs in the fibers. As shown in the insets of **Figures 3A–C**, the fiber diameters of the fiber membranes SF2, SF1, and SF3 were 428 ± 146 nm, 336 ± 93 nm, and 467 ± 141 nm, respectively. As shown in the insets of **Figures 3D–F**, the average sizes of Ag NPs in the fiber membranes SF2, SF1, and SF3 were 10.05 ± 3.48 nm, 7.98 ± 3.04 nm, and 21.75 ± 5.34 nm, respectively. The specific

TABLE 1 | Size specific distribution of Ag NPs.

Fiber membrane	Ag NP size/nm	Ag NP size ratio (%)
SF1	4–8	72
	8–16	25
	16–28	3
SF2	4–8	36
	8–16	57
	16–24	7
SF3	8–16	19
	16–28	72
	28–36	9

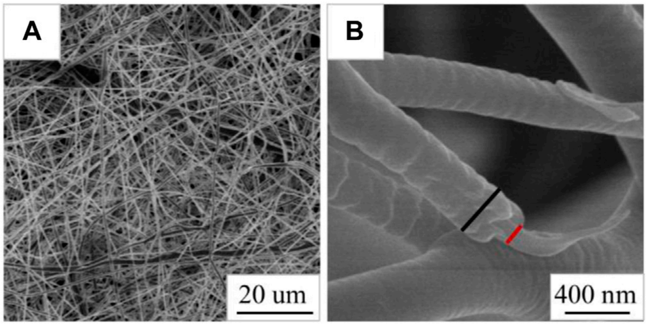

FIGURE 4 | (A) SEM images of CS fibers, the marker in **(B)** is the core-shell structure of the fiber.

distribution of the size of Ag NPs is shown in **Table 1**. It can be seen from **Table 1** that the proportion of Ag NPs of 4–8 nm in SF1 reaches 72%, and the smaller size was conducive to the antibacterial effect of Ag NPs (Wu et al., 2018; Calabrese et al., 2021). Based on the aforementioned analysis, when the silver nitrate concentration increased from 6% to 8%, the average fiber diameter and the average size of Ag NPs became smaller and more uniformly distributed, and the Ag NPs were evenly distributed in the fibers. However, when the silver nitrate concentration increased to 10%, the average fiber diameter and the average size of Ag NPs became larger and unevenly distributed, which may be caused by the aggregation of some Ag NPs into large particles.

Characterization of Cur@Ag Core/Shell Fiber Membrane

As shown in **Figure 4A**, the Cur@Ag fibers are continuous, and the fibers are randomly stacked and packed into a network structure. It can be clearly seen that the Cur@Ag fiber membrane has a core/shell structure from the mark in **Figure 4B**.

Antibacterial Results of PCL/PVP@Cur Electrospun Fiber Membranes Against *Staphylococcus aureus*

Curcumin generates singlet oxygen under irradiation at 405 nm wavelength, which could cause significant structural damage to the membrane structure of *Staphylococcus aureus*, thereby increasing membrane permeability, leading to leakage of intrabacterial substances and bacterial death (Yang et al., 2020). **Figure 5** shows optical photographs of the antibacterial effect of PCL/PVP@Cur electrospun fiber membranes single-loaded with curcumin against *Staphylococcus aureus* for 24 h. It can be seen from the figure that the number of surviving colonies in the blank group and the group of fiber membranes CF2, CF1, and CF3 were 230, 140, 125, and 176, respectively. The calculation showed that the antibacterial rates of the CF2, CF1, and CF3 fiber membranes loaded with curcumin were 39.13, 45.65, and 23.48%, respectively. It can be seen from the antibacterial results that among the electrospinning fibers single-loaded with curcumin, the CF1 fiber membrane with a curcumin loading of 15% has the best antibacterial effect. Compared with CF2, CF1 has higher curcumin loading, so the antibacterial effect of CF1 is better than that of CF2. Among the PCL/PVP@Cur fiber membranes single-loaded with curcumin, CF3 has the highest curcumin loading, but its antibacterial performance is low, which may be related to the adhesion of its fibers and the obvious difference in local fiber diameters (**Figure 1C**).

Antibacterial Results of PVP@Ag Electrospun Fiber Membranes Against *Staphylococcus aureus*

Figure 6 shows optical photographs of the antibacterial effect of PVP@Ag electrospun fiber membranes single-loaded with Ag NPs against *Staphylococcus aureus*. As shown in **Figure 6**, the number of surviving colonies in the blank group and the group of fiber membranes SF2, SF1, and SF3 were 230, 87, 76, and 97, respectively. The calculation showed that the antibacterial rates of the SF2, SF1, and SF3 fiber membranes single-loaded with Ag NPs were 62.17, 66.96, and 57.83%, respectively. The results exhibited that when the amount of silver nitrate increased from 6 to 8%, the antibacterial effect of the obtained SF1 fiber membrane was better than that of SF2, but the antibacterial effect of the obtained SF3 fiber membrane decreased when the concentration increased to 10%. It can be seen from **Figure 3** and **Table 1** that the Ag NPs obtained after the reduction of silver nitrate in the SF1 fiber membrane are small in size and concentrated in 4–16 nm, which accounts for 97%, and is uniformly dispersed in the fiber. Small-sized monodispersed Ag NPs attribute to the superior antibacterial properties of SF1 (Marambio-Jones and Hoek, 2010; Zhou et al., 2022).

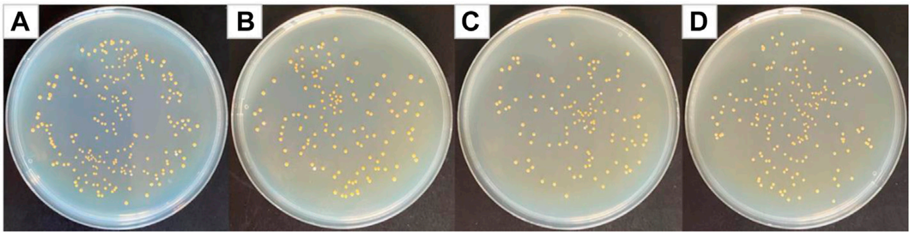

FIGURE 5 | Photographs of antibacterial test result against *Staphylococcus aureus* **(A)** blank group, **(B)** CF2, **(C)** CF1, and **(D)** CF3.

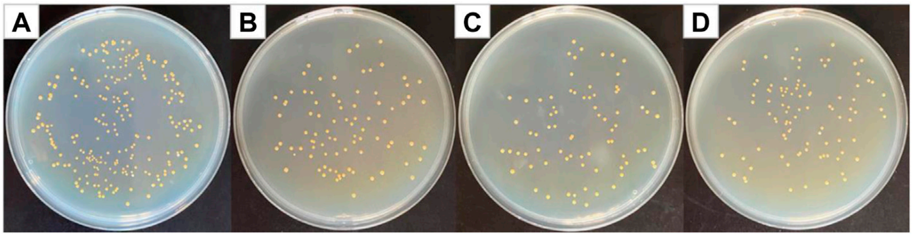

FIGURE 6 | Photographs of antibacterial test result against *Staphylococcus aureus* **(A)** blank group, **(B)** SF2, **(C)** SF1, and **(D)** SF3.

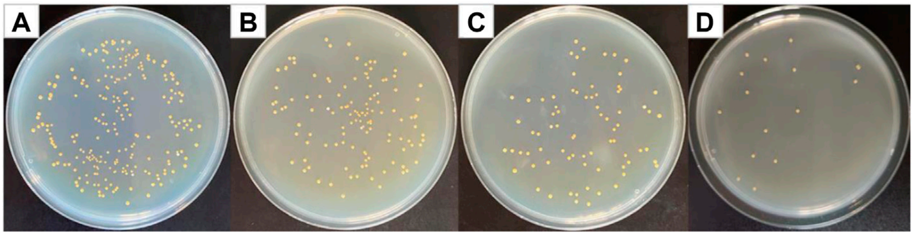

FIGURE 7 | Photographs of antibacterial test result against *Staphylococcus aureus* **(A)** blank group, **(B)** CF1, **(C)** SF1, and **(D)** CS.

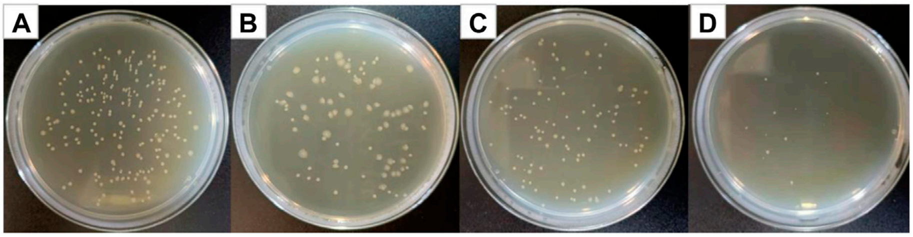

FIGURE 8 | Photographs of antibacterial test result against *Escherichia coli* **(A)** blank group, **(B)** CF1, **(C)** SF1, and **(D)** CS.

Antibacterial Results of Cur@Ag Core/Shell Fibrous Membrane Against *Staphylococcus aureus*, *Escherichia coli*, and MRSA

Figure 7 shows optical photographs of the antibacterial effect of Cur@Ag core/shell fiber membrane against *Staphylococcus aureus*. As shown in **Figure 7**, the number of surviving colonies in the Cur@ Ag core/shell fiber membrane (CS) was 16, and its bacteriostatic rate was as high as 93.04%. Compared with the antibacterial rate 45.65% of the fiber membrane CF1 single-loaded with curcumin and the antibacterial rate 66.96% of the fiber membrane SF1 single-loaded with Ag NPs, the antibacterial rate of Cur@Ag core/shell fiber membrane CS was significantly increased, indicating that curcumin and Ag NPs in the Cur@Ag core/shell fibrous membrane exhibited a clear synergistic inhibitory effect on *Staphylococcus aureus*.

Figure 8 shows optical photographs of the antibacterial effect of Cur@Ag core/shell fiber membrane against *Escherichia coli*. As shown in **Figure 8**, the number of surviving colonies in the blank group and the group of fiber membranes CF1, SF1, and CS were 209, 81, 101, and 15, respectively. The calculation showed that the antibacterial rates of fiber membrane CF1, SF1, and CS were 61.24%, 51.67%, and 92.82%, respectively. Compared with the antibacterial rate 61.24% of the fiber membrane CF1 single-loaded with curcumin, and the antibacterial rate 51.67% of the fiber membrane SF1 single-loaded with Ag NPs, the antibacterial rate of Cur@Ag core/shell fiber membrane CS was significantly increased, indicating that curcumin and Ag NPs could play an obvious synergistic inhibitory effect on *Escherichia coli*.

Figure 9 shows optical photographs of the antibacterial effect of Cur@Ag core/shell fiber membrane against MRSA. As shown in **Figure 9**, the number of surviving colonies in the blank group and the group of fiber membranes CF1, SF1, and CS were 108, 68, 66, and 51, respectively. The calculation showed that the antibacterial rates of fiber membrane CF1, SF1, and CS were 37.04, 38.89, and 52.78%, respectively. Compared with the antibacterial rate 37.04% of the fiber membrane CF1 single-loaded with curcumin, and the antibacterial rate 38.89% of the fiber membrane SF1 single-loaded with Ag NPs, the antibacterial rate of Cur@Ag core/shell fiber membrane CS was increased, indicating that curcumin and Ag NPs could also play a synergistic inhibitory effect on MRSA.

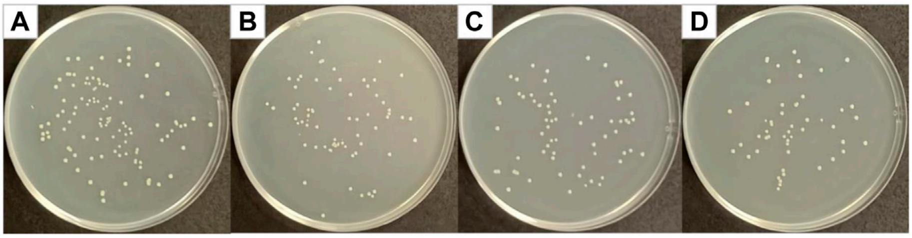

FIGURE 9 | Photographs of antibacterial test result against MRSA **(A)** blank group, **(B)** CF1, **(C)** SF1, and **(D)** CS.

The singlet oxygen test was performed on the fiber membranes CF1 and CS to explore the synergistic antibacterial mechanism of curcumin and Ag NPs. The test results are shown in **Figure 10**.

The singlet oxygen induced by the dispersion of fiber membrane CF1 and fiber membrane CS in pure water can be captured by TEMP and form stable 2, 2, 6, 6-tetramethylpiperidine oxide (TEMPO). The ability of curcumin to generate singlet oxygen in the fiber membrane under different conditions can be known by analyzing the electron paramagnetic resonance (EPR) signal intensity of TEMPO. As shown in **Figure 10**, for CF1, no EPR signal of TEMPO was detected under dark conditions, while three weak EPR signals of TEMPO were observed under light conditions, indicating that curcumin could be induced to produce singlet oxygen under light conditions. Under light conditions, CS detected the strong EPR signals, revealing that the presence of Ag NPs can promote the generation of curcumin singlet oxygen. Ag NPs exerted the metal-enhanced singlet oxygen production effect and improved the singlet oxygen yield (Yu et al., 2020; Wang et al., 2021), so that the antibacterial effect of fiber membrane CS was better than that of CF1 and SF1, and the combined inhibitory effect of Cur and Ag NPs on *Staphylococcus aureus*, *Escherichia coli*, and MRSA was achieved.

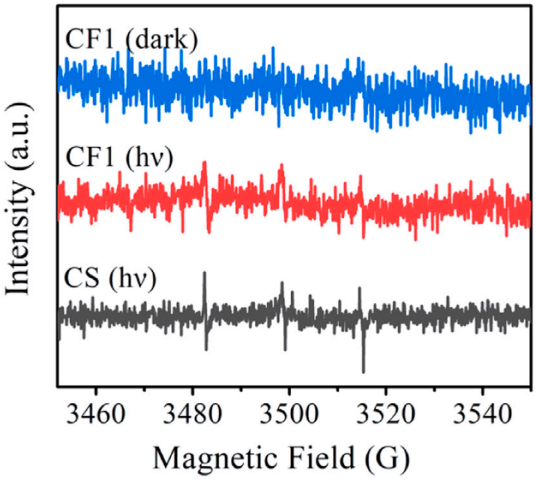

FIGURE 10 | EPR spectra of $^1O_2$ captured by TEMP after CF1 was dispersed in water under dark and light for 10 min, and CS was dispersed in water under light for 10 min.

CONCLUSION

In this study, the curcumin@Ag loaded core/shell nanofiber membrane was constructed by coaxial electrospinning technology. Cur and Ag NPs were uniformly distributed in the core and shell layers of the fiber membrane, respectively. Ag NPs improve the singlet oxygen yield of curcumin through the metal-enhanced singlet oxygen generation effect. The antibacterial experiments showed that compared with the fiber membranes single-loaded with curcumin and Ag NPs, curcumin@Ag loaded core/shell nanofiber membrane exhibited excellent antibacterial effects on both *Staphylococcus aureus* and *Escherichia coli*, and the antibacterial rates reached 93.04% and 92.82%, respectively. At the same time, curcumin@Ag loaded core/shell nanofiber membrane also has synergistic antibacterial effect on methicillin-resistant *Staphylococcus aureus*. In the future, the elucidation of the potential antibacterial mechanism by examining the morphological changes and DNA damage of bacterial cells, and the enhancement of antibacterial effect against drug-resistant bacteria would further favor the application of prepared core/shell nanofiber antimicrobial materials in the field of synergistic antibacterials.

DATA AVAILABILITY STATEMENT

The original contributions presented in the study are included in the article/Supplementary Material, further inquiries can be directed to the corresponding author.

AUTHOR CONTRIBUTIONS

Ideas, formulation of overarching research goals and aims, original draft, QW; formulation of overarching research goals and aims, original draft, SL; original draft, WL; writing—review and editing, PZ, QW, and SL are co-first authors, PZ is the corresponding author.

FUNDING

This work is supported by the academic promotion program of Shandong First Medical University (2019QL011), Shandong Province post-doctoral innovation projects (202003084), and the key projects of industrial science and technology plan in Qiannan prefecture (2017(11)).

REFERENCES

Barros, C. H. N., Hiebner, D. W., Fulaz, S., Vitale, S., Quinn, L., and Casey, E. (2021). Synthesis and Self-Assembly of Curcumin-Modified Amphiphilic Polymeric Micelles with Antibacterial Activity. *J. Nanobiotechnol* 19 (1), 104–118. doi:10.1186/s12951-021-00851-2

Calabrese, G., Petralia, S., Franco, D., Nocito, G., Fabbi, C., Forte, L., et al. (2021). A New Ag-Nanostructured Hydroxyapatite Porous Scaffold: Antibacterial Effect and Cytotoxicity Study. *Mater. Sci. Eng. C* 118, 111394–111403. doi:10.1016/j.msec.2020.111394

Cao, X., Zhu, L., Bai, Y., Li, F., and Yu, X. (2021). Green One-step Synthesis of Silver Nanoparticles and Their Biosafety and Antibacterial Properties. *Green. Chem. Lett. Rev.* 15 (1), 26–32. doi:10.1080/17518253.2021.2018506

Chen, J., Li, H., Fang, C., Cheng, Y., Tan, T., and Han, H. (2019). *In Situ* synthesis and Properties of Ag NPs/carboxymethyl Cellulose/starch Composite Films for Antibacterial Application. *Polym. Composites* 41 (3), 838–847. doi:10.1002/pc.25414

Chen, M., Li, L., Xia, L., Jiang, S., Kong, Y., Chen, X., et al. (2021). The Kinetics and Release Behaviour of Curcumin Loaded pH-Responsive PLGA/chitosan Fibers with Antitumor Activity against HT-29 Cells. *Carbohydr. Polym.* 265, 118077–118084. doi:10.1016/j.carbpol.2021.118077

Dhanalekshmi, K. I., and Meena, K. S. (2016). DNA Intercalation Studies and Antimicrobial Activity of Ag@ZrO 2 Core-Shell Nanoparticles *In Vitro*. *Mater. Sci. Eng. C* 59, 1063–1068. doi:10.1016/j.msec.2015.11.027

Dourado, D., Freire, D. T., Pereira, D. T., Amaral-Machado, L., N. Alencar, É., de Barros, A. L. B., et al. (2021). Will Curcumin Nanosystems Be the Next Promising Antiviral Alternatives in COVID-19 Treatment Trials? *Biomed. Pharmacother.* 139, 111578–111584. doi:10.1016/j.biopha.2021.111578

Farhat, N., Ali, A., Bonomo, R. A., and Khan, A. U. (2020). Efflux Pumps as Interventions to Control Infection Caused by Drug-Resistance Bacteria. *Drug Discov. Today* 25 (12), 2307–2316. doi:10.1016/j.drudis.2020.09.028

Feng, Y., Xiao, K., He, Y., Du, B., Hong, J., Yin, H., et al. (2021). Tough and Biodegradable Polyurethane-Curcumin Composited Hydrogel with Antioxidant, Antibacterial and Antitumor Properties. *Mater. Sci. Eng. C* 121, 111820–111832. doi:10.1016/j.msec.2020.111820

Fu, S., Zhang, Y., Qin, G., and Zhang, E. (2021). Antibacterial Effect of Ti Ag alloy Motivated by Ag-Containing Phases. *Mater. Sci. Eng. C* 128, 112266–112276. doi:10.1016/j.msec.2021.112266

Godoy-Gallardo, M., Eckhard, U., Delgado, L. M., de Roo Puente, Y. J. D., Hoyos-Nogués, M., Gil, F. J., et al. (2021). Antibacterial Approaches in Tissue Engineering Using Metal Ions and Nanoparticles: From Mechanisms to Applications. *Bioactive Mater.* 6 (12), 4470–4490. doi:10.1016/j.bioactmat.2021.04.033

He, F.-L., Deng, X., Zhou, Y.-Q., Zhang, T.-D., Liu, Y.-L., Ye, Y.-J., et al. (2019). Controlled Release of Antibiotics from Poly-ε-Caprolactone/polyethylene Glycol Wound Dressing Fabricated by Direct-Writing Melt Electrospinning. *Polym. Adv. Technol.* 30 (2), 425–434. doi:10.1002/pat.4481

Hou, X., Liang, J., Yang, X., Bai, J., Yang, M., Qiao, N., et al. (2022). Poloxamer188-based Nanoparticles Improve the Anti-oxidation and Anti-degradation of Curcumin. *Food Chem.* 375, 131674–131681. doi:10.1016/j.foodchem.2021.131674

Hu, J., Lin, S., Tan, B. K., Hamzah, S. S., Lin, Y., Kong, Z., et al. (2018). Photodynamic Inactivation of Burkholderia Cepacia by Curcumin in Combination with EDTA. *Food Res. Int.* 111, 265–271. doi:10.1016/j.foodres.2018.05.042

Im, B. N., Shin, H., Lim, B., Lee, J., Kim, K. S., Park, J. M., et al. (2021). Helicobacter Pylori-Targeting Multiligand Photosensitizer for Effective Antibacterial Endoscopic Photodynamic Therapy. *Biomaterials* 271, 120745–120755. doi:10.1016/j.biomaterials.2021.120745

Khalandi, B., Asadi, N., Milani, M., Davaran, S., Abadi, A., Abasi, E., et al. (2017). A Review on Potential Role of Silver Nanoparticles and Possible Mechanisms of Their Actions on Bacteria. *Drug Res. (Stuttg)* 67 (2), 70–76. doi:10.1055/s-0042-113383

Li, H., Chen, X., Lu, W., Wang, J., Xu, Y., and Guo, Y. (2021). Application of Electrospinning in Antibacterial Field. *Nanomaterials* 11 (7), 1822–1850. doi:10.3390/nano11071822

Li, T., Zhao, Y., Matthews, K., Gao, J., Hao, J., Wang, S., et al. (2020). Antibacterial Activity against *Staphylococcus aureus* of Curcumin-Loaded Chitosan spray Coupled with Photodynamic Treatment. *Lwt* 134, 110073–110079. doi:10.1016/j.lwt.2020.110073

Li, W.-R., Xie, X.-B., Shi, Q.-S., Duan, S.-S., Ouyang, Y.-S., and Chen, Y.-B. (2011). Antibacterial Effect of Silver Nanoparticles on *Staphylococcus aureus*. *Biometals* 24 (1), 135–141. doi:10.1007/s10534-010-9381-6

Liu, C.-L., Yang, J., Bai, X.-H., Cao, Z.-K., Yang, C., Ramakrishna, S., et al. (2021). Dual Antibacterial Effect of *In Situ* Electrospun Curcumin Composite Nanofibers to Sterilize Drug-Resistant Bacteria. *Nanoscale Res. Lett.* 16 (1), 54–61. doi:10.1186/s11671-021-03513-2

Liu, Z.-J., Lin, S.-C., Lee, P.-Y., Lin, Y.-T., Lai, Z.-L., Chang, C.-C., et al. (2020). Dual-acting Antibacterial Porous Chitosan Film Embedded with a Photosensitizer. *Sci. Techn. Adv. Mater.* 21 (1), 562–572. doi:10.1080/14686996.2020.1795431

Luraghi, A., Peri, F., and Moroni, L. (2021). Electrospinning for Drug Delivery Applications: A Review. *J. Controlled Release* 334, 463–484. doi:10.1016/j.jconrel.2021.03.033

Lyutakov, O., Hejna, O., Solovyev, A., Kalachyova, Y., and Svorcik, V. (2014). Polymethylmethacrylate Doped with Porphyrin and Silver Nanoparticles as Light-Activated Antimicrobial Material. *RSC Adv.* 4 (92), 50624–50630. doi:10.1039/c4ra08385g

Mahmud, M. M., Zaman, S., Perveen, A., Jahan, R. A., Islam, M. F., and Arafat, M. T. (2020). Controlled Release of Curcumin from Electrospun Fiber Mats with Antibacterial Activity. *J. Drug Deliv. Sci. Techn.* 55, 101386–101425. doi:10.1016/j.jddst.2019.101386

Marambio-Jones, C., and Hoek, E. M. V. (2010). A Review of the Antibacterial Effects of Silver Nanomaterials and Potential Implications for Human Health and the Environment. *J. Nanopart. Res.* 12 (5), 1531–1551. doi:10.1007/s11051-010-9900-y

Mooi, S. M., and Heyne, B. (2014). Amplified Production of Singlet Oxygen in Aqueous Solution Using Metal Enhancement Effects. *Photochem. Photobiol.* 90 (1), 85–91. doi:10.1111/php.12176

Pisani, S., Dorati, R., Chiesa, E., Genta, I., Modena, T., Bruni, G., et al. (2019). Release Profile of Gentamicin Sulfate from Polylactide-Co-Polycaprolactone Electrospun Nanofiber Matrices. *Pharmaceutics* 11 (4), 161–174. doi:10.3390/pharmaceutics11040161

Pontes-Quero, G. M., Benito-Garzón, L., Pérez Cano, J., Aguilar, M. R., and Vázquez-Lasa, B. (2021). Amphiphilic Polymeric Nanoparticles Encapsulating Curcumin: Antioxidant, Anti-inflammatory and Biocompatibility Studies. *Mater. Sci. Eng. C* 121, 111793–111808. doi:10.1016/j.msec.2020.111793

Qiu, L., Wang, C., Lei, X., Du, X., Guo, Q., Zhou, S., et al. (2021). Gelatinase-responsive Release of an Antibacterial Photodynamic Peptide against *Staphylococcus aureus*. *Biomater. Sci.* 9 (9), 3433–3444. doi:10.1039/d0bm02201b

Rathore, P., and Schiffman, J. D. (2021). Beyond the Single-Nozzle: Coaxial Electrospinning Enables Innovative Nanofiber Chemistries, Geometries, and Applications. *ACS Appl. Mater. Inter.* 13 (1), 48–66. doi:10.1021/acsami.0c17706

Sun, J., Fan, Y., Ye, W., Tian, L., Niu, S., Ming, W., et al. (2021). Near-infrared Light Triggered Photodynamic and Nitric Oxide Synergistic Antibacterial Nanocomposite Membrane. *Chem. Eng. J.* 417, 128049–128059. doi:10.1016/j.cej.2020.128049

Sun, Y., Cheng, S., Lu, W., Wang, Y., Zhang, P., and Yao, Q. (2019). Electrospun Fibers and Their Application in Drug Controlled Release, Biological Dressings, Tissue Repair, and Enzyme Immobilization. *RSC Adv.* 9 (44), 25712–25729. doi:10.1039/c9ra05012d

Tong, C., Zhong, X., Yang, Y., Liu, X., Zhong, G., Xiao, C., et al. (2020). PB@PDA@Ag Nanosystem for Synergistically Eradicating MRSA and Accelerating Diabetic Wound Healing Assisted with Laser Irradiation. *Biomaterials* 243, 119936–119949. doi:10.1016/j.biomaterials.2020.119936

Tsekova, P. B., Spasova, M. G., Manolova, N. E., Markova, N. D., and Rashkov, I. B. (2017). Electrospun Curcumin-Loaded Cellulose Acetate/polyvinylpyrrolidone Fibrous Materials with Complex Architecture and Antibacterial Activity. *Mater. Sci. Eng. C* 73, 206–214. doi:10.1016/j.msec.2016.12.086

Wang, H., Hao, L., Wang, P., Chen, M., Jiang, S., and Jiang, S. (2017). Release Kinetics and Antibacterial Activity of Curcumin Loaded Zein Fibers. *Food Hydrocolloids* 63, 437–446. doi:10.1016/j.foodhyd.2016.09.028

Wang, H., Jiang, Y., Zhang, Y., Zhang, Z., Yang, X., Ali, M. A., et al. (2018). Silver Nanoparticles: A Novel Antibacterial Agent for Control of Cronobacter Sakazakii. *J. Dairy Sci.* 101 (12), 10775–10791. doi:10.3168/jds.2018-15258

Wang, J., Zhang, X., Liu, Y., Wang, Z., Wang, P., Zheng, Z., et al. (2021). Enhanced Singlet Oxygen Production over a Photocatalytic Stable Metal Organic Framework Composed of Porphyrin and Ag. *J. Colloid Interf. Sci.* 602, 300–306. doi:10.1016/j.jcis.2021.05.087

Wu, M.-Y., Liu, L., Zou, Q., Leung, J.-K., Wang, J.-L., Chou, T. Y., et al. (2020). Simple Synthesis of Multifunctional Photosensitizers for Mitochondrial and Bacterial Imaging and Photodynamic Anticancer and Antibacterial Therapy. *J. Mater. Chem. B* 8, 9035–9042. doi:10.1039/d0tb01669a

Wu, S., Xu, C., Zhu, Y., Zheng, L., Zhang, L., Hu, Y., et al. (2021). Biofilm-Sensitive Photodynamic Nanoparticles for Enhanced Penetration and Antibacterial Efficiency. *Adv. Funct. Mater.* 31 (33), 2103591–2103601. doi:10.1002/adfm.202103591

Wu, Y., Yang, S., Fu, F., Zhang, J., Li, J., Ma, T., et al. (2022). Amino Acid-Mediated Loading of Ag NPs and Tannic Acid onto Cotton Fabrics: Increased Antibacterial Activity and Decreased Cytotoxicity. *Appl. Surf. Sci.* 576, 151821–151832. doi:10.1016/j.apsusc.2021.151821

Wu, Y., Yang, Y., Zhang, Z., Wang, Z., Zhao, Y., and Sun, L. (2018). A Facile Method to Prepare Size-Tunable Silver Nanoparticles and its Antibacterial Mechanism. *Adv. Powder Techn.* 29 (2), 407–415. doi:10.1016/j.apt.2017.11.028

Xiao, Q., Mai, B., Nie, Y., Yuan, C., Xiang, M., Shi, Z., et al. (2021). *In Vitro* and *In Vivo* Demonstration of Ultraefficient and Broad-Spectrum Antibacterial Agents for Photodynamic Antibacterial Chemotherapy. *ACS Appl. Mater. Inter.* 13 (10), 11588–11596. doi:10.1021/acsami.0c20837

Yakub, G., Toncheva, A., Kussovski, V., Toshkova, R., Georgieva, A., Nikolova, E., et al. (2020). Curcumin-PVP Loaded Electrospun Membranes with Conferred Antibacterial and Antitumoral Activities. *Fibers Polym.* 21 (1), 55–65. doi:10.1007/s12221-020-9473-z

Yang, Q.-Q., Farha, A. K., Kim, G., Gul, K., Gan, R.-Y., and Corke, H. (2020). Antimicrobial and Anticancer Applications and Related Mechanisms of Curcumin-Mediated Photodynamic Treatments. *Trends Food Sci. Techn.* 97, 341–354. doi:10.1016/j.tifs.2020.01.023

Yu, F., Chen, C., Yang, G., Ren, Z., Cao, H., Zhang, L., et al. (2021). An Acid-Triggered Porphyrin-Based Block Copolymer for Enhanced Photodynamic Antibacterial Efficacy. *Sci. China Chem.* 64 (3), 459–466. doi:10.1007/s11426-020-9904-7

Yu, Y., Mei, L., Shi, Y., Zhang, X., Cheng, K., Cao, F., et al. (2020). Ag-Conjugated Graphene Quantum Dots with Blue Light-Enhanced Singlet Oxygen Generation for Ternary-Mode Highly-Efficient Antimicrobial Therapy. *J. Mater. Chem. B* 8 (7), 1371–1382. doi:10.1039/c9tb02300c

Zhang, J., Cao, R., Song, W., Liu, L., and Li, J. (2022). One-step Method to Prepare Core-Shell Magnetic Nanocomposite Encapsulating Silver Nanoparticles with superior Catalytic and Antibacterial Activity. *J. Colloid Interf. Sci.* 607 (Pt 2), 1730–1740. doi:10.1016/j.jcis.2021.09.053

Zhao, Y., Zhu, Y., Yang, G., Xia, L., Yu, F., Chen, C., et al. (2021). A pH/H2O2 Dual Triggered Nanoplatform for Enhanced Photodynamic Antibacterial Efficiency. *J. Mater. Chem. B* 9 (25), 5076–5082. doi:10.1039/d1tb00441g

Zhou, F., Zhu, Y., Yang, L., Yang, D.-Q., and Sacher, E. (2022). Ag NP Catalysis of Cu Ions in the Preparation of AgCu NPs and the Mechanism of Their Enhanced Antibacterial Efficacy. *Colloids Surf. A: Physicochemical Eng. Aspects* 632, 127831–127842. doi:10.1016/j.colsurfa.2021.127831

Conflict of Interest: The authors declare that the research was conducted in the absence of any commercial or financial relationships that could be construed as a potential conflict of interest.

frontiers in Chemistry

REVIEW
published: 24 March 2022
doi: 10.3389/fchem.2022.868630

Multifunctional Nanomaterials for Ferroptotic Cancer Therapy

Zhiyuan Shi[1†], *Jianzhong Zheng*[1†], *Wenbin Tang*[1†], *Yang Bai*[1], *Lei Zhang*[2], *Zuodong Xuan*[1], *Huimin Sun*[3*] and *Chen Shao*[1*]

[1]Department of Urology, Xiang'an Hospital of Xiamen University, School of Medicine, Xiamen University, Xiamen, China, [2]School of Public Health, Xiamen Univerisity, Xiamen, China, [3]Central Laboratory, Xiang'an Hospital of Xiamen University, School of Medicine, Xiamen University, Xiamen, China

Patient outcomes from the current clinical cancer therapy remain still far from satisfactory. However, in recent years, several biomedical discoveries and nanotechnological innovations have been made, so there is an impetus to combine these with conventional treatments to improve patient experience and disease prognosis. Ferroptosis, a term first coined in 2012, is an iron-dependent regulated cell death (RCD) based on the production of reactive oxygen species (ROS) and the consequent oxidization of polyunsaturated fatty acids (PUFAs). Many nanomaterials that can induce ferroptosis have been explored for applications in cancer therapy. In this review, we summarize the recent developments in ferroptosis-based nanomaterials for cancer therapy and discuss the future of ferroptosis, nanomedicine, and cancer therapy.

Keywords: cancer therapy, ferroptosis, nanomaterial, ferroptosis inducers, reactive oxygen species

Edited by:
Yan Zhang,
University of Jinan, China

Reviewed by:
Xin Pang,
First Affiliated Hospital of Zhengzhou University, China
Lisi Xie,
Sun Yat-sen Memorial Hospital, China

***Correspondence:**
Huimin Sun
hmsun@xah.xmu.edu.cn
Chen Shao
cshao@xah.xmu.edu.cn

†These authors have contributed equally to this work

Specialty section:
This article was submitted to Analytical Chemistry, a section of the journal Frontiers in Chemistry

Received: *03 February 2022*
Accepted: *02 March 2022*
Published: *24 March 2022*

Citation:
Shi Z, Zheng J, Tang W, Bai Y, Zhang L, Xuan Z, Sun H and Shao C (2022) Multifunctional Nanomaterials for Ferroptotic Cancer Therapy. Front. Chem. 10:868630. doi: 10.3389/fchem.2022.868630

1 INTRODUCTION

Cancer is one of the leading causes of death and one of the most important diseases affecting human health worldwide (Bray et al., 2021). According to the recent global cancer statistics, there were over 19 million new cancer cases and 10.0 million cancer deaths in 2020, and the cancer burden might be expected to reach 28.4 million cases by 2040 (Sung et al., 2021). Therefore, the development of cancer prevention and treatment strategies is crucial to achieve global cancer control. Conventional approaches, such as surgery, radiotherapy, and chemotherapy, have been utilized; however, the prognosis does not achieve both the doctor's and patient's satisfaction due to the hallmarks of cancer, such as sustaining proliferative signaling, evading growth suppressors, nonmutational epigenetic reprograming, avoiding immune destruction, activating invasion and metastasis, inducing vasculature, genome instability and mutation, resisting cell death, and deregulating cellular metabolism (Hanahan 2022). Accompanied with the significant scientific and technological advancements in recent times, several new technologies are currently under research in clinical trials, and some of them have already been approved for clinical application, including stem cell therapy, targeted therapy, ablation therapy, photodynamic therapy (PDT), photothermal therapy (PTT), chemodynamic therapy (CDT), sonodynamic therapy (SDT), and ferroptosis-based therapy (FBT) (Debela et al., 2021).

Ferroptosis is a novel type of regulated cell death (RCD) that is iron-dependent and characterized by the oxidization of polyunsaturated fatty acids (PUFAs) and subsequently accumulation of lipid peroxides (LPOs) (**Figure 1**) (Shi et al., 2021). During the past two decades, Brent R. Stockwell et al. focused on ferroptosis, and their research studies have attracted global attention. Specifically, in 2003, they identified a novel compound and named it "erastin" (Dolma et al., 2003). Intriguingly, they found that although cell death occurred, characteristics of apoptosis were not observed when erastin

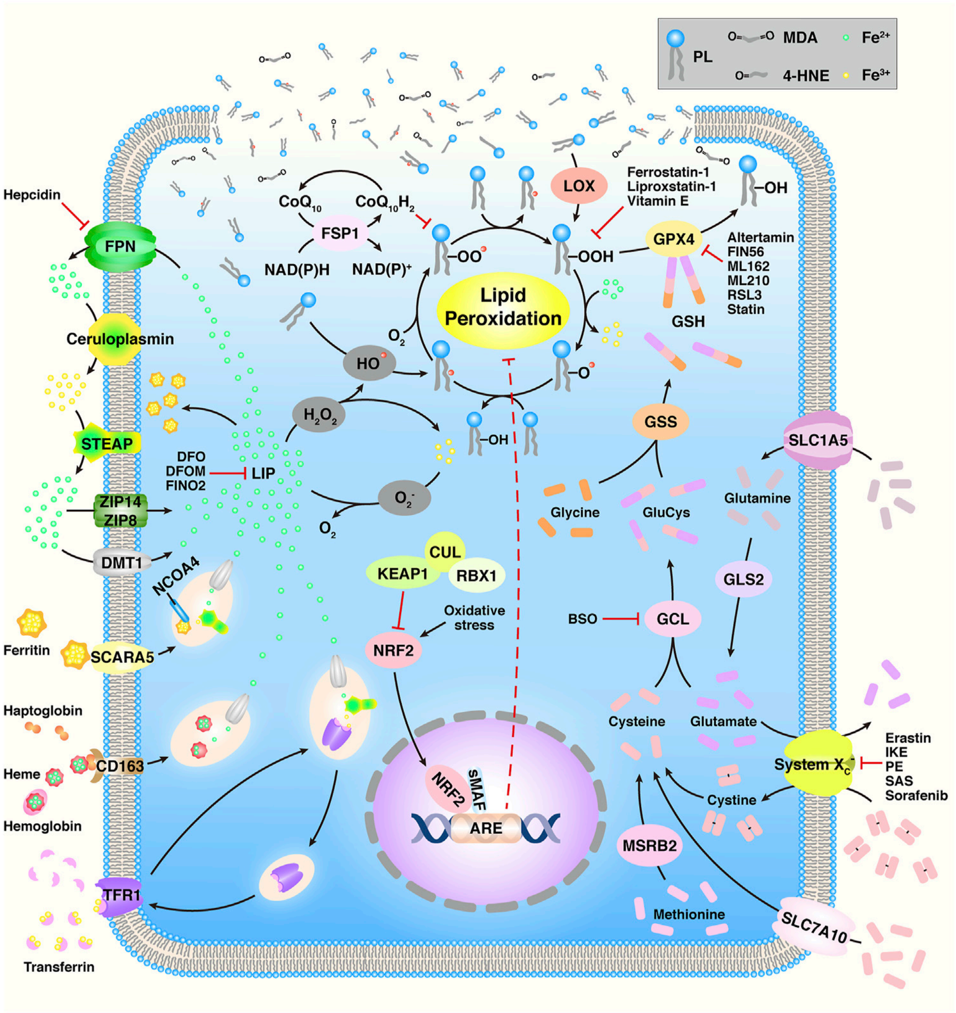

FIGURE 1 | Overview of the ferroptosis mechanism. Adapted from Shi et al., (2021) Copyright @ 2021 (Frontiers).

was present in several tumor cells. In 2007, they found that erastin-induced cell death could be suppressed by α-tocopherol (Yagoda et al., 2007). In 2008, they found another small compound, Ras selective lethal 3 (RSL3) that induced analogous iron-dependent nonapoptotic cell death in RAS-enriched cancer cells, and this could also be restrained by the presence of α-tocopherol or desferrioxamine mesylate (DFOM) (Yang and Stockwell, 2008). In 2011, they confirmed that erastin- and RSL3-induced cell death differed from the mechanism of other cell deaths (Wolpaw et al., 2011). Therefore, in 2012, they named this phenomenon 'ferroptosis' (Dixon et al., 2012). Ferroptosis is distinct from apoptosis, autophagy, and necroptosis in terms of morphology, biochemistry, and genetics (Cao and Dixon, 2016). Cells experiencing ferroptosis show special hallmarks, including the fracture of the cell membrane, smaller mitochondria, increased density of the mitochondrial membrane, reduced/vanished mitochondrial cristae, and outer mitochondrial membrane breakup; however, the nuclei remain normal (Li, J. et al., 2020).

Many nanotechnologists have focused on cancer therapy in recent years because of the promising physicochemical properties of nanomaterials (Liang et al., 2019), and an increasing number of biomedical nanomaterials have been widely investigated as nanomaterial-based drug delivery systems for anticancer therapeutics, with enhanced drug availability, improved efficacy, targeted delivery, and reduced treatment-related toxicity, which could better solve the disadvantages of anticancer drugs with low solubility and poor membrane permeability (Luo et al., 2014; Asghari et al., 2019; Fei et al., 2020a). Nanomaterials possess an exceptional advantage of the enhanced permeability and retention (EPR) effect, which is related to anatomical and pathophysiological differences between the tumor tissue and normal tissue. Crucially, the solid tumors are highly vascularized and have large gaps between the endothelial cells in tumor vessels; as a result, macromolecular drugs are selectively extravasated and retained by the tumor tissues (Fang et al., 2011). Nevertheless, the EPR effect can be influenced by the systolic blood pressure and is

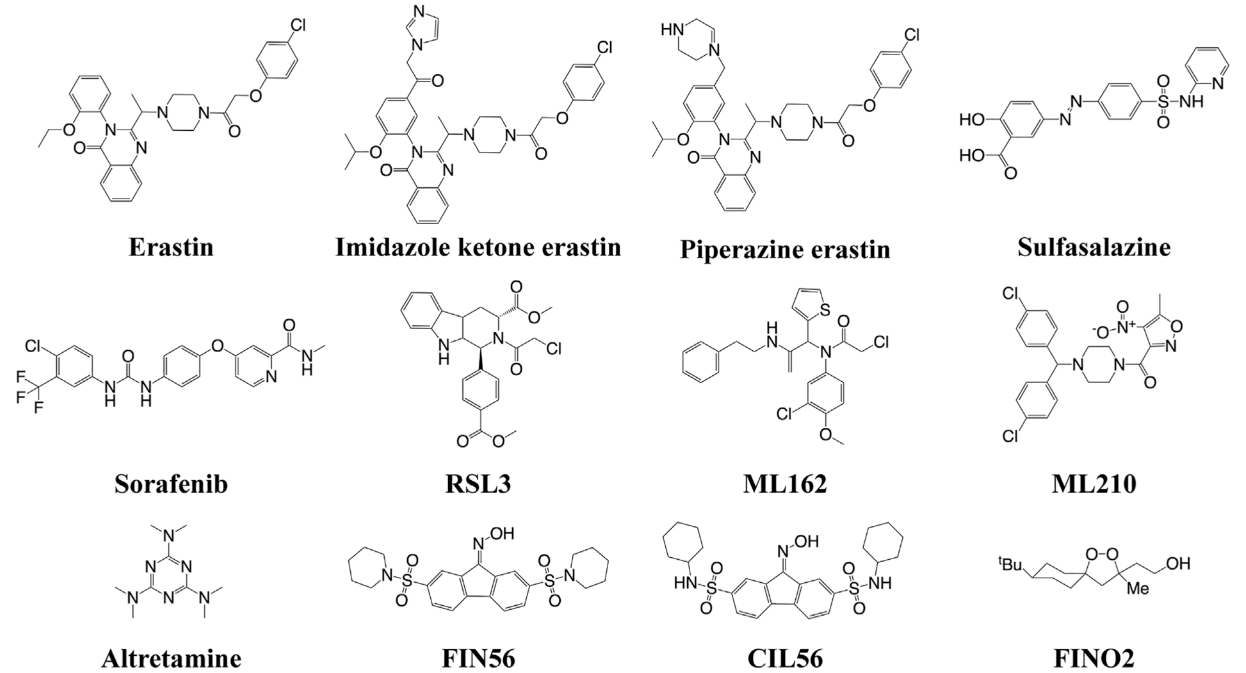

FIGURE 2 | Structures of the small-molecule ferroptosis inducers.

negligible in advanced cancers (Maeda 2015; Golombek et al., 2018; Shan et al., 2020). In addition to the EPR effect, several strategies were taken into advantage by the researchers, such as modifying targeting molecules, remodeling the tumor microenvironment (TME), and enabling tumor stimuli–responsive properties (Shi et al., 2017; Youn and Bae, 2018; Park et al., 2019). Thus, nanomaterials can be used as delivery agents for anticancer drugs, but they can also be used to convert energy to kill cancer cells, such as light, ultrasound (US), electricity, and magnetothermal energy (Fei et al., 2020a). As a result, in the last few years, the Food and Drug Administration (FDA) has approved a large number of anticancer nanomaterials, demonstrating the huge potential of nanomaterials for the precision and personalized cancer therapies in future.

Ferroptosis, as a novel RCD, has become a popular area of cancer research, and, thus, numerous nanomaterials that induce ferroptosis have been developed for cancer therapy because of their potential antitumor properties. In this review, we try to summarize and discuss the multifunctional ferroptosis-based nanomaterials on the recent advances and breakthroughs in cancer therapies.

2 FERROPTOSIS INDUCERS (FINS)

The FINs can be classified into four types **(Figure 2)**. Class I FINs could block the biosynthesis of glutathione (GSH) or deplete it. Many small compounds (such as erastin, imidazole ketone erastin, piperazine erastin, sulfasalazine, and sorafenib) can inhibit system X_c^-, which could transfer cystine into the cells and export glutamate out of the cells (Feng and Stockwell, 2018). The system X_c^- consists of solute carrier family 7 member A11 (SLC7A11, also known as xCT) and SLC3A2 (4F2hc) (Shi et al., 2021). GSH is a cofactor of GSH peroxidase 4 (GPX4), which is a crucial regulator for the conversion of LPOs to the corresponding hydroxyl compounds (LOH). Therefore, the depletion of GSH can inactivate GPX4, subsequently resulting in the accumulation of LPOs to induce ferroptosis. Class II FINs directly inhibit GPX4. Small compounds (such as RSL3, ML162, ML210, and altretamine) can interact with the active selenocyteine site of GPX4 and inhibit its enzymatic activity, resulting in the accumulation of LPOs (Cao and Dixon 2016). Class III FINs deplete the GPX4 protein. For example, the compounds FIN56 and caspase-independent lethal 56 (CIL56) could induce ferroptosis by directly degrading the GPX4 and synchronously depleting the mevalonate-derived coenzyme Q_{10} (CoQ_{10}) (Shimada et al., 2016). Class IV FINs could induce lipid peroxidation, but there is only one small compound, FIN endoperoxide (FINO2), that can directly oxidize iron, indirectly inactivate GPX4, and ultimately cause lipid peroxidation (Gaschler et al., 2018). This compound is suitable *in vitro*; however, it might not be effective *in vivo*.

3 NANOMATERIALS AS FINS

The design of the multifunctional nanomaterials with precisely tuned physicochemical properties could enhance the drug delivery for cancer therapy. The first ferroptosis-inducing nanomaterial was reported by Kim et al. in 2016 (**Figure 3**) (Kim et al., 2016). They coated the near-infrared (NIR) fluorescent silica nanoparticles (NPs) with ploy (ethylene

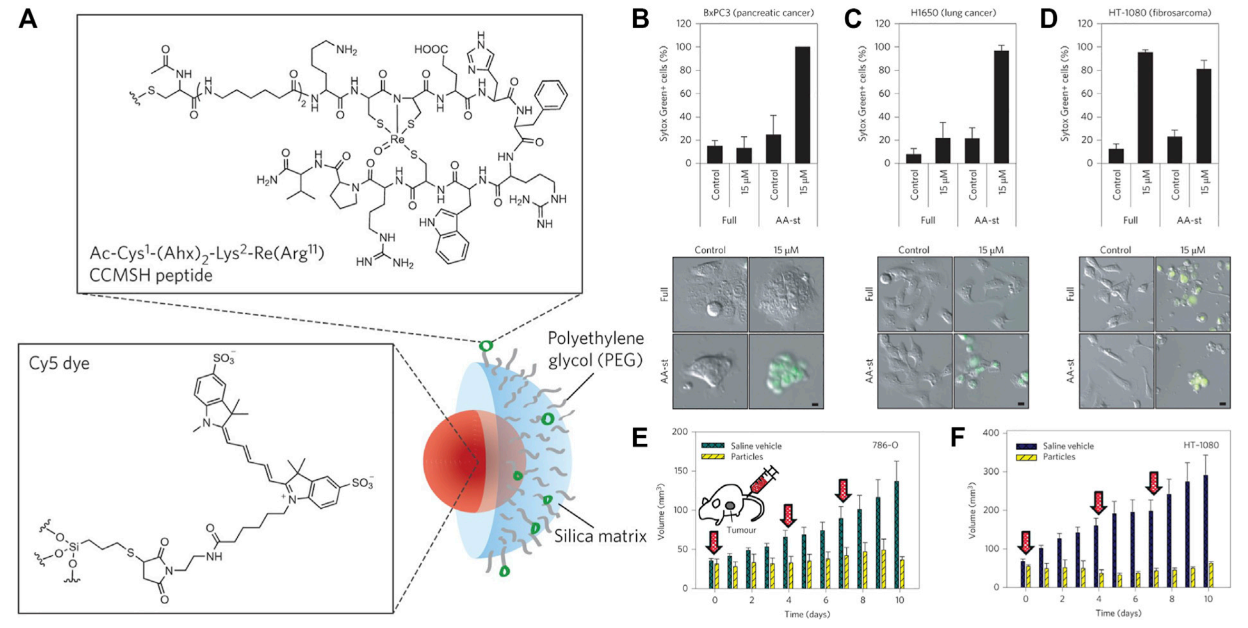

FIGURE 3 | (A) Synthesis scheme of αMSH-PEG-C′ dots. **(B–D)** Cell death about BxPC3 cells with different treatments **(B)**, H1650 cells **(C)**, and HT-1080 cells **(D)**. **(E)** 786-O and **(F)** HT-1080 tumor volume with different treatments. Reproduced with permission from Kim et al., (2016) Copyright @ 2016 (Springer Nature).

glycol)-coated (PEGylated) and Cornell dots (C′ dots) and surface-modified with the melanoma-targeting peptide and alpha-melanocyte stimulating hormone (αMSH). The C′ dots could absorb and incorporate extracellular iron into their structure to increase the intracellular iron level with the subsequent production of reactive oxygen species (ROS) and depletion of GSH, ultimately leading to ferroptosis in different cancer models. The research laid the groundwork for investigating nanomaterials as effective FINs in sensitive tumors.

3.1 Iron-Contained Nanomaterials

Owing to the crucial role of iron in ferroptosis, iron-contained nanomaterials have become the most popular nanomaterials for FBT. In recent years, several types of iron-contained nanomaterials have been explored to induce ferroptosis.

3.1.1 Iron Ion–Based Nanomaterials

The different valence states of iron have been exploited to develop nanomaterials that act as FINs to kill cancer cells. In the zero-valent iron NP (ZVI NPs)–sensitive cancer cells, Fe^0 could be oxidized to Fe^{2+} (Huang et al., 2019). The increased iron induced intracellular ROS surge *via* Fenton reaction, followed by the accumulation of mitochondrial LPOs. The monodispersed ferrihydrite NPs were synthesized and demonstrated the light-triggered Fe^{2+} generation at the tumor sites (Yang, Y. et al., 2021). Ferrihydrite NPs, 20~30 nm, could release a large amount of Fe^{2+} to promote the iron/ROS-related irreversible DNA fragmentation and GPX4 inhibition under a common blue light illumination. In addition, it simultaneously induced polarization of the tumor-associated macrophage (TAM) from the tumor-promoting M2 phenotype to the tumor-killing M1 type, which concomitantly inhibited the tumor growth and prevented lung metastasis under illumination *in vivo*. The sulfasalazine and disulfide-bridged levodopa (DSSD) assembled as sulfasalazine@DSSD that could chelate Fe^{2+} to form the prodrug nanosystem sulfasalazine–Fe^{2+}@DSSD (Xin et al., 2021). The disulfide bonds could consume GSH in tumor cells, triggering the leakage of sulfasalazine and Fe^{2+}. Fe^{2+} induced ferroptosis *via* the Fenton reaction, and this was enhanced by the presence of sulfasalazine to improve the therapeutic efficacy. In another system, doxorubicin (DOX) was chelated with Fe^{2+}, yielding Fe^{2+}-DOX, which was condensed with calcium-containing precursors to form amorphous calcium carbonate (ACC)–encapsulated Fe^{2+}-DOX cores *via* a one-step synthetic approach (**Figure 4**) (Xue et al., 2020). The nanoplatform was simultaneously modified with matrix metalloproteinase-2 (MMP-2)–sheddable PEG and folic acid (FA) to achieve circulation stability and targeting capability. The therapeutic nanomaterial could release Fe^{2+} that produced H_2O_2 and DOX that amplified the effect of Fe^{2+} under a pH-triggered and self-regulated manner.

Recently, Cui et al. prepared a nanoenzyme in which Fe^{3+} was substantially reserved in the polypyrrole NPs (FePPy NPs) (Cui et al., 2021). The FePPy NPs generated hydroxyl radicals (•OH) by the degradation of H_2O_2 to induce ferroptosis. Upon irradiation, the FePPy NPs induced low-temperature PTT, which accelerated the Fenton reaction and enhanced ferroptosis and photoacoustic imaging (PAI) *in vitro* and *in vivo*. In addition, nanomaterials based on Fe^{3+} and tannic acid (TA) with the DOX-loaded dendrimers could combat multidrug resistance (MDR) in cancer cells *via* the apoptosis/ferroptosis pathway (Guo et al., 2019). The DOX-induced apoptosis elevated the intracellular ROS levels, thus sensitizing cancer cells to

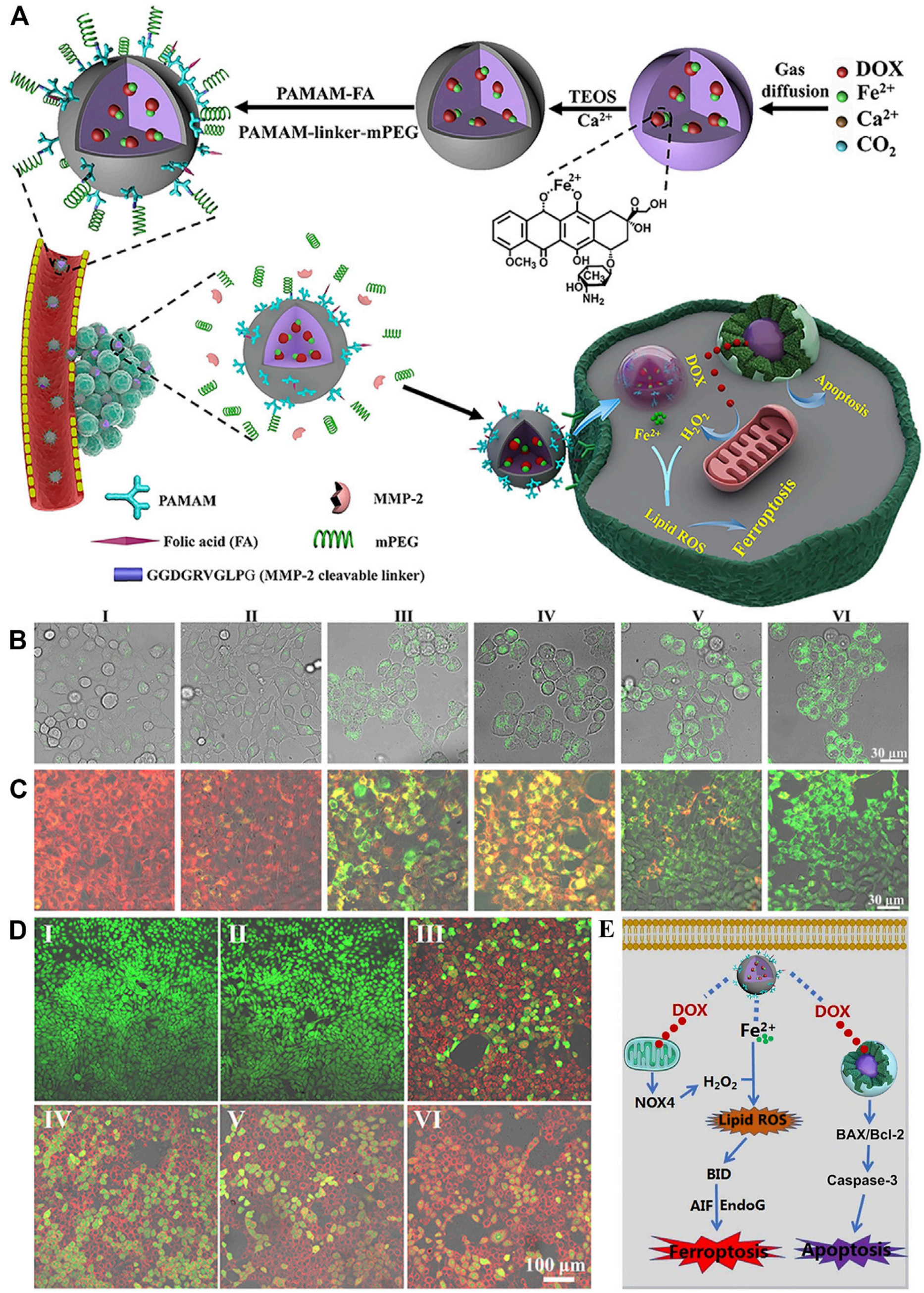

FIGURE 4 | (A) Synthesis scheme of ACC@DOX-Fe^{2+}-Ca-FA/mPEG and its therapeutic action. **(B–D)** Confocal laser scanning microscopy observation in 4T1 tumor cells about the intracellular distribution of the LPOs **(B)**, the changes in the mitochondrial membrane potential **(C)** and apoptosis levels **(D)** after treatment with (I) PBS, (II) ACC-Ca-FA/mPEG, (III) DOX, (IV) ACC@DOX-Ca-FA/mPEG, (V) ACC@DOX-Fe^{2+}-Ca-FA/mPEG, and (VI) MMP-2–treated ACC@DOX-Fe^{2+}-Ca-FA/mPEG. **(E)** Molecular mechanism for ACC@DOX-Fe^{2+}-Ca-FA/mPEG-induced ferroptosis/apoptosis. Reproduced with permission from Xue et al., (2020) Copyright @ 2020 (AAAS).

ferroptosis. The efficiency of CDT, in which H_2O_2 is decomposed into toxic •OH in tumor cells, was improved. Chen H. et al. reported a nanodrug delivery system based on TA, Pluronic F-68, and Fe^{3+} (Chen, H. et al., 2021). DOX, Pluronic F-68, and TA were first assembled to form DOX@Pluronic F-68/TA by π–π interactions and hydrophobic bonds. Subsequently, Fe^{3+} was introduced onto the surface of DOX@Pluronic F-68/TA to form DOX@Pluronic F-68/TA/Fe^{3+} *via* elaborate coordination interactions. The nanodrug DOX@Pluronic F-68/TA/Fe^{3+} efficiently targeted the tumor and primely suppressed tumor growth. In addition, the hollow mesoporous silica NP (MSNP)–loaded ferrate and DOX were followed by

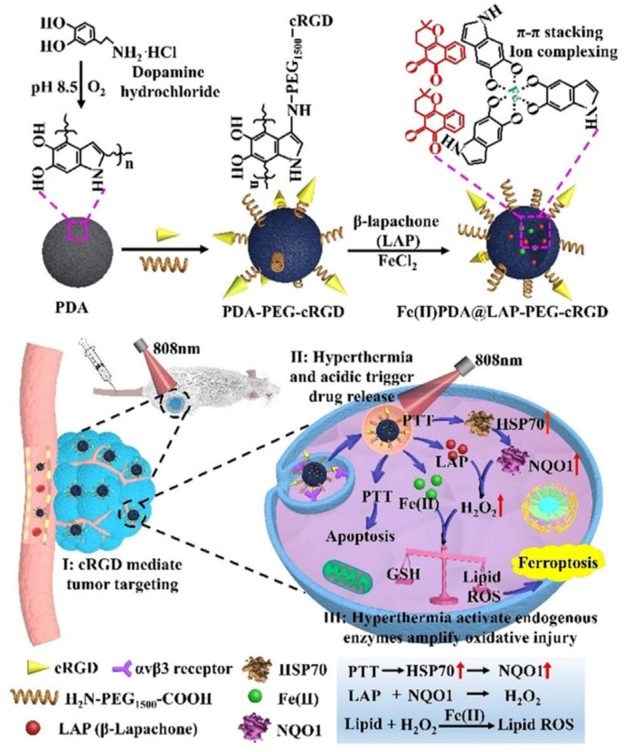

FIGURE 5 | Synthesis scheme of the Fe^{2+}PDA@LAP-PEG-cRGD nanomaterial and mechanism of PTT/FBT for cancer. Adapted from Xue et al., (2021) Copyright @ 2021 (Wiley).

incorporating n-heneicosane (Fu et al., 2021). The mild hyperthermia induced by US initiated the phase change of n-heneicosane and enabled the co-release of ferrate and DOX. The ferrate then reacted with H_2O to form H_2O_2, which released O_2, thus causing TME-independent reoxygenation and downregulation of the expression of hypoxia-inducible factor 1α and MDR gene/transporter P-glycoprotein in tumor cells. Overall, the cooperation of chemotherapy and FBT resulted in enhanced suppression of hypoxic osteosarcoma growth *in vivo*.

Dopamine can be used to load hydrophobic drugs and metal ions due to its aromatic rings and catechol groups (Cheng et al., 2019). Furthermore, polydopamine (PDA) shows strong absorption in the NIR region at approximately 808 nm and can efficiently convert the light energy into thermal energy (Rahim et al., 2019;Yamagishi et al., 2019). PDA nanosubstrates could efficiently load Fe^{2+} and β-lapachone, which initiated ferroptosis in the tumor cells subjected to NIR illumination (Xue et al., 2021). Crucially, cellular hyperthermia was generated by PDA nanostructures under NIR irradiation and triggered the release of Fe^{2+}. The NIR-enabled PTT also activated heat shock response and upregulated NADPH: quinone oxidoreductase protein (NQO1) *via* the heat shock protein 70 (HSP70)/NQO1 axis to promote bioreduction of β-lapachone and boost the intracellular H_2O_2 levels to facilitate the Fe^{2+}-dependent lipid peroxidation, while minimizing the potential damage to normal tissues (**Figure 5**) (Xue et al., 2021). The Fe^{2+} and Fe^{3+} also could be loaded into the core of the ultrasmall PEG-modified PDA NPs (UPDA-PEG NPs, 8.4 nm), thus yielding a novel ferroptosis agent (Chen et al., 2019). Seventy percent of the iron ions could be released at pH 5.0, suggesting applications in the acidic TME. The ferroptosis induced by UPDA-PEG@Fe^{2+} NPs was dependent on ROS, whereas UPDA-PEG@Fe^{3+} NPs induced LPO-dependent ferroptosis. In another research, DOX was loaded onto the PDA NPs to achieve a synergistic effect (Nieto et al., 2021). The pH determined the Fe^{3+} state and the selectivity and therapeutic activity of the resultant Fe^{3+}-loaded PDA NPs. Furthermore, the antitumor activity could be enhanced by DOX, which also increased ROS production in the cancer cells, and PDA NPs with different concentrations of Fe^{3+} and drugs could be tailor-synthesized and administered depending on the therapeutic need. The Fe^{3+} and the catechol of dopamine molecules could self-polymerize Fe^{3+}-PDA cores with an Fe loading efficiency of 5.3% (Chen et al., 2020). Subsequently, the hyaluronic acid (HA) cross-linked cisplatin shells were constructed onto the Fe^{3+}-PDA cores, and the core-shell nanomaterial was highly sensitive to an acidic or reductive TME, while its disassembly led to the continuous release of cisplatin and Fe^{3+}. The cisplatin could enhance ferroptosis *via* activating the NADPH oxidases (NOXs) and suppressing GPX4. Thus, the core-shell nanomaterial provided a new antitumor strategy for synergistic chemotherapy/FBT/PTT with a low dosage.

Iron ions could also be coordinated to some nanomaterials. For example, Jiang Y. et al. reported a hybrid semiconducting nanozyme (HSN) possessing high photothermal (PT) conversion efficiency and NIR-II PAI-guided PTT/FBT (Jiang, Y. et al., 2020). HSN comprised the amphiphilic semiconducting polymer as a PT converter, PA emitter, and iron-chelating Fenton catalyst. Upon NIR-II irradiation, HSN induced PT transduction, which triggered PTT and potentiated the Fenton reaction. Furthermore, •OH transformed HSN to approximately 1.7 nm–sized fragments. The noninvasive therapy possesses several advantages, such as deep ablation, reduced expression of metastasis-related proteins, and inhibition of distant metastasis. Recently, artemisinin and its derivatives have been investigated as potential FINs for cancer treatment. The nanocarrier-containing artemisinin was based on TA and Fe^{2+} coated on the zeolitic imidazolate framework-8 (ZIF-8) (Li, Z. et al., 2021). After 10 h, 59% artemisinin was released from TA-Fe^{2+}/artemisinin@ZIF-8 in pH 5.0. The intracellular ROS production and GPX4 inhibition could lead to suppression of triple-negative breast cancer growth.

3.1.2 Iron-Based Metal-Organic Frameworks (MOFs)

The nanoscale MOFs formed by Fe^{2+} and 2-aminoterephthalic acid (BDC-NH_2) possessed excellent stability and pH-responsive degradation to release Fe^{2+} in the acidic TME, which could catalyze the Fenton reaction and produce considerable quantities of ROS to induce Fe^{2+}-mediated ferroptosis (Xu et al., 2020). The perfluoropentane@Fe/Cu-SS MOF is displayed as an effective FIN because it could increase the production of LPO through the Fenton reaction and inhibit the GPX4 that prevents LPO transfer to LOH in the presence

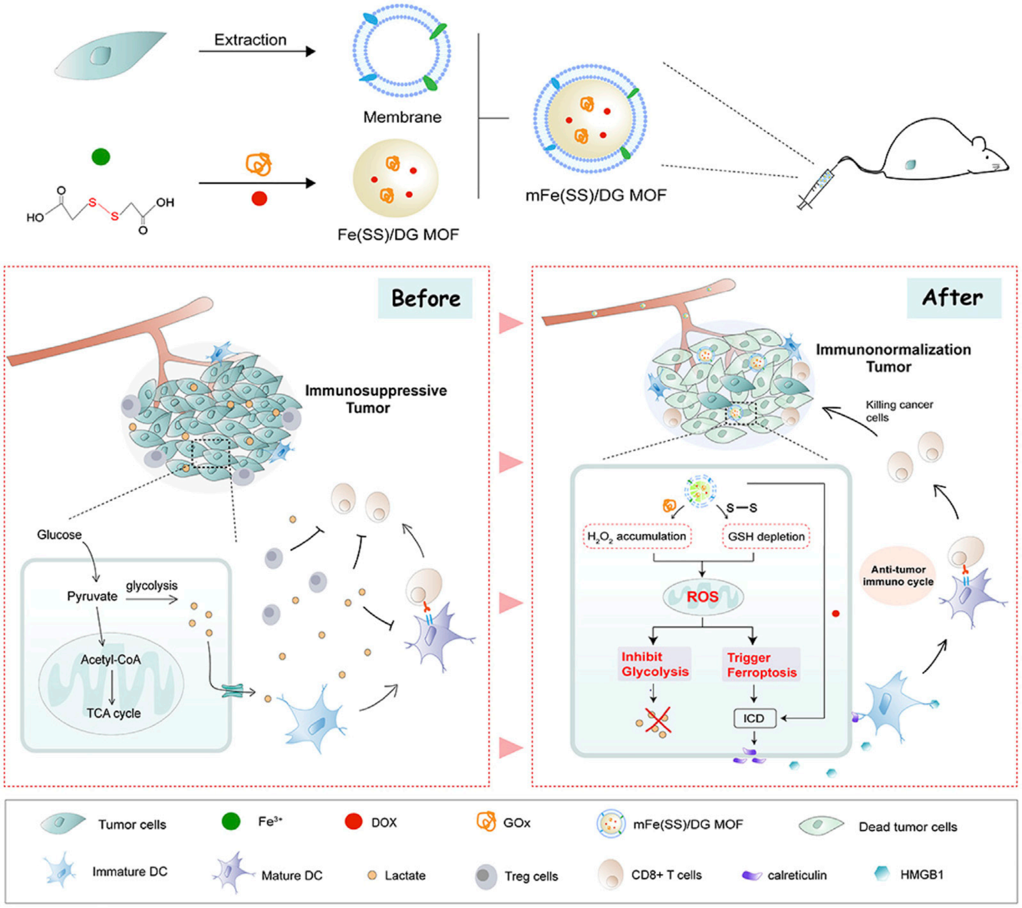

FIGURE 6 | Schematic illustration of mFe (SS)/DG and the mechanism based on ferroptosis–glycolysis regulation. Adapted from Yang J et al., (2021); Yang Y et al., (2021) Copyright @ 2021 (Elsevier).

of GSH, whereas the Fe^{3+} and Cu^{2+} in the MOF could consume GSH, further inhibiting GPX4 activity. Perfluoropentane@Fe/Cu-SS MOF also enabled T1-weighted magnetic resonance imaging (MRI), US imaging, and PTT (He, H. et al., 2020). Au1Ag24 nanoclusters and Fe^{3+} could be effortlessly assembled in an oil phase and modified by the vesicles of the PEG block grafted polyketal copolymer (PbP). The core-shell cancer theranostic nanomaterial Fe^{3+}@Au1Ag24@PbP possessed several excellent multiproperties, including NIR laser/TME co-responsiveness and PAI/PT imaging-guided PTT/PDT/FBT both *in vitro* and *in vivo* (Cheng, H. et al., 2021). In addition, the iron-chelated hybrid polymeric NPs comprising Fe^{3+} and an amphiphilic semiconducting complex have been reported, in which these components acted as PT transducers and Fe^{3+} chelators, respectively (He, S. et al., 2020). In the acidic TME, Fe^{3+} was released to generate •OH; in addition, local heat was generated under the NIR laser irradiation to enhance the Fenton reaction and achieve PAI-guided PTT.

The addition of cancer cell membranes to nanomaterials enables homologous targeting and immune escaping capabilities. Wan et al. reported a nanomaterial containing Fe^{3+}-based MIL-100 and glucose oxidase (GOx) that catalyzed the degradation of glucose to generate sufficient H_2O_2 for FBT (Wan et al., 2020). When the nanomaterial was obtained by the tumor cells, intracellular GSH triggered the disruption of MOF *via* reducing Fe^{3+} to release Fe^{2+} and GOx. The nanomaterial exhibited highly effective tumor inhibition and enabled precise collaborative tumor therapy with spatiotemporal controllability. Another MOF nanomaterial loading with GOx and DOX was also coated with the cancer cell membrane (denoted as mFe(SS)/DG) (**Figure 6**) (Yang, J. et al., 2021). The mFe(SS)/DG system based on Fe^{3+} and disulfide-bearing ligands depleted GSH and suppressed GPX4 activity to induce ferroptosis. The increasing ROS facilitated ferroptosis and restrained glycolysis. Thus, immunogenic cell death (ICD) induced by the synergistic effect of ferroptosis and DOX released tumor antigens to trigger antitumor immunity when the inhibition of glycolysis remodeled the tumor immunogenicity and immunosuppressive microenvironment to strengthen the antitumor immunity.

In addition, iron-based MOFs can be loaded with FINs to enhance ferroptosis. For example, MIL88B loaded with RSL3 forced M2 macrophages to increase the glycolytic metabolism (Gu et al., 2021). MIL88B/RSL3 downregulated the expression of M2-associated signaling pathways and activated M1-related

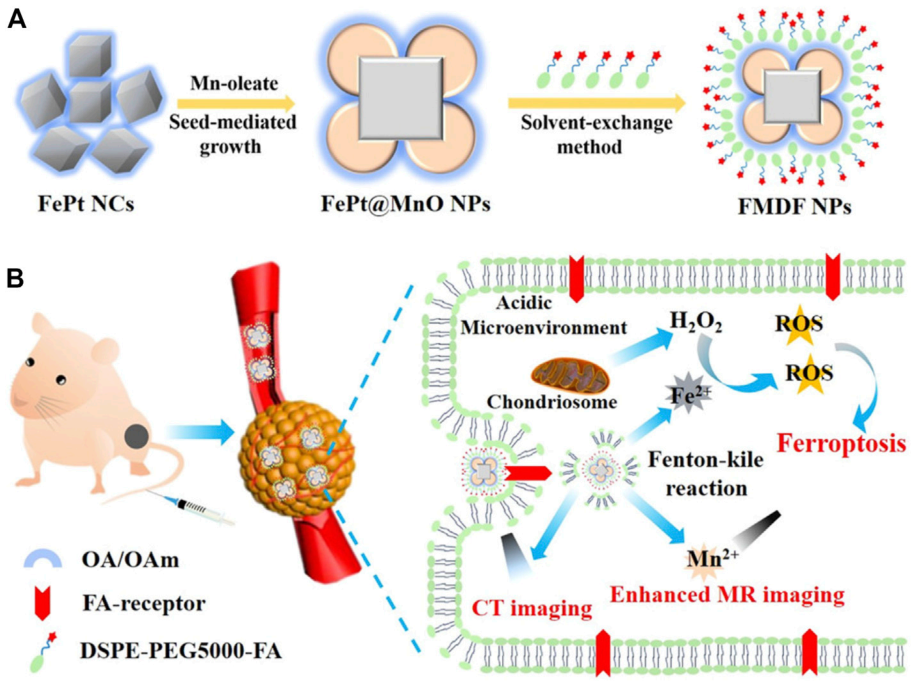

FIGURE 7 | (A) Synthesis scheme of FMDF NPs. **(B)** Acidic-responsive and dual-model imaging-guided FBT/CDT. Adapted from Yang et al., (2019) Copyright @ 2019 (ACS).

signaling. The ferroptosis-strengthened macrophage regulation strategy had great potential for TAM-centered antitumoral applications. In the same year, the surface of MIL-101 (Fe)-loaded sorafenib was modified with an iRGD peptide that could bind to neruopilin-1 receptor yielding a nanodrug that induced ferroptosis of the hepatocellular carcinoma by consuming GSH, decreasing GPX4 expression, and enhancing LPO generation (Liu et al., 2021). Fe^{3+} and TA spontaneously formed a network-like corona onto the sorafenib nanocores that were loaded with methylene blue (Liu et al., 2018). The corona is disrupted in the lysosomal acid environment, whereas TA could reduce Fe^{3+} to Fe^{2+}, paving the way for iron redox cycling to produce LPO. Furthermore, the concomitant methylene blue release induced fluorescence recovery, endowing the nanomaterials with multimodal imaging-guided PDT/FBT. In another example, Fe^{3+}-containing MOFs loaded with piperlongumine (a FIN) were coated with a transferrin-decorated pH sensitive lipid layer to form the nanodrug (Xu, R. et al., 2021). Crucially, after treatment with this nanoagent, the cellular iron concentration increased dramatically due to the iron-containing MOF, and piperlongumine strengthened the ferroptosis *via* providing H_2O_2 for the dual induction system.

3.1.3 FePt-Based Nanomaterials

FePt-based nanomaterials have potential clinical applications in cancer therapy. For example, a ferroptosis nanotheranostic agent was designed by integrating FePt as the core, Eu^{3+}-based luminescent molecule, and FA as the targeting molecule (Yue et al., 2018). FePt-based nanomaterials exhibited an excellent MRI, computed tomography (CT), and time-gated luminescence properties in the clinical diagnosis and had excellent capacity to trigger ferroptosis of cancer *in vitro* and *in vivo*.

The FePt NPs can also be loaded onto diverse nanomaterials to show their advantages. An acidic responsive nanoagent FePt@MnO@DSPE-PEG-FA NP was successfully constructed for MRI-guided FBT/CDT of cancer (**Figure 7**) (Yang et al., 2019). It could release active Fe^{2+} to elevate ROS production *via* the Fenton reaction to induce ferroptosis. In addition, Mn^{2+} could be released from the nanomaterial in the acidic TME and scavenge GSH to enhance the T1/T2-weighted MRI, which could obviously distinguish the solid tumors. Prussian blue (PB) nanocubes were utilized as PT agents, and FePt NPs were loaded onto the surface of the nanocube *via in situ* reduction (Hu et al., 2020). The surface of the nanocomposite PB@FePt was wrapped with HA and PEG, and the nanoagent PB@FePt–HA-g-PEG served as a multifunctional nanomaterial, enabling CDT/PTT and triple-modal imaging (MRI/CT/PT imaging) capability. Covalent organic polymers (COPs) possess specific surface area and good biocompatibility, making them promising nano delivery carriers (Shi et al., 2019). FePt@COP-FA with excellent PT potential was developed for cancer treatment (Meng et al., 2020). It could efficiently ablate the primary tumors with the presentation of NIR irradiation and release a mass of tumor-associated antigens *in situ*. With the assistance of anticytotoxic T-lymphocyte antigen-4 (anti-CTLA4), the specific immune response was triggered to suppress the growth of metastatic tumors. In particular, the synergistic therapy could form a valid immunological memory

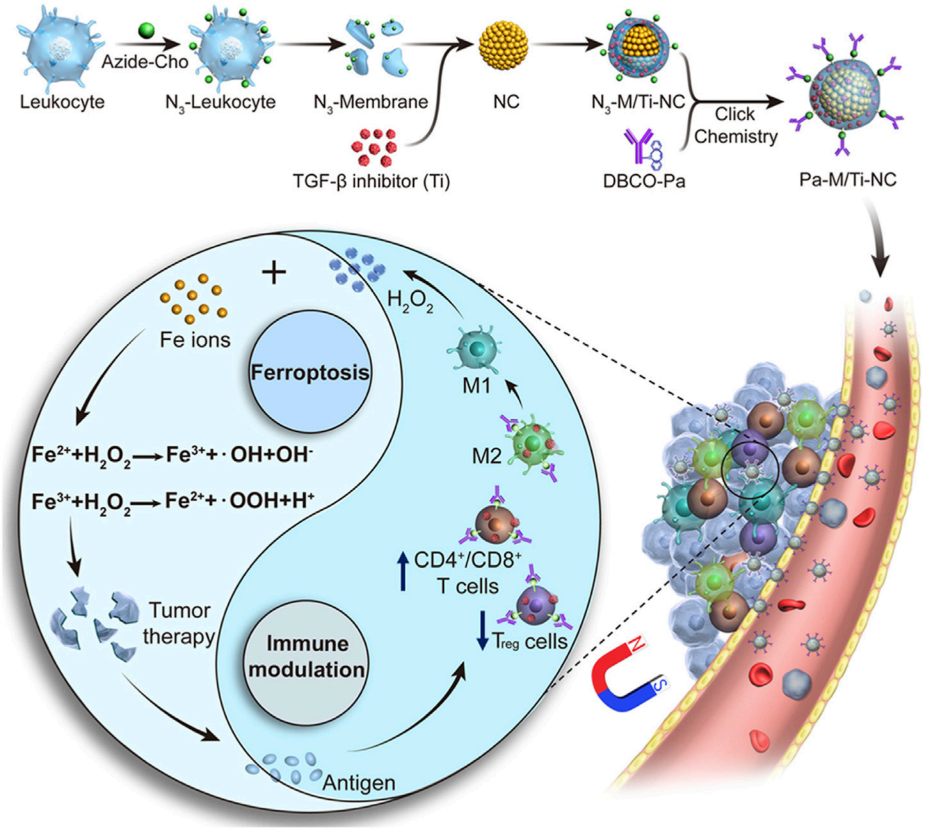

FIGURE 8 | Synthesis scheme and mechanism of the magnetosome for FBT/immunomodulation in cancer. Adapted from Zhang et al., (2019) Copyright @ 2019 (ACS).

to further restrain tumor relapses. FePt NPs could also be loaded onto polyethylenimine (PEI)-modified ultrathin black phosphorus (BP) nanosheets, and this nanomaterial showed enhanced synergistic PTT/PDT/CDT for targeting primary tumors (Yao et al., 2020). More significantly, combined with the CTLA-4 checkpoint blockade, PTT induced by FePt/BP–PEI–FA could control the growth of both the primary and untreated distant tumor.

3.1.4 Iron Oxide (IO)–Based Nanomaterials

IONPs, which have been approved by the FDA, have been widely applied in cancer therapy because they produce ROS *via* the Fenton reaction.

An innovative local chemotherapy combined with a gene therapy–based IONP was developed as a treatment for patients with glioblastoma (Zhang et al., 2020). The porous structure of IONPs attached -COOH groups and could encapsulate the small interfering RNA (siRNA) targeting GPX4 (siGPX4) and cisplatin. After uptake, the IONPs degraded and released Fe^{2+}/Fe^{3+}, and the H_2O_2 level increased owing to the activating reduced NOX. Furthermore, the cisplatin destroyed both nuclear and mitochondrial DNA, while siGPX4 restrained GPX4 expression. The manganese-deposited IO (FMO) NPs were loaded with the cisplatin prodrug Pt (IV) to form Pt-FMO, which was modified with PEG to increase colloidal stability (Cheng, J. et al., 2021). FMO released Mn^{2+} and Fe^{2+}/Fe^{3+} in the weakly acidic TME, and the Pt (IV) could deplete GSH to generate cisplatin. Mn^{2+} enhanced the ferroptosis induced by Fe^{2+}/Fe^{3+} released from FMO, and cisplatin elevated the intracellular H_2O_2 levels, which obviously strengthened ferroptosis *via* the Fenton reaction. Therefore, the synergism between the ferroptosis induced by FMO and the apoptosis induced by cisplatin resulted in tumor ablation.

Biomimetic magnetic NPs coated with platelets can make the cancer cells sensitize to ferroptosis, generate mild immunogenicity, and improve the response rate of noninflammatory tumors to immunotherapy (Jiang, Q. et al., 2020). Thus, a Fe_3O_4-sulfasalazine@platelet system was designed by using mesoporous magnetic Fe_3O_4 NPs, sulfasalazine, and platelet membranes. Fe_3O_4–sulfasalazine@platelet-mediated ferroptosis could evidently improve the potency of programed cell death 1 (PD-1) and achieve persistent tumor elimination in 4T1 metastatic tumors. Moreover, the Fe_3O_4–sulfasalazine@platelet-mediated ferroptosis also repolarize macrophages from the M2 phenotype to M1 phenotype. The magnetosomes contained Fe_3O_4 magnetic nanoclusters and pre-engineered the leukocyte membranes as the core and shell, and the transforming growth factor-β (TGF-β) inhibitor and PD-1 antibody were, respectively, loaded inside and on the surface of the membrane (**Figure 8**) (Zhang et al., 2019). The membrane camouflage endowed the nanomaterial with a long circulation time, and the nanocluster core enabled magnetic targeting under MRI guidance. When the nanomaterial reached the tumor site, the cooperation of the TGF-β inhibitor and PD-1 antibody increased the rates of $CD4^+$ T/Treg cells, $CD8^+$ T/Treg cells, and M1/M2 macrophages to create an immunogenic TME, and the elevated H_2O_2 from M1 polarization enhanced the Fenton reaction. The production of •OH subsequently induced ferroptosis of the cancer cells and the released tumor antigens, thus increasing TME immunogenicity.

IONPs can also be loaded onto or into different nanomaterials. Superparamagnetic IONPs (SPIONPs) are considered excellent carriers to deliver nucleic acid and drug because of the controllable properties, outstanding stability, and easy modification. The sorafenib and ultrasmall SPIONPs (approximately 8.5 nm) were, respectively, loaded onto the mesopores of mesoporous PDA (MDPA) NPs and onto the surface of the MDPA NPs to form sorafenib@MPDA-SPIONP (Guan et al., 2020). The heat generated by the MPDA NPs upon NIR laser irradiation boosted the effect of ferroptosis. Furthermore, the application of moderate heat (45°C) in the presence of the IONPs could significantly suppress the expression of the antioxidative proteins and cause tumor cells to undergo specific lipid metabolism (Xie et al., 2021). By virtue of the IONPs and 1H-perfluoropentane (1H-PFP), a heat-responsive ferroptosis strategy was rationally designed by utilizing a polypeptide-modified, IO-containing nanomaterial that loaded 1H-PFP. The phase transition of 1H-PFP was triggered under 808-nm laser irradiation, which led to the release of IONPs *in situ* to produce ROS in the TME. The inhibition of GSH synthesis restrained the antioxidant response of tumors due to heat stress. Furthermore, the combined treatments reprogramed the lipid metabolism by generating a large amount of LPO and inducing acyl-CoA synthetase bubblegum family member 1 (ACSBG1)–dependent ferroptosis in the C4-2 tumor model. More recently, the polypeptide vehicle-based theranostics (Pt&IONPs@PP) were self-assembled by mixing poly (L-glutamic acid) (PGA), poly (L-lysine) (PLL), Pt prodrug, and carboxyl-modified IONPs through electrostatic interactions, and the surface of this nanomaterial was modified with PEG (Gao et al., 2020). The acidic TME degraded Pt&IONPs@PP to release Pt drug and Fe^{2+}/Fe^{3+}. Moreover, Pt&IONPs@PP could induce T2-weighted, MRI-guided chemotherapy/FBT to inhibit cancer cell growth without systemic toxicity *in vitro* and *in vivo*.

A nanosystem containing Fe_3O_4 and chlorin E6 (Ce6) was designed for the synergistic cancer therapy (Chen, Q. et al., 2021). The poly (lactic-co-glycolic acid) (PLGA) was used as the shell to load Fe_3O_4 and Ce6, which degraded in the acidic TME and released Fe^{2+}/Fe^{3+} and Ce6. The reaction between Fe^{2+}/Fe^{3+} and intracellular H_2O_2 produced •OH to induce ferroptosis of tumor cells. The released Ce6 could increase the ROS levels upon laser irradiation to offer PDT, and this boosted the ferroptosis effect in 4T1 tumors. A gel-delivery platform with embedded Au nanorods (AuNRs) and IONPs was reported, the so-called AuNRs&IONPs@Gel, for bladder cancer therapy (Guo, P. et al., 2020). The gel platform was based on a dextran aldehyde that could selectively adhere with the cancer collagen. AuNRs could induce imaging-guided PTT under NIR radiation, and the locally high concentration of IONPs induced ferroptosis. Moreover, TAMs would be repolarized by the IONPs from the M2 phenotype into M1 phenotype to achieve a direct antitumor effect and antigen presentation of dead cells. This process triggered an effective innate and adaptive immune response to protect against tumor rechallenge in the long term. The black hole quencher (BHQ)–based fluorescence 'off–on' nanomaterials were self-assembled with chitosan oligosaccharide (CSO), IR780, hexadecane (Hex), magnetic IONPs (MIONPs), and sorafenib to form CSO-BHQ-IR780-Hex/MIONPs/sorafenib (Sang et al., 2019a). BHQ and IR780 were combined *via* a GSH-responsive ether bond. After uptake, the CSO–BHQ–IR780–Hex NPs collapsed and IR780–Hex anchored the mitochondrial membrane. When NIR irradiation was applied to the NPs, the iron level increased, and the xCT/GSH/GPX4 system was triggered. In addition, a similar nanomaterial (CSO–SS–Cy7–Hex/SPIONP/sorafenib) was developed to overcome the therapy-resistant state of cancer (Sang et al., 2019b). This system could scavenge GSH and increase the concentration of iron and LPO, and the ferroptosis induced by CSO-SS-Cy7-Hex/SPIONP/sorafenib complex defeated MDR, reduced invasion, and limited the metastasis of cancers undergoing the epithelial-to-mesenchymal transition.

The IO-hydroxide (IOOH) nanospindles have been used as MRI contrast agents for cancer diagnosis; thus, a biocompatible H_2S-responsive IOOH nanospindle for colon cancer is developed (Li, Y. et al., 2020). The IOOH nanospindles, synthesized from Fe^{3+} and dopamine and modified by PEG, could efficiently deplete endogenous H_2S *via* the reduction reaction to inhibit CT26 colon cancer growth. Crucially, the overproduction of H_2S drove a cascade reaction producing FeS; thus, this system could be used for NIR-responsive PTT and Fe^{2+}-induced ferroptosis.

3.1.5 Iron-Containing Organic Transition Metal Compound–Based Nanomaterials

Ferrocene (Fc) is a stable organic transition metal compound that can produce ROS under physiological condition, and thus, is a potential adjuvant to enhance the therapeutic effect of chemotherapy drugs (Patra and Gasser, 2017). As known to all, the iron in Fc is Fe^{2+}, (Xu et al., 2013) making it an ideal exogenous Fe^{2+} to induce ferroptosis. For example, sequential release of the NPs based on the presence of heparinase was reported; these NPs were modified with β-cyclodextrin and coloaded with DOX, Fc, and TGF-β receptor inhibitor SB431542 (**Figure 9**) (Zhang et al., 2021). DOX and Fc could increase the intracellular ROS levels to activate ferroptosis and apoptosis and reduce MMP-9 expression to enhance FBT in the tumor. SB431542 could be gradually released due to the heparanase-driven nature, which prevented the tumor metastasis *via* modulating the TME, decreasing tumor-associated fibroblast activation, and reducing TGF-β secretion. Furthermore, ferroptosis-induced antitumor immune response

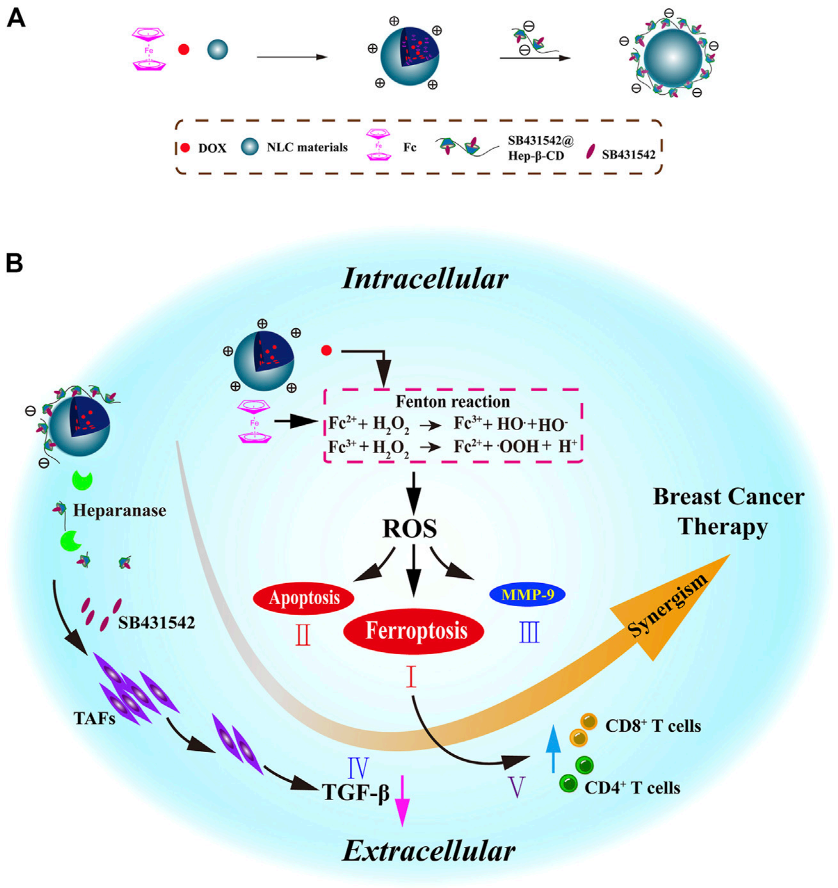

FIGURE 9 | (A) Synthesis scheme of NLC/H (DOX + Fc + SB431542) NPs. **(B)** Mechanism of NLC/H (DOX + Fc + SB431542) NPs for breast cancer therapy. Adapted from Zhang et al., (2021) Copyright @ 2021 (Elsevier).

enhanced the tumor therapy. A CDT nanomaterial, RSL3@COF–Fc, was fabricated by the covalent organic framework (COF), Fc, and RSL3 (Zhou et al., 2021). The RSL3@COF–Fc could promote the production of •OH in cancer cells, and the repair mechanism under oxidative stress was attenuated by the irreversible inhibition of the GPX4. Finally, these two ways synergistically resulted in massive LPO accumulation.

A multifunctional carbon monoxide (CO)/thermo/chemotherapy nanoplatform comprises the mesoporous carbon NPs (MCNPs) as NIR-responsive drug carriers and DOX and hydrophobic iron carbonyl (FeCO) as thermosensitive CO prodrug (Yao et al., 2019). The nanoplatform produced sufficient heat upon NIR illumination to trigger the release of CO and DOX in the acidic TME. The CO successfully increased the sensitivity of the cancer cells to chemotherapeutics through the ferroptosis pathway. Subsequently, the FeCO-DOX@MCNP nanoplatform showed high therapeutic efficacy in combination with chemotherapy, PTT, and gas therapy both *in vitro* and *in vivo*.

3.1.6 Ferritin-Based Nanomaterials

Ferritin is an iron-sequestering protein that plays key roles in iron delivery, cell proliferation, and immunosuppression (Shi et al., 2021). The novel protein-based nanomaterial BCFe@sorafenib was developed by covalently crosslinking the Ce6-conjugated bovine serum albumin (BSA) and ferritin, together with the sorafenib encapsulated inside the protein shell (Wang et al., 2021). Under hypoxic condition, the BCFe@sorafenib could be degraded to release more Ce6 after light irradiation, whereas the ferritin released Fe^{3+} to consume GSH to produce more ROS. In addition, the released sorafenib destroyed the tumor's antioxidative defense to enhance oxidative damage. In addition, a novel carrier-free nanodrug NFER containing ferritin, erastin, and rapamycin was prepared by using an emulsification technique (Li et al., 2019). The NFER displayed strong ferroptosis capability by downregulating the GPX4 and increasing LPO production, which was increased by the presence of rapamycin. Using this nanodrug, tumor recurrence of the 4T1 tumor resection model was controlled.

3.1.7 Iron-Based Up-Conversion (UC) Nanomaterials

The photic UC is achieved by the UCNPs that contain lanthanide or actinide metals. The Fe^{3+}-containing UCNP and DOX were capsulated into the oxidized starch-based gel NPs (**Figure 10**) (Bao et al., 2019). As the core, the UCNPs that convert NIR light to ultraviolet (UV) light overcome the obstacle of limited penetration depth and reduced Fe^{3+} to Fe^{2+}, which led to the

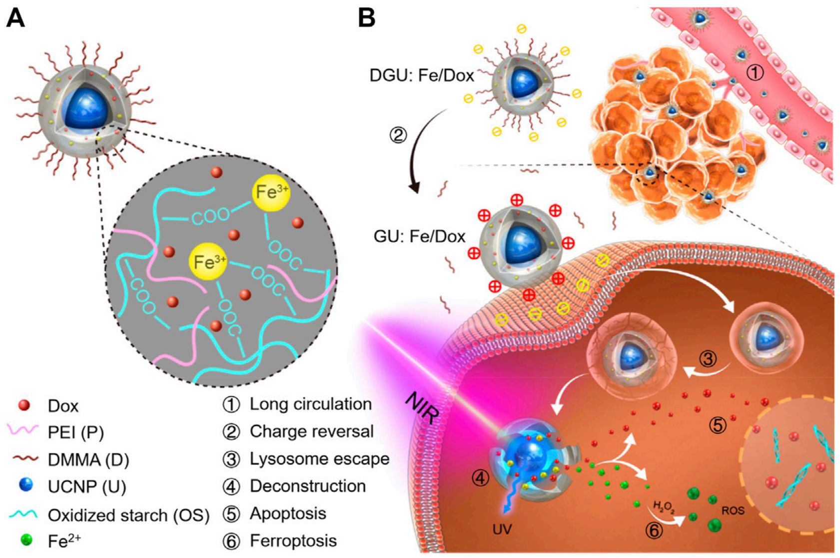

FIGURE 10 | (A) Schematic illustration of DGU:Fe/DOX NPs. **(B)** Mechanism of DGU:Fe/DOX NPs for cancer therapy. Adapted from Bao et al., (2019) Copyright @ 2019 (ACS).

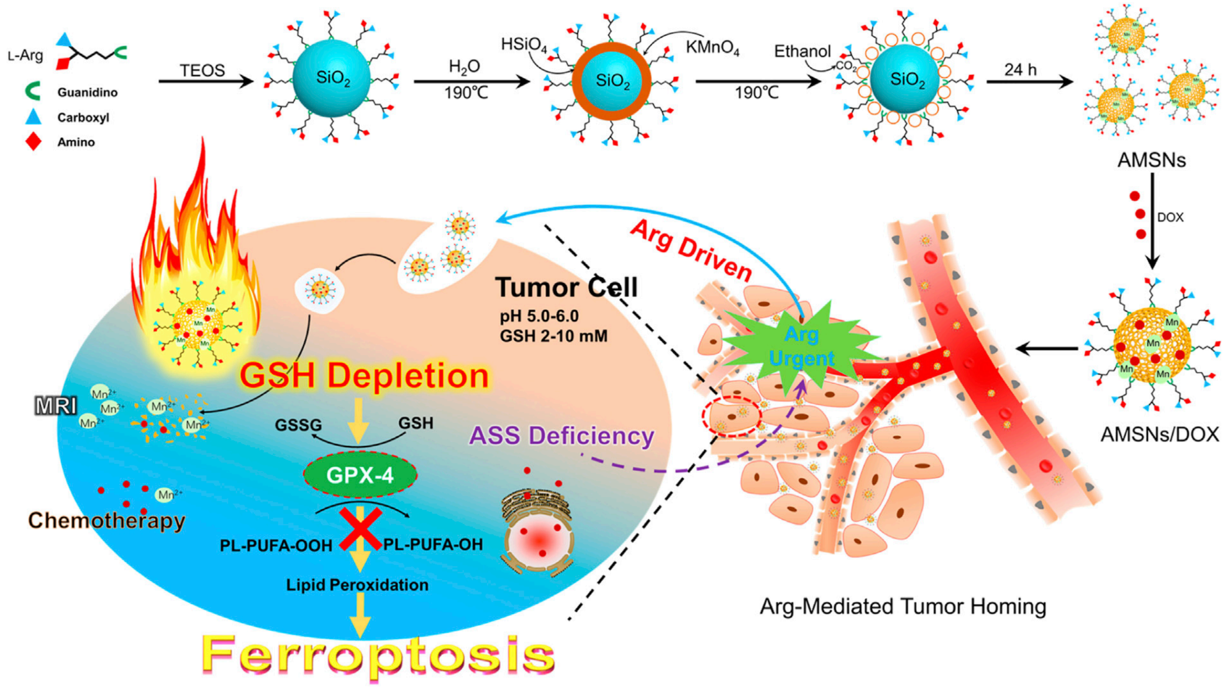

FIGURE 11 | Schematic illustration of AMSNs/DOX for cancer therapy. Adapted from Wang et al., (2018) Copyright @ 2018 (ACS).

deconstruction of gel networks of this nanomaterial and subsequently rapid release of Fe^{2+} and DOX. As a result, this nanomaterial could provide a safe and efficient platform for ferroptosis-/apoptosis-based anticancer therapy.

3.2 Iron-Free Nanomaterials

In addition to the iron-contained nanomaterials, there are several types of nanomaterials without iron that could induce ferroptosis of the cancer cells.

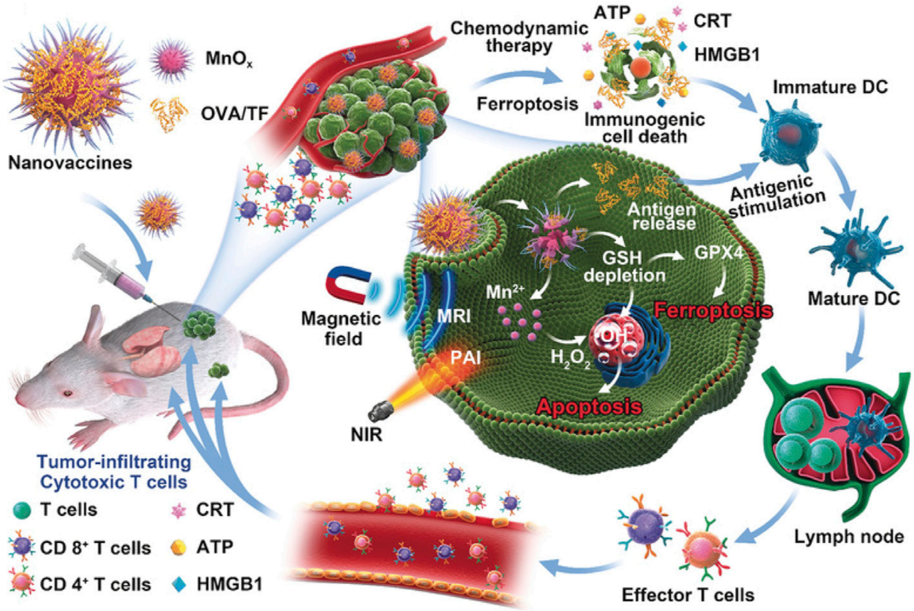

FIGURE 12 | Schematic illustration of MnOx-OVA/tumor cell fragment (TF) nanovaccines for MRI-/PAI-induced cancer immunotherapy. Adapted from Ding et al., (2020) Copyright @ 2020 (ACS).

3.2.1 Manganese-Based Nanomaterials

A versatile porphyrin-based manganese MOF (Mn-MOF) nanoplatform exhibited high catalase activity for the conversion of H_2O_2 to O_2, thus decreasing the intracellular GSH content and GPX4 activity and inhibiting the tumor growth and metastasis *via* inducing SDT and FBT (**Figure 11**) (Xu, Q. et al., 2021). In addition, the Mn-MOF efficiently reshaped the tumor immune microenvironment upon US treatment by increasing the activated CD8$^+$ T cells and matured dendritic cells (DCs) and decreasing the myeloid-derived suppressor cells in tumor tissue. The arginine-rich manganese silicate nanobubbles (AMSNs) could be synthesized through a one-pot method with highly efficient GSH depletion (Wang et al., 2018). The arginine component provides ideal dispersibility, biocompatibility, and tumor-targeting capacity. Compared with the traditional NPs, the arginine-based ultrathin surface coating and nanobubble structure significantly improved the ability of the AMSNs to consume GSH, which led to GPX4 inactivation. In addition, the degradation of AMSNs led to the corelease of Mn^{2+} and DOX, which resulted in T1-weighted MRI and on-demand chemotherapeutic drug release for the synergistic cancer therapy. In addition, manganese-doped MSNPs (MMSNPs) possess the manganese–oxygen bonds that could consume GSH rapidly (Tang et al., 2019). MMSNPs were modified with FA-PFG and loaded with dihydroartemisinin (DHA) to form an innovative nanomaterial (Fei et al., 2020b). After endocytosis, the degradation of nanomaterials consumed intracellular GSH due to the reaction between the manganese–oxygen bonds and GSH, which resulted in the release of DHA and Mn^{2+}. The sorafenib could also be loaded into MMSNPs to induce ferroptosis of tumor cells (Tang et al., 2019; Tang et al., 2020).

3.2.2 Manganese Oxide–Based Nanomaterials

The $MnO_2@HMCu_{2-x}S$ nanocomposites (HMCMs) for tumor ablation were reported (An et al., 2019). The HMCMs had the ability of depletion of GSH enhanced by PTT, thus inducing PTT-enhanced ferroptosis of cells by GPX4 inactivation. The GSH-responsive Mn^{2+} release increased the ROS concentration by a Fenton-like reaction, thus resulting in the accumulation of LPO. The rapamycin was encapsulated into the HMCM to improve sensitization of the tumor cells to ferroptosis. The HMCM showed an outstanding anticancer effect *in vitro* and *in vivo*. In addition, MnO$_x$ nanospikes and ICD drugs were developed as cancer nanovaccines (**Figure 12**) (Ding et al., 2020). Because of the double induction of CDT mediated by Mn^{2+} and FBT that depleted GSH, MnO$_x$ nanospikes could be used as an immune adjuvant for efficient antigen loading and ICD drugs. The nanovaccines achieved the TME-responsive, dual-mode MRI/PAI, while effectively inhibiting tumor growth and metastasis.

3.2.3 Gold-Based Nanomaterials

The salinomycin that conjugated with the Au NPs was used to kill breast cancer stem cells that were derived from CD24^{low}/CD44^{high} subpopulation (Zhao et al., 2019). The salinomycin-AuNPs exhibited higher ability to induce ferroptosis *via* higher iron accumulation and GPX4 inactivation. Pt-decorated Au nanostars were presented as novel nanoprodrugs for FBT against MDR tumors (Del Valle et al., 2020). Upon NIR light irradiation, Pt and Au were released, which resulted in GSH depletion, GPX4 inactivation, and accumulation of lipid hydroperoxides. The NIR light-activation of the prodrugs showed efficacy of FBT against tumors without long-term side effects *in vivo*.

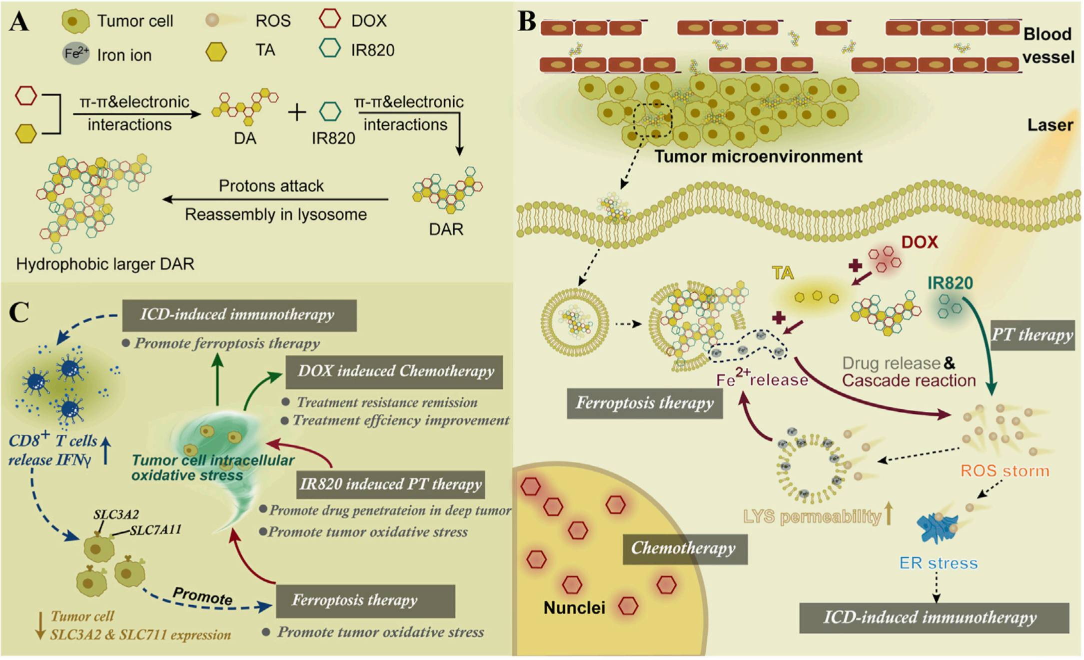

FIGURE 13 | (A) Synthesis scheme of DAR. **(B)** Mechanism of DAR for cancer therapy. **(C)** Combined therapy mechanisms of DAR. Adapted from Xiong et al., (2021) Copyright @ 2021 (Elsevier).

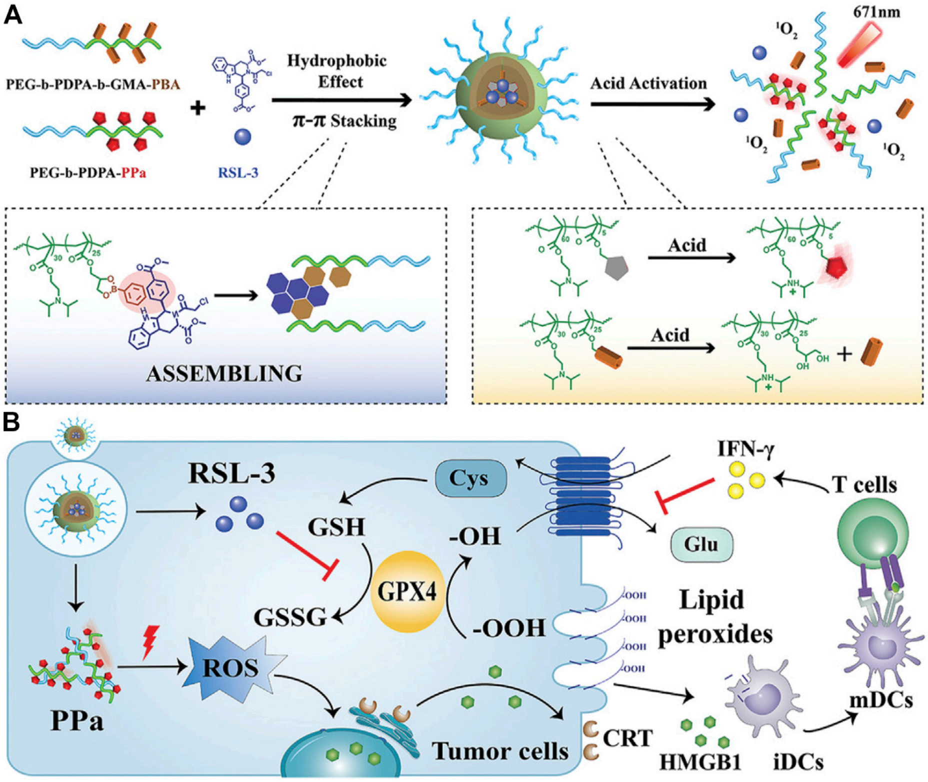

FIGURE 14 | (A) Synthesis scheme of NPs. **(B)** Schematic illustration of the mechanism. Adapted from Song et al., (2021) Copyright @ 2021 (Wiley).

3.2.4 Photosensitizer-Based Nanomaterials

The Ce6 and erastin could be self-assembled to form a novel nanodrug *via* hydrogen bonding and π–π interactions (Zhu et al., 2019). The erastin could induce accumulation of LPO *via* the Fenton reaction. Under the light irradiation, the generation of O_2 ensured efficient photochemical reactions to produce ROS. The imidazole ligand containing disulfide and Zn^{2+} was coordinated to form an MOF nanocarrier for Ce6 loading. Regardless of the light irradiation, nanocarriers loaded with Ce6 induced GSH depletion through the disulfide–thiol exchange reaction in 4T1 tumor cells (Meng et al., 2019). In the 4T1 tumor–bearing mouse model, the nanomaterials showed excellent *in vivo* tumor growth inhibition, and the animal survival rate was improved. However, the combined use of iron chelating agents weakened the antitumor ability of the nanocarrier because it restrained ferroptosis.

The nanoactivator was assembled by DOX, TA, and IR820. The endogenous iron stored in the endo-lysosome was fully utilized. In addition, the ferroptosis and its related oxidative stress were induced by an artificial intracellular positive feedback loop (**Figure 13**) (Xiong et al., 2021). Interestingly, this process could also promote the ICD-related immunotherapy through the endoplasmic reticulum stress. After the laser treatment, the intracellular ROS in cells could be effectively distributed in the lysosomes and endoplasmic reticulum to promote FBT and immunotherapy, respectively.

3.2.5 RSL3-Loaded Nanomaterials

RSL3 can be loaded onto the non-iron nanomaterials. The ionizable block copolymer and phenylboronate ester (PBE) were integrated by covalent bonds to prepare a platform for RSL-3 delivery (**Figure 14**) (Song et al., 2021). At neutral pH, the NPs could stably embed RSL-3 in the hydrophobic core through π–π interaction with the PBE groups and release the payload in the endogenous vesicles through acidity-triggered cleavage of dynamic covalent bonds of PBE. In addition, the NPs could perform acid-activatable PDT by ionizing nuclear protonation and significantly recruiting tumor infiltrating T lymphocytes to secrete IFN-γ, and thus make the B16–F10 melanoma tumor sensitive to RSL-3–induced ferroptosis. The maltose ligand and azobenzene were linked by PEG and self-assembled to load RSL3, yielding Malt-PEG-Abz@RSL3 (Li et al., 2022). Malt-PEG-Abz@RSL3 micelles could actively target HepG2 because of the high expression of glucose transporters, thus achieving RSL3 delivery. Malt-PEG

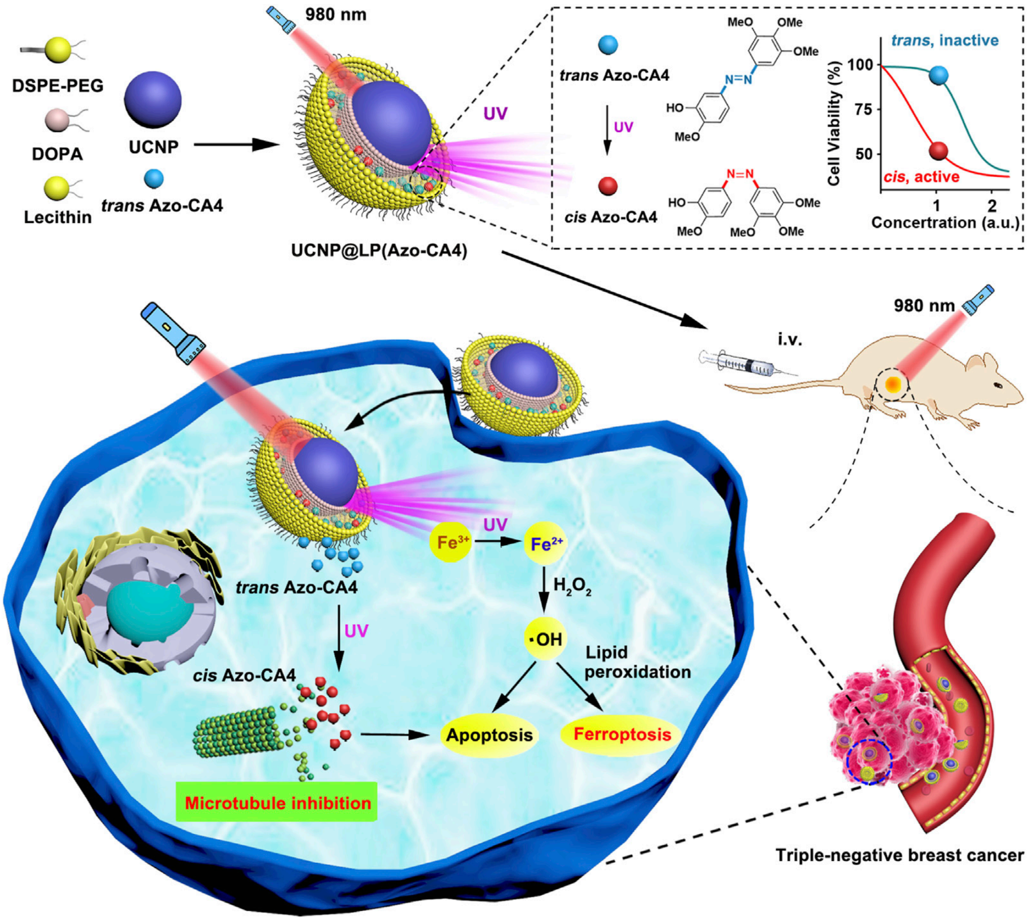

FIGURE 15 | Synthesis scheme and mechanism of UCNP@LP (Azo-CA4). Adapted from Zhu et al., (2020) Copyright @ 2020 (ACS).

degraded to release RSL3 for inhibiting GPX4 activity, whereas NADPH that took part in synthesis of GSH and thioredoxin-SH2 [Trx (SH) 2] was consumed by the azobenzene moiety, resulting in the reduction of GSH and Trx (SH) 2. The azobenzene was also connected to a nitroimidazole-conjugated polypeptide and self-assembled with RSL3 (Guo, X. et al., 2020). Under anoxic conditions, the azobenzene moiety caused PEG to be removed and reinforced micelle uptake in 4T1 cells, while the nitroimidazole moiety not only resulted in the rapid release of RSL3 but also exhausted intracellular NADPH with the help of overexpression of nitroreductase in the tumor site.

3.2.6 UC Nanomaterials

The core-shell UCNPs (NaGdF4:20%Yb, 0.5%Tm^{3+}@NaGdF4) could absorb NIR light and emit UV to transfer azobenzene combretastatin A4 (azobenzene-CA4) to activate azobenzene-CA4, while UV light could induce reduction of intracellular Fe^{3+} to Fe^{2+} (**Figure 15**) (Zhu et al., 2020). Upon NIR irradiation, the viability of the triple-negative breast cancer cells treated with nanocarriers loaded with azobenzene-CA4 evidently decreased. Another UCNP (NaYF4:20%Yb, 2%Er@NaYF4) was coated by the MS and liposome to encapsulate Ce6 and buthionine sulfoximine (BSO) (Li D et al., 2021; Li Z et al., 2021). Notably, Ce6-induced ROS production, BSO-caused GSH depletion, and inactivation of GPX4 could amplify apoptosis and ferroptosis. Efficient tumor destruction led to increased exposure of high mobility group box 1 (HMGB1) and calreticulin enhancing antitumor immune responses, including maturation of DCs and effector function of tumor-infiltrating T lymphocytes, which resulted in the elimination of the residual melanoma cells.

4 CONCLUSIONS AND FUTURE PERSPECTIVES

With the development of life sciences and medicine, the genetic and molecular mechanisms of cancer have been extensively investigated by researchers worldwide. Many countries have invested considerable material and financial resources in this endeavor. However, tumorigenesis, progression, metastasis, recurrence, and death caused by cancer are still poorly understood because of the tumor complexity including diverse molecular types and heterogeneity; thus, the therapeutic outcomes remain unsatisfactory. Therefore, finding novel therapeutic strategies to solve the human cancer issue has become the most significant problem that needs to be urgently addressed to protect human health. Ferroptosis, termed in 2012, has been widely researched concerning the cellular mechanisms and signaling pathways in cancers. As a novel type of cell death, ferroptosis has great potential as a new cancer therapy, and several ferroptosis-inducing small molecules (such as erastin, sorafenib, sulfasalazine, altretamine, and artemisinin) and various genes related to ferroptosis (e.g., xCT, GPX4, p53, NQO1, and NOX) have been discovered by the researchers. Nonetheless, there are also some disadvantages: 1) there are potential adverse effects of ferroptosis on normal tissues due to the low specificity of small-molecule compounds; 2) small-molecule compounds have short half-lives in blood and low accumulation at tumor sites because of rapid renal clearance; 3) gene-based FBT for cancer is essentially one type of gene therapy, which might bring controversy at ethics and law (Shen et al., 2018). Hence, although FBT based on small molecules and genes is promising, significant research is required before it can be applied clinically.

With the rapid development of nanomedicine, numerous ferroptosis-inducing nanomaterials have been developed by chemists, pharmacists, and material scientists. The adverse effects on normal tissues could be decreased because of the precise targetability of the nanomaterials to tumor sites, and the nanomaterials possess long circulating half-lives in the blood, which enhances the accumulation of the nanomaterials at tumor sites. The ferroptosis-based nanomaterials could be triggered by several factors (such as light, US, and TME) to induce the release of metal irons, metal oxides, or drugs to induce or enhance ferroptosis. The FBT of cancer could integrate with different models of imaging guidance (such as US imaging, PAI, and MRI) and combine with diverse cancer therapies (such as CDT, SDT, PDT, PTT, and immunotherapy). In this review, we roughly divide the reported ferroptosis-based nanomaterials into two types: iron-contained nanomaterials and iron-free nanomaterials. The former induces ferroptosis *via* increasing the external iron to enhance the Fenton reaction; meanwhile, the latter induces ferroptosis *via* GSH depletion, GPX4 inactivation, or increasing intracellular ROS, which leads to the prospective that it is difficult for the iron-free nanomaterials to achieve satisfactory treatment. Therefore, iron-contained nanomaterials might be more promising than iron-free nanomaterials because the latter is limited by utilizing the intracellular restricted iron to produce ROS *via* the Fenton reaction.

Undoubtedly, in the future, a mass of ferroptosis-based nanomaterials will be investigated for cancer therapy. The future research might focus on the following aspects: 1) more ferroptosis small-molecular compounds will be discovered and synthesized, and subsequently they might be utilized to be encapsulated into the iron-contained nanomaterials for FBT; 2) the siRNAs targeting ferroptosis-related genes (e.g., p53, GPX4, and xCT) might be used to enhance the effect of FBT; 3) the ferroptosis-based nanomaterials might combine with radiotherapy to make tumor sensitized to radiation; 4) more nanomedical research about the combination treatment of FBT and immunotherapy needs to be brought to the forefront because of its great clinical application prospects. Meanwhile, multiple issues should be taken into consideration in the rational design of the nanomaterials based on ferroptosis in the future, such as safety and feasibility of clinical application, possible toxicity, and industrial feasibility.

AUTHOR CONTRIBUTIONS

ZS, JZ, WT, and CS designed and conceptualized the review. All authors contributed to the writing of the manuscript.

FUNDING

This work was supported by the National Natural Science Foundation of China (No. 81972373), the Natural Science Foundation of Fujian Province of China (No.2019J01016), the funding of the Science and Technology Planned Project of Medical and Health of Xiamen City (No. 3502Z20194038), The Scientific Research Foundation for Advanced Talents of Xiang'an Hospital of Xiamen University (No. PM201809170001), and the Medical Leading Talents of Xiamen City.

ACKNOWLEDGMENTS

ZS would like to thank his wife Meiying Huang and his parents who have given him strong spiritual and financial support during his hard times. Thanks to editor and typesetter for their kind help.

REFERENCES

An, P., Gao, Z., Sun, K., Gu, D., Wu, H., You, C., et al. (2019). Photothermal-Enhanced Inactivation of Glutathione Peroxidase for Ferroptosis Sensitized by an Autophagy Promotor. *ACS Appl. Mater. Inter.* 11 (46), 42988–42997. doi:10.1021/acsami.9b16124

Asghari, F., Khademi, R., Esmaeili Ranjbar, F., Veisi Malekshahi, Z., and Faridi Majidi, R. (2019). Application of Nanotechnology in Targeting of Cancer Stem Cells: A Review. *Ijsc* 12 (2), 227–239. doi:10.15283/ijsc19006

Bao, W., Liu, X., Lv, Y., Lu, G.-H., Li, F., Zhang, F., et al. (2019). Nanolongan with Multiple On-Demand Conversions for Ferroptosis-Apoptosis Combined Anticancer Therapy. *ACS Nano* 13 (1), 260–273. doi:10.1021/acsnano.8b05602

Bray, F., Laversanne, M., Weiderpass, E., and Soerjomataram, I. (2021). The Ever-increasing Importance of Cancer as a Leading Cause of Premature Death Worldwide. *Cancer* 127 (16), 3029–3030. doi:10.1002/cncr.33587

Cao, J. Y., and Dixon, S. J. (2016). Mechanisms of Ferroptosis. *Cell. Mol. Life Sci.* 73 (11-12), 2195–2209. doi:10.1007/s00018-016-2194-1

Chen, G., Yang, Y., Xu, Q., Ling, M., Lin, H., Ma, W., et al. (2020). Self-Amplification of Tumor Oxidative Stress with Degradable Metallic Complexes for Synergistic Cascade Tumor Therapy. *Nano Lett.* 20 (11), 8141–8150. doi:10.1021/acs.nanolett.0c03127

Chen, H., Yan, Z., Wu, S., and Li, F. (2021). A Glutathione-Responsive Polyphenol - Constructed Nanodevice for Double Roles in Apoptosis and Ferroptosis. *Colloids Surf. B: Biointerfaces* 205, 111902. doi:10.1016/j.colsurfb.2021.111902

Chen, L., Lin, Z., Liu, L., Zhang, X., Shi, W., Ge, D., et al. (2019). Fe2+/Fe3+ Ions Chelated with Ultrasmall Polydopamine Nanoparticles Induce Ferroptosis for Cancer Therapy. *ACS Biomater. Sci. Eng.* 5 (9), 4861–4869. doi:10.1021/acsbiomaterials.9b00461

Chen, Q., Ma, X., Xie, L., Chen, W., Xu, Z., Song, E., et al. (2021). Iron-based Nanoparticles for MR Imaging-Guided Ferroptosis in Combination with Photodynamic Therapy to Enhance Cancer Treatment. *Nanoscale* 13 (9), 4855–4870. doi:10.1039/d0nr08757b

Cheng, H., Wang, X., Liu, X., Wang, X., Wen, H., Cheng, Y., et al. (2021). An Effective NIR Laser/tumor-Microenvironment Co-responsive Cancer Theranostic Nanoplatform with Multi-Modal Imaging and Therapies. *Nanoscale* 13 (24), 10816–10828. doi:10.1039/d1nr01645h

Cheng, J., Zhu, Y., Xing, X., Xiao, J., Chen, H., Zhang, H., et al. (2021). Manganese-deposited Iron Oxide Promotes Tumor-Responsive Ferroptosis that Synergizes the Apoptosis of Cisplatin. *Theranostics* 11 (11), 5418–5429. doi:10.7150/thno.53346

Cheng, W., Zeng, X., Chen, H., Li, Z., Zeng, W., Mei, L., et al. (2019). Versatile Polydopamine Platforms: Synthesis and Promising Applications for Surface Modification and Advanced Nanomedicine. *ACS Nano* 13 (8), 8537–8565. doi:10.1021/acsnano.9b04436

Cui, X., Lu, G., Fang, F., Xiong, Y., Tian, S., Wan, Y., et al. (2021). Iron Self-Boosting Polymer Nanoenzyme for Low-Temperature Photothermal-Enhanced Ferrotherapy. *ACS Appl. Mater. Inter.* 13 (26), 30274–30283. doi:10.1021/acsami.1c01658

Debela, D. T., Muzazu, S. G., Heraro, K. D., Ndalama, M. T., Mesele, B. W., Haile, D. C., et al. (2021). New Approaches and Procedures for Cancer Treatment: Current Perspectives. *SAGE Open Med.* 9, 205031212110343. doi:10.1177/20503121211034366

Ding, B., Zheng, P., Jiang, F., Zhao, Y., Wang, M., Chang, M., et al. (2020). MnO X Nanospikes as Nanoadjuvants and Immunogenic Cell Death Drugs with Enhanced Antitumor Immunity and Antimetastatic Effect. *Angew. Chem. Int. Ed.* 59 (38), 16381–16384. doi:10.1002/anie.202005111

Dixon, S. J., Lemberg, K. M., Lamprecht, M. R., Skouta, R., Zaitsev, E. M., Gleason, C. E., et al. (2012). Ferroptosis: an Iron-dependent Form of Nonapoptotic Cell Death. *Cell* 149 (5), 1060–1072. doi:10.1016/j.cell.2012.03.042

Dolma, S., Lessnick, S. L., Hahn, W. C., and Stockwell, B. R. (2003). Identification of Genotype-Selective Antitumor Agents Using Synthetic Lethal Chemical Screening in Engineered Human Tumor Cells. *Cancer Cell* 3 (3), 285–296. doi:10.1016/s1535-6108(03)00050-3

Fang, J., Nakamura, H., and Maeda, H. (2011). The EPR Effect: Unique Features of Tumor Blood Vessels for Drug Delivery, Factors Involved, and Limitations and Augmentation of the Effect. *Adv. Drug Deliv. Rev.* 63 (3), 136–151. doi:10.1016/j.addr.2010.04.009

Fei, W., Chen, D., Tang, H., Li, C., Zheng, W., Chen, F., et al. (2020b). Targeted GSH-Exhausting and Hydroxyl Radical Self-Producing Manganese-Silica Nanomissiles for MRI Guided Ferroptotic Cancer Therapy. *Nanoscale* 12 (32), 16738–16754. doi:10.1039/d0nr02396e

Fei, W., Zhang, Y., Ye, Y., Li, C., Yao, Y., Zhang, M., et al. (2020a). Bioactive Metal-Containing Nanomaterials for Ferroptotic Cancer Therapy. *J. Mater. Chem. B* 8 (46), 10461–10473. doi:10.1039/d0tb02138e

Feng, H., and Stockwell, B. R. (2018). Unsolved Mysteries: How Does Lipid Peroxidation Cause Ferroptosis? *Plos Biol.* 16 (5), e2006203. doi:10.1371/journal.pbio.2006203

Fu, J., Li, T., Yang, Y., Jiang, L., Wang, W., Fu, L., et al. (2021). Activatable Nanomedicine for Overcoming Hypoxia-Induced Resistance to Chemotherapy and Inhibiting Tumor Growth by Inducing Collaborative Apoptosis and Ferroptosis in Solid Tumors. *Biomaterials* 268, 120537. doi:10.1016/j.biomaterials.2020.120537

Gao, Z., He, T., Zhang, P., Li, X., Zhang, Y., Lin, J., et al. (2020). Polypeptide-Based Theranostics with Tumor-Microenvironment-Activatable Cascade Reaction for Chemo-Ferroptosis Combination Therapy. *ACS Appl. Mater. Inter.* 12 (18), 20271–20280. doi:10.1021/acsami.0c03748

Gaschler, M. M., Andia, A. A., Liu, H., Csuka, J. M., Hurlocker, B., Vaiana, C. A., et al. (2018). FINO2 Initiates Ferroptosis through GPX4 Inactivation and Iron Oxidation. *Nat. Chem. Biol.* 14 (5), 507–515. doi:10.1038/s41589-018-0031-6

Golombek, S. K., May, J.-N., Theek, B., Appold, L., Drude, N., Kiessling, F., et al. (2018). Tumor Targeting via EPR: Strategies to Enhance Patient Responses. *Adv. Drug Deliv. Rev.* 130, 17–38. doi:10.1016/j.addr.2018.07.007

Gu, Z., Liu, T., Liu, C., Yang, Y., Tang, J., Song, H., et al. (2021). Ferroptosis-Strengthened Metabolic and Inflammatory Regulation of Tumor-Associated Macrophages Provokes Potent Tumoricidal Activities. *Nano Lett.* 21 (15), 6471–6479. doi:10.1021/acs.nanolett.1c01401

Guan, Q., Guo, R., Huang, S., Zhang, F., Liu, J., Wang, Z., et al. (2020). Mesoporous Polydopamine Carrying Sorafenib and SPIO Nanoparticles for MRI-Guided Ferroptosis Cancer Therapy. *J. Controlled Release* 320, 392–403. doi:10.1016/j.jconrel.2020.01.048

Guo, P., Wang, L., Shang, W., Chen, J., Chen, Z., Xiong, F., et al. (2020). Intravesical *In Situ* Immunostimulatory Gel for Triple Therapy of Bladder Cancer. *ACS Appl. Mater. Inter.* 12 (49), 54367–54377. doi:10.1021/acsami.0c15176

Guo, X., Liu, F., Deng, J., Dai, P., Qin, Y., Li, Z., et al. (2020). Electron-Accepting Micelles Deplete Reduced Nicotinamide Adenine Dinucleotide Phosphate and Impair Two Antioxidant Cascades for Ferroptosis-Induced Tumor Eradication. *ACS Nano* 14 (11), 14715–14730. doi:10.1021/acsnano.0c00764

Guo, Y., Zhang, X., Sun, W., Jia, H.-R., Zhu, Y.-X., Zhang, X., et al. (2019). Metal-Phenolic Network-Based Nanocomplexes that Evoke Ferroptosis by Apoptosis:

Promoted Nuclear Drug Influx and Reversed Drug Resistance of Cancer. *Chem. Mater.* 31 (24), 10071–10084. doi:10.1021/acs.chemmater.9b03042

Hanahan, D. (2022). Hallmarks of Cancer: New Dimensions. *Cancer Discov.* 12 (1), 31–46. doi:10.1158/2159-8290.CD-21-1059

He, H., Du, L., Guo, H., An, Y., Lu, L., Chen, Y., et al. (2020). Redox Responsive Metal Organic Framework Nanoparticles Induces Ferroptosis for Cancer Therapy. *Small* 16 (33), 2001251. doi:10.1002/smll.202001251

He, S., Jiang, Y., Li, J., and Pu, K. (2020). Semiconducting Polycomplex Nanoparticles for Photothermal Ferrotherapy of Cancer. *Angew. Chem. Int. Ed.* 59 (26), 10633–10638. doi:10.1002/anie.202003004

Hu, Z., Wang, S., Dai, Z., Zhang, H., and Zheng, X. (2020). A Novel Theranostic Nano-Platform (PB@FePt-HA-g-PEG) for Tumor Chemodynamic-Photothermal Co-therapy and Triple-Modal Imaging (MR/CT/PI) Diagnosis. *J. Mater. Chem. B* 8 (24), 5351–5360. doi:10.1039/d0tb00708k

Huang, K.-J., Wei, Y.-H., Chiu, Y.-C., Wu, S.-R., and Shieh, D.-B. (2019). Assessment of Zero-Valent Iron-Based Nanotherapeutics for Ferroptosis Induction and Resensitization Strategy in Cancer Cells. *Biomater. Sci.* 7 (4), 1311–1322. doi:10.1039/c8bm01525b

JiangQ, ., Wang, K., Zhang, X., Ouyang, B., Liu, H., Pang, Z., et al. (2020). Platelet Membrane-Camouflaged Magnetic Nanoparticles for Ferroptosis-Enhanced Cancer Immunotherapy. *Small* 16 (22), 2001704. doi:10.1002/smll.202001704

JiangY, ., Zhao, X., Huang, J., Li, J., Upputuri, P. K., Sun, H., et al. (2020). Transformable Hybrid Semiconducting Polymer Nanozyme for Second Near-Infrared Photothermal Ferrotherapy. *Nat. Commun.* 11 (1), 1857. doi:10.1038/s41467-020-15730-x

Kim, S. E., Zhang, L., Ma, K., Riegman, M., Chen, F., Ingold, I., et al. (2016). Ultrasmall Nanoparticles Induce Ferroptosis in Nutrient-Deprived Cancer Cells and Suppress Tumour Growth. *Nat. Nanotech* 11 (11), 977–985. doi:10.1038/nnano.2016.164

Li, D., Ren, J., Li, J., Zhang, Y., Lou, Y., Zhu, J., et al. (2021). Ferroptosis-apoptosis Combined Anti-melanoma Immunotherapy with a NIR-Responsive Upconverting mSiO2 Photodynamic Platform. *Chem. Eng. J.* 419, 129557. doi:10.1016/j.cej.2021.129557

Li, J., Cao, F., Yin, H.-l., Huang, Z.-j., Lin, Z.-t., Mao, N., et al. (2020). Ferroptosis: Past, Present and Future. *Cell Death Dis* 11 (2), 88. doi:10.1038/s41419-020-2298-2

Li, W., Liu, X., Cheng, X., Zhang, W., Gong, C., Gao, C., et al. (2022). Effect of Malt-PEG-Abz@RSL3 Micelles on HepG2 Cells Based on NADPH Depletion and GPX4 Inhibition in Ferroptosis. *J. Drug Target.* 30 (2), 208–218. doi:10.1080/1061186X.2021.1953511

Li, Y., Chen, W., Qi, Y., Wang, S., Li, L., Li, W., et al. (2020). H 2 S-Scavenged and Activated Iron Oxide-Hydroxide Nanospindles for MRI-Guided Photothermal Therapy and Ferroptosis in Colon Cancer. *Small* 16 (37), 2001356. doi:10.1002/smll.202001356

Li, Y., Wang, X., Yan, J., Liu, Y., Yang, R., Pan, D., et al. (2019). Nanoparticle Ferritin-Bound Erastin and Rapamycin: a Nanodrug Combining Autophagy and Ferroptosis for Anticancer Therapy. *Biomater. Sci.* 7 (9), 3779–3787. doi:10.1039/c9bm00653b

Li, Z., Wu, X., Wang, W., Gai, C., Zhang, W., Li, W., et al. (2021). Fe(II) and Tannic Acid-Cloaked MOF as Carrier of Artemisinin for Supply of Ferrous Ions to Enhance Treatment of Triple-Negative Breast Cancer. *Nanoscale Res. Lett.* 16 (1), 37. doi:10.1186/s11671-021-03497-z

Liang, C., Zhang, X., Yang, M., and Dong, X. (2019). Recent Progress in Ferroptosis Inducers for Cancer Therapy. *Adv. Mater.* 31 (51), 1904197. doi:10.1002/adma.201904197

Liu, T., Liu, W., Zhang, M., Yu, W., Gao, F., Li, C., et al. (2018). Ferrous-Supply-Regeneration Nanoengineering for Cancer-cell-specific Ferroptosis in Combination with Imaging-Guided Photodynamic Therapy. *ACS Nano* 12 (12), 12181–12192. doi:10.1021/acsnano.8b05860

Liu, X., Zhu, X., Qi, X., Meng, X., and Xu, K. (2021). Co-Administration of iRGD with Sorafenib-Loaded Iron-Based Metal-Organic Framework as a Targeted Ferroptosis Agent for Liver Cancer Therapy. *Ijn* Vol. 16, 1037–1050. doi:10.2147/IJN.S292528

Luo, C., Sun, J., Sun, B., and He, Z. (2014). Prodrug-based Nanoparticulate Drug Delivery Strategies for Cancer Therapy. *Trends Pharmacol. Sci.* 35 (11), 556–566. doi:10.1016/j.tips.2014.09.008

Maeda, H. (2015). Toward a Full Understanding of the EPR Effect in Primary and Metastatic Tumors as Well as Issues Related to its Heterogeneity. *Adv. Drug Deliv. Rev.* 91, 3–6. doi:10.1016/j.addr.2015.01.002

Meng, X., Deng, J., Liu, F., Guo, T., Liu, M., Dai, P., et al. (2019). Triggered All-Active Metal Organic Framework: Ferroptosis Machinery Contributes to the Apoptotic Photodynamic Antitumor Therapy. *Nano Lett.* 19 (11), 7866–7876. doi:10.1021/acs.nanolett.9b02904

Meng, Y., Zhang, D., Sun, Y., Dai, Z., Zhang, T., Yu, D., et al. (2020). Core-shell FePt-Cube@covalent Organic Polymer Nanocomposites: a Multifunctional Nanocatalytic Agent for Primary and Metastatic Tumor Treatment. *J. Mater. Chem. B* 8 (48), 11021–11032. doi:10.1039/d0tb01981j

Nieto, C., Vega, M. A., and Martín del Valle, E. M. (2021). Tailored-Made Polydopamine Nanoparticles to Induce Ferroptosis in Breast Cancer Cells in Combination with Chemotherapy. *Ijms* 22 (6), 3161. doi:10.3390/ijms22063161

Park, J., Choi, Y., Chang, H., Um, W., Ryu, J. H., and Kwon, I. C. (2019). Alliance with EPR Effect: Combined Strategies to Improve the EPR Effect in the Tumor Microenvironment. *Theranostics* 9 (26), 8073–8090. doi:10.7150/thno.37198

Patra, M., and Gasser, G. (2017). The Medicinal Chemistry of Ferrocene and its Derivatives. *Nat. Rev. Chem.* 1 (9), 0066. doi:10.1038/s41570-017-0066

Rahim, M. A., Kristufek, S. L., Pan, S., Richardson, J. J., and Caruso, F. (2019). Phenolic Building Blocks for the Assembly of Functional Materials. *Angew. Chem. Int. Ed.* 58 (7), 1904–1927. doi:10.1002/anie.201807804

Sang, M., Luo, R., Bai, Y., Dou, J., Zhang, Z., Liu, F., et al. (2019a). BHQ-Cyanine-Based "Off-On" Long-Circulating Assembly as a Ferroptosis Amplifier for Cancer Treatment: A Lipid-Peroxidation Burst Device. *ACS Appl. Mater. Inter.* 11 (46), 42873–42884. doi:10.1021/acsami.9b12469

Sang, M., Luo, R., Bai, Y., Dou, J., Zhang, Z., Liu, F., et al. (2019b). Mitochondrial Membrane Anchored Photosensitive Nano-Device for Lipid Hydroperoxides Burst and Inducing Ferroptosis to Surmount Therapy-Resistant Cancer. *Theranostics* 9 (21), 6209–6223. doi:10.7150/thno.36283

Shan, X., Li, S., Sun, B., Chen, Q., Sun, J., He, Z., et al. (2020). Ferroptosis-driven Nanotherapeutics for Cancer Treatment. *J. Controlled Release* 319, 322–332. doi:10.1016/j.jconrel.2020.01.008

Shen, Z., Song, J., Yung, B. C., Zhou, Z., Wu, A., and Chen, X. (2018). Emerging Strategies of Cancer Therapy Based on Ferroptosis. *Adv. Mater.* 30 (12), 1704007. doi:10.1002/adma.201704007

Shi, J., Kantoff, P. W., Wooster, R., and Farokhzad, O. C. (2017). Cancer Nanomedicine: Progress, Challenges and Opportunities. *Nat. Rev. Cancer* 17 (1), 20–37. doi:10.1038/nrc.2016.108

Shi, Y., Liu, S., Liu, Y., Sun, C., Chang, M., Zhao, X., et al. (2019). Facile Fabrication of Nanoscale Porphyrinic Covalent Organic Polymers for Combined Photodynamic and Photothermal Cancer Therapy. *ACS Appl. Mater. Inter.* 11 (13), 12321–12326. doi:10.1021/acsami.9b00361

Shi, Z., Zhang, L., Zheng, J., Sun, H., and Shao, C. (2021). Ferroptosis: Biochemistry and Biology in Cancers. *Front. Oncol.* 11, 579286. doi:10.3389/fonc.2021.579286

Shimada, K., Skouta, R., Kaplan, A., Yang, W. S., Hayano, M., Dixon, S. J., et al. (2016). Global Survey of Cell Death Mechanisms Reveals Metabolic Regulation of Ferroptosis. *Nat. Chem. Biol.* 12 (7), 497–503. doi:10.1038/nchembio.2079

Song, R., Li, T., Ye, J., Sun, F., Hou, B., Saeed, M., et al. (2021). Acidity-Activatable Dynamic Nanoparticles Boosting Ferroptotic Cell Death for Immunotherapy of Cancer. *Adv. Mater.* 33 (31), 2101155. doi:10.1002/adma.202101155

Sung, H., Ferlay, J., Siegel, R. L., Laversanne, M., Soerjomataram, I., Jemal, A., et al. (2021). Global Cancer Statistics 2020: GLOBOCAN Estimates of Incidence and Mortality Worldwide for 36 Cancers in 185 Countries. *CA A. Cancer J. Clin.* 71 (3), 209–249. doi:10.3322/caac.21660

Tang, H., Chen, D., Li, C., Zheng, C., Wu, X., Zhang, Y., et al. (2019). Dual GSH-Exhausting Sorafenib Loaded Manganese-Silica Nanodrugs for Inducing the Ferroptosis of Hepatocellular Carcinoma Cells. *Int. J. Pharmaceutics* 572, 118782. doi:10.1016/j.ijpharm.2019.118782

Tang, H., Li, C., Zhang, Y., Zheng, H., Cheng, Y., Zhu, J., et al. (2020). Targeted Manganese Doped Silica Nano GSH-Cleaner for Treatment of Liver Cancer by Destroying the Intracellular Redox Homeostasis. *Theranostics* 10 (21), 9865–9887. doi:10.7150/thno.46771

Valle, A. C., Yeh, C. K., and Huang, Y. F. (2020). Near Infrared-Activatable Platinum-Decorated Gold Nanostars for Synergistic Photothermal/Ferroptotic Therapy in Combating Cancer Drug Resistance. *Adv. Healthc. Mater.* 9 (20), 2000864. doi:10.1002/adhm.202000864

Wan, X., Song, L., Pan, W., Zhong, H., Li, N., and Tang, B. (2020). Tumor-Targeted Cascade Nanoreactor Based on Metal-Organic Frameworks for Synergistic Ferroptosis-Starvation Anticancer Therapy. *ACS Nano* 14 (9), 11017–11028. doi:10.1021/acsnano.9b07789

Wang, S., Li, F., Qiao, R., Hu, X., Liao, H., Chen, L., et al. (2018). Arginine-Rich Manganese Silicate Nanobubbles as a Ferroptosis-Inducing Agent for Tumor-Targeted Theranostics. *ACS Nano* 12 (12), 12380–12392. doi:10.1021/acsnano.8b06399

Wang, X., Wu, M., Zhang, X., Li, F., Zeng, Y., Lin, X., et al. (2021). Hypoxia-responsive Nanoreactors Based on Self-Enhanced Photodynamic Sensitization and Triggered Ferroptosis for Cancer Synergistic Therapy. *J. Nanobiotechnol* 19 (1), 204. doi:10.1186/s12951-021-00952-y

Wolpaw, A. J., Shimada, K., Skouta, R., Welsch, M. E., Akavia, U. D., Pe'er, D., et al. (2011). Modulatory Profiling Identifies Mechanisms of Small Molecule-Induced Cell Death. *Proc. Natl. Acad. Sci.* 108 (39), E771–E780. doi:10.1073/pnas.1106149108

Xie, S., Sun, W., Zhang, C., Dong, B., Yang, J., Hou, M., et al. (2021). Metabolic Control by Heat Stress Determining Cell Fate to Ferroptosis for Effective Cancer Therapy. *ACS Nano* 15 (4), 7179–7194. doi:10.1021/acsnano.1c00380

Xin, H., Huang, Y., Tang, H., Chen, Y., Xia, H., Zhang, F., et al. (2021). Delivery of a System Xc– Inhibitor by a Redox-Responsive Levodopa Prodrug Nanoassembly for Combination Ferrotherapy. *J. Mater. Chem. B* 9 (35), 7172–7181. doi:10.1039/d1tb00742d

Xiong, H., Wang, C., Wang, Z., Lu, H., and Yao, J. (2021). Self-assembled Nano-Activator Constructed Ferroptosis-Immunotherapy through Hijacking Endogenous Iron to Intracellular Positive Feedback Loop. *J. Controlled Release* 332, 539–552. doi:10.1016/j.jconrel.2021.03.007

Xu, C., Lin, Y., Wang, J., Wu, L., Wei, W., Ren, J., et al. (2013). Nanoceria-Triggered Synergetic Drug Release Based on CeO2-Capped Mesoporous Silica Host-Guest Interactions and Switchable Enzymatic Activity and Cellular Effects of CeO2. *Adv. Healthc. Mater.* 2 (12), 1591–1599. doi:10.1002/adhm.201200464

Xu, Q., Zhan, G., Zhang, Z., Yong, T., Yang, X., and Gan, L. (2021). Manganese Porphyrin-Based Metal-Organic Framework for Synergistic Sonodynamic Therapy and Ferroptosis in Hypoxic Tumors. *Theranostics* 11 (4), 1937–1952. doi:10.7150/thno.45511

Xu, R., Yang, J., Qian, Y., Deng, H., Wang, Z., Ma, S., et al. (2021). Ferroptosis/pyroptosis Dual-Inductive Combinational Anti-cancer Therapy Achieved by Transferrin Decorated nanoMOF. *Nanoscale Horiz.* 6 (4), 348–356. doi:10.1039/d0nh00674b

Xu, X., Chen, Y., Zhang, Y., Yao, Y., and Ji, P. (2020). Highly Stable and Biocompatible Hyaluronic Acid-Rehabilitated Nanoscale MOF-Fe2+induced Ferroptosis in Breast Cancer Cells. *J. Mater. Chem. B* 8, 9129–9138. doi:10.1039/d0tb01616k

Xue, C.-C., Li, M.-H., Zhao, Y., Zhou, J., Hu, Y., Cai, K.-Y., et al. (2020). Tumor Microenvironment-Activatable Fe-Doxorubicin Preloaded Amorphous CaCO 3 Nanoformulation Triggers Ferroptosis in Target Tumor Cells. *Sci. Adv.* 6 (18), eaax1346. doi:10.1126/sciadv.aax1346

Xue, C., Li, M., Liu, C., Li, Y., Fei, Y., Hu, Y., et al. (2021). NIR-Actuated Remote Activation of Ferroptosis in Target Tumor Cells through a Photothermally Responsive Iron-Chelated Biopolymer Nanoplatform. *Angew. Chem. Int. Ed.* 60 (16), 8938–8947. doi:10.1002/anie.202016872

Yagoda, N., von Rechenberg, M., Zaganjor, E., Bauer, A. J., Yang, W. S., Fridman, D. J., et al. (2007). RAS-RAF-MEK-dependent Oxidative Cell Death Involving Voltage-dependent Anion Channels. *Nature* 447 (7146), 865–869. doi:10.1038/nature05859

Yamagishi, K., Kirino, I., Takahashi, I., Amano, H., Takeoka, S., Morimoto, Y., et al. (2019). Tissue-adhesive Wirelessly Powered Optoelectronic Device for Metronomic Photodynamic Cancer Therapy. *Nat. Biomed. Eng.* 3 (1), 27–36. doi:10.1038/s41551-018-0261-7

Yang, B., Liu, Q., Yao, X., Zhang, D., Dai, Z., Cui, P., et al. (2019). FePt@MnO-Based Nanotheranostic Platform with Acidity-Triggered Dual-Ions Release for Enhanced MR Imaging-Guided Ferroptosis Chemodynamic Therapy. *ACS Appl. Mater. Inter.* 11 (42), 38395–38404. doi:10.1021/acsami.9b11353

Yang, J., Ma, S., Xu, R., Wei, Y., Zhang, J., Zuo, T., et al. (2021). Smart Biomimetic Metal Organic Frameworks Based on ROS-Ferroptosis-Glycolysis Regulation for Enhanced Tumor Chemo-Immunotherapy. *J. Controlled Release* 334, 21–33. doi:10.1016/j.jconrel.2021.04.013

Yang, W. S., and Stockwell, B. R. (2008). Synthetic Lethal Screening Identifies Compounds Activating Iron-dependent, Nonapoptotic Cell Death in Oncogenic-RAS-Harboring Cancer Cells. *Chem. Biol.* 15 (3), 234–245. doi:10.1016/j.chembiol.2008.02.010

Yang, Y., Tian, Q., Wu, S., Li, Y., Yang, K., Yan, Y., et al. (202112073). Blue Light-Triggered Fe2+-Release from Monodispersed Ferrihydrite Nanoparticles for Cancer Iron Therapy. *Biomaterials* 271, 120739. doi:10.1016/j.biomaterials.2021.120739

Yao, X., Yang, B., Wang, S., Dai, Z., Zhang, D., Zheng, X., et al. (2020). A Novel Multifunctional FePt/BP Nanoplatform for Synergistic Photothermal/photodynamic/chemodynamic Cancer Therapies and Photothermally-Enhanced Immunotherapy. *J. Mater. Chem. B* 8 (35), 8010–8021. doi:10.1039/d0tb00411a

Yao, X., Yang, P., Jin, Z., Jiang, Q., Guo, R., Xie, R., et al. (2019). Multifunctional Nanoplatform for Photoacoustic Imaging-Guided Combined Therapy Enhanced by CO Induced Ferroptosis. *Biomaterials* 197, 268–283. doi:10.1016/j.biomaterials.2019.01.026

Youn, Y. S., and Bae, Y. H. (2018). Perspectives on the Past, Present, and Future of Cancer Nanomedicine. *Adv. Drug Deliv. Rev.* 130, 3–11. doi:10.1016/j.addr.2018.05.008

Yue, L., Dai, Z., Chen, X., Liu, C., Hu, Z., Song, B., et al. (2018). Development of a Novel FePt-Based Multifunctional Ferroptosis Agent for High-Efficiency Anticancer Therapy. *Nanoscale* 10 (37), 17858–17864. doi:10.1039/c8nr05150j

Zhang, F., Li, F., Lu, G.-H., Nie, W., Zhang, L., Lv, Y., et al. (2019). Engineering Magnetosomes for Ferroptosis/Immunomodulation Synergism in Cancer. *ACS Nano* 13 (5), 5662–5673. doi:10.1021/acsnano.9b00892

Zhang, J., Yang, J., Zuo, T., Ma, S., Xokrat, N., Hu, Z., et al. (2021). Heparanase-driven Sequential Released Nanoparticles for Ferroptosis and Tumor Microenvironment Modulations Synergism in Breast Cancer Therapy. *Biomaterials* 266, 120429. doi:10.1016/j.biomaterials.2020.120429

Zhang, Y., Fu, X., Jia, J., Wikerholmen, T., Xi, K., Kong, Y., et al. (2020). Glioblastoma Therapy Using Codelivery of Cisplatin and Glutathione Peroxidase Targeting siRNA from Iron Oxide Nanoparticles. *ACS Appl. Mater. Inter.* 12 (39), 43408–43421. doi:10.1021/acsami.0c12042

Zhao, Y., Zhao, W., Lim, Y. C., and Liu, T. (2019). Salinomycin-Loaded Gold Nanoparticles for Treating Cancer Stem Cells by Ferroptosis-Induced Cell Death. *Mol. Pharmaceutics* 16 (6), 2532–2539. doi:10.1021/acs.molpharmaceut.9b00132

Zhou, L. L., Guan, Q., Li, W. Y., Zhang, Z., Li, Y. A., and Dong, Y. B. (2021). A Ferrocene-Functionalized Covalent Organic Framework for Enhancing Chemodynamic Therapy via Redox Dyshomeostasis. *Small* 17 (32), 2101368. doi:10.1002/smll.202101368

Zhu, J., Dai, P., Liu, F., Li, Y., Qin, Y., Yang, Q., et al. (2020). Upconverting Nanocarriers Enable Triggered Microtubule Inhibition and Concurrent Ferroptosis Induction for Selective Treatment of Triple-Negative Breast Cancer. *Nano Lett.* 20 (9), 6235–6245. doi:10.1021/acs.nanolett.0c00502

Zhu, T., Shi, L., Yu, C., Dong, Y., Qiu, F., Shen, L., et al. (2019). Ferroptosis Promotes Photodynamic Therapy: Supramolecular Photosensitizer-Inducer Nanodrug for Enhanced Cancer Treatment. *Theranostics* 9 (11), 3293–3307. doi:10.7150/thno.32867

Conflict of Interest: The authors declare that the research was conducted in the absence of any commercial or financial relationships that could be construed as a potential conflict of interest.

ORIGINAL RESEARCH
published: 06 April 2022
doi: 10.3389/fchem.2022.872582

A Flexible Electrochemiluminescence Sensor Equipped With Vertically Ordered Mesoporous Silica Nanochannel Film for Sensitive Detection of Clindamycin

Xinjie Wei[1†], *Xuan Luo*[2†], *Shuai Xu*[2], *Fengna Xi*[2*] and *Tingting Zhao*[1*]

[1]*Guangxi Medical University Cancer Hospital, Guangxi Medical University, Nanning, China,* [2]*Department of Chemistry, Key Laboratory of Surface and Interface Science of Polymer Materials of Zhejiang Province, Zhejiang Sci-Tech University, Hangzhou, China*

Fast, convenient, and highly sensitive detection of antibiotic is essential to avoid its overuse and the possible harm. Owing to enrichment effect and antifouling ability of ultrasmall nanochannels, the vertically ordered mesoporous silica nanochannel film (VMSF) has great potential in the development of the facile electrochemiluminescence (ECL) sensor for direct and sensitive analysis of antibiotics in complex samples. In this study, we demonstrated a flexible ECL sensor based on a cost-effective electrode covered with a VMSF for sensitive detection of clindamycin. Polyethylene terephthalate coated with indium tin oxide (PET-ITO) is applied as a flexible electrode to grow VMSF using the electrochemically assisted self-assembly (EASA) method. The negatively charged VMSF nanochannels exhibit significant enrichment toward the commonly used cationic ECL luminophores, tris(2,2-bipyridyl) dichlororuthenium (II) (Ru (bpy)$_3^{2+}$). Using the enhanced ECL of Ru (bpy)$_3^{2+}$ by clindamycin, the developed VMSF/PET-ITO sensor can sensitively detect clindamycin. The responses were linear in the concentration range of 10 nM–25 μM and in the concentration range of 25–70 μM. Owing to the nanoscale thickness of the VMSF and the high coupling stability with the electrode substrate, the developed flexible VMSF/PET-ITO sensor exhibits high signal stability during the continuous bending process. Considering high antifouling characteristic of the VMSF, direct analysis of clindamycin in a real biological sample, human serum, is realized.

Keywords: electrochemiluminescence sensor, flexible electrode, vertically ordered mesoporous silica nanochannel film, sensitive detection, clindamycin

Edited by:
Yan Zhang,
University of Jinan, China

Reviewed by:
Chuanxiang Chen,
Jiangsu University of Science and Technology, China
Qiang Ma,
Jilin University, China

***Correspondence:**
Fengna Xi
fengnaxi@zstu.edu.cn
Tingting Zhao
gxzhaott@163.com

[†]*These authors have contributed equally to this work*

Specialty section:
This article was submitted to Analytical Chemistry, a section of the journal Frontiers in Chemistry

Received: *09 February 2022*
Accepted: *11 March 2022*
Published: *06 April 2022*

Citation:
Wei X, Luo X, Xu S, Xi F and Zhao T (2022) A Flexible Electrochemiluminescence Sensor Equipped With Vertically Ordered Mesoporous Silica Nanochannel Film for Sensitive Detection of Clindamycin. Front. Chem. 10:872582. doi: 10.3389/fchem.2022.872582

INTRODUCTION

Antibiotics, drugs that can inhibit and kill bacteria, have been widely used in medical and healthcare, livestock and poultry breeding, agricultural production, and other industries. However, the excessive and irrational use of antibiotics is now widespread. Antibiotic residues can cause serious harm to human health including carcinogenic, teratogenic, and mutagenic effects (Wang et al., 2008; Wong et al., 2016; Hadi and Honarmand, 2017; Paul et al., 2017). In addition, prolonged exposure to such drugs can lead to severe antibiotic-resistant infections. For instance, clindamycin is a lincosamide antibiotic, which is widely used for the treatment of bacterial infections. The side effects of clindamycin include dry skin, nausea, vomiting, and constipation (Liu et al., 2010; Habib et al., 2011; Girondi et al., 2018; Mohammad Beigi et al., 2020; Liang et al., 2021). Researchers are also highly concerned about the bacterial resistance of clindamycin due to its overuse. Therefore, rapid, low-cost, and highly sensitive detection of antibiotics is crucial to standardize the use of antibiotics and avoid harm.

Until now, the developed technologies for the detection of antibiotics include capillary electrophoresis (CE), high-performance liquid chromatography (HLPC), ultrahigh-performance liquid chromatography–electrospray tandem mass spectrometry (UPLC-ESI-MS/MS), and electrochemical sensors (Liu et al., 2010; Habib et al., 2011; Hadi and Honarmand, 2017; Girondi et al., 2018; Mohammad Beigi et al., 2020; Liang et al., 2021). However, these methods usually suffer time-consuming detection, expensive instruments, complicated operation, or low sensitivity. Electrochemiluminescence (ECL), where chemiluminescence (CL) is triggered and controlled by electrochemical methods, elegantly combines the electrochemical and optical methods (Chen et al., 2011; Li et al., 2017; Zhai et al., 2017; Ma et al., 2019). Compared with photoluminescence with photo-excitation, ECL has advantages of near-zero background, high detection sensitivity, simplified optical instrument, and good temporal/spatial resolution (Wang et al., 2020; Zhang et al., 2020; Wang et al., 2021a; Huang et al., 2021; Ma et al., 2021; Yang et al., 2021; Zhu et al., 2021). Thus, ECL has emerged as a powerful tool in clinical diagnosis, drug analysis, immunoassay, environmental analysis, etc. In addition to constructing an ECL sensor on conventional electrochemical electrodes, development of a flexible, cost-efficient, and disposable ECL sensor with high sensitivity and its application in sensitive detection of antibiotic is of great significance.

The modification of the supporting electrode can significantly affect the performance of ECL sensors. As functional nanomaterials in molecular sieves, nanofluids, sensing and energy conversion, solid-state nanofilms (SSN) have attracted great attention owing to advantages of tunable nanopores, high specific surface area, and intelligent control of molecular transport (Zhou et al., 2019a; Zhou et al., 2019b; Zhou et al., 2020a; Ding et al., 2020; Li et al., 2020). Among the developed SSN, vertically ordered mesoporous silica nanochannel film (VMSF) exhibits high chemical and thermal stability, ordered and vertically aligned nanochannels (nanopores), uniform pore size distribution, high pore density, and ease of modification (Nasir et al., 2018; Jiokeng et al., 2019; Ullah et al., 2021; Walcarius, 2021). The ultrasmall (usually 2–3 nm) and high-density (up to 4~8 × 10^{12}/cm^2) nanochannel arrays make it possible to significantly improve the sensor performance as electrode modification materials (Mi et al., 2020; Li et al., 2021a; Asadpour et al., 2021; Li et al., 2021b; Xiao et al., 2021). On the one hand, a large number of silanol groups (Si-OH) with low pKa (~2) endow the VMSF with a negatively charged surface, which can accelerate the transfer of positively charged molecules to the electrode surface, leading to a significant enrichment effect. On the other hand, ultrasmall nanochannels of the VMSF can exclude large-sized substances, which can effectively suppress the interference of coexisting substances in complex samples, providing high antifouling ability and good signal stability (Yan et al., 2020a; Yan et al., 2020b; Lin et al., 2020; Liu et al., 2020; Ma et al., 2020; Yan et al., 2021a; Wang et al., 2021b; Yan et al., 2021b; Qiu et al., 2021; Yanyan et al., 2021). Therefore, the VMSF has great potential in the development of facile ECL sensors for direct and sensitive analysis of antibiotics in complex samples.

In this work, we demonstrate a flexible electrochemiluminescence sensor based on covering the electrode with vertically ordered mesoporous silica nanochannel films, which enable direct and sensitive detection of clindamycin in human serum. As shown in **Figure 1**, polyethylene terephthalate coated with indium tin oxide (PET-ITO), which is flexible, cheap, and suitable for the fabrication of portable, integrated, or disposable sensors, is used as the supporting electrode to grow VMSFs using the electrochemically assisted self-assembly (EASA) method. The significant enrichment toward the commonly used cationic ECL luminophores tris(2,2-bipyridyl) dichlororuthenium (II) [Ru $(bpy)_3^{2+}$] is proved resulting from the negatively charged VMSF nanochannels. As clindamycin can act as coreactant to promote the ECL of Ru $(bpy)_3^{2+}$, the developed VMSF/PET-ITO sensor can detect clindamycin with high sensitivity. In addition, high signal stability during the continuous blending process is revealed, showing the unique properties of flexible electrodes. Owing to the high antifouling characteristic of the VMSF, direct analysis of clindamycin in real biological sample, human serum, is also realized.

MATERIALS AND METHODS

Chemicals and Materials

Cetyltrimethylammonium bromide (CTAB), tetraethoxysilane (TEOS), clindamycin hydrochloride, tris(2, 2′-bipyridyl) ruthenium (II), acetone, Na_2HPO_4, NaH_2PO_4, potassium hydrogen phthalate (KHP), NH_4OH (25%), and H_2O_2 (30%) were purchased from Aladdin Chemistry Co., Ltd. (China). Polyethylene terephthalate coated with indium tin oxide (PET-ITO) with surface resistivity of 5.5–6.1 Ω/sq was purchased from Zhuhai Kaivo Optoelectronic Technology (China). Human blood serum was provided by the Center for Disease Control and Prevention (Hangzhou, China). Ultrapure water (18.2 MΩ cm) prepared using Mill-Q system (Millipore, United States) was used to prepare the aqueous solutions in this work.

Measurements and Instrumentations

Transmission electron microscopic (TEM) images were taken on a JEM-2100 transmission electron microscope (JEOL Ltd., Japan) using an operating voltage of 200 kV. Before measurement, the VMSF was scrapped from PET-ITO and dispersed in ethanol. Copper grid was applied to support the VMSF in TEM characterization. Scanning electron microscopic

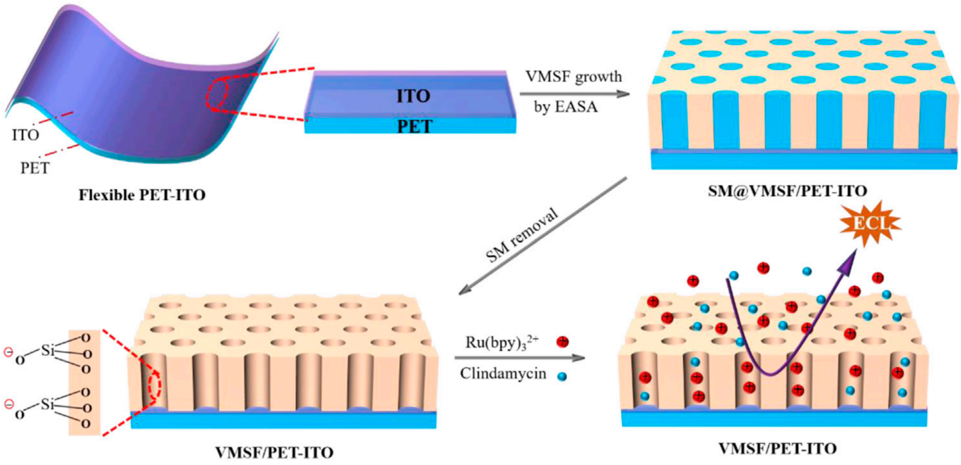

FIGURE 1 | Illustration for the preparation of VMSF/PET-ITO using the EASA method and the enrichment of Ru (bpy)$_3^{2+}$ on negatively charged VMSF for detection of clindamycin.

(SEM) image was taken under a field-emission scanning electron microscopy (S-4800, Hitachi, Japan). CHI 832C electrochemical workstation (CH Instrument, China) and MPI-E workstation (Remex Analysis, China) were used for ECL measurement. The detection cell was fixed in a dark detection chamber and had a volume of ~7 ml. Electrochemical measurements including cyclic voltammetry (CV) and electrochemical impedance spectroscopy (EIS) were carried out on an AutoLab electrochemical station (PGSTAT302N, Metrohm, Switzerland). Three electrode system was used in both electrochemical and ECL investigations. Briefly, bare or modified PET-ITO electrodes act as a working electrode. Ag/AgCl electrode (saturated with KCl solution) is applied as the reference electrode and Pt sheet electrode is the counter electrode.

Growth of Vertically Ordered Mesoporous Silica Nanochannel Film on Polyethylene Terephthalate Coated With Indium Tin Oxide

To improve the hydrophilicity of PET-ITO, the electrode was immersed in a mixed solution containing ultrapure water/hydrogen peroxide/ammonium hydroxide (5:1:1, v/v) under dark conditions for 1.5 h. Then, the electrode was washed thoroughly with ultrapure water. The VMSF was equipped on PET-ITO using the electrochemically assisted self-assembly method. Briefly, 20 ml $NaNO_3$ (0.1 mol/L, pH = 3), 20 ml ethanol, 2.833 g TEOS, and 1.585 g CTAB were mixed, and the obtained mixture was stirred for 2.5 h to obtain the precursor solution. For VMSF growth, a constant current (-0.35 mA/cm^2) was applied on PET-ITO for 10 s. Then the electrode was quickly rinsed with ultrapure water. After drying under N_2 stream, the electrode with surfactant micelles (SM) in the nanochannels (SM@VMSF/PET-ITO) was aged at 120°C for 10 h. Then, SM was removed by treating the SM@VMSF/PET-ITO in acetone and stirring for 30 min. Finally, the VMSF/PET-ITO with open nanochannels was obtained.

Electrochemiluminescence Determination of Clindamycin

Phosphate-buffered saline (PBS, 0.01 mol/L, pH 7.0) containing Ru (bpy)$_3^{2+}$ (10 µmol/L) was used as the supporting solution to detect clindamycin. When different concentrations of clindamycin were added, the ECL signal on the VMSF/PET-ITO electrode generated during CV scan (potential ranged from 0 to 1.4 V at a scan rate of 100 mV/s) was recorded. The standard addition method was used to evaluate the reliability of the developed ECL sensor in analysis of a real sample. Briefly, the human serum was diluted by a factor of 50 with PBS. Then, ECL detection was carried out after adding a certain amount of clindamycin.

RESULTS AND DISCUSSION

Facile Coupling Vertically Ordered Mesoporous Silica Nanochannel Film on Flexible Polyethylene Terephthalate Coated With Indium Tin Oxide Electrode and Charge Selectivity of Nanochannels

The flexible electrode is a research hotspot in recent years (Zhou et al., 2020b; İnce and Sezgintürk, 2021; Avelino et al., 2021). Compared with traditional hard electrodes, the flexible electrode has great potential in flexible or wearable sensors owing to the unique abilities of folding, bending, and multi-layer winding. Therefore, a simple and efficient modification of the flexible electrode to improve the detection sensitivity and antifouling ability in the complex sample is of great significance. **Figure 1** is

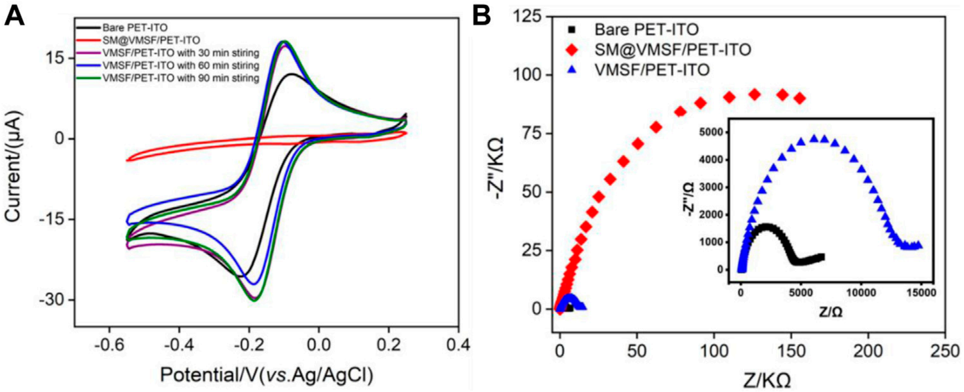

FIGURE 2 | (A) Cyclic voltammetry (CV) curves on bare PET-ITO, VMSF/PET-ITO, or SM@VMSF/PET-ITO electrodes in Ru $(NH_3)_6{}^{3+}$ solution (0.5 mmol/L in 0.05 mol/L KHP). The VMSF/PET-ITO electrode was prepared through the removal of SM using different soaking time with stirring in acetone as indicated. **(B)** EIS curves obtained on are PET-ITO, VMSF/PET-ITO, or SM@VMSF/PET-ITO in $[Fe(CN)_6]^{3-/4}$ (2.5 mmol/L in 1 mol/L KCl). Inset in **(B)** is the magnified plots of bare PET-ITO and VMSF/PET-ITO.

the schematic illustration for coupling VMSF on the flexible PET-ITO electrode using the electrochemically assisted self-assembly (EASA) method. Among the developed strategies to prepare the VMSF, the EASA method is fast and efficient which can achieve rapid growth of the VMSF within 5–30 s at room temperature. Briefly, the VMSF with a pore diameter of 2–3 nm is formed by using cetyltrimethylammonium bromide (CTAB) micelles (SM) as the template. The mechanism lies in the controlled condensation kinetics of siloxane around the SM template under the *in situ* pH gradient resulting from the reduction of protons and water molecules when a negative voltage is applied to the electrode. Researchers have systematically investigated the effects of experimental conditions on the film formation and properties of VMSF (Herzog et al., 2013). It has been proven that the electrode surface cannot be completely covered by the VMSF, if a short electrodeposition time and a small current density are employed. On the contrary, a long electrodeposition time and a large current density lead to a thick film, which in turn weakens the permeability of the film. If the concentration of silane precursor is too small, the electrodes will not be fully covered by the film. However, a higher precursor concentration will result in a film that is too thick and prone to cracking during the aging stage. After VMSF growth, the resulting electrode contains surfactant SM (SM@VMSF/PET-ITO), which blocks the nanochannels. The efficient removal of SM in the VMSF is the key to obtain open nanochannels. The most common method to remove SM is to soak the SM@VMSF/PET-ITO electrode in HCl-ethanol solution. However, PET will get damaged in HCl medium because of its hydrolysis reaction in strong acid. Thus, acetone is applied to remove SM in this work. **Figure 2A** shows the CV curves of Ru $(NH_3)^{3+}$ obtained on different electrodes including bare PET-ITO, SM@VMSF/PET-ITO and VMSF/PET-ITO, respectively. To investigate the effect of soaking time in acetone on the removal of SM, VMSF/PET-ITO electrodes prepared using different soaking time under stirring are studied. As shown, no Faraday current is observed on the SM@VMSF/PET-ITO electrode. This is because the micelles block the nanochannels so that the redox probes cannot reach the electrode surface. The result also proves that the VMSF is a complete film without cracks. In contrast, the VMSF/PET-ITO electrode without SM has significant current responses. In addition, the signal of Ru $(NH_3)_6{}^{3+}$ on the VMSF/PET-ITO electrode remains unchanged after the VMSF/PET-ITO electrode is soaked in acetone for 30 min, indicating efficient removal of SM. Thus, 30 min of soaking in acetone is chosen for further investigation.

Compared with bare PET-ITO, the VMSF/PET-ITO electrode shows enhanced signal for Ru $(NH_3)^{3+}$, proving remarkable enrichment effect toward positively charges species. The deprotonation of silanols (pKa ~2) on the surface of VMSF nanochannels leads to negatively charged surface, which attracts the positively charged Ru $(NH_3)^{3+}$ through electrostatic interactions. The successful growth of the VMSF and the charge selectivity of nanochannels are also confirmed by electrochemical impedance spectroscopy (EIS) obtained in the anionic $[Fe(CN)_6]^{3-/4}$ probe (**Figure 2B**). As shown, bare PET-ITO, SM@VMSF/PET-ITO, and VMSF/PET-ITO exhibit significantly different charge transfer resistance (*Rct*), which is related to the diameter of the curve semicircle in the high-frequency region. When SM exist in nanochannels, the SM@VMSF/PET-ITO electrode exhibits the largest *Rct* owing to the blocking of nanochannels. When SM is removed, the *Rct* for VMSF/PET-ITO electrode remarkably decreases. However, the *Rct* for the VMSF/PET-ITO electrode is still larger than that of bare PET-ITO, indicating the electrostatic repulsion of negatively charged nanochannels to negatively charged probes.

Morphology of Vertically Ordered Mesoporous Silica Nanochannel Film Nanochannels

The structure and morphology of the VMSF are characterized by TEM and SEM. **Figure 3A** is the top-view TEM images of

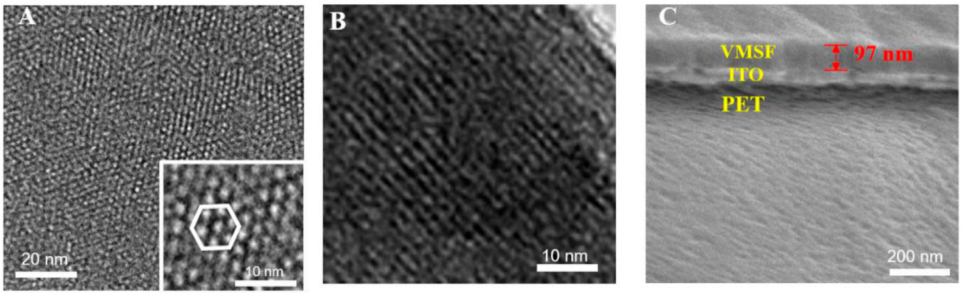

FIGURE 3 | (A) Top-view and **(B)** cross-sectional TEM images of VMSF. Inset in **(A)** is the image at high magnification. **(C)** Cross-sectional SEM images of VMSF/PET-ITO electrode.

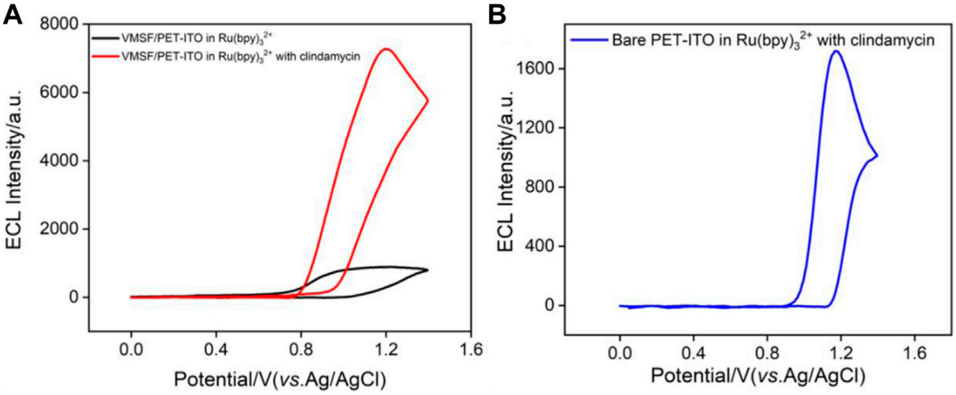

FIGURE 4 | (A) ECL signals obtained on VMSF/PET-ITO electrode in PBS containing Ru (bpy)$_3^{2+}$ (10 μmol/L) before and after adding clindamycin (30 μmol/L). **(B)** ECL signal obtained on bare PET-ITO in the mixture of Ru (bpy)$_3^{2+}$ (10 μmol/L) and clindamycin (30 μmol/L).

the VMSF at different magnification. As shown, the VMSF has a uniformly distributed nanopore structure without cracks or defects in the observed range. The highly ordered nanopores have a diameter of 2–3 nm. The cross-sectional TEM image of the VMSF in **Figure 3A** reveals nanochannels parallel to each other. The cross-sectional SEM image of the VMSF/PET-ITO electrode shows a three-layered structure, which corresponds to PET substrate, ITO layer, and VMSF layer from bottom to top. In addition, VMSF has a flat structure with a thickness of ~97 nm.

Enhanced Electrochemiluminescence by Clindamycin and Vertically Ordered Mesoporous Silica Nanochannel Film Nanochannels

Electrochemiluminescence has the unique advantage of simple instruments, low background, and easy operation. Although many ECL luminophores such as acridan ester, ruthenium chelate, luminol, and nanoemitters have been developed, tris(2,2′-bipyridyl) ruthenium (II) [Ru (bpy)$_3^{2+}$] is still widely used due to high stability, solubility, and reversible electrochemical behavior (Zhou et al., 2019a; Zhou et al., 2020a; Ding et al., 2020; Li et al., 2020). As shown in **Figure 4A**, when clindamycin is added to Ru (bpy)$_3^{2+}$, the ECL signal significantly enhances, indicating that clindamycin can promote the ECL emission. Owing to the quaternary amine structure in the clindamycin molecule, the possible ECL mechanism might be similar to that of Ru (bpy)$_3^{2+}$/tri-n-propylamine (TPrA) system. The ECL reaction pathway can be elucidated in the following equations (**Eqs 1–5**). Briefly, Ru (bpy)$_3^{2+}$ can be oxidized to Ru (bpy)$_3^{3+}$ when an oxidation potential of 1.4 V is applied to the electrode. At the same time, clindamycin is oxidized to radical cation (clindamycin$^{\cdot+}$) followed with deprotonation to form the reduced product 1(clindamycin$^{\cdot}$), which undergoes redox reaction with Ru (bpy)$_3^{3+}$ to generate the excited state [Ru (bpy)$_3^{2+*}$]. Then, ECL is observed when the excited state returns to the ground state.

$$\mathrm{Ru(bpy)_3^{2+}} - e^- \rightarrow \mathrm{Ru(bpy)_3^{3+}} \tag{1}$$

$$\text{Clindamycin} - e^- \rightarrow \text{Clindamycin}^{\bullet+} \tag{2}$$

$$\text{Clindamycin}^{\bullet+} \rightarrow \text{Clindamycin}^{\bullet} + H^+ \tag{3}$$

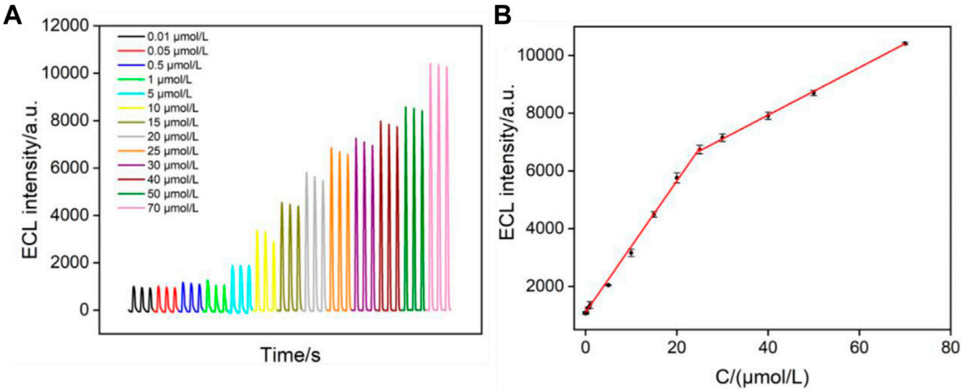

FIGURE 5 | (A) ECL intensity of Ru (bpy)$_3^{2+}$ in the presence of different concentrations of clindamycin. **(B)** Linear dependence between the ECL intensity and the concentration of clindamycin.

$$\mathrm{Ru(bpy)_3^{3+}} + \mathrm{Clindamycin}^{\bullet} \rightarrow \mathrm{Ru(bpy)_3^{2+*}} + \text{Clindamycin fragment} \quad (4)$$

$$\mathrm{Ru(bpy)_3^{2+*}} \rightarrow \mathrm{Ru(bpy)_3^{2+}} + h\nu \quad (5)$$

It is worth noting that the ECL signal on the VMSF/PET-ITO electrode is about 7 times of that on the bare PET-ITO electrode (**Figure 4B**), indicating that the nanochannels of the VMSF have significant signal amplification effect. This was attributed to the enrichment of positively charged ECL probes by VMSF nanochannels.

Optimized Conditions for Electrochemiluminescence Detection of Clindamycin

To achieve the best detection performance, the concentration and pH of the supporting electrolyte are optimized. As shown in **Supplementary Figure S1A** (in supporting information, SI), the ECL intensity gradually decreases when the ionic strength of the supporting buffer increases. This is because the thickness of the electric double layer of VMSF nanochannels is inversely proportional to the ionic strength. The increase in thickness of the electric double layer of the nanochannels enhances the electrostatic adsorption of Ru (bpy)$_3^{2+}$, resulting in more ECL probes on the electrode surface. As can be seen from **Supplementary Figure S1B** (SI), the ECL intensity on the electrode gradually increases as the pH of the buffer increases from 4 to 8. This might be ascribed to the enhanced deprotonation of the radical cation of clindamycin (clindamycin$^{\cdot+}$) to form strong reducing agent (clindamycin, **Eq. 3**), which facilitates the redox reaction with Ru (bpy)$_3^{3+}$ and the formation of the excited state (Ru (bpy)$_3^{2+*}$) (Leland and Powell, 1990). The phenomenon further confirms the coreactant mechanism for the enhanced ECL signal. The decrease of ECL signal at pH 9 might result from the instability of the VMSF at high alkaline medium. Considering the stability of the VMSF and the neutral environment of common physiological samples, pH 7 is chosen for further experiments.

Sensitive Electrochemiluminescence Detection of Clindamycin

Under the optimized conditions, ECL detection of clindamycin is investigated. **Figure 5A** illustrates the ECL intensity on the VMSF/PET-ITO electrode in the presence of different concentrations of clindamycin. The ECL intensity (I_{ECL}) is linearly correlated to the concentration of clindamycin (C) in the range from 10 nmol/L to 25 μmol/L ($I_{ECL} = 227.2C + 1{,}106$, $R^2 = 0.9941$) and from 25 μmol/L to 70 μmol/L ($I_{ECL} = 82.45C + 4{,}635$, $R^2 = 0.9995$) (**Figure 5B**). The limit of detection (LOD) is based on a signal-to-noise ratio of 3 ($S/N = 3$) is 4 nmol/L. Owing to the enrichment effect of VMSF nanochannels toward Ru (bpy)$_3^{2+}$, the LOD from the VMSF/PET-ITO electrode is lower than that obtained using square wave voltammetry (SWV) detection on a glassy carbon electrode modified with graphene oxide and gold nanoparticles within a film of cross-linked chitosan with epichlorohydrin (AuNP-GO-CTS-ECH/GCE electrode) or CV detection on edge-plane pyrolytic graphite electrode (EPPG) (Wong et al., 2016; Hadi and Honarmand, 2017). The LOD is also lower than that obtained using capillary electrophoresis (CE) or CE-ECL (Wang et al., 2008; Paul et al., 2017). Thus, the constructed ECL sensor has the advantages of simple preparation and high detection performance.

High Stability of Vertically Ordered Mesoporous Silica Nanochannel Film/ Polyethylene Terephthalate Coated With Indium Tin Oxide Electrode Under Continuous Bending

The signal stability under large deformation is a key factor in evaluating the performance of flexible electrodes. We compared the signals on the VMSF/PET-ITO electrode

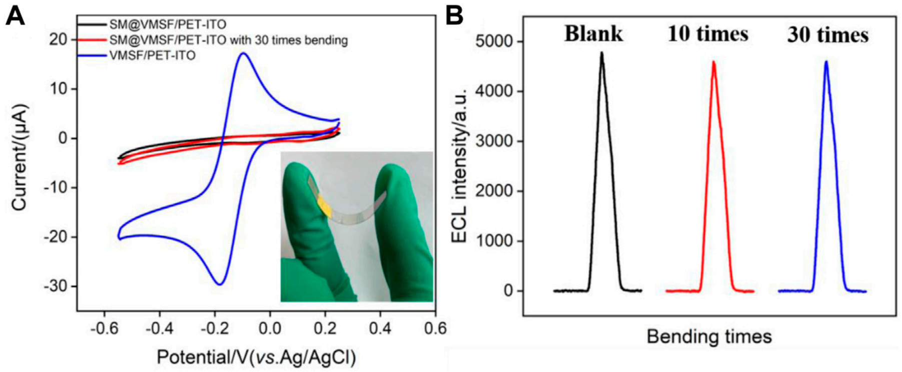

FIGURE 6 | (A) CV curves of SM@VMSF/PET-ITO and VMSF/PET-ITO electrodes in Ru $(NH_3)_6^{3+}$ solution (0.5 mmol/L in 0.05 mol/L KHP). Inset is the image of the electrode in case of bending. **(B)** ECL signals obtained on original or blended VMSF/PET-ITO in the mixture containing Ru $(bpy)_3^{2+}$ (10 μmol/L) and clindamycin (15 μmol/L) in PBS solution.

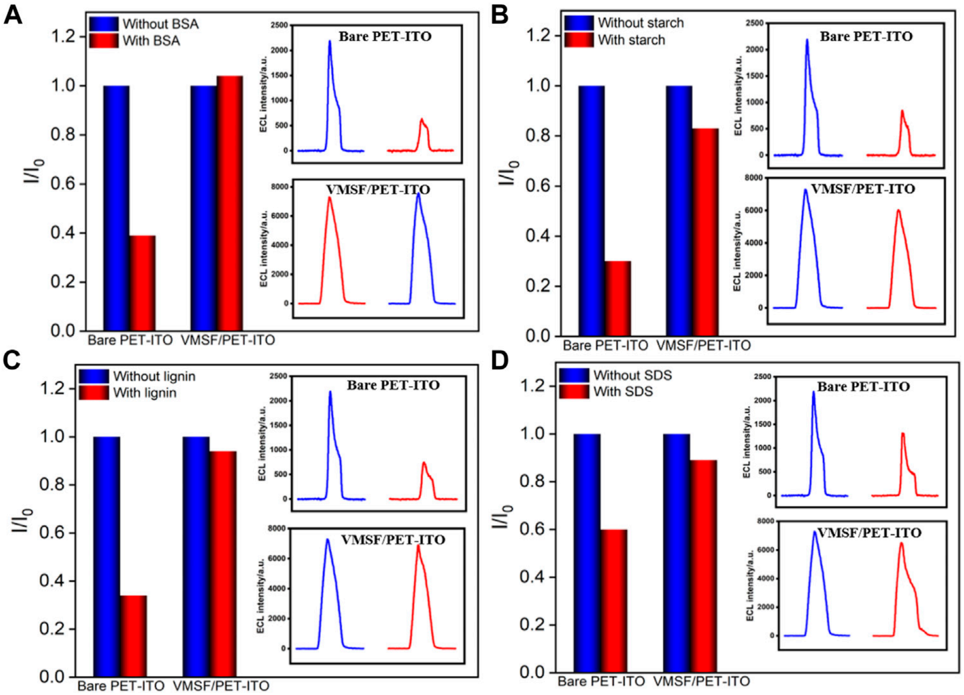

FIGURE 7 | Normalized ECL intensity ratio on bare PET-ITO or VMSF/PET-ITO toward clindamycin (30 μM). I and I_0 represent the ECL intensity obtained in the absence and present of 50 μg/ml **(A)** BSA, **(B)** starch, **(C)** lignin, or **(D)** SDS in PBS (0.01 mol/L, pH = 7). The insets are the corresponding ECL intensity obtained on bare PET-ITO and VMSF/PET-ITO in the absence or presence of fouling species.

before and after continuous bending. The micelle-containing electrode, SM@VMSF/PET-ITO electrode, is first investigated with continuous bending for 30 times. As shown in **Figure 6A**, CV curves of Ru $(NH_3)_6^{3+}$ on the original or bended electrode are quite similar. There was no significant Faraday signal before and after folding of the electrode. Thus, no crack of the VMSF layer appears during the continuous bending process, proving high stability of the flexible electrode. When the micelles are removed from the electrode that was folded 30 times, the opening of the nanochannels leads to significant electrochemical signals of the redox probe. In addition, the stability of the ECL signal on the electrode during the continuous bending is also investigated. As shown in **Figure 6B**, the electrode before and after bending for 10 or 30 times exhibits unchanged ECL intensity, indicating high signal stability. This phenomenon is attributed to the nanoscale thickness of the VMSF and the high coupling stability with the electrode substrate.

Antifouling of Vertically Ordered Mesoporous Silica Nanochannel Film/Polyethylene Terephthalate Coated With Indium Tin Oxide Electrode and Real Sample Analysis

Biological, food, and environmental samples usually have complex matrix containing proteins, starch, surfactants, etc., which often contaminates the electrode surface and reduces signal accuracy. Thus, improving the antifouling ability of the electrode is of great significance for direct electroanalysis of complex samples. To evaluate the antifouling ability of the developed VMSF/PET-ITO sensor, bovine serum albumin (BSA), starch, lignin and sodium dodecyl sulfonate (SDS) are applied as the possible interfering substances. The ECL of Ru $(bpy)_3^{2+}$ with clindamycin in the absence or presence of one of these substances on both VMSF/PET-ITO and PET-ITO electrodes are given in **Figure 7**. As shown, the ECL signal significantly reduced on PET-ITO when one of the aforementioned substances is added, indicating remarkable fouling of the electrode. On the contrary, no significant change of ECL signal is observed on the VMSF/PET-ITO electrode, indicating high antifouling performance resulting from the remarkable molecular sieving ability of the VMSF.

Considering the antifouling ability of the VMSF, the developed VMSF/PET-ITO sensor is applied to detect clindamycin in human serum samples (diluted by a factor by 50) using the standard addition method (**Supplementary Table S1** in SI). The recovery rate of other three artificial added clindamycin concentration is between 97.6 and 104.0% with low relative standard deviation (RSD, ≤4.7%), indicating good reliability in the direct measurement of clindamycin in real complex samples.

CONCLUSION

In summary, we demonstrate a cost-effective and disposable electrochemiluminescence sensor based on the flexible electrode covered with a vertically ordered mesoporous silica nanochannel film for sensitive detection of clindamycin. The polyethylene terephthalate coated with indium tin oxide (PET-ITO) is applied as the flexible electrode to easily grow the VMSF using the electrochemically assisted self-assembly (EASA) method. The negatively charged VMSF nanochannels exhibit significant enrichment toward the commonly used cationic ECL luminophores, tris(2,2-bipyridyl) dichlororuthenium (II) [Ru $(bpy)_3^{2+}$]. Using the enhanced ECL of Ru $(bpy)_3^{2+}$ by clindamycin, the developed VMSF/PET-ITO sensor can detect clindamycin with high sensitivity. Owing to the nanoscale thickness of the VMSF and the high coupling stability with the electrode substrate, the developed VMSF/PET-ITO sensor exhibits high signal stability during the continuous bending process. Considering high antifouling characteristic of the VMSF, direct analysis of clindamycin in human serum is realized. Because the PET-ITO electrode is easy to be miniaturized or patterned, the proposed strategy of modifying flexible electrode based on the nanochannel is expected to open up a new research field in flexible, wearable, or miniaturized sensors.

DATA AVAILABILITY STATEMENT

The original contributions presented in the study are included in the article/**Supplementary Material**; further inquiries can be directed to the corresponding author.

AUTHOR CONTRIBUTIONS

XW, XL, and SX curated the data. FX supervised and wrote and edited the review. TZ wrote and edited the review.

FUNDING

The authors gratefully acknowledge the financial support from the National Natural Science Foundation of China (No. 81860512), and the Zhejiang Provincial Natural Science Foundation of China (LY20B050007).

SUPPLEMENTARY MATERIAL

The Supplementary Material for this article can be found online at: https://www.frontiersin.org/articles/10.3389/fchem.2022.872582/full#supplementary-material

REFERENCES

Asadpour, F., Mazloum-Ardakani, M., Hoseynidokht, F., and Moshtaghioun, S. M. (2021). *In Situ* monitoring of Gating Approach on Mesoporous Silica Nanoparticles Thin-Film Generated by the EASA Method for Electrochemical Detection of Insulin. *Biosens. Bioelectron.* 180, 113124. doi:10.1016/j.bios.2021.113124

Avelino, K. Y. P. S., Oliveira, L. S., Lucena-Silva, N., Andrade, C. A. S., and Oliveira, M. D. L. (2021). Flexible Sensor Based on Conducting Polymer and Gold Nanoparticles for Electrochemical Screening of HPV Families in Cervical Specimens. *Talanta* 226, 122118. doi:10.1016/j.talanta.2021.122118

Chen, X.-m., Su, B.-y., Song, X.-h., Chen, Q.-a., Chen, X., and Wang, X.-r. (2011). Recent Advances in Electrochemiluminescent Enzyme Biosensors. *Trac Trends Anal. Chem.* 30, 665–676. doi:10.1016/j.trac.2010.12.004

Ding, J., Li, X., Zhou, L., Yang, R., Yan, F., and Su, B. (2020). Electrodeposition of Nickel Nanostructures Using Silica Nanochannels as Confinement for Low-Fouling Enzyme-free Glucose Detection. *J. Mater. Chem. B* 8, 3616–3622. doi:10.1039/c9tb02472g

Girondi, N. G., Barreto., F., Pigatto, M. C., and Dalla Costa, T. (2018). Sensitive Analytical Method to Quantify Clindamycin in Plasma and Microdialysate Samples: Application in a Preclinical Pharmacokinetic Study. *J. Pharm. Biomed. Anal.* 153, 57–62. doi:10.1016/j.jpba.2018.02.005

Habib, I. H. I., Rizk, M. S., and El-Aryan, T. R. (2011). Determination of Clindamycin in Dosage Forms and Biological Samples by Adsorption Stripping Voltammetry with Carbon Paste Electrode. *Pharm. Chem. J.* 44, 705–710. doi:10.1007/s11094-011-0548-4

Hadi, M., and Honarmand, E. (2017). Application of Anodized Edge-Plane Pyrolytic Graphite Electrode for Analysis of Clindamycin in Pharmaceutical Formulations and Human Urine Samples. *Russ. J. Electrochem.* 53, 380–390. doi:10.1134/s1023193517040061

Herzog, G., Sibottier, E., Etienne, M., and Walcarius, A. (2013). Electrochemically Assisted Self-Assembly of Ordered and Functionalized Mesoporous Silica Films: Impact of the Electrode Geometry and Size on Film Formation and Properties. *Faraday Discuss.* 164, 259–273. doi:10.1039/c3fd00021d

Huang, Z., Li, Z., Chen, Y., Xu, L., Xie, Q., Deng, H., et al. (2021). Regulating Valence States of Gold Nanocluster as a New Strategy for the Ultrasensitive Electrochemiluminescence Detection of Kanamycin. *Anal. Chem.* 93, 4635–4640. doi:10.1021/acs.analchem.1c00063

İnce, B., and Sezgintürk, M. K. (2021). A High Sensitive and Cost-Effective Disposable Biosensor for Adiponectin Determination in Real Human Serum Samples. *Sens. Actuators, B* 328, 129051. doi:10.1016/j.snb.2020.129051

Jiokeng, S. L. Z., Tonle, I. K., and Walcarius, A. (2019). Amino-attapulgite/mesoporous Silica Composite Films Generated by Electro-Assisted Self-Assembly for the Voltammetric Determination of Diclofenac. *Sensors Actuators B: Chem.* 287, 296–305. doi:10.1016/j.snb.2019.02.038

Leland, J. K., and Powell, M. J. (1990). Electrogenerated Chemiluminescence: An Oxidative-Reduction Type ECL Reaction Sequence Using Tripropyl Amine. *J. Electrochem. Soc.* 137, 3127–3131. doi:10.1149/1.2086171

Li, G., Belwal, T., Luo, Z., Li, Y., Li, L., Xu, Y., et al. (2021). Direct Detection of Pb2+ and Cd2+ in Juice and Beverage Samples Using PDMS Modified Nanochannels Electrochemical Sensors. *Food Chem.* 356, 129632. doi:10.1016/j.foodchem.2021.129632

Li, L., Chen, Y., and Zhu, J.-J. (2017). Recent Advances in Electrochemiluminescence Analysis. *Anal. Chem.* 89, 358–371. doi:10.1021/acs.analchem.6b04675

Li, X., Zhou, L., Ding, J., Sun, L., and Su, B. (2020). Platinized Silica Nanoporous Membrane Electrodes for Low-Fouling Hydrogen Peroxide Detection. *ChemElectroChem* 7, 2081–2086. doi:10.1002/celc.202000321

Li, Z., He, Y., Klausen, L. H., Yan, N., Liu, J., Chen, F., et al. (2021). Growing Vertical Aligned Mesoporous Silica Thin Film on Nanoporous Substrate for Enhanced Degradation, Drug Delivery and Bioactivity. *Bioactive Mater.* 6, 1452–1463. doi:10.1016/j.bioactmat.2020.10.026

Liang, X., Gou, Z., Wang, X., Wang, Y., Yue, J., Li, N., et al. (2021). Simultaneous Quantification of Cefuroxime and Clindamycin in Human Lumbar Anulus Fibrosus, Nucleus Pulposus and Serum via UPLC-MS/MS. *J. Chromatogr. B* 1165, 122522. doi:10.1016/j.jchromb.2021.122522

Lin, J., Li, K., Wang, M., Chen, X., Liu, J., and Tang, H. (2020). Reagentless and Sensitive Determination of Carcinoembryonic Antigen Based on a Stable Prussian Blue Modified Electrode. *RSC Adv.* 10, 38316–38322. doi:10.1039/d0ra06751b

Liu, X., Li, H., Zhou, H., Liu, J., Li, L., Liu, J., et al. (2020). Direct Electrochemical Detection of 4-aminophenol in Pharmaceuticals Using ITO Electrodes Modified with Vertically-Ordered Mesoporous Silica-Nanochannel Films. *J. Electroanalytical Chem.* 878, 114568. doi:10.1016/j.jelechem.2020.114568

Liu, Y.-M., Shi, Y.-M., Liu, Z.-L., and Peng, L.-F. (2010). Sensitive Determination of Tilmicosin, Erythromycin Ethylsuccinate and Clindamycin by CE with Electrochemiluminescence Detection Using Azithromycin as Internal Standard and its Applications. *J. Sep. Sci.* 33, 1305–1311. doi:10.1002/jssc.200900843

Ma, C., Cao, Y., Gou, X., and Zhu, J.-J. (2019). Recent Progress in Electrochemiluminescence Sensing and Imaging. *Anal. Chem.* 92, 431–454. doi:10.1021/acs.analchem.9b04947

Ma, C., Wu, S., Zhou, Y., Wei, H. F., Zhang, J., Chen, Z., et al. (2021). Bio-Coreactant-Enhanced Electrochemiluminescence Microscopy of Intracellular Structure and Transport. *Angew. Chem. Int. Ed.* 60, 4907–4914. doi:10.1002/anie.202012171

Ma, X., Liao, W., Zhou, H., Tong, Y., Yan, F., Tang, H., et al. (2020). Highly Sensitive Detection of Rutin in Pharmaceuticals and Human Serum Using ITO Electrodes Modified with Vertically-Ordered Mesoporous Silica-Graphene Nanocomposite Films. *J. Mater. Chem. B* 8, 10630–10636. doi:10.1039/d0tb01996h

Mi, X., Li, H., Tan, R., and Tu, Y. (2020). Dual-modular Aptasensor for Detection of Cardiac Troponin I Based on Mesoporous Silica Films by Electrochemiluminescence/electrochemical Impedance Spectroscopy. *Anal. Chem.* 92, 14640–14647. doi:10.1021/acs.analchem.0c03130

Mohammad Beigi, S., Mesgari, F., and Hosseini, M. (2020). Detection of Clindamycin in Pharmaceutical Products Using an Electrochemiluminescence Electrode Based on a Composite of Ru(bpy)$_2$$^{3+}$, Eu$_2O_3$ Nanoparticle and Chitosan. *Anal. Bioanal. Electrochem.* 12, 733–746.

Nasir, T., Herzog, G., Hébrant, M., Despas, C., Liu, L., and Walcarius, A. (2018). Mesoporous Silica Thin Films for Improved Electrochemical Detection of Paraquat. *ACS Sens.* 3, 484–493. doi:10.1021/acssensors.7b00920

Paul, P., Duchateau, T., Sänger-van de Griend, C., Adams, E., and Van Schepdael, A. (2017). Capillary Electrophoresis with Capacitively Coupled Contactless Conductivity Detection Method Development and Validation for the Determination of Azithromycin, Clarithromycin, and Clindamycin. *J. Sep. Sci.* 40, 3535–3544. doi:10.1002/jssc.201700560

Qiu, G., Han, Y., Zhu, X., Gong, J., Luo, T., Zhao, C., et al. (2021). Sensitive Detection of Sulfide Ion Based on Fluorescent Ionic Liquid–Graphene Quantum Dots Nanocomposite. *Front. Chem.* 9, 316. doi:10.3389/fchem.2021.658045

Ullah, W., Herzog, G., Vilà, N., and Walcarius, A. (2021). Electrografting and Electropolymerization of Nanoarrays of PANI Filaments through Silica Mesochannels. *Electrochemistry Commun.* 122, 106896. doi:10.1016/j.elecom.2020.106896

Walcarius, A. (2021). Electroinduced Surfactant Self-Assembly Driven to Vertical Growth of Oriented Mesoporous Films. *Acc. Chem. Res.* 54, 3563–3575. doi:10.1021/acs.accounts.1c00233

Wang, F., Liu, Y., Fu, C., Li, N., Du, M., Zhang, L., et al. (2021). Paper-based Bipolar Electrode Electrochemiluminescence Platform for Detection of Multiple miRNAs. *Anal. Chem.* 93, 1702–1708. doi:10.1021/acs.analchem.0c04307

Wang, J., Peng, Z., Yang, J., Wang, X., and Yang, N. (2008). Detection of Clindamycin by Capillary Electrophoresis with an End-Column Electrochemiluminescence of tris(2,2′-bypyridine)Ruthenium(II). *Talanta* 75, 817–823. doi:10.1016/j.talanta.2007.12.019

Wang, M., Lin, J., Gong, J., Ma, M., Tang, H., Liu, J., et al. (2021). Rapid and Sensitive Determination of Doxorubicin in Human Whole Blood by Vertically-Ordered Mesoporous Silica Film Modified Electrochemically Pretreated Glassy Carbon Electrodes. *RSC Adv.* 11, 9021–9028. doi:10.1039/d0ra10000e

Wang, Y., Zhao, G., Chi, H., Yang, S., Niu, Q., Wu, D., et al. (2020). Self-luminescent Lanthanide Metal-Organic Frameworks as Signal Probes in Electrochemiluminescence Immunoassay. *J. Am. Chem. Soc.* 143, 504–512. doi:10.1021/jacs.0c12449

Wong, A., Razzino, C. A., Silva, T. A., and Fatibello-Filho, O. (2016). Square-wave Voltammetric Determination of Clindamycin Using a Glassy Carbon Electrode Modified with Graphene Oxide and Gold Nanoparticles within a Crosslinked Chitosan Film. *Sensors Actuators B: Chem.* 231, 183–193. doi:10.1016/j.snb.2016.03.014

Xiao, Y., Chen, S., Zhang, S., Wang, G., Yi, H., Xin, G.-Z., et al. (2021). Mesoporous Silica-Mediated Controllable Electrochemiluminescence Quenching for Immunosensor with Simplicity, Sensitivity and Tunable Detection Range. *Talanta* 231, 122399. doi:10.1016/j.talanta.2021.122399

Yan, F., Ma, X., Jin, Q., Tong, Y., Tang, H., Lin, X., et al. (2020). Phenylboronic Acid-Functionalized Vertically Ordered Mesoporous Silica Films for Selective Electrochemical Determination of Fluoride Ion in Tap Water. *Mikrochim Acta* 187, 470–478. doi:10.1007/s00604-020-04422-4

Yan, F., Chen, J., Jin, Q., Zhou, H., Sailjoi, A., Liu, J., et al. (2020). Fast One-step Fabrication of a Vertically-Ordered Mesoporous Silica-Nanochannel Film on Graphene for Direct and Sensitive Detection of Doxorubicin in Human Whole Blood. *J. Mater. Chem. C* 8, 7113–7119. doi:10.1039/d0tc00744g

Yan, F., Luo, T., Jin, Q., Zhou, H., Sailjoi, A., Dong, G., et al. (2021). Tailoring Molecular Permeability of Vertically-Ordered Mesoporous Silica-Nanochannel Films on Graphene for Selectively Enhanced Determination of Dihydroxybenzene Isomers in Environmental Water Samples. *J. Hazard. Mater.* 410, 124636. doi:10.1016/j.jhazmat.2020.124636

Yan, F., Wang, M., Jin, Q., Zhou, H., Xie, L., Tang, H., et al. (2021). Vertically-ordered Mesoporous Silica Films on Graphene for Anti-fouling

Electrochemical Detection of Tert-Butylhydroquinone in Cosmetics and Edible Oils. *J. Electroanalytical Chem.* 881, 114969. doi:10.1016/j.jelechem.2020.114969

Yang, X.-y., Wang, Y.-z., Wang, L.-l., Zhu, J. W., Zhao, J., Zong, H.-l., et al. (2021). Bipolar Electrode Ratiometric Electrochemiluminescence Biosensing Analysis Based on boron Nitride Quantum Dots and Biological Release System. *Biosens. Bioelectron.* 191, 113393. doi:10.1016/j.bios.2021.113393

Yanyan, Z., Lin, J., Xie, L., Tang, H., Wang, K., and Liu, J. (2021). One-step Preparation of Nitrogen-Doped Graphene Quantum Dots with Anodic Electrochemiluminescence for Sensitive Detection of Hydrogen Peroxide and Glucose. *Front. Chem.* 9, 394. doi:10.3389/fchem.2021.688358

Zhai, Q., Li, J., and Wang, E. (2017). Recent Advances Based on Nanomaterials as Electrochemiluminescence Probes for the Fabrication of Sensors. *ChemElectroChem* 4, 1639–1650. doi:10.1002/celc.201600898

Zhang, Y., Xu, J., Zhou, S., Zhu, L., Lv, X., Zhang, J., et al. (2020). DNAzyme-Triggered Visual and Ratiometric Electrochemiluminescence Dual-Readout Assay for Pb(II) Based on an Assembled Paper Device. *Anal. Chem.* 92, 3874–3881. doi:10.1021/acs.analchem.9b05343

Zhou, L., Cheng, C., Li, X., Ding, J., Liu, Q., and Su, B. (2020). Nanochannel Templated Iridium Oxide Nanostructures for Wide-Range pH Sensing from Solutions to Human Skin Surface. *Anal. Chem.* 92, 3844–3851. doi:10.1021/acs.analchem.9b05289

Zhou, L., Hou, H., Wei, H., Yao, L., Sun, L., Yu, P., et al. (2019). *In Vivo* monitoring of Oxygen in Rat Brain by Carbon Fiber Microelectrode Modified with Antifouling Nanoporous Membrane. *Anal. Chem.* 91, 3645–3651. doi:10.1021/acs.analchem.8b05658

Zhou, P., Yao, L., Chen, K., and Su, B. (2020). Silica Nanochannel Membranes for Electrochemical Analysis and Molecular Sieving: a Comprehensive Review. *Crit. Rev. Anal. Chem.* 50, 424–444. doi:10.1080/10408347.2019.1642735

Zhou, P., Yao, L., and Su, B. (2019). Fabrication, Characterization, and Analytical Application of Silica Nanopore Array-Modified Platinum Electrode. *ACS Appl. Mater. Inter.* 12, 4143–4149. doi:10.1021/acsami.9b20165

Zhu, L., Lv, X., Li, Z., Shi, H., Zhang, Y., Zhang, L., et al. (2021). All-sealed Paper-Based Electrochemiluminescence Platform for On-Site Determination of lead Ions. *Biosens. Bioelectron.* 192, 113524. doi:10.1016/j.bios.2021.113524

Conflict of Interest: The authors declare that the research was conducted in the absence of any commercial or financial relationships that could be construed as a potential conflict of interest.

frontiers | Frontiers in Chemistry

ORIGINAL RESEARCH
published: 08 April 2022
doi: 10.3389/fchem.2022.871013

Colorimetric and Fluorescence Dual-Mode Biosensors Based on Peroxidase-Like Activity of the Co_3O_4 Nanosheets

Jingying Tan[1†], Weifu Geng[2†], Junde Li[3], Zhen Wang[1], Shaohao Zhu[1] and Xiuzhong Wang[1]*

[1]College of Chemistry and Pharmaceutical Sciences, Qingdao Agricultural University, Qingdao, China, [2]College of Plant Health and Medicine, Qingdao Agricultural University, Qingdao, China, [3]Hospital of Qingdao Agricultural University, Qingdao Agricultural University, Qingdao, China

The mimic enzyme has become a research hotspot in recent years because of its advantages of high stability, convenient preparation, and low price. In this article, Co_3O_4 nanosheets synthesized by a simple hydrothermal method possess the characteristics of a peroxidase-like activity. The results demonstrated that 3,3′,5,5′-Tetramethylbenzidine (TMB) could be oxidized by H_2O_2 to produce a typical blue product (oxTMB) which has a strong absorption at 650 nm wavelength with the help of the Co_3O_4 nanosheets. Thus, a simple and sensitive colorimetric detection method for H_2O_2 was established with a good linear relationship (2–200 μM) and a low limit of detection (0.4 μM). Meanwhile, the colorimetric product can effectively quench the fluorescence emitted by $Ru(bpy)_3^{2+}$. Therefore, a colorimetric and fluorescence dual detection mode photochemical sensor for H_2O_2 detection is constructed based on the principle of the inner filter effect (IFE) between the colorimetric product (oxTMB) and $Ru(bpy)_3^{2+}$. It can effectively avoid the false positive problem of a single detection mode. In the presence of glucose oxidase, glucose can be catalyzed to produce gluconic acid and H_2O_2; therefore, the sensor can also be used for the determination of glucose with a good linear relationship (0.02–2 μM) and a low limit of detection (5 nM). Experimental results showed that the sensor has a high sensitivity and strong anti-interference ability which can be used for the detection of actual samples.

Keywords: biosensor, dual modes, mimic enzyme, hydrogen peroxide, glucose

Edited by:
Yan Zhang,
University of Jinan, China

Reviewed by:
Wei-Lung Tseng,
National Sun Yat-sen University, Taiwan
Xiangjuan Kong,
Jiangxi Science and Technology Normal University, China
Qingyun Liu,
Shandong University of Science and Technology, China

****Correspondence:***
Xiuzhong Wang
xzwang@qau.edu.cn

†These authors have contributed equally to this work

Specialty section:
This article was submitted to Analytical Chemistry, a section of the journal Frontiers in Chemistry

Received: *07 February 2022*
Accepted: *09 March 2022*
Published: *08 April 2022*

Citation:
Tan J, Geng W, Li J, Wang Z, Zhu S and Wang X (2022) Colorimetric and Fluorescence Dual-Mode Biosensors Based on Peroxidase-Like Activity of the Co_3O_4 Nanosheets. Front. Chem. 10:871013. doi: 10.3389/fchem.2022.871013

INTRODUCTION

Enzymes are generally biological catalysts (or biocatalysts) that can accelerate the biochemical reactions in living organisms (Hemalatha et al., 2013; Meghwanshi et al., 2020). However, natural enzymes are usually made up of proteins (or RNAs); therefore these biocatalysts with high costs are vulnerable to inactivation (Sharma et al., 2021). They are often not optimal for practical applications (Lancaster et al., 2018). Thus, artificial enzymes have been developed by scientists as an alternative to natural enzymes (Li et al., 2014; Neelam et al., 2019). Since it was reported first that the Fe_3O_4 magnetite nanoparticles possess an intrinsic mimetic enzyme activity (Gao et al., 2007), nanozymes and nanomaterials with enzyme-mimicking activities have become a research hotspot in recent years due to their facile synthesis, tunable catalytic activities, high stability, and low cost (Lin Y. et al., 2014;

Wang H. et al., 2019; Liang and Han, 2020). Many nanomaterials, such as cobaltosic oxide nanoparticles (Wang P. et al., 2019), manganese dioxide (Zou et al., 2021), graphene oxide hybrid (Wang Q. et al., 2021; Zhang et al., 2021e), nanoceria (Zhang J. et al., 2021), carbon dots (Li et al., 2022), VS_2 (Huang et al., 2018), PtS_2 (Zhang W. et al., 2021), MoS_2 (Zhang X. et al., 2021; Tan et al., 2021), and WS_2 (Nandu et al., 2021), had been shown to possess a similar peroxidase-like activity. These nanozymes had been used in various fields including biosensing (Wang L. et al., 2021; Liu et al., 2021), bioimaging (Gao et al., 2017; Liu et al., 2019), therapeutics (Chen et al., 2021; Zhang et al., 2021d; Zhang et al., 2021e; Hai et al., 2021), and biofuel cells (Le and Il, 2021) as substitutes for natural enzymes. Among these nanozymes, Co_3O_4 nanomaterials exhibit multienzyme activities at different pH conditions (Wang P. et al., 2019) which had been used to construct enzyme-free glucose sensors and other biosensing applications. Although various Co_3O_4 nanostructures such as nanoflowers, polyhedral, and spherical shapes have been successfully synthesized (Balouch et al., 2015; Liu et al., 2020; Cao et al., 2022), some disadvantages and several challenges in the synthetic routes need to be overcome, such as the need for special instruments, the cost and assisted agents, and the complicated process of the operation.

Two-dimensional (2D) layered nanomaterials have attracted an increasing research interest recently because they possess a larger surface area and more accessible active sites with a smaller diffusion barrier for the substrate molecules (Zhang et al., 2020; Hasan et al., 2021). There are few reports about 2D layered Co_3O_4 nanosheets in biosensing fields (Zhao et al., 2021). Herein, Co_3O_4 nanosheets were synthesized by a simple hydrothermal process, and the intrinsic peroxidase-like catalytic activity of the Co_3O_4 nanosheets has been discussed.

As one of the reactive oxygen species (ROS), hydrogen peroxide (H_2O_2) plays critical roles in some biological processes, such as biosynthesis and cell signaling (Liu et al., 2015). However, abnormally elevated ROS levels can destroy redox homeostasis and cause oxidative stress and serious damage to the structure and function of macromolecules in the cell (Pratsinis et al., 2017; Lin et al., 2020). So excessive H_2O_2 is associated with the occurrence and development of many diseases. Several techniques have been used for the detection of H_2O_2. Among these techniques, colorimetric detection of hydrogen peroxide has been widely reported due to its obvious advantage of simplicity, visualization, and low cost. In this system, Co_3O_4 nanosheets can catalyze the oxidation of 3,3′,5,5′-Tetramethylbenzidine (TMB) to afford a blue oxidized TMB (oxTMB) form in the presence of H_2O_2. Thus, a simple and sensitive colorimetric method to detect H_2O_2 was established. Interestingly, the colorimetric product (oxTMB) with a strong absorption at 650 nm wavelength can effectively quench the fluorescence emitted by $Ru(bpy)_3^{2+}$. The inner filter effect (IFE) occurred between oxTMB and $Ru\ (bpy)_3^{2+}$ because the fluorescence emission spectrum of $Ru\ (bpy)_3^{2+}$ is from 550 to 750 nm (with a maximum emission wavelength at 610 nm) which is overlapped with the absorption spectrum of oxTMB. Therefore, a colorimetric and fluorescence dual-mode photochemical sensor for the detection of H_2O_2 is constructed based on the principle of the IFE. Glucose can be catalyzed to produce gluconic acid and H_2O_2; therefore, we further designed a sensitive and facile fluorescence sensor based on the Co_3O_4 nanosheets for the determination of glucose, which is one of the most common analysts providing an assessment of metabolic disorders and diabetes mellitus (Chaianantakul et al., 2018). It has been successfully applied for the determination of glucose in fruit juice and human blood samples (**Scheme 1**).

MATERIALS AND METHODS

Chemicals and Materials

3,3′,5,5′-Tetramethylbenzidine (TMB), $Co\ (NO_3)_2.6H_2O$, glucose, fructose, maltose, sucrose, ascorbic acid, and dopamine were purchased from Aladdin (Shanghai, China). Ruthenium bipyridine was purchased from Sigma-Aldrich (Shanghai, China). Hexamethylenetetramine, Na_2HPO_4, NaH_2PO_4, H_2O_2, acetic acid, sodium acetate, hydrochloric acid, and NaOH were purchased from Sinopharm Chemical Reagent Co., Ltd (Shanghai, China). All the chemical reagents were of analytical grade. Deionized water (18.2 MΩ cm at room temperature), obtained from a Milli-Q water purification system (Millipore Corp., MA), was used to prepared all of the aqueous solutions.

Measurement and Apparatus

FT-IR spectra were obtained from the KBr slice with a Nicolet iS10 FT-IR spectrophotometer (Thermo Fisher Scientific,

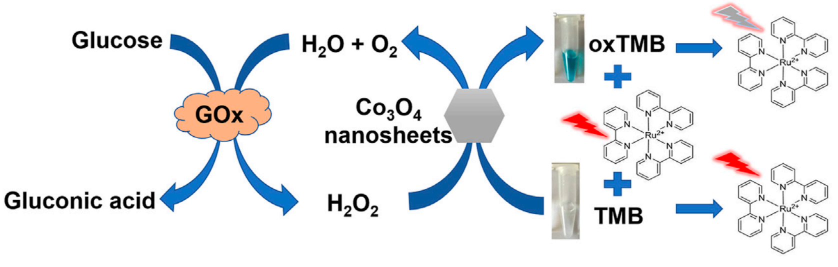

Scheme 1 | Schematic illustration for the determination of H_2O_2 and glucose based on Co_3O_4 nanozymes colorimetric/fluorescent dual mode sensing strategy.

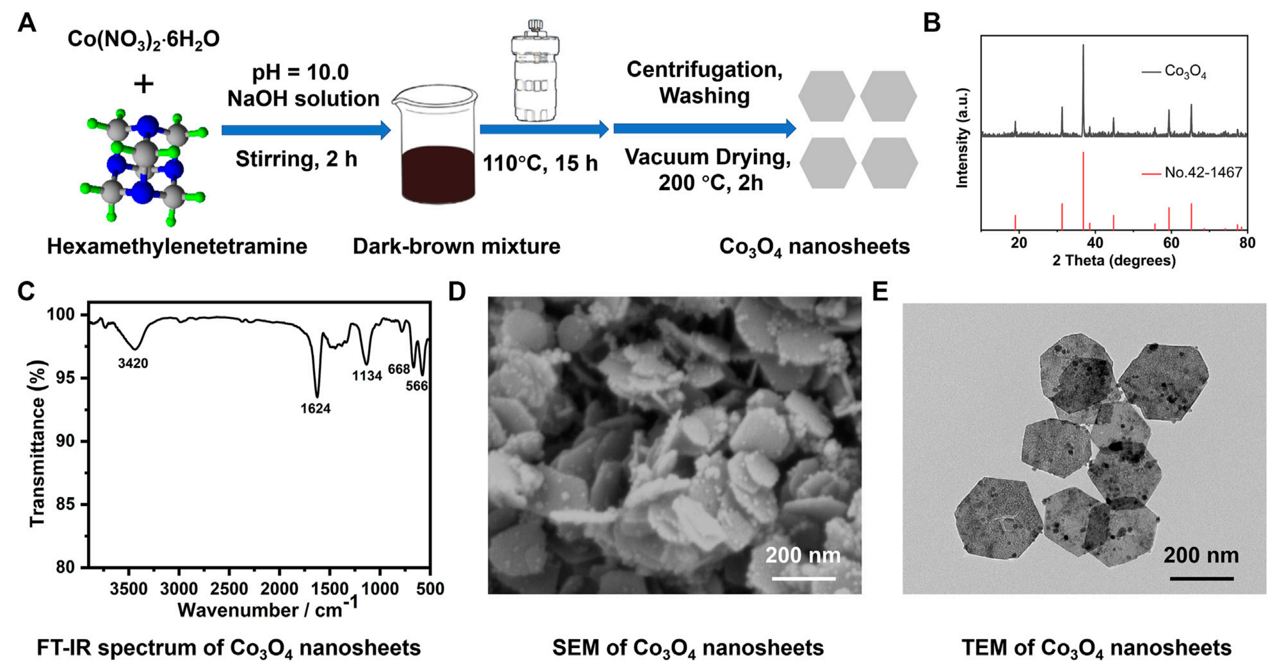

FIGURE 1 | Synthetic process and structural characterizations of the layered Co_3O_4 nanosheets **(A)** Illustration for the hydrothermal synthesis of the layered Co_3O_4 nanosheets; **(B)** XRD pattern; **(C)** FT-IR spectrum; **(D)** SEM; and **(E)** TEM image of the as-prepared Co_3O_4 nanosheets.

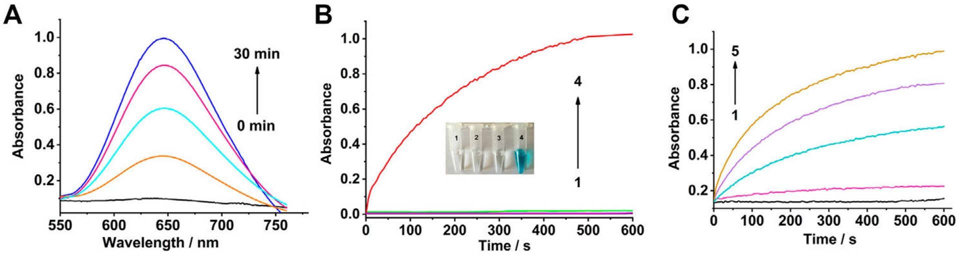

FIGURE 2 | Peroxidase-like activity of the Co_3O_4 nanosheets. **(A)** UV–Vis spectra of the mixed solution of TMB, H_2O_2, and Co_3O_4 nanosheets with different times. **(B)** Time-dependent absorbance changes at 650 nm of TMB solutions in different conditions: (1) $Co_3O_4 + H_2O_2$, (2) Co_3O_4 + TMB, (3) H_2O_2 + TMB, and (4) Co_3O_4 + TMB + H_2O_2. **(C)** Time-dependent absorbance changes at 650 nm in the absence (black) or presence of different concentrations of the Co_3O_4 nanosheets: (1)–(5) are 0, 0.5, 5, 10, and 20 μg ml^{-1}, respectively.

Shanghai). X-ray diffraction (XRD) patterns were recorded on a Bruker D8 Advance diffractometer (Germany) with a Cu Kα (1.5406 Å) radiation source. All pH measurements were performed with a Sartorius PB-10 digital pH meter (Shanghai, China). Transmission electron microscopy (TEM) and scanning electron microscopy (SEM) were performed with a HITACHI model HT7700 instrument operating at 80 kV accelerating voltage and a ZEISS Gemini 300 with OXFORD Xplore, respectively. The ultraviolet-visible (UV-Vis) absorption spectra were recorded by using a U3900 spectrophotometer (Hitachi, Japan). All fluorescence measurements were performed on a Hitachi F-7000 fluorescence spectrometer. The excitation wavelength was set at 496 nm, and the emission spectra from 550 to 750 nm were observed. The fluorescence intensity at 610 nm was used to evaluate the performance of the proposed strategy.

Synthesis of Co_3O_4 Nanosheets

Co_3O_4 nanosheets were prepared in accordance with the method previously reported with a minor modification (Hwang et al., 2011). Under continuous stirring conditions, 1.3 g of $Co(NO_3)_2·6H_2O$ and 0.6 g of hexamethylenetetramine were dissolved in 100 ml of deionized water, respectively. Then, the aforementioned two solutions were mixed together. The resultant solution was maintained at pH 10 with 1 M sodium hydroxide solution and was vigorously stirred for 2 h. Next, the resultant solution was transferred into a pressure-tight teflon-lined stainless-steel autoclave, and then, it was heated up to 110°C. After 15 h, the autoclave cooled down naturally to room temperature. Then, the

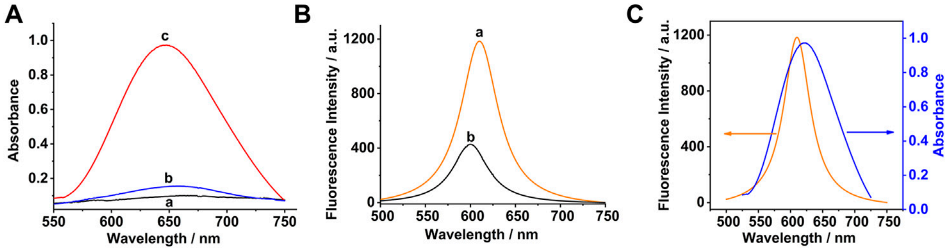

FIGURE 3 | (A) Absorbance spectra of TMB under different conditions: **(a)** TMB, **(b)** Co_3O_4 + TMB, and **(c)** Co_3O_4 + TMB + H_2O_2 **(B)** Fluorescence spectra of Ru $(bpy)_3^{2+}$ under different experimental conditions: **(a)** Ru $(bpy)_3^{2+}$; **(b)** Co_3O_4 + TMB + H_2O_2 + Ru $(bpy)_3^{2+}$; and **(C)** Fluorescence quenching mechanism. The concentrations of Co_3O_4, TMB, H_2O_2, and Ru $(bpy)_3^{2+}$ were 20 μg/ml, 0.5, 0.05, and 0.5 mM, respectively.

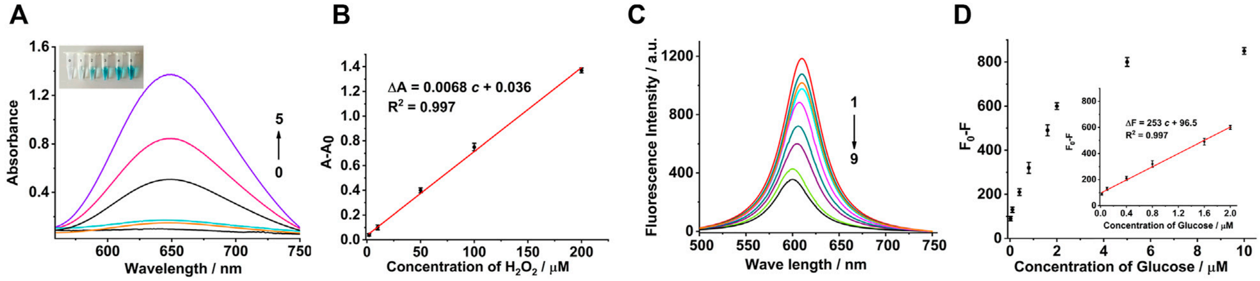

FIGURE 4 | H_2O_2 and glucose assays using Co_3O_4 nanosheet mimetics. **(A)** UV-Vis absorption spectra in the presence of different H_2O_2 concentrations: (0) 0, (1) 2, (2) 10, (3) 50, (4) 100, and (5) 200 μM. The inset photograph shows the visible color change of the reaction system, accordingly. **(B)** Calibration curve corresponding to the absorbance (at the wavelength of 650 nm) as a function of H_2O_2 concentration. **(C)** Fluorescence spectra of Ru $(bpy)_3^{2+}$ in the presence of different concentrations of glucose: (1) 0, (2) 0.02, (3) 0.1, (4) 0.4, (5) 0.8, (6) 1.6, (7) 2.0, (8) 5.0, and (9) 10.0 μM. **(D)** Calibration curve corresponding to the fluorescence intensity (at the emission wavelength of 610 nm) as a function of glucose concentration. Inset shows the linear relationship between the fluorescence intensity and the glucose concentration. The error bars represent the standard deviation of the three measurements. The concentrations of Co_3O_4, TMB, and Ru $(bpy)_3^{2+}$ were 20 μg/ml, 0.5, and 0.5 mM, respectively.

obtained products were washed with water, ethanol, and acetone, in turn, and vacuum dried at 60°C for 4 h. At last, the dried products were calcined for 2 h at 200°C. The obtained products were studied for their morphological characteristics and the peroxidase mimetic activity test.

Kinetic Study and Peroxidase Mimetic Activity of Co_3O_4 Nanosheets

The Co_3O_4 nanosheets were added into HAc-NaAc buffer (100 mM, pH 4.5) in the presence of H_2O_2 by varying concentrations of TMB. The reactions were monitored in time at a wavelength 650 nm by using a U3900 spectrophotometer. The steady-state kinetic catalytic parameters were determined based on the Michaelis–Menten equation(Huang et al., 2018).

Detection of H_2O_2 and Glucose Using the Co_3O_4/TMB/Ru$(bpy)_3^{2+}$ System

H_2O_2 detection was conducted as follows: different concentrations of H_2O_2 were introduced into the mixture of 20 μg/ml Co_3O_4 nanosheets and 0.5 mM TMB in HAc-NaAc buffer (100 mM, pH 4.5). The solution was incubated for 30 min at 37°C, and the absorbance of the solution was detected.

Glucose detection was conducted as follows: 5 μL of 50 mgmL^{-1} glucose oxidase was added into 95 μL PBS (10 mM, pH 7.4) containing different concentrations of glucose, and then, the mixture was incubated for 30 min at 37°C. Subsequently, the abovementioned reaction solution was transferred into 400 μL acetate buffer (100 mM, pH 4.5) containing 0.5 mM TMB, 20 μg/ml Co_3O_4 nanosheets, and 0.5 mM Ru $(bpy)_3^{2+}$. After incubating for another 30 min at 37°C, the reaction solution was monitored by using the fluorescence spectrophotometer. In the control experiments, fructose, maltose, sucrose, ascorbic acid, and dopamine were used instead of glucose, respectively.

For glucose determination in human serum samples, they were pretreated according to the literature (Peng and Weng, 2017) with a minor modification: 50 μL of the serum sample was diluted with 50 μL water and then were added into 900 μL solution containing 0.11 M $Ba(OH)_2$ and 0.0765 M $ZnSO_4$. The resultant solution was centrifuged for 10 min with 4,000 rpm. The supernatant was collected for the determination of glucose.

All the experiments involving human beings were approved by the Ethics Committee Approval of China and operated in strict compliance with the Ethics Committee of Qingdao Agricultural University.

RESULTS AND DISCUSSION

Synthesis and Characterization of Co_3O_4 Nanosheets

Co_3O_4 nanosheets were synthesized through a hydrothermal method, using $Co(NO_3)_2{\cdot}6H_2O$ and hexamethylenetetramine as precursor materials, as shown in **Figure 1A**. The XRD pattern of the synthetic Co_3O_4 nanosheets is shown in **Figure 1B**. It is obvious that all the characteristic peaks are keeping in with the reported data (JCPDS Card No. 42-1467). The IR spectrum of the Co_3O_4 nanosheets is presented in **Figure 1C**. The two distinct adsorption peaks at 566 cm^{-1} and 668 cm^{-1} are ν1 and ν2, respectively, stretching vibrations of the metal–oxygen bonds which confirm the formation of Co_3O_4 (Hwang et al., 2011). The broad absorption bands at 3,420 cm^{-1} and the peak at 1,624 cm^{-1} are due to O-H stretching and the bending vibration of the adsorbed water at the surface. The band at 1,134 cm^{-1} is corresponding to the Co-OH bending vibration. The synthesized nanosheets were also examined by SEM and TEM, which are shown in **Figures 1D,E**. It is obvious that the synthesized products are hexagonal nanosheets in large quantities. The stacking densities of the nanosheets are very high even though most of them are attached with each other through their surface. Most of them reveal a hexagonal shape with an internal angle of ~120°; however, there are also some deformed hexagonal-structured nanosheets among them. The nanosheets are about 200 ± 10 nm in diagonal.

Design Principle of the Biosensor

The colorless TMB solution can be oxidized into a blue solution by H_2O_2 in the presence of a catalyst. Therefore, TMB and H_2O_2 were used as the reaction substrates to evaluate the peroxidase-like activity of the Co_3O_4 nanosheets. The absorbance of oxTMB (the oxidation product of TMB) increased with time in the mixture of Co_3O_4 nanosheets, H_2O_2, and TMB (**Figure 2A**).

It can be seen from **Figure 2B** that the mixture of Co_3O_4 and H_2O_2 have no absorption at 650 nm (curve 1). It was also obvious that the oxidation reaction of TMB cannot take place in the presence of Co_3O_4 or H_2O_2 alone (curves 2 and 3). As a result, TMB was oxidized by H_2O_2 in the presence of as-synthesized Co_3O_4 nanosheets (curve 4). The absorbance of the mixture at wavelength 650 nm obviously increased with the increasing concentration of the Co_3O_4 nanosheets from 0 to 20 $\mu g\ ml^{-1}$ which are shown in **Figure 2C**. As a comparison, the activity of the earlier published peroxidase-like nanomaterials MnO_2 and 2D Co-MOF (Wang et al., 2022) have also been examined, which are shown in **Supplementary Figure S1**. To further investigate the catalytic activity of the Co_3O_4 nanosheets, the steady-state kinetic parameters were examined for the reaction between H_2O_2 and TMB, as shown in **Supplementary Figure S2**. The results demonstrated that the catalysis of Co_3O_4 nanosheets showed typical Michaelis–Menten curves (**Supplementary Figure S2A**). The curves were fitted to the Lineweaver–Burk plots (**Supplementary Figure S2B**). According to the plots, the Michaelis–Menten constants (K_m) and the maximum initial reaction rates (V_{max}) were calculated to be 0.42 mM and 5.7×10^{-7} M· s^{-1}, respectively, which are superior to the previously published peroxidase-like materials (Lin et al., 2014a; Lin et al., 2014b; Huang et al., 2018). In a word, Co_3O_4 nanosheets can facilitate the oxidation of TMB in the presence of H_2O_2. So the content of H_2O_2 can be detected based on this catalytic reaction principle.

As H_2O_2 was the primary catalyzed reaction product of glucose oxidase, the glucose content can also be detected using the Co_3O_4 nanosheets as the catalyst (Illustrated as **Scheme 1**). Additionally, the colorimetric product oxTMB can effectively quench the fluorescence emitted by Ru $(bpy)_3{}^{2+}$ due to the IFE. Thus, glucose also can be indirectly detected by the fluorescence method which can not only improve detection sensitivity but also avoid the false positives caused by a single colorimetric signal response (Shin et al., 2020; Munzi et al., 2021; Wan et al., 2021).

Feasibility Study

The absorbance spectra of TMB under different conditions were measured to prove the feasibility of the sensing strategy. As shown in **Figure 3A**, a very weak absorption was obtained in the presence of TMB independently (curve a). There is a slight increase of absorption compared with TMB in the mixture of Co_3O_4 and TMB (curve b), which might be a weak catalytic effect of Co_3O_4 to TMB. The biggest absorption signal (curve c) was obtained when H_2O_2 was added into the aforementioned solution.

Figure 3B shows fluorescence spectra of Ru $(bpy)_3{}^{2+}$ under different experimental conditions. As shown in **Figure 3B**, the biggest fluorescence signal (curve a) was obtained in the presence of $Ru(bpy)_3{}^{2+}$ independently. However, the fluorescence intensity significantly decreased when an amount of the Co_3O_4 nanosheets, TMB, and H_2O_2 were added into the aforementioned solution (curve b). It is worth noting that the maximum emission wavelength is blue-shifted slightly. The experimental results demonstrated that a certain amount of oxTMB was produced in the solution, which quenched the fluorescence emitted by $Ru(bpy)_3{}^{2+}$ due to the IFE . The fluorescence quenching mechanism of $Ru(bpy)_3{}^{2+}$ by the Co_3O_4 nanosheets raised from the IFE process are demonstrated in **Figure 3C**. The reduced fluorescence intensity has a quantitative relationship with the concentration of H_2O_2. Thus, the content of glucose can also be detected indirectly by this fluorescence sensing strategy.

Optimization of Experimental Conditions

To improve the detection sensitivity, the experimental conditions have been optimized. Absorption is dependent on the concentration of the chromogenic reagent, so the concentrations of TMB were initially optimized. The results are shown in **Supplementary Figure S3** in SI which showed that the absorption increased gradually with the increase of concentration from 0.1 to 0.4 mM and then increased slightly and kept stable. To ensure the experimental results, therefore, 0.5 mM TMB was selected as the optimal concentration.

All the experimental results confirmed that the Co_3O_4 nanosheets revealed a peroxidase-like activity. It was noted that the catalytic activity of peroxidase was associated with the pH and temperature. Therefore, the optimal reaction conditions were investigated. The results demonstrated that Co_3O_4 nanosheets have the best catalytic activity in pH 4.5 at 37°C (**Supplementary Figures S4, S5** in SI).

The fluorescence detection method in this strategy is based on the inhibition capability of the colorimetric reaction products on the fluorescence emitted by Ru $(bpy)_3^{2+}$. Therefore, only Ru $(bpy)_3^{2+}$ concentrations have been optimized to obtain the biggest difference of the fluorescence intensity in the presence of Co_3O_4, TMB, H_2O_2, and Ru $(bpy)_3^{2+}$ compared with Ru $(bpy)_3^{2+}$ independently. The difference of the fluorescence intensity gradually increased with increasing Ru $(bpy)_3^{2+}$ concentrations, as shown in **Supplementary Figure S6** in SI; the biggest difference was obtained at the concentration of 0.5 mM. Therefore, 0.5 mM Ru $(bpy)_3^{2+}$ was selected as the optimal concentration for this procedure.

Colorimetric Detection for H_2O_2 and Fluorescence Detection for Glucose

A colorimetric sensor for the detection of H_2O_2 was constructed based on the peroxidase-like activity of the Co_3O_4 nanosheets. Under the optimal conditions, the concentration-response curve of H_2O_2 to TMB at wavelength 650 nm is shown in **Figure 4A**. A good linear relationship was established between 2 and 200 μM (**Figure 4B**). The linear regression equation was $\Delta A = 0.0068\ c + 0.036$ with the correlation coefficient of 0.997 [ΔA: difference of absorbance and c: concentration of H_2O_2 (μM)]. The limit of detection for H_2O_2 was estimated to be 0.4 μM (based on the signal-to-noise ratio of 3). Similarly, the fluorescence response of the system was examined with different concentrations of glucose which demonstrated that the fluorescence intensity gradually decreased with the increase in the concentration of glucose (**Figure 4C**). These results verified that with the greater concentration of glucose, more H_2O_2 were produced, which inhibited the fluorescence of $Ru(bpy)_3^{2+}$. The difference of the fluorescence intensity showed a good linear relationship with the concentration of glucose ranging from 0.02 to 2 μM (the inset of **Figure 4D**). The linear regression equation was $\Delta F = 253\ c + 96.5$ with the correlation coefficient of 0.997 [ΔF: difference of fluorescence intensity and c: concentration of glucose (μM)]. The limit of detection was estimated to be 5.0 nM (based on the signal-to-noise ratio of 3), which are superior to the reported methods (**Supplementary Table S1**).

To prove the anti-interference capability of the strategy for the detection of glucose, five other analogs, such as fructose, maltose, sucrose, ascorbic acid, and dopamine, were also determined by the fluorescence method, which are shown in **Supplementary Figure S7** in SI. The results showed that the other analogs hardly interfered with the determination of glucose under this experimental condition. The stability of the assay system has also been investigated. **Supplementary Figure S8** in SI showed the fluorescence response of the sensing system with the concentration of 0.2 and 1.5 μM glucose based on the six-time detections, respectively. The fluorescence intensity was relatively stable with the relative standard deviation of 2.61 and 3.93%, respectively.

Determination of H_2O_2 and Glucose in Real Samples

H_2O_2 in artificial lake water, glucose in fruit juice, and blood samples were detected by colorimetric and fluorescence methods, respectively. The water sample was obtained from the artificial lake in Qingdao Agricultural University, and fruit juice was purchased from the local supermarket. They have been processed according to the literature studies (Wang et al., 2016a; Wang et al., 2016b). Blood samples, provided by the Hospital of Qingdao Agricultural University by collecting from healthy volunteers with informed consent, were processed according to the literature (Peng and Weng, 2017). In addition, the recovery tests were examined by adding a known concentration of the standard to the pretreated solution in real samples (**Supplementary Tables S2, S3** in SI). The results demonstrated that the recoveries obtained ranged from about 99.2 to 106.6% and 94–108%, respectively.

CONCLUSION

In summary, two-dimensional layered Co_3O_4 nanosheets with an intrinsic peroxidase-like catalytic activity have been successfully synthesized by a simple hydrothermal method. The catalytic activity of the Co_3O_4 nanosheets has been investigated by the oxidation of TMB by H_2O_2 in acidic conditions. The blue oxidation product (oxTMB) was easily visualized and quantified by using a spectrophotometer. Based on this discovery, a simple, cheap colorimetric assay for H_2O_2 was successfully developed. Interestingly, we found that the colorimetric product can effectively quench the fluorescence emitted by Ru $(bpy)_3^{2+}$ due to the IFE. So we further constructed a sensitive and facile fluorescence sensor for the determination of glucose by the catalyzed reaction of glucose oxidase (GOx) with a low detection limit of 5 nM. It has been applied to assay the glucose content in fruit juices and human serum samples. This sensing strategy would facilitate the application of Co_3O_4 nanosheets in the fields of biomedicine diagnosis and analytical chemistry.

DATA AVAILABILITY STATEMENT

The original contributions presented in the study are included in the article/**Supplementary Material**, further inquiries can be directed to the corresponding author.

ETHICS STATEMENT

The studies involving human participants were reviewed and approved by Qingdao Agricultural University. The patients/participants provided their written informed consent to participate in this study.

AUTHOR CONTRIBUTIONS

XW conceived and supervised the work. JT and WG contributed equally to this work. WG designed the colorimetric assay and supervised the fluorescence experiments. JL performed the human serum sample assay experiments. ZW and SZ performed the experiments including synthesis and characterization of Co_3O_4 nanosheets. XW wrote the manuscript with input from all the other coauthors. All the coauthors analyzed the results and revised the manuscript.

FUNDING

This work was financially supported by the National Innovation Training Program for College Students (No. 202110435184), the Shandong Provincial Higher Education Research Project on Undergraduate Teaching Reform (No. Z2021220), the Syncretic of Professional and Innovation Education Reform of Qingdao Agricultural University (No. ZCJG202105), and the Shandong Provincial Natural Science Foundation, China (No. ZR2018MB030).

ACKNOWLEDGMENTS

We acknowledge Prof. Lei Han of Qingdao Agricultural University for providing valuable help for synthesis and characterization of Co_3O_4 nanosheets.

SUPPLEMENTARY MATERIAL

The Supplementary Material for this article can be found online at: https://www.frontiersin.org/articles/10.3389/fchem.2022.871013/full#supplementary-material

REFERENCES

Balouch, Q., Ibupoto, Z. H., Khaskheli, G. Q., Soomro, R. A., Sirajuddin, M. K., Samoon, M. K., et al. (2015). Cobalt Oxide Nanoflowers for Electrochemical Determination of Glucose. *J. Elec. Materi.* 44, 3724–3732. doi:10.1007/s11664-015-3860-z

Cao, X., Liu, M., Zhao, M., Li, J., Xia, J., Zou, T., et al. (2022). Synergetic PtNP@ Co3O4 Hollow Nanopolyhedrals as Peroxidase-like Nanozymes for the Dual-Channel Homogeneous Biosensing of Prostate-specific Antigen. *Anal. Bioanal. Chem.* 414, 1921–1932. doi:10.1007/s00216-021-03827-1

Chaianantakul, N., Wutthi, K., Kamput, N., Pramanpol, N., Janphuang, P., Pummara, W., et al. (2018). Development of Mini-Spectrophotometer for Determination of Plasma Glucose. *Spectrochimica Acta A: Mol. Biomol. Spectrosc.* 204, 670–676. doi:10.1016/j.saa.2018.06.107

Chen, L., Xing, S., Lei, Y., Chen, Q., Zou, Z., Quan, K., et al. (2021). A Glucose-Powered Activatable Nanozyme Breaking pH and H 2 O 2 Limitations for Treating Diabetic Infections. *Angew. Chem. Int. Ed.* 60, 23534–23539. doi:10.1002/anie.202107712

Gao, L., Fan, K., and Yan, X. (2017). Iron Oxide Nanozyme: A Multifunctional Enzyme Mimetic for Biomedical Applications. *Theranostics* 7, 3207–3227. doi:10.7150/thno.19738

Gao, L., Zhuang, J., Nie, L., Zhang, J., Zhang, Y., Gu, N., et al. (2007). Intrinsic Peroxidase-like Activity of Ferromagnetic Nanoparticles. *Nat. Nanotech.* 2, 577–583. doi:10.1038/nnano.2007.260

Hai, X., Li, Y., Yu, K., Yue, S., Li, Y., Song, W., et al. (2021). Synergistic *In-Situ* Growth of Silver Nanoparticles with Nanozyme Activity for Dual-Mode Biosensing and Cancer Theranostics. *Chin. Chem. Lett.* 32, 1215–1219. doi:10.1016/j.cclet.2020.09.013

Hasan, M. A. M., Wang, Y., Bowen, C. R., and Yang, Y. (2021). 2D Nanomaterials for Effective Energy Scavenging. *Nano-micro Lett.* 13, 82. doi:10.1007/s40820-021-00603-9

Hemalatha, T., Umamaheswari, T., Krithiga, G., Sankaranarayanan, P., and Puvanakrishnan, R. (2013). Enzymes in Clinical Medicine: An Overview. *Indian J. Exp. Biol.* 51, 777–788.

Huang, L., Zhu, W., Zhang, W., Chen, K., Wang, J., Wang, R., et al. (2018). Layered Vanadium(Iv) Disulfide Nanosheets as A Peroxidase-like Nanozyme for Colorimetric Detection of Glucose. *Microchim Acta* 185, 7. doi:10.1007/s00604-017-2552-1

Hwang, S. W., Umar, A., Kim, S. H., Al-Sayari, S. A., Abaker, M., Al-Hajry, A., et al. (2011). Low-temperature Growth of Well-Crystalline Co3O4 Hexagonal Nanodisks as Anode Material for Lithium-Ion Batteries. *Electrochimica Acta* 56, 8534–8538. doi:10.1016/j.electacta.2011.07.033

Lancaster, L., Abdallah, W., Banta, S., and Wheeldon, I. (2018). Engineering Enzyme Microenvironments for Enhanced Biocatalysis. *Chem. Soc. Rev.* 47, 5177–5186. doi:10.1039/c8cs00085a

Le, P. G., and Kim, M. I. (2021). Research Progress and Prospects of Nanozyme-Based Glucose Biofuel Cells. *Nanomaterials* 11, 2116. doi:10.3390/nano11082116

Li, X., Zhang, Z., and Li, Y. (2014). Artificial Enzyme Mimics for Catalysis and Double Natural Enzyme Co-immobilization. *Appl. Biochem. Biotechnol.* 172, 1859–1865. doi:10.1007/s12010-013-0625-0

Li, Z., Liu, W., Ni, P., Zhang, C., Wang, B., Duan, G., et al. (2022). Carbon Dots Confined in N-Doped Carbon as Peroxidase-like Nanozyme for Detection of Gastric Cancer Relevant D-Amino Acids. *Chem. Eng. J.* 428, 131396. doi:10.1016/j.cej.2021.131396

Liang, X., and Han, L. (2020). White Peroxidase-Mimicking Nanozymes: Colorimetric Pesticide Assay without Interferences of O 2 and Color. *Adv. Funct. Mater.* 30, 2001933. doi:10.1002/adfm.202001933

Lin, S., Cheng, Y., Zhang, H., Wang, X., Zhang, Y., Zhang, Y., et al. (2020). Copper Tannic Acid Coordination Nanosheet: A Potent Nanozyme for Scavenging ROS from Cigarette Smoke. *Small* 16, e1902123. doi:10.1002/smll.201902123

Lin, T., Zhong, L., Guo, L., Fu, F., and Chen, G. (2014a). Seeing Diabetes: Visual Detection of Glucose Based on the Intrinsic Peroxidase-like Activity of MoS2 Nanosheets. *Nanoscale* 6, 11856–11862. doi:10.1039/c4nr03393k

Lin, T., Zhong, L., Song, Z., Guo, L., Wu, H., Guo, Q., et al. (2014b). Visual Detection of Blood Glucose Based on Peroxidase-like Activity of WS2 Nanosheets. *Biosens. Bioelectron.* 62, 302–307. doi:10.1016/j.bios.2014.07.001

Lin, Y., Ren, J., and Qu, X. (2014c). Catalytically Active Nanomaterials: A Promising Candidate for Artificial Enzymes. *Acc. Chem. Res.* 47, 1097–1105. doi:10.1021/ar400250z

Liu, B., Sun, Z., Huang, P.-J. J., and Liu, J. (2015). Hydrogen Peroxide Displacing DNA from Nanoceria: Mechanism and Detection of Glucose in Serum. *J. Am. Chem. Soc.* 137, 1290–1295. doi:10.1021/ja511444e

Liu, F., Lin, L., Zhang, Y., Wang, Y., Sheng, S., Xu, C., et al. (2019). A Tumor-Microenvironment-Activated Nanozyme-Mediated Theranostic Nanoreactor for Imaging-Guided Combined Tumor Therapy. *Adv. Mater.* 31, e1902885. doi:10.1002/adma.201902885

Liu, H. Y., Xu, H. X., Zhu, L. L., Wen, J. J., Qiu, Y. B., Gu, C. C., et al. (2021). Colorimetric Detection of Hydrogen Peroxide and Glutathione Based on Peroxidase Mimetic Activity of Fe_3O_4-Sodium Lignosulfonate Nanoparticles. *Chin. J. Anal. Chem.* 49, E21160–E21169. doi:10.1016/s1872-2040(21)60113-5

Liu, P., Wang, Y., Han, L., Cai, Y., Ren, H., Ma, T., et al. (2020). Colorimetric Assay of Bacterial Pathogens Based on Co3O4 Magnetic Nanozymes Conjugated with Specific Fusion Phage Proteins and Magnetophoretic Chromatography. *ACS Appl. Mater. Inter.* 12, 9090–9097. doi:10.1021/acsami.9b23101

Meghwanshi, G. K., Kaur, N., Verma, S., Dabi, N. K., Vashishtha, A., Charan, P. D., et al. (2020). Enzymes for Pharmaceutical and Therapeutic Applications. *Biotechnol. Appl. Biochem.* 67, 586–601. doi:10.1002/bab.1919

Munzi, G., Failla, S., and Di Bella, S. (2021). Highly Selective and Sensitive Colorimetric/fluorometric Dual Mode Detection of Relevant Biogenic Amines. *Analyst* 146, 2144–2151. doi:10.1039/d0an02336a

Nandu, N., Smith, C. W., Kachwala, M. J., and Yigit, M. V. (2021). Regulation of the Peroxidase-Like Activity of nGO, MoS 2 and WS 2 Nanozymes by Using Metal Cations. *ChemBioChem* 22, 662–665. doi:10.1002/cbic.202000617

Neelam, A., Chhillar, A. K., and Rana, J. S. (2019). Enzyme Nanoparticles and Their Biosensing Applications: A Review. *Anal. Biochem.* 581, 113345. doi:10.1016/j.ab.2019.113345

Peng, J., and Weng, J. (2017). Enhanced Peroxidase-like Activity of MoS2/graphene Oxide Hybrid with Light Irradiation for Glucose Detection. *Biosens. Bioelectron.* 89, 652–658. doi:10.1016/j.bios.2015.12.034

Pratsinis, A., Kelesidis, G. A., Zuercher, S., Krumeich, F., Bolisetty, S., Mezzenga, R., et al. (2017). Enzyme-Mimetic Antioxidant Luminescent Nanoparticles for Highly Sensitive Hydrogen Peroxide Biosensing. *ACS Nano* 11, 12210–12218. doi:10.1021/acsnano.7b05518

Sharma, A., Gupta, G., Ahmad, T., Mansoor, S., and Kaur, B. (2021). Enzyme Engineering: Current Trends and Future Perspectives. *Food Rev. Int.* 37, 121–154. doi:10.1080/87559129.2019.1695835

Shin, B., Park, J.-S., Chun, H.-S., Yoon, S., Kim, W.-K., and Lee, J. (2020). A Fluorescence/colorimetric Dual-Mode Sensing Strategy for miRNA Based on Graphene Oxide. *Anal. Bioanal. Chem.* 412, 233–242. doi:10.1007/s00216-019-02269-0

Tan, Y., Jiang, H., Wang, B., and Zhang, X. (2021). MoS2-based Composite Nanozymes with superior Peroxidase-like Activity for Ultrasensitive SERS Detection of Glucose. *New J. Chem.* 45, 19593–19604. doi:10.1039/d1nj02451e

Wan, Y., Zhao, J., Deng, X., Chen, J., Xi, F., and Wang, X. (2021). Colorimetric and Fluorescent Dual-Modality Sensing Platform Based on Fluorescent Nanozyme. *Front. Chem.* 9, 774486. doi:10.3389/fchem.2021.774486

Wang, H., Wan, K., and Shi, X. (2019a). Recent Advances in Nanozyme Research. *Adv. Mater.* 31, 1805368. doi:10.1002/adma.201805368

Wang, L., Li, B., You, Z., Wang, A., Chen, X., Song, G., et al. (2021a). Heterojunction of Vertically Arrayed MoS2 Nanosheet/N-Doped Reduced Graphene Oxide Enabling a Nanozyme for Sensitive Biomolecule Monitoring. *Anal. Chem.* 93, 11123–11132. doi:10.1021/acs.analchem.1c01550

Wang, P., Cao, L., Chen, Y., Wu, Y., and Di, J. (2019b). Photoelectrochemical Biosensor Based on Co3O4 Nanoenzyme Coupled with PbS Quantum Dots for Hydrogen Peroxide Detection. *ACS Appl. Nano Mater.* 2, 2204–2211. doi:10.1021/acsanm.9b00165

Wang, Q., Niu, D., Shi, J., and Wang, L. (2021b). A Three-In-One ZIFs-Derived CuCo(O)/GOx@PCNs Hybrid Cascade Nanozyme for Immunotherapy/Enhanced Starvation/Photothermal Therapy. *ACS Appl. Mater. Inter.* 13, 11683–11695. doi:10.1021/acsami.1c01006

Wang, X., Dong, S., Hou, T., Liu, L., Liu, X., and Li, F. (2016a). Exonuclease I-Aided Homogeneous Electrochemical Strategy for Organophosphorus Pesticide Detection Based on Enzyme Inhibition Integrated with a DNA Conformational Switch. *Analyst* 141, 1830–1836. doi:10.1039/c5an02374b

Wang, X., Hou, T., Dong, S., Liu, X., and Li, F. (2016b). Fluorescence Biosensing Strategy Based on Mercury Ion-Mediated DNA Conformational Switch and Nicking Enzyme-Assisted Cycling Amplification for Highly Sensitive Detection of Carbamate Pesticide. *Biosens. Bioelectron.* 77, 644–649. doi:10.1016/j.bios.2015.10.034

Wang, Z., Zhang, Y., Wang, X., and Han, L. (2022). Flow-homogeneous Electrochemical Sensing System Based on 2D Metal-Organic Framework Nanozyme for Successive microRNA Assay. *Biosens. Bioelectron.* 206, 114120. doi:10.1016/j.bios.2022.114120

Zhang, J., Chen, H., Zhao, M., Liu, G., and Wu, J. (2020). 2D Nanomaterials for Tissue Engineering Application. *Nano Res.* 13, 2019–2034. doi:10.1007/s12274-020-2835-4

Zhang, J., Wang, J., Liao, J., Lin, Y., Zheng, C., and Liu, J. (2021a). *In Situ* Fabrication of Nanoceria with Oxidase-like Activity at Neutral pH: Mechanism and Boosted Bio-Nanozyme Cascades. *ACS Appl. Mater. Inter.* 13, 50236–50245. doi:10.1021/acsami.1c14831

Zhang, W., Li, X., Cui, T., Li, S., Qian, Y., Yue, Y., et al. (2021b). PtS2 Nanosheets as a Peroxidase-Mimicking Nanozyme for Colorimetric Determination of Hydrogen Peroxide and Glucose. *Microchim Acta* 188, 174. doi:10.1007/s00604-021-04826-w

Zhang, X., Zhang, S., Yang, Z., Wang, Z., Tian, X., and Zhou, R. (2021c). Self-cascade MoS2 Nanozymes for Efficient Intracellular Antioxidation and Hepatic Fibrosis Therapy. *Nanoscale* 13, 12613–12622. doi:10.1039/d1nr02366g

Zhang, Y., Wang, Y., Zhou, Q., Chen, X., Jiao, W., Li, G., et al. (2021d). Precise Regulation of Enzyme-Nanozyme Cascade Reaction Kinetics by Magnetic Actuation toward Efficient Tumor Therapy. *ACS Appl. Mater. Inter.* 13, 52395–52405. doi:10.1021/acsami.1c15717

Zhang, Y., Yang, Y., Shi, J., and Wang, L. (2021e). A Multimodal Strategy of Fe3O4@ZIF-8/GOx@MnO2 Hybrid Nanozyme via TME Modulation for Tumor Therapy. *Nanoscale* 13, 16571–16588. doi:10.1039/d1nr04196g

Zhao, Q., Zheng, X., Xing, L., Tang, Y., Zhou, X., Hu, L., et al. (2021). 2D Co3O4 Stabilizing Rh Nano Composites Developed for Visual Sensing Bioactive Urea and Toxic P-Aminophenol in Practice by Synergetic-Reinforcing Oxidase Activity. *J. Hazard. Mater.* 409, 125019. doi:10.1016/j.jhazmat.2020.125019

Zou, N., Wei, X. Y., Zong, Z. M., Li, X., Meng, F. N., and Wang, Z. X. (2021). Preparation of Manganese Dioxide Nanozyme as Catalyst for Electrochemical Sensing of Hydrogen Peroxide. *Int. J. Electrochem. Sci.* 16, 210324. doi:10.20964/2021.03.47

Conflict of Interest: The authors declare that the research was conducted in the absence of any commercial or financial relationships that could be construed as a potential conflict of interest.

frontiers | Frontiers in Chemistry

ORIGINAL RESEARCH
published: 10 May 2022
doi: 10.3389/fchem.2022.872251

Quantitative Determination of Whey Protein to Casein Ratio in Infant Formula Milk Powder

Tao Xu[1,2,3], *Jingyao Chen*[2,3], *Kai Yang*[2,3], *Weicang Qiao*[2,3], *Junying Zhao*[2,3,4] *and Lijun Chen*[2,3,4]*

[1]*School of Bioengineering, Dalian Polytechnic University, Dalian, China,* [2]*National Engineering Research Center of Dairy Health for Maternal and Child, Beijing Sanyuan Foods Co. Ltd, Beijing, China,* [3]*Beijing Engineering Research Center of Dairy, Beijing Sanyuan Foods Co. Ltd., Beijing, China,* [4]*South Asia Branch of National Engineering Center of Dairy for Maternal and Child Health, Guilin University of Technology, Guilin, China*

This study was aimed to establish a method for quantitatively determining the ratio of whey protein in the total protein of infant formula by respectively selecting two characteristic peptides from whey protein and casein and calculating the ratio between the characteristic peptides. A nanoliter high-performance liquid chromatography tandem high-resolution mass spectrometry (Q Exactive) was used to simultaneously detect the characteristic peptides of two main whey proteins and two main caseins. The characteristic peptides were calculated, predicted, and screened using the ExPASy website, and peptide information was confirmed by database retrieval after the analysis by using a high-resolution mass spectrometer. The matrix effect was compensated by comparing the characteristic peptides in whey protein with those in casein protein, in which isotope internal standards were not required. The influence of the changes of the protein content in whey protein and casein on the detection method was eliminated by the calculation formula designed by ourselves. In this detection method, the sample was stable in the total protein concentration range of between 0.1 and 0.4 mg/ml. In the simulated industrial processing environment, with desalted whey powder, the recovery rate was 98.63–113.33% under different spiked levels with good reproducibility (RSD<8%). The RSDs of intraday and interday precisions were 2.03–9.35% and 0.61–11.02%, respectively. The different processing procedures of samples had no significant impact on the detection of whey protein (RSD% for milk samples treated by different processing techniques was 2.97%). The quantitation method of whey protein was applied to evaluate the whey protein content in different brands of commercially available milk powder. In summary, the proposed method was applicable for quantitative analysis of whey proteins in the infant formula.

Keywords: relative quantitative, mass spectrometry, infant formula, protein, peptides

Edited by:
Roberto Romero González,
University of Almeria, Spain

Reviewed by:
Marco Iammarino,
Experimental Zooprophylactic Institute of Puglia and Basilicata (IZSPB), Italy
Silvia Vincenzetti,
University of Camerino, Italy

***Correspondence:**
Lijun Chen
chenlijun@sanyuan.com.cn

Specialty section:
This article was submitted to Analytical Chemistry, a section of the journal Frontiers in Chemistry

Received: *09 February 2022*
Accepted: *22 March 2022*
Published: *10 May 2022*

Citation:
Xu T, Chen J, Yang K, Qiao W, Zhao J and Chen L (2022) Quantitative Determination of Whey Protein to Casein Ratio in Infant Formula Milk Powder.
Front. Chem. 10:872251.
doi: 10.3389/fchem.2022.872251

INTRODUCTION

As an important nutrient with high-nutritional value and rich active substances, whey protein is often added to various foods such as infant formula. The infant formula is used as a substitute for human milk for the newborns unavailable to adequate human milk, in which the content of whey protein is particularly important. It has been established that whey protein accounts for about 18% of the total protein content in cow milk, and it accounts for 60%–70% of the total protein content in human milk. To meet the nutritional needs of infants for growth and development, adequate whey protein is often added in the formula to make it closer to human milk. In the past few years, several commonly used methods for detecting whey protein in formula milk powder have been proposed and applied in practice, such as sodium dodecyl sulfate–polyacrylamide gel electrophoresis (SDS–PAGE), amino acid conversion algorithm, capillary electrophoresis (CE), high-performance liquid chromatography (HPLC), and liquid chromatography–mass spectrometry (LC–MS) (Kinghorn et al., 1995; Czerwenka et al., 2007; Bonfatti et al., 2013; Feng and Baugh, 2013).

The invention of polyacrylamide gel electrophoresis in 1959 ushered in a new era of modern electrophoresis. Nowadays, due to its simple operation, fast detection speed, and low cost, it is often used for the qualitative and quantitative detections of biological macromolecules (Restani et al., 1995; Aludatt et al., 2017). But when this method is used to detect whey protein in infant formula milk powder, the detected electrophoresis band will change, thus affecting the detection result, which might be caused by the complicated process under high temperature and high pressure in the production process of the infant formula (Lemos et al., 2015; Krause and Goldring, 2019). As one of the most commonly used detection methods, HPLC separates and analyzes the components in the mixture according to their difference in retention time. Modern capillary electrophoresis was invented by Jorgenson and Lukacs in 1981. Due to its high selectivity and superior separation effect of proteins, it has been widely used in protein analysis (Veledo et al., 2005; Grochocki et al., 2015), but when it was used to separate the proteins in formula milk powder with complex matrices, adhesion occurred in the related protein peak. In the latest ISO standard (ISO 23293-2020), the sub-protein peaks in whey protein are compared with casein as a whole, thus a more accurate capillary electrophoresis method can be obtained for the detection of whey protein in formula milk powder (Feng et al., 2018). In 2013, Wesley proposed to quantify whey protein in formula milk powder with the amino acid model, so as to avoid the influence of protein structure changes on the detection of whey protein, and to quantify whey protein more accurately from the amino acid level (Feng and Baugh, 2013). However, because amino acids are present in each protein, the conversion of the amino acid amount to the whey protein content can only be completed by summarizing experimental experience. On the other hand, the incorporation of other miscellaneous proteins will cause great changes in the test results (Feng and Baugh, 2013). At the end of the 1980s, John Fenn invented electrospray electrolysis and created a new era of proteomics analysis. The extremely sensitive and selective ability of mixture analysis was obtained using the combination of physical separation capabilities of LC and universal mass analysis capabilities of MS (Fenn et al., 2012; Ke et al., 2017; Wang et al., 2018). The absolute quantification of whey protein in formula milk powder can be achieved using the internal standard method of isotope peptides. However, it has been found in recent years that isotope-labeled peptides and characteristic peptides may behave differently in the pretreatment process, and some peptides and the peptides labeled with isotope might mutually interfere with each other, causing distortion of the mass spectrum signal (Qian et al., 2006; Higgs et al., 2008; Chen and Pramanik, 2009; Winter et al., 2009).

TABLE 1 | Gradient elution conditions.

(Time, min)	0 (%)	5 (%)	65 (%)	70 (%)	75 (%)	76 (%)
A	96	96	78	10	96	96
B	4	4	22	90	4	4

To precisely quantify whey protein in formula milk powder, the influence of the denaturation behavior of whey protein during processing on the detection result should be prevented. This denaturation behavior can further amplify the error of some protein detection methods (SDS–PAGE, CE, and HPLC). The influence of protein denaturation can be effectively prevented using the method of protein quantification at the levels of amino acid and peptide. On the other hand, the unpracticability of the method limits the application of the detection method in the production process. The high price of synthetic internal standards for LC–MC detection greatly increases the detection costs. However, when internal standards are not used, the difference in the matrix effect and ionization efficiency leads to great error in the detection results.

This study detected the labeled isotope with HC–MC and made corrections according to other peptides in the sample without using the isotope internal standard, determined the whey protein content according to the relationship between the ratio of whey protein to casein and the peak area ratio of the respective characteristic peptides, and eliminated the difference between the matrix effect and ionization efficiency.

MATERIALS AND METHODS

Materials

Nanoliter high-performance liquid chromatography UltiMate 3000 RSLCnano (Thermo Fisher Scientific Company) was used in this study.

Q Exactive-combined quadrupole Orbitrap mass spectrometer (Thermo Fisher Scientific Company) was used in this study.

The chemicals and reagents used in this study were purchased from Sigma-Aldrich, including the standard protein product with the purity of 85% α-lactalbumin, 90% *β*-lactoglobulin, 70% *α*-casein, 98% *β*-casein, and alkaline bovine trypsin (Sigma, ≥10,000 N-benzoyl-L-arginine-ethyl ester, BAEE). The polyethersulfone fiber membrane was purchased from Agela and Phenomenex (Article No. AS051320-19). Mass spectrometry analysis software: Thermo Proteome Discoverer (version 1.4) from Thermo Fisher Scientific Company; Xcalibur (Thermo Fisher Scientific Company) ingredient list for desalting whey powder. A commercial infant formula powder has been used. Desalted whey powder from the model D90 was used (protein 14.01%, lactose 83.69%, and moisture 1%, Fonterra Company, New Zealand).

METHODS

Enzymolysis Condition

The enzymolysis efficiency of whey protein and casein was different, which was related to the enzyme content and enzymolysis time. To reduce the detection error, it is very important to ensure the stability of the peptide obtained by protease hydrolysis. The change of peptide ratio of whey protein and casein in formula milk powder with enzymatic hydrolysis time was detected. Experiments were performed using formulated milk powder as the substrate and an enzymatic digestion using bovine-derived alkaline trypsin, where samples were configured using formulated milk powder at a protein concentration of 0.2 mg/ml (see pretreatment conditions for detailed procedure). The optimal enzymatic hydrolysis conditions were finally determined to be as follows: enzyme concentration:substrate concentration of 1:40; lysed for 28 h.

Pretreatment Conditions

Formula milk powder was dissolved in ultrapure water so that the protein concentration was between 0.1 mg/ml and 0.4 mg/ml, 250 μL solution was taken into the centrifuge tube, 150 μl of 500 mmol/L ammonium bicarbonate and 10 μl of 500 mmol/L dithiothreitol were added for reduction in the water bath at 70°C for 30 min. After cooling, 30 μl of 500 mmol/L iodoacetamide was added for alkylation in the dark for 30 min. After the aforementioned mixture was exposed to light for 10 min (to decompose iodoacetamide), 10 μl of 100 mmol/L calcium chloride solution and 50 μl of 0.5 mg/ml trypsin solution were added for enzyme digestion at 37°C for more than 28 h. After 10 μL of formic acid solution was added, the aforementioned mixture was set aside for 15 min to terminate the digestion. Pure water (490 μL) was added into the centrifuge tube and mixed well. After filtration with a 0.22 μm polyethersulfone fiber membrane, nanoliter liquid chromatography was applied for selective ion scanning analysis.

Preparation of Mixed Standards

Four protein standards of α-lactalbumin, *β*-lactoglobulin, α-casein, and *β*-casein were used to prepare mixed protein standards. For the milk produced by cows of different breeds in different seasons and regions, the contents of protein components in milk are different, resulting in changes in the contents of protein components in whey protein and casein protein. In this study, by referring to relevant literature (Kinghorn et al., 1995; Lönnerdal, 2014) and considering the actual processing loss and the error of detection method, the protein content of each component was set as follows: α-lactalbumin and *β*-lactoglobulin accounted for 20% and 50% of whey protein, respectively, and α-casein and *β*-casein accounted for 50 and 40% of casein, respectively (Tegge and Strke, 1982; Kunz and Lönnerdal, 1992; Kinghorn et al., 1995; Lara-Villoslada et al., 2005). According to the proportion of each protein component in whey protein and casein, the whey protein standard solution (20% *α*-lactalbumin and 50% *β*-lactoglobulin) and the casein standard solution (50% *α*-casein and 40% *β*-casein) were prepared. The prepared whey protein standard solution had the same protein concentration with that of the casein standard solution.

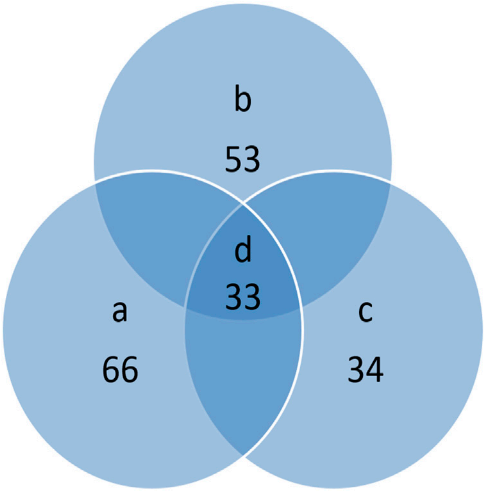

FIGURE 1 | Comparison of actual number of detected peptides with theoretical peptides.

Liquid Chromatographic Conditions

Acclaim® PepMap RSLC (75 μm × 15 cm, nanoViper C18, 2 μm, 100A Thermo Fisher Scientific) was selected as the separation column. Acclaim PepMapTM 100 (75 μm × 2 cm, nanoViper C18, 3 μm, 100A Thermo Fisher Scientific) was chosen as the enrichment column. The aqueous solution of 0.1% formic acid and 2% acetonitrile was taken as the mobile phase A; the solution of 0.1% formic acid acetonitrile and 20% water as the mobile phase B. The column temperature of 50°C, the flow rate of 0.25 μl/min, and the injection volume of 1 μl were adopted as the chromatographic parameters. The sample was enriched on the enriching column with the aqueous solution of 2% acetonitrile at the flow rate of 0.3 μl/min. The elution procedure was as follows. (**Table 1**).

Mass Detection Conditions

The Q Exactive-combined quadrupole Orbitrap mass spectrometer equipped with the Nanospray Flex nanoliter electrospray source was applied, in which the full mass was used to search for characteristic peptides, and parallel reaction monitoring (PRM) mode was used for quantitative detection of characteristic peptides. The data collection (ESI^+) mode of electrospray positive ion was adopted; Thermo Proteome Discoverer (version 1.4) was used to search the sequence database for analysis. The parameter settings of a relevant instrument and software (Xcalibur) were as follows: full scan mode was adopted for the data-dependent acquisition mode; Orbitrap acquisition was used for the primary mass spectrometer with the scanning range of 200–1,000 m/z and the resolution of 17500. MS1 was selected for the initial mass-to-charge ratio with the separation window of 1.0 m/z and the collision energy of NCE

TABLE 2 | Ion information of characteristic peptides.

Protein	Peptide	Mass (KDa)	Daughter ion (KDa)	Time (Min)
β-lg	TPEVDDEALEK	623.29	199.10	27.5
α-la	LDQWLCEK	546.23	268.16	55.2
α-cs	FALPQYLK	490.19	120.08	57.8
β-cs	VLPVPQK	390.75	372.22	23.7

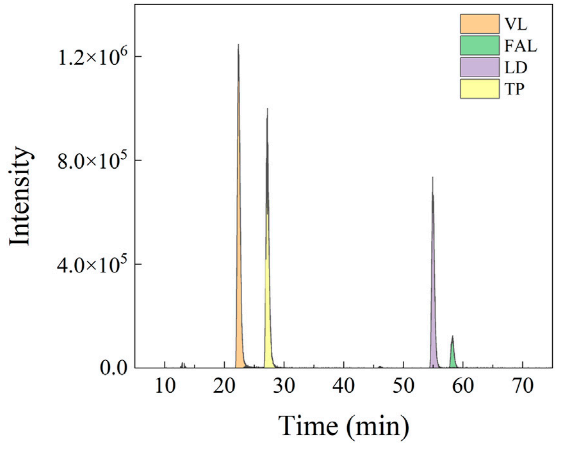

FIGURE 2 | Quantitative ion peak shape of four peptides.

27/28. The PRM mode was used as the quantitative scanning mode, and the parent ion information of characteristic peptide was set in the inclusion list.

Analysis of Mass Spectrometric Data

The raw data files of the obtained samples were compared with the database using Thermo Proteome Discoverer 1.4 software. SEQUEST HT was used as the search software of the comparison database, and the database was derived from UniProt (*Homo sapiens* and *Bos taurus* were used for the human and cattle, respectively). The specific parameters were set as follows: enzyme of trypsin (full), maximum missed cleavage site of 2, parent ion mass deviation of 10 ppm, and daughter ion mass deviation of 0.02Da. Dynamic modification was set as oxidation/M +15.995 Da and deamidation/N, Q +0.984Da, and fixed modification was set as carbamidomethyl/C +57.021Da.

The Calculation Formula

The final test results are not only affected by the changes in the protein content of each composition in whey protein and casein during the production process but also by the differences in the raw materials and the nutrients supplemented by the manufacturer. In order to eliminate the errors caused by the changes of the protein content, the ratios of two groups of proteins were chosen in the experiment, which were further corrected by formula calculation.

The main proteins in whey protein and casein in each group were compared. The ratios of the two groups of peptides were TP: FAL (β-Lg:α-cs) and LD:VL (α-La:β-cs) (TP, LD, FAL, and VL are the amino acids at the beginning of each peptide. TP: threonine and proline; FAL: phenylalanine, alanine, and leucine; LD: leucine and aspartic acid; VL: valine and leucine. They are used here to represent each peptide; the two peptides from whey protein were randomly compared with the two peptides from casein), respectively. According to the standard curve of the detected peptide response area ratio and protein ratio, two ratios of whey protein to casein of M (TP:FAL) and N (LD:VL) were obtained. The ratios of M and N can be changed into the fraction form as shown in the following **Eqs 1**, **2**:

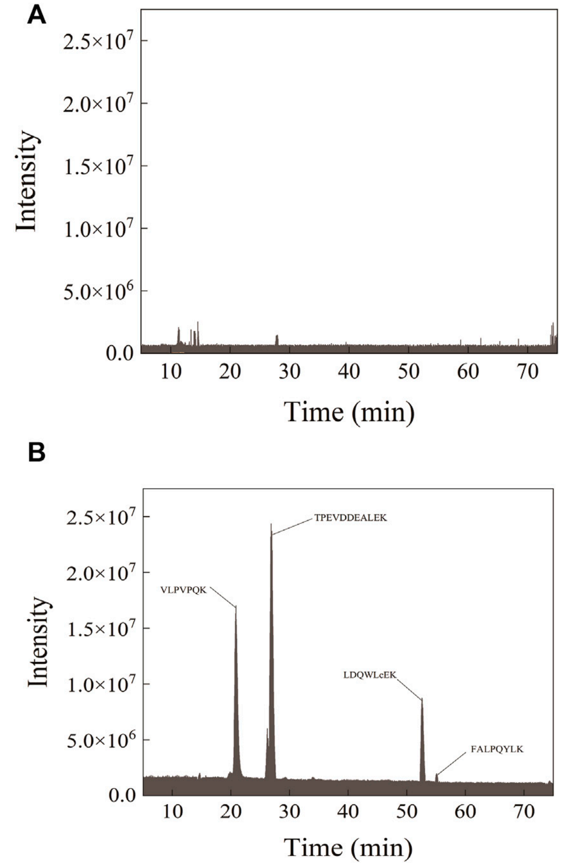

FIGURE 3 | Peptide ion diagrams of mass spectrometry PRM before **(A)** and after **(B)** enzymatic digestion of the sample.

$$M = \frac{m1}{m2} \tag{1}$$

$$N = \frac{n1}{n2}. \tag{2}$$

The ratios of the two groups of peptides were obtained from one analysis in the same matrix. It was specified that m1+m2 = n1+n2 = 1, and postulated that the protein concentration was X. Since the standard curve is drawn by mixing the standard protein solutions, the four main proteins of β-lg, α-la, α-cs, and β-cs in the mixed standard solution are shown in the following formulas:

Whey protein = 20% α-la + 50% β-lg + 30% miscellaneous protein.

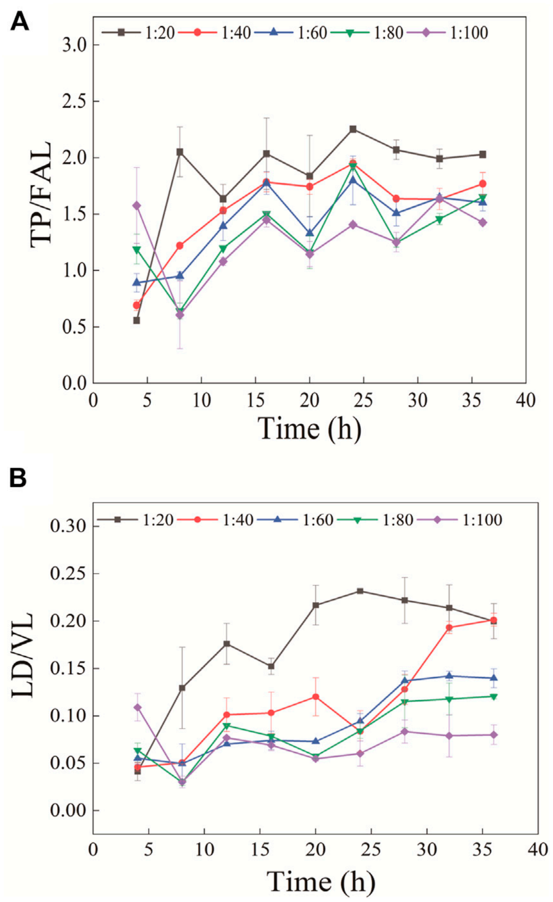

FIGURE 4 | Ratio of peptides **(A)** TP/FAL and **(B)** LD/VL changes with enzyme concentration and enzymatic hydrolysis time (*n* = 3).

Casein = 50% α-cs + 40% β-cs + 10% miscellaneous protein.

The true value of the four proteins is obtained in the following **Eqs 3–6**:

$$\beta-1g=\frac{m1}{m1+m2}X*50\%, \tag{3}$$

$$\alpha-cs=\frac{m2}{m1+m2}X*50\%, \tag{4}$$

$$\alpha-1a=\frac{n1}{n1+n2}X*20\%, \tag{5}$$

$$\beta-cs=\frac{n2}{n1+n2}X*40\%. \tag{6}$$

According to the proportion of each protein in the corresponding protein, the actual ratio of whey protein:casein is obtained by the following **Eq. 7**:

$$\frac{\frac{n1}{n1+n2}X*20\%+\frac{m1}{m1+m2}X*50\%}{0.7}\bigg/\frac{\frac{m2}{m1+m2}X*50\%+\frac{n2}{n1+n2}X*40\%}{0.9}=\frac{18n1+45m1}{35m2+28n2}=\frac{63MN+18N+45M}{35N+28M+63}. \tag{7}$$

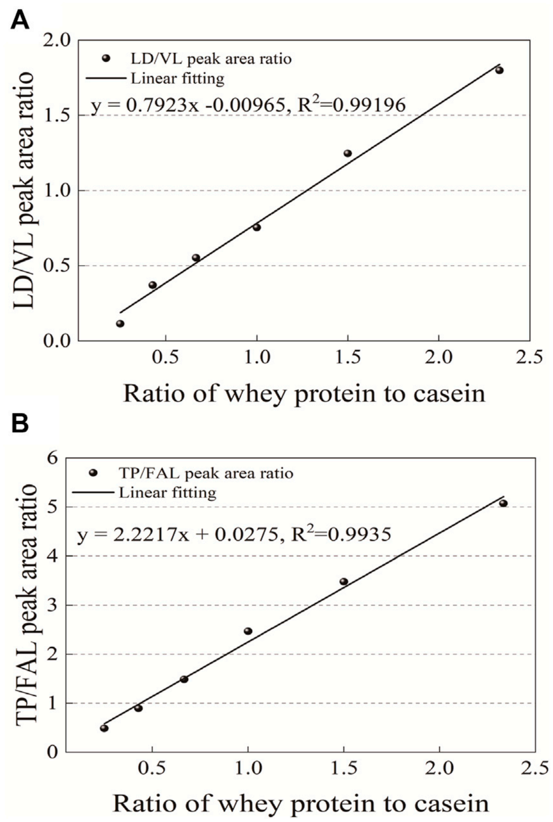

FIGURE 5 | Standard curve of the ratio of peptides in **(A)** LD/VL and **(B)** TP/FAL.

TABLE 3 | Linear regression equation of the ratio of peptides in the two groups (*n* = 3).

	Linear regression equation	R^2	RSD (%)
TP/FAL	y = 2.2217x + 0.0275	0.9935	2.88–8.06
LD/VL	y = 0.7923x-0.0096	0.992	3.01–9.75

The percentage of whey protein in total protein is obtained by the following **Eq. 8**:

$$\frac{63MN+18N+45M}{63MN+53N+73M+63}\times 100\%, \tag{8}$$

where M and N are the ratios of whey protein to casein determined by the two peptides of TP:FAL and LD:VL, respectively.

RESULTS AND DISCUSSION

Choice of Protein and Characteristic Peptides

To bring the protein content of milk formula closer to that of human milk, a certain amount of milk protein is industrially

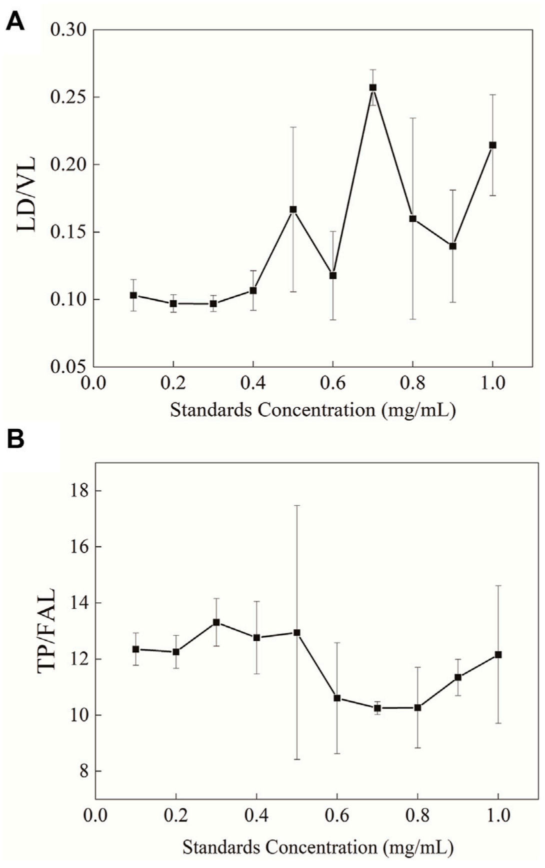

FIGURE 6 | Changes in the ratio of peptide in the samples with different protein concentrations after enzymolysis **(A)** LD/VL and **(B)** TP/FAL.

added to meet the criterion of whey protein:casein ratio of 60:40 in the infant formula (Kunz and Lönnerdal, 1992; Wood et al., 2021). Milk protein is composed of whey protein and casein, in which α-lactalbumin and β-lactoglobulin account for 70–80% of whey protein (Lara-Villoslada et al., 2005; Lönnerdal, 2014) and α-casein and β-casein account for about 90% of casein (Kunz and Lönnerdal, 1992). Therefore, the two main types of whey protein and two main types of casein were used to detect the ratio of whey protein to casein in the infant formula. Four cow protein standard substances and commercially available formula milk powder were chosen to perform a full scan of peptides and simulate enzyme digestion of all the aforementioned protein with the Peptide Mass tool provided by the ExPASy website (https://web.expasy.org/peptide_mass/) to get the theoretically calculated peptides and screen the specific peptides of target protein (**Figure 1**). As shown in **Figure 1** , the letter a represents the theoretical digestion peptides; the letter b represents the whey protein peptides detected after the enzyme digestion of formula milk powder; the letter c represents the peptides detected after standard protease digestion; the letter d represents the common peptides detected in all three samples. To ensure the representativeness of the selected peptides, BLAST comparison analysis of proteins was performed on the NCBI website (https://www.ncbi.nlm.nih.gov/). Considering that the difference in peptide length might have an impact on mass spectrometry detection, peptide sequences are selected with similar lengths as much as possible, and finally the characteristic peptides of four kinds of proteins are selected (**Table 2**).

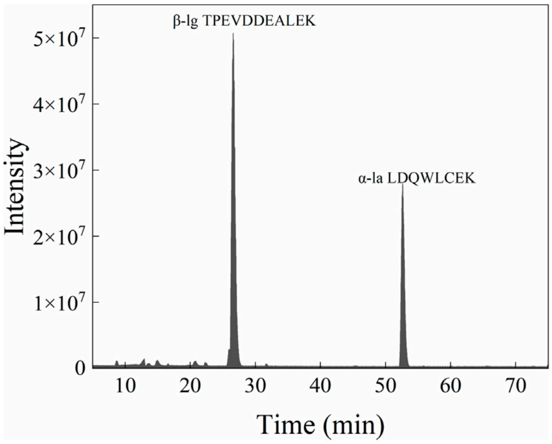

FIGURE 7 | Mass spectrometric analysis results of desalted whey powder with protein concentration of 0.2 mg/ml.

METHOD VALIDATION

Peptide Specificity

In the detected sample, the parent ions of the four characteristic peptides and the selected single-daughter ions showed steep and symmetrical peaks without interference (**Figure 2**). Separation of four peptides from infant formula milk powder was detected by mass spectrometry, with the protein concentration 0.2 mg/ml. There was no target peak in the chromatogram of the milk powder sample undigested by trypsin (**Figure 3**).

Complete Enzymolysis

In the experiment, the enzymolysis conditions for stable protein cleavage were obtained by changing enzymolysis time and enzyme concentration. The finally balanced peptide ratios obtained at different enzyme concentrations were different (**Figure 4**). This might be caused by the enzyme inactivation due to autohydrolysis during the enzymolysis process, which made it impossible to further enzymatically hydrolyze protein. Therefore, the ratio of peptides after stable enzymatic hydrolysis changes in a certain trend with the enzyme concentration. The final peptide ratio was consistent in the TP/FAL digestion curve. Compared with TP/FAL, this phenomenon was more evident in LD/VL. In the LD/VL enzymatic hydrolysis curve, the final peptide ratio of the enzyme concentration tended to be consistent when the enzyme concentration was greater than 1:40. Therefore, we believe that the protein in this group can be completely digested into peptides at the enzyme concentration of

TABLE 4 | Spiked recovery rate (n = 3).

	Spiked level (mg)	Theoretical value (mg)	Detection value (mg)	Recovery (%)	RSD (%)
Substrate	0	—	19.48	—	7.35
Desalted whey powder	30	23.08	23.03	98.63	0.84
	60	26.68	26.90	103.06	7.42
	90	30.28	31.72	113.33	1.83
	120	33.88	34.11	101.62	0.84

TABLE 5 | Intragroup and intergroup precisions of formula milk powder (n = 3).

Sample	Peptide	Day	Intraday			Interday		
			Average	SD	RSD (%)	Average	SD	RSD (%)
1	TP/FAL	1	6.10	0.36	5.83	6.07	0.037	0.61
		2	6.03	0.29	4.88			
		3	6.09	0.16	2.61			
	LD/VL	1	0.59	0.022	3.69	0.60	0.014	2.28
		2	0.61	0.029	4.75			
		3	0.59	0.023	3.92			
2	TP/FAL	1	6.03	0.24	4.05	5.83	0.24	4.19
		2	5.60	0.17	3.05			
		3	5.62	0.13	2.24			
	LD/VL	1	0.59	0.031	5.26	0.61	0.032	5.29
		2	0.63	0.013	2.03			
		3	0.56	0.022	3.95			
3	TP/FAL	1	7.39	0.22	3.01	7.69	0.30	3.93
		2	7.69	0.16	2.07			
		3	7.99	0.66	8.32			
	LD/VL	1	0.54	0.045	8.29	0.60	0.066	11.02
		2	0.58	0.032	5.55			
		3	0.67	0.063	9.35			

TABLE 6 | Quantitative detection of whey protein with different processing techniques (n = 3).

	TP/FAL	LD/VL	Whey protein content (%)
Raw milk	0.42	0.0021	17.23
Homogenization	0.42	0.0021	17.39
Pasteurization	0.44	0.0020	17.93
Ultrahigh-temperature sterilization	0.45	0.0023	18.14
Spray drying	0.39	0.0024	16.59
Average value	0.42	0.0022	17.51
SD	0.024	0.00016	0.052
RSD (%)	5.65	7.50	2.97

TABLE 7 | Whey protein content of different brands of domestic and international formula milk powders.

Milk powder	TP/FAL	LD/VL	Whey protein content (%)
Sample 1	7.49	0.58	63.71
Sample 2	5.82	0.57	60.86
Sample 3	5.85	0.61	61.40
Sample 4	4.97	0.56	58.72
Sample 5	4.09	0.94	60.76
Sample 6	4.78	0.83	61.77
Sample 7	6.92	0.64	63.80
Sample 8	6.75	0.79	65.48
Sample 9	8.59	0.45	62.96
Sample 10	6.67	0.46	60.54
Sample 11	4.05	0.85	59.71

1:40. It was shown that with the concentration ratio of enzyme and substrate of 1:20, the ratio of peptides in the two groups tended to be stable after 28 h, and the error range was smaller.

Linearity Verification

The relationship between the ratios of the two peptides was observed according to the gradient of six different concentration ratios of whey protein to casein (20:80, 30:70, 40:60, 50:50, 60:40, and 70:30) in the standard solution prepared with different ratios of whey protein and casein. Using this as a standard, the mass ratio of the two proteins in the sample can be obtained from the peak area ratio of peptides in the two groups after enzymatic hydrolysis (**Figure 5**). The 2-level linear regression equations of the characteristic peptides had a good linear relationship and a determination coefficient ($r^2 > 0.99$) (**Table 3**).

The Concentration Range for the Method

Whey protein was quantified with peptide ratios in four different proteins in the study. In order to ensure the stability of enzymatic hydrolysis under the experimental conditions, the sample detection range of this method was determined. The changes in the ratio of peptides in two groups after the aforementioned pretreatment were observed using 10 different protein concentration gradients (**Figure 6**). It was shown that when the protein concentration in the sample was below 0.4 mg/ml, the ratio of peptides in the two groups remained stable with small variation in the error.

Verification of the Recovery Rate

To simulate the change of whey protein in the industrial production process, the demineralized whey powder that was used to offer whey protein in the production process of formula milk powder (**Figure 7**) (it was determined that the protein in the demineralized whey powder did not contain casein, and the content of whey protein accounted for 14% in the total whey powder) was used as the spiked standard, and the spiked samples were pretreated and analyzed by the aforementioned method. The recovery test was performed by comparing the measured concentration of the control sample and the spiked sample with the theoretical concentration (**Table 4**). The recovery rate of the spiked sample was between 98.63% and 113.33%, and the RSD was between 0.84% and 7.42%, which indicated that the method had good accuracy.

Intraday and Daytime Precision

According to the aforementioned experimental operation, three different commercial formula milk powders were pretreated in three consecutive days to evaluate the intraday and interday accuracies of the method. The whey protein content of the products varied according to the manufacturers of commercially available milk powder, and the TP/FAL value in sample three was higher than that in the other two samples (**Table 5**). The RSDs of intraday and interday precisions were 2.03–9.35% and 0.61–11.02%, respectively. It was shown that the method had good intragroup and intergroup precisions.

Considering the purity issues of the experimentally used protein standards and the possible errors during experimental procedures, we considered the detection precision when the RSD of repeated detection was less than 10%. When verifying the interday precision, the samples to be tested are prone to change on their own due to the large time span, so we considered the precision of the assay to be qualified when the RSD was less than 12% (Ke et al., 2017).

The Impact of Production and Processing on Testing Methods

The processing process of formula milk powder will affect the detection of whey protein, leading to changes in the content of whey protein in the same batch of samples before and after processing, so it was explored whether the production process might have an impact on this method. The changes of the whey protein content in milk powder were measured using the processes of sterilization (here, including pasteurization and ultrahigh-temperature sterilization), spray drying, and so on during the production of formula milk powder with raw milk as the starting material, so as to study the impact of processing technology on the detection method (**Table 6**). It was shown that the content of the finally detected whey protein was similar after the treatment using different processes, with an RSD of 2.97%, and the average value was almost the same as that of raw milk. This proves that processing technology in the industrial production process has no significant influence on the detection of the whey protein content by this method.

Application of the Method in Actual Sample Detection

Whey protein was detected in the infant formula of 11 domestic and international brands in this trial. The results showed that whey protein accounted for more than 60% of the total protein content in 81.8% of the formula milk powder, it was also very close to the 60% content standard in the remaining ones. (**Table 7**).

CONCLUSION

This study established an analytical method to quantitatively determine the percentage of whey protein in the infant formula. By detecting the characteristic peptides of two whey proteins and two caseins, an ultrahigh-performance liquid chromatography–mass spectrometry (UHPLC–MS/MS) method was established for simultaneous quantification of two whey proteins and two caseins. In mass spectrometry analysis, matrix interference was avoided by comparing the two groups of peptides. The accuracy, sensitivity, and selectivity of the current method were verified by the calibration curve, intraday and interday precisions, and recovery rate (recovery rate 98.63–113.33%, determination coefficient $r^2 > 0.99$, intraday RSD <10%, and interday RSD <12%). A specific formula has been established to calculate the content of whey protein in formula milk powder. Through the detection of different processed samples, it was determined that the production process of formula milk powder would not change the testing results of this method. The method was applied to the routine testing of infant formulas of different commercial brands ($n = 11$). The results showed that the whey protein content accounted for more than 60% of the total protein in infant milk powders of most brands, and it was slightly less than 60% in only a small part of milk powder. Compared with other quantitative methods, this method is simple to operate in production practice, offers substantial savings in testing costs, and the test results are not affected by production and processing operations.

DATA AVAILABILITY STATEMENT

The original contributions presented in the study are included in the article/Supplementary Material, further inquiries can be directed to the corresponding author.

AUTHOR CONTRIBUTIONS

TX: formal analysis, writing—original draft, visualization, validation, methodology. LC: conceptualization and funding acquisition. JC and JZ: related technical guidance and formal analysis. KY and WQ: writing—review and editing.

FUNDING

Guangxi Science and Technology project (AD20297088), the National Natural Science Foundation of China (Grant No. 32072191), the National Key R&D Program of China (Grant No. 2021YFD2100700), Daxing District Major Scientific and Technological Achievements Transformation Project (Grant No. 2020006), Beijing Science and Technology Plan (Grant No. Z201100008020005), and the National Key R&D Program of China (Grant No. 2019YFF0216702).

REFERENCES

Aludatt, M. H., Rababah, T., Alhamad, M. N., Alodat, M., Al-Mahasneh, M. A., Gammoh, S., et al. (2017). Molecular Characterization and Bio-Functional Property Determination Using SDS-PAGE and RP-HPLC of Protein Fractions from Two Nigella Species. *Food Chem.* 230, 125–134. doi:10.1016/j.foodchem.2017.03.025

Bonfatti, V., Giantin, M., Rostellato, R., Dacasto, M., and Carnier, P. (2013). Separation and Quantification of Water buffalo Milk Protein Fractions and Genetic Variants by RP-HPLC. *Food Chem.* 136, 364–367. doi:10.1016/j.foodchem.2012.09.002

Chen, G., and Pramanik, B. N. (2009). Application of LC/MS to Proteomics Studies: Current Status and Future Prospects. *Drug Discov. Today* 14, 465–471. doi:10.1016/j.drudis.2009.02.007

Czerwenka, C., Maier, I. N., Potocnik, N., Pittner, F., and Lindner, W. (2007). Absolute Quantitation of β-Lactoglobulin by Protein Liquid Chromatography−Mass Spectrometry and its Application to Different Milk Products. *Anal. Chem.* 79, 5165–5172. doi:10.1021/ac062367d

Feng, P., and Baugh, S. (2013). Determination of Whey Protein Content in Bovine Milk-Based Infant Formula Finished Products Using Amino Acids Calculation Method: AOAC First Action 2012.08. *J. AOAC Int.* 96, 795–797. doi:10.5740/jaoacint.13-076

Feng, P., Fuerer, C., McMahon, A., Arendse, K., Chanady, A., Chen, H., et al. (2018). Quantification of Whey Protein Content in Milk-Based Infant Formula Powders by Sodium Dodecyl Sulfate-Capillary Gel Electrophoresis (SDS-CGE): Multilaboratory Testing Study, Final Action 2016.15. *J. AOAC Int.* 101, 1566–1577. doi:10.5740/jaoacint.18-0057

Fenn, J. B., Mann, M., Meng, C. K., Wong, S. F., and Whitehouse, C. M. (2012). Electrospray Ionization for Mass Spectrometry of Large Biomolecules. *Science* 246, 64–71. doi:10.1126/science.2675315

Grochocki, W., Markuszewski, M. J., and Quirino, J. P. (2015). Multidimensional Capillary Electrophoresis. *Electrophoresis* 36, 135–143. doi:10.1002/elps.201400416

Higgs, R. E., Knierman, M. D., Gelfanova, V., Butler, J. P., and Hale, J. E. (2008). Label-Free LC-MS Method for the Identification of Biomarkers. *Methods Mol. Biol.* 428, 209–230. doi:10.1007/978-1-59745-117-8_12

Ke, X., Zhang, J., Lai, S., Chen, Q., Zhang, Y., Jiang, Y., et al. (2017). Quantitative Analysis of Cow Whole Milk and Whey Powder Adulteration Percentage in Goat and Sheep Milk Products by Isotopic Dilution-Ultra-High Performance Liquid Chromatography-Tandem Mass Spectrometry. *Anal. Bioanal. Chem.* 409, 213–224. doi:10.1007/s00216-016-9987-9

Kinghorn, N. M., Norris, C. S., Paterson, G. R., and Otter, D. E. (1995). Comparison of Capillary Electrophoresis with Traditional Methods to Analyse Bovine Whey Proteins. *J. Chromatogr. A* 700, 111–123. doi:10.1016/0021-9673(95)00117-6

Krause, R. G. E., and Goldring, J. P. D. (2019). Crystal Violet Stains Proteins in SDS-PAGE Gels and Zymograms. *Anal. Biochem.* 566, 107–115. doi:10.1016/j.ab.2018.11.015

Kunz, C., and Lönnerdal, B. (1992). Re-evaluation of the Whey Protein/casein Ratio of Human Milk. *Acta Paediatr.* 81, 107–112. doi:10.1111/j.1651-2227.1992.tb12184.x

Lara-Villoslada, F., Olivares, M., and Xaus, J. (2005). The Balance between Caseins and Whey Proteins in Cow's Milk Determines its Allergenicity. *J. Dairy Sci.* 88, 1654–1660. doi:10.3168/jds.s0022-0302(05)72837-x

Lemos, V. F., Guaraná, E. L. S., Afonso, J. A. B., Fagliari, J. J., Silva, P. C., Soares, P. C., et al. (2015). Effects of Intramammary Infection on Whey Proteinograms of Sheep during Lactation. *Pesq. Vet. Bras.* 35, 230–236. doi:10.1590/s0100-736x2015000300004

Lönnerdal, B. (2014). Infant Formula and Infant Nutrition: Bioactive Proteins of Human Milk and Implications for Composition of Infant Formulas. *Am. J. Clin. Nutr.* 99, 712S–717S. doi:10.3945/ajcn.113.071993

Qian, W.-J., Jacobs, J. M., Liu, T., Camp, D. G., 2nd, and Camp, D. G. (2006). Advances and Challenges in Liquid Chromatography-Mass Spectrometry-Based Proteomics Profiling for Clinical Applications. *Mol. Cell Proteomics* 5, 1727–1744. doi:10.1074/mcp.m600162-mcp200

Restani, P., Velona, T., Plebani, A., Ugazio, A. G., Poiesi, C., Muraro, A., et al. (1995). Evaluation by SDS-PAGE and Immunoblotting of Residual Antigenicity in Hydrolysed Protein Formulas. *Clin. Exp. Allergy* 25, 651–658. doi:10.1111/j.1365-2222.1995.tb01113.x

Tegge, G., and Strke, S.-. (1982). *Lehrbuch der Lebensmittelchemie (Text-book of Food Chemistry).* New York: Springer-Verlag.

Veledo, M. T., de Frutos, M., and Diez-Masa, J. C. (2005). Development of a Method for Quantitative Analysis of the Major Whey Proteins by Capillary Electrophoresis with On-Capillary Derivatization and Laser-Induced Fluorescence Detection. *J. Sep. Sci.* 28, 935–940. doi:10.1002/jssc.200500016

Wang, Z., Chen, Q., Wu, Q., Li, Q., Chen, D., and Chu, X. (2018). Evaluation of Mutual Interference between Bovine α-lactalbumin Peptide and its Isotope-Labeled Peptide in Whey Protein Analysis Using Liquid Chromatography-Tandem Mass Spectrometry. *J. Chromatogr. A* 1533, 94–101. doi:10.1016/j.chroma.2017.12.024

Winter, D., Seidler, J., Ziv-Lehrman, S., Shiloh, Y., and Lehmann, W. D. (2009). Simultaneous Identification and Quantification of Proteins by Differential 16O/18O Labeling and UPLC-MS/MS Applied to Mouse Cerebellar Phosphoproteome Following Irradiation. *Anticancer Res.* 29, 4949–4958.

Wood, E. L., Christian, D. G., Arafat, M., McColl, L. K., Prosser, C. G., Carpenter, E. A., et al. (2021). Adjustment of Whey:Casein Ratio from 20:80 to 60:40 in Milk Formulation Affects Food Intake and Brainstem and Hypothalamic Neuronal Activation and Gene Expression in Laboratory Mice. *Foods* 10, 658. doi:10.3390/foods10030658

Conflict of Interest: TX, JC, KY, WQ, JZ and LC were employed by Beijing Sanyuan Foods Co. Ltd.

The remaining author declares that the research was conducted in the absence of any commercial or financial relationships that could be construed as a potential conflict of interest.

ORIGINAL RESEARCH
published: 10 May 2022
doi: 10.3389/fchem.2022.888587

A Pyridazinone Compound for Effectively Treating Non-alcoholic Steatohepatitis by Targeting THRβ

Hao Cheng[1,2,3,4], *Xiao-Bo Wang*[2,4], *Ying Zhi*[1,2,3,4], *Bo Liu*[1,2,3,4], *Na Liu*[1], *Meng-Jun Li*[1] *and Yan-Ling Mu*[1,2,3,4]*

[1]School of Pharmacy and Pharmaceutical Sciences, Shandong First Medical University, Jinan, China, [2]Institute of Materia Medica, Shandong Academy of Medical Sciences, Jinan, China, [3]Key Laboratory for Biotech-Drugs Ministry of Health, Jinan, China, [4]Key Laboratory for RareUncommon Diseases of Shandong Province, Jinan, China

Developing effective therapies and medicines to conquer nonalcoholic steatohepatitis (NASH) is of great significance for public health and is faced with a major challenge. The activation of the thyroid hormone receptor agonist THRβ could be regulated by target drugs that has brought huge potential to the treatment of NASH. In this work, pyridazinone compound YWS01125 was synthesized for the first time. In this study, an ultra-performance liquid chromatography–tandem mass spectrometry (UPLC-MS/MS) method for YWS01125 determination was established, and the pharmacokinetics of YWS01125 was evaluated. The half-life values (t1/2)of three different doses of YWS01125 was 189.12 ± 95.27, 152.64 ± 37.98, and 181.95 ± 64.25 min, respectively, and the tissue distribution studies demonstrated that YWS01125 was quickly distributed to various tissues. With successful application in the pharmacokinetics study of YWS01125, the UPLC-MS/MS method has shown characteristics of high sensitivity, rapidity, and good selectivity.

Keywords: pyridazinones, UPLC-MS/MS, pharmacokinetics, NASH, tissue distribution

Edited by:
Dejin Zang,
Tsinghua University, China

Reviewed by:
Pengju Zhang,
Shandong University, China
Xinhua Liu,
Fudan University, China
Ziying Wang,
Shandong University, China

Correspondence:
Yan-Ling Mu
807787252@qq.com

Specialty section:
This article was submitted to Analytical Chemistry, a section of the journal Frontiers in Chemistry

Received: *03 March 2022*
Accepted: *17 March 2022*
Published: *10 May 2022*

Citation:
Cheng H, Wang X-B, Zhi Y, Liu B, Liu N, Li M-J and Mu Y-L (2022) A Pyridazinone Compound for Effectively Treating Non-alcoholic Steatohepatitis by Targeting THRβ. Front. Chem. 10:888587. doi: 10.3389/fchem.2022.888587

INTRODUCTION

Nonalcoholic fatty liver disease (NAFLD) is characterized by heterotopic liver fat and steatosis (Dibba et al., 2018; Pierantonelli and Svegliati, 2019). NAFLD included a series of liver diseases, such as nonalcoholic fatty liver (NAFL), Nonalcoholic steatohepatitis (NASH), and liver fibrosis (Abdelbasset et al., 2019). With the increase of obesity and diabetes patients, the global incidence of NAFLD has shown an upward trend year by year. A few studies (Hannah et al., 2016; Friedman et al., 2018a; Kefala and Tziomalos, 2019; Janssen et al., 2020; Harrison et al., 2021) have reported that the global prevalence of NAFLD approximately accounted for 24–25% of the total population, which has been predicted to reach 28.40% in 2030.

The pathogenesis of NASH is very complicated. The "two-hit" theory is a widely accepted mechanism for NASH (Sumida et al., 2018) in which excess food intake leads to the accumulation of fat in the liver. However, with further research (Takahashi et al., 2014; Park et al., 2018; Peng et al., 2020), the "two-hit" theory can no longer reveal the complexity of this disease (Orci et al., 2016). Therefore, the "multiple-hit" theory proposed by Tilg and Moschen, 2010 (Younossi, et al., 2019) has gradually replaced the "two-hit" as the most widely accepted theory. The proposed mechanisms under this theory include disorders of lipid metabolism, lipid toxicity, insulin resistance, oxidative stress, mitochondrial dysfunction,

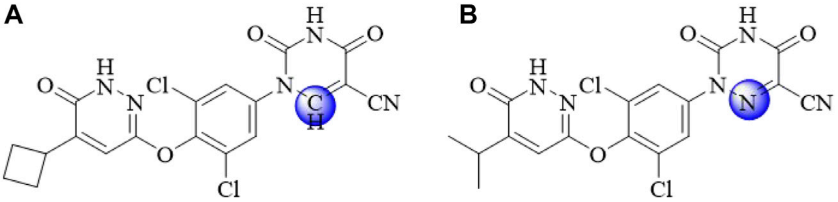

FIGURE 1 | The chemical structures of **YWS01125 (A)** and **MGL-3196 (B)**.

changes in the intestinal microbiota, apoptosis, inflammation, and genetic susceptibility as the main components of this hypothesis (Janssen, et al., 2020). NASH can not only affect the functional structure of the liver but also increase the incidence of type II diabetes, cardiovascular disease, and chronic kidney disease (Castera et al., 2019).

Treatments for NASH can be divided into two main categories: drug therapy and nondrug therapy. Nondrug treatment is used to make appropriate adjustments in diet, physical exercise, and psychological stress relief, while drug therapy may include antioxidant therapy, lipid-lowering drugs, and weight-loss drugs; however, no highly effective drugs are available in the treatment of NASH in the present.

Therefore, it is extremely urgent to find drug targets to develop effective treatments. Thyroid hormone receptor agonist THR (namely, T3 and T4) includes two subtypes: THRα and THRβ. THRα is highly expressed in the skeletal muscle and heart, mainly regulating the heart rate, while THRβ is highly expressed in the liver, kidneys, and pituitary gland, mainly regulating the release of thyroid stimulating hormone (Younossi, 2019). THRβ selective agonist improves blood lipids, reduces Low density lipoprotein cholesterol (LDL) cholesterol levels, increases High density lipoprotein cholesterol (HDL) cholesterol reuptake, and reduces plasma triglyceride levels. Due to some side effects of THRα, THRβ was selected for a series of studies. Clinical trials (Tacke, 2018) have found that THRβ has good lipid-lowering properties in animals and small clinical trials. **MGL-3196** (**Figure 1B**), a selective THRβ agonist, is currently being evaluated in phase 3 clinical trials. It has been reported that resmetirom reduced both low density lipoprotein and triglyceride effectively and showed a liver-specific distribution, endowing it with good safety and making it a promising compound in the treatment of NASH (Harrison et al., 2019).

With regard to the fact that the azauracil moiety is a privilege scaffold for selective THRβ activation, we designed and synthesized a series of pyrazinone compounds bearing azauracil structure or its bioisostere. As a novel bioisostere of cynoazauracils, uracil derivatives **YWS01125** possesses the best selectivity and activity for THRβ with low cytotoxicity and was selected as the lead compound. In the pharmacodynamic study, it showed good *in vivo* efficacy in rat, such as hepatoprotective effect in an acute liver injury model, lipid-lowering function on acute hyperlipidemia mice, and alleviation of NASH. Therefore, we further conducted pharmacodynamics and pharmacokinetics research of **YWS01125** (**Figure 1A**). Firstly, we detected the metabolization of YWS01125 based on ultra-performance liquid chromatography–tandem mass spectrometry (UPLC-MS/MS). Then, the pharmacokinetics and tissue distribution of **YWS01125** in mice were further studied. As far as we know, this is the first reported study on the synthesis, pharmacokinetics, and tissue distribution of a novel THRβ selective agonist after oral administration.

MATERIALS AND METHODS

Chemicals and Reagents

Pyridazinones: **YWS01125** (purity of 98.83%) was supplied by the Institute of Materia Medica, Shandong Academy of Medical Sciences (Jinan, China); **MGL-3196** (internal standard, IS) was purchased from Selleck Corporation (Beijing, China). The structural equations of the two compounds are shown in **Figure 1**. Nicotinamide adenine dinucleotide sodium phosphate (NADP), glucose-6-phosphate disodium salt (G-6-P), and glucose-6-phosphate dehydrogenase (G-6-PDH) were purchased from Sigma (Sigma, Germany). The reagent was purchased from Sigma Company (St. Louis, MO) and was chromatographically pure. The rat and human liver microsomes were purchased from Red Company (Shanghai, China). HPLC-grade methanol was supplied by Thermo Fisher Scientific Co. Ltd. (Shanghai, China); HPLC-grade acetonitrile was offered by Thermo Fisher Scientific Co. Ltd. (Shanghai, China); HPLC-grade formic acid was provided by Tianjin Kermel Chemical Reagent Co. Ltd. (Tianjin, China); purified water used for the all analysis was employed by Wahaha Co. Ltd. (Hangzhou, China).

Chemistry

The synthetic route of pyrazinone compound YWS01125 is as depicted in **Scheme 1**. Synthesis of 1-(3,5-dichloro-4-((5-cyclobutyl-6-oxo-1,6-dihydropyridazin-3-yl) oxy) phenyl)-2,4-dioxo-1,2,3,4-tetrahydropyrimidine-5-carbonitrile (YWS01125).

Synthesis of ethyl (2-cyano-3-methoxyacryloyl) carbamate (1).

Ethyl (2-cyanoacetyl) carbamate (3.12 g, 20 mmol), trimethyl orthoformate (3.5 ml, 40 mmol), acetic anhydride (20 ml), and acetonitrile (40 ml) were added to a 100-ml flask. The solution was stirred at 80°C for 4 h, and then the reaction stopped. The solvent was evaporated. Diethyl ether (50 ml) was added to the mixture, and the resulting suspension was kept at 2–8°C overnight. The suspension was filtered and rinsed several times with ether (3 × 50 ml) to give target

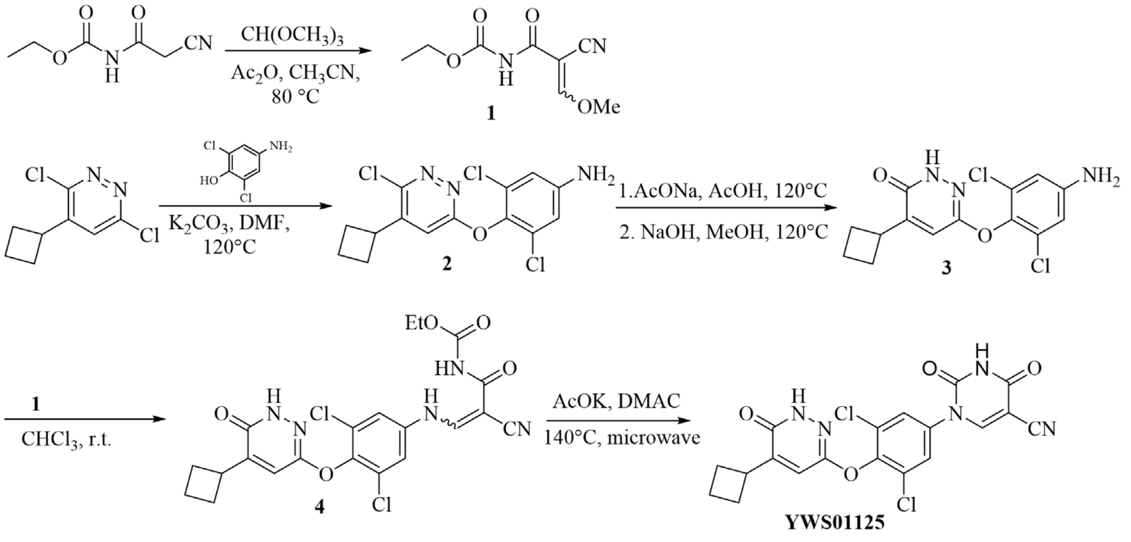

SCHEME 1 | (A) $CH(OCH_3)_3$, Ac_2O, CH_3CN, 80°C; **(B)** 6-dichloro-4-cyclobutylpyridine, K_2CO_3, DMF, 120°C; **(C)** 1. AcONa, AcOH, 120°C; 2. NaOH, MeOH, 100°C; **(D)** ethyl (2-cyano-3-methoxyacryloyl) carbamate, $CHCl_3$, r.t.; **(E)** AcOK, DMAC, 140°C, microwave.

compound **1** as a white solid (2.20 g, 56%). ESI m/z: $C_8H_{11}N_2O_4$ (M + H)+m/z = 199.1; molecular weight, 198.1780.

Synthesis of 3,5-dichloro-4-((6-chloro-5-cyclobutylpyridazin-3-yl) oxy) aniline (2).

The solution of 6-dichloro-4-cyclobutylpyridine (1.62 g, 8.00 mmol), 2, 6-dichloro-4-aminophenol (1.42 g, 8.00 mmol), and potassium carbonate (2.21 g, 16.00 mmol) in *N, N*-dimethylformamide (20 ml) was stirred at 120°C for 3 h. The reaction was stopped. An appropriate amount of diatomite was added into the sand core funnel, and the reaction solution was pumped and filtered to collect the filtrate. The filtrate was washed with 10% sodium chloride aqueous solution and saturated sodium chloride and was dried with anhydrous sodium sulfate. The solvent was evaporated to give a crude product which was purified by column chromatography (petroleum ether/ethyl acetate = 4/1) to obtain compound **2** as a light-brown solid (1.36 g, 50%). ESI m/z: $C_{14}H_{13}Cl_3N_3O$ (M + H)+344.0; molecular weight, 344.6200.

Synthesis of 6-(4-amino-2,6-dichlorophenoxy)-4-cyclobutylpyridazin-3(2H)-one (3).

In a 100-ml round-bottom flask, the solution of compound **2** (1.36 g, 3.97 mmol), sodium acetate (1.30 g, 15.86 mmol), and glacial acetic acid (20 ml) was stirred at 120°C for 24 h. The reaction was stopped and the mixture cooled to room temperature. Then, 10 ml of water was added. The pH was adjusted to 9–10 with 1N HCl. The aqueous phase was extracted with ethyl acetate (25 ml × 3). The organic phase was combined, washed with brine, and dried over anhydrous sodium sulfate. The solvent was evaporated to give a crude product which was used directly in the next step without further purification.

The above obtained solid was dissolved in methanol (24 ml), and NaOH solution (1N, 24 ml) was added. The resulting mixture was stirred at 100°C for 24 h. The reaction was stopped. The solvent was evaporated. The suspension was extracted with ethyl acetate (25 ml × 3), and then the organic phase was combined, washed with brine, and dried over anhydrous sodium sulfate. The solution was concentrated under pressure and purified by column chromatography (petroleum ether/ethyl acetate = 2/1) to give compound **3** as a gray solid (0.57 g, 44%). ESI m/z: $C_{14}H_{14}Cl_2N_3O_2$ (M + H)+326.0; molecular weight, 326.1770.

Synthesis of ethyl (2-cyano-3-((3,5-dichloro-4-((5-cyclobutyl-6-oxo-1,6-dihydropy-ridazin-3-yl) oxy) phenyl) amino) acryloyl) carbamate (4).

To a 10-ml reaction tube were added **1** (71 mg, 0.36 mmol), **3** (98 mg, 0.30 mmol), and chloroform (5 ml). The reaction mixture was stirred at reflux for 1 h and the reaction stopped. The mixture was then cooled to room temperature. The suspension was filtered and rinsed with ether. The filtrate cake was dried at 50°C. Compound **4** was obtained as a white solid (80 mg, 54%). ESI m/z: $C_{21}H_{20}Cl_2N_2O_5$ (M + H)+492.1; molecular weight, 492.2130.

1-(3,5-dichloro-4-((5-cyclobutyl-6-oxo-1,6-dihydropyridazin-3-yl)oxy)phenyl)-2,4-dioxo-1,2,3,4-tetrahydropyrimidine-5-carbonitrile (YWS01125).

Compound **4** (80 mg, 0.17 mmol) was added into a 10-ml microwave reaction tube, followed by the addition of potassium acetate (33 mg, 0.34 mmol) and N, N-dimethylacetamide (2 ml). The mixture reacted at 140°C for 30 min, then stopped. The reaction solution was diluted with ethyl acetate (20 ml), transferred into a 150-ml separating funnel, and diluted with water (10 ml). The organic phase was separated, washed with brine, and dried over anhydrous sodium sulfate. The solvent was evaporated to give a crude mixture which was purified by column chromatography (methylene chloride/methanol = 30/1 to 10/1) to give the target compound **YWS01125** as a light-yellow solid (37 mg, 52%). 1H NMR (600 MHz, DMSO-d6) δ 12.31 (s, 1H), 12.22 (s, 1H), 8.90 (s, 1H), 7.88 (s, 2H), 7.50 (s, 1H), 3.59–3.53

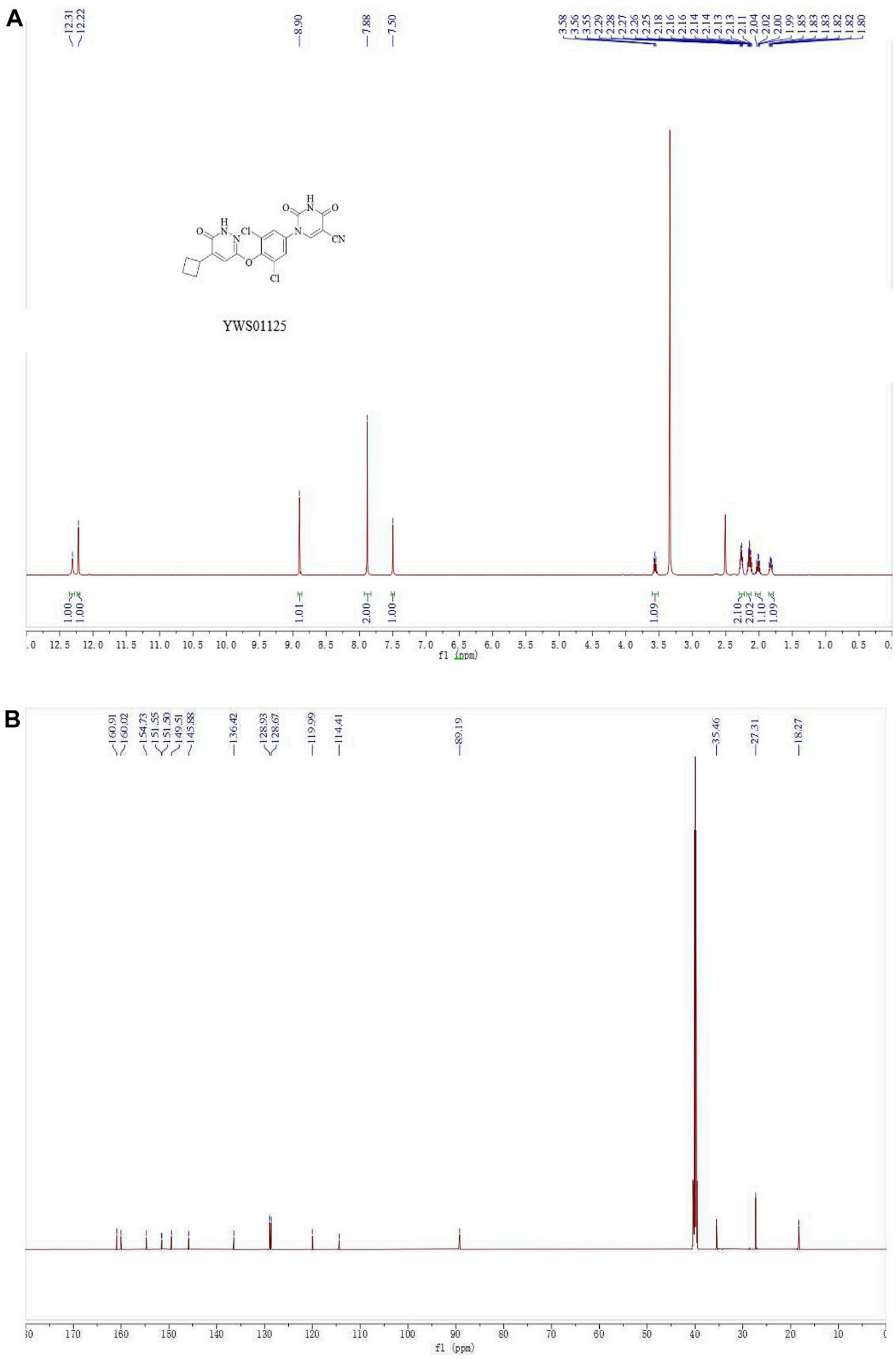

FIGURE 2 | (A) ^{1}H NMR spectra of **YWS01125**. **(B)** ^{13}C NMR spectra of **YWS01125.**

(m, 1H), 2.30–2.24 (m, 2H), 2.19–2.10 (m, 2H), 2.07–1.97 (m, 1H), 1.85–1.80 (m, 1H) ppm; 13C NMR (150 MHz, DMSO-d6) δ 160.9, 160.0, 154.7, 151.5, 151.4, 149.5, 145.9, 136.4, 128.9 (2C), 128.7 (2C), 120.0, 114.4, 89.2, 35.5, 27.3 (2C), 18.3 ppm; ESI-HRMS m/z calculated for $C_{19}H_{14}Cl_2N_5O_4$ (M + H)+446.0423; molecular weight, 446.0420 (**Figure 2**).

Animals

A total of 60 male C57BL/6J mice, weighting 23 ± 5 g, were obtained from Jinan Peng Yue Experimental Animal Breeding Co. Ltd. (Jinan, China). The permit number was SCXK (Lu) 20190003. The mice were allowed free laboratory sterile feed and sterile water and were housed in controlled environment conditions since at least 1 week before the experiment. The adjustable temperature was set at 20 ± 5°C and the moisture was 55 ± 15%, with a 12-h dark–light cycle. The tested mice were carried out according to the National Institute of Health Guideline for the Care and Use of Laboratory Animals, and performed by the Animal Ethics Committee of Institute of Materia Medica, Shandong Academy of Medical Sciences (Jinan, China). Before the pharmacokinetic study, all experimental mice had fasted for 12 h with free drinking water.

Preparation of Stock Solution, Calibration Standard, and Quality Control Samples

The stock solution of **YWS01125** was prepared by accurately weighing a lot of the medicine, then dissolving it in methanol, yielding a final concentration of 1 mg/ml, and storing at 4°C. It was gradually diluted before use into a series of working solutions at concentrations of 4–400 ng/ml with acetonitrile. **MGL-3196** powder was prepared as a 1 mg/mL internal standard stock solution and stored in refrigerator at 4°C. Immediately before use, use chromatographic acetonitrile to dilute step by step to prepare an internal standard solution with a concentration of 2 ng/ml **MGL-3196**, and placed in 4°C standby. These standards of the quality control (QC) samples were prepared by diluting the stock solution of **YWS01125** to the blank plasma at low, medium, and high concentrations of 10, 50, and 300 ng/ml, respectively, and by depositing them at 4°C until analysis. All solutions were kept at 4°C before use.

High-Performance Liquid Chromatography Conditions

Hypersil GOLD C18 column (4.6 × 150 mm, 5 μm, Thermo). A 0.025% ammonia aqueous solution in water (solvent A) and acetonitrile (solvent B) were used as mobile phases with gradient elution. The gradient was as follows: 0.01 min, 15% B; 5 min, 20% B; 12 min, 80% B; 16 min, 80% B; 16.01 min, 15% B; 19 min, 15% B; and 19.01 min, stopped. The timing interval was 19 min, and the flow rate was set at 1 ml/min.

Chromatographic and Ultra-Performance Liquid Chromatography–Tandem Mass Spectrometry Conditions

Sorvall Biofuge Stratos high-speed refrigerated centrifuge was bought from the Thermo Fisher Scientific Co. Ltd. (Shanghai, China); EL204 electronic balance was selected from Shanghai Mettler-Toledo Instruments Co. Ltd. (Shanghai, China); IKA Vortex Genius 3 Vortex Mixer was purchased from Aika Instrument Equipment Co. Ltd. (Guangzhou, China); and the test was carried out using an AB SCIEX™ 5500 Q-Trap® mass spectrometer (Applied Biosystems, United States) coupled to a Shimadzu Prominence UPLC (ultra-performance liquid chromatography, Shimadzu, United States) system. It was equipped with a binary pump, a degasser, an auto sampler, and an automatic thermostatic column compartment. The column was utilized from Agela Technologies UHP Innoval C18 (2.1 × 50 mm, 1.9 μm; Agela Technologies; Made in China). The whole process with a gradient elution program is as follows: 0.00–0.50 min, 5% B; 0.50–1.50 min, 90% B; 1.50–3.00 min, 90% B; 3.00–3.10 min, 15% B; and 3.10–5.00 min, 15% B. The mobile phase was made up of 0.10% formic acid in water (A) and acetonitrile (B), and the velocity of flow was 0.50 ml/min. The auto sampler and column temperature were set at 15 and 40°C, respectively. The injection volume was 1 μl. The Q-Trap mass spectrometer was operated with positive electrospray ionization source (ESI) and scanned using the multiple-reaction monitoring (MRM) mode. The Analyst® software version 1.6.3 (Applied Bio-systems, AB SCIEX™, United States) was used to control the UPLC-MS/MS system. The best of the **YWS01125** parameters was curtain gas, 35 psi; collision gas, medium; ion spray voltage, 5500 V; temperature, 500°C; ion source gas 1, 50 psi; and ion source gas 2, 50 psi. The quantitative analysis ion pairs of **YWS01125** and **MGL-3196** (IS) were m/z 446.2 → 375 and m/z 435.2 → 182, individually. The suitable collision energy (CE) of **YWS01125** and IS was 42 and 50 eV, respectively, and the decluttering voltage (DP) was 160 and 180 V, respectively.

Sample Preparation

The frozen mice plasma samples and tissue homogenates were thawed at room temperature, vortexed for 1 min, then taken out in 10-μl aliquots in a 1.50-ml centrifuge tube, and this was then mixed with 1 μl of standard solution and 50 μl of internal standard (IS) solution, which was then dissolved and diluted with acetonitrile. Subsequently, it was vortexed for 3 min and at 14,000 rpm centrifugation for 5 min. The adopted 1 μl of the supernatant was used for sample injection analysis.

Method Validation

The validation was carried out by the US Food and Drug Administration bioanalytical method guidance (Bioanalytical Method Validation, 2018; US Food and Drug Administration, 2018; Chen et al., 2019), namely evaluating selectivity, linearity, accuracy and precision, recovery, matrix effect, and stability. Selectivity was assessed by contrasting the normal blank plasma samples' and analyst plasma samples' chromatograms from six different specimens. Linearity was appraised by different concentrations of the standard medicated plasma samples for 3 days continuously. The peak area was recorded (Booth et al., 2015), and weighted ($1/x^2$) least-squares analysis was used to acquire the standard curve equations. The accuracy and precision were assessed by three different (low, medium, and high) QC samples by diluting with acetonitrile; each concentration had six samples and was continuously accessed for 3 days, and the accuracy, intra-day precision, and inter-day precision were obtained. Recovery was evaluated by comparing the peak area of protein precipitated with acetonitrile first and finally using it to calculate the recovery of the analyst. The matrix effect was measured by comparing the analyst peak area with the saline

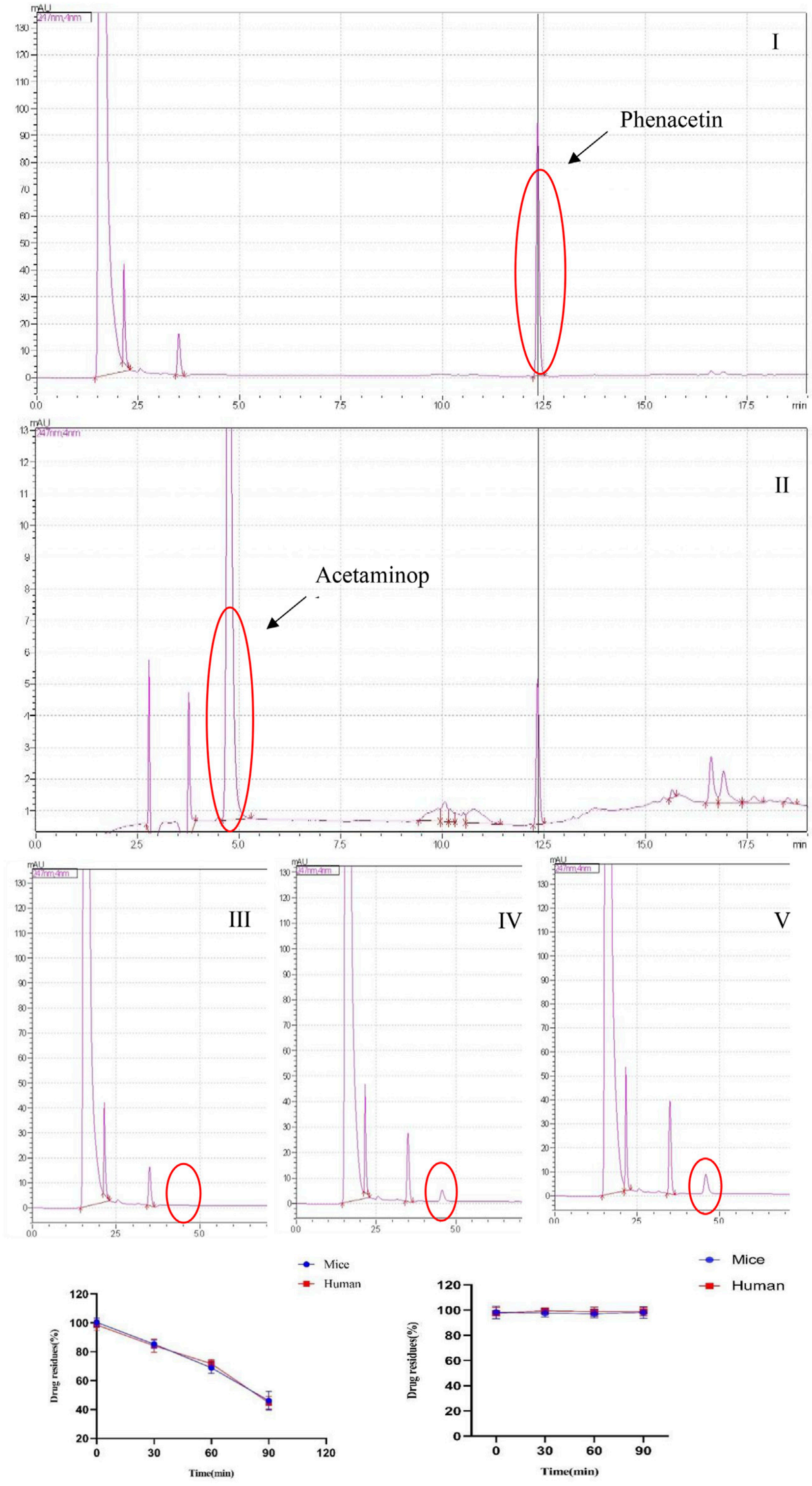

FIGURE 3 | (A) Selected reaction monitoring chromatograms of phenacetin (I), acetaminophen (II), the peak of metabolite acetaminophen at 0 min (III), the peak of metabolite acetaminophen at 30 min (IV), and the peak of metabolite acetaminophen at 60 min (V) in the human liver microsomes. **(B)** Stability of phenacetin (I) and **YWS01125** (II) in mice and human liver microsomes.

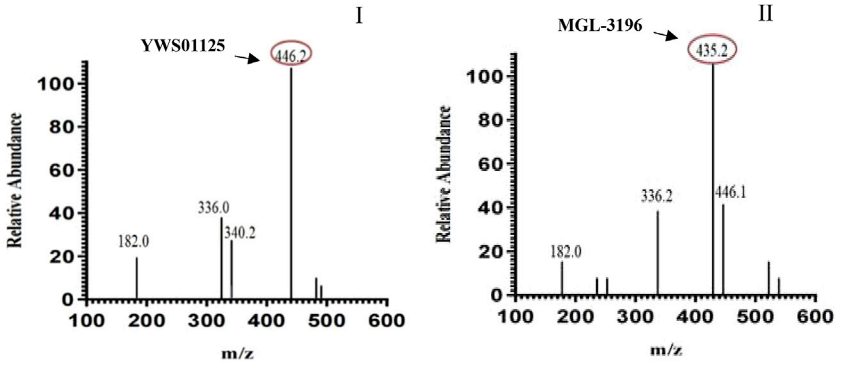

FIGURE 4 | Positive-ion electrospray mass spectra of **YWS01125** (I) and IS (II).

solution samples and QC samples at the three concentrations. The stability was assessed by defining the three QC levels in several different storage conditions: at room temperature for 6 h, injector stability at 15 °C for a whole night, and after three freeze–thaw cycles.

Stability of Liver Microsomes Study

The incubation system was carried out in 0.05 M Tris/KCl buffer (PH = 7.4) and included the following: pyrazinone compounds dissolved with dimethyl sulfoxide (DMSO), mouse liver microsomes and human liver microsomes at 0.50 mg/ml, 1.30 mM nicotinamide adenine dinucleotide sodium phosphate (NADP), 3.30 mM glucose-6-phosphate disodium salt (G-6-P), 0.40 units/mL glucose-6-phosphate dehydrogenase (G-6-PDH), and 3.30 mM magnesium chloride. The volume of the organic solvent did not exceed 1% of the reaction system. After preincubation for 3 min in an 850-rpm blender (37°C), liver microsomes were added to initiate the incubation reaction (37°C). The incubation time was 0, 30, 60, and 90 min. After incubation, an equal volume of cold acetonitrile was added to stop the reaction, and an internal standard (0.05 mg/ml acetaminophen solution) was added. The samples were centrifuged at 10,000 rpm for 10 min to precipitate proteins (Day et al., 2017; Manne et al., 2018), and the 10 μL of the supernatant was taken for HPLC analysis.

Pharmacokinetic Study

A total of 18 C57BL/6J mice were given **YWS01125** by oral administration with a dose of 10, 20, and 40 mg/kg, respectively (Lally et al., 2019; Kelly et al., 2014; Motamed et al., 2017) (with the concentration of drug administration selected according to the study by Kelly et al.). The blood samples of 20 μl were collected and placed in heparinized tubes from the ophthalmic venous plexus before and at 0.03, 0.08, 0.16, 0.25, 0.50, 1, 2, 4, 6, 8, 12, and 24 h. The samples were immediately centrifuged at 14,000 rpm for 10 min at 4°C. The plasma was separated and stored below −80°C until UHPLC-MS/MS analysis.

Tissue Distribution Study

A total of 24 male C57/BL6J mice were divided into 4 groups at random, with 6 mice in a group for tissue distribution at 0.25, 1, 6, and 24 h. They were given **YWS01125** after oral administration of 20 mg/kg, and then sacrificed at 0.25, 1, 6, and 24 h. Tissues from the heart, liver, spleen, lungs, kidneys, stomach, small intestine, colon, fat, muscle, testes, and brain were taken and rinsed with saline solution to remove the blood and connective tissues (Geng et al., 2015; He et al., 2017; Jiang et al., 2017), then put on the filter paper and weighed, quickly. Each tissue sample was homogenized by using five times of the tissue weight saline (w/v). All homogenates were stored at−80 °C until analysis.

Statistical Analysis

In this study, the comparison of the pharmacokinetic data between the normal and experimental groups was done using IBM SPSS Statistics 22.0 (Statistical Product and Service Solutions, United States) with an independent-samples *t*-test. The value of $p < 0.05$ was considered statistically significant.

RESULTS AND DISCUSSION

Stability of Liver Microsomes Study

The liver microsomal metabolic system was established. Phenacetin was used as a positive control, and its metabolite paracetamol were used for liquid phase analysis. The concentration of phenacetin peaked at 12.50 min, and its metabolite paracetamol peaked in about 5 min. In addition, phenacetin was added into the metabolic system and cultured for 0, 30, and 60 min. The results showed that its metabolite acetaminophen appeared in a time-dependent manner. However, **YWS01125** had no metabolites during the culture time in mice and human liver microsomes, suggesting that **YWS01125** was not metabolized in the liver microsomal system (**Figure 3**).

Ultra-Performance Liquid Chromatography–Tandem Mass Spectrometry Chromatograms

Under the above chromatographic conditions, the retention time for **YWS01125** and **MGL-3196** (IS) was 1.60 and 1.80 min, respectively. The production scan MS spectra of **MGL-3196** and **YWS01125** is shown in **Figure 4**. **Figure 5**

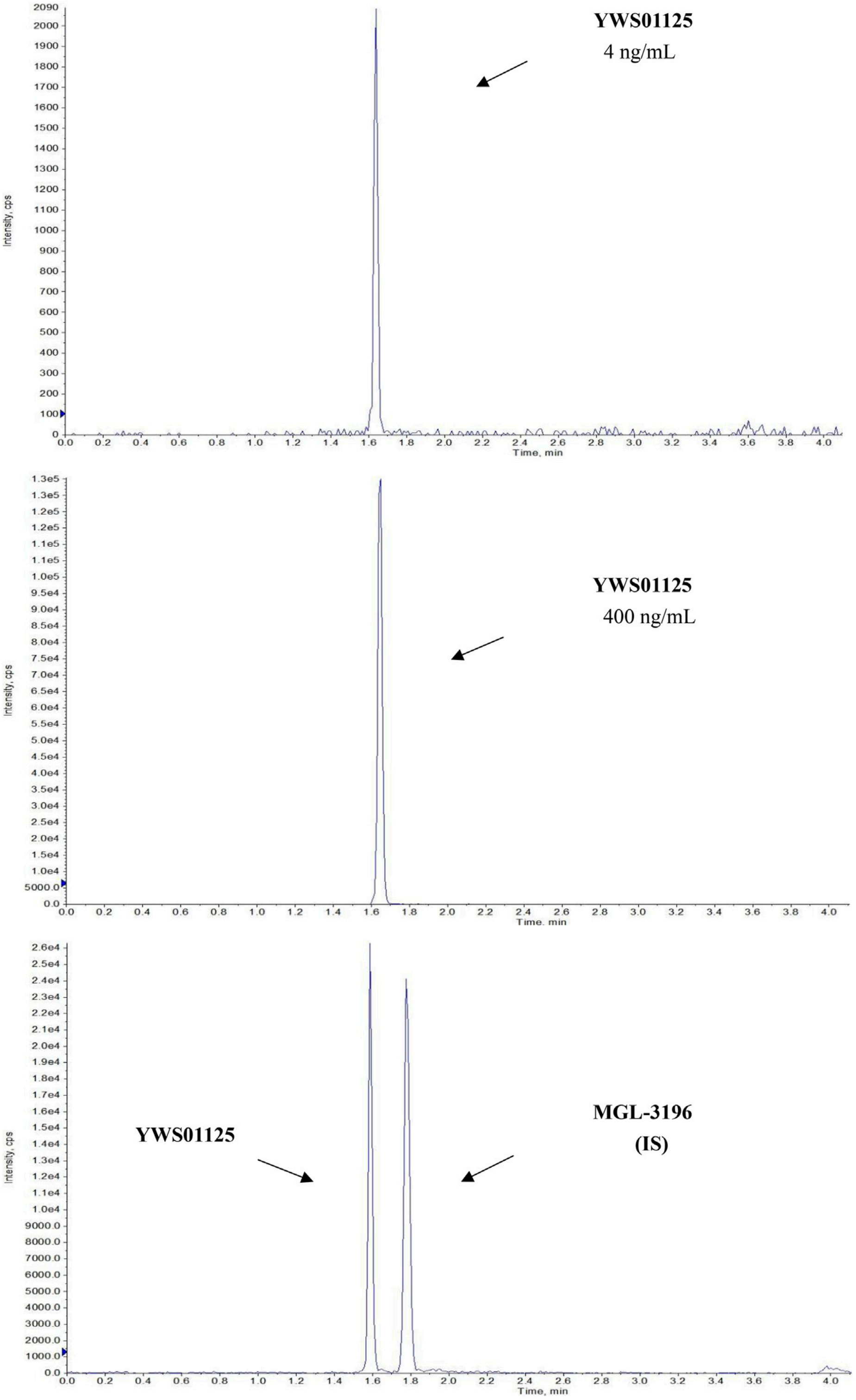

FIGURE 5 | Representative LC-MS/MS chromatograms of **YWS01125** (4 and 400 ng/ml) and **MGL-3196** (IS) samples.

shows **YWS01125** of 4 and 400 ng/ml, and IS of 2 ng/ml UPLC chromatographic images. During optimization of the mass spectrometric parameters, a higher response was observed in the positive mode than in the negative mode for all of the analysts. The deprotonated precursor molecular ions (M – H)– were chosen to be monitored. The quantitative analysis

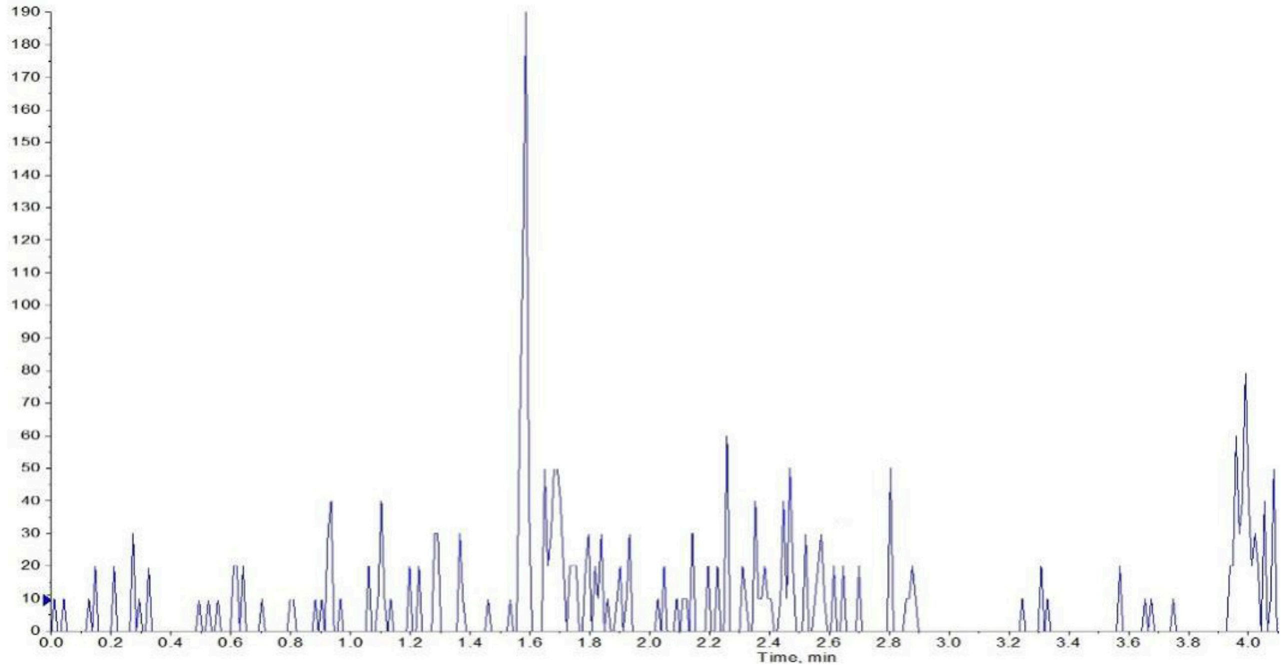

FIGURE 6 | Chromatographic profile of the plasma of control mouse.

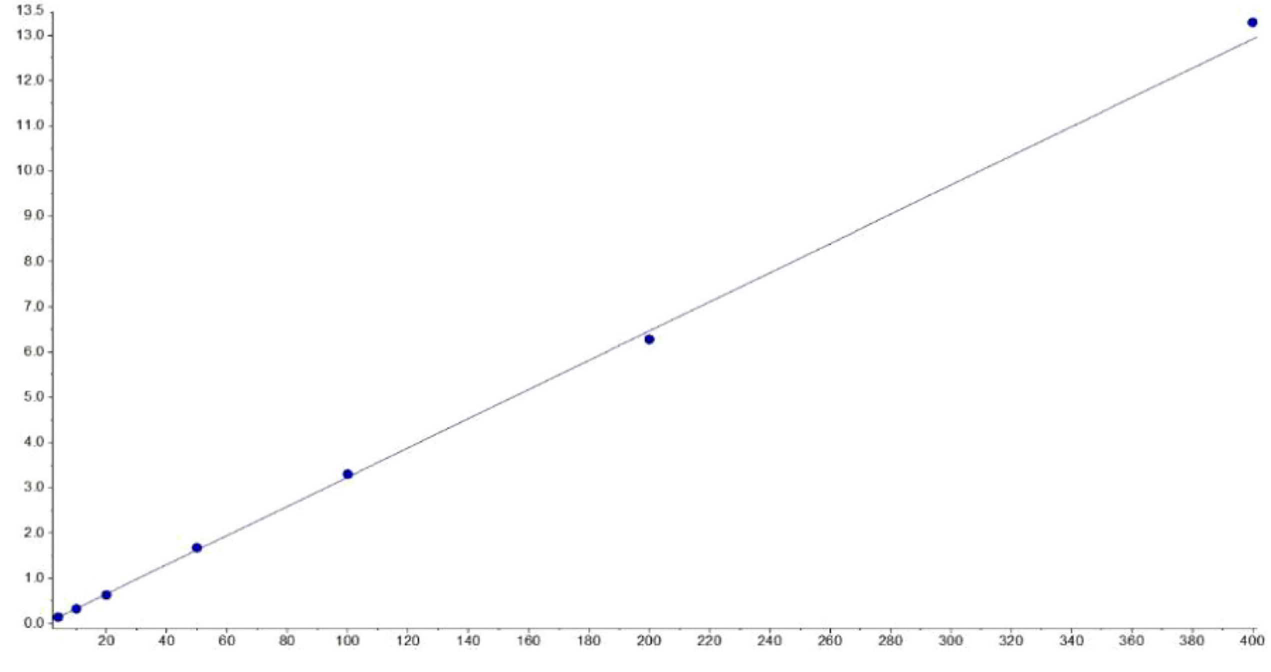

FIGURE 7 | The linearity of the calibration curve.

was carried out in the MRM mode at m/z 446.2 → 336 for **YWS01125** and m/z 435.2 → 182 for MGL-3196 (IS). Meanwhile, the transitions were regarded as qualitative analysis. Finally, for **YWS01125**, the decluttering potential (DP), entrance potential (EP), cell exit potential (CXP), and collision energy (CE) were 160, 42, 15, and 28 V, respectively, while for MGL-3196, the DP, EP, CXP, and CE were 180, 50, 43, and 20 V, respectively.

TABLE 1 | Precision and accuracy of UPLC-MS/MS for drugs in the mouse plasma (*n* = 6).

Analyze	Added concentration (ng/ml)	Intra-day			Inter-day		
		Calculated concentration (ng/ml)	Precision (RSD, %)	Accuracy (RE, %)	Calculated concentration (ng/ml)	Precision (RSD, %)	Accuracy (RE, %)
YWS01125	4	4.07 ± 0.22	5.45	1	4.09 ± 0.26	6.43	2.25
	10	9.34 ± 0.56	6.06	−6.6	10.34 ± 0.53	5.16	3.40
	50	47.66 ± 4.40	9.24	−4.68	48.95 ± 2.58	5.27	-2.10
	300	289.16 ± 12.76	4.41	−3.61	314.66 ± 10.85	3.45	4.88

TABLE 2 | The mean extraction recoveries and matrix effect of **YWS01125** and IS in the mouse plasma (n = 6).

Analyze	Added concentration (ng/ml)	Recovery (%, mean ± SD)	Matrix effect (%, mean ± SD)
YWS01125	10	86.66 ± 2.84	110 ± 0.08
	50	86.56 ± 2.21	112 ± 0.06
	300	85.47 ± 2.08	115 ± 0.12
IS	2	93.70 ± 2.84	111 ± 0.06

TABLE 3 | Stabilities of **YWS01125** in the mouse plasma (n = 6).

Storage conditions	YWS01125			
	Added concentration (ng/ml)	Mean ± SD (ng/ml)	Precision (RSD, %)	Accuracy (RE, %)
Injector stability	10	10.67 ± 0.52	4.91	5.00
	50	49.91 ± 2.15	9.24	−4.68
	300	295.17 ± 29.36	9.94	−1.60
Room temperature for 6 h	10	10.29 ± 0.82	9.06	1.20
	50	52.62 ± 1.73	4.29	−0.46
	300	299.33 ± 10.07	2.98	3.88
Three freeze–thaw cycles	10	9.45 ± 0.57	8.87	−1.80
	50	47.80 ± 3.96	4.80	−2.20
	300	289.17 ± 12.77	2.80	−2.66

Method Validation

Specificity and Selectivity

The selectivity of the method toward endogenous biological matrices was assessed with the plasma, heart, liver, spleen, lungs, kidneys, stomach, small intestine, colon, fat, muscle, testes, and brain from six mice. The retention times of **YWS01125** and IS were detected at 1.60 and 1.80 min, respectively (**Figure 5**). Comparing with the images of the control plasma samples (**Figure 6**) indicates that **YWS01125** and IS are well separated.

Linearity of Calibration Curve

The plasma calibration standard curve had a reliable reproducibility over the standard concentrations across the calibration range. The calibration curves' linear relationship was good in the range of 4–400 ng/ml, with a correlation coefficient (r^2) of 0.99 or better, and these were acquired on three consecutive days. The concentration of **YWS01125** as abscissa and the peak area ratio of **YWS01125** to IS as the ordinate implemented the regression equation with the weighted ($1/x^2$) least squares method in acquiring the linearity of the calibration curve. The typical regression equations for the calibration curves were obtained as follows: $Y = 0.0323\ x + 0.00756$ ($r = 0.9994$) for **YWS01125**. The The lower limit of

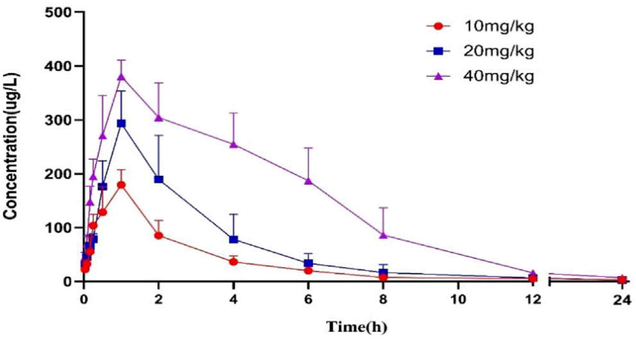

FIGURE 8 | Mean plasma concentration–time curves after oral administration of **YWS01125** (10, 20, and 40 mg/kg) to C57BL/6J mice (mean ± SD, n = 6).

TABLE 4 | Pharmacokinetic parameters of **YWS01125** after oral administration in the mice plasma (mean ± SD, n = 6).

Parameter		Oral administration		
		10 mg/kg	20 mg/kg	40 mg/kg
AUC0-t	mg/L*min	30921.38 ± 6261.12	54062.38 ± 18240.93	132269.96 ± 26808.23
AUC0-∞	mg/L*min	31378.67 ± 6086.08	54907.00 ± 19018.92	133818.83 ± 27275.44
MRT (0-t)	Min	205.41 ± 51.83	183.51 ± 23.10	274.15 ± 23.35
MRT (0-∞)	Min	242.69 ± 62.15	204.15 ± 25.50	296.57 ± 34.84*
$t_{1/2z}$	Min	189.12 ± 95.27	152.64 ± 37.98	181.95 ± 64.25
T_{max}	Min	55.00 ± 12.25	60.00 ± 0.01	55.00 ± 12.25
$C_{Lz/F}$	L/min/kg	0.16 ± 0.02	0.25 ± 0.28	0.28 ± 0.05*
$V_{z/F}$	L/kg	0.08 ± 0.04	0.09 ± 0.02	0.08 ± 0.03
C_{max}	ng/mL	188.50 ± 30.03	293.42 ± 60.43	381.58 ± 30.55

$p < 0.05$ compared with normal mice.

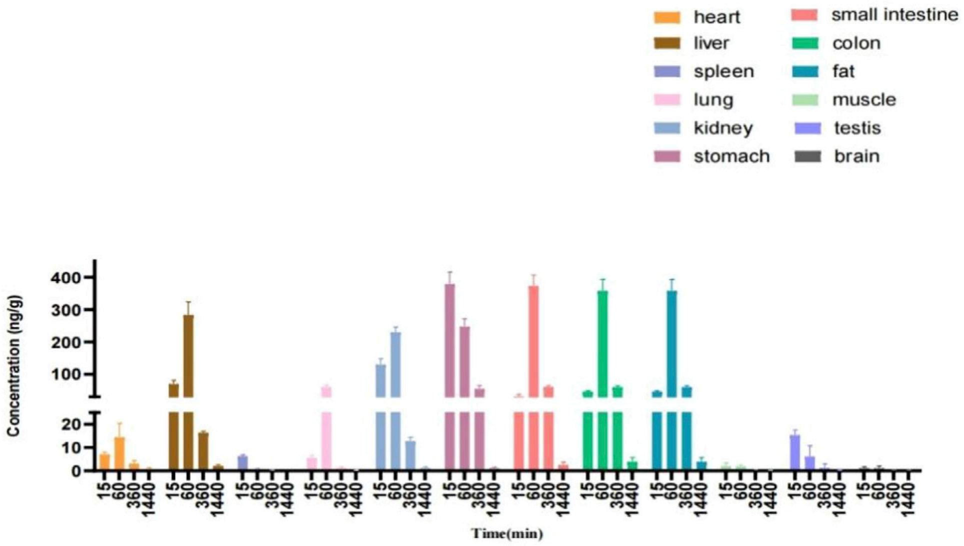

FIGURE 9 | Tissue distribution of **YWS01125** (20 mg/kg) in C57/BL6J mice (mean ± SD, n = 6).

quantification (LLOQ) with the relative standard deviation (RSD) ≤20% was found to be 4.00 ng/ml, with an RSD <9.24% (**Figure 7** and **Table 1**) indicating of good sensitivity of the UPLC-MS/MS method.

Accuracy and Precision

The intra- and inter-day precision and accuracy data of **YWS01125** in the plasma are summarized in **Table 1**. The precision and accuracy of the developed method were validated by assaying the QC samples at four concentration levels (LLOQ, and low, medium, and high QC) in the plasma on three consecutive days (n = 6). In this assay, the intra- and inter-day precision (RSD, %) values were measured to be <9.24 and 6.43%, respectively, with the intra- and inter-day accuracy (%) in the range −6.60–4.88% in all biological matrices. The results met the requirements for the biological analysis with RSD ≤15% and RE within ±15%, suggesting a satisfactory precision and accuracy for the quantifications of all analysts in the mice plasma.

Extraction Recovery and Matrix Effect

The results of extraction recovery and matrix effects for **YWS01125** in biological matrices are summarized at three different QCs levels in **Table 2**. The recovery for each analysis at the three QC concentration levels range from 85.47 to 86.66% (n = 6) and the matrix effect from 110.00 to 115.00%, which indicates that the matrix effects under the current conditions are acceptable. The recovery of IS is 93.70% and the matrix effect of IS is 111.00%. These results show that the recovery of **YWS01125** in all biological matrices is consistent, reproducible, and independent; the values are all within the acceptable limit for extraction recovery. There is no significant matrix effect on analyses in this method. It is considered as negligible or insignificant matrix effect under the present conditions.

Stability

This experiment investigated the stability of **YWS01125** in the mouse plasma at different temperature conditions, namely the auto sampler (15°C) for 12 h of injector stability, room

TABLE 5 | Linear ranges, correlation coefficients, weight factors, and regression equations for all analytes in the mouse plasma and tissue homogenates.

Analysts	Matrix	Linear range	r^2	Weight factor	Regression equations
YWS01125	Heart	4–400 ng/ml	0.9959	$1/X^2$	Y = 0.0217 x + 0.0242
	Liver		0.9976		Y = 0.0226 x + 0.0563
	Spleen		0.9993		Y = 0.0237 x + 0.0223
	Lung		0.9960		Y = 0.022 x + 0.0311
	Kidneys		0.9988		Y = 0.0252 x + 0.00717
	Stomach		0.9989		Y = 0.0211 x + 0.0287
	Small intestine		0.9987		Y = 0.0223 x + 0.00278
	Colon		0.9989		Y = 0.0246 x + 0.0126
	Fat		0.9966		Y = 0.0244 x + 0.0337
	Muscle		0.9965		Y = 0.02 x + 0.00988
	Testes		0.9925		Y = 0.0244 x + 0.0423
	Brain		0.9986		Y = 0.0217 x + 0.00903

TABLE 6 | Main organ tissue concentrations in mice after oral administration of **YWS01125**.

Organs	15 min, mean ± SD	1 h, mean ± SD	6 h, mean ± SD	24 h, mean ± SD
Heart	7.00 ± 1.05	14.41 ± 5.97	4.01 ± 1.27	ND
Liver	69.93 ± 11.25	283.67 ± 40.72	16.63 ± 1.72	ND
Spleen	6.26 ± 0.60	ND	ND	ND
Lungs	5.51 ± 1.22	60.76 ± 4.97	ND	ND
Kidneys	129.83 ± 18.31	230.50 ± 15.53	12.73 ± 1.65	ND
Stomach	378.67 ± 36.89	247.17 ± 24.96	54.49 ± 10.20	ND
Small intestine	31.30 ± 6.38	373.00 ± 33.88	61.03 ± 4.06	ND
Colon	46.70 ± 2.27	357.67 ± 35.31	60.23 ± 3.87	ND
Fat	9.37 ± 0.88	8.69 ± 1.45	ND	ND
Muscle	ND	ND	ND	ND
Testes	15.37 ± 2.15	6.08 ± 4.70	ND	ND
Brain	ND	ND	ND	ND

ND: not detected.

temperature for 6 h, and three freeze–thaw cycles. The results revealed RSD ≤ ± 15% and RE ≤ ± 15%, which has indicated that **YWS01125** maintains stability in the above three environments. The measured results of **YWS01125** are all within the acceptable limits during the entire process (**Table 3**).

Pharmacokinetic Study

The validated method was applied to the pharmacokinetic study of **YWS01125** in normal C57BL/6J mice after oral administration, at doses of 10, 20, and 40 mg/kg suspensions with sodium carboxymethyl cellulose (CMCNa). **YWS01125** was measured in the plasma until the last blood collection time (24 h). The plasma concentration–time profiles of **YWS01125** following the single oral administration in C57/BL6J are presented in **Figure 8**. The main pharmacokinetic parameters of **YWS01125** were processed by a no compartmental model using the DAS 2.0 software package, and the pharmacokinetic parameters are summarized in **Table 4**. As can be seen, the peak concentration (C_{max}) of each concentration of **YWS01125** in the mice plasma is 188.50 ± 30.03 ng/ml at 55.00 ± 12.25 min for 10 mg/kg, 293.42 ± 60.43 ng/ml at 60.00 ± 0.01 min for 20 mg/kg, and 381.58 ± 30.55 ng/ml at 55 ± 12.25 min for 40 mg/kg. From a comparison of the maximum plasma concentration (C_{max}), the time to reach C_{max} (T_{max}) and areas under the plasma drug concentration–time curve (AUC0–t and AUC0–∞) of **YWS01125** in the C57BL/6J mice were markedly increased, and there were statistically significant differences in these parameters ($p < 0.05$).

Tissue Distribution

The tissue distributions of **YWS01125** were investigated in C57BL/6J mice at 0.25, 1, 6, and 24 h after oral administration. The examined organs or tissues included the heart, liver, spleen, lungs, kidneys, stomach, small intestine, colon, fat, muscle, testes, and brain. The results are presented in **Figure 9**. The linear ranges, correlation coefficients, weight factors, and regression equations for all analytes in the mouse plasma and tissue homogenates are shown in **Table 5**. The concentration of each tissue at 0.25 h is indicated as stomach > kidneys > liver > colon > small intestine > testes > heart > spleen > lungs > fat; concentration of each tissue at 1 h is small intestine > colon > liver > stomach > kidneys > lungs > heart > fat > testes; concentration of each tissue at 6 h is small intestine > colon > stomach > liver > kidneys > heart; and concentration of each tissue at 24 h is that the whole tissues were not detected (**Table 6**). After oral administration, the concentrations of **YWS01125** were not detected in the brain and muscle, suggesting that the blood–brain barrier may block the entry of the drug into the brain. The content of the compound in the stomach was much higher than that in any other organ. The highest levels were reached 0.25 h after oral administration, then decreased thereafter. For the heart, liver, kidneys, lungs, small intestine, colon, and fat, the highest level was reached 1 h after oral administration, and it reached the highest levels at 0.25 h in the spleen, stomach, and testes. These data show that **YWS01125** is quickly distributed throughout the mice body after oral administration; however, long-term accumulation might not be observed.

CONCLUSION

In this study, a rapid, specific, and sensitive UPLC-MS/MS method for the determination of YWS01125 was developed and validated in the mouse plasma for the first time. In this method, carboxymethyl cellulose sodium suspension was used to dissolve drugs to maintain the homogeneity of the analytes. With the advantage of simple sample preparation procedure, short analysis time, and high sensitivity, the present method was successfully applied to the preliminary pharmacokinetic study of oral **YWS01125** in mice. This study demonstrated that as a precursor drug, **YWS01125** was absorbed very quickly and distributed extensively in C57BL/6J mice after oral administration. In addition, the UPLC-MS/MS method proved to be valuable in determining plasma **YWS01125**. *In vitro* experiments showed that **YWS01125** was stable and may not be metabolized in the mouse and human liver microsomes. Subsequently, the retention of **YWS01125** in the blood and its distribution in the various organs of mice were studied by *in vivo* experiments. It was found that **YWS01125** reached its highest concentration in the blood of mice at 1 h, and no drug distribution was detected in the muscle and brain of the mice group. In summary, **YWS01125**, a pyridazinone compound which we newly designed and synthesized, as an effective target, exhibited excellent activity targeting THRβ, and we studied its pharmacokinetics *in vivo* and found that it is a potential drug for the treatment of nonalcoholic fatty liver disease. The results are beneficial to further investigate the mechanism of YWS01125 and provide useful information for its clinical application.

DATA AVAILABILITY STATEMENT

The original contributions presented in the study are included in the article/Supplementary Material, further inquiries can be directed to the corresponding author.

ETHICS STATEMENT

The animal study was reviewed and approved by Ethics Committee of Institute of Materia Medica, Shandong Academy of Medical Sciences.

AUTHOR CONTRIBUTIONS

BL, YZ and X-BW conceptualized experiments and analyses. HC, M-JL and NL performed the animal experiments. HC wrote the article. M-YL guided the whole experiment process.

REFERENCES

Abdelbasset, W. K., Tantawy, S. A., Kamel, D. M., Alqahtani, B. A., and Soliman, G. S. (2019). A Randomized Controlled Trial on the Effectiveness of 8-Week High-intensity Interval Exercise on Intrahepatic Triglycerides, Visceral Lipids, and Health-Related Quality of Life in Diabetic Obese Patients with Nonalcoholic Fatty Liver Disease. *Medicine (Baltimore)* 98 (12), e14918. doi:10.1097/MD.0000000000014918

Bioanalytical Method Validation (2018). Guidance for Industry; Availability[J]. *The Fed. Regist./FIND* 83 (99).

Booth, B., Arnold, M. E., DeSilva, B., Amaravadi, L., Dudal, S., Fluhler, E., et al. (2015). Workshop Report: Crystal City V-Quantitative Bioanalytical Method Validation and Implementation: The 2013 Revised FDA Guidance. *AAPS J.* 17 (2), 277–288. doi:10.1208/s12248-014-9696-2

Castera, L., Friedrich-Rust, M., and Loomba, R. (2019). Noninvasive Assessment of Liver Disease in Patients with Nonalcoholic Fatty Liver Disease. *Gastroenterology* 156 (5), 1264–1281. Apre 4. doi:10.1053/j.gastro.2018.12.036

Chen, E. Y., Raghunathan, V., and Prasad, V. (2019). An Overview of Cancer Drugs Approved by the US Food and Drug Administration Based on the Surrogate End Point of Response Rate. *JAMA Intern. Med.* 179 (7), 915–921. Jul 1 doi:10.1001/jamainternmed.2019.0583

Day, E. A., Ford, R. J., and Steinberg, G. R. (2017). AMPK as a Therapeutic Target for Treating Metabolic Diseases. *Trends Endocrinol. Metab.* 28, 545–560. doi:10.1016/j.tem.2017.05.004

Dibba, P., Li, A., Perumpail, B., John, N., Sallam, S., Shah, N., et al. (2018). Emerging Therapeutic Targets and Experimental Drugs for the Treatment of NAFLD. *Diseases* 6 (3), 83. doi:10.3390/diseases6030083

Friedman, S. L., Neuschwander-Tetri, B. A., and Rinella, M. (2018b). Mechanisms of NAFLD Development and Therapeutic Strategies[J]. *Nat. Med.*, 24 (7), 908–922.doi:10.1038/s41591-018-0104-9

Friedman, S. L., Ratziu, V., Harrison, S. A., Abdelmalek, M. F., Aithal, G. P., Caballeria, J., et al. (2018a). A Randomized, Placebo-Controlled Trial of Cenicriviroc for Treatment of Nonalcoholic Steatohepatitis with Fibrosis. *Hepatology* 67 (5), 1754–1767. May. doi:10.1002/hep.29477

Geng, C., Yin, J.-y., Yu, X.-h., Liu, J.-y., Yang, Y.-x., Sun, D.-y., et al. (2015). Tissue Distribution and Excretion Study of Neopanaxadiol in Rats by Ultra-performance Liquid Chromatography Quadrupole Time-Of-Flight Mass Spectrometry. *Biomed. Chromatogr.* 29 (3), 333–340. doi:10.1002/bmc.3274

Hannah, W. N., and Harrison, S. A. (2016). Nonalcoholic Fatty Liver Disease and Elastography: Incremental Advances but Work Still to be Done. *Hepatology* 63 (6), 1762–1764. doi:10.1002/hep.28504

Harrison, S. A., Bashir, M., Moussa, S. E., McCarty, K., Pablo Frias, J., Taub, R., et al. (2021). Effects of Resmetirom on Noninvasive Endpoints in a 36-Week Phase 2 Active Treatment Extension Study in Patients with NASH. *Hepatol. Commun.* 5 (4), 573–588. doi:10.1002/hep4.1657

Harrison, S. A., Bashir, M. R., Guy, C. D., Zhou, R., Moylan, C. A., Frias, J. P., et al. (2019). Resmetirom (MGL-3196) for the Treatment of Non-alcoholic Steatohepatitis: a Multicentre, Randomised, Double-Blind, Placebo-Controlled, Phase 2 Trial. *The Lancet* 394 (10213), 2012–2024. doi:10.1016/s0140-6736(19)32517-6

He, M., Ouyang, H., He, M., Tan, T., Li, J., Zhang, X., et al. (2017). Application of a Liquid Chromatography-Tandem Mass Spectrometry Method to the Pharmacokinetics, Tissue Distribution and Excretion in the Study of Anemoside B4, a Novel Antiviral Agent Candidate, in Rats. *Biomed. Chromatogr.* 31 (7). doi:10.1002/bmc.3914

Janssen, A., Grobbee, D. E., and Dendale, P. (2020). Non-alcoholic Fatty Liver Disease, a New and Growing Risk Indicator for Cardiovascular Disease. *Eur. J. Prev. Cardiol.* 27 (10), 1059–1063. doi:10.1177/2047487319891783

Jiang, Z., Zheng, X., Gong, X., Zhao, C., Zhou, X., Zhao, Y., et al. (2017). Relative Tissue Distribution and Excretion Studies of Gastrodin and Parishin from Powder and Extract of Gastrodiae Rhizoma in Rat by UHPLC-ESI-MS/MS. *Biomed. Chromatogr.* 31 (7). doi:10.1002/bmc.3909

Kefala, G., and Tziomalos, K. (2019). Apoptosis Signal-Regulating Kinase-1 as a Therapeutic Target in Nonalcoholic Fatty Liver Disease. *Expert Rev. Gastroenterol. Hepatol.* 13 (3), 189–191. doi:10.1080/17474124.2019.1570136

Kelly, M. J., Pietranico-Cole, S., Larigan, J. D., Haynes, N. E., Reynolds, C. H., Scott, N., et al. (2014). Discovery of 2-[3,5-Dichloro-4-(5-Isopropyl-6-Oxo-1,6-Dihydropyridazin-3-Yloxy)phenyl]-3,5-Dioxo-2,3,4,5-Tetrahydro[1,2,4] triazine-6-Carbonitrile (MGL-3196), a Highly Selective Thyroid Hormone Receptor β Agonist in Clinical Trials for the Treatment of Dyslipidemia. *J. Med. Chemjournal Medicinal Chemistry* 57 (10), 3912–3923. doi:10.1021/jm4019299

Lally, J. S. V., Ghoshal, S., DePeralta, D. K., Moaven, O., Wei, L., Masia, R., et al. (2019). Inhibition of Acetyl-CoA Carboxylase by Phosphorylation or the Inhibitor ND-654 Suppresses Lipogenesis and Hepatocellular Carcinoma. *Cell Metab* 29 (1), 174–182. e5. doi:10.1016/j.cmet.2018.08.020

López-Sánchez, G. N., Dóminguez-Pérez, M., Uribe, M., Chávez-Tapia, N. C., and Nuño-Lámbarri, N. (2021). Non-alcoholic Fatty Liver Disease and microRNAs Expression, How it Affects the Development and Progression of the Disease. *Ann. Hepatol.* 21, 100212.

Manne, V., Handa, P., and Kowdley, K. V. (2018). Pathophysiology of Nonalcoholic Fatty Liver Disease/Nonalcoholic Steatohepatitis. *Clin. Liver Dis.* 22 (1), 23–37. doi:10.1016/j.cld.2017.08.007

Motamed, N., Rabiee, B., Poustchi, H., Dehestani, B., Hemasi, G. R., Khonsari, M. R., et al. (2017). Non-alcoholic Fatty Liver Disease (NAFLD) and 10-year Risk of Cardiovascular Diseases. *Clin. Res. Hepatol. Gastroenterol.* 41 (1), 31–38. doi:10.1016/j.clinre.2016.07.005

Orci, L. A., Gariani, K., Oldani, G., Delaune, V., Morel, P., Toso, C., et al. (2016). Exercise-based Interventions for Nonalcoholic Fatty Liver Disease: A Meta-analysis and Meta-regression. *Clin Gastroenterol Hepatol* 14 (10), 1398–1411. doi:10.1016/j.cgh.2016.04.036

Park, H. J., Min, T. R., Chi, G. Y., Choi, Y. H., and Park, S. H. (2018). Induction of Apoptosis by Morusin in Human Non-small Cell Lung Cancer Cells by Suppression of EGFR/STAT3 Activation. *Biochem. Biophysical Res. Commun.* 505, 194–200. doi:10.1016/j.bbrc.2018.09.085

Peng, C., Stewart, A. G., Woodman, O. L., Ritchie, R. H., and Qin, C. X. (2020). Non-Alcoholic Steatohepatitis: A Review of its Mechanism, Models and Medical Treatments. *Front. Pharmacol.* 11, 603926. doi:10.3389/fphar.2020.603926

Pierantonelli, I., and Svegliati-Baroni, G. (2019). Nonalcoholic Fatty Liver Disease: Basic Pathogenetic Mechanisms in the Progression from NAFLD to NASH. *Transplantation* 103 (1), e1–e13. doi:10.1097/tp.0000000000002480

Sumida, Y., and Yoneda, M. (2018). Current and Future Pharmacological Therapies for NAFLD/NASH. *J Gastroenterol* 53 (3), 362–376. doi:10.1007/s00535-017-1415-1

Tacke, F. (2018). Cenicriviroc for the Treatment of Non-alcoholicsteatohepatitis and Liver Fibrosis [J]. *Expert Opin. Investig. Drugs* 27 (3), 301–311. doi:10.1080/13543784.2018.1442436

Takahashi, N., Asano, Y., Maeda, K., and Watanabe, N. (2014). *In Vivo* evaluation of 1-Benzyl-4-Aminoindole-Based Thyroid Hormone Receptor β Agonists: Importance of Liver Selectivity in Drug Discovery. *Biol. Pharm. Bull.* 37 (7), 1103–1108. doi:10.1248/bpb.b13-00915

Tilg, H., and Moschen, A. R. (2010). Evolution of Inflammation in Nonalcoholic Fatty Liver Disease: the Multiple Parallel Hits Hypothesis. *Hepatology* 52 (5), 1836–1846. doi:10.1002/hep.24001

US Food and Drug Administration (2018). *Guidance for Industry: Bioanalytical Method validationFood and Drug Administration*. US Department of Health and Human ServicesCenter for Drug Evaluation and Research and Center for Veterinary Medicine.

Younossi, Z. (2019). Emerging Research on MGL-3196 for the Treatment of Nonalcoholic Steatohepatitis. *Gastroenterol. Hepatol. (N Y).* 15 (6), 317–319.

Younossi, Z. M., Golabi, P., de Avila, L., Paik, J. M., Srishord, M., Fukui, N., et al. (2019). The Global Epidemiology of NAFLD and NASH in Patients with Type 2 Diabetes: A Systematic Review and Meta-Analysis. *J. Hepatol.* 71 (4), 793–801. doi:10.1016/j.jhep.2019.06.021

Conflict of Interest: The authors declare that the research was conducted in the absence of any commercial or financial relationships that could be construed as a potential conflict of interest.

ORIGINAL RESEARCH
published: 19 May 2022
doi: 10.3389/fchem.2022.911795

One-Shot Full-Range Quantification of Multi-Biomarkers With Different Abundance by a Tandem Giant Magnetoresistance Assay

Fanda Meng[1,2,3]*, Lei Zhang[4], Jie Lian[5], Weisong Huo[4], Xizeng Shi[4] and Yunhua Gao[6,7]*

[1]Department of Clinical Laboratory Medicine, The First Affiliated Hospital of Shandong First Medical University & Shandong Provincial Qianfoshan Hospital, Shandong Medicine and Health Key Laboratory of Laboratory Medicine, Jinan, China, [2]School of Clinical and Basic Medicine, Shandong First Medical University & Shandong Academy of Medical Sciences, Jinan, China, [3]Department of Chemistry and Chemical Engineering, Chalmers University of Technology, Gothenburg, Sweden, [4]Shenzhen Bosh Biotechnologies, Ltd., Shenzhen, China, [5]College of Criminal Investigation, People's Public Security University of China, Beijing, China, [6]Key Laboratory of Photochemical Conversion and Optoelectronic Materials, Technical Institute of Physics and Chemistry, Chinese Academy of Sciences, Beijing, China, [7]University of Chinese Academy of Sciences, Beijing, China

Edited by:
Chengchao Chu,
Eye Institute, Xiamen University, China

Reviewed by:
Chengjun Wu,
Dalian University of Technology, China
Xin Du,
University of Science and Technology
Beijing, China

***Correspondence:**
Fanda Meng
mengfind@163.com
Yunhua Gao
yhgao@mail.ipc.ac.cn

Specialty section:
This article was submitted to
Analytical Chemistry,
a section of the journal
Frontiers in Chemistry

Received: 03 April 2022
Accepted: 20 April 2022
Published: 19 May 2022

Citation:
Meng F, Zhang L, Lian J, Huo W, Shi X and Gao Y (2022) One-Shot Full-Range Quantification of Multi-Biomarkers With Different Abundance by a Tandem Giant Magnetoresistance Assay.
Front. Chem. 10:911795.
doi: 10.3389/fchem.2022.911795

In this study, we reported a tandem giant magnetoresistance (GMR) assay that realized the one-shot quantification of multi-biomarkers of infection, C-reactive protein (CRP) with procalcitonin (PCT), and neutrophil gelatinase-associated lipocalin (NGAL), all of which could cover their clinically relevant concentration ranges under a different principle. In the presence of co-determined assay, we quantified these three biomarkers in undiluted human blood serum in a single test. The tandem principle, based on which quantification of CRP occurs, combines a sandwich assay and an indirect competitive assay, which allows for the discrimination of the concentration values resulting from the multivalued dose-response curve ('Hook' effect), which characterizes the one-step sandwich assay at high CRP concentrations. However, the entire diagnostically dynamic range, in the quantification of PCT and NGAL, was achieved by differential coating of two identical GMR sensors operated in tandem and by combining two standard curves. The sensor quantified low detection limits and a broader dynamic range for the detection of infection biomarkers. The noticeable features of the assay are its dynamic range and small sample volume requirement (50 μL), and the need for a short measurement time of 15 min. These figures of merit render it a prospective candidate for practical use in point-of-care analysis.

Keywords: 'hook' effect, multi-biomarker detection, giant magnetoresistance, biosensor, POCT

1 INTRODUCTION

The levels of C-reactive protein (CRP), neutrophil gelatinase-associated lipocalin (NGAL), and procalcitonin (PCT), which have different abundance in blood, show good responses to inflammation (Yavuz et al., 2014; Zhu et al., 2014; Nielsen et al., 2021). In this era of rising antimicrobial resistance, infection biomarkers are gradually becoming a convenient and effective tool to guide the antimicrobial use (Nielsen et al., 2021).

In clinical settings, combinations of multi-biomarkers have outperformed single biomarkers for early diagnosis of the disease (Lian et al., 2013; Bhide et al., 2019; Muinao et al., 2019), especially the combined detection of infection markers could define the precise level of inflammation. But there is a giant challenge that lies in the multi-detection caused by their different abundance and dynamic range, which also limits the widespread use of the one-shot detection of multi-biomarkers.

CRP is always used in combination with low abundance biomarkers in clinical settings (Buch and Rishpon, 2008; Pultar et al., 2009; Kilpatrick et al., 2012; Pay and Shaw, 2019); the dilution of serum is a serious problem indeed in multi-biomarker detection in one shot, where the dynamic ranges of different analytes are very different. Dilution would prevent the detection of low abundance biomarkers, and avoiding it is one of the primary concerns. Typically, detection of CRP in the undiluted human serum is usually limited by the 'Hook' effect (Byun et al., 2013; Oh et al., 2014; He et al., 2022), which also limits the combination with other biomarkers. In our previous work (Meng et al., 2021a), a competition assay was utilized as a complementary assay as an indicator to monitor the 'Hook effect' curve, so the 'Hook' effect curve could be utilized as the standard curve which actually contains two standard curves.

PCT and NGAL are always combined with CRP in clinical settings to predict and diagnose infection levels (Zhu et al., 2014). For the biomarkers of PCT and NGAL with low concentrations in serum, the detection method should be with high sensitivity while covering the concentrations relevant for infection diagnosis. Two sensors in tandem in one assay system were utilized to widen the detection range of N-terminal pro-B-type natriuretic peptides in our previous work (Meng et al., 2021b), which also maintain the good sensitivity. Differential coating of two identical GMR sensors operated in tandem and combining two standard curves could be ultimate in detecting PCT and NGAL biomarkers. In the tandem assay, two pairs of antibodies of different affinities to the specific biomarker were used simultaneously in one assay, in which two signals were applied to quantify the bio target.

The quantification principle of the GMR sensor is based on the change in resistance when the local magnetic field is changed due to magnetic materials binding to the surface (Nesvet et al., 2021). In the GMR assay, magnetic nanoparticles (MNPs) are always used as labels to create a magnetic field that is detected by the GMR sensor, which could realize real-time detection. Compared to traditional optical detection, the GMR biosensor has been shown to have high sensitivity and specificity, which also retained low costs and rapid testing time in bio-analysis assays (Gani et al., 2019; Ravi et al., 2022).

With these figures of merit, we developed a multiplexed quantitative platform for the detection of CRP, PCT, and NGAL, which are all bacterial infection biomarkers in clinical settings. The one-shot GMR chip realized accurate detection of infection, which also provides valuable clinical information and could aid in infection management.

2 MATERIALS AND METHODS

2.1 Regents and Materials

All reagents used in this work were of analytical grade. $NaHCO_3$, Na_2CO_3, Na_2HPO_4, NaH_2PO_4, KCl, NaCl, and BSA were purchased from Sigma-Aldrich (Merck). Tween 20 was purchased from AMRESCO (United States). NHS-biotin was purchased from Thermo Fisher Scientific, Inc. (United States). Streptavidin-conjugated magnetic particles (MNP, 100 nm) were purchased from Ademtech (France). A sample of polystyrene-grafted maleic anhydride (PS-g-MA, graft ratio 17%) was provided as a free sample by Longjia Plastics Fabrication (Jilin, China). Heterophilic blocking reagent (HBR1) was obtained from Scantibodies Laboratory, Inc. (United States). Heterophilic immunoglobulin elimination reagent (Fapon Block: HIER-E-010) was obtained from Fapon Biotech Inc. (China).

Anti-human CRP antibodies (capture antibody: MCP01 and detection antibody:MCP02) and CRP antigen were purchased from Hangzhou Yibaixin Biotechnology Co., Ltd. (China). Anti-human PCT antibodies (capture-detection antibody: pair I: MPT33-MPT34 and pair II: MPT31-MPT34) and PCT antigen were purchased from Hangzhou Yibaixin Biotechnology Co., Ltd. (China). Anti-human NGAL antibodies (capture-detection antibody: pair I: 1F2-1G2 and pair II: 4H11-1G2) and NGAL antigen were purchased from Fantibody Co., Ltd. (China). Undiluted clinical serum samples were received as a donation from the Zhujiang Hospital of Southern Medical University (China). The detection antibody was biotinylated using NHS-biotin (Zhang et al., 2015).

The GMR immunoassay analyzer (Bosh M16) (**Figure 1A**) and the polymer assay cartridge (**Figure 1B**) were manufactured by Shenzhen Bosh Biotechnologies, Ltd. (China).

2.2 Giant Magnetoresistance Chip Preparation

The GMR biosensor arrays comprise 2 × 6 sensors (**Figure 1C**). For the quantification of all three biomarkers, two sensors were selected in combination to realize each biomarker assay (**Figure 1C**). The detection of CRP (**Figure 2A**) combines a sandwich assay and an indirect competitive assay, which utilizes the multivalued dose-response curve ('Hook' effect) to realize the whole-range quantification of CRP. The detection of PCT (**Figure 2B**) and NGAL (**Figure 2C**) were all realized by a combination sandwich assay, which used two pairs of antibodies with different affinities to widen the detection range.

The GMR chip preparation procedure was described in our previous work (Meng et al., 2021a). The CRP, PCT, NGAL capture antibody, and CRP antigen solutions (50 μg/ml) were deposited onto the selected sensors. The antibody/antigen could be covalent to the sensor surface (Meng et al., 2016).

2.3 Immunoassay Procedure

For quantification of multi-biomarkers, six sensors were selected in the tandem assay (**Figure 1C**). Two sensors, combining a sandwich assay and competitive assay (**Figure 2A**), realized the CRP detection. In the one-step reaction, the sandwich assay forms a 'Hook' effect curve in the whole-range concentration of CRP, whereas the competitive assay could monitor the reaction in combination with the sandwich assay. The combination of these two assays makes the 'Hook' effect curve a possible standard curve, which extremely expanded the quantification range of the sandwich assay.

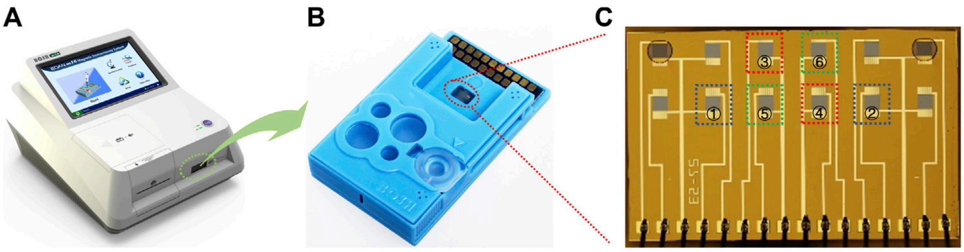

FIGURE 1 | GMR immunoassay analyzer **(A)**, the polymer assay cartridge **(B)**, and the GMR sensor array chip **(C)**. The two selected sensor units used for CRP detection are marked in blue squares (① and ②). The two selected sensor units used for PCT detection are marked in red squares (③ and ④). The two selected sensor units used for NGAL detection are marked in green squares (⑤ and ⑥).

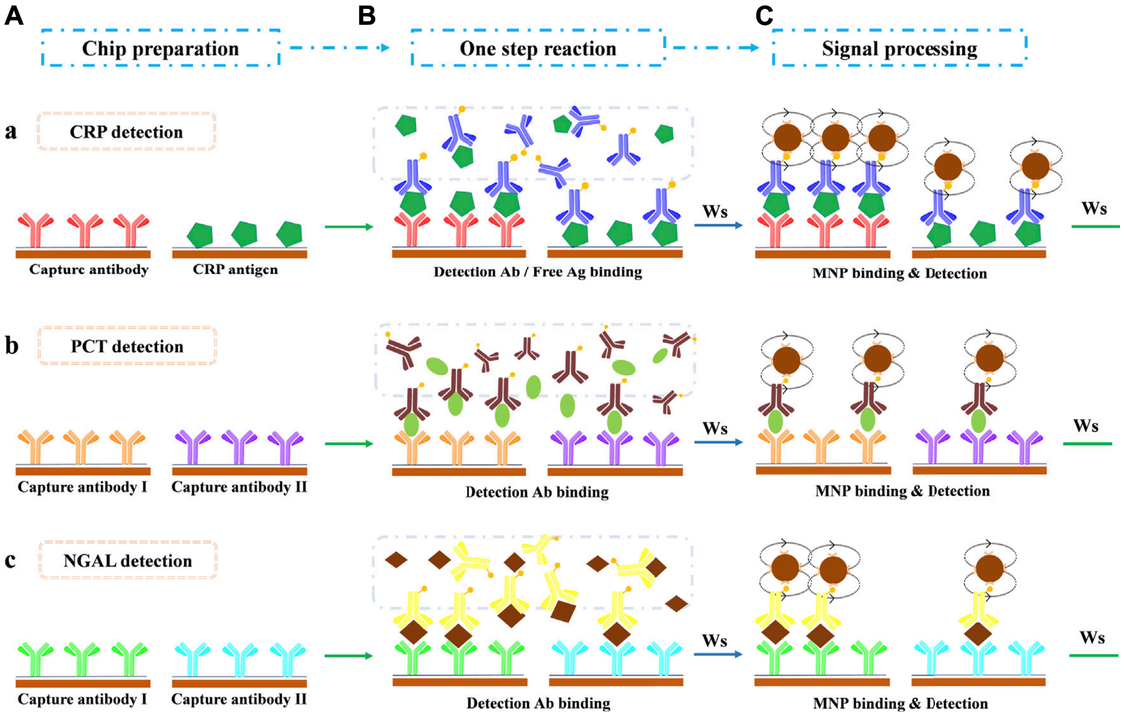

FIGURE 2 | Assay protocol for multi-biomarker detection in a one-shot chip. **(A)** Chip preparation. **(B)** One-step antibody-antigen reaction after sample loading. **(C)** Magnetic particle binding and detection. Ws: washing step. **(a)** CRP detection: the combination of sandwich assay and indirect competitive assay. **(b)** PCT detection: the combination of two sandwich assays with two antibody pairs that share the same detection antibody. **(c)** NGAL detection: the combination of two sandwich assays with two antibody pairs that share the same detection antibody.

For PCT (**Figure 2B**) and NGAL (**Figure 2C**) detection, two sensors were combined for each, which realized two different affinity sandwich assays at the same time. The ultimate two pairs of antibodies with different affinities, which with a shared detection antibody, broadened the detection range and ensured the detection sensitivity as well.

As described in our previous work (Meng et al., 2021a) on the assay protocol, 50 µL sample or standard was pipetted into the sample port of the cartridge in the first step. Then, the cartridge was inserted immediately into the detector to autorun the immune reaction and to obtain the results in 15 min. The sample/standard first re-dissolved the freeze-dried detection antibodies and reacted to form the antigen-antibody complex simultaneously (**Figure 2B**). Washing steps by PBST (10 mM, pH = 7.4, 0.5% Tween 20) were applied to remove the extra sample/regents. Afterward, the mixture was pumped to flow through the sensor surface (flow back and forth 5 min at RT), where the free antigen/detection antibody reacted with the capture antibody/antigen and was captured. Subsequently, the carbonate buffer (0.1 M, pH = 9.6, 0.05% Tween 20, and 10% BSA) was pumped to dissolved freeze-dried avidin-coated MNPs and initiated to react with the captured biotin-modified detection antibody (5 min at RT, **Figure 2C**). The captured MNPs on the specified sensors were finally detected by the GMR detector, and the results were reported automatically.

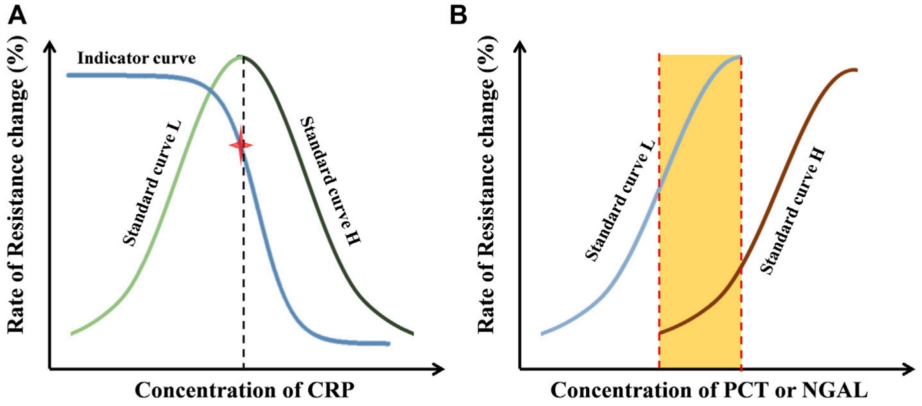

FIGURE 3 | Principle of data processing. **(A)** Standard curves and indicator curves of CRP obtained with external standards from sensor ① and ②. **(B)** Standard curves of PCT (sensor ③ and ④) or NGAL (sensor ⑤ and ⑥) obtained with external standards.

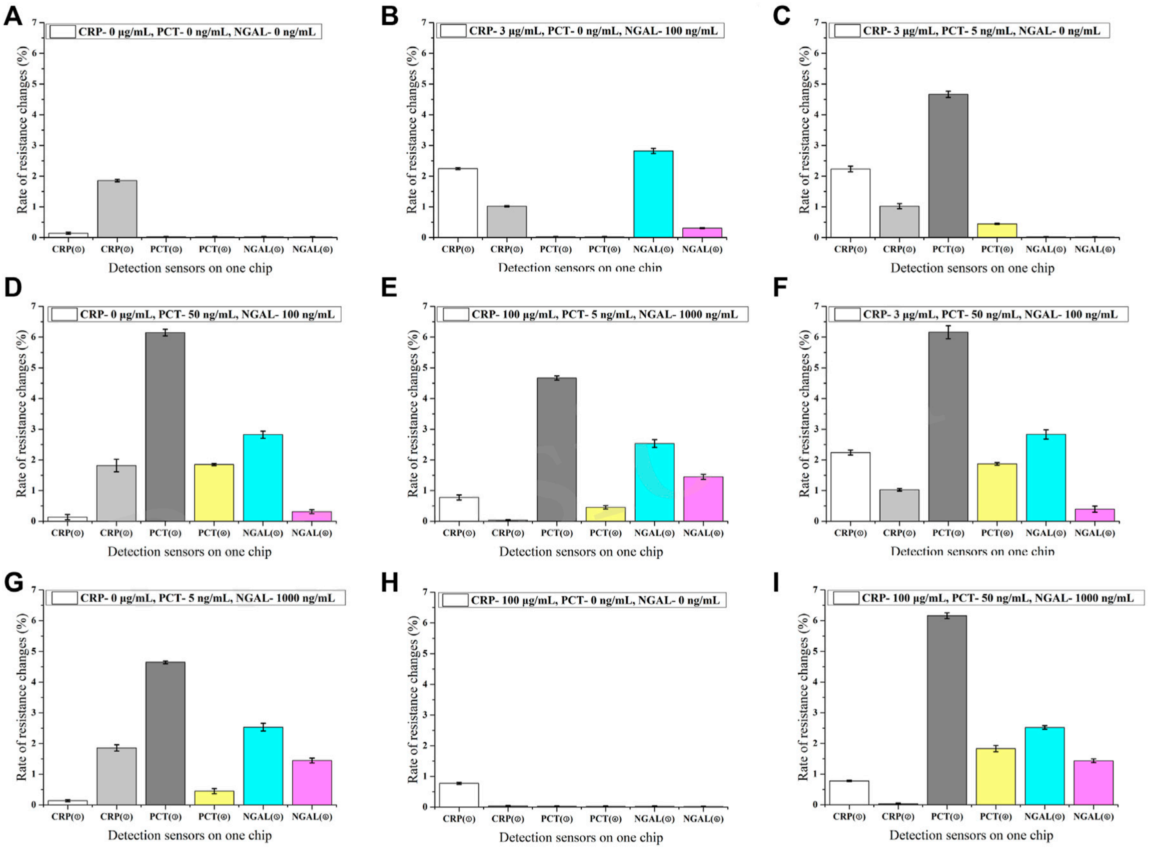

FIGURE 4 | Specificity of the assay (*n* = 3) **(A–I)**. ①-⑥ in the horizontal axis represents different sensors labeled in **Figure 1**.

2.4 Fitting Software and Algorithm

All standard curves were fitted by the four-parameter logistic model ($y = A_2+(A_1-A_2)/(1+(x/x_0)^p)$) (O'Connell et al., 1993), by Origin 9.1 software.

2.5 Data Processing

For the establishment of standard curves of all three biomarkers, each concentration point of the mixed standard was measured four times. A total of 91 clinical

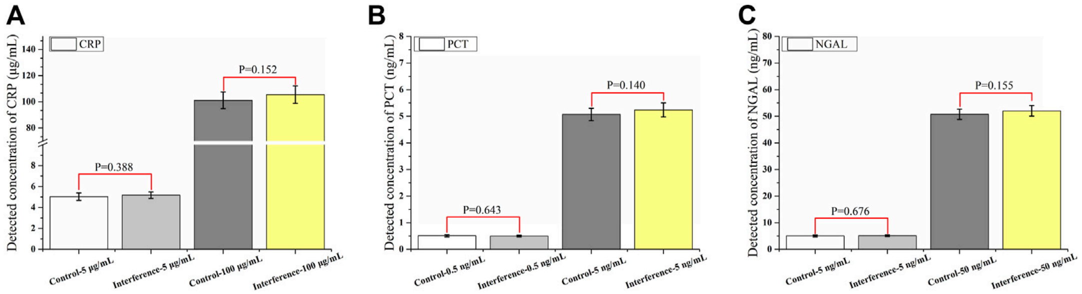

FIGURE 5 | Specificity of the assay under the interference of substances (*n* = 10) **(A–C)**.

TABLE 1 | Precision of the assay (*n* = 80).

Marker	Concentration	Mean	Intra-assay Precision		Inter-assay Precision	
			SD	RSD/%	SD	RSD/%
CRP	5 μg/ml	5.012	0.437	8,71	0.465	9.28
	100 μg/ml	99.41	8.485	8,54	7.359	7.40
PCT	0.5 ng/ml	0.504	0.032	6.30	0.038	7.48
	5 ng/ml	5.036	0.313	6.22	0.305	6.06
NGAL	5 ng/ml	5.406	0.370	7.34	0.480	9.51
	50 ng/ml	49.727	1.991	4.00	1.954	3.93

samples were analyzed, and measurement was performed once per sample.

In the evaluation of CRP (**Figure 3A**), signals on sensor ① formatted a 'HOOK'-shaped curve, which covered the low (standard curve L) and high (standard curve H)-concentration situations. Signals on sensor ② formatted the indictor curve, which contains an indicator point to measure whether the 'Hook' effect occurs or not. The indicator is not used in quantification. In the real sample measurement, if the value on sensor ② is higher than the indictor point, the value on sensor ① would be calculated with standard curve L. Otherwise, the standard curve H would be appropriate in quantification.

In the evaluation of PCT or NGAL (**Figure 3B**), two standard curves covering the low (standard curve L) and high (standard curve H)-concentration situations were obtained, which extremely expanded the detection range. The standard curve L was used in low-concentration situations; in the other case, the standard curve H was used. The quantification in the middle range (the orange area in **Figure 3B**) was determined by calculating the mean of the data from both standard curves.

3 RESULTS AND DISCUSSION

3.1 Specificity of the Assay

3.1.1 Interference of Three Markers

The specificity of the antibody pairs is the key factor in the multi-detection assay. The interference of the detection of three markers was evaluated at a crossing concentration (**Figure 4**). It shows that the combinational sensors designed for detecting the same biomarker presented undifferentiated signals at varying concentrations of two other markers. So it proves that there is no interference during the combined detection of three markers, which indicates that the assay has good specificity.

3.1.2 Interference of Substances

Many ingredients, especially some big proteins, in the human serum may result in nonspecific binding. To further verify the specificity of the assay, a mixture of interfering substances (1,000 μg/ml hemoglobin, 60 μg/ml bilirubin, 1,000 μg/ml triglycerides, and 1200 IU/ml rheumatoid factor) was added to the sample. Two levels (CRP: 5 and 100 μg/ml; PCT: 0.5 and 5 ng/ml; and NGAL: 5 and 50 ng/ml) were evaluated for each biomarker (**Figure 5**), and the results showed that there was no significant difference after the substances were added. It also proved the function of the commercial blockers we added to the assay, which helped keep the excellent specificity of the assay.

3.2 Precision and Long-Term Stability of the Assay

The precision was calculated by the measurements (*n* = 80), which were split into two concentration levels (**Table 1**). The measurement period was 20 consecutive days with two measurements per day and one concentration level. The assay cartridges used were newly fabricated on the day of detection. Measurements on the same day were denominated as intra-assay, when all other measurements were

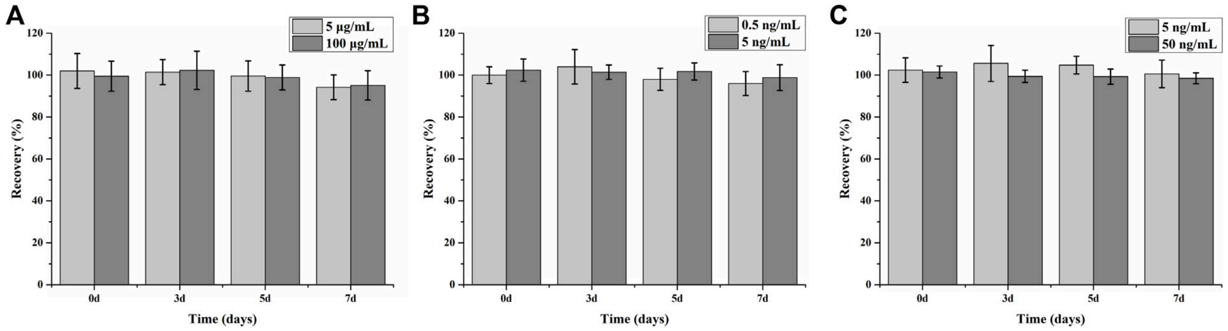

FIGURE 6 | Long-term stability of assay for CRP **(A)**, PCT **(B),** and NGAL **(C)** detection (*n* = 6).

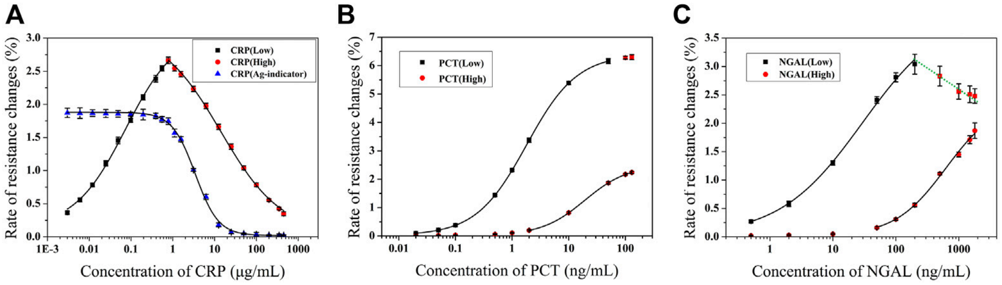

FIGURE 7 | Standard curves for CRP **(A)** (Adapted with permission from (Meng et al., 2021a) Copyright © 2021 Fanda Meng, etc. Published by American Chemical Society), PCT **(B),** and NGAL **(C)** detection (*n* = 4).

denominated as inter-assay. The RSD all under 10% shows that the precision was excellent.

The long-term stability was investigated by incubating the fabricated cartridge at 37°C over 7 days (**Figure 6**). The determined recovery >94.2% and RSD <10% (*n* = 6) indicate that the assay can maintain good function for several months at 4°C. The antibody/antigen deposited onto the selected sensors was sufficient to bind to the surface; the excessive antibody/antigen on the outside could work as a protector to keep the activity of the covalently captured antibody/antigen. The method of freeze-drying we used in the assay could also greatly protect the activity of protein reagents.

3.3 Establishment of Standard Curves

The relationships between the rate of resistance change and concentration were calculated to establish the standard curves. All standard curves were fitted by the four-parameter logistic model ($y = A_2+(A_1-A_2)/(1+(x/x_0)^p)$). The parameters are listed as follows:

CRP: there was good linearity in the range of 3 ng/ml–350 μg/ml, as shown in **Figure 7A**. The standard curve L (black square) covers a dynamic range of 3 ng/ml–0.781 μg/ml (LOD = 1 ng/ml), $A_1 = 0.11964$, $A_2 = 3.05252$, $x_0 = 0.06783$, $p = 0.73045$, and $R^2 = 0.9988$. The standard curve H (red square) covers a dynamic range of 0.781–350 μg/ml, $A_1 = 3.0816$, $A_2 = -0.04743$, $x_0 = 17.27685$, $p = 0.58217$, and $R^2 = 0.9998$. The value of indicators in the indicator curve (blue triangle) was calculated by combination with the standard curves L and H, which was set at the point of 1.745%.

PCT: there was good linearity in the range of 0.02–100 ng/ml, as shown in **Figure 7B**. The standard curve L (black square) covers a dynamic range of 0.02–50 ng/ml (LOD = 0.011 ng/ml), $A_1 = 0.02$, $A_2 = 6.4$, $x_0 = 1.80248$, $p = 0.97454$, and $R^2 = 0.9999$. The standard curve H (red circle) covers a dynamic range of 2–100 ng/ml, $A_1 = 0.02571$, $A_2 = -2.49554$, $x_0 = 19.28237$, $p = 1.13747$, and $R^2 = 0.9999$.

NGAL: there was good linearity in the range of 0.5–1,500 ng/ml, as shown in **Figure 7C**. The standard curve L (black square) covers a dynamic range of 0.5–100 ng/ml (LOD = 0.085 ng/ml), $A_1 = 0.02$, $A_2 = 4$, $x_0 = 29.53935$, $p = 0.66192$, and $R^2 = 0.9984$. The standard curve H (red circle) covers a dynamic range of 50–1,500 ng/ml, $A_1 = 0.02$, $A_2 = -2.4$, $x_0 = 623.48545$, $p = 1.07164$, and $R^2 = 0.99682$. The green line that connects the red square in **Figure 7C** shows the multivalued dose response, which demonstrates the 'HOOK' effect occurred in that value.

3.4 Measurement and Validation of the Chip for Multi-Detection

The assay results obtained with the GMR detection system were validated against the commercialized assay (**Figures 8A–C**). Fitness analysis (*n* = 91) yielded the following

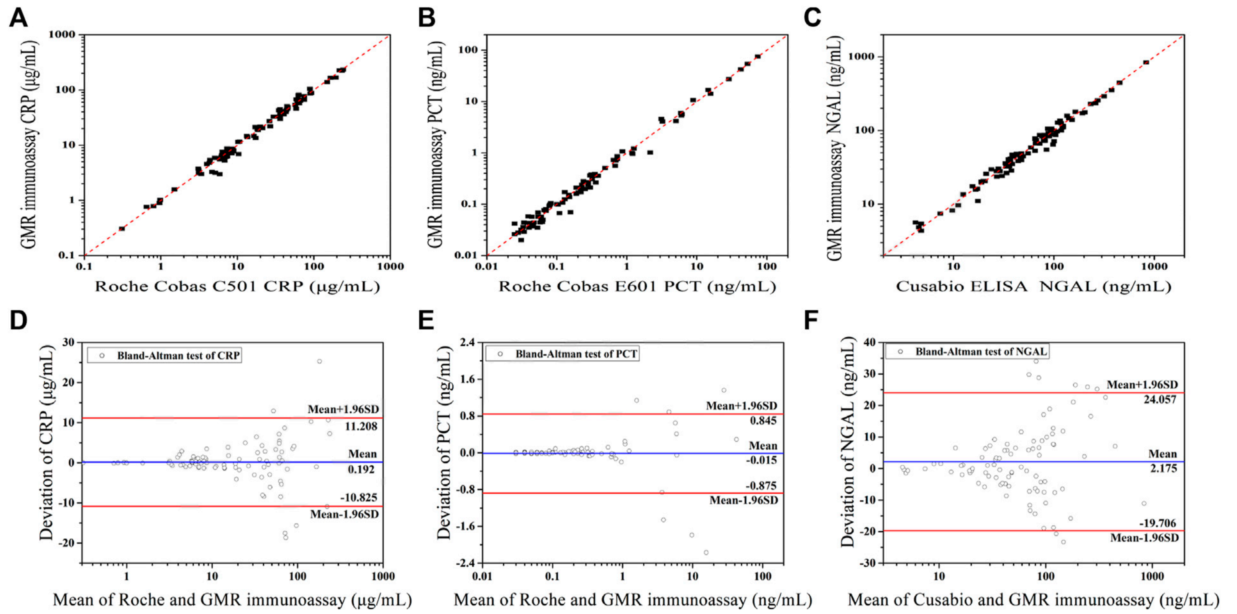

FIGURE 8 | Method comparison between two assays: fitness analysis and Bland–Altman analysis of the agreement of CRP **(A,D)** (Adapted with permission from (Meng et al., 2021a) Copyright © 2021 Fanda Meng, etc. Published by American Chemical Society), PCT **(B,E),** and NGAL **(C,F)** detection between the GMR and commercialized assay.

equation for the data set, covering the entire concentration range.

The CRP assay results obtained with the GMR detection system were validated against the Roche Cobas C501 assay (**Figure 8A**). The PCT assay results obtained with the GMR detection system were validated against the Roche Cobas E601 assay (**Figure 8B**). The NGAL assay results obtained with the GMR detection system were validated against the Cusabio ELISA assay (**Figure 8C**).

For PCT detection, there were five samples with the concentration under the LOD (the results were reported <0.02 ng/ml), so only 86 samples were calculated.

All correlation coefficients were above 0.95(CRP: $r = 0.9881$, PCT: $r = 0.9936$, and NGAL: $r = 0.9898$). In **Figures 8D–F**, Bland–Altman plots of the relative differences between the data sets of the two compared assays were displayed. There were above 90% of points within the 95% confidence limit for all three biomarkers' evaluation (CRP: 86 of 91 and 94.5%; PCT: 80 of 86 and 93.0%; and NGAL: 83 of 91 and 91.2%.).

There is no statistically significant bias between the GMR assay and commercialized assays, which shows the good potential clinical application of our established assay.

4 CONCLUSION

The multi-detection of combinational biomarkers in clinical settings with different abundance and dynamic ranges attracted wide attention in the area of the point-of-care test. Traditional assays are hard to balance the various sensitivities and different dynamic ranges of multi-biomarkers at the same time. Even though many combinations of biomarkers could better support the diagnosis of disease in clinical settings, they are hardly detected in one assay. Rapid quantification of multi-biomarkers in blood with a sensitive tool could, therefore, serve as a diagnostic of diseases, which also could be assessed for further clinical utility.

In the tandem GMR assay, two methods of expanding the dynamic range to cover the full clinically relevant concentration range were provided. The competitive assay was conjoined with a sandwich assay as the indicator, which could monitor the 'HOOK' effect. Therefore, the 'HOOK' effect curve was creatively ultimate as the standard curve, which provides an alternative method to analyze the bio target in the undiluted sample. In addition, the tandem operation of two pairs of antibodies with different affinities also effectively widens the dynamic range and guaranteed sensitivity.

Our portable GMR sensor in tandem realized the quantitative and multiplexed measurement of infection biomarker abundance. Three biomarkers (CRP, PCT, and NGAL) were simultaneously quantified. We combined two wide-range dynamic methods in a tandem GMR assay that realized the one-shot full-range quantification of multi-biomarkers of infection in clinical settings, which were not only with different abundance analytically but were also with totally different clinically relevant concentration ranges. In addition, simultaneous quantification of multi-biomarkers with both higher and lower abundance in one assay was achieved.

There is no interference in the combined detection of three markers and after an interfering substance is added, showing that the assay has good specificity. Validation with commercial assays revealed that the accuracy of the assay was excellent in clinical settings. The developed concept of tandem assay provides a convincing way to detect multi-analytes in one shot with the undiluted clinical sample, which also perfectly meet the requirement of clinical application, and the tandem assay would be explored to realize more simultaneous protein detection. Future studies would be involved to develop a unique set of biomarkers specific to other diseases and render the assay onto the current platform.

DATA AVAILABILITY STATEMENT

The original contributions presented in the study are included in the article/Supplementary Material; further inquiries can be directed to the corresponding authors.

REFERENCES

Bhide, A., Cheeran, S., Muthukumar, S., and Prasad, S. (2019) Enzymatic Low Volume Passive Sweat Based Assays for Multi-Biomarker Detection. *Biosensors* 9 (1, 13). doi:10.3390/bios9010013

Buch, M., and Rishpon, J. (2008) An Electrochemical Immunosensor for C-Reactive Protein Based on Multi-Walled Carbon Nanotube-Modified Electrodes. *ELECTROANALYSIS* 20 (23):2592–2594. doi:10.1002/elan.200804358

Byun, J.-Y., Shin, Y.-B., Kim, D.-M., and Kim, M.-G. (2013) A Colorimetric Homogeneous Immunoassay System for the C-Reactive Protein. *ANALYST* 138 (5):1538–1543. doi:10.1039/c3an36592a

Gani, A. W., Wei, W., Shi, R.-Z., Ng, E., Nguyen, M., Chua, M.-S., et al. (2019) An Automated, Quantitative, and Multiplexed Assay Suitable for Point-of-Care Hepatitis B Virus Diagnostics. *Sci. Rep.* 9 (1):15615. doi:10.1038/s41598-019-52147-z

He, G., Dong, T., Yang, Z., and Jiang, Z. (2022) Mitigating Hook Effect in One-step Quantitative Sandwich Lateral Flow Assay by Timed Conjugate Release. *TALANTA* 240, 123157. doi:10.1016/j.talanta.2021.123157

Kilpatrick, E. L., Liao, W.-L., Camara, J. E., Turko, I. V., and Bunk, D. M. (2012) Expression and Characterization of 15N-Labeled Human C-Reactive Protein in *Escherichia coli* and Pichia pastoris for Use in Isotope-Dilution Mass Spectrometry. *PROTEIN Expr. Purif.* 85 (1):94–99. doi:10.1016/j.pep.2012.06.019

Lian, J., Zhou, W.-W., Shi, X.-Z., and Gao, Y.-H. (2013) Development of Integrated Microfluidic Magnetic Bioprocessor for Multi-Biomarker Detection. *Chin. J. Anal. Chem.* 41 (9):1302–1307. doi:10.3724/SP.J.1096.2013.30231doi:10.1016/s1872-2040(13)60681-7

Meng, F.-D., Huo, W.-S., He, M.-L., Li, H., Lian, J., Shi, X.-Z., et al. (2016) A Microfluidic Fluorescence Immunoassay Test Card for Rapid Detection of Heart-type Fatty Acid Binding Protein. *Chin. J. Anal. Chem.* 44 (4):633–639. doi:10.1016/S1872-2040(16)60926-X

Meng, F., Huo, W., Lian, J., Zhang, L., Shi, X., Jesorka, A., et al. (2021) A Tandem Giant Magnetoresistance Assay for One-Shot Quantification of Clinically Relevant Concentrations of N-Terminal Pro-B-type Natriuretic Peptide in Human Blood. *Anal. Bioanal. Chem.* 413 (11):2943–2949. doi:10.1007/s00216-021-03227-5

Meng, F., Zhang, L., Huo, W., Lian, J., Jesorka, A., Shi, X., et al. (2021) Dynamic Range Expansion of the C-Reactive Protein Quantification with a Tandem Giant Magnetoresistance Biosensor. *ACS OMEGA* 6 (19):12923–12930. doi:10.1021/acsomega.1c01603

Muinao, T., Deka Boruah, H. P., and Pal, M. (2019) Multi-biomarker Panel Signature as the Key to Diagnosis of Ovarian Cancer. *HELIYON* 5 (12, e02826). doi:10.1016/j.heliyon.2019.e02826

Nesvet, J. C., Antilla, K. A., Pancirer, D. S., Lozano, A. X., Preiss, J. S., Ma, W., et al. (2021) Giant Magnetoresistive Nanosensor Analysis of Circulating Tumor DNA Epidermal Growth Factor Receptor Mutations for Diagnosis and Therapy Response Monitoring. *Clin. Chem.* 67 (3):534–542. doi:10.1093/clinchem/hvaa307

Nielsen, M. J., Baines, P., Jennings, R., Siner, S., Kolamunnage-Dona, R., Newland, P., et al. (2021) Procalcitonin, C-Reactive Protein, Neutrophil Gelatinase-Associated Lipocalin, Resistin and the APTT Waveform for the Early Diagnosis of Serious Bacterial Infection and Prediction of Outcome in Critically Ill Children. *PLOS ONE* 16 (2, e0246027). doi:10.1371/journal.pone.0246027

O'Connell, M. A., Belanger, B. A., and Haaland, P. D. (1993) Calibration and Assay Development Using the Four-Parameter Logistic Model. *Chemom. Intelligent Laboratory Syst.* 20 (2):97–114. doi:10.1016/0169-7439(93)80008-6

Oh, Y. K., Joung, H.-A., Han, H. S., Suk, H.-J., and Kim, M.-G. (2014) A Three-Line Lateral Flow Assay Strip for the Measurement of C-Reactive Protein Covering a Broad Physiological Concentration Range in Human Sera. *Biosens. Bioelectron.* 61:285–289. doi:10.1016/j.bios.2014.04.032

Pay, J. B., and Shaw, A. M. (2019) Towards Salivary C-Reactive Protein as a Viable Biomarker of Systemic Inflammation. *Clin. Biochem.* 68:1–8. doi:10.1016/j.clinbiochem.2019.04.006

Pultar, J., Sauer, U., Domnanich, P., and Preininger, C. (2009) Aptamer-antibody On-Chip Sandwich Immunoassay for Detection of CRP in Spiked Serum. *Biosens. Bioelectron.* 24 (5):1456–1461. doi:10.1016/j.bios.2008.08.052

Ravi, N., Chang, S. E., Franco, L. M., Nagamani, S. C. S., Khatri, P., Utz, P. J., et al. (2022) A GMR-Based Assay for Quantification of the Human Response to Influenza. *Biosens. Bioelectron.* 205:114086. doi:10.1016/j.bios.2022.114086

Yavuz, S., Anarat, A., Acartürk, S., Dalay, A. C., Kesiktaş, E., Yavuz, M., et al. (2014) Neutrophil Gelatinase Associated Lipocalin as an Indicator of Acute Kidney Injury and Inflammation in Burned Children. *BURNS* 40 (4):648–654. doi:10.1016/j.burns.2013.09.004

Zhang, L., Huo, W., Gao, Y., Shi, S., and Gao, Y. (2015) Determination of Affinity and Kinetic Constants of the Biotin-Streptavidin Complex Using Microfluidic GMR Biosensors. *IEEE Trans. Magn.* 51 (11):1–4. doi:10.1109/TMAG.2015.2443125

Zhu, W., Liu, M., Wang, G.-C., Che, J.-P., Xu, Y.-F., Peng, B., et al. (2014) Urinary Neutrophil Gelatinase-Associated Lipocalin, a Biomarker for Systemic Inflammatory Response Syndrome in Patients with Nephrolithiasis. *J. Surg. Res.* 187 (1):237–243. doi:10.1016/j.jss.2013.09.036

AUTHOR CONTRIBUTIONS

All authors listed have made a substantial, direct, and intellectual contribution to the work and approved it for publication.

FUNDING

This work was funded by the National Key Technology R&D Program of China (2013BAI03B03) and the Medical Health Science and Technology Project of Shandong Province (202011000657).

Conflict of Interest: Author LZ, WH, and XS were employed by Shenzhen Bosh Biotechnologies, Ltd.

The remaining authors declare that the research was conducted in the absence of any commercial or financial relationships that could be construed as a potential conflict of interest.

frontiers | Frontiers in Chemistry

ORIGINAL RESEARCH
published: 23 May 2022
doi: 10.3389/fchem.2022.865847

Efficient Interfacial Charge Transfer Based on 2D/2D Heterojunctions of Fe-C_3N_4/Ti_3C_2 for Improving the Photocatalytic Degradation of Antibiotics

Zhaohui Huo[1,2]*, Yanmin Liao[1], Yongyi He[1], Yifan Zhang[1], Xiaolin Liao[1], Qitong Zhang[1], Haojie Wu[1], Junjie Shi[1], Genglong Wen[1], Haixia Su[1] and Suyang Yao[1,2]

[1]School of Chemistry and Materials Science, Guangdong University of Education, Guangzhou, China, [2]Engineering Technology Development Center of Advanced Materials & Energy Saving and Emission Reduction in Guangdong Colleges and Universities, Guangzhou, China

Graphitic carbon nitride (g-C_3N_4) has shown to be a promising photocatalyst that, however, suffers from strong charge recombination and poor conductivity, while MXenes have shown to be perfect cocatalysts for the photocatalytic process but show poor stability. In this study, we successfully constructed 2D/2D heterojunctions of Fe-C_3N_4/Ti_3C_2 for the photocatalytic degradation of antibiotics. In this study, multilayer Ti_3C_2 was obtained by etching Ti_3AlC_2, and then Fe-C_3N_4/Ti_3C_2 photocatalyst was prepared by the one-pot microwave method and high-temperature calcination method. The synthesized samples were characterized by XRD, SEM, TEM, XPS, TGA, BET, DRS, PL, and other means. The photocatalytic degradation of tetracycline hydrochloride by Fe-C_3N_4/Ti_3C_2 was in accordance with the first-order reaction kinetics model, and the apparent rate constant k was 2.83, 2.06, and 1.77 times that of g-C_3N_4, Fe-C_3N_4, and g-C_3N_4/Ti_3C_2, respectively. Through the mechanism study, it was shown that the most active species in the reaction system was $\bullet O_2^-$, while h^+ and •OH had a relatively lower effect on the degradation system.

Keywords: g-C_3N_4, Ti_3C_2, Fe, 2D/2D heterojunction, photocatalytic degradation

OPEN ACCESS

Edited by:
Dejin Zang,
Tsinghua University, China

Reviewed by:
Zhao-Qing Liu,
Guangzhou University, China
Qitao Zhang,
Shenzhen University, China

****Correspondence:***
Zhaohui Huo
huozhaohui@gdei.edu.cn

Specialty section:
This article was submitted to Analytical Chemistry, a section of the journal Frontiers in Chemistry

Received: *30 January 2022*
Accepted: *05 April 2022*
Published: *23 May 2022*

Citation:
Huo Z, Liao Y, He Y, Zhang Y, Liao X, Zhang Q, Wu H, Shi J, Wen G, Su H and Yao S (2022) Efficient Interfacial Charge Transfer Based on 2D/2D Heterojunctions of Fe-C_3N_4/Ti_3C_2 for Improving the Photocatalytic Degradation of Antibiotics. Front. Chem. 10:865847. doi: 10.3389/fchem.2022.865847

INTRODUCTION

With the rapid development of modern industry, the problems of environmental pollution and energy shortage are increasingly prominent. Water pollution is particularly prominent among many environmental pollution problems, and antibiotic wastewater is recognized as organic wastewater, that is, difficult to treat (Lindberg et al., 2005). Tetracycline antibiotics are widely used in clinics and belong to broad-spectrum antibiotics. However, tetracycline drugs cannot be completely absorbed after being ingested by organisms, and most of them are discharged in their original form or metabolites (Gibson and Skett, 1986). Moreover, the production process of this class of antibiotics is complex, and a large number of them remain in pharmaceutical wastewater. Tetracycline antibiotics can damage the aquatic environment and cause chronic effects on the behavior, reproduction, and growth of organisms. At the same time, these antibiotics have bactericidal and bacteriostatic effects, resulting in the disappearance of some microbial populations and ecological function damage, which may lead to changes in methane generation, sulfate reduction, nitrogen transformation, and organic matter degradation, bringing great threats to the ecosystem and human health (Pei et al., 2020). At present, the treatment of tetracycline antibiotic wastewater mainly includes the biological method (Xu et al., 2017b), physical method (Wei et al., 2019), and chemical method (Lee et al., 2011), but these methods have disadvantages such as low degradation rate, complex technological process, and high cost, and may produce some new pollutants. Therefore, the development of a green, efficient, and low energy consumption antibiotic degradation technology has become an urgent need. Semiconductor photocatalytic technology can convert renewable solar energy into chemical energy under mild conditions, promote the REDOX reaction, and degrade antibiotics into nontoxic small molecules, so it has become a research hotspot. The core of photocatalytic technology lies in semiconductor materials. At present, a large number of semiconductor materials have been explored and applied in this technology, such as titanium dioxide (TiO_2) (Gao et al., 2020; Galeano et al., 2019), black phosphorus (P) (Bian et al., 2020; Liu D. et al., 2020), tungsten trioxide (WO_3) (Fu et al., 2019; Sun et al., 2019), and graphitic carbon nitride (g-C_3N_4) (Tong et al., 2017). At present, there are two main aspects that restrict the photocatalytic effect of semiconductors (Liu N. et al., 2018): 1) Low utilization rate of light. Most semiconductor photocatalysts can only be excited by ultraviolet light, which greatly limits the utilization rate of materials to sunlight; 2) the single-component semiconductor materials often have the defect of a high recombination rate of electron–hole pairs, which seriously restricts the photocatalytic effect. Therefore, we need to develop efficient photocatalytic materials with high visible light response and low carrier recombination rate, so as to promote the application of photocatalytic technology. In numerous semiconductor photocatalysts, the nonmetallic photocatalyst g-C_3N_4 stands out because of its visible light response, good chemical stability, suitable conduction band (CB) and valence band (VB) location, low cost, and nontoxic advantages; is considered as a metal-free photocatalyst with broad prospects; and has a great research value in the field of photocatalytic treatment of water pollution and hydrolysis of H_2. However, because of its poor conductivity, high carrier recombination rate, and small specific surface area (Xu et al., 2017a), the practical application of g-C_3N_4 is limited. Therefore, researchers modified g-C_3N_4 by means of element doping (Li et al., 2018; Zhao et al., 2019), semiconductor recombination (Yang et al., 2020; Yi et al., 2020; Liu et al., 2021), morphology control (Cui et al., 2018), and noble metal deposition (Li et al., 2019), to improve the photocatalytic performance. Among these strategies, doping (metal or non-metal) has been extensively used as a valid method to modulate the energy gap of semiconductors for the treatment of conductive, optical, or other physical properties (Fu et al., 2017; Liu N. et al., 2018). Doping Fe has been recognized as a facile and efficient approach to amending g-C_3N_4 (Zheng et al., 2015). g-C_3N_4 is rich in N atoms, which are filed with six lone pair electrons (Wang et al., 2009). This unique unit structure is quite appropriate for Fe inclusion. For example, Xu et al., 2019, designed Fe-doped surface alkalization g-C_3N_4 photocatalyst, showing good photocatalytic activity, and the degradation rate of tetracycline hydrochloride (TC) within 80 min was 63.70%, which was 1.29 times of that before doping. And, Liu G. et al., 2020, designed $CNFe_x$ samples with different Fe doping ratios, and the results showed that when the Fe doping ratio was 0.25, the samples showed the best photocatalytic activity, and the degradation rate of RhB was 87.00% within 60 min, 2.90 times that of pure g-C_3N_4. Liu et al. carried out a series of studies about Fe_2O_3 (He et al., 2020; Huang et al., 2021a), they have demonstrated that the combination of α-Fe_2O_3 can further improve the transfer of photogenerated charges and improved the photoelectric conversion efficiency. In particular, Fe_2O_3 combined with g-C_3N_4 could improve h^+ injection efficiency (Huang et al., 2021b). The results show that due to the lower reduction potential of Fe^{2+}/Fe^{3+} than that of g-C_3N_4, the addition of Fe species can effectively capture the photogenerated carriers of g-C_3N_4 and inhibit the recombination of electron–hole pairs. At the same time, the modification of high conductive materials on g-C_3N_4 nanosheets to construct heterojunctions is one of the feasible ways to promote charge separation.

MXene is an emerging two-dimensional layered material that shows great potential in the field of photocatalysis due to its superior ability to capture light and metal conductivity. The general formula for MXene is $M_{n+1}X_nT_x$, where M represents the early transition metal, X represents carbon or nitrogen, and T_x represents the functional groups (such as -OH, -F, and =O) produced in the etching process and attached to the surface of MXene material. In other words, MXene material is a new type of two-dimensional material composed of transition metal carbides, nitrides, and carbonitrides. Among them, Ti_3C_2 is a typical MXene material composed of transition metal carbide, which was successfully synthesized for the first time by Naguib et al. (2011). With the advantages of multilayer structure, good electrical conductivity, large specific surface area, and excellent chemical stability, Ti_3C_2 has become a research hotspot in the energy field in recent years. At present, a variety of hybrid materials based on Ti_3C_2 appear in the field of photocatalysis, such as Ti_3C_2/Bi_2WO_6 (Huang et al., 2020), $Ti_3C_2/CdLa_2S_4$ (Cheng et al., 2020), and Ti_3C_2/CdS (Yang et al., 2019, Huang et al., 2020) prepared Ti_3C_2/Bi_2WO_6 composites by electrostatic assembly method, showing excellent performance in photodegradation of formaldehyde and acetone, and the degradation rate was 2 times and 6.6 times of pure Bi_2WO_6, respectively. Studies have shown that this may be attributed to the strong adsorption of formaldehyde and acetone by Ti_3C_2 and the effective promotion of photogenerated electron–hole recombination of Bi_2WO_6 by Ti_3C_2. A large number of studies have shown that (Xiao et al., 2016; Anasori et al., 2017) Ti_3C_2 can effectively promote the separation of photogenerated electrons and holes by forming heterojunctions between Ti_3C_2 and other semiconductors due to its excellent metal-like conductivity. Therefore, Ti_3C_2 is widely used as a cocatalyst to improve the photocatalytic performance of semiconductors. Currently, there was also some work on the

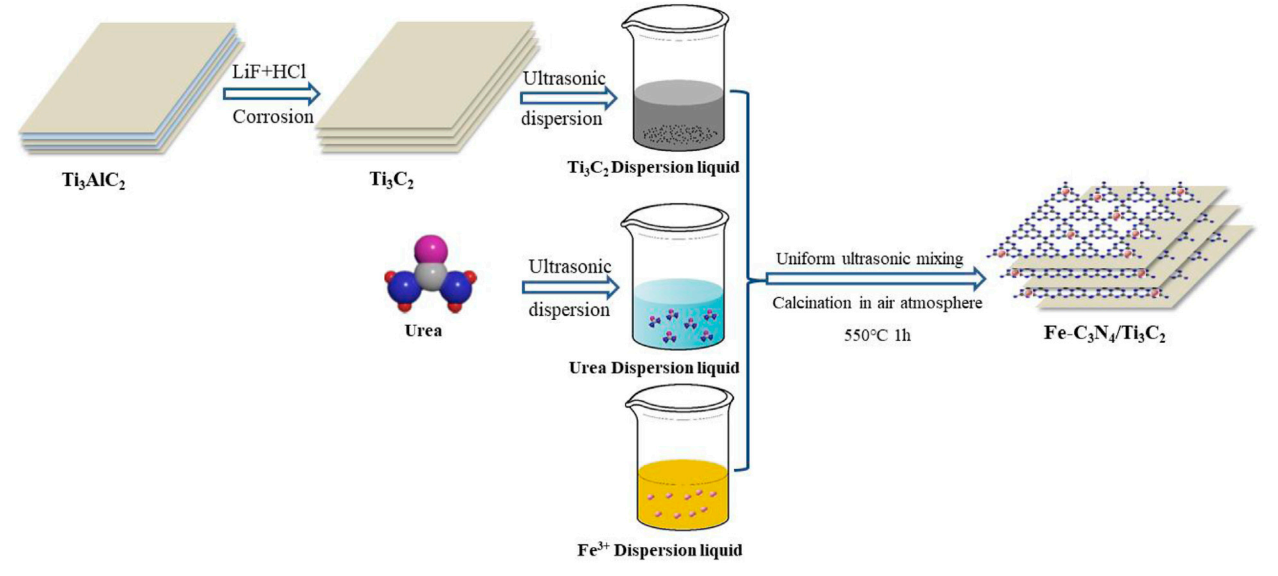

SCHEME 1 | Scheme illustration for Fe-C_3N_4/Ti_3C_2.

research of Ti_3C_2 and g-C_3N_4 composites. For example, Liu S. et al. (2018) prepared Ti_3C_2/g-C_3N_4 composites by means of evaporative self-assembly. The heterojunction formed between g-C_3N_4 and Ti_3C_2 effectively inhibited the photogenerated electric–hole pair composite of g-C_3N_4, and ciprofloxacin could be completely decomposed within 150 min, which was about 10% higher than that of pure g-C_3N_4. Composites show better performance. Liu et al., 2022, designed a 3D/2D g-C_3N_4/Ti_3C_2 heterojunction and found that benefiting from the 3D interconnected morphology and the incorporation of Ti_3C_2 nanosheets, it exhibited high specific surface area and efficient charge transfer. Yi et al., 2020, designed the compound of alkalized g-C_3N_4 with less layer Ti_3C_2 to prepare Ti_3C_2/g-C_3N_4 complex, which could effectively remove TC under visible light irradiation, with a yield of 77.0%. The kinetic constant was 1.8 times higher than that of alkalized g-C_3N_4, and the photocatalytic performance was effectively enhanced. Liu et al., 2021, prepared Ti_3C_2/g-C_3N_4 photocatalysts with different mass ratios. The results showed that when the mass ratio was 1%, Ti_3C_2/g-C_3N_4 had the best degradation performance for levofloxacin. It was 72.0%, which was 2.14 times that of the g-C_3N_4 monomer. Yang et al., 2020, prepared the ultrathin Ti_3C_2/g-C_3N_4 complex by directly calcining the mixture of massive Ti_3C_2 and urea, which showed good performance in the photoreduction of CO_2, and the total CO_2 conversion rate was 8.1 times higher than that of pure g-C_3N_4. These results showed that the 2D/2D heterojunction formed by g-C_3N_4 and Ti_3C_2 could effectively promote the charge separation of g-C_3N_4 and improve photocatalytic performance. In view of the disadvantages of g-C_3N_4, such as small specific surface area, easy recombination of electron–hole pairs, and low visible light utilization, the peeling process of Ti_3C_2 reported at present was complicated and had certain risks, and the "accordion" lamellar structure is unstable and easy to recombine.

In this study , Fe-C_3N_4/Ti_3C_2 was prepared by the one-pot microwave method and high-temperature calcination method. The photocatalytic performance of g-C_3N_4 was improved by the Fe doping and Ti_3C_2 composite, and TC was used as the target degradation material to investigate the photocatalytic performance of the sample and explore the photodegradation mechanism. The experimental results showed that both Fe doping and Ti_3C_2 composite could reduce the bandgap energy of g-C_3N_4 and improve the visible light utilization of the material; at the same time, it could effectively inhibit the recombination of electron–hole pairs of g-C_3N_4, improve the quantum efficiency, and enhance the photocatalytic performance. The highlights of this work were as follows: 1) simple preparation method: the synthesis of g-C_3N_4, the intercalation and peeling multilayer Ti_3C_2, and the composite of Ti_3C_2 and g-C_3N_4 were realized simultaneously by the combination of one-pot microwave method and high-temperature calcination method. Specificaly, urea was used as the precursor to prepare g-C_3N_4 in this study. NH_3 was produced in the process of calcination. As a small molecular substance, NH_3 could intercalate multilayer Ti_3C_2, effectively prevent the stacking of Ti_3C_2 layers and play a supporting role, promote the expansion of the spacing of multilayer Ti_3C_2 layers, and better form a tight 2D/2D interlayer interface with g-C_3N_4. The conventional relatively complex synthesis path of synthesizing monomer g-C_3N_4 and multilayer Ti_3C_2, and then intercalation and peeling multilayer Ti_3C_2 with dimethyl sulfoxide, and then recombination was simplified effectively (Li et al., 2020). 2) For the first time, Fe and Ti_3C_2 were introduced to modify g-C_3N_4, and the reduction potential of Fe^{2+}/Fe^{3+} was lower than that of g-C_3N_4, to effectively capture the photogenerated carriers of g-C_3N_4. At the same time, the 2D/2D heterojunction formed by g-C_3N_4 and Ti_3C_2 could effectively promote the charge separation of the g-C_3N_4 and explored whether there was a synergistic effect between these two modification methods to further promote the photocatalytic performance of the g-C_3N_4.

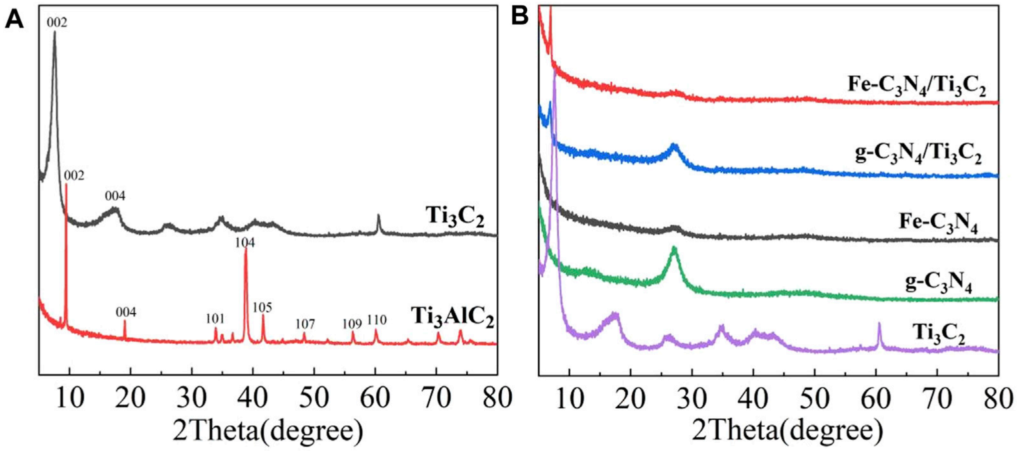

FIGURE 1 | (A) XRD pattern of Ti_3C_2 and Ti_3AlC_2. **(B)** XRD pattern of the Ti_3C_2, g-C_3N_4, Fe-C_3N_4, g-C_3N_4/Ti_3C_2, and Fe-C_3N_4/Ti_3C_2.

EXPERIMENTAL SECTION

Materials

Urea, p-benzoquinone (BQ), and ethylenediamine tetraacetic acid disodium (EDTA-2Na) were purchased from Tianjin Damao Chemical Reagent Factory. Lithium fluoride (LiF), tetracycline hydrochloride (TC), and isopropanol (IPA) were purchased from Shanghai Aladdin Biochemical Technology Co., Ltd. Iron nitrate [$Fe(NO_3)_3{\cdot}9H_2O$] was purchased from Shanghai McLean Biochemical Technology Co., Ltd. Ti_3AlC_2 MAX phase was purchased from Hangzhou Namao Technology Co., Ltd. Hydrochloric acid (37% wt.) was purchased from Guangzhou Chemical Reagent Factory. And, all the chemicals are analytically pure except for special marked, and they were directly used without further purification.

Preparation of Multilayer Ti_3C_2

HCl solution (20 ml of 9 mol/L) was added to the Teflon beaker, and 1.0 g of LiF powder was slowly added to the beaker under the action of a magnetic agitator. After it gets fully dissolved, the solution was stirred for 10 min. To avoid overheating, 1.0 g of Ti_3AlC_2 powder was added slowly for about 20 min. After continuous stirring at 35°C for 48 h, they were centrifuged at 4,000 rpm for 20 min, washed with 3 mol/L HCl solution several times to remove the residual LiF after reaction, and then washed repeatedly with deionized water until the pH of the supernatant was close to 7. The collected Ti_3C_2 precipitate was freeze-dried thoroughly, and the obtained powder was multilayer Ti_3C_2 powder.

Preparation of Fe-C_3N_4/Ti_3C_2

$Fe(NO_3)_3{\cdot}9H_2O$ (0.06 g) was dissolved and dispersed in 50 ml of deionized water, 10 g of urea was added to dissolve completely, and 0.08 g of Ti_3C_2 powder was added under an ultrasonic environment to form a uniform dispersion solution, dried thoroughly, and ground evenly. Calcination was carried out in a 50 ml crucible with a lid in a muffle furnace under an air atmosphere. The temperature rose to 550°C at a rate of 50°C/min, and the temperature was held for 1 h. The resulting brown-yellow solid was ground thoroughly to form Fe-C_3N_4/Ti_3C_2 powder (see **Scheme 1**).

Testing and Characterization of Materials

The phase characterization of the samples was determined by an X-ray powder diffract graph (D8 Advance, Brock AXS, Germany), using Cu-Kα rays with a wavelength of 154 p.m. and a scanning range of 2θ = 5°~80°; the morphology and structure of the samples were characterized by MIRA 3 LMU scanning electron microscope SEM (TESCAN Brno, S.R.O., Czech Republic) at a voltage of 15 kV; the morphology and microstructure were also observed by transmission electron microscopy TEM and high-resolution transmission electron microscopy HR-TEM (FEI Talos F200x G2,United States); the element was mapped by the energy-dispersive spectroscopy EDS (FEI Talos F200x G2, Super-X, United States); the element composition and existence form of the samples were determined by X-ray photoelectron spectroscopy XPS (Thermo Scientific K-Alpha Hangzhou Yanqu Information Technology Co., LTD) using the Al-Kα rays; the thermal stability of the samples was characterized by using a thermogravimetric analyzer TGA (TGA-4000, Platinum Elmer, United States); the specific surface area of the samples was analyzed by an automatic specific surface adsorption instrument BET (BELSORP-max, DKSH Commercial Co., LTD., Japan); the optical absorption performance of the sample was reflected by using the UV-visible diffuse reflector DRS (Shimadzu UV-2600, Japan) and calculating the bandgap of the photocatalyst. $BaSO_4$ was used as the reference sample; the photocatalytic activity of the samples was analyzed by fluorescence PL (Shimadzu RF-5301PC, Japan), and the excitation wavelength was 322 nm.

Adsorption Properties of the Material

50 ml of 20 mg/L TC solution was added into the beaker, then 20 mg of Fe-C_3N_4/Ti_3C_2 powder was added, and shook well. The mixture was stirred away from light, the proper amount of mixture was absorbed every 10 min, and the absorbance was measured at 356 nm by using a visible spectrophotometer.

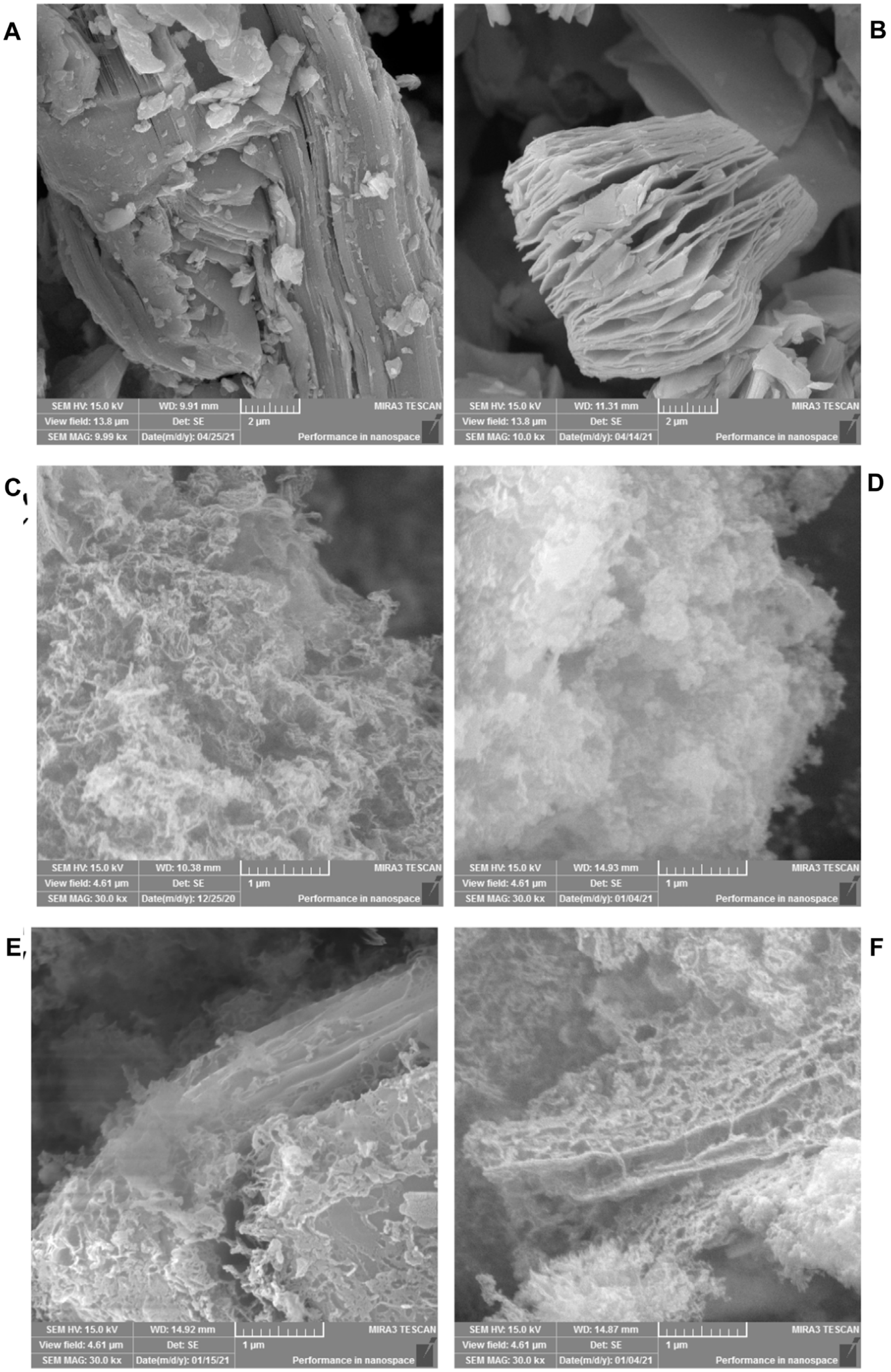

FIGURE 2 | SEM images of **(A)** Ti_3AlC_2, **(B)** Ti_3C_2, **(C)** g-C_3N_4, **(D)** Fe-C_3N_4, **(E)** g-C_3N_4/Ti_3C_2 and **(F)** Fe-C_3N_4/Ti_3C_2.

Photocatalytic Performance of the Material

50 ml of 20 mg/L TC solution was added into the beaker, 20 mg of Fe-C_3N_4/Ti_3C_2 powder was added, and shook well. The mixture was stirred away from light until the adsorption–desorption is balanced, then placed it in a xenon lamp source (λ > 420 nm, 280W), the proper amount of mixture was absorbed every 20 min, and the absorbance was measured at 356 nm by using a visible spectrophotometer. Benzoquinone (BQ), isopropyl

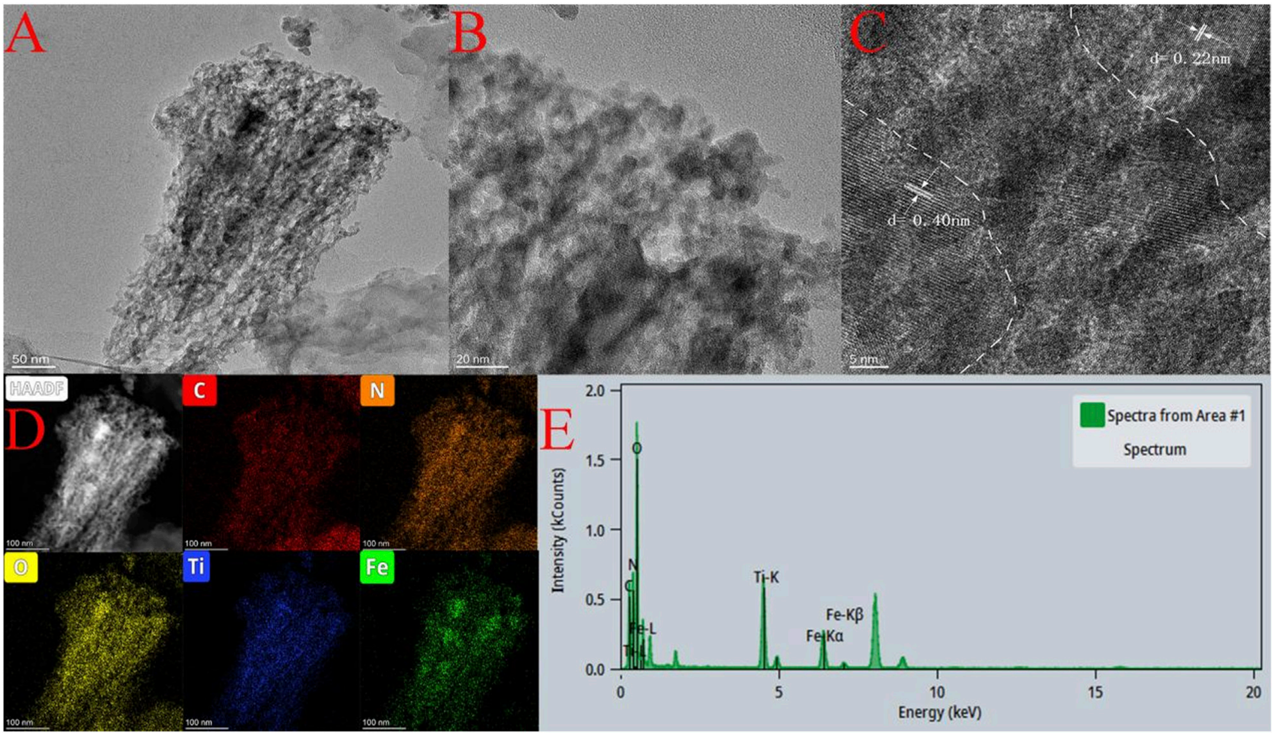

FIGURE 3 | (A,B) TEM images of Fe-C_3N_4/Ti_3C_2, **(C)** HR-TEM of Fe-C_3N_4/Ti_3C_2, **(D,E)** EDS of Fe-C_3N_4/Ti_3C_2.

alcohol (IPA), and ethylenediamine tetraacetic acid disodium (EDTA-2Na) were used as the trapping agent of superoxide free radical (•O_2^-), hydroxyl free radical (•OH), and hole (h^+), respectively, to explore the degradation mechanism of pollutants in the photocatalytic reaction.

Photoelectrochemical Measurements

The photoelectrochemical measurements were conducted on a three-electrode electrochemical workstation (A4602, Wuhan Kesite Instrument Co., LTD.), in which the working electrode, counter electrode, and reference electrode were the obtained samples, platinum foil, and Ag/AgCl electrode, respectively. The working electrodes were prepared by the drop-coating method: typically, 2 mg of catalyst and 15 μl Nafion solution were dispersed in 1 ml of ethanol and sonicated for 30 min. Afterward, the resulted homogeneous suspension was dripped onto the FTO and dried at room temperature. Here, all photoelectrochemical measurements were carried out in 0.5 m Na_2SO_4 electrolyte, and the light source was identical to that of photocatalytic measurements. Mott–Schottky was recorded at a frequency of 1,000 Hz.

RESULTS AND DISCUSSION

XRD Characterization

The phase of the sample was characterized by an X-ray powder diffractometer, and the results are reflected in **Figure 1A** which shows the XRD patterns of Ti_3AlC_2 and multilayer Ti_3C_2. A series of diffraction peaks corresponding to (002), (004), (101), (104), (105), (107), (109), and (110) crystal planes can be observed from the XRD spectra of Ti_3AlC_2. After being etched by HF, the strongest peak of Ti_3C_2 at 39.0° disappeared, and the peaks corresponding to (002) and (004) crystal planes widened and shifted to a lower angle, indicating that the Al layer in Ti_3AlC_2 had been removed, and Ti_3AlC_2 was successfully converted to Ti_3C_2. At the same time, the Ti_3C_2 layer structure becomes thinner. From **Figure 1B**, two evident diffraction peaks located at 12.83° and 27.05° for g-C_3N_4 are observed, corresponding to (100) and (002) crystal planes, respectively. Fe-C_3N_4 mainly had a peak at 27.05°, corresponding to the (002) crystal plane of g-C_3N_4. The characteristic peak of Fe was not observed, probably due to the small amount of doped Fe or the weak characteristic peak. The XRD pattern of g-C_3N_4/Ti_3C_2 shows two distinct peaks at 6.93° and 27.05°, respectively, corresponding to the (002) crystal plane of Ti_3C_2 and the (002) crystal plane of g-C_3N_4, indicating that g-C_3N_4 and Ti_3C_2 have achieved good recombination. The XRD pattern of Fe-C_3N_4/Ti_3C_2 is similar to that of g-C_3N_4/Ti_3C_2. The characteristic peaks of Ti_3C_2 and g-C_3N_4 are observed, and the characteristic peaks of Fe are not observed, on account of the small amount of Fe doped or the weak characteristic peaks.

Compared with multilayer Ti_3C_2, the intensity of characteristic peaks on the (002) plane of g-C_3N_4/Ti_3C_2 and Fe-C_3N_4/Ti_3C_2 at 6.93° is much weaker. It is speculated

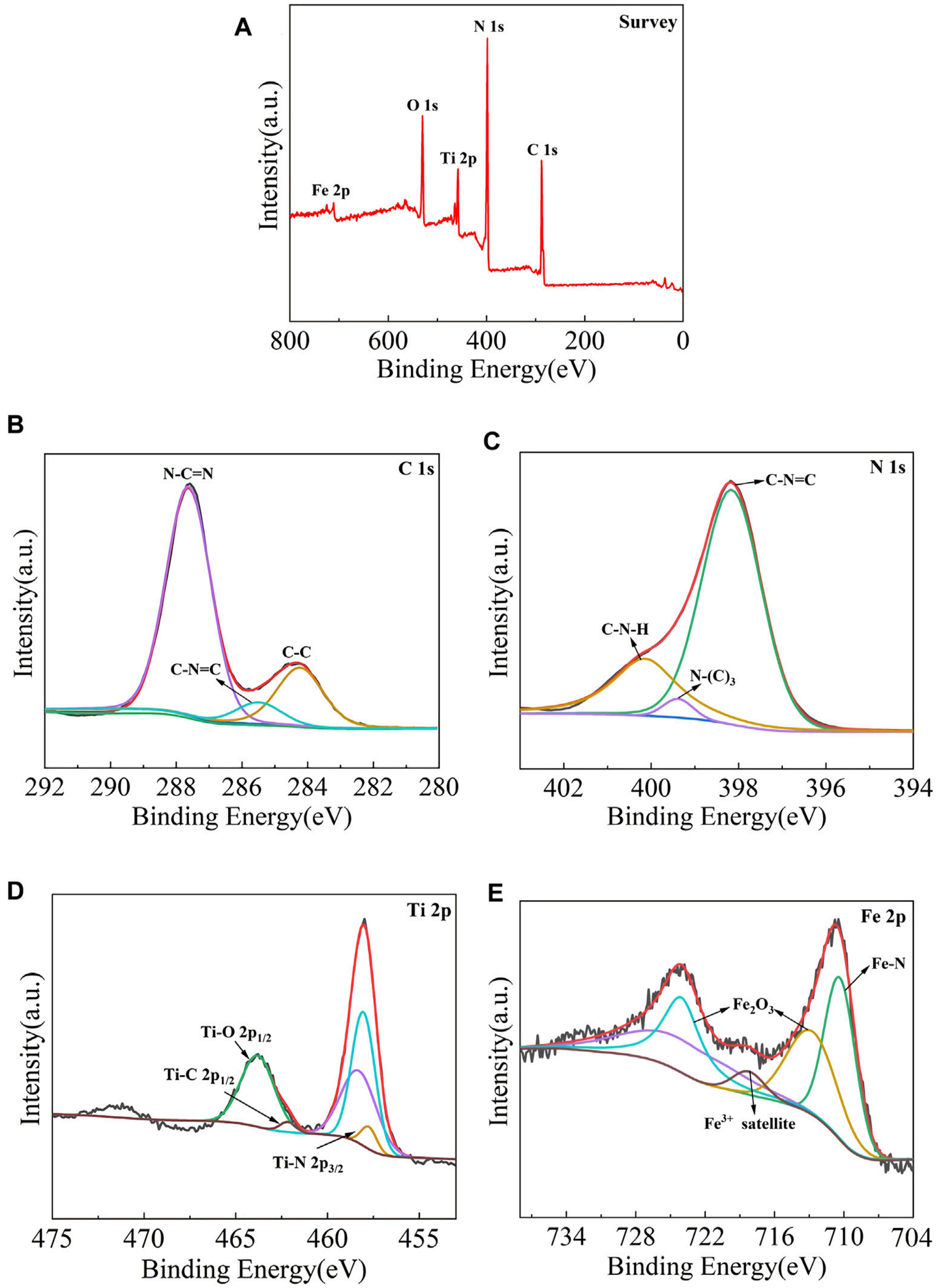

FIGURE 4 | XPS pattern of **(A)** Fe-C_3N_4/Ti_3C_2 composites, High-resolution XPS spectra comparison of **(B,C)** 1s and **(C)** N 1s and **(D)** Ti 2pand **(E)** Fe 2p.

that NH_3 released during urea calcination can be inserted into the interlayer of multilayer Ti_3C_2 as a small molecule in the process of compounding with Ti_3C_2, which effectively prevents the stacking of Ti_3C_2 interlayers, plays a supporting role, promotes the expansion of interlayer spacing of multilayer Ti_3C_2, and forms a close 2D/2D interlayer contact surface with g-C_3N_4. At the same time, it is speculated that Fe doping causes different degrees of polycondensation of g-C_3N_4 and delays the phase transition process, resulting in the decrease of cell parameters and crystal plane spacing of g-C_3N_4 and the increase of specific surface area. Moreover, Ti_3C_2 and g-C_3N_4 form a 2D/2D contact surface, which directly affects the periodic stacking interlayer structure of g-C_3N_4, resulting in the decrease of the diffraction peak intensity of g-C_3N_4 at 27.05° and the broadening.

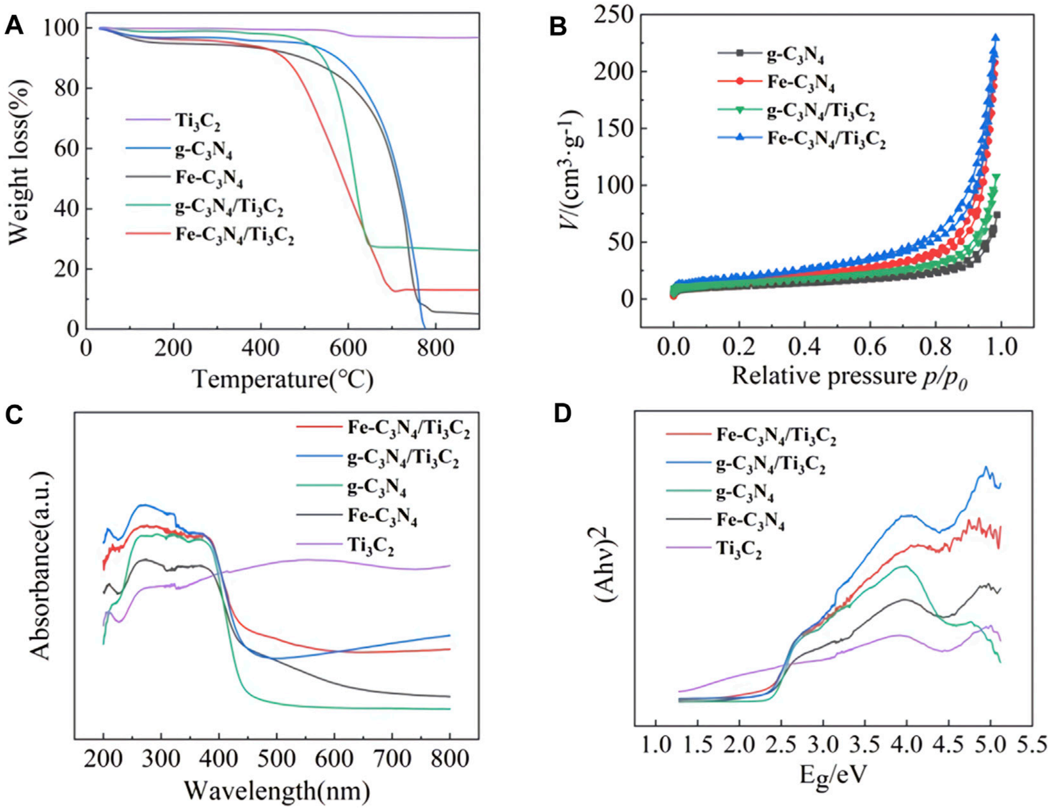

FIGURE 5 | (A) The TGA curves of Ti_3C_2, g-C_3N_4, Fe-C_3N_4, g-C_3N_4/Ti_3C_2, and Fe-C_3N_4/Ti_3C_2. **(B)** N_2 adsorption-desorption isotherms of different materials. **(C)** UV-Vis diffuse reflectance spectra and **(D)** band gap of g-C_3N_4, Ti_3C_2, Fe-C_3N_4, g-C_3N_4/Ti_3C_2 and Fe-C_3N_4/Ti_3C_2.

SEM Characterization

The microstructure of the samples was characterized by SEM, and the results are shown in **Figure 2**. It can be seen from **Figure 2A** that the unetched Ti_3AlC_2 is a bulk stacking structure. The morphology of Ti_3C_2 obtained by etching is shown in **Figure 2B**. Clear interlamellar spacing can be observed visually, showing a two-dimensional layered structure of MXene. Multilayer Ti_3C_2 stacked together changed into an accordion-like structure. It is observed from **Figure 2C** that g-C_3N_4 is mostly agglomerated and a small part is thin. It is observed from **Figure 2D** that the aggregation of g-C_3N_4 after Fe-doping is weakened, showing a thin lamellar structure. It is observed from **Figure 2E** that, after the combination of g-C_3N_4 and Ti_3C_2, the two form a close interlayer structure. From **Figure 2F**, it can be observed that there is a close interlayer structure between g-C_3N_4 and Ti_3C_2 in Fe-C_3N_4/Ti_3C_2. It is assumed that urea releases NH_3 during the calcination, and small molecule NH_3 inserts into the interlayer structure of Ti_3C_2 and acts as a gas template to strip Ti_3C_2, effectively preventing the accumulation of Ti_3C_2 layers (Yang et al., 2020).

TEM Characterization

The morphology and microstructure of the Fe-C_3N_4/Ti_3C_2 catalyst were observed by TEM (**Figure 3A**). It can be seen that the sample exhibits a typical layered structure. In **Figure 3B**, the shallowest area is g-C_3N_4, the darker overlying layer is Ti_3C_2, and the darkest black area is Fe species. More information about Fe-C_3N_4/Ti_3C_2 can be obtained from **Figure 3C**. The lattice spacing of Ti_3C_2 is 0.22 nm, and the lattice spacing of Fe species is 0.40 nm. In addition, the EDS element map (**Figure 3D**) of the sample further confirms that there is good interaction between Fe, Ti_3C_2, and g-C_3N_4. The elements C, N, O, Ti, and Fe are distributed uniformly in the samples. According to **Figure 3E**, the contents of Fe and Ti are 13.34 and 25.16%, respectively. These results show that g-C_3N_4 is uniformly modified by Ti_3C_2 and Fe and has close contact.

XPS Characterization

The chemical composition and valence state of the samples were characterized by X-ray photoelectron spectroscopy, and the results are shown in **Figure 4**. It is observed from **Figure 4A** that the measured spectra of Fe-C_3N_4/Ti_3C_2 show the existence of C, N, Ti, O, and Fe elements, indicating that Fe-doping and the composite of Ti_3C_2 were successfully realized in g-C_3N_4. It can be seen from the C 1s spectrum (**Figure 4B**) that the C 1s peak can be fitted into three peaks, namely, graphite phase carbon (C–C) at 284.38 eV, sp^3-hybridized carbon (C-N=C) at 285.48 eV, and sp^2-hybridized carbon (N-C=N) at 287.58 eV. The N 1s spectrum (**Figure 4C**)

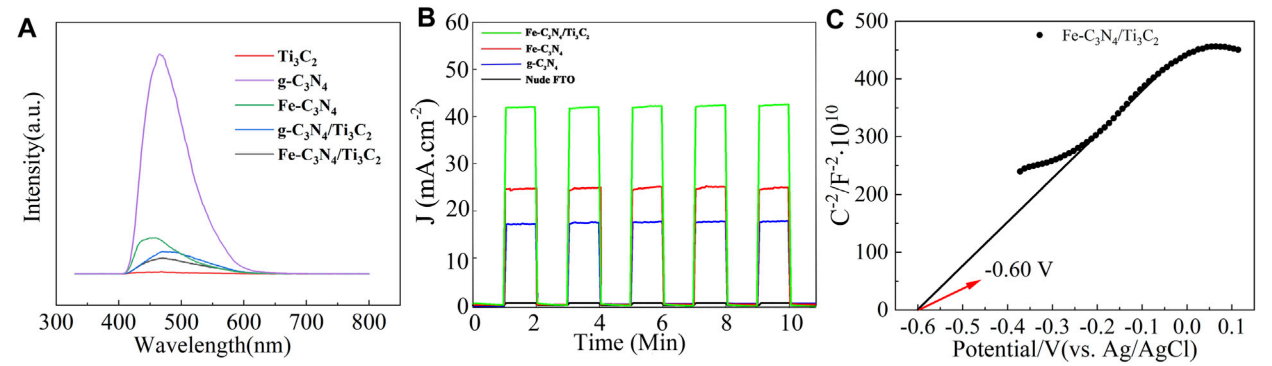

FIGURE 6 | (A) PL spectra of g-C_3N_4, Ti_3C_2, Fe-C_3N_4, g-C_3N_4/Ti_3C_2, and Fe-C_3N_4/Ti_3C_2. **(B)** The transient photocurrent density of nude FTO, g-C_3N_4, Fe-C_3N_4 and Fe-C_3N_4/Ti_3C_2. **(C)** Mott-Schottky curves of Fe-C_3N_4/Ti_3C_2.

shows three distinct peaks, which are ascribed to sp^2-hybridized nitrogen (C-N=C) at 398.18 eV, tertiary nitrogen group (N-(C)$_3$) at 399.38 eV, and free amino groups (C-N-H) at 400.10 eV, respectively. According to the Ti 2p spectrum (**Figure 4D**), Ti 2p XPS peaks are deconvoluted into three peaks, namely, Ti-N bond at 457.70 eV, Ti-C 2p$^{1/2}$ bond at 462.20 eV, and Ti-O 2p$^{1/2}$ bond at 463.84 eV. The existence of the Ti-O 2p$^{1/2}$ bond may be related to the slight oxidation of Ti_3C_2. According to the Fe 2p spectra (**Figure 4E**), there are three chemical states of Fe, namely, Fe-N bond at 710.48 eV, trivalent iron satellite peak at 718.30 eV, and trivalent iron in Fe_2O_3 at 713.08 and 724.28 eV, which indicates that there are both iron–nitrogen chemical bonds and Fe_2O_3 in the material. From the above analysis, Fe-doping and Ti_3C_2 composite were successfully realized in g-C_3N_4. In Fe-C_3N_4/Ti_3C_2, Fe mainly exists in the form of the Fe-N bond and Fe_2O_3, Ti forms the key existence in the Ti-N bond and Ti-C bond, which further confirms that Fe and Ti_3C_2 have been successfully combined with g-C_3N_4.

TGA Characterization

The thermal stability of the sample was characterized by a thermogravimetric analyzer, and the results are shown in **Figure 5A**. It can be observed from **Figure 5A** that the mass change of Ti_3C_2 is not obvious with the increase in temperature, showing excellent stability. The mass loss of g-C_3N_4, Fe-C_3N_4, g-C_3N_4/Ti_3C_2, and Fe-C_3N_4/Ti_3C_2 was very rapid within a certain temperature range, which was due to the decomposition of the C-N bond of g-C_3N_4 in the material to generate CO_2 and NO_2. At the same time, pure g-C_3N_4 was completely decomposed when the temperature exceeded 777°C, while Fe-C_3N_4, g-C_3N_4/Ti_3C_2, and Fe-C_3N_4/Ti_3C_2 were not completely decomposed, which was attributed to the stability of Fe and Ti_3C_2 residues in the sample.

BET Characterization

The specific surface area of the sample was analyzed by an automatic surface adsorption instrument. **Figure 5B** shows that the specific surface areas of g-C_3N_4, Fe-C_3N_4, g-C_3N_4/Ti_3C_2, and Fe-C_3N_4/Ti_3C_2 are 38.55 m^2/g, 54.13 m^2/g, 49.25 m^2/g, and 68.58 m^2/g, respectively. Both Fe-doping and composite Ti_3C_2 are conducive to expanding the specific surface area of photocatalyst, providing more active sites and improving the adsorption performance of materials. At the same time, the larger the specific surface area, the e$^-$ generated by g-C_3N_4 can migrate to the surface of the catalyst more quickly, which effectively reduces the recombination rate of electron and hole pairs and improves the photocatalytic performance of the material.

UV-Vis-DRS Characterization

The absorption properties of the samples were recorded by UV-Vis diffuse reflectance spectroscopy. The results are shown in **Figures 5C,D**. It is observed from **Figure 5C** that the Ti_3C_2 shows broad absorption in the whole region (200~800 nm), and there is no obvious absorption with the edge, indicating that Ti_3C_2 has metallic properties. The pristine g-C_3N_4 displays a typical absorption region at about 450 nm, which is consistent with the literature (Gebreslassie et al., 2019). The optical cutoff wavelengths of Fe-C_3N_4, g-C_3N_4/Ti_3C_2, and Fe-C_3N_4/Ti_3C_2 are 467 nm, 458, and 470 nm, respectively. It can be seen that after Fe-doping and Ti_3C_2 composite, the sample shows a redshift compared with the monomer g-C_3N_4, and the visible light absorption capacity is enhanced, indicating that Fe-doping and composite Ti_3C_2 can effectively improve the visible light absorption performance of g-C_3N_4. Due to the strong absorption of dark Ti_3C_2 in the whole wavelength range (200~800 nm), the absorption edge of g-C_3N_4 can readily shift after recombination, so Ti_3C_2 composite can effectively enhance the light absorption of g-C_3N_4. According to the energy level theory, it is suggested that the bandgap of g-C_3N_4 forms the impurity energy level after Fe-doping. The electrons only need to absorb photons with small energy to realize the indirect transition of energy level, which can absorb photons with long-wavelength, broaden the visible light absorption range of g-C_3N_4 and improve the utilization rate of visible light. From **Figure 5D** the band gaps of g-C_3N_4, Fe-C_3N_4, g-C_3N_4/Ti_3C_2, and Fe-C_3N_4/Ti_3C_2 are 2.38, 2.26, 2.21, and 2.19 eV, respectively. It shows that Fe-doping and composite Ti_3C_2 can reduce the bandgap energy of g-C_3N_4, reduce the bandgap width, expand the visible light response range, and improve the visible light utilization.

PL Characterization

The photocatalytic activity of the samples was analyzed by fluorescence spectroscopy. The results are shown in

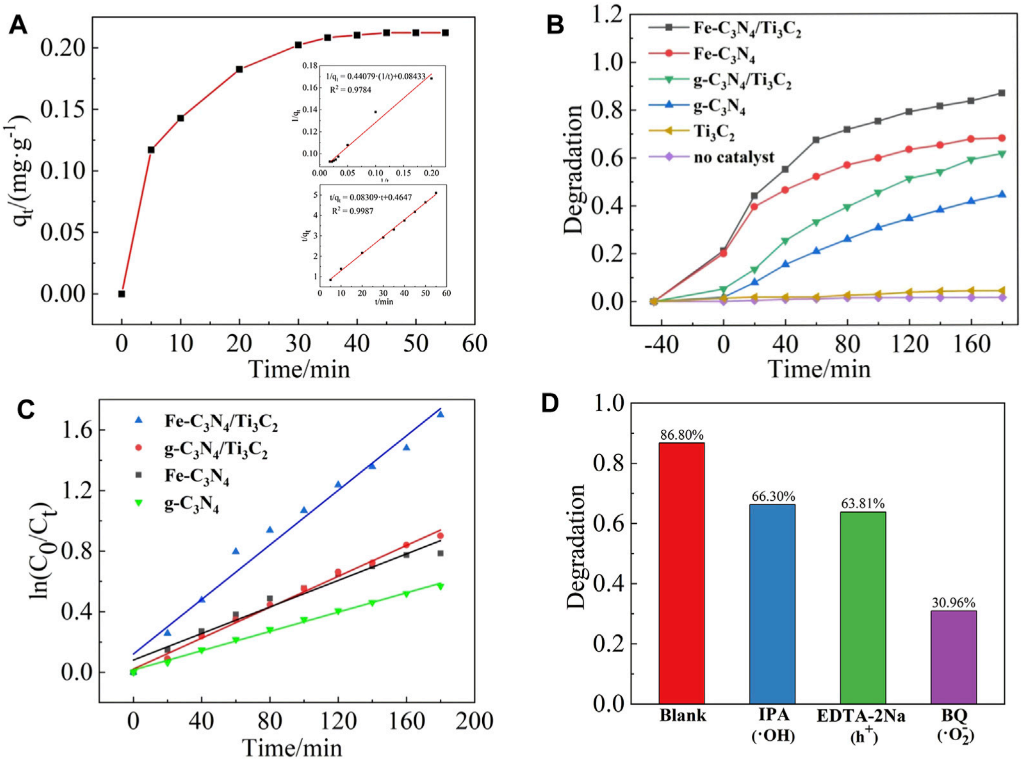

FIGURE 7 | (A) Absorption curve of TC on Fe-C_3N_4/Ti_3C_2。Dynamic model: quasi-first order,quasi-second order. **(B)** Photocatalytic degradation curves of TC by different photocatalysts. **(C)** Kinetic fitting curve. **(D)** Photocatalytic activity changes of Fe-C_3N_4/Ti_3C_2 for TC degradation with different sacrificial agents.

TABLE 1 | First-order reaction kinetic parameters.

Photocatalyst	First order kinetic equation	Correlation R^2	Degradation rate (%)	Reaction Rate Constant k (min)
g-C_3N_4	ln (C_0/C_t) = 0.00318t+0.01508	0.9957	44.37	0.00318^{-1}
Fe-C_3N_4	ln (C_0/C_t) = 0.00438t+0.08071	0.9664	68.01	0.00438^{-1}
g-C_3N_4/Ti_3C_2	ln (C_0/C_t) = 0.00510t+0.02109	0.9937	61.53	0.00510^{-1}
Fe-C_3N_4/Ti_3C_2	ln (C_0/C_t) = 0.00901t+0.12033	0.9794	86.80	0.00901^{-1}

Figure 6A. It can be seen from **Figure 6A** that g-C_3N_4 shows a strong fluorescence emission peak at 466 nm. After Fe-doping and composite Ti_3C_2, the intensity of this peak was inhibited significantly. Confirming that Fe-doping and composite Ti_3C_2 can effectively reduce the electrons and holes recombination probability of g-C_3N_4, and the quantum efficiency is improved.

According to the relevant literature (Li et al., 2008), Fe^{2+}/Fe^{3+} has a reduction potential lower than the conduction band potential of g-C_3N_4, so Fe-doping can effectively capture the photogenerated carriers of g-C_3N_4 and inhibit the recombination of electron and hole pairs. When the g-C_3N_4 layer is inserted into the Ti_3C_2 sheet, the two form many intimate interfaces, thus providing the maximum contact surface between the two phases. On such a platform, electrons can be easily transferred from g-C_3N_4 nanosheets to metal Ti_3C_2 sheets with high conductivity (Su et al., 2019), inhibiting the recombination of electron and hole pairs. At the same time, it can be observed from **Figure 6A** that the fluorescence intensity of Fe-C_3N_4/Ti_3C_2 is the lowest, indicating that there is a synergistic effect between Fe-doping and composite Ti_3C_2 in g-C_3N_4. The recombination rate of the excited electrons and holes in g-C_3N_4 is greatly reduced, the quantum efficiency shows excellent improvement, and the sample may show better photocatalytic activity.

As it is known to all, a higher photocurrent means a higher separation efficiency for the photogenerated charge, which is finally reflected in the better photocatalytic performance. As displayed in **Figure 6B**, compared with naked FTO, the photocurrent responses of g-C_3N_4, Fe-C_3N_4, and Fe-C_3N_4/Ti_3C_2 samples gradually increase, with average photocurrent densities of 17.3, 24.6, and 41.7 μA/cm^2. Fe-C_3N_4/Ti_3C_2 shows the highest photocurrent density, which is 2.4-fold higher than g-C_3N_4 and 1.7-fold higher than Fe-C_3N_4. The enhanced photocurrent density of Fe-C_3N_4 and Fe-C_3N_4/Ti_3C_2 electrodes, respectively, shows that Fe doping and Ti_3C_2 composite can promote g-C_3N_4 to provide more

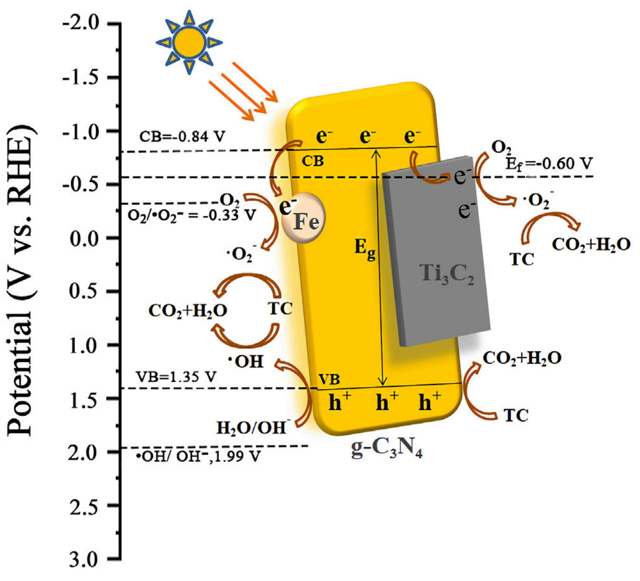

FIGURE 8 | Photocatalytic degradation mechanism diagram of Fe-C_3N_4/Ti_3C_2 to TC.

carriers to the external circuit, resulting in the greater the photocurrent and the higher the photogenerated charge. The higher the separation efficiency, the better the photocatalytic performance. The results here are mainly due to the following reasons: the reduction potential of Fe^{2+}/Fe^{3+} is lower than the conduction band potential of g-C_3N_4, so Fe can effectively capture the photogenerated carriers generated by g-C_3N_4, and the e^-–h^+ pair recombination rate is greatly reduced (Hu et al., 2018), and Fe doping weakens the degree of polymerization of g-C_3N_4, increases its surface area, and provides more photocatalytically active sites. The Ti_3C_2 layer is embedded in thin g-C_3N_4 nanosheets, forming a heterojunction and interfacial effect between them. The photogenerated electrons tend to transfer from g-C_3N_4 to Ti_3C_2, which improves the interfacial charge transfer ability of g-C_3N_4, which can effectively inhibit the recombination of e^-–h^+ pairs. (Li et al., 2020). Metal Fe-doped and g-C_3N_4 composite Ti_3C_2 act simultaneously, and the photocatalytic performance is better than Fe-C_3N_4.

Adsorption Performance

When the catalyst dosage was 20 mg and the initial concentration of TC is 20 mg/L, the adsorption curve of Fe-C_3N_4/Ti_3C_2 on TC is shown in **Figure 7A**. In the first 5 min of the dark reaction, the adsorption amount of TC on Fe-C_3N_4/Ti_3C_2 increased rapidly and reached the adsorption-desorption equilibrium after 45 min. The equilibrium adsorption amount was 10.78 mg/g, and the adsorption rate was 21.03%. The adsorption kinetics of TC on Fe-C_3N_4/Ti_3C_2 was investigated by pseudo-first-order and pseudo-second-order adsorption kinetics models. The results are shown in **Figure 7A**. The graph shows that the correlation coefficient of the pseudo-first-order kinetic equation $R^2 = 0.9784$, and the correlation coefficient of the pseudo-second-order kinetic equation $R^2 = 0.9987$, indicating that the adsorption of TC by Fe-C_3N_4/Ti_3C_2 is a second-order kinetic model, that is, chemical adsorption. The equilibrium adsorption amount $q_e = 10.78$ mg/g, and the adsorption rate constant $k = 0.01852$ g/(mgmin) can be obtained from the slope and intercept of the straight line, respectively.

Photocatalytic Activity

When the catalyst dosage was 20 mg and the initial concentration of TC was 20 mg/L, the photocatalytic degradation curves of different samples are shown in **Figure 7B**. When no photocatalyst was added, TC was almost not degraded under xenon lamp irradiation, and the degradation rate was only about 1.41%, indicating that TC was relatively stable and difficult to be photodegraded. When only Ti_3C_2 was added, the photocatalytic degradation rate of TC under xenon lamp irradiation was only 4.30%, indicating that Ti_3C_2 cannot be used as a catalyst for photocatalytic degradation of TC alone. After 180 min of illumination, the photocatalytic degradation rates of TC by g-C_3N_4, g-C_3N_4/Ti_3C_2, Fe-C_3N_4, and Fe-C_3N_4/Ti_3C_2 were 44.37, 61.53, 68.01, and 86.80%, respectively. It can be seen that compared with g-C_3N_4, the degradation rate of TC by g-C_3N_4 is improved after Fe-doping and composite Ti_3C_2. The degradation rate of TC by Fe-C_3N_4/Ti_3C_2 within 180 min is 86.80%, 1.96 times that of g-C_3N_4, which greatly improves the photocatalytic degradation efficiency of TC by photocatalyst. It can be speculated that there is a synergistic effect between Fe-doping and composite Ti_3C_2 in g-C_3N_4, and the photocatalytic ability of the sample is better.

Linear fitting with $\ln(C_0/C_t)$ to t, and the results are shown in **Figure 7C**. The photocatalytic degradation of TC by Fe-C_3N_4/Ti_3C_2 conforms to the first-order reaction kinetics model, and the

TABLE 2 | Comparison of photocatalytic properties of different systems.

Years	Photocatalyst	Dosage (mg)	Target degradation amount	Degrading time (min)	Source power (W)	Light source wavelength	Degradation rate (%)	Rate constant	References
2021	Fe-C_3N_4/Ti_3C_2	20	TC	180	280	>420 nm	86.80	0.0090 min^{-1}	Our work
2021	Ti_3C_2/g-C_3N_4	20	LEV	30	300	>420 nm	72.00	0.0392 min^{-1}	Liu et al. (2021)
2021	cPTA/g-C_3N_4	30	TC	180	500	>420 nm	78.00	0.0084 min^{-1}	Yang et al. (2021)
2020	Ti_3C_2/alkalized g-C_3N_4	10	TC	60	300	>420 nm	77.00	0.0307 min^{-1}	Yi et al. (2020)
2020	Fe-doped g-C_3N_4	50	RhB	60	300	>420 nm	87.00	-	Liu et al. (2020a)
2018	Fe-doped alkalinized g-C_3N_4	30	TC	80	300	>420 nm	63.70	0.0164 min^{-1}	Xu et al. (2018)

relevant parameters are shown in **Table 1**. The apparent rate constants k of Fe-C_3N_4, g-C_3N_4/Ti_3C_2, and Fe-C_3N_4/Ti_3C_2 are 1.38, 1.60, and 2.83 times of g-C_3N_4, respectively. It shows that Fe-doping and composite Ti_3C_2 are beneficial to improve the photocatalytic degradation activity of g-C_3N_4.

Degradation Mechanism

By adding sacrificial agents such as BQ, IPA, and EDTA-2Na to detect the common active radicals $\bullet O_2^-$, •OH, and h^+ to explore the degradation mechanism of the photocatalytic reaction system. The results are shown in **Figure 7D**. When no radical scavengers were in the solution, the degradation rate of TC by Fe-C_3N_4/Ti_3C_2 was 86.80%. When •OH and h^+ capture agents were added, the photocatalytic degradation of TC by Fe-C_3N_4/Ti_3C_2 was inhibited to a certain extent, and the degradation rates were reduced to 66.30 and 63.81%, respectively. When $\bullet O_2^-$ capture agent was added, the photocatalytic degradation of TC by Fe-C_3N_4/Ti_3C_2 was greatly inhibited, and the degradation rate decreased to 30.96%. Therefore, the influence of active species on the degradation of TC in the photocatalytic degradation system was as follows: $\bullet O_2^- > h^+ > \bullet OH$.

Based on the above results, we speculated on the photocatalytic degradation mechanism of Fe-C_3N_4/Ti_3C_2 to TC (**Figure 8**). The electrons of g-C_3N_4 in Fe-C_3N_4/Ti_3C_2 were excited to CB under visible light irradiation. Thus, the photogenerated holes (h^+) were left in the VB. In the Mott–Schottky test (**Figure 6C**), we made a tangent along the longest straight line in the figure, and the slope was found to be positive, indicating that g-C_3N_4 was an *n*-type semiconductor. According to the formula ($E_g = E_{VB} + E_{CB}$) and the DRS results, the theoretical estimation of the E_{VB} and E_{CB} of g-C_3N_4 were 1.35 V and −0.84 V vs. NHE. In addition, the Fermi level (E_f, vs. NHE, pH = 0) of Ti_3C_2 was −0.60 V, which was higher than the E_{CB} of g-C_3N_4 (Su et al., 2019). In Fe-C_3N_4/Ti_3C_2 composites, a close 2D/2D contact interface is formed between Ti_3C_2 and g-C_3N_4. Electrons could be easily transferred from g-C_3N_4 nanosheets to Ti_3C_2 surfaces, which inhibits recombination of photoinduced electrons and holes. Moreover, because the reduction potential of Fe^{2+}/Fe^{3+} ($Fe^{2+}/Fe^{3+} = -0.77$ V) was lower than the E_{CB} of g-C_3N_4 (Li et al., 2008), Fe could effectively capture the photogenerated electrons of g-C_3N_4 and inhibit recombination of electron and hole pairs. Then, the electrons reacted with oxygen adsorbed on the surface of the photocatalyst or dissolved in solution to form strongly oxidized $\bullet O_2^-$ ($O_2/\bullet O_2^- = -0.33$ V). It oxidized TC to CO_2 and H_2O. At the same time, the h^+ of g-C_3N_4 reacted with H_2O or OH^- in the solution to form the •OH ($\bullet OH/OH^- = 1.99$ V) with strong oxidizability. •OH could degrade TC into CO_2 and H_2O. The holes in the valence band of g-C_3N_4 also had strong oxidation which could react with TC and degrade it. The process of Fe-C_3N_4/Ti_3C_2 photocatalytic degradation of TC is as follows.

Material Performance Comparison

Comparing the experimental system with other related systems, the results are shown in **Table 2**. It can be seen from **Table 2** that the experimental system has a certain value in practicability and economy. A small amount of Fe-doping and a small amount of Ti_3C_2 composite were used to modify g-C_3N_4, and the prepared Fe-C_3N_4/Ti_3C_2 photocatalyst could be used to degrade TC efficiently with a degradation rate of 86.80%. Compared with the following table, there are certain differences in the degradation rates of different substances in different systems. The main reasons are that the types and ratios of materials, the dosage of photocatalyst, the degradation time, and the power and wavelength of the light source are different.

CONCLUSION

In this study, Fe-C_3N_4/Ti_3C_2 photocatalyst was synthesized *via* one-pot microwave method and high-temperature calcination method. When the catalyst dosage was 20 mg and the initial concentration of TC was 20 mg/L, the degradation rate of TC by Fe-C_3N_4/Ti_3C_2 was 86.80%, which was 1.96, 1.28, and 1.41 times that of g-C_3N_4, Fe-C_3N_4 and g-C_3N_4/Ti_3C_2. The influence of active species on the degradation of TC in the photocatalytic degradation system was $\bullet O_2^- > h^+ > \bullet OH$. During the synthesis of Fe-C_3N_4/Ti_3C_2, the byproduct NH_3 could intercalate multilayer Ti_3C_2, effectively preventing the stacking of Ti_3C_2 layers. Fe-doping and the composite of Ti_3C_2 would decrease the bandgap energy of g-C_3N_4 and effectively inhibited the recombination of electron and hole pairs of g-C_3N_4. It is expected that this work provides new insight into the construction of 2D/2D heterojunction materials used in the photocatalytic application.

DATA AVAILABILITY STATEMENT

The original contributions presented in the study are included in the article/Supplementary Material, further inquiries can be directed to the corresponding author.

AUTHOR CONTRIBUTIONS

ZH contributed to the conception, design of the study, and writing the original draft. YL was responsible for the data processing and the experimental part. ZH and YL contributed equally to this work. YH, XL, and QZ were in charge of the experimental part and wrote sections of the manuscript. YZ and SY were responsible for the TEM. HW, JS, GW, and HS wrote sections of the manuscript. All authors contributed to manuscript revision and read and approved the submitted version.

FUNDING

The project was supported by the special fund for scientific and technological innovation strategy of Guangdong Province ("Climbing" Program, nos. pdjh 2022b0385 and pdjh 2021b0371), Guangzhou Basic and Applied Basic Project (no.

202102020424), and College Students' Scientific and Technological Innovation Project (nos. 202114278078 and 202114278087), Key Scientific Research Projects of General Universities in Guangdong Province (no. 2021KCXTD086) and Scientific Research Project of Guangdong University of Education (Student Work Project) (no. 2021XKY009).

REFERENCES

Anasori, B., Lukatskaya, M. R., and Gogotsi, Y. (2017). 2D Metal Carbides and Nitrides (MXenes) for Energy Storage. *Nat. Rev. Mater.* 2, 16098. doi:10.1038/natrevmats.2016.98

Bian, S., Wen, M., Wang, J., Yang, N., Chu, P. K., and Yu, X.-F. (2020). Edge-Rich Black Phosphorus for Photocatalytic Nitrogen Fixation. *J. Phys. Chem. Lett.* 11, 1052–1058. doi:10.1021/acs.jpclett.9b03507

Cheng, L., Chen, Q., Li, J., and Liu, H. (2020). Boosting the Photocatalytic Activity of $CdLa_2S_4$ for Hydrogen Production Using Ti_3C_2 MXene as a Co-catalyst. *Appl. Catal. B: Environ.* 267, 118379. doi:10.1016/j.apcatb.2019.118379

Cui, L., Song, J., McGuire, A. F., Kang, S., Fang, X., Wang, J., et al. (2018). Constructing Highly Uniform Onion-ring-like Graphitic Carbon Nitride for Efficient Visible-Light-Driven Photocatalytic Hydrogen Evolution. *ACS Nano* 12 (6), 5551–5558. doi:10.1021/acsnano.8b01271

Fu, J., Xu, Q., Low, J., Jiang, C., and Yu, J. (2019). Ultrathin 2D/2D WO_3/g-C_3N_4 Step-Scheme H_2-Production Photocatalyst. *Appl. Catal. B: Environ.* 243, 556–565. doi:10.1016/j.apcatb.2018.11.011

Fu, J., Zhu, B., Jiang, C., Cheng, B., You, W., and Yu, J. (2017). Hierarchical Porous O-Doped g-C_3N_4 With Enhanced Photocatalytic CO_2 Reduction Activity. *Small* 13 (15), 1603938. doi:10.1002/smll.201603938

Galeano, L., Valencia, S., Restrepo, G., and Marín, J. M. (2019). Dry-co-grinding of Doped TiO_2 With Nitrogen, Silicon or Selenium for Enhanced Photocatalytic Activity under UV/visible and Visible Light Irradiation for Environmental Applications. *Mater. Sci. Semiconductor Process.* 91, 47–57. doi:10.1016/j.mssp.2018.10.032

Gao, B., Sun, M., Ding, W., Ding, Z., and Liu, W. (2021). Decoration of γ-graphyne on TiO_2 Nanotube Arrays: Improved Photoelectrochemical and Photoelectrocatalytic Properties. *Appl. Catal. B: Environ.* 281, 119492. doi:10.1016/j.apcatb.2020.119492

Gebreslassie, G., Bharali, P., Chandra, U., Sergawie, A., Baruah, P. K., Das, M. R., et al. (2019). Hydrothermal Synthesis of g-C_3N_4/$NiFe_2O_4$ Nanocomposite and its Enhanced Photocatalytic Activity. *Appl. Organometal Chem.* 33 (8), e5002. doi:10.1002/aoc.5002

Gibson, G. G., and Skett, P. (1986). *Introduction to Drug Metabolism.* London: Chapman & Hall.

He, S., Yan, C., Chen, X.-Z., Wang, Z., Ouyang, T., Guo, M.-L., et al. (2020). Construction of Core-Shell Heterojunction Regulating α-Fe_2O_3 Layer on CeO_2 Nanotube Arrays Enables Highly Efficient Z-Scheme Photoelectrocatalysis. *Appl. Catal. B: Environ.* 276, 119138. doi:10.1016/j.apcatb.2020.119138

Hu, J., Zhang, P., An, W., Liu, L., Liang, Y., and Cui, W. (2019). *In-situ* Fe-Doped g-C_3N_4 Heterogeneous Catalyst *via* Photocatalysis-Fenton Reaction with Enriched Photocatalytic Performance for Removal of Complex Wastewater. *Appl. Catal. B: Environ.* 245, 130–142. doi:10.1016/j.apcatb.2018.12.029

Huang, G., Li, S., Liu, L., Zhu, L., and Wang, Q. (2020). Ti_3C_2 MXene-Modified Bi_2WO_6 Nanoplates for Efficient Photodegradation of Volatile Organic Compounds. *Appl. Surf. Sci.* 503, 144183. doi:10.1016/j.apsusc.2019.144183

Huang, S., Ouyang, T., Zheng, B. F., Dan, M., and Liu, Z. Q. (2021b). Enhanced Photoelectrocatalytic Activities for CH_3OH-to-HCHO Conversion on Fe_2O_3/MoO_3 : Fe-O-Mo Covalency Dominates the Intrinsic Activity. *Angew. Chem. Int. Ed.* 60, 9546–9552. doi:10.1002/anie.202101058

Huang, S., Zheng, B.-F., Tang, Z.-Y., Mai, X.-Q., Ouyang, T., and Liu, Z.-Q. (2021a). CH_3OH Selective Oxidation to HCHO on Z-Scheme Fe_2O_3/g-C_3N_4 Hybrid: The Rate-Determining Step of C-H Bond Scission. *Chem. Eng. J.* 422, 130086. doi:10.1016/j.cej.2021.130086

Lee, H., Lee, E., Lee, C.-H., and Lee, K. (2011). Degradation of Chlorotetracycline and Bacterial Disinfection in Livestock Wastewater by Ozone-Based Advanced Oxidation. *J. Ind. Eng. Chem.* 17 (3), 468–473. doi:10.1016/j.jiec.2011.05.006

Li, B., Song, H., Han, F., and Wei, L. (2020). Photocatalytic Oxidative Desulfurization and Denitrogenation for Fuels in Ambient Air over Ti_3C_2/g-C_3N_4 Composites under Visible Light Irradiation. *Appl. Catal. B: Environ.* 269, 118845. doi:10.1016/j.apcatb.2020.118845

Li, J., Wu, D., Iocozzia, J., Du, H., Liu, X., Yuan, Y., et al. (2019). Achieving Efficient Incorporation of π-Electrons into Graphitic Carbon Nitride for Markedly Improved Hydrogen Generation. *Angew. Chem. Int. Ed.* 58 (7), 1985–1989. doi:10.1002/anie.201813117

Li, K., Cui, W., Li, J., Sun, Y., Chu, Y., Jiang, G., et al. (2019). Tuning the Reaction Pathway of Photocatalytic NO Oxidation Process to Control the Secondary Pollution on Monodisperse Au Nanoparticles@g-C_3N_4. *Chem. Eng. J.* 378, 122184. doi:10.1016/j.cej.2019.122184

Li, X., Wang, D., Cheng, G., Luo, Q., An, J., and Wang, Y. (2008). Preparation of Polyaniline-Modified TiO_2 Nanoparticles and Their Photocatalytic Activity under Visible Light Illumination. *Appl. Catal. B: Environ.* 81 (3-4), 267–273. doi:10.1016/j.apcatb.2007.12.022

Lindberg, R. H., Wennberg, P., Johansson, M. I., Tysklind, M., and Andersson, B. A. V. (2005). Screening of Human Antibiotic Substances and Determination of Weekly Mass Flows in Five Sewage Treatment Plants in Sweden. *Environ. Sci. Technol.* 39 (10), 3421–3429. doi:10.1021/es048143z

Liu, D., Li, C., Ge, J., Zhao, C., Zhao, Q., Zhang, F., et al. (2022). 3D Interconnected g-C_3N_4 Hybridized with 2D Ti_3C_2 MXene Nanosheets for Enhancing Visible Light Photocatalytic Hydrogen Evolution and Dye Contaminant Elimination. *Appl. Surf. Sci.* 579, 152180. doi:10.1016/j.apsusc.2021.152180

Liu, D., Wang, J., Bian, S., Liu, Q., Gao, Y., Wang, X., et al. (2020a). Photoelectrochemical Synthesis of Ammonia with Black Phosphorus. *Adv. Funct. Mater.* 30 (24), 2002731. doi:10.1002/adfm.202002731

Liu, G., Dong, G., Zeng, Y., and Wang, C. (2020b). The Photocatalytic Performance and Active Sites of g-C_3N_4 Effected by the Coordination Doping of Fe(III). *Chin. J. Catal.* 41, 1564–1572. doi:10.1016/S1872-2067(19)63518-7

Liu, N., Lu, N., Su, Y., Wang, P., and Quan, X. (2018a). Fabrication of g-C_3N_4/Ti_3C_2 Composite and its Visible-Light Photocatalytic Capability for Ciprofloxacin Degradation. *Separat. Purif. Techn.* 211, 782–789. doi:10.1016/j.seppur.2018.10.027

Liu, S., Zhu, H., Yao, W., Chen, K., and Chen, D. (2018b). One Step Synthesis of P-Doped g-C_3N_4 With the Enhanced Visible Light Photocatalytic Activity. *Appl. Surf. Sci.* 430, 309–315. doi:10.1016/j.apsusc.2017.07.108

Liu, W., Sun, M., Ding, Z., Gao, B., and Ding, W. (2021). Ti_3C_2 MXene Embellished g-C_3N_4 Nanosheets for Improving Photocatalytic Redox Capacity. *J. Alloys Compd.* 877, 160223. doi:10.1016/j.jallcom.2021.160223

Naguib, M., Kurtoglu, M., Presser, V., Lu, J., Niu, J., Heon, M., et al. (2011). Two-Dimensional Nanocrystals Produced by Exfoliation of Ti_3AlC_2. *Adv. Mater.* 23 (52), 4248–4253. doi:10.1002/adma.201102306

Pei, Z., Jia, H., Zhang, Y., Wang, P., Liu, Y., Cui, W., et al. (2020). A One-Pot Hydrothermal Synthesis of Eu/$BiVO_4$ Enhanced Visible-Light-Driven Photocatalyst for Degradation of Tetracycline. *J. Nanosci. Nanotechnol.* 20 (5), 3053–3059. doi:10.1166/jnn.2020.17446

Su, T., Hood, Z. D., Naguib, M., Bai, L., Luo, S., Rouleau, C. M., et al. (2019). 2D/2D Heterojunction of Ti_3C_2/g-C_3N_4 Nanosheets for Enhanced Photocatalytic Hydrogen Evolution. *Nanoscale* 11 (17), 8138–8149. doi:10.1039/c9nr00168a

Sun, Z., Huo, R., Choi, C., Hong, S., Wu, T.-S., Qiu, J., et al. (2019). Oxygen Vacancy Enables Electrochemical N_2 Fixation over WO_3 with Tailored Structure. *Nano Energy* 62, 869–875. doi:10.1016/j.nanoen.2019.06.019

Tong, Z., Yang, D., Li, Z., Nan, Y., Ding, F., Shen, Y., et al. (2017). Thylakoid-Inspired Multishell g-C_3N_4 Nanocapsules with Enhanced Visible-Light Harvesting and Electron Transfer Properties for High-Efficiency Photocatalysis. *ACS Nano* 11 (1), 1103–1112. doi:10.1021/acsnano.6b08251

Wang, X., Chen, X., Thomas, A., Fu, X., and Antonietti, M. (2009). Metal-Containing Carbon Nitride Compounds: A New Functional Organic-Metal Hybrid Material. *Adv. Mater.* 21, 1609–1612. doi:10.1002/adma.200802627

Wei, X., Zhang, R., Zhang, W., Yuan, Y., and Lai, B. (2019). High-efficiency Adsorption of Tetracycline by the Prepared Waste Collagen Fiber-Derived Porous Biochar. *RSC Adv.* 9 (67), 39355–39366. doi:10.1039/C9RA07289F

Xiao, Y., Hwang, J.-Y., and Sun, Y.-K. (2016). Transition Metal Carbide-Based Materials: Synthesis and Applications in Electrochemical Energy Storage. *J. Mater. Chem. A.* 4, 10379–10393. doi:10.1039/C6TA03832H

Xu, J., Wang, Z., and Zhu, Y. (2017a). Enhanced Visible-Light-Driven Photocatalytic Disinfection Performance and Organic Pollutant Degradation Activity of Porous g-C_3N_4 Nanosheets. *ACS Appl. Mater. Inter.* 9 (33), 27727–27735. doi:10.1021/acsami.7b07657

Xu, R., Wu, Z., Zhou, Z., and Meng, F. (2017b). Removal of Sulfadiazine and Tetracycline in Membrane Bioreactors: Linking Pathway to Microbial Community Shift. *Environ. Techn.* 40 (2), 134–143. doi:10.1080/09593330.2017.1380714

Xu, Y., Ge, F., Chen, Z., Huang, S., Wei, W., Xie, M., et al. (2019). One-step Synthesis of Fe-Doped Surface-Alkalinized g-C_3N_4 and Their Improved Visible-Light Photocatalytic Performance. *Appl. Surf. Sci.* 469, 739–746. doi:10.1016/j.apsusc.2018.11.062

Yang, C., Tan, Q., Li, Q., Zhou, J., Fan, J., Li, B., et al. (2020). 2D/2D Ti_3C_2 MXene/g-C_3N_4 Nanosheets Heterojunction for High Efficient CO_2 Reduction Photocatalyst: Dual Effects of Urea. *Appl. Catal. B: Environ.* 268, 118738. doi:10.1016/j.apcatb.2020.118738

Yang, D., Wang, W., An, K., Chen, Y., Zhao, Z., Gao, Y., et al. (2021). Bioinspired Construction of Carbonized Poly(tannic Acid)/g-C_3N_4 Nanorod Photocatalysts for Organics Degradation. *Appl. Surf. Sci.* 562, 150256. doi:10.1016/j.apsusc.2021.150256

Yang, Y., Zhang, D., and Xiang, Q. (2019). Plasma-modified Ti_3C_2Tx/CdS Hybrids with Oxygen-Containing Groups for High-Efficiency Photocatalytic Hydrogen Production. *Nanoscale* 11, 18797–18805. doi:10.1039/C9NR07242J

Yi, X., Yuan, J., Tang, H., Du, Y., Hassan, B., Yin, K., et al. (2020). Embedding Few-Layer Ti_3C_2Tx into Alkalized g-C_3N_4 Nanosheets for Efficient Photocatalytic Degradation. *J. Colloid Interf. Sci.* 571, 297–306. doi:10.1016/j.jcis.2020.03.061

Zhao, D., Dong, C. L., Wang, B., Chen, C., Huang, Y. C., Diao, Z., et al. (2019). Synergy of Dopants and Defects in Graphitic Carbon Nitride with Exceptionally Modulated Band Structures for Efficient Photocatalytic Oxygen Evolution. *Adv. Mater.* 31 (43), 1903545. doi:10.1002/adma.201903545

Zheng, Y., Lin, L., Wang, B., and Wang, X. (2015). Graphitic Carbon Nitride Polymers toward Sustainable Photoredox Catalysis. *Angew. Chem. Int. Ed.* 54 (44), 12868–12884. doi:10.1002/anie.201501788

Conflict of Interest: The authors declare that the research was conducted in the absence of any commercial or financial relationships that could be construed as a potential conflict of interest.

frontiers | Frontiers in Chemistry

TYPE Original Research
PUBLISHED 01 August 2022
DOI 10.3389/fchem.2022.865006

EDITED BY
Yan Zhang,
University of Jinan, China

REVIEWED BY
Makoto Tamura,
Mitsubishi Tanabe Pharma Holdings America, United States
Hayder Amin,
German Center for Neurodegenerative Diseases (DZNE), Germany

*CORRESPONDENCE
Liping Du,
duliping@xjtu.edu.cn
Chunsheng Wu,
wuchunsheng@xjtu.edu.cn

SPECIALTY SECTION
This article was submitted to Analytical Chemistry,
a section of the journal
Frontiers in Chemistry

RECEIVED 29 January 2022
ACCEPTED 28 June 2022
PUBLISHED 01 August 2022

CITATION
Zhu P, Liu S, Tian Y, Chen Y, Chen W, Wang P, Du L and Wu C (2022), Odor-induced modification of oscillations and related theta-higher gamma coupling in olfactory bulb neurons of awake and anesthetized rats.
Front. Chem. 10:865006.
doi: 10.3389/fchem.2022.865006

Odor-induced modification of oscillations and related theta-higher gamma coupling in olfactory bulb neurons of awake and anesthetized rats

Ping Zhu[1,2], Shuge Liu[1,2], Yulan Tian[1,2], Yating Chen[1,2], Wei Chen[1,2], Ping Wang[3,4], Liping Du[1,2,3,4]* and Chunsheng Wu[1,2]*

[1]Department of Biophysics, Health Science Center, Institute of Medical Engineering, School of Basic Medical Sciences, Xi'an Jiaotong University, Xi'an, China, [2]Key Laboratory of Environment and Genes Related to Diseases, Ministry of Education of China, Xi'an Jiaotong University, Xi'an, China, [3]Biosensor National Special Laboratory, Department of Biomedical Engineering, Zhejiang University, Hangzhou, China, [4]Key Laboratory for Biomedical Engineering of Ministry of Education, Department of Biomedical Engineering, Zhejiang University, Hangzhou, China

Olfactory gamma oscillations (40–100 Hz) are generated spontaneously in animals and represent the activity of local olfactory bulb (OB) networks, which play important roles in cognitive mechanisms. In addition, high-frequency oscillations (HFO, 130–180 Hz) have attracted widespread attention and are novel neuronal oscillations with a frequency range closer to high gamma oscillations (60–100 Hz, HGOs). Both HGOs and HFOs are distinctly regulated by θ rhythm in the hippocampus. To understand their mediation mechanisms in the OB, we investigated whether local field potential (LFP) oscillations including HGOs and HFOs and even their coupling with theta rhythm are modified by odor stimulation in both freely moving and anesthetized rats. Therefore, we combined electrophysiological technology and cross-frequency coupling analysis approaches to determine the difference in the odor-modulated LFP oscillations between awake and anesthetized rats. The obtained results indicate that LFP oscillations including HGOs and HFOs were differently modified by odor stimulation in animals of both states. However, θ-HGO and θ-HFO coupling were modified in only awake animals. It is suggested that these oscillations and their interactions with theta oscillations may play crucial roles in olfactory network activity. This could pave the way for further understanding the underlying mechanisms of oscillations in OB neurons towards odor sensation.

KEYWORDS

neuronal oscillations, high gamma, high-frequency oscillations, cross-frequency coupling, odor stimulation

Introduction

Neuronal oscillations are ubiquitous in various brain networks, including the thalamus, hippocampus, neocortex, and olfactory bulb (OB), which provide a temporal structure for brain networks communication and processing (Zhang et al., 2018; Urbain et al., 2019; Naggar et al., 2020; Średniawa et al., 2021). This regular electrical activity in neurons is described as several different oscillation bands, including respiration-related δ oscillations (1–4 Hz), θ rhythm (4–12 Hz), faster oscillations in β (15–30 Hz), and γ (40–100 Hz) frequency ranges. B-frequency activity is related to odor sampling and discrimination (Martin and Ravel, 2014). Gamma oscillations are the important symbols of neural network function in the sensory system and play crucial roles in cognitive functions (Vinck et al., 2013).

Gamma oscillations in the OB are dependent on dendritic synaptic interactions between the main output neurons (mitral and tufted cells, M/T cells) and GABAergic interneurons (granule cells) (Osinski and Kay, 2016), which are not only generated spontaneously (Manabe and Mori, 2013) but also modified by odor stimulation (Frederick et al., 2016). Gamma oscillations composed of distinct subbands generated in awake animals exhibit a unique characteristic (Kay, 2003). Low γ (LG, 40–60 Hz) and high γ oscillations (HGOs, 60–100 Hz) represent different patterns of network interaction. It is considered that paired remote mitral cells are specially synchronized in the LG band. However, HGOs are more restricted in space, representing the local network activity (Lepousez and Lledo, 2013). In addition, scientists described a novel cortical oscillating activity (HFOs) in a frequency range of 130–180 Hz (Scheffer-Teixeira et al., 2012), which was also termed fast γ oscillations (Jackson et al., 2011; Tort et al., 2013). In addition to the hippocampus (Jackson et al., 2011; Scheffer-Teixeira et al., 2012) and neocortex (Scheffzük et al., 2011), it is reported that the OB of rodents can generate fast rhythms and is also a source of HFO (Chery et al., 2013; Hunt et al., 2019). Neuron oscillations in different frequency bands represent distinct physiological implications and can interact with each other. The interaction of rhythms in different frequency bands is generally called cross-frequency coupling (CFC). The most famous example of CFC is in the hippocampus, where the amplitude of the γ oscillation is modulated by the θ rhythm (Li et al., 2019; Nakazono et al., 2019; Salimi et al., 2021). Recent studies have shown that this θ-γ coupling reflects the general mechanism of dynamic information processing in the brain and the strength of coupling changes during learning, long-term, and working memory processes (van Wingerden et al., 2014; Griffiths et al., 2019; Jones et al., 2020; Vivekananda et al., 2021). In addition, there has been evidence that the θ-γ coupling is involved in the sensory processing of the cortex, such as olfactory, auditory, and vision (Shusterman et al., 2011; Hamm et al., 2012; Murphy et al., 2020). The OB is an ideal site to investigate whether the phase amplitude coupling (PAC) is involved in sensory processing because of its inherent oscillatory activity associated with odor signal processing. The oscillation activity in the OB can powerfully drive the coherent rhythmic activity in the remote brain region (Ito et al., 2014). In addition, the θ-γ coupling in the OB changed during the process of awake immobile and exploring (Zhong et al., 2017).

According to previous studies in extracellular recording or imaging of the OB in anesthetized and awake animals, odor responses of mitral and tufted cells were significantly different (Buzsáki and Watson, 2012). The changes in the OB neuron activity in awake animals are related to the olfactory stimulation, which conveys information about odor recognition and odor value. Therefore, it is crucial to study the odor response of neurons in awake animals. Among many studies involving local field potential information in awake animals, a large number of studies have focused on the critical role of neuronal γ oscillations in olfactory perception and cognition, as well as olfactory-related learning and memory (Rosero and Aylwin, 2011; Manabe and Mori, 2013). Scientists found that the PAC between the θ phase and the high γ amplitude in the OB of awake rats varied during the learning process (Losacco et al., 2020). Therefore, this modulation plays a role in the early sensory processing of olfaction during the learning phase. This work highlights the important original information about the influences of learning on the γ oscillations of OB, providing new insight into the mechanisms of OB information processing. These discoveries about γ oscillations also led us to investigate the influences of odor stimulation on the HFO of OB in awake rats. Several studies on the local field potential (LFP) in the OB of anesthetized animals have discussed the mechanism of HFO generation and occurrence in mammals (Średniawa et al., 2021). Although studies on anesthetized animals provide much information, it is crucial to study the neuronal responses of awake animals. We examined the changes in the oscillatory activity of the OB neurons and their coupling activity in rats under two states and how these changes are related to odor stimulation.

Here, we implanted multi-channel micro-electrodes into the OBs of rats, which were utilized to record the LFP signal of M/T cells in the OB of awake and anesthetized rats. We examined the changes in HGOs and HFOs and their coupling with θ oscillations during odor stimulation. It is indicated that the neural oscillations in different frequency bands and their interactions are modified by odor stimulation. Moreover, the differences in odor-induced LFP and HFOs activity between anesthetized and awake animals are clear. In addition, the differences in HGOs and HFOs and even their coupling with θ rhythm during odor stimulation is also obvious. These findings provide new clues for understanding the mechanism of neuronal oscillations participating in the communication of the OB network.

Experiment

Materials and instruments

We used three adult male Sprague–Dawley rats (250–300 g) purchased from the experimental animal center of Xi'an Jiaotong University. An 8-channel microelectrode array was handmade with a 38-μm diameter formvar-coated nichrome microwire electrode (AM system, WA; #761500). The signal recording system used was a wireless W2100-system (Multichannel Systems, Germany), a data acquisition system consists of a receiver and interface board. The system can be connected to a computer *via* a USB. The odorants used in the experiment include nonanoic acid ($CH_3(CH_2)_7COOH$, NA, Tokyo Chemical Industry, P0952) and amyl hexanoate ($C_{11}H_{22}O_2$, AH, Macklin, P859158, China). Dental cement was purchased from luxatemp (Dental Milestones Guaranteed, America). A brain stereotaxic instrument was used (RWD Life Science, China) and the fixative was paraformaldehyde (4%, PI105, ZHONGHUIHECAI, China).

Surgery, odor stimulation, and signal recording

The microwire electrode array was implanted into the OB of rats. After being anesthetized with chloral hydrate (intraperitoneal injection, 4 ml/kg), the rats were individually fixed on a brain stereotaxic instrument. A craniotomy was performed to expose the OB and related brain areas (Supplementary Figure S1A). The microelectrode array was implanted into the mitral/tufted (M/T) cell layer of OB according to specific coordinates (Anterior-Position: +8.2 mm, Medial-Lateral: −1.0 mm, and Doral-Ventral: +0.8 mm) with the real-time synchronous recording of signals (Supplementary Figure S1B). The depth of the electrode tip was determined by monitoring the configuration of neuron activity of OB (Supplementary Figures S1C,D). After implantation, the microelectrode array was fixed onto the head with the dental cement. Then, the headstage was disconnected from the microelectrode array. The use of animals was approved by the Medical Ethics Committee of Xi'an Jiaotong University.

We performed the electrophysiological LFP signal recording after the rats recovered from the surgery (3–5 days). Before the odorant stimulation, we connected the microelectrode array with the headstage of a multichannel system with a sampling rate of 25 kHz. The odorant was diluted in the mineral oil to 10^{-3} M. Then, the odor was delivered to the nose of the awake rat through a glass dish containing an odor-saturating filter paper. Each stimulation lasted 2 s. Nonanoic acid is a colorless, oily liquid with a specific smell. It is naturally found in bananas, beer, and bread. Amyl hexanoate has a sweet, fragrant smell, naturally found in apples, grapes, and other fruits. Obvious sniffing behavior could be observed during the odor stimulus. This could be used to determine the duration of the odor sample. The cases in which the animal did not have a reliable odor-related behavioral response after the odor presentation were not included in the trial. A 5 min refreshing was performed between each odor stimulation to refresh the room. Three rats were used in this study. Two kinds of odor stimulation were applied to each rat under anesthesia and awake state. Each rat received four odor stimuli (nonanoic acid and amyl hexanoate twice each) under each state (anesthesia and awake). Three rats received 12 trials of odor stimulation in total in each state.

After being anesthetized, the rats were perfused through the left ventricle with 400 ml of paraformaldehyde. The bilateral OB was removed and post-fixed with paraformaldehyde to inspect the recording region.

Data analysis

Filter and spectral analysis: The recorded electrophysiological data were analyzed offline using the software of MATLAB (Mathworks, Inc.) and the software program Spike2 (Cambridge Electronic Design). LFPs were obtained by filtering the original signals using a 2nd-odor Butterworth band-pass filter at 0.1–200 Hz, which were then divided into different frequency bands: θ oscillations (4–12 Hz), high γ oscillations (60–100 Hz), and high-frequency oscillations (130–180 Hz). The wavelet transform of the signal was realized by a MATLAB function 'cwt.' The fast Fourier transform was used to calculate the power spectra of oscillations for the 0–1 s period after the stimulus onset and compared with the 1 s pre-stimulus baseline. The Data were analyzed using the repeated-measures ANOVA followed by the Fisher's least significant difference (LSD) post hoc test, with the statistical difference determined at $p < 0.05$. Graphpad Prism (Graphpad Software Inc., United States) was used for the statistical analysis.

For the cross-frequency coupling (CFC), the modulation index (MI) was used to measure the intensity of phase-amplitude coupling between the two frequency ranges of interest: The phase modulating (f_P) and amplitude modulating (f_A) frequency bands. The computation of the MI was as described elsewhere (Tort et al., 2010). Briefly, the steps required are as follows: The raw signal was filtered at the two frequency ranges (f_P and f_A) (Supplementary Figures S2A–C). The standard Hilbert transform was applied to the raw signal to obtain the time series of the phase of f_P and the amplitude envelope of f_A (Supplementary Figures S2D,E). The phase of f_P was then binned into eighteen 20° intervals, and the mean amplitude of f_A over each phase bin was calculated. Next, the mean amplitude of f_A in each bin was normalized so that the sum of all bins equaled to 1 giving rise to a phase-amplitude distribution (Supplementary Figure S2F). A uniform distribution of phase-amplitude indicated no phase-amplitude coupling between the two frequency ranges of interest. Therefore, MI estimating the KL distance is defined as the measure that quantifies the

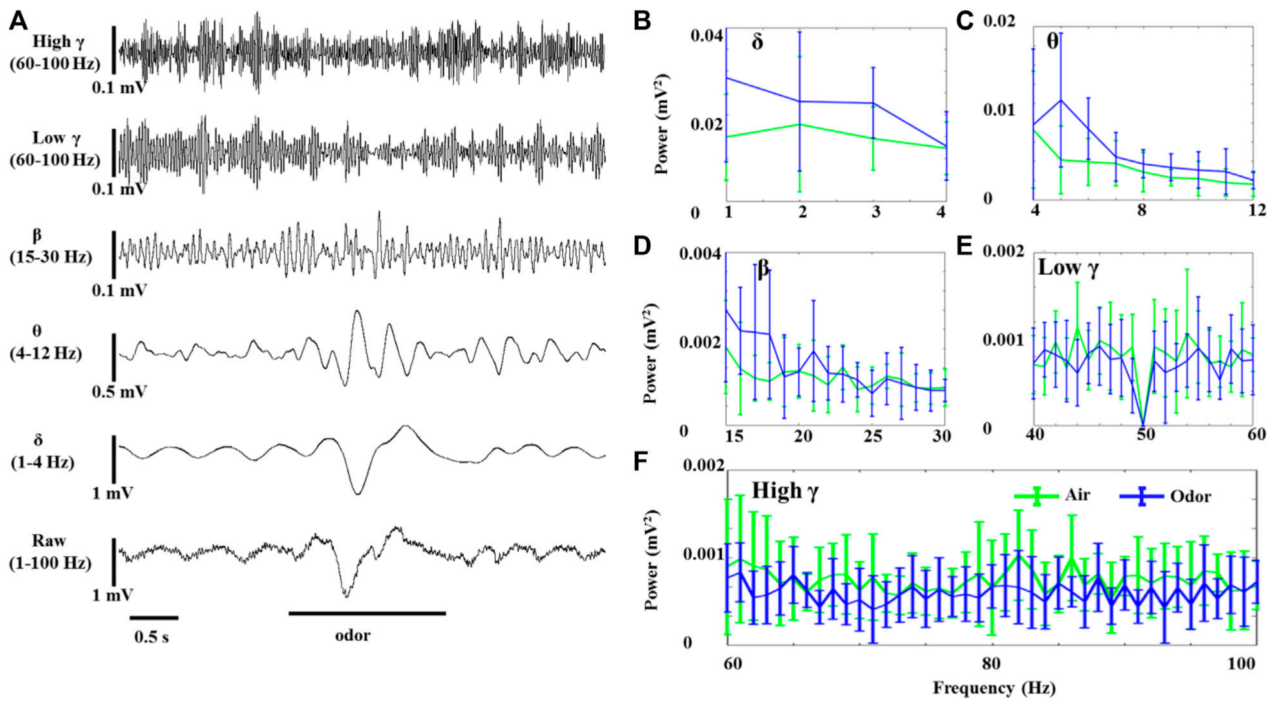

FIGURE 1
Odor-evoked LFP (1–100 Hz) responses in the OB of awake rats. **(A)** Typical OB LFP traces recorded under nonanoic acid (NA) stimulation. Shown are the band-pass filtered traces of δ (1–4 Hz), θ (4–12 Hz), *β* (15–30 Hz), low *γ* (40–60 Hz), and high *γ* (60–100 Hz) activity, as well as full band LFP (1–100 Hz). The mean fast Fourier transform (FFT) power spectrum shows the distribution of energy from the δ- **(B)**, θ- **(C)**, *β*- **(D)**, low *γ*- **(E)**, and high *γ*-bands **(F)** across three rats under air (green line) and nonanoic acid (NA) (blue line) stimulation. The trial-averaged data are presented as the mean ± SEM, *n* = 12, 4 trials per rat.

deviation of the phase-amplitude distribution from the uniform distribution (Tort et al., 2010). The stronger the phase-to-amplitude modulation, the larger the MI value (Tort et al., 2008). The comodulogram was obtained by calculating the MI of multiple band pairs and displaying the results on the two-dimensional pseudo-color map (Supplementary Figure S2G). The bandwidths of phase-frequency and amplitude-frequency were 4 and 10 Hz, respectively. The coordinate of each MI was its center frequency. Here, the phase modulating frequency (θ oscillation) is denoted as one dimension in the comodulogram. Amplitude modulating frequency (*γ* oscillation) is denoted as another dimension. The color in the comodulogram refers to the strength of the modulation.

Results

Odor responses in anesthetized and awake rats

The LFP oscillation of the OB was modulated by odor stimulation. This modulation of LFP oscillations in the OB by odor has been widely described in anesthetized and awake animals (Cenier et al., 2008; Aylwin et al., 2009; Kum et al., 2019). In the olfactory system of awake mammals, particularly when animals freely explore new environments without any olfactory stimulation, the OB exhibits regular *γ* oscillations, which has been widely studied (Rojas-Líbano and Kay, 2008). We compared how the LFP frequency band oscillations of the OB neurons in the anesthetized and awake rats were modulated by odors. In our study, multichannel microelectrodes were implanted into the OB in the anesthetized and awake rats. These electrodes were then used to record olfactory neuron oscillations in surgically recovered rats. The detected oscillations were explored in the time and frequency domains. In the time-domain index, we focused on the included signal waveform and amplitude of the oscillating frequency band. While in the frequency domain, the power spectrum and spectrum diagram were calculated to analyze the maximum power and time-frequency information in the pseudo-color mode, respectively. Pseudo-color window functions can be used to display the energy density spectrum of each short period so that time-frequency analysis can be carried out visually.

LFP odor responses of three rats were recorded under anesthesia and awake conditions. The spontaneous activity of the OB neurons was composed of slow oscillation with high

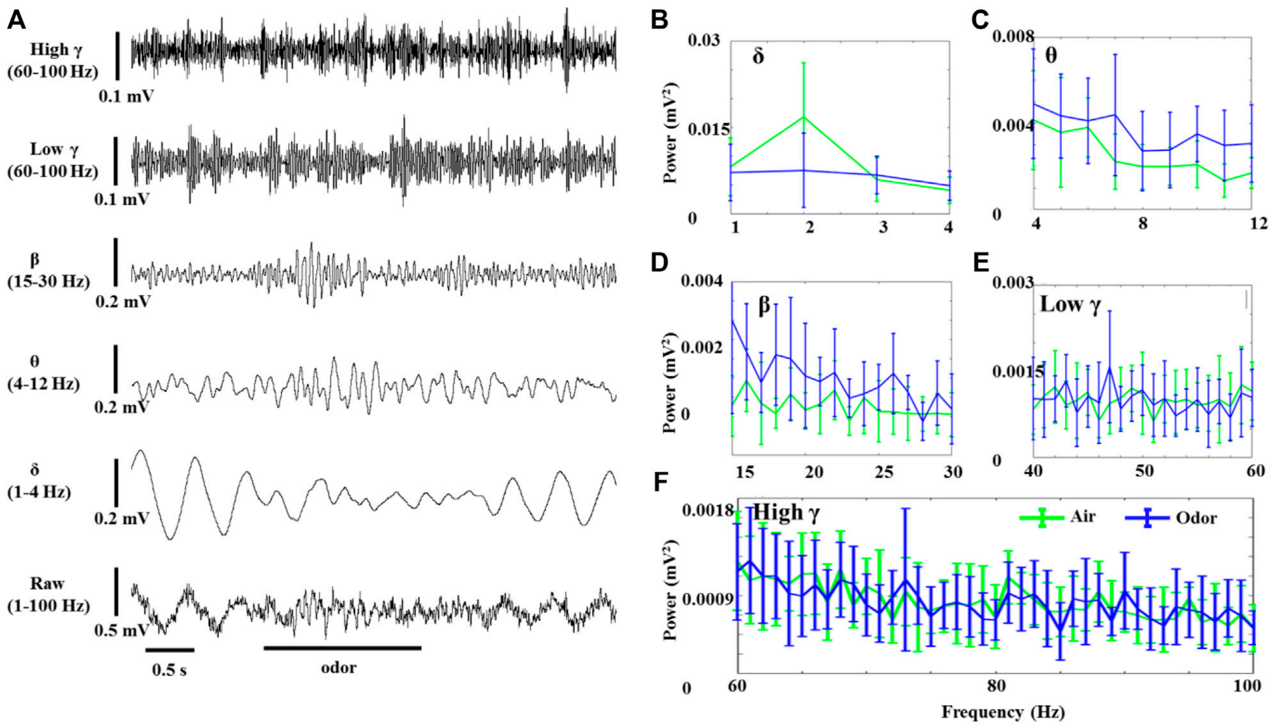

FIGURE 2
Odor-evoked LFP (1–100 Hz) responses in the OB of anesthetized rats. **(A)** Typical OB LFP traces recorded under nonanoic acid (NA) stimulation. Shown are the band-pass filtered traces of δ (1–4 Hz), β (15–30 Hz), low γ (40–60 Hz), and high γ (60–100 Hz) activity, as well as full band LFP (1–100 Hz). The Mean fast Fourier transform (FFT) power spectrum showing the distribution of energy from the δ- **(B)**, θ- **(C)**, β- **(D)**, low γ- **(E)**, and high γ-bands **(F)** across three rats under air (green line) and NA (blue line) stimulation. The trial-averaged data are presented as the mean ± SEM, n = 12, 4 trials per rat.

amplitude and regular fluctuation and fast wave with low amplitude and irregular fluctuation. Rhythmicity changes were observed in all the recorded animals in significant ways in response to odor stimuli. Figure 1 shows the effects of odor stimulation on the δ-, θ-, β-, LG-, and HG-bands' powers recorded in the OB of awake rats (Figure 1A). In the OB of awake animals, odor exposure caused significant δ-, θ-, and β-oscillations, accompanied by rapid responses. The δ-, θ-, and β-bands powers increased during odor stimulation and gradually returned to baseline after odor stimulation (Figures 1B–D). However, the OB's low γ- and high γ-bands' powers in the awake rats decreased under odor stimulation (Figures 1E,F). As reported in the previous articles that studied γ oscillations in the olfactory system, odor stimulation modifying HGOs does not mean that γ oscillations increase induced by odor but significantly decrease (Ravel et al., 2003; Liu et al., 2020).

The OB neurons of anesthetized rats also showed significant LFP oscillations without odor stimulation. Figure 2 shows the effects of odor stimulation on the δ-, θ-, β-, low γ-, and high γ-powers recorded in the OB of anesthetized rats (Figure 2A). In contrast to awake rats, odor stimulation significantly reduced the δ oscillations of the OB neurons in the anesthetized rats (Figure 2B). However, the increase of θ and β power in the odor-induced anesthetized rats was similar to that in the awake rats (Figures 2C,D). The γ power (Including low γ and high γ) of the OB in the anesthetized rats did not change significantly before and after odor stimulation.

Another pattern of odorant-induced olfactory oscillations was found in some recorded neurons, which erupted in weak but steady bursts of rapid LFP oscillations (130–180 Hz, HFO) in the absence of odor stimulation in both the awake and anesthetized rats. Interestingly, odor stimulation led to a significant increase in the HFO power in awake rats (Figure 3A,B). After odor stimulation, the recorded neurons recovered their spontaneous weak HFO. The anesthetized rats also showed significant HFO oscillations, but odorant stimuli did not modulate these high-frequency oscillations (Figure 3C,D). To the best of our knowledge, our study is the first to describe that HFOs produced by the OB neurons in awake rats are modified by odor stimulation, providing new insights into the role of OB neuron HFOs in olfactory processing. There is some evidence that tufted cells, rather than mitral cells, generate outputs in this frequency range (Nagayama et al., 2004; Manabe and Mori, 2013). Previous studies introduced high-frequency neural

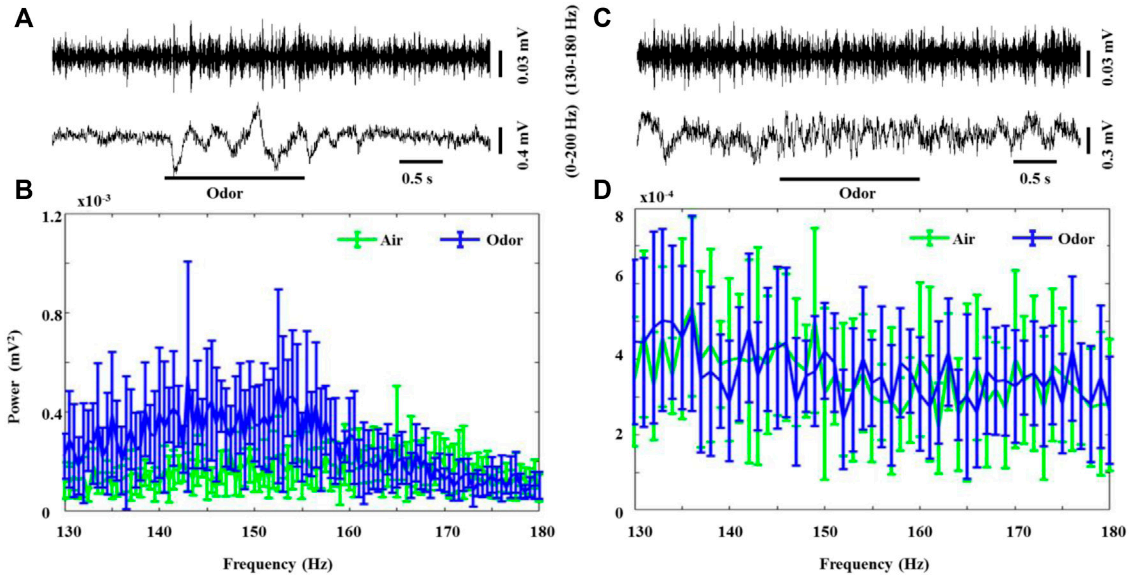

FIGURE 3
Odor-evoked high-frequency oscillations (130–180 Hz) responses in the OB of awake and anesthetized rats. **(A)** Typical OB 0–200 Hz activity and HFO traces from an awake rat under nonanoic acid (NA) stimulation. Shown are the HFO activity and 0–200 Hz activity. The mean fast Fourier transform (FFT) power spectrum showing the distribution of energy from HFO-bands **(B)** across three awake rats under air (green line) and NA (blue line) stimulation. The trial-averaged data are presented as the mean ± SEM, *n* = 12, 4 trials per rat. **(C)** Typical OB 0–200 Hz activity and HFO traces from an anesthetized rat under nonanoic acid (NA) stimulation. Shown are the HFO activity and 0–200 Hz activity. The mean fast Fourier transform (FFT) power spectrum showing the distribution of energy from HFO-bands **(B)** across the three anesthetized rats under air (green line) and NA (blue line) stimulation. The trial-averaged data are presented as the mean ± SEM, *n* = 12, 4 trials per rat. The short black line represents the duration of 0.5s, and the long black line represents the duration of the odor stimulation.

population oscillations generated by the OB of rats under ketamine anesthesia (Hunt et al., 2019). Our study describes for the first time that HFOs generated by the OB neurons of awake rats are modified by odor stimulation, which provides a new understanding of the role of HFOs in the OB neurons in olfactory processing.

To more accurately examine the difference of odor-modulated LFP activity of the OB neurons between the anesthetized and awake rats, the LFP power was quantitatively analyzed. For the δ power, the increase of odor-induced power in the awake rats was significant, and the decrease of odor -induced power in the anesthetized rats was also significant (Figure 4A). A quantitative comparison of the mean power before and during odor stimulation showed that odor stimulation caused a significant increase in θ and *β* powers in both the anesthetized and awake rats (Figures 4B,C). At the same time, odor stimulation also caused a significant decrease in the *γ* power (low *γ* and high *γ*) of the OB in the awake rats (Figures 4D,E). The enhancement of HFO power of OB in the awake rats induced by odor stimulation was also significant (Figure 4F). In addition, some interesting results were obtained in the quantitative analysis of LFP power. First, there was no significant difference in the LFP responses of different frequency bands in the OB neurons between the conscious and anesthetized rats induced by the two odors used in the study. The decrease in LFP power caused by the odor sampling did not depend on the chemical nature of stimuli but on the behavioral significance. As reported by Frederick et al. (2016), the modulation of *γ* power showed differences in different olfactory tasks. Second, in the absence of odor stimulation, the OB neurons of awake rats exhibited stronger HGO and weaker HFO than anesthetized rats, which is consistent with that reported in previous studies (Manabe and Mori, 2013; Średniawa et al., 2021).

Modifying θ-HGO/HFO coupling during odors

Neural oscillations in distinct frequency bands play different roles in the brain network communication and computation, and interacting oscillations help to regulate this integration of brain activity (Mofleh and Kocsis, 2021). Interactions between different frequency bands termed CFC, particularly the phase-amplitude CFC, have been reported in several brain regions, highlighting their importance in learning and memory. We first used multichannel microelectrodes to record LFPs from the three freely moving rats with odor presentation to characterize the phase-amplitude CFC in the OB during the odorant presentation.

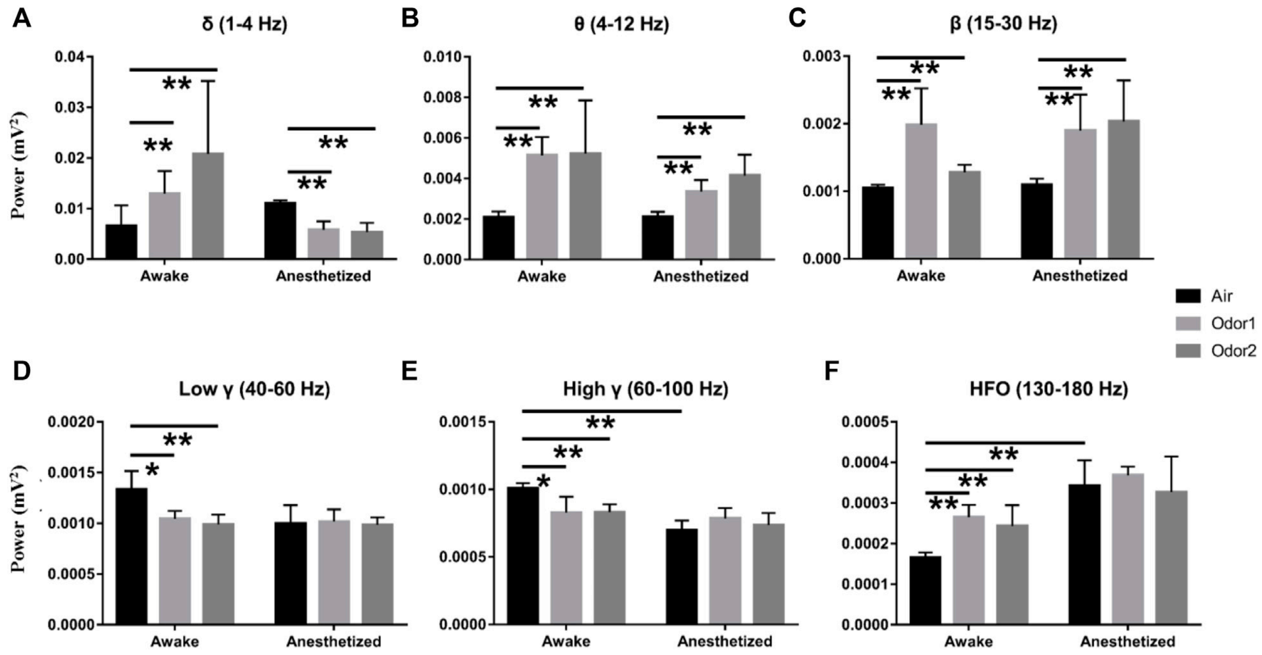

FIGURE 4
Histogram displaying the quantification of power spectrum in the δ- **(A)**, θ- **(B)**, β- **(C)**, low γ- **(D)**, high γ- **(E)**, and HFO-bands **(F)** in 3 awake and 3 anesthetized rats under the stimulation of air, nonanoic acid (NA, odor 1), and amyl hexanoate (AH, odor 2) with 2 trials per odor per rat. $**p < 0.01$, $*p < 0.05$,and ANOVA followed by Fisher's least significant difference (LSD).

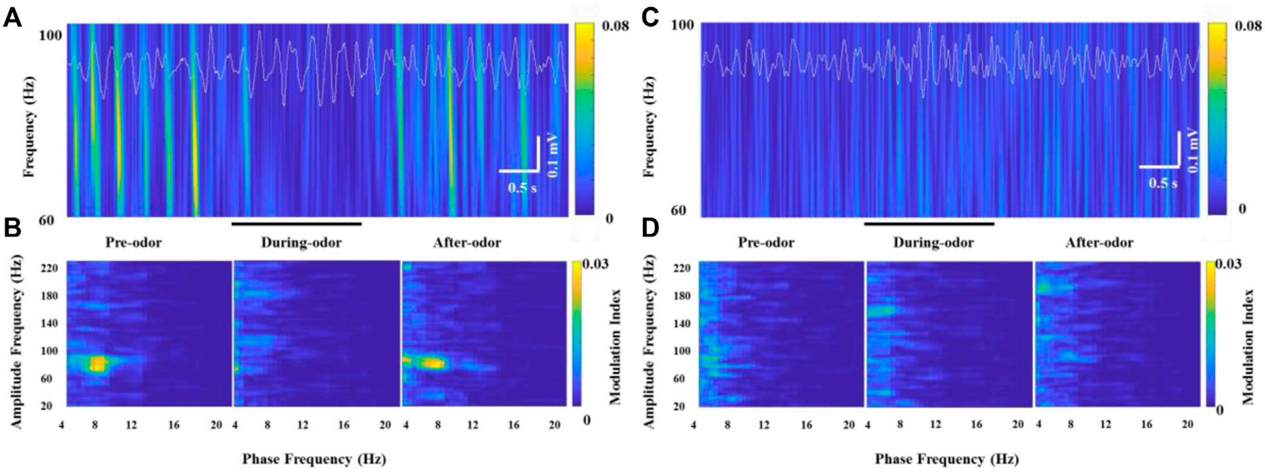

FIGURE 5
Example of specific coupling between θ and high γ oscillations (60–100 Hz) in an awake rat **(A,B)** and an anesthetized rat **(C,D)** during odor stimulation. **(A)** Wavelet spectrograms and superimposed θ signals (4–12 Hz, white traces) from the recorded OB neurons in an awake rat pre-odor (left), during odor (middle), and after odor (right). **(B)** Comodulation maps obtained from the OB neurons of a freely moving rat pre-odor (left), during odor (middle), and after odor (right). **(C)** Wavelet spectrograms and superimposed θ signals (4–12 Hz, white traces) from the recorded OB neurons in an anesthetized rat pre-odor (left), during odor (middle), and after odor (right). **(D)** Comodulation maps obtained from the OB neurons of an anesthetized rat pre-odor (left), during odor (middle), and after odor (right).

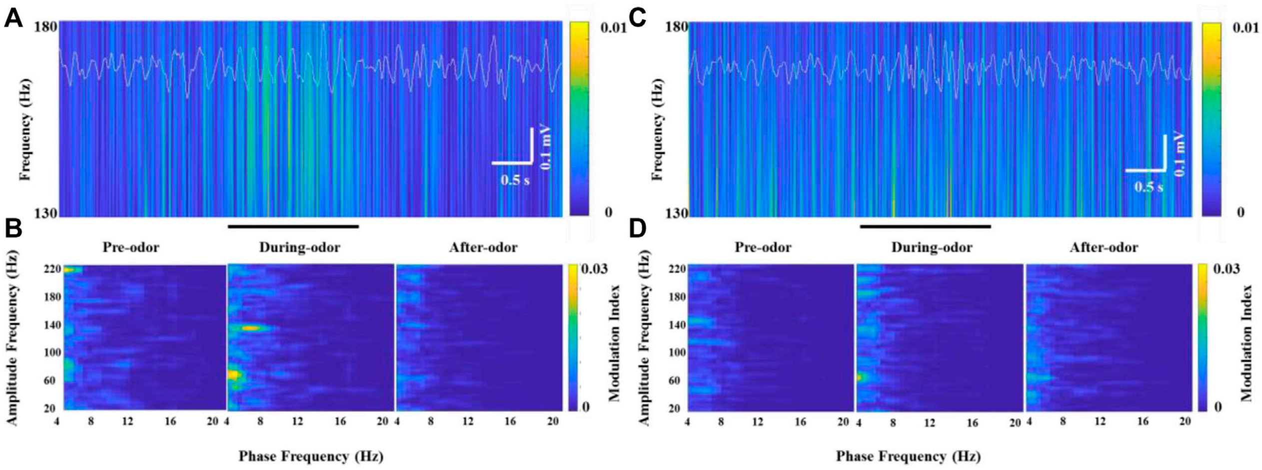

FIGURE 6

Example of specific coupling between θ and high-frequency oscillations (130–180 Hz) in an awake rat **(A,B)** and an anesthetized rat **(C,D)** during odor stimulation. **(A)** Wavelet spectrograms and superimposed θ signals (4–12 Hz, white traces) from the recorded OB neurons in an awake rat pre-odor (left), during odor (middle), and after odor (right). **(B)** Comodulation maps obtained from the OB neurons of a freely moving rat pre-odor (left), during odor (middle), and after odor (right). **(C)** Wavelet spectrograms and superimposed θ signals (4–12 Hz, white traces) from the recorded OB neurons in an anesthetized rat pre-odor (left), during odor (middle), and after odor (right). **(D)** Comodulation maps obtained from the OB neurons of an anesthetized rat pre-odor (left), during odor (middle), and after odor (right).

Then, we analyzed the CFC between the θ phase and the amplitude of the two γ subbands in the LFP recorded in the OB by referring to the previously reported method (Tort et al., 2010).

In all the awake freely moving rats, we found prominent coupling between θ and γ oscillations in the OB. Scheffer-Teixeira et al. (2012) observed the θ-high γ coupling and θ-high frequency oscillation coupling with different simultaneously recorded electrodes in the CA1 region of the hippocampus. Similarly, we observed the θ phase modulation of two non-overlapping frequency oscillations, HGO or HFO, in simultaneously recorded electrodes implanted into the OB. More specifically, the HGO amplitude was visibly phase-locked to the phase of the θ rhythm according to wavelet spectrograms and θ traces in recorded HG burst neurons (Figure 5A). We confirmed the phase-amplitude coupling between θ and HGO by cross-frequency comodulation analysis and power spectrum of θ in awake rats (Figure 5B, left panel). However, along with the decrease of the γ power during odor stimulation, this phase-amplitude coupling was also significantly weakened or even disappeared (Figure 5B, middle panel), which resumed as before after the odor stimulus was completed (Figure 5B, right panel). It is worth noting that during each repeated trial (2 min, in which the odor stimulation lasted for 2 s), the rats were freely moving, during which the OB exhibited a strong θ-γ coupling. Unlike the transition of phase-amplitude coupling in different behavioral states (Zhong et al., 2017), the decrease of the γ power during odor stimulation led to a significant decrease in the modulation of the θ phase to the γ amplitude. However, we did not find this cross-frequency coupling in the OB of anesthetized rats, nor was it modulated by odor stimulation (Figures 5C,D).

Unlike HGO, we did not find a prominent θ-HFO coupling activity in the neurons that generated significant HFOs in the OBs of freely moving rats without odor stimulation when the neurons burst weak but stable HFOs (Figure 6A and Figure 6B, left panel). Along with the significantly increasing HFO power and amplitude, prominent modulation of HFO activity by the θ phase in the OB was observed during odor stimulation (Figure 6B, middle panel). Similarly, the amplitude and power of HFO and CFC resumed as before and after odor stimulation (Figure 6B, right panel). This odor-modulated cross-frequency coupling was not observed in anesthetized rats (Figures 6C,D).

To quantify the θ-HGO coupling and θ-HFO coupling in the OB, we calculated the mean value of the modulation index of multiple frequency pairs in the two sets of frequency bands. For the θ-HGO coupling, we calculated the mean modulation index of 12 repeated trials of 369 pairs of frequencies from 2–6 Hz (central frequency at 4 Hz) and 55–65 Hz (central frequency at 60 Hz) to 10–14 Hz (central frequency at 12 Hz) and 95–105 Hz (central frequency at 100 Hz) (Figure 7A). For the θ-HFO coupling, we calculated the mean modulation index of 12 repeated trials of 459 pairs of frequencies from 2–6 Hz (central frequency at 4 Hz) and 125–135 Hz (central frequency at 130 Hz) to 10–14 Hz (central frequency at 12 Hz) and 175–185 Hz (central frequency at 180 Hz) (Figure 7B). The results showed that the average modulation index of θ-HGO

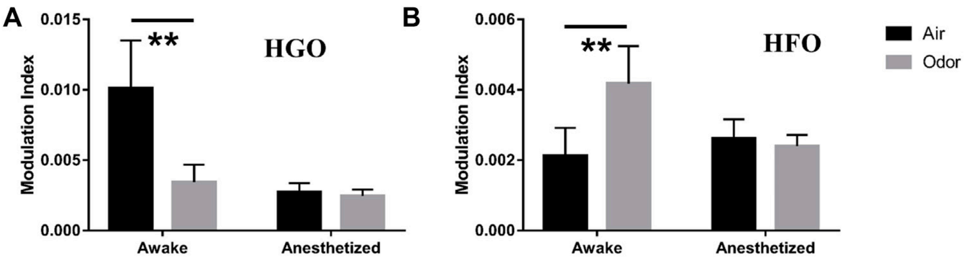

FIGURE 7
(A) Mean modulation index values of Θ-HGO coupling (pair of frequencies ranging 4–12 Hz for phase frequency, 60–100 Hz for Amplitude Frequency) in three awake and three anesthetized rats under air and odors stimulation. **(B)** Mean modulation index values of Θ-HFO coupling (pair of frequencies ranging from 4–12 Hz for phase frequency, 130–180 Hz for Amplitude Frequency) in 3 awake and 3 anesthetized rats under air and odors stimulation. The trial-averaged data are presented as the mean ± SEM, $n = 12$, 4 trials per rat. $^{**}p < 0.01$, $^{*}p < 0.05$, and ANOVA followed by Fisher's least significant difference (LSD).

coupling in the OB of awake rats decreased significantly under odor stimulation. In contrast, the modulation index of θ-HFO coupling increased significantly. Thus, the θ-HGO coupling and θ-HFO coupling activity in the OB of awake rats were both modulated significantly by odor stimulation. A significant θ-HFO coupling was observed in the OB, the prefrontal cortex (PFC), and ventral striatum (VS.) after injection of ketamine (Hunt et al., 2019), indicating the association between olfactory networks and oscillatory activity in the limbic areas. A cross-frequency coupling between the olfactory and hippocampus in a new context provides evidence of the hippocampus participating in the OB sensory processing (Pena et al., 2017). The finding that odor stimulation enhanced the θ-HFO coupling in the OB of freely moving rats suggests that odor stimulation may modify the communication between the olfactory system and the brain network through oscillation activity.

Discussion

In this study, we recorded the LFP of the OB neurons in the anesthetized and awake rats under odor stimulation. We observed that the LFP oscillations of anesthetized and awake rats were modulated to varying degrees by odor stimulation. Our results showed that the δ, θ, β, and high-frequency power were enhanced, and the γ power decreased in the awake rats during odor stimulation. In addition, the δ power of anesthetized rats decreased during odor stimulation, θ and β power increased, and γ and high-frequency oscillations did not respond to odor stimulation. The decrease of γ power in awake animals was accompanied by the enhancement of β power, consistent with the findings of previous studies (Beshel et al., 2007; Fuentes et al., 2008). However, we did not observe this phenomenon in anesthetized animals. Previous studies have shown that γ oscillation is more prominent in awake animals than in anesthetized animals (Li et al., 2012). As a result, we observed more robust γ oscillation and γ responses to odor stimuli in awake animals. The slow oscillation of 1–4 Hz exists in the OB of anesthetized and awake rats, also called respiratory rhythm. Recent studies have shown that this slow oscillation is affected by the respiratory input and by internal processing (Lockmann et al., 2016; Kocsis et al., 2018). Our study found that the δ rhythm is modulated differently by the odor stimuli during anesthesia and when awake, suggesting that this slow oscillation is also related to the brain state during sensory processing. In addition, our study found that the odor stimuli also modulated the high-frequency oscillations of awake animals. This rapid oscillation in the anesthetized animals has been reported numerous times in other studies. Based on the quantitative analysis of the power spectrum of high-frequency oscillations in the rats under two states, we found that HFO has more substantial power under anesthesia, which may be due to the effect of anesthesia. Previous studies have shown that the subanesthetic state significantly enhanced HFO in the OB (Hunt et al., 2019). The θ oscillation in the OB in this study distinctly modulated the HGO and HFO amplitude activity during the free movement, and odor presentation significantly modified these modulations. Changes in the activity of frequency bands and their interactions in the OB suggest distinct physiological processes subserving different functions. For instance, the θ-HG coupling in CA1 may play a role in memory encoding (Colgin and Moser, 2010), while θ-HFO has a possible role for inhibitory interneurons (Klausberger and Somogyi, 2008). Therefore, appropriate behavior tasks need to be designed in the future to explore further the specific physiological significance of oscillations in different frequency bands in the OB and how their interaction participates in olfactory processing.

Data availability statement

The original contributions presented in the study are included in the article/Supplementary Material; further inquiries can be directed to the corresponding authors.

Ethics statement

The animal study was reviewed and approved by Xi'an Jiaotong University.

Author contributions

PZ: conceptualization, methodology, investigation, validation, formal analysis, data curation, and writing—original draft. SL: methodology, validation, and visualization. YT: methodology, visualization, and writing—review and editing. YC: methodology, writing—review and editing, and visualization. WC: conceptualization, methodology, validation, data curation, visualization, and writing—review and editing. PW: conceptualization, resources, and writing—review and editing. LD: conceptualization, methodology, resources, writing—review and editing, supervision, project administration, and funding acquisition. CW: conceptualization, methodology, resources, writing—review and editing, supervision, project administration, and funding acquisition. All authors contributed to the article and approved the submitted version.

Funding

This work was supported by the National Natural Science Foundation of China (Grant Nos 32071370, 51861145307, and 31700859), and the Key Research and Development Program of Shaanxi Province-International Science and Technology Cooperation General Project (Grant No. 2022KW-23).

Conflict of interest

The authors declare that the research was conducted in the absence of any commercial or financial relationships that could be construed as a potential conflict of interest.

Publisher's note

Supplementary material

The Supplementary Material for this article can be found online at: https://www.frontiersin.org/articles/10.3389/fchem.2022.865006/full#supplementary-material

References

Beshel, J., Kopell, N., and Kay, L. M. (2007). Olfactory bulb gamma oscillations are enhanced with task demands. *J. Neurosci.* 27, 8358–8365. doi:10.1523/jneurosci.1199-07.2007

Buzsáki, G., and Watson, B. O. (2012). Brain rhythms and neural syntax: Implications for efficient coding of cognitive content and neuropsychiatric disease. *Dialogues Clin. Neurosci.* 14, 345–367. doi:10.31887/dcns.2012.14.4/gbuzsaki

Chery, R., Gurden, H., and Martin, C. (2013). Anesthetic regimes modulate the temporal dynamics of local field potential in the mouse olfactory bulb. *J. Neurophysiol.* 111, 908–917. doi:10.1152/jn.00261.2013

Colgin, L. L., and Moser, E. I. (2010). Gamma oscillations in the Hippocampus. *Physiology* 25, 319–329. doi:10.1152/physiol.00021.2010

Frederick, D. E., Brown, A., Brim, E., Mehta, N., Vujovic, M., Kay, L. M., et al. (2016). Gamma and beta oscillations define a sequence of neurocognitive modes present in odor processing. *J. Neurosci.* 36, 7750–7767. doi:10.1523/jneurosci.0569-16.2016

Fuentes, R. A., Aguilar, M. I., Aylwin, M. L., and Maldonado, P. E. (2008). Neuronal activity of mitral-tufted cells in awake rats during passive and active odorant stimulation. *J. Neurophysiol.* 100, 422–430. doi:10.1152/jn.00095.2008

Griffiths, B. J., Parish, G., Roux, F., Michelmann, S., Van Der Plas, M., Kolibius, L. D., et al. (2019). Directional coupling of slow and fast hippocampal gamma with neocortical alpha/beta oscillations in human episodic memory. *Proc. Natl. Acad. Sci. U. S. A.* 116, 21834–21842. doi:10.1073/pnas.1914180116

Hamm, J. P., Dyckman, K. A., Mcdowell, J. E., and Clementz, B. A. (2012). Pre-cue fronto-occipital alpha phase and distributed cortical oscillations predict failures of cognitive control. *J. Neurosci.* 32, 7034–7041. doi:10.1523/jneurosci.5198-11.2012

Hunt, M. J., Adams, N. E., Średniawa, W., Wójcik, D. K., Simon, A., Kasicki, S., et al. (2019). The olfactory bulb is a source of high-frequency oscillations (130–180 Hz) associated with a subanesthetic dose of ketamine in rodents. *Neuropsychopharmacology* 44, 435–442. doi:10.1038/s41386-018-0173-y

Ito, J., Roy, S., Liu, Y., Cao, Y., Fletcher, M., Lu, L., et al. (2014). Whisker barrel cortex delta oscillations and gamma power in the awake mouse are linked to respiration. *Nat. Commun.* 5, 3572. doi:10.1038/ncomms4572

Jackson, J., Goutagny, R., and Williams, S. (2011). Fast and slow gamma rhythms are intrinsically and independently generated in the subiculum. *J. Neurosci.* 31, 12104–12117. doi:10.1523/jneurosci.1370-11.2011

Jones, K. T., Johnson, E. L., and Berryhill, M. E. (2020). Frontoparietal theta-gamma interactions track working memory enhancement with training and tDCS. *NeuroImage* 211, 116615. doi:10.1016/j.neuroimage.2020.116615

Kay, L. M. (2003). Two species of gamma oscillations in the olfactory bulb: dependence on behavioral state and synaptic interactions. *J. Integr. Neurosci.* 2, 31–44. doi:10.1142/s0219635203000196

Klausberger, T., and Somogyi, P. (2008). Neuronal diversity and temporal dynamics: the unity of hippocampal circuit operations. *Sci. (New York, N.Y.)* 321, 53–57. doi:10.1126/science.1149381

Kocsis, B., Pittman-Polletta, B. R., and Roy, A. (2018). Respiration-coupled rhythms in prefrontal cortex: beyond if, to when, how, and why. *Brain Struct. Funct.* 223, 11–16. doi:10.1007/s00429-017-1587-8

Lepousez, G., and Lledo, P.-M. (2013). Odor discrimination requires proper olfactory fast oscillations in awake mice. *Neuron* 80, 1010–1024. doi:10.1016/j.neuron.2013.07.025

Li, A., Zhang, L., Liu, M., Gong, L., Liu, Q., Xu, F., et al. (2012). Effects of different anesthetics on oscillations in the rat olfactory bulb. *J. Am. Assoc. Lab. Anim. Sci.* 51, 458–463.

Li, Q., Yang, C., Zhang, X., Yang, Z., and Zhang, T. (2019). Arginine vasopressin attenuates dysfunction of hippocampal theta and gamma oscillations in chronic cerebral hypoperfusion via V1a receptor. *Brain Res. Bull.* 153, 84–92. doi:10.1016/j.brainresbull.2019.08.012

Liu, P., Cao, T., Xu, J., Mao, X., Wang, D., Li, A., et al. (2020). Plasticity of sniffing pattern and neural activity in the olfactory bulb of behaving mice during odor sampling, anticipation, and reward. *Neurosci. Bull.* 36, 598–610. doi:10.1007/s12264-019-00463-9

Lockmann, A. L. V., Laplagne, D. A., Leão, R. N., and Tort, A. B. L. (2016). A respiration-coupled rhythm in the rat Hippocampus independent of theta and slow oscillations. *J. Neurosci.* 36, 5338–5352. doi:10.1523/jneurosci.3452-15.2016

Losacco, J., Ramirez-Gordillo, D., Gilmer, J., and Restrepo, D. (2020). Learning improves decoding of odor identity with phase-referenced oscillations in the olfactory bulb. *Elife* 9, e52583. doi:10.7554/elife.52583

Manabe, H., and Mori, K. (2013). Sniff rhythm-paced fast and slow gamma-oscillations in the olfactory bulb: Relation to tufted and mitral cells and behavioral states. *J. Neurophysiol.* 110, 1593–1599. doi:10.1152/jn.00379.2013

Martin, C., and Ravel, N. (2014). Beta and gamma oscillatory activities associated with olfactory memory tasks: different rhythms for different functional networks? *Front. Behav. Neurosci.* 8, 218. doi:10.3389/fnbeh.2014.00218

Mofleh, R., and Kocsis, B. (2021). Delta-range coupling between prefrontal cortex and hippocampus supported by respiratory rhythmic input from the olfactory bulb in freely behaving rats. *Sci. Rep.* 11, 8100. doi:10.1038/s41598-021-87562-8

Murphy, N., Ramakrishnan, N., Walker, C. P., Polizzotto, N. R., and Cho, R. Y. (2020). Intact auditory cortical cross-frequency coupling in early and chronic schizophrenia. *Front. Psychiatry* 11, 507. doi:10.3389/fpsyt.2020.00507

Nagayama, S., Takahashi, Y. K., Yoshihara, Y., and Mori, K. (2004). Mitral and tufted cells differ in the decoding manner of odor maps in the rat olfactory bulb. *J. Neurophysiol.* 91, 2532–2540. doi:10.1152/jn.01266.2003

Naggar, I., Stewart, M., and Orman, R. (2020). High frequency oscillations in rat hippocampal slices: Origin, frequency characteristics, and spread. *Front. Neurol.* 11, 326. doi:10.3389/fneur.2020.00326

Nakazono, T., Takahashi, S., and Sakurai, Y. (2019). Enhanced theta and high-gamma coupling during late stage of rule switching task in rat Hippocampus. *Neuroscience* 412, 216–232. doi:10.1016/j.neuroscience.2019.05.053

Osinski, B. L., and Kay, L. M. (2016). Granule cell excitability regulates gamma and beta oscillations in a model of the olfactory bulb dendrodendritic microcircuit. *J. Neurophysiol.* 116, 522–539. doi:10.1152/jn.00988.2015

Pena, R. R., Medeiros, D. D. C., Guarnieri, L. D. O., Guerra, J. B., Carvalho, V. R., Mendes, E. M. a. M., et al. (2017). Home-cage odors spatial cues elicit theta phase/gamma amplitude coupling between olfactory bulb and dorsal hippocampus. *Neuroscience* 363, 97–106. doi:10.1016/j.neuroscience.2017.08.058

Ravel, N., Chabaud, P., Martin, C., Gaveau, V., Hugues, E., Tallon-Baudry, C., et al. (2003). Olfactory learning modifies the expression of odour-induced oscillatory responses in the gamma (60-90 Hz) and beta (15-40 Hz) bands in the rat olfactory bulb. *Eur. J. Neurosci.* 17, 350–358. doi:10.1046/j.1460-9568.2003.02445.x

Rojas-Líbano, D., and Kay, L. M. (2008). Olfactory system gamma oscillations: the physiological dissection of a cognitive neural system. *Cogn. Neurodyn.* 2, 179–194. doi:10.1007/s11571-008-9053-1

Rosero, M. A., and Aylwin, M. L. (2011). Sniffing shapes the dynamics of olfactory bulb gamma oscillations in awake behaving rats. *Eur. J. Neurosci.* 34, 787–799. doi:10.1111/j.1460-9568.2011.07800.x

Salimi, M., Ghazvineh, S., Nazari, M., Dehdar, K., Garousi, M., Zare, M., et al. (2021). Allergic rhinitis impairs working memory in association with drop of hippocampal – prefrontal coupling. *Brain Res.* 1758, 147368. doi:10.1016/j.brainres.2021.147368

Scheffer-Teixeira, R., Belchior, H., Caixeta, F. V., Souza, B. C., Ribeiro, S., Tort, A. B. L., et al. (2012). Theta phase modulates multiple layer-specific oscillations in the CA1 region. *Cereb. Cortex* 22, 2404–2414. doi:10.1093/cercor/bhr319

Scheffzük, C., Kukushka, V. I., Vyssotski, A. L., Draguhn, A., Tort, A. B., Brankačk, J., et al. (2011). Selective coupling between theta phase and neocortical fast gamma oscillations during REM-sleep in mice. *PLoS One* 6, e28489. doi:10.1371/journal.pone.0028489

Shusterman, R., Smear, M. C., Koulakov, A. A., and Rinberg, D. (2011). Precise olfactory responses tile the sniff cycle. *Nat. Neurosci.* 14, 1039–1044. doi:10.1038/nn.2877

Średniawa, W., Wróbel, J., Kublik, E., Wójcik, D. K., Whittington, M. A., Hunt, M. J., et al. (2021). Network and synaptic mechanisms underlying high frequency oscillations in the rat and cat olfactory bulb under ketamine-xylazine anesthesia. *Sci. Rep.* 11, 6390. doi:10.1038/s41598-021-85705-5

Tort, A. B. L., Kramer, M. A., Thorn, C., Gibson, D. J., Kubota, Y., Graybiel, A. M., et al. (2008). Dynamic cross-frequency couplings of local field potential oscillations in rat striatum and hippocampus during performance of a T-maze task. *Proc. Natl. Acad. Sci. U. S. A.* 105, 20517–20522. doi:10.1073/pnas.0810524105

Tort, A. B. L., Komorowski, R., Eichenbaum, H., and Kopell, N. (2010). Measuring phase-amplitude coupling between neuronal oscillations of different frequencies. *J. Neurophysiol.* 104, 1195–1210. doi:10.1152/jn.00106.2010

Tort, A. B. L., Scheffer-Teixeira, R., Souza, B. C., Draguhn, A., and Brankačk, J. (2013). Theta-associated high-frequency oscillations (110–160Hz) in the hippocampus and neocortex. *Prog. Neurobiol.* 100, 1–14. doi:10.1016/j.pneurobio.2012.09.002

Urbain, N., Fourcaud-Trocmé, N., Laheux, S., Salin, P. A., and Gentet, L. J. (2019). Brain-state-dependent modulation of neuronal firing and membrane potential dynamics in the somatosensory thalamus during natural sleep. *Cell Rep.* 26, 1443–1457.e5. doi:10.1016/j.celrep.2019.01.038

van Wingerden, M., Van Der Meij, R., Kalenscher, T., Maris, E., and Pennartz, C. M. A. (2014). Phase-amplitude coupling in rat orbitofrontal cortex discriminates between correct and incorrect decisions during associative learning. *J. Neurosci.* 34, 493–505. doi:10.1523/jneurosci.2098-13.2014

Vinck, M., Womelsdorf, T., Buffalo, Elizabeth a., Desimone, R., and Fries, P. (2013). Attentional modulation of cell-class-specific gamma-band synchronization in awake monkey area V4. *Neuron* 80, 1077–1089. doi:10.1016/j.neuron.2013.08.019

Vivekananda, U., Bush, D., Bisby, J. A., Baxendale, S., Rodionov, R., Diehl, B., et al. (2021). Theta power and thetagamma coupling support long-term spatial memory retrieval. *Hippocampus* 31, 213–220. doi:10.1002/hipo.23284

Zhang, H., Watrous, A. J., Patel, A., and Jacobs, J. (2018). Theta and alpha oscillations are traveling waves in the human neocortex. *Neuron* 98, 1269–1281.e4. doi:10.1016/j.neuron.2018.05.019

Zhong, W., Ciatipis, M., Wolfenstetter, T., Jessberger, J., Müller, C., Ponsel, S., et al. (2017). Selective entrainment of gamma subbands by different slow network oscillations. *Proc. Natl. Acad. Sci. U. S. A.* 114, 4519–4524. doi:10.1073/pnas.1617249114

frontiers | Frontiers in Chemistry

TYPE Original Research
PUBLISHED 08 August 2022
DOI 10.3389/fchem.2022.939736

A reagentless electrochemical immunosensor for sensitive detection of carcinoembryonic antigen based on the interface with redox probe-modified electron transfer wires and effectively immobilized antibody

Jing Zhang[1,2], Luoxing Yang[3], Jie Pei[1,2], Yanzhang Tian[1,2]* and Jiyang Liu[3]*

[1]Shanxi Bethune Hospital, Shanxi Academy of Medical Sciences, Tongji Shanxi Hospital, Third Hospital of Shanxi Medical University, Taiyuan, China, [2]Tongji Hospital, Tongji Medical College, Huazhong University of Science and Technology, Wuhan, China, [3]Key Laboratory of Surface & Interface Science of Polymer Materials of Zhejiang Province, Department of Chemistry, Zhejiang Sci-Tech University, Hangzhou, China

Convenient and sensitive detection of tumors marked in serum samples is of great significance for the early diagnosis of cancers. Facile fabrication of reagentless electrochemical immunosensor with efficient sensing interface and high sensitivity is still a challenge. Herein, an electrochemical immunosensor was easily fabricated based on the easy fabrication of immunoassay interface with electron transfer wires, confined redox probes, and conveniently immobilized antibodies, which can achieve sensitive and reagentless determination of the tumor marker, carcinoembryonic antigen (CEA). Carboxyl multi-walled carbon nanotubes (MWCNTs) were firstly modified with an electrochemical redox probe, methylene blue (MB), which has redox potentials distinguished from those of redox molecules commonly existing in biological samples (for example, ascorbic acid and uric acid). After the as-prepared MB-modified MWCNT (MWCNT-MB) was coated on the supporting glassy carbon electrode (GCE), the MWCNT-MB/GCE exhibited improved active area and electron transfer property. Polydopamine (PDA) was then *in situ* synthesized through simple self-polymerization of dopamine, which acts as the bio-linker to covalently immobilize the anti-CEA antibody (Ab). The developed immunosensor could be applied for electrochemical detection of CEA based on the decrease in the redox signal of MB after specific binding of CEA and immobilized Ab. The fabricated immunosensor can achieve sensitive determination of CEA ranging from 10 pg/ml to 100 ng/ml with a limit of detection (LOD) of 0.6 pg/ml. Determination of CEA in human serum samples was also realized with high accuracy.

EDITED BY
Yan Zhang,
University of Jinan, China

REVIEWED BY
Ghazala Ashraf,
Huazhong University of Science and Technology, China
Ali Benvidi,
Yazd University, Iran
Yun Shu,
Yangzhou University, China

*CORRESPONDENCE
Yanzhang Tian,
tyz2030@163.com
Jiyang Liu,
liujyxx@126.com

SPECIALTY SECTION
This article was submitted to Analytical Chemistry,
a section of the journal
Frontiers in Chemistry

RECEIVED 09 May 2022
ACCEPTED 27 June 2022
PUBLISHED 08 August 2022

CITATION
Zhang J, Yang L, Pei J, Tian Y and Liu J (2022), A reagentless electrochemical immunosensor for sensitive detection of carcinoembryonic antigen based on the interface with redox probe-modified electron transfer wires and effectively immobilized antibody.
Front. Chem. 10:939736.
doi: 10.3389/fchem.2022.939736

KEYWORDS

electrochemical determination, immunosensor, label free, sensitive detection, carcinoembryonic antigen

Introduction

Cancer nowadays seriously threatens human health owing to high morbidity and mortality. Early diagnosis and treatment of cancer is the most effective way to reduce mortality (Ashraf et al., 2022a; Asif et al., 2022). Tumor markers (TM) are effective indicators for early diagnosis of cancer and monitoring of therapeutic effects (Sadighbayan et al., 2019; Farzin et al., 2020; Zheng et al., 2021; Laraib et al., 2022). It is well known that carcinoembryonic antigen (CEA) is the most sensitive tumor marker (Liu et al., 2015; Pirsaheb et al., 2019). Thus, convenient and highly sensitive detection of CEA in serum is crucial for the early diagnosis of cancers (Jozghorbani et al., 2021). Until now, the detection of CEA commonly uses immunoassay methods based on signals of radiation, time-resolved fluorescence, chemiluminescence, or electrochemiluminescence (Liu et al., 2015; Pirsaheb et al., 2019; Jozghorbani et al., 2021). These detection strategies usually suffer from expensive instruments, special reagents, and skilled operations. In comparison with other detection strategies (for example, optical technology) (Zhang et al., 2020; Zhao et al., 2020; Deng et al., 2021; Wan et al., 2021; Zhu et al., 2022a), electrochemical sensing has attracted extensive attention because of its fast detection speed, a simple instrument, easy integration, and miniaturization (Asif et al., 2018; Ashraf et al., 2019; Aziz et al., 2019; Liu et al., 2020; Ashraf et al., 2021a; Ashraf et al., 2021b; Deng et al., 2021; Zhang et al., 2022a; Zhu et al., 2022b; Wei et al., 2022; Zhong et al., 2022; Zhou et al., 2022). The development of a novel electrochemical immunosensor for simple and highly sensitive detection of CEA is of great significance.

The detection modes in electrochemical immunoassay are usually divided into two categories (Farzin et al., 2020; Zheng et al., 2021; Laraib et al., 2022). One is based on the free electrochemical probes in solution. Usually, the specific recognition between antigen and antibody will affect the diffusion of the electrochemical probe to the electrode surface or reduce its electron transfer on the electrode interface. However, the use of a solution-phase probe might compromise the detection efficiency due to the increased complexity of the operation and possible contamination of the target system. The other detection mode is based on the immobilized electrochemical probes, which can realize reagentless detection with convenient operation. Fabrication of reagentless electrochemical immunoassay with convenient antibody immobilization and effective signal amplification is highly desirable.

The immobilization of antibody (Ab) is crucial for the construction of an efficient immuno-recognitive interface and the subsequent detection performance. Biomimetic modification of the micro/nano interface is commonly effective to immobilize antibodies. Inspired by the structure of marine mussels, polydopamine (PDA) chemistry has been used as a simple and versatile approach for the (bio) functionalization of materials (Alfieri et al., 2022). On the one hand, PDA coating can improve the hydrophilicity and biocompatibility of materials. Polydopamine is the product of the self-polymerization of dopamine (DA) under alkaline conditions with air or oxygen as the oxidant. Usually, PDA can form and stably combine on the surface of almost all materials (for example, ceramics, semiconductors, metals, and even synthetic polymers) (Samyn, 2021; Alfieri et al., 2022; Prabhu et al., 2022). On the other hand, polydopamine has secondary reactivity and can be directly used as the bio-linker for covalent immobilization of recognitive antibodies (Ding et al., 2016; Huang et al., 2020; Li et al., 2021). It has been proven that under alkaline conditions, the catechol groups in the polydopamine matrix can be oxidized to dopaquinone, which can undergo Schiff base reaction or Michael addition reaction with nucleophilic groups (for example, amine or thiol groups). Thus, PDA can be applied to directly immobilize antibodies since proteins contain $-NH_2$ or $-SH$ groups. This antibody immobilization process based on PDA is convenient with no need for complex reaction conditions or equipment.

In this work, a simple strategy for the convenient construction of electrochemical immunosensor and its application for reagentless and sensitive determination of CEA are demonstrated. As shown in Figure 1, methylene blue (MB) was selected as the electrochemical redox probe because its redox potential is distinguishable from that of common redox molecules (for example, ascorbic acid and uric acid) in biological samples. Owing to good electrical conductivity, carboxyl multi-walled carbon nanotube (MWCNT) was employed as one-dimensional quantum wires to improve the performance of the fabricated electrochemical sensor (Mazloum-Ardakani et al., 2013; Benvidi et al., 2015; Benvidi et al., 2016; Asif et al., 2018; Yazdanparast et al., 2019; Ashraf et al., 2020; Ashraf et al., 2021b; Iftikhar et al., 2021). After MWCNT was modified by MB, the obtained composite (MB-MWCNT) was applied to modify the glassy carbon electrode (GCE), so that electron transfer wires and immobilized probes were integrated on the surface of GCE. Under alkaline conditions, polydopamine (PDA) was synthesized *in situ* through simple self-polymerization of dopamine in alkaline conditions. Subsequently, the covalent immobilization of the CEA antibody (Ab) was easily achieved by using PDA as the biological linker. When CEA specifically recognized Ab, the redox signal of MB was weakened because the antigen-antibody complex hindered the electron transfer on the electrode surface. Based on this principle, sensitive, and reagentless, electrochemical detection of CEA was achieved.

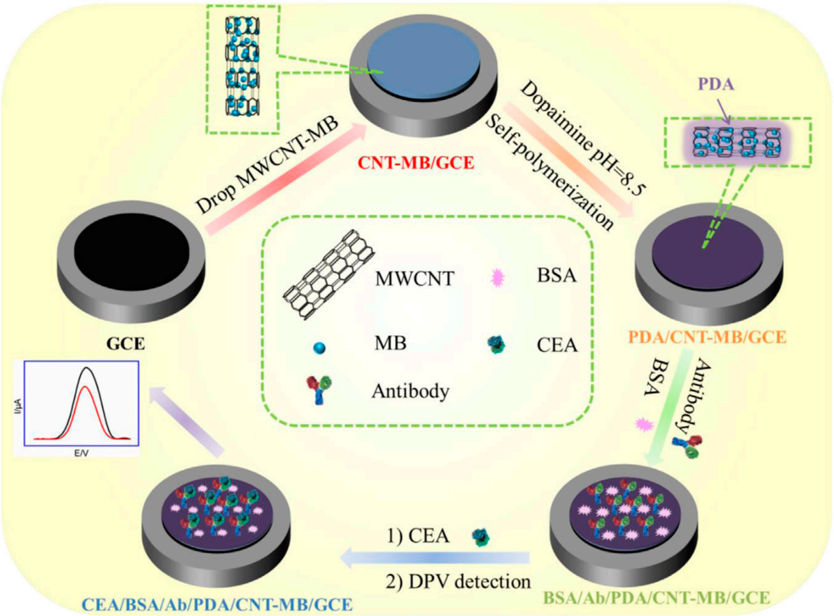

FIGURE 1
Schematic illustration for the fabrication of immunoanalysis interface and the following label-free electrochemical determination of CEA.

The advantages of the fabrication of the electrochemical method lie in the easy fabrication of an immunoassay interface with electron transfer wires, confined redox probes, and conveniently immobilized antibodies, which can be used as a universal platform to construct an electrochemical sensor for reagentless determination of tumor marker.

Materials and methods

Chemicals and materials

Carcinoembryonic antigen (CEA), anti-CEA (Ab), prostate specific antigen (PSA), and carcinoma antigen 125 (CA125) were purchased from Beijing KEY-BIO Biotech Co., Ltd. (China). S100 calcium-binding protein β was purchased from Proteintech (China). Bovine serum albumin (BSA), 3-hydroxytyramine hydrochloride (DA), and sodium phosphate dibasic dodecahydrate ($Na_2HPO_4{\cdot}12H_2O$) were obtained from Aladdin (China). Sodium dihydrogen phosphate dehydrates ($NaH_2PO_4{\cdot}2H_2O$) were obtained from Macklin (China). Phosphate buffer solution (PBS) was prepared using Na_2HPO_4 and NaH_2PO_4. Methylene Blue trihydrate (MB) was obtained from Tianjin Yongda Chemical Reagent Co. Ltd. (China). Carboxyl multiwall carbon nanotubes (MWCNTs) were purchased from Chengdu organic chemicals Co. Ltd. (China). Human blood serum (healthy man) was provided by Shanxi Bethune Hospital (Taiyuan, China). All other chemicals were of analytical grade and used without further treatment. Ultrapure water (18.2 MΩ cm) was prepared by the Mill-Q system and used throughout the work.

Measurements and instrumentations

Scanning electron microscopy (SEM) images were obtained at an acceleration voltage of 2 kV on a SU8010 microscope (Hitachi, Japan). All electrochemical investigations including cyclic voltammetry (CV), electrochemical impedance spectroscopy (EIS), and differential pulse voltammetry (DPV) were performed on the electrochemical workstation (Autolab PGSTAT302N, Metrohm, Switzerland) in the laboratory with constant temperature (25°C) and humidity (75%). The traditional three electrode system was applied in all electrochemical experiments. Briefly, bare or modified GCE was used as the working electrode. The silver/silver chloride electrode (Ag/AgCl, saturated with sodium chloride) was adopted as the reference electrode and the platinum wire electrode was the counter electrode. Before use, GCE was sequentially polished with 0.3 μM, 0.3 μM, and 0.05 μM Al_2O_3 slurry, respectively. Afterward, the electrode was sonicated in ethanol and then in ultrapure water to obtain a clean mirror surface. EIS investigation was performed with the frequencies ranging from 10^4 to 10^{-1} Hz in $Fe(CN)_6^{3/4-}$ (2.5 mM) containing KCl (0.1 M). The Brunauer-Emmette-Teller (BET) surface areas were measured on an ASAP 2020 analyzer (Belsorp-max, United States) by using N_2 as the adsorption gas. X-ray photoelectron spectroscopy (XPS) measurements were carried out using Mg Ká as the excitation source (Thermo Fisher, United States). The X-ray powder diffraction (XRD) patterns were obtained on a Bruker D8 A8 Advance diffractometer with Cu K radiation (40 kV, 20 mA, λ= 1.54056 Å) (Bruker AXS, United States). The zeta potential was analyzed using a Nano Particle Analyzer (SZ-100V2, HORIBA Jobin Yvon, France).

Preparation of methylene blue-modified carboxyl multi-walled carbon nanotubes

To synthesize MB modified carbon nanotube (MWCNT-MB), carboxyl multiwall carbon nanotubes (0.5 mg/ml) were added to MB solution (2 mg/ml). A dispersion was obtained by sonication for 30 min. Then, the dispersion was centrifuged at 14,000 rpm for 10 min to remove the supernatant. The obtained precipitate was the MWCNT-MB, which can be further re-dispersed in ultrapure water.

Fabrication of immunosensor

The immuno-recognitive interface was a fabrication on GCE through three steps. First, 10 μL of MWCNT-MB dispersion was dropped to the surface of GCE and dried at 60°C (Yan et al., 2020). The obtained electrode was denoted as MWCNT-MB/GCE. The second step was the *in-situ* coating of PDA through self-polymerization of DA. Briefly, the MWCNT-MB/GCE electrode was immersed in DA solution (0.38 mg/ml in 0.1 M PBS, pH = 8.5). After self-polymerization of DA for 1 h, the PDA-coated electrode (PDA/MWCNT-MB/GCE) was thoroughly rinsed with ultrapure water to remove the residual DA on the electrode surface. The third step was the covalent immobilization of Ab using PDA as the linker. Commonly, the CEA antibody (30 μl, 100 μg/ml in 0.1 M PBS, pH = 7.4) was dropped on the surface of PDA/MWCNT-MB/GCE and incubated at 37°C for 1 h. After the residual antibody on the obtained electrode (Ab/PDA/MWCNT-MB/GCE) was washed with PBS (0.1 M, pH = 7.4), non-specific sites were blocked by incubation in BSA (1%, in 0.1 M PBS, pH = 7.4) for 1 h at room temperature to produce a CEA immunosensor, which was denoted as BSA/Ab/PDA/MWCNT-MB/GCE.

Electrochemical determination of carcinoembryonic antigen

PBS (0.1 M, pH 7.4) was used as the electrolyte for the electrochemical determination of CEA. Briefly, the immunosensor, BSA/Ab/PDA/MWCNT-MB/GCE, was incubated with different concentrations of CEA (antigen) at 37°C for 60 min. The electrochemical signals of MB in the immunosensor before and after CEA binding was measured using differential pulse voltammetry. The determination of CEA in human serum (healthy women) was investigated to evaluate the application of developed immunosensor for real sample analysis. Before determination, the serum was diluted by a factor of 50.

Results and discussion

Strategy for facile fabrication of the immunoassay interface with electron transfer wires, confined redox probes, and conveniently immobilized antibodies

Figure 1 demonstrates the facile fabrication of the immunoassay interface and the subsequent reagentless determination of CEA based on the electrochemical signals of an immobilized mediator. As shown, electron transfer wires, immobilized redox probes, and antibodies were integrated into the immunosensor interface. Amongst, multi-walled carbon nanotubes (MWCNTs) were chosen as electron transfer wires due to their excellent electron transfer, high specific surface area, and low price. (Rivas et al., 2017; Eguílaz et al., 2019; Xie et al., 2019). Carboxylated carbon nanotubes were directly applied because of the good hydrophilicity. At the same time, methylene blue (MB), a commonly used cationic redox probe ($pK_1 = 11.2$), was used as the electrochemical probe. (Zhang et al., 2022b; Liu et al., 2022; Prado et al., 2022; Suo et al., 2022). Since the redox peaks of MB are at a negative potential, the electrochemical interference of redox small molecules (for example, ascorbic acid-AA, uric acid-UA, dopamine-DA, tryptophan, etc) in biological samples (for example, serum) can be effectively avoided because of their positive redox potentials. MB modified MWCNT (MWCNT-MB) can be easily synthesized through their electrostatic interaction due to the negative charge of carboxylated MWCNT and the positive charge of MB.

Three steps were involved in the construction of the immunosensor. First, the MWCNT-MB composite was drop-coated on the surface of GCE to improve the active electrode area, facilitate electron transfer and introduce a redox probe. The π-π interaction or hydrophobic interactions between sp (Asif et al., 2022) carbon atoms from both GCE and MWCNTs was beneficial to the stable binding of MWCNT-MB composites. Second, a layer of PDA was *in-situ* covered on an MWCNT-MB modified electrode (MWCNT-MB/GCE) through the self-polymerization of dopamine (DA) under alkaline conditions with dissolved oxygen as the oxidant. Third, the anti-CEA antibody (Ab) was covalently linked to the PDA layer followed by the blocking of non-specific sites using bovine serum albumin (BSA). It has been shown that PDA has a structure similar to the byssin protein in marine mussels and thus has secondary reactivity. Due to the $-NH_2$ or $-SH$ groups in amino acids of proteins, PDA can be used as a linking layer to achieve covalent attachment of Ab through Michael addition or Schiff-based reactions under mild conditions.

Characterization of carboxyl multi-walled carbon nanotubes-methylene blue nanocomposite

XRD was employed to investigate the change in the crystalline structure of MWCNT. As shown in Supplementary Figure S1 (in Supporting information, SI), two peaks located at 26.0° (d value of 3.4 Å) and 43.6° (d value of 3.25 Å) were observed as (002) and (100) reflections of graphite, respectively, which are attributed to the distance between walls and interwall spacing of MWCNT (Ömür and Alanyalıoğlu, 2017; Alimohammady et al., 2019). In addition, the formation of nanocomposite with MB did not change the crystal structure of MWCNT. The changes in chemical composition between MWCNT and MWCNT-MB were further confirmed by X-ray photoelectron spectroscopy (XPS, Supplementary Figure S2 in SI). As shown, MWCNT displayed C_{1s} and O_{1s} peaks resulting from its sp (Asif et al., 2022) carbon structure and carboxylated groups. In addition to the C_{1s} and O_{1s} peaks, N_{1s} and S_{2p} peaks appeared in MWCNT-MB, proving the successful composite of MB on MWCNT. The surface potentials of MWCNT and MWCNT-MB were determined using zeta potential measurements. The zeta potential of MWCNT was −27.2 mV, which was attributed to the ionization of carboxyl groups on its surface. For MWCNT-MB, the zeta potential was −14.9 mV. The decrease in zeta potential originated from the binding of positively charged MB on the surface of MWCNT through electrostatic interaction. Brunauer-Emmett-Teller (BET) analysis revealed a specific surface area of 405.3 m^2/g for MWCNT, which was higher than that of MWCNT-MB (337.3 m^2/g). The slight decrease in the specific surface area might result from the increase in mass after MB binding and the possible entanglement of MWCNTs due to the electrostatic interaction with MB.

Electrochemical characterization of the immobilized redox probes and morphology of the electrode

In comparison with other detection strategies (for example, optical Analysis), electrochemical detection has advantages including fast detection speed, a simple instrument, easy integration, and miniaturization. (Cui et al., 2020; Cui et al., 2021; Duan et al., 2021; Liu et al., 2022). The immobilization of redox probes on the electrode surface was investigated by detecting the electrochemical signals of MB. Figure 2A is a cyclic voltammogram of different electrodes in PBS electrolyte. As shown, no redox peak was observed on bare GCE. When GCE was modified by the MWCNT-MB composite, a pair of redox peaks was revealed on MWCNT-MB/GCE with the anodic potential (E_{pa}) and cathodic potential (E_{pc}) of −0.2 V and −0.32 V, respectively. These peaks were consistent with the redox potential of MB, indicating the successful immobilization of MB on the surface of the electrode. In addition, the charging current of MWCNT-MB/GCE significantly increased, proving that the introduction of carbon nanotubes effectively increased the active area of the electrode. When the PDA layer was further modified on MWCNT-MB/GCE, the redox peak current of MB slightly decreased owing to the poor conductivity of the PDA layer. These results were also proven by DPV curves in the inset of Figure 2A.

The stability of redox probes is crucial for the performance of reagentless detection. In order to investigate the stability of the immobilized probe, the prepared PDA/MWCNT-MB/GCE was continuously scanned for 20 cycles. As shown in Figure 2B, the peak current of MB hardly changed with the increase of the scanning cycles. This phenomenon indicated that MB on MWCNT could be stably immobilized on the surface of the electrode. This was due to the following two reasons. On the one hand, the electrostatic interaction and π-π interaction between MB and MWCNT endowed the MWCNT-MB composite with good stability. On the other hand, the coated PDA layer can further stabilize the components in the inner layer.

The electrochemical behaviors of MB on the electrode surface were further investigated at different scan rates. As shown in Figure 3A, the redox peak currents of MB increased with the increase in scan rate. Linear correlations between the anodic peak current (I_{pa}) or cathodic peak current (I_{pc}) and scan rate (v) were revealed (Figure 3B, $I_{pa} = 0.709\ v + 5.86$, $R^2 = 0.995$, $I_{pc} = -0.747\ v - 10.3$, $R^2 = 0.993$), demonstrating a characteristic surface-controlled electrochemical process of the immobilized probe.

The morphology of MWCNT-MB/GCE and PDA/MWCNT-MB/GCE were investigated using a scanning electron microscopy (SEM). The left image in Figure 4 displayed the rough surface of MWCNT-MB/GCE with uniform distribution of MWCNT. The characteristics signals including C and O elements mainly form MWCNT, and N and S elements from MB in SEM-energy dispersive spectroscopy (SEM-EDS) also prove the successful modification of electrodes with MWCNT-MB nanocomposites. After the coating of PDA, the rough and porous network of carbon nanotubes was not obvious, indicating the effective coverage of the PDA layer (the right image in Figure 4).

Optimized conditions for the fabrication of immunosensor

Figure 5 presents the CV curves obtained on different electrodes during antibody binding. The dopaquinone structure in PDA can react with $-NH_2$ or $-SH$ groups of proteins to achieve covalent immobilization of antibodies. As

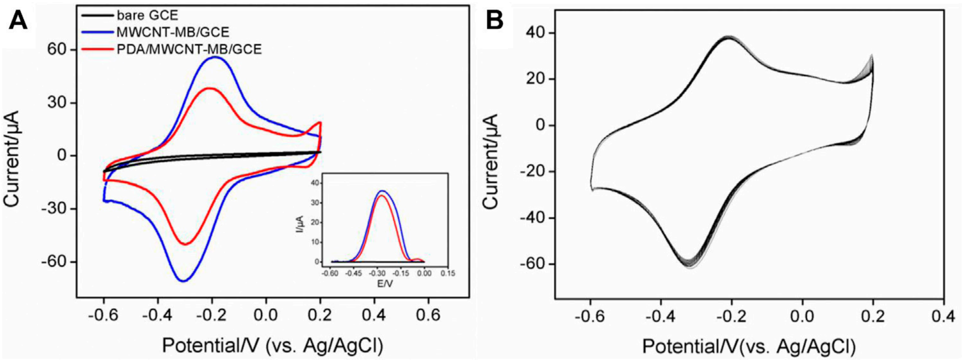

FIGURE 2
(A) CV and DPV (inset) curves obtained on different electrodes in PBS electrolyte (0.1M, pH = 7.4). **(B)** CV curves obtained on PDA/MWCNT-MB/GCE during continuous cyclic voltammetry scanning.

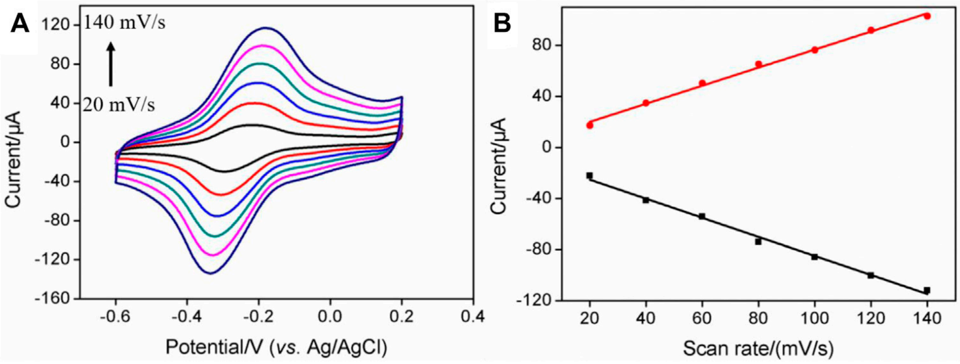

FIGURE 3
(A) CV curves of PDA/MWCNT-MB/GCE at different scan rate. The electrolyte solution is 0.1 M PBS (pH = 7.4). **(B)** The linear regression curve between the oxidation peak current or reduction peak current and scan rate.

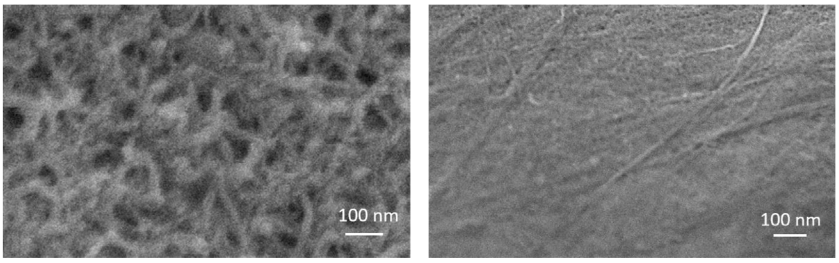

FIGURE 4
SEM images of MWCNT-MB **(left)** and PDA/MWCNT **(right)** modified glassy carbon sheet.

seen, the electrochemical signal of MB on Ab/MWCNT-MB/GCE significantly reduced after Ab binding (Figure 5A). This was due to the insulating properties of the protein, which hindered the interfacial electron transfer. After subsequent blocking of non-specific sites with BSA, the immunosensor BSA/Ab/MWCNT-MB/GCE is finally obtained. This blocking process

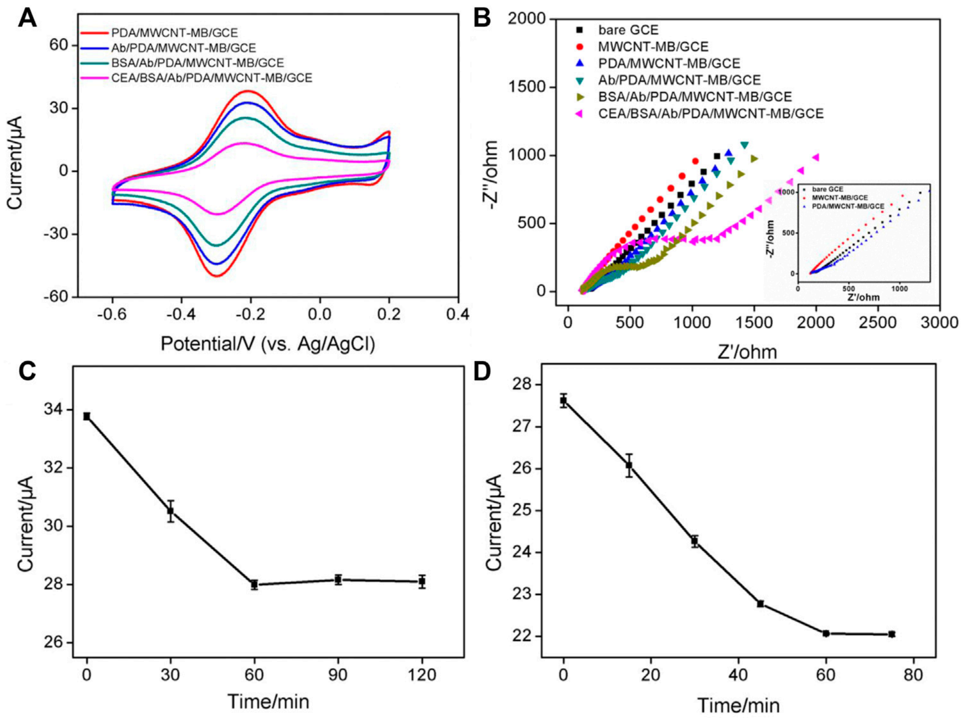

FIGURE 5
(A) CV obtained on different electrodes. **(B)** Nyquist plots obtained in KCl (0.1 M) containing $Fe(CN)_6{}^{3/4-}$ (2.5 mM). Inset is the magnified Nyquist plots, respectively. **(C)** The peak current obtained after CEA binding on different immunosensors fabricated using different reaction time between PDA and Ab. **(D)** The peak current obtained after CEA binding using different incubation time between CEA and Ab. The concentration of Ab for the fabrication of the immunosensor is 100 μg/ml. The used concentration of CEA is 1 ng/ml.

further leads to a decrease in the peak current of immobilized MB. When the constructed immunosensor is further incubated with CEA, the electrochemical signal of MB is remarkably reduced, suggesting the specific binding of antigen to antibody. The changes in the electrode surface during the construction of the immunosensor were also characterized by electrochemical impedance spectroscopy (EIS, Figure 5B). It is well known that the charge transfer resistance (R_{ct}) of an electrode is related to the diameter of the semicircle of the Nyquist plots in the high-frequency region. (Ashraf et al., 2020; Iftikhar et al., 2021). In comparison with that of bare GCE (R_{ct} of 128 Ω), the R_{ct} of MWCNT-MB/GCE decreased (42 Ω) resulting from the good electronic conductivity of MWCNT. The *in-situ* formation of the PDA layer increased the R_{ct} of the PDA/MWCNT/GCE electrode (144 Ω) because of the non-conductive property of PDA. During the subsequent covalent immobilization of Ab followed by BSA blocking, the R_{ct} of immunosensor (BSA/Ab/PDA/MWCNT/GCE) became larger (410 Ω) because the protein layer acted as an inert layer and hindered electron transfer. When the fabricated immunosensor was incubated with CEA, a significant increase in impedance values (634 Ω) was observed, indicating successful capture of antigen at the immuno-recognitive interface. Randles-Sevcik equation is used to calculate the electrochemically active surface area (EASA) of different electrodes as follows:

$$Ip = (2.69 \times 10^5) n^{3/2} ACD^{1/2} v^{1/2}, \qquad (1)$$

where n, A, C, D, and v are the number of electron transfer, electrode area, the molecular concentration of redox solution, diffusion coefficient, and scan rate respectively (He et al., 2015; Asif et al., 2019; Alam and Deen, 2020; Ashraf et al., 2022b) The calculated EASA of MWCNT-MB/GCE (0.346 cm^2) notably increased in comparison with that of bare GCE (0.0584 cm^2), owing to the generation of conductive MWCNT network. On the other hand, the EASA of electrodes obtained after the growth of PDA (0.307 cm^2 for PDA/MWCNT/GCE) or the fabrication of immuno-recognitive interface (0.202 cm^2 for BSA/Ab/PDA/MWCNT/GCE) gradually decreased because of the coverage of non-conductive substances.

To achieve the best detection sensitivity, the parameters for the construction of the immunosensor include the applied concentrations of MWCNT and dopamine, the reaction time between Ab and PDA, and the incubation time for the binding of antigen, and antibody, and the used concentration of Ab are optimized. When the concentration of MB was fixed, too low a concentration of MWCNT resulted in a low peak current of MB on the electrode due to less amount of bound MB (Supplementary Figure S3 in SI). The highest peak current was obtained when the concentration of MWCNT was 0.5 mg/ml. Then, even though the concentration of MWCNT continued to increase, the current value of MB decreased resulting in the decreased water dispersibility of MWCNT. Thus, the concentration of MWCNT was set as 0.5 mg/mL. As revealed in Supplementary Figure S4 (SI), the used concentration of dopamine had little effect on the electrochemical response of the electrode. High concentrations of dopamine only resulted in a weak decrease of the current signal, which was attributed to the larger deposition amount of non-conductive PDA. The chosen dopamine concentration was 0.38 mg/ml. Figure 5C shows the peak currents of MB obtained on immunosensor that are fabricated using different reaction time between Ab and PDA. As revealed, the current of MB decreased with the increase of reaction time and then reached a stable plateau when the reaction time was 60 min. This indicated that the immobilization of the antibody was saturated at 60 min. Therefore, the reaction time between Ab and PDA layer was chosen to be 60 min for further investigation. Figure 5D presents the electrochemical signals of MB obtained under different incubation times of antigen and antibody. When the incubation time was too short, the reaction equilibrium of antigen and antibody can not be reached, leading to insufficient reduction of MB signal. When the incubation time reached 1 h, further increasing the incubation time did not cause changes in the current signal of MB, suggesting a reaction balance between antigen and antibody. Thus, the incubation time between antigen and antibody was set as 1 h for the subsequent experiments. The binding amount of the Ab on the electrode surface reached saturation when the used concentration of Ab was 100 μg/ml (Supplementary Figure S5 in SI). In addition, the effect of pH of the electrochemical support solution was also studied. As shown in Supplementary Figure S6 (in SI), the current signal of MB after CEA binding decreased with increasing pH. This was due to the participation of protons in the electrochemical redox process of MB. As the pH value increased, the H^+ concentration in the solution decreased, which was not beneficial for the electrochemical oxidation of MB, resulting in a decreased peak current (He et al., 2015; Yang et al., 2018).

Reagentless electrochemical determination of carcinoembryonic antigen

Based on the decrease of the electrochemical signal of MB after CEA binding with Ab, the fabricated immunosensor was applied for reagentless detection of CEA. After incubating the immunosensors with different concentrations of CEA, differential pulse voltammetry is used to detect the signal of MB on the electrode. The DPV curves are shown in Figure 6A. When the concentration of CEA ranged from 10 pg/ml to 100 ng/ml, as shown in the inset in Figure 6A, the peak current of MB (I) had a good linear relationship with the logarithm of CEA concentration ($\lg C_{CEA}$) ($I = -1.77 \lg C_{CEA} + 22.33$, $R^2 = 0.997$). The limit of detection (LOD) based on three times signal-to-noise ratio (S/N = 3) was 0.6 pg/ml, where the signal was calculated as 3 times of noise and represented the decreased current resulting from the binding of CEA. The noise was the standard deviation (SD) of the blank current of the immunosensor before incubation of CEA. Supplementary Table S1 (SI) shows the comparison of the detection of CEA using different methods (Li et al., 2017; Barman et al., 2018; Han et al., 2018; Ma et al., 2019; Li et al., 2020; Tang et al., 2020; Wu et al., 2021). The LOD is lower than that obtained using nanopipette analysis based on CEA aptamer modified magnetic Fe_3O_4-Au nanoparticles (Apt-MNPs), (Tang et al., 2020), or fluorescence determination using CEA aptamer modified Cu^{2+}-loaded UiO-66 metal-organic framework (Cu-UiO-66/CEA-Apt) (Wu et al., 2021), or photoelectrochemical determination based on WO_3@BiOI modified indium-tin oxide electrode followed with loading CdS NWs (CdS@BiOI@WO_3/ITO) (Han et al., 2018), or electrochemical determination based on immobilization of Ab on poly(ethyleneglycol)-NH_2 connected pyrenebutyric acid functionalized graphene/gold nanoparticles (BSA/Ab/AuNPs/PPYGR/GCE) (Li et al., 2017), and Pd@Au@Pt nanocomposite/-COOH terminated reduced graphene oxide (Barman et al., 2018). The LOD is higher than the that obtained using sandwich-type electrochemical determination based on trimetallic yolk-shell Au@AgPt nanocubes loaded on amino-functionalized MoS_2 nanoflowers (MoS_2 NFs/Au@AgPt YNCs) and Au triangular nanoprisms (Au TNPs) (Ma et al., 2019), and immunointerface using NH_2-functionalized CEA aptamer on Fe-MOF modified with self-polymerized dopamine-decorated Au (NH_2-aptamer/Au@PDA@Fe-MOF/GCE) (Li et al., 2020).

Selectivity, reproducibility, and stability of the fabricated immunosensor

Selectivity is important to evaluate the performance of immunosensors. The selectivity of the fabricated immunosensor was examined by performing detection of CEA in the absence or presence of one or the mixture of other tumor markers including prostate-specific antigen (PSA), and carcinoma antigen 125 (CA125), and calcium-binding protein β (S-100). As shown in Figure 6B, both one or several other tumor markers almost had no effect on the detection of CEA, proving the specificity of the constructed immuno-recognitive interface and the selectivity of the immunosensor. To evaluate the reproducibility of the fabricated immunosensor, five electrodes were prepared in parallel. The relative standard deviation (RSD) for the detection of CEA was 0.5%, indicating high reproducibility (Figure 6C). When electrodes were stored at 4°C for 15 days, the response of the

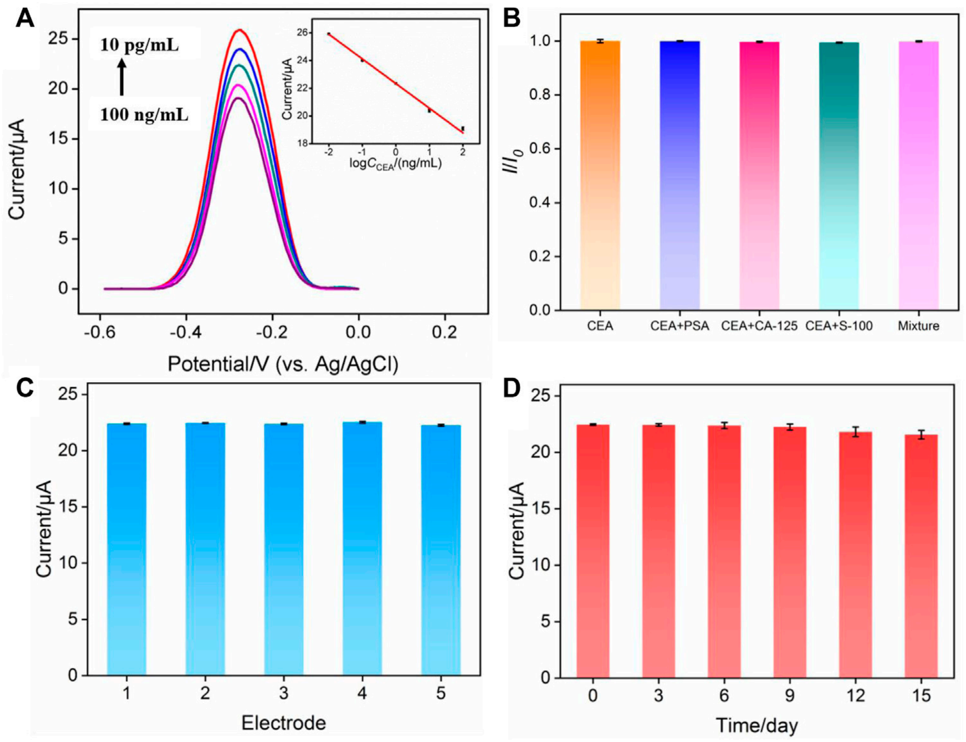

FIGURE 6
(A) Electrochemical response of the immunosensor in presence of different concentrations of CEA. Inset is the calibration curve for the determination of CEA. **(B)** Relative ratio of peak current before (I_0) and after (I) incubation with CEA, CEA + PSA, CEA + CA125, CEA + S-100 or the mixture containing CEA, PSA, CA125, S-100. The concentration of CEA and other proteins are 0.1 ng/ml and 10 ng/ml, respectively. **(C)** The peak current obtained using five different electrodes. **(D)** The peak current obtained using electrodes stored for different time.

immunosensor towards CEA remained at 98.3% of the initial signal, demonstrating the high stability of the sensor (Figure 6C).

Real sample analysis

The feasibility of immunosensors in the analysis of the real sample is the prerequisite for their clinical application. To investigate the detection reliability of the sensor, determination of CEA in human serum was performed. The CEA concentration values determined in a human serum sample (a healthy woman) by the proposed immunosensor and ROCHE ELISA electrochemiluminescence analyzer were 2.10 ± 0.08 ng/ml (mean ± SD, $n = 3$) and 2.18 ± 0.05 ng/ml (mean ± SD, $n = 3$), respectively. F-test and t-test were performed to assess whether there was statistical significance between the two means. The obtained F-value (2.56) was lower than the critical F-value (19.00), suggesting that the precision of the two data was not significantly different from each other. The obtained t-value (1.47) was lower than the t-critical two-tail value (2.13), indicating that there was no statistical significance between the two methods.

Conclusion

In summary, a simple and convenient electrochemical immunosensor was constructed to realize rapid, highly sensitive, and reagentless detection of the tumor marker, carcinoembryonic antigen. To realize direct detection of CEA without adding additional solution-based electrochemical probes, the redox probe methylene blue (MB), which had distinguished potential with the common electroactive interferences in biological samples, was immobilized on the surface of the electrode. To increase the active area and conductivity of the electrode, a multi-walled carbon nanotube composite was employed as an electronic wire to improve the performance of the development. Efficient immobilization of the antibody was achieved by an *in-situ* coating of polydopamine layer, which acts as the linkage to covalently immobilize the antibody. Based on the decrease of the electrochemical signal of confined MB after the binding of antigen, the fabricated immunosensor can achieve reagentless and sensitive detection of CEA. As the electrode interface simultaneously contains electron transfer wires, confined redox probes, and effectively immobilized recognition antibodies, the fabricated immunosensor exhibits simple preparation, sensitive detection, and good selectivity, demonstrating great potential in the sensitive detection of tumor markers.

Data availability statement

The original contributions presented in the study are included in the article/Supplementary Material; further inquiries can be directed to the corresponding author.

Author contributions

JZ: data curation and writing—original draft preparation, LY: data curation, JP: data curation, YT: supervision and writing—reviewing and editing, and JL: supervision and writing—reviewing and editing.

Acknowledgments

This study was funded by Shanxi Province 136 Revitalization Medical Project Construction Funds, Fundamental Research Program of Shanxi Province (201901D211510), the National Natural Science Foundation of China (21904117) and the Zhejiang Provincial Natural Science Foundation of China (LY20B050007).

Conflict of interest

The authors declare that the research was conducted in the absence of any commercial or financial relationships that could be construed as a potential conflict of interest.

Publisher's note

Supplementary material

The Supplementary Material for this article can be found online at: https://www.frontiersin.org/articles/10.3389/fchem.2022.939736/full#supplementary-material

References

Alam, A. U., and Deen, M. J. (2020). Bisphenol A electrochemical sensor using graphene oxide and β-cyclodextrin-functionalized multi-walled carbon nanotubes. *Anal. Chem.* 92, 5532–5539. doi:10.1021/acs.analchem.0c00402

Alfieri, M., Weil, T., Ng, D., and Ball, V. (2022). Polydopamine at biological interfaces. *Adv. Colloid Interface Sci.* 305, 102689. doi:10.1016/j.cis.2022.102689

Alimohammady, M., Jahangiri, M., Kiani, F., and Tahermansouri, H. (2019). Preparation and characterization of functionalized MWCNTs-COOH with 3-amino-5-phenylpyrazole as an adsorbent and optimization study using central composite design. *Carbon Lett.* 29, 1–20. doi:10.1007/s42823-019-00001-7

Ashraf, G., Asif, M., Aziz, A., Dao, A. Q., Zhang, T., Iftikhar, T., et al. (2020). Facet-energy inspired metal oxide extended hexapods decorated with graphene quantum dots: sensitive detection of bisphenol a in live cells. *Nanoscale* 12, 9014–9023. doi:10.1039/c9nr10944g

Ashraf, G., Asif, M., Aziz, A., Iftikhar, T., and Liu, H. (2021). Rice-Spikelet-like copper oxide decorated with platinum stranded in the CNT network for electrochemical *in vitro* detection of serotonin. *ACS Appl. Mat. Interfaces* 13, 6023–6033. doi:10.1021/acsami.0c20645

Ashraf, G., Asif, M., Aziz, A., Iftikhar, T., Zhong, Z.-T., Zhang, S., et al. (2022). Advancing interfacial properties of carbon cloth via anodic-induced self-assembly of MOFs film integrated with α-MnO_2: a sustainable electrocatalyst sensing acetylcholine. *J. Hazard. Mater.* 426, 128133. doi:10.1016/j.jhazmat.2021.128133

Ashraf, G., Asif, M., Aziz, A., Wang, Z., Qiu, X., Huang, Q., et al. (2019). Nanocomposites consisting of copper and copper oxide incorporated into MoS4 nanostructures for sensitive voltammetric determination of bisphenol A. *Microchim. Acta* 186, 337. doi:10.1007/s00604-019-3406-9

Ashraf, G., Aziz, A., Qaisrani, R. N., Chen, W., and Asif, M. (2021). Detecting and inactivating severe acute respiratory syndrome coronavirus-2 under the auspices of electrochemistry. *Curr. Res. Chem. Biol.* 1, 100001. doi:10.1016/j.crchbi.2021.100001

Ashraf, G., Zhong, Z.-T., Asif, M., Aziz, A., Song, L., Zhang, S., et al. (2022). Extension of duplex specific nuclease sensing application with RNA aptamer. *Talanta* 242, 123314. doi:10.1016/j.talanta.2022.123314

Asif, M., Aziz, A., Ashraf, G., Iftikhar, T., Sun, Y., Xiao, F., et al. (2022). Unveiling microbiologically influenced corrosion engineering to transfigure damages into benefits: A textile sensor for H_2O_2 detection in clinical cancer tissues. *Chem. Eng. J.* 427, 131298. doi:10.1016/j.cej.2021.131398

Asif, M., Aziz, A., Ashraf, G., Wang, Z., Wang, J., Azeem, M., et al. (2018). Facet-inspired core-shell gold nanoislands on metal oxide octadecahedral heterostructures: high sensing performance toward sulfide in biotic fluids. *ACS Appl. Mat. Interfaces* 10, 36675–36685. doi:10.1021/acsami.8b12186

Asif, M., Aziz, A., Wang, Z., Ashraf, G., Wang, J., Luo, H., et al. (2019). Hierarchical CNTs@CuMn layered double hydroxide nanohybrid with enhanced electrochemical performance in H2S detection from live cells. *Anal. Chem.* 91, 3912–3920. doi:10.1021/acs.analchem.8b04685

Aziz, A., Asif, M., Ashraf, G., Azeem, M., Majeed, I., Ajmal, M., et al. (2019). Advancements in electrochemical sensing of hydrogen peroxide, glucose and dopamine by using 2D nanoarchitectures of layered double hydroxides or metal dichalcogenides. a review. *Microchim. Acta* 186, 671. doi:10.1007/s00604-019-3776-z

Barman, S. C., Hossain, M. F., Yoon, H., and Park, J. Y. (2018). Trimetallic Pd@Au@Pt nanocomposites platform on -COOH terminated reduced graphene oxide for highly sensitive CEA and PSA biomarkers detection. *Biosens. Bioelectron.* 100, 16–22. doi:10.1016/j.bios.2017.08.045

Benvidi, A., Rajabzadeh, N., Mazloum-Ardakani, M., and Heidari, M. M. (2015). Comparison of impedimetric detection of DNA hybridization on chemically and electrochemically functionalized multi-wall carbon nanotubes modified electrode. *Sensors Actuators B Chem.* 207, 673–682. doi:10.1016/j.snb.2014.10.043

Benvidi, A., Tezerjani, M. D., Jahanbani, S., Mazloum Ardakani, M., and Moshtaghioun, S. M. (2016). Comparison of impedimetric detection of DNA hybridization on the various biosensors based on modified glassy carbon electrodes with PANHS and nanomaterials of RGO and MWCNTs. *Talanta* 147, 621–627. doi:10.1016/j.talanta.2015.10.043

Cui, Y., Duan, W., Jin, Y., Wo, F., Xi, F., and Wu, J. (2021). Graphene quantum dot-decorated luminescent porous silicon dressing for theranostics of diabetic wounds. *Acta Biomater.* 131, 544–554. doi:10.1016/j.actbio.2021.07.018

Cui, Y., Duan, W., Jin, Y., Wo, F., Xi, F., and Wu, J. (2020). Ratiometric fluorescent nanohybrid for noninvasive and visual monitoring of sweat glucose. *ACS Sens.* 5, 2096–2105. doi:10.1021/acssensors.0c00718

Deng, X., Zhao, J., Ding, Y., Tang, H., and Xi, F. (2021). Iron and nitrogen co-doped graphene quantum dots as highly active peroxidases for the sensitive detection of L-cysteine. *New J. Chem.* 45, 19064. doi:10.1039/d1nj03559b

Ding, Y. H., Floren, M., and Tan, W. (2016). Mussel-inspired polydopamine for bio-surface functionalization. *Biosurface Biotribology* 2, 121–136. doi:10.1016/j.bsbt.2016.11.001

Duan, W., Jin, Y., Cui, Y., Xi, F., Liu, X., Wo, F., et al. (2021). A co-delivery platform for synergistic promotion of angiogenesis based on biodegradable, therapeutic and self-reporting luminescent porous silicon microparticles. *Biomaterials* 272, 120772. doi:10.1016/j.biomaterials.2021.120772

Eguílaz, M., Dalmasso, P., Rubianes, M., Gutierrez, F., Rodríguez, M., Gallay, P., et al. (2019). Recent advances in the development of electrochemical hydrogen peroxide carbon nanotube–based (bio)sensors. *Curr. Opin. Electrochem* 14, 157–165. doi:10.1016/j.coelec.2019.02.007

Farzin, L., Shamsipur, M., Samandari, L., Sadjadi, S., and Sheibani, S. (2020). Biosensing strategies based on organic-scaffolded metal nanoclusters for ultrasensitive detection of tumor markers. *Talanta* 214, 120886. doi:10.1016/j.talanta.2020.120886

Han, Q., Wang, R., Xing, B., Zhang, T., Khan, M. S., Wu, D., et al. (2018). Label-free photoelectrochemical immunoassay for CEA detection based on CdS sensitized WO3@BiOI heterostructure nanocomposite. *Biosens. Bioelectron.* 99, 493–499. doi:10.1016/j.bios.2017.08.034

He, Y., Ding, L., and Su, B. (2015). Vertically ordered silica mesochannels as preconcentration materials for the electrochemical detection of methylene blue. *Sci. China Chem.* 58, 1593–1599. doi:10.1007/s11426-015-5365-2

Huang, Q., Chen, J., Liu, M., Huang, H., Zhang, X., and Wei, Y. (2020). Polydopamine-based functional materials and their applications in energy, environmental, and catalytic fields: state-of-the-art review. *Chem. Eng. J.* 387, 124019. doi:10.1016/j.cej.2020.124019

Iftikhar, T., Xu, Y., Aziz, A., Ashraf, G., Li, G., Asif, M., et al. (2021). Tuning electrocatalytic aptitude by incorporating α-MnO_2 nanorods in Cu-MOF/rGO/CuO hybrids: electrochemical sensing of resorcinol for practical applications. *ACS Appl. Mat. Interfaces* 13, 31462–31473. doi:10.1021/acsami.1c07067

Jozghorbani, M., Fathi, M., Kazemi, S. H., and Alinejadian, N. (2021). Determination of carcinoembryonic antigen as a tumor marker using a novel graphene-based label-free electrochemical immunosensor. *Anal. Biochem.* 613, 114017. doi:10.1016/j.ab.2020.114017

Laraib, U., Sargazi, S., Rahdar, A., Khatami, M., and Pandey, S. (2022). Nanotechnology-based approaches for effective detection of tumor markers: a comprehensive state-of-the-art review. *Int. J. Biol. Macromol.* 195, 356–383. doi:10.1016/j.ijbiomac.2021.12.052

Li, H., Yin, D., Li, W., Tang, Q., Zou, L., and Peng, Q. (2021). Polydopamine-based nanomaterials and their potentials in advanced drug delivery and therapy. *Colloids Surfaces B Biointerfaces* 199, 111502. doi:10.1016/j.colsurfb.2020.111502

Li, J., Liu, L., Ai, Y., Liu, Y., Sun, H., and Liang, Q. (2020). Self-polymerized dopamine-decorated Au NPs and coordinated with Fe-mof as a dual binding sites and dual signal-amplifying electrochemical aptasensor for the detection of CEA. *ACS Appl. Mat. Interfaces* 12, 5500–5510. doi:10.1021/acsami.9b19161

Li, Y., Chen, Y., Deng, D., Luo, L., He, H., and Wang, Z. (2017). Water-dispersible graphene/amphiphilic pyrene derivative nanocomposite: high AuNPs loading capacity for CEA electrochemical immunosensing. *Sensors Actuators B Chem.* 248, 966–972. doi:10.1016/j.snb.2017.02.138

Liu, J., Wang, J., Wang, T., Li, D., Xi, F., Wang, J., et al. (2015). Three-dimensional electrochemical immunosensor for sensitive detection of carcinoembryonic antigen based on monolithic and macroporous graphene foam. *Biosens. Bioelectron.* 65, 281–286. doi:10.1016/j.bios.2014.10.016

Liu, Q., Zhong, H., Chen, M., Zhao, C., Liu, Y., Xi, F., et al. (2020). Functional nanostructure-loaded three-dimensional graphene foam as a non-enzymatic electrochemical sensor for reagentless glucose detection. *RSC Adv.* 10, 33739–33746. doi:10.1039/d0ra05553k

Liu, X., Chen, Z., Wang, T., Jiang, X., Qu, X., Duan, W., et al. (2022). Tissue imprinting on 2D nanoflakes-capped silicon nanowires for lipidomic mass spectrometry imaging and cancer diagnosis. *ACS Nano* 16, 6919–6928. doi:10.1021/acsnano.2c02616

Ma, E., Wang, P., Yang, Q., Yu, H., Pei, F., Li, Y., et al. (2019). Electrochemical immunosensor based on MoS2 NFs/Au@AgPt YNCs as signal amplification label for sensitive detection of CEA. *Biosens. Bioelectron.* 142, 111580. doi:10.1016/j.bios.2019.111580

Mazloum-Ardakani, M., Naser-Sadrabadi, A., Sheikh-Mohseni, M. A., Naeimi, H., Benvidi, A., and Khoshroo, A. (2013). Oxidized multiwalled carbon nanotubes for improving the electrocatalytic activity of a Schiff base modified electrode in determination of isoprenaline. *J. Electroanal. Chem.* 705, 75–80. doi:10.1016/j.jelechem.2013.07.028

Ömür, T., and Alanyalıoğlu, M. (2017). Amperometric nitrite sensor based on free-standing carbon nanotube/methylene blue composite paper. *Ionics* 23, 3507. doi:10.1007/s11581-017-2142-6

Pirsaheb, M., Mohammadi, S., and Salimi, A. (2019). Current advances of carbon dots based biosensors for tumor marker detection, cancer cells analysis and bioimaging. *TrAC Trends Anal. Chem.* 115, 83–99. doi:10.1016/j.trac.2019.04.003

Prabhu, A., Crapnell, R. D., Eersels, K., van Grinsven, B., Kunhiraman, A. K., Singla, P., et al. (2022). Reviewing the use of chitosan and polydopamine for electrochemical sensing. *Curr. Opin. Electrochem.* 32, 100885. doi:10.1016/j.coelec.2021.100885

Prado, N. S., Silva, L. A. J., Takeuchi, R. M., Richter, E. M., Santos, A. L. d., and Falcão, E. H. L. (2022). Graphite sheets modified with poly(methylene blue) films: a cost-effective approach for the electrochemical sensing of the antibiotic nitrofurantoin. *Microchem. J.* 177, 107289. doi:10.1016/j.microc.2022.107289

Rivas, G. A., Rodríguez, M. C., Rubianes, M. D., Gutierrez, F. A., Eguílaz, M., Dalmasso, P. R., et al. (2017). Carbon nanotubes-based electrochemical (bio)sensors for biomarkers. *Appl. Mater. Today* 9, 566–588. doi:10.1016/j.apmt.2017.10.005

Sadighbayan, D., Sadighbayan, K., Tohid-kia, M. R., Khosroushahi, A. Y., and Hasanzadeh, M. (2019). Development of electrochemical biosensors for tumor marker determination towards cancer diagnosis: recent progress. *TrAC Trends Anal. Chem.* 118, 73–88. doi:10.1016/j.trac.2019.05.014

Samyn, P. (2021). A platform for functionalization of cellulose, chitin/chitosan, alginate with polydopamine: A review on fundamentals and technical applications. *Int. J. Biol. Macromol.* 178, 71–93. doi:10.1016/j.ijbiomac.2021.02.091

Suo, Z., Niu, X., Liu, R., Xin, L., Liu, Y., and Wei, M. (2022). A methylene blue and Ag+ ratiometric electrochemical aptasensor based on Au@Pt/Fe-N-C signal amplification strategy for zearalenone detection. *Sensors Actuators B Chem.* 362, 131825. doi:10.1016/j.snb.2022.131825

Tang, H., Wang, H., Yang, C., Zhao, D., Qian, Y., and Li, Y. (2020). Nanopore-based strategy for selective detection of single carcinoembryonic antigen (CEA) molecules. *Anal. Chem.* 92, 3042–3049. doi:10.1021/acs.analchem.9b04185

Wan, Y., Zhao, J., Deng, X., Chen, J., Xi, F., and Wang, X. (2021). Colorimetric and fluorescent dual-modality sensing platform based on fluorescent nanozyme. *Front. Chem.* 9, 774486. doi:10.3389/fchem.2021.774486

Wei, X., Luo, X., Xu, S., Xi, F., and Zhao, T. (2022). A flexible electrochemiluminescence sensor equipped with vertically ordered mesoporous silica nanochannel film for sensitive detection of clindamycin. *Front. Chem.* 10, 872582. doi:10.3389/fchem.2022.872582

Wu, Y., Chen, X., Luo, X., Yang, M., Hou, C., and Huo, D. (2021). Bimetallic organic framework Cu/UiO-66 mediated "fluorescence turn-on" method for ultrasensitive and rapid detection of carcinoembryonic antigen (CEA). *Anal. Chim. Acta* 1183, 339000. doi:10.1016/j.aca.2021.339000

Xie, F., Yang, M., Jiang, M., Huang, X.-J., Liu, W.-Q., and Xie, P.-H. (2019). Carbon-based nanomaterials - a promising electrochemical sensor toward persistent toxic substance. *TrAC Trends Anal. Chem.* 119, 115624. doi:10.1016/j.trac.2019.115624

Yan, F., Chen, J., Jin, Q., Zhou, H., Sailjoi, A., Liu, J., et al. (2020). Fast one-step fabrication of a vertically-ordered mesoporous silica-nanochannel film on graphene for direct and sensitive detection of doxorubicin in human whole blood. *J. Mat. Chem. C* 8, 7113–7119. doi:10.1039/d0tc00744g

Yang, S., Liu, D., Meng, Q. B., Wu, S., and Song, X.-M. (2018). Reduced graphene oxide-supported methylene blue nanocomposite as a glucose oxidase-mimetic for electrochemical glucose sensing. *RSC Adv.* 8, 32565–32573. doi:10.1039/c8ra06208k

Yazdanparast, S., Benvidi, A., Abbasi, S., and Rezaeinasab, M. (2019). Enzyme-based ultrasensitive electrochemical biosensor using poly(l-aspartic acid)/MWCNT bio-nanocomposite for xanthine detection: a meat freshness marker. *Microchem. J.* 149, 104000. doi:10.1016/j.microc.2019.104000

Zhang, C., You, X., Li, Y., Zuo, Y., Wang, W., Li, D., et al. (2022). A novel electrochemical aptasensor for serum dopamine detection based on methylene blue-integrated m-PdNFs signal material. *Sensors Actuators B Chem.* 354, 131233. doi:10.1016/j.snb.2021.131233

Zhang, M., Zou, Y., Zhou, X., Yan, F., and Ding, Z. (2022). Vertically-ordered mesoporous silica films for electrochemical detection of Hg(II) ion in pharmaceuticals and soil samples. *Front. Chem.* doi:10.3389/fchem.2022.952936

Zhang, Y., Xu, J., Zhou, S., Zhu, L., Lv, X., Zhang, J., et al. (2020). DNAzyme-triggered visual and ratiometric electrochemiluminescence dual-readout assay for Pb(II) based on an assembled paper device. *Anal. Chem.* 92, 3874–3881. doi:10.1021/acs.analchem.9b05343

Zhao, J., Zheng, Y., Pang, Y., Chen, J., Zhang, Z., Xi, F., et al. (2020). Graphene quantum dots as full-color and stimulus responsive fluorescence ink for information encryption. *J. Colloid Interface Sci.* 579, 307–314. doi:10.1016/j.jcis.2020.06.077

Zheng, Y., Li, J., Zhou, B., Ian, H., and Shao, H. (2021). Advanced sensitivity amplification strategies for voltammetric immunosensors of tumor marker: state of the art. *Biosens. Bioelectron.* 178, 113021. doi:10.1016/j.bios.2021.113021

Zhong, Z.-T., Ashraf, G., Chen, W., Song, L.-B., Zhang, S.-J., Liu, B., et al. (2022). A new strategy based on duplex-specific nuclease and DNA aptamer with modified hairpin structure for various analytes detection. *Microchem. J.* 179, 107510. doi:10.1016/j.microc.2022.107510

Zhou, H., Ding, Y., Su, R., Lu, D., Tang, H., and Xi, F. (2022). Silica nanochannel array film supported by ß-cyclodextrin-functionalized graphene modified gold film electrode for sensitive and direct electroanalysis of acetaminophen. *Front. Chem.* 9, 812086. doi:10.3389/fchem.2021.812086

Zhu, L., Lv, X., Yu, H., Tan, X., Rong, Y., Feng, W., et al. (2022). Paper-based bipolar electrode electrochemiluminescence platform combined with pencil-drawing trace for the detection of M.SssI methyltransferase. *Anal. Chem.* 94, 8327–8334. doi:10.1021/acs.analchem.2c00803

Zhu, X., Xuan, L., Gong, J., Liu, J., Wang, X., Xi, F., et al. (2022). Three-dimensional macroscopic graphene supported vertically-ordered mesoporous silica-nanochannel film for direct and ultrasensitive detection of uric acid in serum. *Talanta* 238, 123027. doi:10.1016/j.talanta.2021.123027

frontiers | Frontiers in Chemistry

TYPE Original Research
PUBLISHED 26 August 2022
DOI 10.3389/fchem.2022.940795

Simple immunosensor for ultrasensitive electrochemical determination of biomarker of the bone metabolism in human serum

Qiang Chang[1,2], Jie Huang[3], Liming He[1,2] and Fengna Xi[3]*

[1]Shanxi Bethune Hospital, Shanxi Academy of Medical Sciences, Tongji Shanxi Hospital, Third Hospital of Shanxi Medical University, Taiyuan, China, [2]Tongji Hospital, Tongji Medical College, Huazhong University of Science and Technology, Wuhan, China, [3]Department of Chemistry, Key Laboratory of Surface & Interface Science of Polymer Materials of Zhejiang Province, Zhejiang Sci-Tech University, Hangzhou, China

Ultrasensitive and selective determination of biomarkers of the bone metabolism in serum is crucial for early screening, timely treatment, and monitoring of the curative effect of osteoporosis, which is a silent disease with serious health threats. Immunoassay with a simple sensing interface and ultrahigh sensitivity is highly desirable. Herein, a simple electrochemical immunosensor is demonstrated based on gold nanoparticles (AuNPs) electrodeposited on chitosan-reduced graphene oxide (CS-G) composite modified electrode, which can achieve sensitive determination of the important biomarker of bone metabolism, bone gamma-carboxyglutamate protein (BGP). To overcome the agglomeration of graphene and introduce a biocompatible matrix with functional amino groups, CS-G is prepared and modified on the supporting glassy carbon electrode (GCE). Then, AuNPs are electrodeposited on CS-G through their interaction between amine groups of CS. The immobilized AuNPs provide numerous binding sites to immobilize anti-BGP antibodies (Ab_{BGP}). The specific recognition between BGP and Ab_{BGP} results in a reduction in the mass transfer of the electrochemical probe ($Fe(CN)_6^{3-/4-}$) in solution, leading to a reduced electrochemical signal. Based on this mechanism, fast and ultrasensitive electrochemical detection of BGP is achieved when the concentration of BGP ranges from 100 ag ml^{-1} to 10 μg mL^{-1} with a limit of detection (LOD) of 20 ag ml^{-1} (S/N = 3). The determination of BGP in human serum is also realized with high reliability.

KEYWORDS

immunosensor, electroanalysis, ultrasensitive detection, biomarker of bone metabolism, osteocalcin

Check for updates

OPEN ACCESS

EDITED BY
Yan Zhang,
University of Jinan, China

REVIEWED BY
Zhiwei Lu,
Sichuan Agricultural University, China
Zhanjun Yang,
Yangzhou University, China

*CORRESPONDENCE
Fengna Xi,
fengnaxi@zstu.edu.cn

SPECIALTY SECTION
This article was submitted to Analytical Chemistry,
a section of the journal
Frontiers in Chemistry

RECEIVED 10 May 2022
ACCEPTED 01 August 2022
PUBLISHED 26 August 2022

CITATION
Chang Q, Huang J, He L and Xi F (2022), Simple immunosensor for ultrasensitive electrochemical determination of biomarker of the bone metabolism in human serum.
Front. Chem. 10:940795.
doi: 10.3389/fchem.2022.940795

Introduction

Osteoporosis is a silent disease that has become a serious health problem after cardiovascular disease. Osteoporosis is a systemic bone disease characterized by decreased bone mass and damage to the microstructure of bone tissue, leading to increased bone fragility and susceptibility to fractures (Walker-Bone et al., 2002; Rachner et al., 2011; Cheatham et al., 2017). In addition, the incidence of osteoporosis increases significantly with age. It is well known that fractures are the most common manifestation of osteoporosis. For instance, an osteoporotic fracture occurs every 3 s in the world. About 50% of women and 20% of men will experience the first osteoporotic fracture after the age of 50 years, and 50% of these patients might have a second osteoporotic fracture. Fractures may affect daily activities in mild cases, and patients will lose their ability to move independently or lead to cardiovascular and cerebrovascular accidents in severe cases (Price and Thompson, 1995; Afsarimanesh et al., 2018a; Lima et al., 2019). Bone mineral density (BMD) is mainly used to diagnose and monitor the curative effect of osteoporosis. Until now, methods to measure BMD include dual-energy X-ray absorptiometry (DXA), quantitative computed tomography (QCT), peripheral DXA, and quantitative ultrasound (QUS). However, these methods cannot accurately and quantitatively assess bone quality and are susceptible to problems such as osteophytes and calcification. In addition, the optimal treatment stage is often missed when bone density is abnormal. Unlike the slowly changing parameters of BMD, abnormal situations in markers of the bone metabolism might be detectable only within a few weeks (Farley et al., 1981; Christenson, 1997; Ivaska et al., 2005; Afsarimanesh et al., 2016; Afsarimanesh et al., 2018b). Combining imaging data and level of bone metabolism markers can realize early screening, timely treatment, and monitoring of curative effects of osteoporosis. Therefore, rapid and sensitive detection of bone metabolism markers is of great significance.

Osteocalcin, also known as bone gamma-carboxyglutamate protein (BGP), is an important biomarker of the bone metabolism. BGP has a molecular weight of ~5.8 kDa and consists of 49 amino acids. Its total amount accounts for 15–20% of the non-collagen protein in bone tissue. BGP is synthesized and secreted by osteoblasts and ~50% of its content enters the blood circulation. The main physiological function of BGP is to maintain the normal mineralization rate of bone, inhibit the formation of abnormal hydroxyapatite crystals, and inhibit the mineralization rate of cartilage (Calvo et al., 1996; Ivaska et al., 2005). Thus, serum BGP level can reflect the activity state of osteoblasts. Generally, the faster the bone turnover rate, the higher the BGP value. For instance, primary osteoporosis is the high conversion type, so BGP is significantly elevated. On the contrary, senile osteoporosis is a low-conversion type, resulting in no obvious increase in BGP (Ingram et al., 1994; Gundberg et al., 2002). Therefore, changes in BGP can be used to identify the types of osteoporosis and provide important references for studying the pathogenesis of bone diseases. The development of a convenient analysis of BGP with convenient fabrication, high sensitivity, good reliability, and low cost is highly desirable.

Electrochemical techniques have shown great potential in biological and environmental analyses (Yan et al., 2021a; Zheng et al., 2021; Gong et al., 2022a; Ma et al., 2022a; Wang et al., 2022). The electrochemical sensing platforms have been proven to offer the advantages of simple instrumentation, convenient to use, free of tedious pretreatment, easy integration, and miniaturization compared to chromatography methods which need trained operators and costly equipment (Lu et al., 2021a; Lu et al., 2021b; Zhang Y. et al., 2022). Furthermore, matrix effects caused by colorful contaminants can be effectively avoided compared with colorimetric and spectrographic strategies (Lu et al., 2021c). The construction of modified electrodes with good biocompatibility, high electron transfer rate, and easy immobilization of recognitive ligands is crucial to improving the performance of electrochemical sensors (Lin et al., 2020; Ma et al., 2020; Yan et al., 2020; Yan et al., 2021b; Wang et al., 2021). Recently, the introduction of functional nanomaterials to improve detection sensitivity and stability has become an important strategy to fabricate electrochemical sensors (Ma et al., 2022b; Zhang M. et al., 2022). Reduced graphene oxide (G) is a carbon nanomaterial with sp^2-hybridized carbon atoms tightly packed into a single-layer two-dimensional (2D) honeycomb lattice structure. Owing to excellent optical, electrical, and mechanical properties and high charge transport properties, graphene has shown great potential in the fields of sensors, energy storage, and drug delivery (Gong et al., 2022b; Zou et al., 2022). However, G is prone to agglomerate because of the strong π–π interaction between graphene sheets. Biofunctionalization of graphene is effective to improve its hydrophilicity and biocompatibility (Kang et al., 2009; Jirakunakorn et al., 2020). Chitosan (CS), the product from natural polysaccharide chitin obtained through the removal of part of the acetyl group, has the characteristics of easy degradation and good biocompatibility. Numerous amino groups in CS can be used to immobilize functional substances such as proteins or nanoparticles (Qiu et al., 2009; Zhang J. et al., 2022). However, direct modification of electrodes using CS suffers from high interfacial resistance as CS is a non-conductive material. When G and chitosan are combined, the intercalation of CS between graphene layers can prevent the agglomeration of G sheets. On the other hand, reduced graphene oxide with a large conjugated structure can improve the conductivity of chitosan materials. In addition, chitosan-reduced graphene oxide nanocomposites (CS-G) can also provide a biocompatible microenvironment for biomolecules, which effectively promotes the maintenance of their activity (Kang et al., 2009). Gold nanoparticles (AuNPs) have also been widely used in bioanalysis due to their excellent electron transport ability, easy preparation, good biocompatibility, and

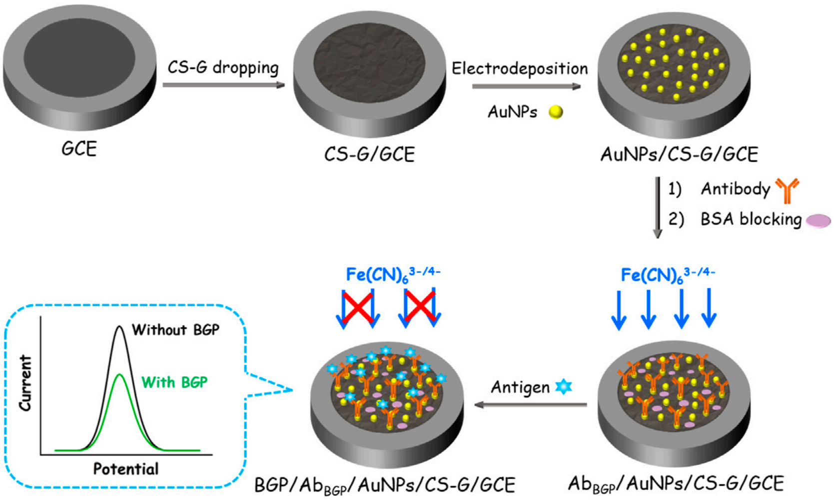

FIGURE 1
Schematic illustration for the simple fabrication of immunoanalysis interface and the following electrochemical detection of BGP.

controllable surface characteristics (Chen et al., 2018; Sarfraz and Khan, 2021; Tai et al., 2022). Combining CS-G with AuNPs is expected to easily construct high-performance electrochemical biosensors for highly sensitive detection of BGP.

In this work, we present a simple electrochemical immunoassay platform for sensitive detection of the important biomarker of the bone metabolism, bone gamma-carboxyglutamate protein (BGP), in human serum. As illustrated in Figure 1, chitosan–graphene nanocomposite (CS-G) is easily prepared and modified on the supporting glassy carbon electrode (GCE). Then, AuNPs are electrodeposited on CS-G through their interaction between amine groups of CS. The immunosensor (Ab_{BGP}/AuNPs/CS-G/GCE) is finally obtained after anti-BGP antibodies (Ab_{BGP}) are immobilized on AuNPs followed by the blocking of the non-specific sites with bovine serum albumin (BSA). The specific binding of BGP on the immunorecognitive interface results in a reduction in the mass transfer of the electrochemical probe ($Fe(CN)_6^{3-/4-}$) in solution, which leads to a reduced electrochemical signal. Based on this mechanism, fast and sensitive electrochemical detection of BGP is achieved. Combined with the advantages of simple fabrication, high sensitivity, good selectivity, and reproductivity, the immunosensor has great potential for sensitive and convenient detection of BGP in biological samples.

Materials and methods

Chemicals and materials

BGP antigen and anti-BGP antibody were purchased from Nanjing Okay Biotechnology Co., Ltd. (China). Prostate-specific antigen (PSA), carcinoembryonic antigen (CEA), carcinoma antigen 125 (CA125), and carcinoma antigen 199 (CA199) were purchased from Beijing KEY-BIO Biotech Co., Ltd. (China). S100 calcium-binding protein β was purchased from Proteintech (China). Potassium ferricyanide ($K_3[Fe(CN)_6]$, 99.5%), potassium ferricyanide ($K_4[Fe(CN)_6]$, 99.5%), bovine serum albumin (BSA), potassium chloride (KCl, analytical reagent-AR), chloroauric acid ($HAuCl_4{\cdot}3H_2O$, 99.9%), sodium borohydride ($NaBH_4$, 98%), sodium citrate (98%), and chitosan were purchased from Aladdin Biochemical Technology Co., Ltd. (China). Ethanol (99.8%) was purchased from Hangzhou Gaojing Fine Chemical Co., Ltd. (China). A glassy carbon electrode (GCE, 3 mm in diameter) was purchased from CHI instrument Co., Ltd. (China). Phosphate buffer solution (PBS) is prepared by Na_2HPO_4 and NaH_2PO_4. Ultrapure water (18.2 MΩ cm) used in the experiments is prepared by the Mill-Q system (Millipore Company).

Measurements and instrumentations

The morphologies of G synthesized without the protection of CS, CS-G, and AuNPs/CS-G were investigated by scanning electron microscope (SEM, SU8010, Hitachi, Japan) with an acceleration voltage of 10 kV. The morphologies of GO and CS-G were investigated by transmission electron microscope (TEM, JEM-2100, JEOL, Japan) with an acceleration voltage of 200 kV. Energy dispersive X-ray spectroscopy (EDS) was performed on SU8010 SEM. The UV-Vis spectrum was measured using an ultraviolet spectrophotometer (UV-2450, Shimadzu, Japan). Fourier transform infrared spectroscopy (FT-IR) was measured using a Vertex 70 spectrometer

(Bruker, United States) through the KBr tablet method. X-ray photoelectron spectroscopy (XPS) analysis was carried out on a PHI5300 electron spectrometer using 250 W, 14 kV, Mg Kα radiation (PE Ltd., United States). Raman spectra were measured using a 960FT-Raman spectrometer (Thermo Nicolet, United States). The XRD pattern was measured using a D8 Advance X-ray diffractometer (Bruker, Germany). Electrochemical impedance spectroscopy (EIS), cyclic voltammetry (CV), and differential pulse voltammetry (DPV) measurements were performed on an Autolab (PGSTAT302N) electrochemical workstation (Metrohm, Switzerland). All electrochemical measurements were performed at room temperature using a conventional three-electrode system. In brief, Ag/AgCl was used as the reference electrode. A platinum wire electrode was used as the counter electrode, and bare or modified GCE was used as the working electrode. The scanning rate for CV scanning was 50 mV/s. The parameters for DPV measurements included step potential (0.005 V), pulse amplitude (0.05 V), pulse time (0.05 s), and interval time (0.2 s).

Synthesis of CS-G

Graphene oxide (GO) was prepared from natural graphite by a modified Hummers method (Santhiago et al., 2015). To prepare chitosan-modified composites (CS-G), GO dispersion (4 ml, 1 mg ml^{-1}) was mixed with an aqueous solution of CS (36 ml, 0.25%, wt%, pH = 3) (Liu et al., 2012). A homogeneous dispersion was obtained by sonicating for 30 min. Then, hydrazine hydrate (50 wt%, 20 ml) was added to the above dispersion under rapid stirring and reacted in a water bath at 80°C for 3 h. The solid was collected by centrifugation at 15,000 rpm followed by washing three times with 0.1 mM HCl solution to remove the remaining CS. The CS-G was subsequently obtained and re-dispersed.

Synthesis of AuNPs

Gold nanoparticles (AuNPs) were prepared by the electrodeposition method (Wu et al., 2015). A typical three-electrode system was adopted including a modified GCE as the working electrode, an Ag/AgCl electrode (saturated KCl) as the reference electrode, and a platinum sheet electrode as the counter electrode. In brief, the modified GCE was immersed in 0.5% $HAuCl_4$, and a constant potential of −0.5 V for 2 s was applied. The electrode was then rinsed with ultrapure water.

Fabrication of the immunosensor

GCE is used as the supporting electrode for the construction of the immunosensors. Before use, GCE was sequentially polished with 0.3 and 0.05 μm alumina slurry, and then ultrasonically cleaned in ethanol and ultrapure water for 60 s, respectively. The polished GCE has a glossy mirror under natural light. Then, 10 μL CS-G (0.25 mg ml^{-1}) was drop-coated on the polished GCE. The obtained electrode was dried at 60 °C and denoted as CS-G/GCE. To electrodeposit AuNPs, CS-G/GCE was further immersed in 0.5% $HAuCl_4$ and a constant potential of −0.5 V (vs. Ag/AgCl) for 2 s was applied. The electrode was then rinsed with ultrapure water to obtain AuNPs/CS-G/GCE. To fabricate the immunorecognitive interface, the BGP antibody (40 μL, 100 μg ml^{-1}) was drop-coated on the surface of AuNPs/CS-G/GCE. After incubation at 37°C for 60 min, the electrode surface was rinsed with PBS (0.1 M, pH = 7.4) to remove unbound antibodies. The obtained electrode was then incubated with BSA solution (1%, wt%) for 60 min to block the non-specific sites followed by rinsing with PBS (0.1 M, pH = 7.4). The as-prepared immunosensor was denoted as Ab_{BGP}/AuNPs/CS-G/GCE.

Electrochemical determination of BGP

The Ab_{BGP}/AuNPs/CS-G/GCE immunosensor was incubated with different concentrations of BGP (antigen) at 37°C for 40 min. KCl (0.1 M) containing $Fe(CN)_6^{3-/4-}$ (2.5 mM) was applied as the electrolyte. The electrochemical signal of the $Fe(CN)_6^{3-/4-}$ in the electrolyte before and after BGP binding was measured. For the real sample analysis, BGP in human serum (healthy male, provided by Shanxi Bethune Hospital, China) was determined using the standard addition method. To simulate the different BGP concentrations of osteoporosis patients, artificial BGP was added to the serum. Then, serum with added BGP was diluted by a factor of 50 with electrolyte and determined using the developed immunosensor.

Results and discussion

Easy fabrication of the immunosensor

Figure 1 illustrates the fabrication of the immunosensing interface. As illustrated, chitosan–graphene nanocomposite (CS-G) is prepared and modified on a glassy carbon electrode (GCE). The nanocomposite could overcome the agglomeration of reduced graphene oxide and introduce a biocompatible matrix with functional amino groups. Then, AuNPs are electrodeposited on CS-G, and the interaction between amine groups of CS and AuNPs/CS-G/GCE is obtained. Electrochemical synthesis of AuNPs has received much interest due to its controllable and green procedure. It is a simple, rapid, and convenient technique that can produce AuNPs with controlled characteristics (e.g., particle size, crystallographic orientation, mass, thickness, and morphology) by simply adjusting the electrodeposition parameters (Mohanty, 2010). The time-saving and

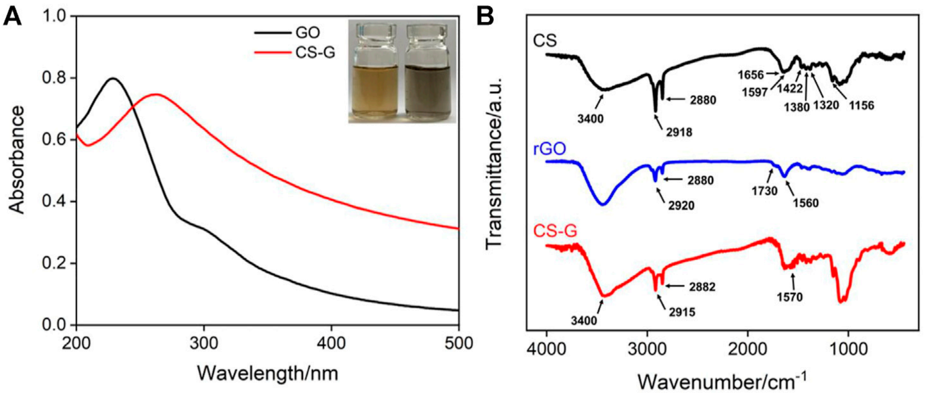

FIGURE 2
(A) UV-Vis absorption spectrum of GO and CS-G. Insets are photographs of GO (left) and CS-G (right) solutions. **(B)** FT-IR spectra of CS, rGO, and CS-G. The rGO was synthesized by reduction of GO using the same procesure but without CS.

environment-friendly electrodeposition process overcomes the drawbacks of chemical synthesis including the use of extra reagents, contamination from precursor molecules, and unwished by-products (Shein et al., 2009; Shedbalkar et al., 2014). Furthermore, more firm AuNP adherence to substrates can be realized by the electrodeposition method and facilitates the construction of the ultimate electrochemical device (Tai et al., 2022). The electrodeposited AuNPs provide numerous binding sites to immobilize anti-BGP antibodies (Ab_{BGP}). After blocking the non-specific sites with bovine serum albumin (BSA), the immunosensor, denoted as Ab_{BGP}/AuNPs/CS-G/GCE, is finally obtained. For the determination of BGP, the commonly used electrochemical probe, $Fe(CN)_6^{3-/4-}$, is applied as the solution-based redox indicator. When BGP specifically interacts with Ab_{BGP} on the surface of the electrode, the formed antigen–antibody complex hinders the mass transfer of $Fe(CN)_6^{3-/4-}$ in solution, leading to a significantly reduced electrochemical signal. Based on this mechanism, fast and sensitive electrochemical detection of BGP is achieved.

Characterization of CS-G composite and AuNPs/CS-G-modified electrode

The structure and morphology of CS-G are characterized by ultraviolet-visible spectroscopy (UV-Vis), Fourier transform infrared spectroscopy (FT-IR), and scanning electron microscopy (SEM). As shown in the inset of Figure 2A, the GO dispersion is a brown solution, while the CS-G dispersion is a black solution. The doping amount of chitosan on the CS-G nanocomposite is investigated by changing the mass ratio between the original GO and CS. Three ratios between CS and GO (5.62, 11.2, and 22.5) are employed to synthesize the CS-G nanocomposite. However, the synthesized dispersion can produce a large amount of precipitation after standing for 2 h at the low GO/CS ratio (5.62 and 11.2), which is attributed to the agglomeration of G when the protective agent CS is less. On the contrary, the high ratio between the used CS and GO (22.5) leads to stable dispersion of CS-G nanocomposite without precipitation. Thus, this doping amount of chitosan is chosen for further investigation. Figure 2A shows the UV-Vis absorption spectra of GO and CS-G. It can be seen that GO has two characteristic absorption peaks at 230 and 300 nm, corresponding to the π–π^* transition of conjugated C-C=C and the n-π^* transition of C=O, respectively (Ang et al., 2009; Guo et al., 2010). After being composited with CS, the absorption peak at 230 nm is red-shifted to 268 nm, indicating that GO is reduced and the electronic conjugation within the graphene sheets is restored upon hydrazine hydrate reduction (Li et al., 2008). In addition, the absorption peak at 300 nm disappears, further indicating the reduction of GO by hydrazine and the restoration of the conjugated carbon structure (Liu et al., 2012). These results prove the successful preparation of reduced graphene oxide. The changes in chemical composition during the preparation of CS-G are further characterized by FT-IR. As shown in Figure 2B, the characteristic peaks of hydroxyl and amino (3,400 cm^{-1}), amide carbonyl (1,656 cm^{-1}), N-H (1,597 cm^{-1}), C-N (1,320 cm^{-1}), and glycosidic bonds (1,156 cm^{-1}) appear in the FT-IR spectrum of CS. In addition, the spectrum also reveals the characteristic absorption of saturated C-H (2,918 cm^{-1}, 2,880 cm^{-1}, 1,422 cm^{-1}, 1,380 cm^{-1}) (Mauricio-Sánchez et al., 2018). In the case of reduced graphene oxide (rGO), that was synthesized in absence of CS, the absorption peak (1,560 cm^{-1}) attributed to the conjugated C-C=C framework significantly increases, indicating that GO was successfully reduced (Zhou et al., 2022). However, rGO still has a weak O=C-OH absorption peak (1730 cm^{-1}) because the carboxyl group is difficult to be reduced. CS-G shows the absorption peak basically consistent with CS, indicating that CS does not change during the composite process (Li et al., 2008; Mianehrow et al., 2016). At the same time, the absorption peak of C-C=C proves the successful composite between CS and graphene.

X-ray photoelectron spectroscopy (XPS) is employed to analyze the structure and composition of GO and CS-G. As revealed by Supplementary Figures S1A,B (in supporting information-SI), the high-resolution C1s spectrums of GO and CS-G show four types of carbon atoms including C-C/C=C (284.6 eV, sp^2 C), C-O (286.6 eV, epoxy and alkoxy), C=O (287.8 eV), and O-C=O (289.1 eV). However, the peak associated with C-/C=C becomes more dominant in CS-G, and the peaks related to the oxygen-containing carbon bonds especially C-O distinctly decrease, indicating the good reduction of GO (Zhou et al., 2022). Meanwhile, a new peak corresponding to the C-N bond appears at 286.0 eV in the spectrum of CS-G (Su et al., 2009), which is ascribed to the intercalation of chitosan. The N1s spectrum of CS-G shows two peaks at 399.9 and 401.9 eV, attributing to the N atom in $-NH_2$ and/or -NH- groups and protonated species ($-NH_3^+$) of CS, respectively (Supplementary Figure S1C) (Jurado-López et al., 2017). These results confirm the successful synthesis of the CS-G nanocomposite.

Raman spectroscopy is one of the most powerful techniques to characterize the structural and electronic properties of graphene and its derivates (Zhu et al., 2010). There are usually two main features in the Raman spectrum of graphene, including the G band arising from the first order scattering of the E_{2g} phonon of sp^2 C atoms (usually observed at ~1,575 cm^{-1}) and the D band arising from a breathing mode of κ-point photons of A_{1g} symmetry (~1,350 cm^{-1}) (Guo et al., 2010). As shown in Supplementary Figure S2, the G band and D band are observed in spectra of both CS-G and GO. The relative intensity of the D band and G band is proportional to the average size of the sp^2 domains (Guo et al., 2010), which increase from 0.87 of GO to 1.5 of CS-G, indicating the successful reduction of GO and the synthesis of CS-G.

The crystal structures of GO and CS-G are investigated by XRD. Supplementary Figure S3 shows the XRD patterns of CS-G and GO. As shown, GO has a feature diffraction peak at $2\theta = 10.2^\circ$ (*001*) with an interlayer d_{001} spacing of 0.864 nm (Patil et al., 2009; Zhu et al., 2010). For CS-G, the peak located at 10.2° becomes significantly weaker, confirming the great reduction of GO. A new peak located at 22° appears in the case of CS-G, related to the backbone of CS, suggesting the successful synthesis of CS-G (Mianehrow et al., 2016). Transmission electron microscope (TEM) images of GO and CS-G are displayed in Supplementary Figure S4. As shown, GO exhibits a thin stacked lamellar structure with some wrinkles (Rathnayake et al., 2017). After being reduced by hydrazine hydrate and combined with CS, the characteristic wrinkled sheet structure is retained, and some shadows corresponding to CS can be observed, which illustrates the successful synthesis of CS-G.

The morphologies of G synthesized without CS, CS-G, and the following AuNPs/CS-G modified electrode have been characterized by SEM and energy dispersive spectroscopy (EDS). A glassy carbon sheet is used to simulate the surface of GCE. As revealed in Figures 3A rGO that is reduced from GO by hydrazine without the protection of CS exhibits crumpled and aggregated structure owing to the possible aggregation (Abdolhosseinzadeh et al., 2015; Maddumage et al., 2022). When G is reduced in the presence of CS, the obtained CS-G exhibits a characteristic structure with the wrinkled sheet (Figure 3B). In addition, AuNPs with an approximate diameter of 40 nm uniformly distributed on the CS-G surface (Figure 3C). Energy dispersive spectroscopy (EDS) result further suggests the successful synthesis of CS-G and assembling of AuNPs (Figures 3D–F). The optimization of the amount of CS-G modification is studied by dropping 10 μL of CS-G with a different concentration on GCE. The peak currents obtained on the as-prepared CS-G/GCE in $Fe(CN)_6^{3-/4-}$ probe solution are compared. As shown in Supplementary Figure S5, the peak currents decrease as the amount of modified CS-G on the electrode increases, resulting from the poor conductivity of CS which may hinder the electron transfer. Thus, the optimal concentration of CS-G is set as 0.1 mg ml^{-1}.

Fabrication of immunosensor

The feasibility of the construction of the immunosensor is verified by electrochemical monitoring of the changes in the electrode interface during the modification. Figure 4A shows the CV and the corresponding DPV (inset) curves obtained on different electrodes in $Fe(CN)_6^{3-/4-}$ solution. As shown, $Fe(CN)_6^{3-/4-}$ displays a pair of reversible redox peaks on GCE. When a layer of CS-G is modified on the surface of GCE, the peak current decreases, and the peak-to-peak difference increases. This is attributed to the poor electrical conductivity of CS. Further assembly of AuNPs could be achieved by forming Au-amine bonds between AuNPs and abundant $-NH_2$ groups on CS-G. AuNPs/CS-G/GCE has a larger peak current and smaller peak-to-peak difference than CS-G/GCE due to the excellent electrical conductivity of AuNPs. The BGP antibody is then immobilized on AuNPs followed by blocking the non-specific site with BSA. BGP can bind on the as-prepared immunosensor through specific recognition between antigen and antibody. As seen, the peak current of the electrode decreases, and the peak-to-peak difference increases upon BGP binding. When BGP forms a non-conductive layer on the electrode surface, the electron transfer of the electrochemical probes on the electrode interface is hindered. These results demonstrate the successful construction of the immunosensor. According to CV curves obtained on GCE, CS-G/GCE, and AuNPs/CS-G/GCE (Figure 4A), the standard heterogeneous rate constant (k_s)

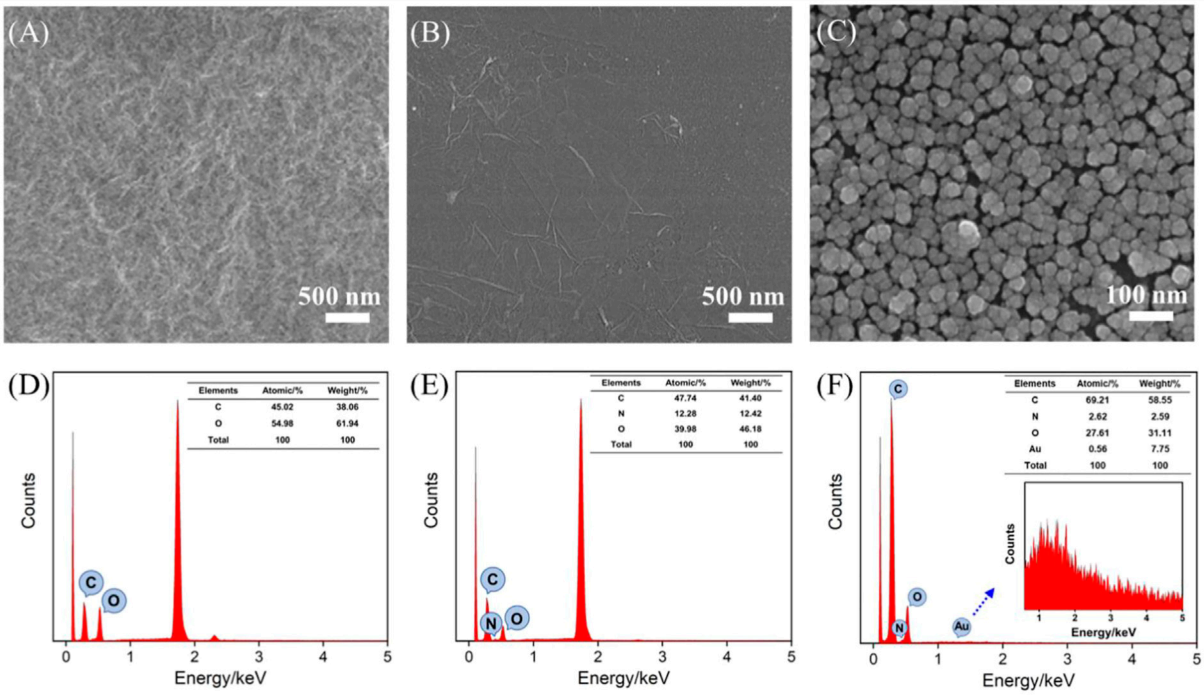

(D)

Elements	Atomic/%	Weight/%
C	45.02	38.06
O	54.98	61.94
Total	100	100

(E)

Elements	Atomic/%	Weight/%
C	47.74	41.40
N	12.28	12.42
O	39.98	46.18
Total	100	100

(F)

Elements	Atomic/%	Weight/%
C	69.21	58.55
N	2.62	2.59
O	27.61	31.11
Au	0.56	7.75
Total	100	100

FIGURE 3
SEM image of G synthesized without the protection of CS **(A)**, CS-G **(B)**, and AuNPs/CS-G **(C)** modified glassy carbon sheet. EDS of GO **(D)**, CS-G **(E)**, and AuNPs/CS-G **(F)**. Inset in **(F)** is the magnified EDS of the Au section.

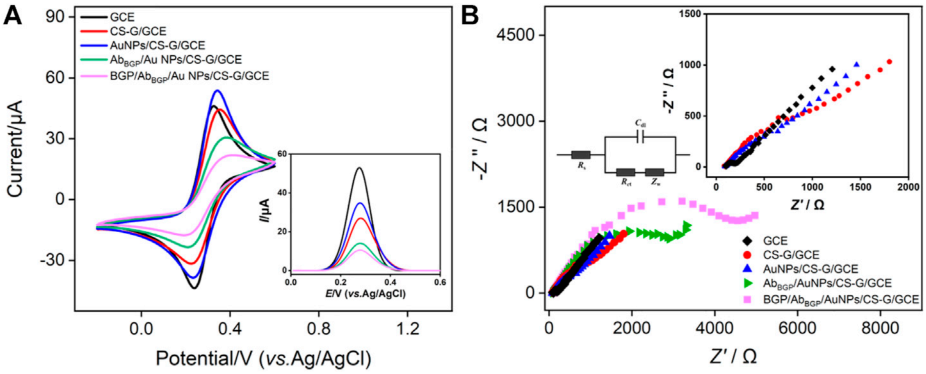

FIGURE 4
CV **(A)** and EIS **(B)** curves obtained on different electrodes including GCE, CS-G/GCE, AuNPs/CS-G/GCE, Ab$_{BGP}$/AuNPs/CS-G/GCE, and BGP/Ab$_{BGP}$/AuNPs/CS-G/GCE. The electrolyte solution is $Fe(CN)_6^{3-/4-}$ (2.5 mM) containing 0.1 M KCl. Inset in **(A)** includes the corresponding DPV curves. Insets in **(B)** are equivalent circuits of detection (left) and the enlarged view of the EIS curves at the high frequency region.

can be calculated by the following Nicholson equation (Nicholson, 1965):

$$\psi = \frac{(D_0/D_R)^{\alpha/2} k_s}{[D_0 \pi v (nF/RT)]^{1/2}},$$

where D_O and D_R are the diffusion coefficients of $Fe(CN)_6^{3-}$ and $Fe(CN)_6^{4-}$, respectively. $D_O = D_R = 1 \times 10^{-5}$ cm^2 s^{-1} v is the scan rate of CV. n is the number of electrons transferred ($n = 1$). F is the Faraday constant (96,485 C mol^{-1}). R is the gas constant (8.314 J mol^{-1} K^{-1}). T is the absolute temperature ($T = 298$ K). The value of ψ can be obtained according to the peak-to-peak difference of CV. Thus, k_s of GCE, CS-G/GCE, and AuNPs/CS-G/GCE are calculated as 9.4×10^{-3} cm s^{-1}, 4.3×10^{-3} cm s^{-1}, and 4.7×10^{-3} cm s^{-1}, respectively. As can be seen, after the modification of poor conductive CS-G, k_s of CS-G/GCE decreased obviously compared to GCE, which can be alleviated by the immobilization of AuNPs with good electrochemical properties.

Supplementary Figure S6A displays CV curves obtained on GCE or AuNPs/CS-G/GCE in PBS (0.1 M, pH = 5), where the non-Faraday current is proportional to the double layer capacitance (C_{dl}) and can act as a quantitative indicator of the electrochemical active surface area (ECSA) of electrodes (Wei et al., 2019). As seen, a remarkably increased capacitive current (~7 fold increasing) is observed on AuNPs/CS-G/GCE compared with that of GCE, suggesting an enlarged ECSA owing to the decoration of AuNPs. In addition, two apparent redox peaks at ~1.1 and ~0.55 V are observed on AuNPs/CS-G/GCE attributing to the decorating of AuNPs (Sierra-Rosales et al., 2018). At the same time, AuNPs/CS-G/GCE demonstrates larger decomposition currents and reduced decomposition potentials for both the anodic and cathodic limits, indicating an improved electroanalytical reactivity. The exact ECSA of GCE is calculated to be 0.06644 cm^2 using reversible probe $K_3[Fe(CN)_6]$ by the Randles-Sevcik equation (Supplementary Figure S6B) (Alam and Deen, 2020). The ECSA of AuNPs/CS-G/GCE is 0.465 cm^2, indicating a highly increased active surface through the modification.

Electrochemical impedance spectroscopy (EIS) is also used to investigate the changes in the electrode interface during sensor construction. As shown in Figure 4B, each EIS curve consists of a semicircle in the high-frequency region and a linear part in the low-frequency region, where the former represents electron transfer-limited processes and the latter represents diffusion-limited processes. The left inset of Figure 4B illustrates the illustration of the equivalent circuit, which contains solution resistance (R_s), double-layer capacitance (C_{dl}), Warburg impedance (Z_w), and apparent charge transfer resistance (R_{ct}). The right inset is an enlarged view of the high-frequency region curves. The equivalent diameter of the semicircle in the high-frequency region is the apparent charge transfer resistance R_{ct}. The R_{ct} of different electrodes is summarized in Supplementary Table S1. As seen, after modifying GCE with CS-G that has CS with poor conductivity, the R_{ct} of CS-G/GCE demonstrates a distinct increasement compared with that of GCE. Thanks to the excellent electrochemical property of AuNPs, the R_{ct} of AuNPs/CS-G/GCE decreases. After the combination of Ab_{BGP} and BGP, the R_{ct} further increases, indicating the successful construction of the immunosensor.

Electrochemical determination of BGP

Differential pulse voltammetry (DPV) is used to investigate the detection performance of the constructed immunosensor. Figure 5A presents the DPV curves obtained after incubating different concentrations of BGP on the immunosensors. As seen, the peak current decreases with increasing BGP concentration. This is attributed to the formation of the antigen–antibody complex through bio-specific recognition, which inhibits the electron transfer of the electrochemical probe on the electrode interface. This hindering effect becomes more obvious with the increase of bound antigen. When the concentration of BGP ranges from 100 ag ml^{-1} to10 μg mL^{-1}, the peak current (I) of the electrode has a linear relationship with the logarithmic value of BGP concentration ($\log C_{BGP}$) (Figure 5B, $I = -0.571 \log C_{BGP} +9.94$, $R^2 = 0.990$). The limit of detection (LOD) is 20 ag ml^{-1} (S/N = 3). A comparison between the determination of BGP using different methods is demonstrated in Supplementary Table S2 (Khashayar et al., 2017; Inal Kabala et al., 2019; Han et al., 2020; Bi et al., 2021). The LOD is lower than that obtained from the iron oxide material modified interdigitated electrode (IOM/IDE) (Bi et al., 2021), chemiluminescent immunoassay (Han et al., 2020), ethyl acetate/1,4-butanediol diglycidyl ether/6-mercaptohexanol modified gold electrode (EA/1,4-BED/6-MCH/AuE) (Inal Kabala et al., 2019), and AuNP-modified gold electrode (AuNPs/AuE) (Khashayar et al., 2017). The detection linear range is wider than that obtained using IOM/IDE, EA/1,4-BED/6-MCH/AuE, and AuNPs/AuE mentioned earlier. In comparison with other detection strategies (e.g., electrochemiluminescence), the electrochemical sensor has the advantages of simple instrumentation, easy operation, and the potential for the detection of colored or opaque samples (Zhang et al., 2020; Zhu et al., 2022).

Selectivity, reproducibility, and stability of the constructed immunosensor

To investigate the selectivity of the constructed immunosensor, the Ab_{BGP}/AuNPs/CS-G/GCE is incubated with other tumor markers including prostate-specific antigen (PSA), carcinoma antigen 125 (CA125), S100 calcium-binding protein β (S-100β), cancer antigen 125 (CA125), and cancer antigen 199 (CA199). As shown in Figure 6A, the peak current of the electrode did not change significantly in the presence of one of these abovementioned proteins. Even if BGP is mixed with all of these tumor markers, the peak current of the electrode is not significantly different from that obtained with BGP alone. This result proves the specific recognition ability between antigen and antibody, indicating the excellent selectivity of the constructed immunosensor. The signal stability, inter-electrode reproductivity, and storage stability of the constructed immunosensor are also investigated. After the immunosensor is incubated with BGP, the electrochemical signal of the electrode was measured five consecutive times. A relative standard deviation (RSD) of the current value is 1.4% (Figure 6B). The reproducibility of the immunosensor electrodes was evaluated by preparing five electrodes in the same batch. The RSD for detecting BGP is 2.4% (Figure 6C). When the immunosensors

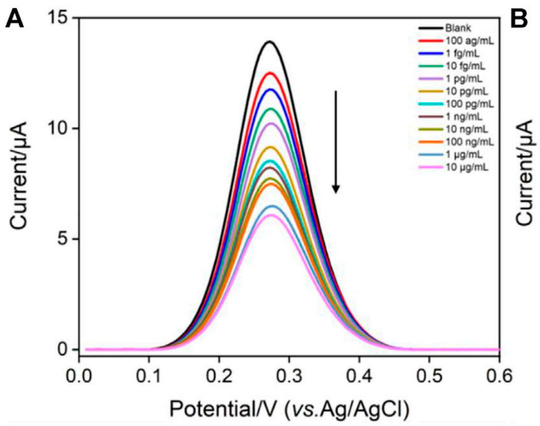

FIGURE 5
(A) DPV curves obtained on the developed immunosensors after incubation with different concentrations of BGP. **(B)** Corresponding linear regression curve. Error bars represent the standard deviation of three measurements.

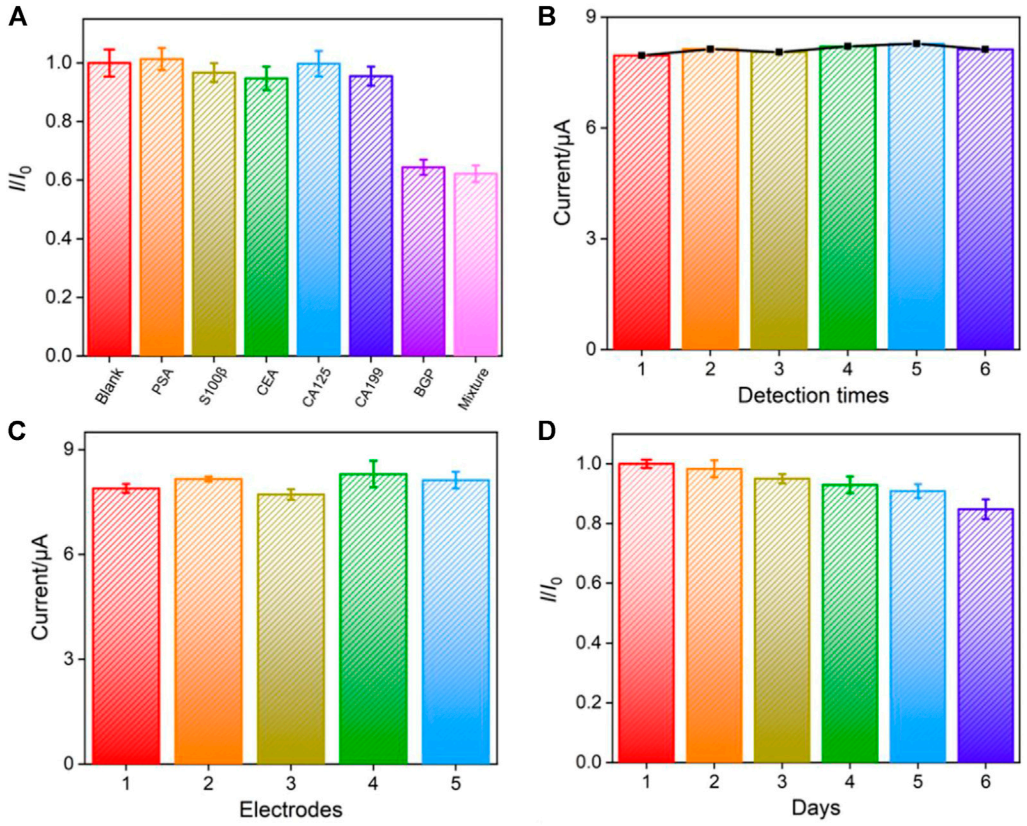

FIGURE 6
(A) Relative ratio of the current (I/I_0) obtained on the developed immunosensors before (I_0) and after (I) incubation with prostate-specific antigen (PSA, 1 ng ml^{-1}), S100 calcium-binding protein β (S100β, 1 ng ml^{-1}), carcinoembryonic antigen (CEA, 1 ng ml^{-1}), carcinoma antigen 125 (CA125, 1 μU mL^{-1}), carcinoma antigen 199 (CA199, 1 μU mL^{-1}), BGP (1 ng ml^{-1}), or the mixture of the above proteins. Repeatability **(B)**, inter-electrode reproducibility **(C)**, and storage stability **(D)** of the fabricated immunosensor. Error bars represent the standard deviation of three measurements.

are stored in a refrigerator at 4°C, the storage stability is studied using the peak measured on the first day and after storage, respectively. The immunosensor retains ~90% of its original performance after 6 days of storage, indicating high stability.

Determination of BGP in human serum

To evaluate the potential of the constructed immunosensor for practical application, the concentrations of BGP in human serum were determined by the standard addition method. Different concentrations of BGP are artificially added to the serum of a healthy man to simulate the different BGP concentrations of patients with osteoporosis. As shown in Supplementary Table S3, the immunosensor exhibits good recoveries ranging from 96.9 to 106.2% and low relative standard deviations (RSD <2.5%), suggesting good reliability and great potential in real sample analysis.

Conclusion

In this article, an immunosensor is easily fabricated through a simple and convenient method, which can realize highly sensitive electrochemical detection of the biomarker of the bone metabolism, bone gamma-carboxyglutamate protein (BGP). The modification of the electrode with the chitosan–graphene nanocomposite (CS-G) increases the active area of the electrode and provides abundant amino sites to further anchor gold nanoparticles (AuNPs). On the one hand, AuNPs further improve the electron transfer at the electrode interface, and on the other hand, AuNPs could be used for the immobilization of recognitive antibodies. The specific binding of BGP to the recognitive antibody hinders the electron transfer of the electrochemical probe on the electrode surface, resulting in the reduction of the electrochemical signal. Based on this mechanism, a highly sensitive electrochemical detection of BGP is achieved when the concentration of BGP ranges from 100 ag ml^{-1} to 10 μg ml^{-1} with a limit of detection of 20 ag ml^{-1} (S/N = 3). The constructed immunosensor exhibits excellent selectivity, good reproducibility, and high stability. The determination of BGP in human serum is also achieved with high reliability. The simple construction and good performance of the developed immunosensor provide an efficient strategy for convenient and sensitive determination of bone metabolic markers.

Data availability statement

The original contributions presented in the study are included in the article/Supplementary Material; further inquiries can be directed to the corresponding author.

Author contributions

QC: data curation and writing—original draft preparation; JH: data curation; LH: data curation; FX: supervision and writing—reviewing and editing.

Funding

We acknowledge the financial support from the National Natural Science Foundation of China (21904117) and the Zhejiang Provincial Natural Science Foundation of China (LY20B050007).

Conflict of interest

The authors declare that the research was conducted in the absence of any commercial or financial relationships that could be construed as a potential conflict of interest.

Publisher's note

Supplementary material

The Supplementary Material for this article can be found online at: https://www.frontiersin.org/articles/10.3389/fchem.2022.940795/full#supplementary-material

References

Abdolhosseinzadeh, S., Asgharzadeh, H., and Seop Kim, H. (2015). Fast and fully-scalable synthesis of reduced graphene oxide. *Sci. Rep.* 5, 10160. doi:10.1038/srep10160

Afsarimanesh, N., Zia, A., Mukhopadhyay, S., Kruger, M., Yu, P., Kosel, J., et al. (2016). Smart sensing system for the prognostic monitoring of bone health. *Sensors* 16, 976–988. doi:10.3390/s16070976

Afsarimanesh, N., Mukhopadhyay, S., and Kruger, M. (2018). Sensing technologies for monitoring of bone-health: a review. *Sensors Actuators A Phys.* 274, 165–178. doi:10.1016/j.sna.2018.03.027

Afsarimanesh, N., Alahi, M., Mukhopadhyay, S., and Kruger, M. (2018). Smart sensing system for early detection of bone loss: current status and future possibilities. *J. Sens. Actuator Netw.* 7, 10–20. doi:10.3390/jsan7010010

Alam, A., and Deen, M. (2020). Bisphenol A electrochemical sensor using graphene oxide and β-cyclodextrin-functionalized multi-walled carbon Nanotubes. *Anal. Chem.* 92, 5532–5539. doi:10.1021/acs.analchem.0c00402

Ang, P., Wang, S., Bao, Q., Thong, J., and Loh, K. (2009). High-throughput synthesis ofgraphene by intercalation-exfoliation ofgraphite oxide and study of ionic screening in graphene transistor. *ACS Nano* 3, 3587–3594. doi:10.1021/nn901111s

Bi, H., Bian, P., Gopinath, S., Marimuthu, K., Lv, G., and Yin, X. (2021). Identifying mineral decrement with bone injury by quantifying osteocalcin on current-volt sensor. *Biotechnol. Appl. Biochem.*, 1–8. doi:10.1002/bab.2267

Calvo, M., Eyret, D., and Gundberg, C. (1996). Molecular basis and clinical application of biological markers of bone turnover. *Endocr. Rev.* 17, 333–368. doi:10.1210/er.17.4.333

Cheatham, S., Hanney, W., Kolber, M., and Salamh, P. (2017). Osteoporosis: exercise programming insight for the sports medicine professional. *Strength Cond. J.* 39, 2–13. doi:10.1519/ssc.0000000000000302

Chen, N., Liu, H., Zhang, Y., Zhou, Z., Fan, W., Yu, G., et al. (2018). A colorimetric sensor based on citrate-stabilized AuNPs for rapid pesticide residue detection of terbuthylazine and dimethoate. *Sensors Actuators B Chem.* 255, 3093–3101. doi:10.1016/j.snb.2017.09.134

Christenson, R. (1997). Biochemical markers of bone metabolism: an overview. *Clin. Biochem.* 30, 573–593. doi:10.1016/s0009-9120(97)00113-6

Farley, J., Chesnut, C., and Baylink, D. (1981). Improved method for quantitative determination in serum of alkaline phosphatase of skeletal origin. *Clin. Chem.* 27, 2002–2007. doi:10.1093/clinchem/27.12.2002

Gong, J., Zhang, T., Luo, T., Luo, X., Yan, F., Tang, W., et al. (2022). Bipolar silica nanochannel array confined electrochemiluminescence for ultrasensitive detection of SARS-CoV-2 antibody. *Biosens. Bioelectron.* 215, 114563–132093. doi:10.1016/j.bios.2022.114563

Gong, J., Tang, H., Wang, M., Lin, X., Wang, K., and Liu, J. (2022). Novel three-dimensional graphene nanomesh prepared by facile electro-etching for improved electroanalytical performance for small biomolecules. *Mat. Des.* 215, 110506–110514. doi:10.1016/j.matdes.2022.110506

Gundberg, C., Looker, A., Nieman, S., and Calvo, M. (2002). Patterns of osteocalcin and bone specific alkaline phosphatase by age, gender, and race or ethnicity. *Bone* 31, 703–708. doi:10.1016/s8756-3282(02)00902-x

Guo, Y., Guo, S., Ren, J., Zhai, Y., Dong, S., and Wang, E. (2010). Cyclodextrin functionalized graphene nanosheets with high supramolecular recognition capability: synthesis and host-guest inclusion for enhanced electrochemical performance. *ACS Nano* 4, 4001–4010. doi:10.1021/nn100939n

Han, S., Xue, Y., Zhang, J., Huang, J., Liu, X., Yang, Y., et al. (2020). A chemiluminescent immunoassay for osteocalcin in human serum and a solution to the "hook effect". *J. Anal. Methods Chem.* 2020, 8891437. doi:10.1155/2020/8891437

Inal Kabala, S., Yagar, H., and Ozcan, H. (2019). A new biosensor for osteoporosis detection. *Prep. Biochem. Biotechnol.* 49, 511–520. doi:10.1080/10826068.2019.1587628

Ingram, R., Park, Y., Clarke, B., and Fitzpatrick, L. (1994). Age- and gender-related changes in the distribution of osteocalcin in the extracellular matrix of normal male and female bone. Possible involvement of osteocalcin in bone remodeling. *J. Clin. Invest.* 93, 989–997. doi:10.1172/jci117106

Ivaska, K., Käkönen, S., Gerdhem, P., Obrant, K., Pettersson, K., and Väänänen, H. (2005). Urinary osteocalcin as a marker of bone metabolism. *Clin. Chem.* 51, 618–628. doi:10.1373/clinchem.2004.043901

Jirakunakorn, R., Khumngern, S., Choosang, J., Thavarungkul, P., Kanatharana, P., and Numnuam, A. (2020). Uric acid enzyme biosensor based on a screen-printed electrode coated with prussian blue and modified with chitosan-graphene composite cryogel. *Microchem. J.* 154, 104624–104632. doi:10.1016/j.microc.2020.104624

Jurado-López, B., Vieira, R., Rabelo, R., Beppu, M., Casado, J., and Rodríguez-Castellón, E. (2017). Formation of complexes between functionalized chitosan membranes and copper: a study by angle resolved XPS. *Mat. Chem. Phys.* 185, 152–161. doi:10.1016/j.matchemphys.2016.10.018

Kang, X., Wang, J., Wu, H., Aksay, I. A., Liu, J., and Lin, Y. (2009). Glucose oxidase-graphene-chitosan modified electrode for direct electrochemistry and glucose sensing. *Biosens. Bioelectron.* 25, 901–905. doi:10.1016/j.bios.2009.09.004

Khashayar, P., Amoabediny, G., Hosseini, M., Verplancke, R., Razi, F., Vanfleteren, J., et al. (2017). An electrochemical biosensor based on AuNP-modified gold electrodes for selective determination of serum levels of osteocalcin. *IEEE Sens. J.* 17, 3367–3374. doi:10.1109/jsen.2017.2684903

Li, D., Müller, M., Gilje, S., Kaner, R., and Wallace, G. (2008). Processable aqueous dispersions of graphene nanosheets. *Nat. Nanotechnol.* 3, 101–105. doi:10.1038/nnano.2007.451

Lima, R., de Oliveira, R., Raposo, R., Neri, S., and Gadelha, A. (2019). Stages of sarcopenia, bone mineral density, and the prevalence of osteoporosis in older women. *Arch. Osteoporos.* 14, 38–45. doi:10.1007/s11657-019-0591-4

Lin, J., Li, K., Wang, M., Chen, X., Liu, J., and Tang, H. (2020). Reagentless and sensitive determination of carcinoembryonic antigen based on a stable Prussian blue modified electrode. *RSC Adv.* 10, 38316–38322. doi:10.1039/d0ra06751b

Liu, J., Guo, S., Han, L., Ren, W., Liu, Y., and Wang, E. (2012). Multiple pH-responsive graphene composites by non-covalent modification with chitosan. *Talanta* 101, 151–156. doi:10.1016/j.talanta.2012.09.013

Lu, Z., Wu, L., Dai, X., Wang, Y., Sun, M., Zhou, C., et al. (2021). Novel flexible bifunctional amperometric biosensor based on laser engraved porous graphene array electrodes: highly sensitive electrochemical determination of hydrogen peroxide and glucose. *J. Hazard. Mat.* 402, 123774–123783. doi:10.1016/j.jhazmat.2020.123774

Lu, Z., Du, X., Sun, M., Zhang, Y., Li, Y., Wang, X., et al. (2021). Novel dual-template molecular imprinted electrochemical sensor for simultaneous detection of CA and TPH based on peanut twin-like $NiFe_2O_4/CoFe_2O_4$/NCDs nanospheres: fabrication, application and DFT theoretical study. *Biosens. Bioelectron.* 190, 113408–113418. doi:10.1016/j.bios.2021.113408

Lu, Z., Dang, Y., Dai, C., Zhang, Y., Zou, P., Du, H., et al. (2021). Hollow MnFeO oxide derived from MOF@MOF with multiple enzyme-like activities for multifunction colorimetric assay of biomolecules and Hg^{2+}. *J. Hazard. Mat.* 403, 123979–123988. doi:10.1016/j.jhazmat.2020.123979

Ma, X., Liao, W., Zhou, H., Tong, Y., Yan, F., Tang, H., et al. (2020). Highly sensitive detection of rutin in pharmaceuticals and human serum using ITO electrodes modified with vertically-ordered mesoporous silica-graphene nanocomposite films. *J. Mat. Chem. B* 8, 10630–10636. doi:10.1039/d0tb01996h

Ma, K., Yang, L., Liu, J., and Liu, J. (2022). Electrochemical sensor nanoarchitectonics for sensitive detection of uric acid in human whole blood based on screen-printed carbon electrode equipped with vertically-ordered mesoporous silica-nanochannel film. *Nanomaterials* 12, 1157–1169. doi:10.3390/nano12071157

Ma, K., Zheng, Y., An, L., and Liu, J. (2022). Ultrasensitive immunosensor for prostate specific antigen based on enhanced electrochemiluminescence by vertically-ordered mesoporous silica-nanochannel film. *Front. Chem.* 10, 851178. doi:10.3389/fchem.2022.851178

Maddumage, D., Panamaldeniya, S., Kimbulapitiya, K., Jayakantha, D., Munasinghe, M., Pemasiri, B., et al. (2022). Effect of substrate temperature on electrical properties of RGO thin films deposited by atomized spray pyrolysis. *Mat. Res. Bull.* 154, 111936–111947. doi:10.1016/j.materresbull.2022.111936

Mauricio-Sánchez, R., Salazar, R., Luna-Bárcenas, J., and Mendoza-Galván, A. (2018). FTIR spectroscopy studies on the spontaneous neutralization of chitosan acetate films by moisture conditioning. *Vib. Spectrosc.* 94, 1–6. doi:10.1016/j.vibspec.2017.10.005

Mianehrow, H., Afshari, R., Mazinani, S., Sharif, F., and Abdouss, M. (2016). Introducing a highly dispersed reduced graphene oxide nano-biohybrid employing chitosan/hydroxyethyl cellulose for controlled drug delivery. *Int. J. Pharm.* 509, 400–407. doi:10.1016/j.ijpharm.2016.06.015

Mohanty, U. (2010). Electrodeposition: a versatile and inexpensive tool for the synthesis of nanoparticles, nanorods, nanowires, and nanoclusters of metals. *J. Appl. Electrochem.* 41, 257–270. doi:10.1007/s10800-010-0234-3

Nicholson, R. (1965). Theory and application of cyclic voltammetry for measurement of electrode reaction kinetics. *Anal. Chem.* 37, 1351–1355. doi:10.1021/ac60230a016

Patil, A., Vickery, J., Scott, T., and Mann, S. (2009). Aqueous stabilization and self-assembly of graphene sheets into layered bio-nanocomposites using DNA. *Adv. Mat.* 21, 3159–3164. doi:10.1002/adma.200803633

Price, C., and Thompson, P. (1995). The role of biochemical tests in the screening and monitoring of osteoporosis. *Ann. Clin. Biochem.* 32, 244–260. doi:10.1177/000456329503200302

Qiu, J., Wang, R., Liang, R., and Xia, X. (2009). Electrochemically deposited nanocomposite film of CS-Fc/AuNPs/GOx for glucose biosensor application. *Biosens. Bioelectron.* 24, 2920–2925. doi:10.1016/j.bios.2009.02.029

Rachner, T., Khosla, S., and Hofbauer, L. (2011). Osteoporosis: now and the future. *Lancet* 377, 1276–1287. doi:10.1016/s0140-6736(10)62349-5

Rathnayake, R., Wijayasinghe, H., Pitawala, H., Yoshimura, M., and Huang, H.-H. (2017). Synthesis of graphene oxide and reduced graphene oxide by needle platy natural vein graphite. *Appl. Surf. Sci.* 393, 309–315. doi:10.1016/j.apsusc.2016.10.008

Santhiago, M., Maroneze, C., Silva, C., Camargo, M., and Kubota, L. (2015). Electrochemical oxidation of glassy carbon provides similar electrochemical response as graphene oxide prepared by tour or hummers routes. *ChemElectroChem* 2, 761–767. doi:10.1002/celc.201402387

Sarfraz, N., and Khan, I. (2021). Plasmonic gold nanoparticles (AuNPs): properties, synthesis and their advanced energy, environmental and biomedical applications. *Chem. Asian J.* 16, 720–742. doi:10.1002/asia.202001202

Shedbalkar, U., Singh, R., Wadhwani, S., Gaidhani, S., and Chopade, B. (2014). Microbial synthesis of gold nanoparticles: current status and future prospects. *Adv. Colloid Interface Sci.* 209, 40–48. doi:10.1016/j.cis.2013.12.011

Shein, J., Lai, L., Eggers, P., Paddon-Row, M., and Gooding, J. (2009). Formation of efficient electron transfer pathways by adsorbing gold nanoparticles to self-assembled monolayer modified electrodes. *Langmuir* 25, 11121–11128. doi:10.1021/la901421m

Sierra-Rosales, P., Torres, R., Sepúlveda, C., Kogan, M., and Arturo Squella, J. (2018). Electrochemical characterization and electrocatalytic application of gold nanoparticles synthesized with different stabilizing agents. *Electroanalysis* 30, 386–396. doi:10.1002/elan.201700633

Su, Q., Pang, S., Alijani, V., Li, C., Feng, X., and Müllen, K. (2009). Composites of graphene with large aromatic molecules. *Adv. Mat.* 21, 3191–3195. doi:10.1002/adma.200803808

Tai, J., Fan, S., Ding, S., and Ren, L. (2022). Gold nanoparticles based optical biosensors for cancer biomarker proteins: a review of the current practices. *Front. Bioeng. Biotechnol.* 10, 877193. doi:10.3389/fbioe.2022.877193

Walker-Bone, K., Walter, G., and Cooper, C. (2002). Recent developments in the epidemiology of osteoporosis. *Curr. Opin. Rheumatol.* 14, 411–415. doi:10.1097/00002281-200207000-00014

Wang, M., Lin, J., Gong, J., Ma, M., Tang, H., Liu, J., et al. (2021). Rapid and sensitive determination of doxorubicin in human whole blood by vertically-ordered mesoporous silica film modified electrochemically pretreated glassy carbon electrodes. *RSC Adv.* 11, 9021–9028. doi:10.1039/d0ra10000e

Wang, K., Yang, L., Huang, H., Lv, N., Liu, J., and Liu, Y. (2022). Nanochannel array on electrochemically polarized screen printed carbon electrode for rapid and sensitive electrochemical determination of clozapine in human whole blood. *Molecules* 27, 2739–2752. doi:10.3390/molecules27092739

Wei, C., Sun, S., Mandler, D., Wang, X., Qiao, S., and Xu, Z. (2019). Approaches for measuring the surface areas of metal oxide electrocatalysts for determining their intrinsic electrocatalytic activity. *Chem. Soc. Rev.* 48, 2518–2534. doi:10.1039/c8cs00848e

Wu, M., Sun, X., Zhu, M., Chen, H., and Xu, J. (2015). Mesoporous silica film-assisted amplified electrochemiluminescence for cancer cell detection. *Chem. Commun.* 51, 14072–14075. doi:10.1039/c5cc06229b

Yan, F., Chen, J., Jin, Q., Zhou, H., Sailjoi, A., Liu, J., et al. (2020). Fast one-step fabrication of a vertically-ordered mesoporous silica-nanochannel film on graphene for direct and sensitive detection of doxorubicin in human whole blood. *J. Mat. Chem. C Mat.* 8, 7113–7119. doi:10.1039/d0tc00744g

Yan, F., Luo, T., Jin, Q., Zhou, H., Sailjoi, A., Dong, G., et al. (2021). Tailoring molecular permeability of vertically-ordered mesoporous silica-nanochannel films on graphene for selectively enhanced determination of dihydroxybenzene isomers in environmental water samples. *J. Hazard. Mat.* 410, 124636–124644. doi:10.1016/j.jhazmat.2020.124636

Yan, F., Wang, M., Jin, Q., Zhou, H., Xie, L., Tang, H., et al. (2021). Vertically-ordered mesoporous silica films on graphene for anti-fouling electrochemical detection of tert-butylhydroquinone in cosmetics and edible oils. *J. Electroanal. Chem. (Lausanne).* 881, 114969–114975. doi:10.1016/j.jelechem.2020.114969

Zhang, Y., Xu, J., Zhou, S., Zhu, L., Lv, X., Zhang, J., et al. (2020). DNAzyme-triggered visual and ratiometric electrochemiluminescence dual-readout assay for Pb(II) based on an assembled paper device. *Anal. Chem.* 92, 3874–3881. doi:10.1021/acs.analchem.9b05343

Zhang, Y., Cui, Y., Sun, M., Wang, T., Liu, T., Dai, X., et al. (2022). Deep learning-assisted smartphone-based molecularly imprinted electrochemiluminescence detection sensing platform: protable device and visual monitoring furosemide. *Biosens. Bioelectron.* 209, 114262–114273. doi:10.1016/j.bios.2022.114262

Zhang, M., Zou, Y., Zhou, X., Yan, F., and Ding, Z. (2022). Vertically-ordered mesoporous silica films for electrochemical detection of Hg(II) ion in pharmaceuticals and soil samples. *Front. Chem.* 10, 952936. doi:10.3389/fchem.2022.952936

Zhang, J., Pei, J., Yang, L., Tian, Y., and Liu, J. (2022). A label-free electrochemiacl immunosensor for sensitive detection of carcinoembryonic antigen based on interface with redox probe modified electron transfer wires and effectively immobilized antibody. *Front. Chem.* 10, 939736. doi:10.3389/fchem.2022.939736

Zheng, Y., Lin, J., Xie, L., Tang, H., Wang, K., and Liu, J. (2021). One-step preparation of nitrogen-doped graphene quantum dots with anodic electrochemiluminescence for sensitive detection of hydrogen peroxide and glucose. *Front. Chem.* 9, 688358. doi:10.3389/fchem.2021.688358

Zhou, H., Ding, Y., Su, R., Lu, D., Tang, H., and Xi, F. (2022). Silica nanochannel array film supported by β-cyclodextrin-functionalized graphene modified gold film electrode for sensitive and direct electroanalysis of acetaminophen. *Front. Chem.* 9, 812086. doi:10.3389/fchem.2021.812086

Zhu, C., Guo, S., Fang, Y., and Dong, S. (2010). Reducing sugar: new functional molecules for the green synthesis of graphene nanosheets. *ACS Nano* 4, 2429–2437. doi:10.1021/nn1002387

Zhu, L., Lv, X., Yu, H., Tan, X., Rong, Y., Feng, W., et al. (2022). Paper-based bipolar electrode electrochemiluminescence platform combined with pencil-drawing trace for the detection of M.SssI methyltransferase. *Anal. Chem.* 94, 8327–8334. doi:10.1021/acs.analchem.2c00803

Zou, Y., Zhou, X., Xie, L., Tang, H., and Yan, F. (2022). Vertically-ordered mesoporous silica films grown on boron nitride-graphene composite modified electrodes for rapid and sensitive detection of carbendazim in real samples. *Front. Chem.* 10, 939510. doi:10.3389/fchem.2022.939510

frontiers | Frontiers in Chemistry

TYPE Review
PUBLISHED 26 September 2022
DOI 10.3389/fchem.2022.994272

OPEN ACCESS

EDITED BY
Yan Zhang,
University of Jinan, China

REVIEWED BY
Xiu Liang,
Qilu University of Technology, China
Haifeng Yang,
Shanghai Normal University, China
Jeon Woong Kang,
Massachusetts Institute of Technology, United States

*CORRESPONDENCE
Biagio Todaro,
biagio.todaro@sns.it
Stefano Luin,
s.luin@sns.it

SPECIALTY SECTION
This article was submitted to Analytical Chemistry,
a section of the journal
Frontiers in Chemistry

RECEIVED 14 July 2022
ACCEPTED 24 August 2022
PUBLISHED 26 September 2022

CITATION
Todaro B, Begarani F, Sartori F and Luin S (2022), Is Raman the best strategy towards the development of non-invasive continuous glucose monitoring devices for diabetes management? *Front. Chem.* 10:994272.
doi: 10.3389/fchem.2022.994272

Is Raman the best strategy towards the development of non-invasive continuous glucose monitoring devices for diabetes management?

Biagio Todaro[1]*, Filippo Begarani[2,3], Federica Sartori[2,3] and Stefano Luin[1,4]*

[1]NEST Laboratory, Scuola Normale SuperiorePisa, Italy, [2]P.B.L. SRL, Solignano, PR, Italy, [3]Omnidermal Biomedics SRL, Solignano, PR, Italy, [4]NEST, Istituto Nanoscienze, CNR, Pisa, Italy

Diabetes has no well-established cure; thus, its management is critical for avoiding severe health complications involving multiple organs. This requires frequent glycaemia monitoring, and the gold standards for this are fingerstick tests. During the last decades, several blood-withdrawal-free platforms have been being studied to replace this test and to improve significantly the quality of life of people with diabetes (PWD). Devices estimating glycaemia level targeting blood or biofluids such as tears, saliva, breath and sweat, are gaining attention; however, most are not reliable, user-friendly and/or cheap. Given the complexity of the topic and the rise of diabetes, a careful analysis is essential to track scientific and industrial progresses in developing diabetes management systems. Here, we summarize the emerging blood glucose level (BGL) measurement methods and report some examples of devices which have been under development in the last decades, discussing the reasons for them not reaching the market or not being really non-invasive and continuous. After discussing more in depth the history of Raman spectroscopy-based researches and devices for BGL measurements, we will examine if this technique could have the potential for the development of a user-friendly, miniaturized, non-invasive and continuous blood glucose-monitoring device, which can operate reliably, without inter-patient variability, over sustained periods.

KEYWORDS

diabetes, Raman spectroscopy, spectral data processing, glycaemia monitoring devices, wearable continuous non-invasive sensors, blood glucose

1 Background

Diabetes is a lifelong disease that affects more than 400 millions of people worldwide (WHO. Diabetes, 2022). Emerging reports from the International Diabetes Federation state that diabetes is set to rise very fast, estimating 700 millions of cases in the next 25 years (IDF Diabetes Atlas, 2019). Among the various types of diabetes, all characterized by high blood glucose levels, the main two types are type 1 diabetes, an autoimmune condition where the pancreas produces little or no insulin, and type 2 diabetes, a metabolic disorder that results in hyperglycaemia due to insulin resistance. Diabetes, and related risk factors such as microvascular (retinopathy, nephropathy, and neuropathy) and macrovascular metabolic disorders, is so widespread that it has been defined "the epidemic of the century" (Kharroubi, 2015). According to the European parameters (Blood Sugar Level Ranges, 2019), the plasma blood glucose level (BGL) of a healthy person under fasting conditions fluctuates during the day between approximately 99.0 and 124.2 mg/dl (5.5–6.9 mmol/L) with maximum levels of up to 140.4 mg/dl (7.8 mmol/L) 2 h post-prandial. Conversely, the plasma BGL of a diabetic person under fasting conditions fluctuates during the day between approximately 124.2 and 198.2 mg/dl (6.9–11.0 mmol/L) with maximum levels up to 250.0 mg/dl (13.7 mmol/L) 2 h post-prandial. In this contest, an adequate therapeutic treatment has a pivotal role to avoid life-threatening health complications, such as risks of heart disease, kidney failure, blindness, up to hypoglycaemic or hyperglycaemic coma. While subcutaneous injection of insulin or oral/nasal administration of sugar-lowering drugs have been proved as the crucial drug delivery systems over the last years, recent pharmacotherapeutic approaches, exploiting i.e., nanotechnologies, provide nowadays important alternatives into resolving some of the most several limitations of conventional anti-diabetes medications (Veiseh et al., 2015; Todaro et al., 2022).

However, despite these technological improvements, it remains difficult to maintain long-lasting ideal blood glucose levels, and people with diabetes (PWD) must monitor the BGL several times per day.

In this regards, great progresses have been made during the past 60 years regarding BGL sensors. Weller and co-workers pioneered the first continuous *in vivo* BGL sensing in 1960 (Weller et al., 1960). Starting from that year, several finger-stick device have been developed, from the traditional Accu-Chek (Roche Diagnostics GmbH, Germany), OneTouch (LifeScan Inc., United States), Freestyle Optium Neo (Abbott Diabetes Care Inc., United States), Contour Next, and Contour Next One (Ascensia Diabetes Care Inc., Canada) to the most novel technologies, such as a device based on a wireless smart pen that can automatically calculate required insulin (Huang et al., 2022). The conception of the traditional finger-stick for blood testing method has further represented a cornerstone of the research efforts, even if nowadays this tool is considered obsolete because painful and time consuming, sometimes resulting in poor compliance and bearing the risk of infections. In the quest for painless alternatives, researchers are attempting with extensive efforts to develop a fully Non-Invasive Continuous Blood Glucose Level (NICBGL) sensing device since the Eighties. (John L. Smith, 2021). Several technologies (Heineman and Jensen, 2006) have been and are being developed globally towards this end; until now, however, a completely user-friendly, cheap, small and reliable NICBGL device is lacking.

This review is organized as follows. Section 2 provides an overview of current optical/wave-based/remote measurement methods for BGL estimation; the main advantages and drawbacks of the technologies are discussed. Section 3 presents a summary of the Raman spectroscopy advances over the years. The main Raman features, advantages, disadvantages as well as the emerging results in Raman biosensors are examined. In Section 4 we discuss more deeply the requirements for the ideal BGL measurement device and how the various techniques can approach this result, provide an intuitive explanation for the data analysis methods, highlight the aspects that are important in particular for avoiding (too frequent) recalibrations, and discuss the advantages of Raman over the other possible techniques, presenting therefore also the perspectives of this work. The manuscript ends with a short conclusions section.

2 Blood glucose monitoring devices

2.1 Overview

The history of blood glucose monitoring (BGM) devices began in the mid-twentieth-century when Leland C. Clark Jr., considered the "father of biosensors," designed the first-generation enzymatic glucose biosensor made to monitor glucose during cardiac surgery. Due to its higher specificity, accuracy and reliability in comparison to the previous chemical/enzymatic tests (i.e., Trommer's test, 1841; Fehling's test, 1848; or Benedict's test, 1908), this device was one of the major breakthroughs in glucose measurement (Dziergowska et al., 2019). Thereafter, many other (invasive and non-continuous) enzyme-based biosensors as well as other continuous glucose monitoring (CGM) devices have been or are being developed exploiting several techniques for measuring various glucose physical parameters (Harman-Boehm et al., 2009; Olliver et al., 2009; Clarke and Foster, 2012; Villena Gonzales et al., 2019; Bolla and Priefer, 2020).

Measuring the concentration of an analyte requires detecting a signal which is related to its amount, and knowing or determining the functional relationship. The signal is usually generated through the interaction of a field or of other molecules (the "source") with some physical-chemical characteristic of the analyte. The source may interact with the analyte in the body because:

1) a quantity of the analyte proportional to its concentration is extracted (Figure 1A),
2) something is inserted inside the tissue of interest (Figure 1B),

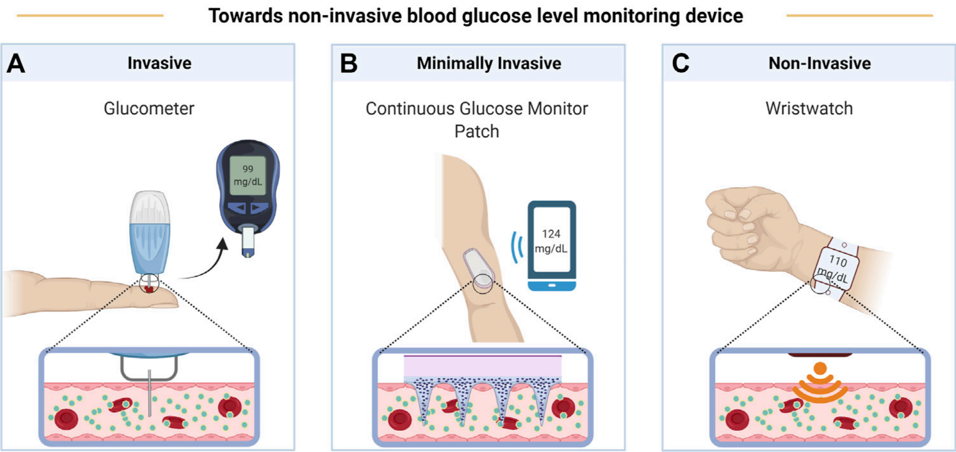

FIGURE 1
Evolution of BGL monitoring devices from invasive glucometer **(A)**, to minimally invasive continuous glucose monitoring patch **(B)**, and finally to non-invasive wristwatch **(C)**. Created with BioRender.com.

3) source and signal can pass through the tissues (Figure 1C).

The different possible sources and signals, linked with the measured physico-chemical characteristic of the analyte, characterize the different possible methods and techniques. In the case of the BGM devices reviewed here, extraction of fluids (case 1) is exploited in finger-pricking methods, in Reverse Iontophoresis (RI, Section 2.7) and Sonophoresis Technology (ST, 2.8) with subsequent enzymatic or surface enhanced Raman scattering (SERS) quantification of glucose (2.6 or 2.3.1, respectively); insertion of a minimally invasive device (case 2) can be used in Enzymatic Detection Technology (EDT, 2.6), in Fluorescence Technology (FT, 2.9), or again with SERS (2.3.1).

Case 3) is maybe the most promising for completely non-invasive CGM devices, and sources and signals are usually pressure/movement waves ("sound") and/or electromagnetic fields ("light"). The various techniques based on electromagnetic fields differ for the frequency at which these vary, and for how the signal is detected. At the lowest frequencies, we will discuss Bioimpedance Spectroscopy (BS, Section 2.11) and ElectroMagnetic Sensing (EMS, 2.14).

Increasing the frequency, there are the different optical spectroscopy techniques, based on absorption by, emission from, or scattering by the analyte. These three different measures would require different geometries, but the possibly relatively low penetration of the used electromagnetic radiation in tissues, and the requirement for a CGM device to be small and wearable, most often constrain the geometry to be (almost) in back-scattering, i.e. with the signal detected very close to the source. In particular, absorption is usually measured as "diffuse reflectance" (or remission), i.e., exploiting the random scattering of penetrating radiation from tissues. Absorption can be observed also by considering the effect of the energy absorbed by the molecules, i.e. the local heating which can be measured directly (sometimes called photothermal spectroscopy) or by the generated pressure wave (photoacoustic spectroscopy, see Section 2.5). Depending on the measured regions of the glucose absorption spectrum, the related devices are based on Near, Mid, and Far Infrared Spectroscopy (NIRS, MIRS, and FIRS, see Section 2.2), or Millimetre and Microwave Sensing (MMS, 2.4). Regarding light scattering: coherent diffused radiation is measured in Optical Coherence Tomography (OCT, Section 2.12), where glucose concentration can be determined because of its influence on the refractive index of biofluids; on the other hand, a vibrational spectrum of glucose can be measured by looking at the inelastic light scattering in Raman Spectroscopy (RS, Sections 2.3, 3). Finally, there are devices that exploit more than one technique and/or measure also quantities different from glycaemia (e.g., to correct its obtained values); these are MultiTechnologies (MT) devices (Section 2.13), among which the ones measuring Metabolic Heat Conformation (MHC), based on various spectroscopies and possibly on gravitometry (for detecting movements, e.g., caused by heart pulse).

In the following, we will provide examples of BGM devices that are available on the market or are or have recently been under development, and we will explain the main complications of each technique. A more comprehensive research on BGM devices on the market or currently under development is presented in (Shang et al., 2022).

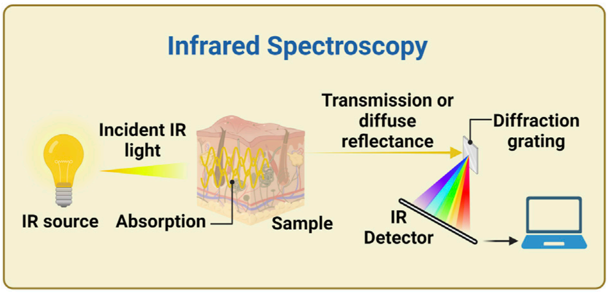

FIGURE 2
Example of experimental setup for infrared spectroscopy. A continuous IR source generates light over a wide range of infrared wavelengths, which irradiates the sample. The light is collected in transmission or diffuse reflectance mode, and the spectrum is measured thanks to a diffraction grating, in this example. Alternative configurations use a Fourier transform interferometer (FTIR) instead of the dispersive element, or use a monochromator or other methods for selecting the wavelength bands between IR source and sample. Created with BioRender.com.

2.2 Infrared spectroscopy

In general, absorption of infrared radiation usually causes a variation in molecular vibrational states. The vibrational spectrum of a molecule is usually composed by relatively sharp peaks, with energies precisely depending on the structure of the molecule (spectral fingerprint region); therefore, studying infrared absorption spectra allows drawing information on distinctive features of the molecules. Infrared spectroscopy can be used as a quantitative analytical method, since the absorption is proportional to the intensity of the incident light and to the concentration of the considered molecule. This, together with the high selectivity of the method, allows the quantitative determination of an analyte in a complex mixture with limited or no prior separation.

A basic configuration for an IR measurement is shown in Figure 2. A Fourier transform infrared interferometer (FTIR) is often used as the dispersive element especially in the mid and far infrared, because it is more efficient than gratings (and prisms, where there could also be high absorption), especially in producing a higher signal to noise ratio (SNR) (Tozzini and Luin, 2012). However, measurements with this instrument are usually slower, measures on only some subsets of wavelengths are not feasible, and the moving part makes them difficult to implement in a wearable device.

2.2.1 Near infrared spectroscopy

NIR absorption spectroscopy is an analysis technique based on the interactions between matter and electromagnetic radiation with wavelengths between ~700 and ~2,500 nm, corresponding to energies between ~14,000 and ~4,000 cm^{-1}. In this region there is the so-called NIR optical window, i.e. a range of wavelengths (~650–1,350 nm) at which light penetrates tissues the most, thanks to the low absorption of water and haemoglobin.

In the NIR region, the active modes are actually overtone or combination bands, with somehow broader spectra. Moreover, there are some peaks in the absorption spectrum of water, also within the optical window; increasing the concentration of an analyte will decrease the absorption of water in these regions, causing negative peaks in the differential absorption between the studied solution and water (water volume-displacement effects). Moreover, other changes in the absorption spectra could arise because of differences in water hydrogen bonds, due to interactions with the solute.

Often, NIR is combined with photoplethysmography (PPG). PPG is a non-invasive optical technique introduced for the first time in 1937 by Hertzman, who was the first suggesting that a pulse oximeter pleth (Plethysmograph), an instrument for measuring blood or air fluctuations, may be used to detect blood volume changes in the skin's vessels. A typical PPG device is composed by a LED, which emits infrared light on the skin, and by a photodetector, which captures and measures the diffused-reflected light. The resultant PPG tracks were intensely studied for several decades until 2015, when for the first time the PPG signals were analysed by means of hard spectral data processing methods for the first BGL estimation. (Monte-Moreno, 2011; Ramasahayam et al., 2015).

Advantages of the NIR technique are that it is suitable in the presence of interfering substances such as plastic, glass and water, needs relatively low-cost materials and the required photoconductive detectors are highly sensitive. Only three NIR-based devices are currently available on the market, i.e. the Combo Glucometer (Cnoga Medical, Israel), where NIR is combined PPG, one from the Tech4Life entreprise (United States) and the HELO Extense (World Global Network, United States); these are little devices providing a non-invasive glucose detection through the finger. Unfortunately, they need frequent and personalized calibration, thus monitoring the glucose in a non-continuous manner, and often do not measure directly glucose spectral characteristics. (Pfützner et al., 2018; Segman, 2018; Vahlsing et al., 2018; Villena Gonzales et al., 2019).

WizmiTM (Wear2b Ltd., Israel), LifeLeaf$^{®}$ (LifePlus, United States) and two devices from the Polytechnic University of Catalunya (Spain) and the Karunya University (India) are under development (Monte-Moreno, 2011; Hadar et al., 2019; Villena Gonzales et al., 2019; Shang et al., 2022; MEET LIFELEAF, 2022$^{®}$). The first one could offer a non-invasive and continuous glucose monitoring when applied to the arm wrist and the other three could harness the PPG technique when applied on the wrist, finger and forearm, respectively.

Other devices, such as NBM-200G (OrSense Ltd., Israel) and Diasensor 1,000 (Biocontrol Technology, United States), or

GluControl® GC300 (Samsung Fine Chemicals Co., Ltd. & Arith. Med Gmb. H, United States) and one from TouchTrack Pro, were withdrawn or never released, respectively, because of their weak sensitivity and stability, mostly caused by the high scattering of tissues. Indeed, almost all NIR devices suffer from the need to perform frequent recalibrations and from poor selectivity (Oliver et al., 2009; Villena Gonzales et al., 2019; Bolla and Priefer, 2020). Even if there are spectra peaks whose intensity is directly proportional to the concentration of the analyte (glucose), its concentration is very low and there can be many reasons for changes in NIR spectra (e.g., the effects on water discussed above). Accordingly, complex machine learning model and multivariate calibration models, such as partial least squares (PLS) regression, support vector regression or Monte-Carlo simulation, are required for extracting a quantification of glucose in the presence of other physiological substances and tissue components (water, haemoglobin, proteins, fat, etc.) (Kino et al., 2016; Althobaiti and Al-Naib, 2021). For better understanding the state of the art of the non-invasively measured NIR signals from tissue, see studies from the Heise group, who reviewed the progress in emerging glucose monitoring techniques exploiting photoplethysmography within the visible and near-infrared range (Delbeck et al., 2019; Heise et al., 2021).

2.2.2 Mid infrared spectroscopy

Mid Infrared Spectroscopy (MIRS) allows collecting spectra where the contribution of different moieties (including blood glucose) are clearer if compared to NIRS, and therefore it can be more specific (Oliver et al., 2009). MIRS is a vibrational spectroscopy technique that exploits radiation in the mid-infrared region (2.5–25 μm, corresponding to 4,000–400 cm^{-1}), where there is lower scattering from the tissues, and high absorption in the so-called fingerprint region of organic molecules. Conversely, the main problem of this technology is related to the fact that the light has limited penetration in tissues (100 μm approximately) for the strong water absorption, thus making necessary the use of expensive complementary technologies. No devices are currently available, but some products are under development. The start-up DiaMonTech AG (Germany) is developing D-Band, D-Pocket and D-Base, three analogous devices exploiting "photothermal detection" of MIR absorption spectra upon excitation with a tuneable mid-infrared quantum cascade laser (QCL) (Shang et al., 2022; DiaMonTech, 2022; DiaMonTech: Non-Invasive Blood Glucose Monitoring.); these products are based on the researches of Mäntele group, who stated that photoacoustic and photothermal detection seem to provide high accuracy in following glucose absorbance signal, overcoming cross-sensitivities and interpersonal variation of skin glucose level measurements (Lubinski et al., 2021). Indeed, also a device under development by the Swiss Federal Institute of Technology (Switzerland) exploits powerful but expensive QCL MIR sources and photoacoustic detection. (Kottmann et al., 2016; Villena Gonzales et al., 2019). Another device (under development in Tohoku University, Japan) is a minimally invasive device applicable on the inner lips, harnessing an attenuated total internal multireflection geometry (Kino et al., 2016; Villena Gonzales et al., 2019). However, the use of attenuated total reflection for this kind of measures has been criticized due to penetration depth limitations (Delbeck and Heise, 2021).

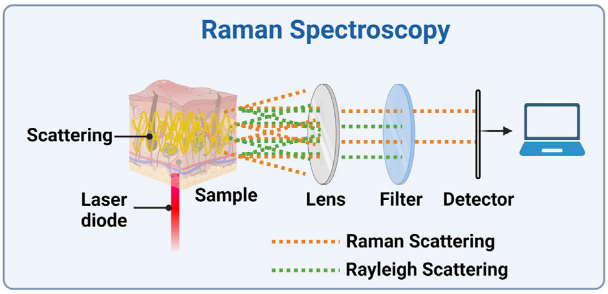

FIGURE 3
Experimental setup for a Raman spectrometer. A laser diode is focused onto the sample and the scattered light is collected by a lens (alternatively, the backscattered light could be collected). The Rayleigh scattered light is then and blocked, while the Raman scattered light can be detected and its spectrum can be analysed. Created with BioRender.com.

2.2.3 Far infrared spectroscopy

At still higher wavelengths there is far infrared radiation (FIR), having wavelengths of ~25–1,000 μm (sub-millimetre waves), corresponding to energies of ~400–10 cm^{-1} or to frequencies between ~12 and 0.3 THz, and therefore it is also known as terahertz radiation. FIR spectroscopy (FIRS), for instance, is less sensitive towards scattering compared to NIR and MIR and does not require frequent calibration. However, the scattered radiation intensity depends on skin temperature and skin thickness, and strong water absorption makes extremely difficult to identify other analytes, such as glucose, in the sample. Therefore, no instrument based on this technology is known to exist or be under development.

Terahertz Time-Domain Spectroscopy (THz-TDS), and Time of Flight (TOF), are nevertheless promising emerging technologies. Despite the long measurement time and the low spatial and depth resolution, these technologies seems more suitable than the IR spectroscopy for the identification of glucose, whatever in solid-state or in aqueous solutions. (Song et al., 2018). Furthermore, the possibility to study broad frequency ranges with a single ultrashort pulse and to make complex permittivity measurement with a single scan are two added values of this approach, which could be exploited in the near future in BGL assessment (Villena Gonzales et al., 2019).

2.3 Raman spectroscopy

Raman spectroscopy allows exploring the vibrational transitions addressed also by MIRS and down to part of the FIRS range; like those, it is a non-destructive optical technique useful for obtaining analytical information on the (bio)chemical composition of a sample (Pandey et al., 2017). This is irradiated by a monochromatic light source usually in the visible or NIR range (typically a laser beam), and the photons scattered by the sample are recorded (Figure 3) (Oliver et al., 2009; Dziergowska et al., 2019). There are two types of scattered light, namely Rayleigh (elastic scattering, at the same frequency of the incident light), and the weaker Raman scattering (anelastic scattering, with different frequencies than the incident light) (Wróbel, 2016; Villena Gonzales et al., 2019). The energy difference between the two scattering modes is the Raman shift, which corresponds to the energy of an excitation of the considered system. As already stated, these excitations are usually vibrational modes, and their spectrum form a unique "fingerprint" of the specific chemical substance (Pandey et al., 2017). Usually, the Stokes Raman peaks (at lower energies than the one of the source photons) are measured, since the Anti-Stokes signal (at higher energies) is much weaker at room and physiological temperatures. Atkins and co-workers (2017) reviewed the literature in the field, listing the published Raman spectroscopy studies of haemoglobin and red blood cells, white blood cells, platelets, plasma and serum, and whole blood (Atkins et al., 2017). RS is so far one of the most promising technologies due to its numerous advantages. The main one is the fact that, by choosing the source in the red region of the spectrum or in the NIR, both source and signal can be within the optical window for tissue transparency, and this allows a good penetration depth (up to millimetres) into human tissue. In this configuration, also an FTIR can be used for obtaining the spectra with the same advantages and disadvantages discussed in Section 2.2; it has been used with 1,064 nm laser excitation also for minimizing the disturbance of fluorescence background (Wang Q. et al., 2021). Other advantages are its unequivocal detection capability (and subsequently high specificity to glucose) without issues of photostability, minimal interference by temperature changes and water presence, and the high amount of developed methods for quantitative data analysis. As a result, Raman spectroscopy has significant potentials to provide precious data in several clinical assessment processes, such as diagnosing cancer, infections or neurodegenerative diseases, as well as for non-invasive BGM (Parlatan et al., 2019).

A more complete review of the research on RS for measuring BGL is reported in Section 3, and the information reported here are for better comparison with the other techniques. Considering devices, apart C8 Medisensors (C8 Medisensors inc., United States), which was never released nominally due to the absence of capital to finalize the design, GlucoBeam (RSP System A/S, Denmark) seems to be the only BGM Raman device under development (Lundsgaard-Nielsen et al., 2018; Villena Gonzales et al., 2019). The authors claim that clinical tests on 600 participants have been already performed and some intrinsic limiting factors typical of Raman, such as the usually low SNR as well as the interference of signals caused by the high complexity of biological tissues and by a strong fluorescence background, have been resolved. However, unstable laser wavelength and intensity, long collection time and accuracy issues need to be solved before future clinical applications (Li et al., 2019; Kang et al., 2020; Pleus et al., 2021; Wróbel et al., 2021).

2.3.1 Surface enhanced Raman spectroscopy

Another strategy to overcome the weakness of Raman signals exploits the high enhancement of the signal when molecules are adsorbed, or at least very close, to metallic surfaces with nanometric features (Tozzini and Luin, 2012). This is exploited in surface enhanced Raman scattering (SERS), where there is both an enhancement of the electromagnetic field for its "storage" in nanoplasmonic modes, and a "chemical" enhancement, due to the interactions of the molecular orbitals with the electronic states in the metal. This technique provides both excellent detection sensitivity (down to single-molecule detection) and the high selectivity of RS (SERS fingerprint spectrum). Reports proved that SERS-active plasmonic devices could represent a useful platform for molecular recognition/sensing inside the body. For instance, Park et al. developed a plasmonic microneedle array coated with gold nanorods and with the pH-sensitive molecule 4-mercaptobenzoic acid as a platform for pH sensing in *ex vivo* human skin (Park et al., 2019). A wearable sensing platform, formed by a flexible SERS-active plasmonic silver superlattice metasurface as key sensing component and by a flexible electronic system for iontophoresis (see Section 2.7), was able to automatically extract sweat and analytes from the body and to reveal trace-amounts of drugs and glucose inside the body (Wang Y. et al., 2021). Over the last years, SERS strategies have opened novel horizons also in diabetes management, as the development of 1) silver-coated intracutaneous microneedle to detect glucose concentrations ranging from 5 to 150 mM (Yuen and Liu, 2014), 2) gold nanorods SERS probe embedded in two-component self-assembled monolayers consisting of 3-mercaptophenylboronic acid and 1-decanethiol, to measure the glucose concentration in the range 2–16 mM (Torul et al., 2014), 3) a subcutaneous glucose sensor by tracking the SERS emission of mercaptophenylboronic acid (MPBA), (Li et al., 2015), 4) composite of gold nanoparticles (AuNPs) onto two-dimensional (2D) nanosheet metalloporphyrinic metal–organic framework (MOF), used for the detection of glucose in saliva (Hu et al., 2020), 5) a glucose sensor based on a poly(methyl methacrylate) (PMMA) microneedle array coated with silver nanoparticles (Ag NPs) to achieve mice intradermal measurements (Ju et al., 2020). Although SERS has been extensively studied for glycaemia management and the usage of such sensors will probably expand more in the coming years, no device is on the market yet. Because of the requirement for the SERS-active surface to touch the analyte, SERS can be used in external or extracted fluids or, in the last reported examples, is not a completely noninvasive technology. Indeed, subcutaneous injection of metal materials can produce toxicity, appropriate microneedles are costly and can easily cause permanent skin damages, and in any case *in-vivo* efficacy has been not completely demonstrated. (Asharani et al., 2008; Ma et al., 2011; Moore et al., 2018; Wang et al., 2022).

2.4 Millimetre and microwave sensing

Millimetre and Microwave sensing (MMS) can be based on reflection, transmission, resonance perturbation and/or radar techniques using electromagnetic fields oscillating at ~30–300 GHz and ~3–30 GHz respectively; in any case, the glucose concentration could be inferred by the dependence of the permittivity of blood and tissues on the glucose concentration, which causes different interactions with the electromagnetic waves (Saha et al., 2017; Shaker et al., 2018). This radiation can penetrate deeper in tissues than more energetic ones, allowing to reach areas with more circulating blood and more glucose, and enhancing therefore the sensitivity for this molecule; always for the deep penetration of these waves, it is possible to perform glucose measurements on different areas of body (hand, abdomen, ear lobe and other portions of skin). Several universities and companies from Europe and United States (MediWise, University of Waterloo and Google, University of Cardiff, Caltech University and University of Erlangen-Nuremberg) are currently developing devices for a non-invasive glycemia tracking exploiting the previously mentioned advantages (Choi et al., 2017; Shaker et al., 2018; Villena Gonzales et al., 2019; Omer et al., 2020). However, it is worth noting that these devices are not suitable for continuous glucose monitoring (i.e. Glucowise™ or Google Soli, both equipped with 60 GHz mm-wave radar, could be not user-friendly after a long exposure) and the penetration of signal can be affected from physiological parameters such as sweating, breathing and cardiac activity; thus, the glucose concentration measurement could be inaccurate.

2.5 PhotoAcoustic spectroscopy

This technology allows developing a relatively simple and compact sensor, employing a nanosecond-pulsed QCL or a modulated laser, with wavelength from the ultraviolet to the MIR ranges, and exploiting the fact that absorption of radiation by an analyte produces microscopically localized heating. This causes a fast and adiabatic thermal expansion of the sample and the generation of detectable acoustic waves as a consequence (Villena Gonzales et al., 2019). Therefore, absorbance spectra in any of the regions discussed above can be measured by detection with ultrasound detectors, and the variations of blood glucose level can be calculated similarly to the all-optical methods, with the advantage that the tissues mostly transmit sound waves (Figure 4). However, the signal may not be intense enough (low SNR) and it may be susceptible to temperature, motion, pulsation and surrounding acoustics; moreover, the integration time could be long (several minutes) (Oliver et al., 2009). Some examples of PAS-based devices under development have been reported above, especially in Section 2.2.2. Other possible examples are Aprise (Glucon, United States) and another device from the Electronics and Telecomm. Research Inst. of Korea (Republic of Korea), but they are almost unknown and not on the market (Kottmann et al., 2016; Sim et al., 2018; Dziergowska et al., 2019; Villena Gonzales et al., 2019).

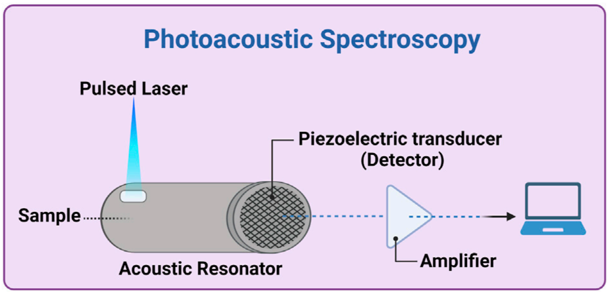

FIGURE 4
Photoacoustic spectroscopy experimental setup. A thermal expansion of the sample (inside or in contact with the acoustic resonator) is generated by a pulsed laser source (e.g., a quantum cascade -QC- laser). The generated acoustic waves propagate through the acoustic resonator and, after amplification and possibly ADC (analogic-digital converter), is analyzed by a computer. Created with BioRender.com.

2.6 Enzymatic detection technology

Enzymatic detection represents the first developed method to reveal glucose level. Through technologies exploiting enzymatic reactions, it is possible to provide a direct and efficient measurement not only from blood, but also from other biological fluids (e.g., tears and interstitial fluid) (Park et al., 2018). The commercially available CGM sensors based on enzymatic detection, without the typical long-term stability issue of enzyme, are: 1) Guardian Sensor 3 (Medtronic Plc., United States) (Cappon et al., 2017; Christiansen et al., 2017; Lee et al., 2021; Shang et al., 2022), 2) Dexcom G6 (DexCom, Inc., United States) (Cappon et al., 2017; Boscari et al., 2021, 2022; Lee et al., 2021; Shang et al., 2022), and 3) Free Style Libre (Abbott Ltd., United States) (Cappon et al., 2017; Blum, 2018; Galindo et al., 2020; Jafri et al., 2020; Lee et al., 2021; Shang et al., 2022). All three electrochemical sensors works by means of an enzymatic sensor, equipped with sterile and fluffy microneedles, which are subcutaneously inserted (on abdomen or upper arm), and the following automatic data sharing on smartphone. However, every 7, 10 and 14 days, respectively for Medtronic, Dexcom and Abbott, the sensors need to be replaced. In the last years, research institutes have been moving towards the development of similar but longer-life CGM devices. It is this case for: 1) K'Watch, a skin patch under development by PKvitality (France); 2) the devices under development by KTH Royal Inst. of Technology (Sweden), to be applied on the forearm; 3) mouthguard glucose sensor, from Tokyo Medical and Dental University (Japan) and 4) the biosensor platform from the iQ Group Global Ltd. (formerly iQnovate, Australia), exploiting the Organic Thin Film Transistor technology, both developed to monitor salivary glucose that is reported to be correlated with the BGL; 5) the device from Ulsan National Inst. of Science and Technology (South Korea) and 6) NovioSense from Novio Tech Campus (Netherlands), both exploiting eye glucose monitoring technology (Dastoor and Belcher, 2017; Kownacka et al., 2018; Park et al., 2018; Ribet et al., 2018; Villena Gonzales et al., 2019; Arakawa et al., 2020; Shang et al., 2022). Data on most of these devices are not in the public domain. However, it should be mentioned that, although all of them are able to check the glycaemia level with a painless scan instead of fingersticks, they are all considered minimally invasive devices (Ventrelli et al., 2015).

2.7 Reverse iontophoresis

Reverse Iontophoresis (RI) is a minimally invasive technique, based on an electrochemical apparatus applicable on the skin that can extract glucose from the interstitial fluid (ISF). Upon application of electrodes and then of an electric field, the flux of the target compound is possible thanks to passive diffusion and electroosmosis, which is a net movement of water across the skin from anode to cathode and results when the electric field is applied across the negatively-charged skin (the isoelectric point of human skin is around 4–4.5); glucose is then revealed through enzymatic methods (Dziergowska et al., 2019). The first two example of RI continue glucose monitoring devices were developed in the United Kingdom. SugarBEAT (Nemaura Medical, United Kingdom), available on the market, is a daily upper arm disposable sensor whilst another device from the University of Bath (United Kingdom), under development, seems to use a graphene-based transdermal platform. (Lipani et al., 2018; Villena Gonzales et al., 2019; Shang et al., 2022). The main advantages of devices employing a RI technology are that electrodes are not difficult to manufacture and they are easily applied to skin; in addition, there is a good correlation between glucose level in the ISF and in the blood under stable conditions. GluCall (K.M.H Co., Ltd., South Korea) is another RI device currently present on the market but not widely used due to its high degree of invasiveness. Common disadvantages of RI devices are high susceptibility to sweating, slowness in responding to rapid changes of glucose concentration, besides provoking skin irritation due to the passage of current. For these reasons, and for the low reliability, another RI continuous monitoring glucose device, named GlucoWatch (Cygnus Inc., United States) was withdrawn (Oliver et al., 2009; Villena Gonzales et al., 2019).

2.8 Sonophoresis technology

Sonophoresis is a well-known drug delivery method relying on low-frequency pressure waves to move molecules into and across the skin. Sonophoresis instruments induce a series of compression and expansion movements and enhance the permeability of the skin; by slight changes in the geometry, they can be used to extract ISF with glucose, similarly to RI, allowing a CGM by means of enzymatic methods (Oliver et al., 2009; Dziergowska et al., 2019). On the other side, determining the relationship between the extracted glucose quantity and the BGL is usually difficult, and can be susceptible to temperature and pressure variations, to environmental parameters, and to the presence of other compounds. Based on sonophoresis approach, the American company Echo Therapeutics is currently trying to develop "Symphony", a CGM device catalogued as a minimally invasive technology, even if it seems to harness a user-friendly approach as there is no side-effect to skin (Villena Gonzales et al., 2019).

2.9 Fluorescence technology

Although an old patent based on an assumptive fluorescence of glucose excited at 308 nm is reported, glucose actually has no detectable fluorescence when excited in the visible or near-UV range (Khalil, 2004; Pullano et al., 2022). Fluorescence technologies make instead use of fluorophores that, once bound to the analyte (e.g., glucose), are able to emit fluorescent light with distinctive optical properties (mostly, excitation and detection wavelengths). Thus, the analyte concentration can be measured in terms of fluorescence intensity and/or decay times. Fluorescence technology is receiving much attention for its high sensitivity and specificity also in scattering media such as blood, skin layers or tears; however, it requires contact between the fluid to be analysed and the fluorophores, likewise enzymatic detection (Dziergowska et al., 2019). In this contest, Eversense® CGM under-skin biosensor (Senseonics, United States) is today available on the market. Furthermore, another under-skin patch (from Profusa, inc., United States) and a contact lens, that can monitor the

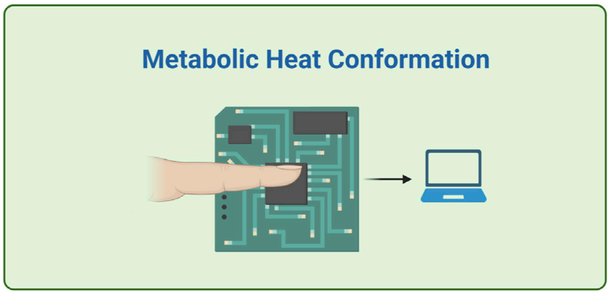

FIGURE 5
A schematics of a simplified MHC device, where the detection system transforms information about temperature, humidity, blood flow rate and degree of blood oxygen saturation into estimation of glucose level. Created with BioRender.com.

glucose concentration in tears, are currently under development (Chen et al., 2017; Badugu et al., 2018; Villena Gonzales et al., 2019; Jafri et al., 2020). The last one is based on an optical fluorescent sensor that monitor the BGL chemically through a boronic-acid derivative support containing the fluorophore; the higher the glucose amount, the more boronic acid converts from neutral to anionic form, and the bigger the spectral variations retrieved by the detector (Badugu et al., 2004, 2018; Gamsey et al., 2006). Despite their ability to reveal glucose at very low concentration (lower than 25 μM for Eversense®), none of these devices is currently widely used worldwide. As a matter of fact, they are not exempt from invasiveness: they need an "exogenous" fluorescence-based sensor/indicator in contact with the analyte, the foreign body containing all this is inserted within biological media, and this may lead to local tissue trauma and potential toxicity issues. In addition, they suffer from the intrinsic FT issues related to autofluorescence and its limitations associated with photostability/photobleaching. Because of these obstacles, the research has quickly moved towards less invasive CGM devices (Oliver et al., 2009; Villena Gonzales et al., 2019). Such is the case of DermalAbyss (Massachusetts Institute of Technology, United States), relying on a colour-based indicator for glucose concentration that can be used in a pioneering tissue-integrating tattoo (Vega et al., 2017). This is now under development and represents a promising biosensor for continuous monitoring, despite issues related to the very high sensitivity to local pH changes and/or oxygen levels.

2.10 Metabolic heat conformation

MHC technology consists in deducing glycaemia level from measurements of physiological indicators related to metabolic heat generation and local oxygen amount, such as pulse rate, oxyhaemoglobin saturation, heat metabolic rate and the blood flow volume, via well-known multi-wavelength (MIR/NIR range) spectroscopy methods (Figure 5) (Dziergowska et al., 2019; Villena Gonzales et al., 2019). GlucoGenius (ESER Health Care Digital Technology Co. Ltd., Taiwan) is the only available device on the market, while other non-invasive devices, one from Health-Care Computer (Japan) and G2 Mobile (Eser Digital, India), are under development. Hitachi Ltd. (Japan) announced in 2004 the development of a unique non-invasive blood sugar monitoring device for diabetics but it was never released (Okura et al., 2018; Villena Gonzales et al., 2019). The main issue of these tools is that they don't provide a direct glucose monitoring; besides, they suffer of high sensitivity towards temperature and sweat; thus, MHC doesn't seems a suitable technology for continuous glucose monitoring purpose (Bolla and Priefer, 2020).

2.11 Bioimpedance spectroscopy

Bioimpedance spectroscopy (BS) was a very popular technology in the early 2000s. It is supposedly based on the fact that the conductivity of the red blood cells membranes can be correlated with variation of blood glycaemia level, since the glucose concentration influences the sodium-potassium currents in cells (Oliver et al., 2009; Dziergowska et al., 2019). Pendra (Pendragon Medical Ltd., Switzerland) and Glucoband (Calisto Medical, Inc., United States) were the first two developed BS devices that allowed an easy CGM measurement on arm wrist cheaply (Villena Gonzales et al., 2019). On the other side, the conductivity was measured by means of the application of a current on the skin for a long time, which could cause irritation. Moreover, as MHC technology, BS is sensitive to variations of temperature, to motion, to sweat and to water content. For these reasons, Pendra and Glucoband were withdrawn few years after their release and are considered obsolete (Huang et al., 2020).

2.12 Optical coherence tomography

Optical Coherence Tomography (OCT) is a medical imaging technique, initially born as an ocular diagnostic test and evolved later as tomographic imaging of different tissues also sensible to various analytes, such as glucose. OCT is typically a non-invasive method, characterized by a good SNR due to NIR light, deeply penetrating in the skin. Although it can suffer from tissue inhomogeneity, this technology does not seem susceptible to blood pressure, haematocrit and cardiac activity (Dziergowska et al., 2019; Villena Gonzales et al., 2019). There's currently only one device from the National Cheng Kung University (Taiwan), considered however not suitable for continuous glucose monitoring (Chen et al., 2018; Villena Gonzales et al., 2019). Researchers are currently trying to overcome some OCT related issues, such as the high sensitivity to temperature changes of the skin and to motion, and the lack of chemical specificity for glucose (Oliver et al., 2009; Wróbel, 2016).

2.13 MultiTechnologies

The technologies already described are analytical methods used for the determination of glucose by using one or more of its intrinsic molecular properties, or by assessing the effects of glucose on the physical properties of blood and/or tissues. However, glucose determination with different methods presents different drawbacks and it is limited by the influence of interfering factors (which could be, e.g., temperature, humidity, motion of the sensor, or other physio-pathological parameters of the PWD). Accordingly, the development of a tool that combines several technologies may decrease the errors derived from each method separately, or can be used to determine the interfering factors in order to correct the glucose measure. Starting from 2009, researchers from the Integrity Applications (Israel) placed on the market GlucoTrack, apparently a combination of ultrasound, thermal and electromagnetic sensing device, a non-invasive glucose monitoring device intended for people with type 2 diabetes for use in home and home-alike environments. (Harman-Boehm et al., 2009; Villena Gonzales et al., 2019; Shang et al., 2022). For measuring BGL upon a personal calibration valid for 1 month, a personal ear clip, equipped with both sensors of hypo- and hyperglycaemia and calibration electronics, is attached to the earlobe. This latter is an interesting site since its accessibility and the abundant supply of blood to it. The device is lightweight, compact and safe and seems to achieve very high accuracy and precision in clinical trials due to combination of multiple technologies (Mohamad Yunos and Nordin, 2020). More recently, other technologies have been developed. Evia Medical Technologies Limited (Saudi Arabia), exploiting similar technology than GlucoTrack, has developed Egm1000™, an ear-lobe glucose monitoring device available for type 2 diabetes (Mosli and Madani, 2021). To date, GlucoTrack and Egm1000™ are not suitable for a CGM because they are not really wearable.

In another kind of multitechnology approach, the United States researchers Xu and Berry are currently trying to exploit graphene's Raman spectroscopy (GRS) as a tool for reading the activity of a glucose oxidase (GOx) enzymatic-based detector or the response to glucose in an affinity-based detector; RS can indeed measure the changes in graphene dopant level and/or Fermi energy caused by these kinds of detectors without employing conventional electrical measurements (Ahmadianyazdi et al., 2022). The reported measurements have been done on fluids containing glucose; however, once device sensitivity, measurement uncertainty, sample-to-sample variation, and compatibility with biological fluids will be overcome, this glucose sensor could represent a complementary tool for the study of molecular interaction phenomena at the interface with graphene and a promising glycaemia continuous monitoring biosensor.

2.14 Other technologies

Besides the above described approaches, there are several other technologies that could be employed in BGL estimation but no BGM devices are currently on the market due to drawbacks mainly related to reliability, size or cost. Optical Polarimetry Technology (OPT) is an optical measurement method that relies on rotation of light polarization due to the optical activity of an analyte. The aqueous humour of the eye has been identified as the fittest tissue for BGL measurements with this technique, because of low protein and erythrocytes contents and therefore negligible scattering. However, OPT is not a front-line technology for glycaemia sensing purpose, firstly due to the intrinsic low optical activity of glucose. Furthermore, several challenges have yet to be addressed such as high sensitivity to interferences (other optically active compounds), temperature, pH changes and motion and the need of an external laser source and proper alignment with eye (Oliver et al., 2009; Dziergowska et al., 2019; Villena Gonzales et al., 2019; Bolla and Priefer, 2020).

Surface Plasmon Resonance Technology (SPRT) is a refractive index-based detection technology not suitable for BGL assessment since glucose and other low molecular weight compounds have insufficient mass to affect a measurable change in the refractive index. Moreover, this technique is very sensitive to temperature, sweat and motion, and the instruments are generally bulky and require a long calibration time (Villena Gonzales et al., 2019).

Electromagnetic sensing (EMS) is a low-cost, easily miniaturized and safe technology, which supposedly exploits the dependence on glucose of the magnetic permittivity of tissues. However, several challenges, such as the low glucose selectivity as well as the high sensitivity to temperature, have to be addressed before making EMS technology available for glycaemia measurement (Villena Gonzales et al., 2019; Bolla and Priefer, 2020).

Ultrasound Technology (UT) is a well-established technology, not harmful to cells, and highly sensitive for qualitative/quantitative analysis due to the long penetration through skin and other tissues of ultrasound waves. Its sensitivity to glucose is linked to the dependence of sound velocity on glucose concentration. However, UT is not a suitable approach for BGL measurement, due to the limited accuracy (pressure changes and temperature fluctuations can cause interferences, and therefore it is often coupled with NIRS) as well as the high cost (Villena Gonzales et al., 2019; Bolla and Priefer, 2020).

Occlusion Spectroscopy (OS), based on red light or NIR scattering often in the reflected-diffusion configuration, is suitable for the non-invasive measurement of arterial glucose. However, due to the susceptibility to many endovascular variables, such as pharmacological treatment, internal erythrocyte aggregation, free fatty acid concentration and chylomicrons (ULDLs), this technology cannot be used to develop BGM devices without a complex algorithm, still lacking, to extract glucose information (Shokrekhodaei and Quinones, 2020).

RadioFrequency Sensor Technology (RFST) is another approach to monitor the different levels of blood glucose concentration (Moore, 2009; Yilmaz et al., 2019; Yunos et al., 2021). Compared to sensors with different mechanisms, Alertgy® (Alertgy Ltd., United States) and UBAND™ (Know Labs, United States) RF devices are advantageous in terms of their fast response (Shang et al., 2022; Meet Alertgy NICGM, 2022. Blood Glucose Monitoring. In The Convenience of a Wristband. For Diabetics. For Healthcare. Using Non-invasive Deep-Gluco®; UBAND-Know Labs, 2021. Bio-RFID™. Transforming Non-Invasive Medical Diagnostics). However, they are not highly sensitive systems, and need to take into account a large number of external factors (such as temperature variability, the effect of pressure and the effect of sweat) to accurately determine the effective permittivity of glucose.

Indigo Diabetes, 2021 (INDIGO DIABETES N.V., Belgium) is a subcutaneous implant which exploit NanoPhotonics Technology (NPT). Indigo Diabetes may work through an on-chip inert and miniature spectrometer by measuring the absorption of light in the individual's interstitial fluid and by quantifying the concentration of multiple metabolites simultaneously without the use of enzymes or fluorophores (INDIGO Giving people with diabetes the extra sense for health).

Regarding urine test strips, although results are quickly displayed, they are not extremely accurate, since there is an uncertain correlation between glucose in blood and urine; moreover, this technique is not adapt to continuous fast measurements (Oliver et al., 2009; Dziergowska et al., 2019).

Skin Suction Blister (SSB) is a technique based on the accumulation and collection of analytes from interstitial fluid (ISF) by applying vacuum to a skin area. The pressure splits the dermis and epidermis, and the blister fluid from the nearby tissues is next extracted by a syringe (Niedzwiecki et al., 2018). Compared to other ISF sampling approaches, such as RI technology, suction blister sampling is more user-friendly since it is a painless procedure but needs to be optimized for the high sensitivity to temperature and pressure variations and to the interference of other compounds (Oliver et al., 2009; Dziergowska et al., 2019).

Exhaled Breath Analysis (EBA) is an emergent methodology for glycaemia estimation: the exhaled breath gases contains several body metabolism biomarkers, such as acetone. Ketone Breathalyzer (KB) could be a possible device to use in blood glucose level (BGL) estimation, if the correlation between blood glucose and breath acetone levels will be better understood and if the sensitivity to variations of temperature could be decreased or corrected. Previous tests demonstrated 1) the possibility to have good correlation between blood glucose and breath acetone levels and 2) the "Keto Diet" should not have significant impact in terms of accuracy standpoint. Ketone Breathalyzer is cheap, fast and user-friendly; however, to date, EBA remains unreliable and challenging because of the huge mixture of volatile organic compounds (more than 3,500) present in the breath (Bolla and Priefer, 2020; Shokrekhodaei and Quinones, 2020; Dixit et al., 2021). The main advantages and drawbacks of each glucose test technology are listed in Supplementary Table S1, while most of the BGL technologies and devices are summarized in Supplementary Table S2 and in the recent review article by David C. Klonoff group. (Shang et al., 2022).

3 Raman

It has been over 24 years since James Lambert, Michael Storrie-Lombardi and Mark Borchert at the Jet Propulsion laboratory, California institute of technology (Caltech), United States, did the first measurement of physiological glucose level using Raman Spectroscopy (RS) (Lambert et al., 1998). They combined this technique with multivariate analysis to measure glucose level in the aqueous humour of a rabbit model. The foremost (most intense) Raman peaks at 911 cm^{-1} and 1,125 cm^{-1} are considered the Raman fingerprints of glucose. The concept of RS would be elegantly developed later for the analysis of other analytes, such as lactate, urea and ascorbate. In 2005, Lambert et al. settled key parameters (laser power, of the order of mW, retinal power density, mW/cm^2, and exposure time, seconds) to achieve, by RS instruments, a reliable aqueous-humour glucose-level estimation within an acceptable range of safety and patient tolerability (see setup instrument Table 1 row B) (Lambert et al., 2005).

The same year, the first non-invasive ("transcutaneous") Raman measurement was made (see setup instrument Table 1 row A). The raw Raman spectra from 17 subjects were dominated by spectral components of the human skin, such as human callus skin, collagen I and III, dermal and epidermal structural proteins, and triolein, as well as of human haemoglobin, water, cholesterol, elastin, phosphatidylcholine and actin, rather than glucose. Consequently, a reliable multivariate calibration method, such as partial least squares (PLS) regression analysis, was employed for the first time in order to analyse the Raman spectra, highlighting the glucose Raman peaks from the other signals (treated as background). In particular, the background was removed by least-squares fitting each spectrum to a fifth order polynomial and subtracting this polynomial from the spectrum. The authors of the study were the first to provide quantitative information about glucose by examining blood samples (Enejder et al., 2005).

TABLE 1 Example of Raman setups.

	Raman excitation source	Beam power (mW)	Spot dimension	Spectral range	Measurement time	Sensitivity, selectivity, accuracy	Spectral data processing	References
A	830 nm diode laser	300	1 mm^2 (area; on human skin)	355–1,545 cm^{-1}	2 s integration time (90 times)	MAE: 5.0%, R^2: 0.93	PLS analysis, Savitsky – Golay algorithm, EGA Analysis	Enejder et al. (2005)
B	785 nm Ti: sapphire laser	100	~1.01 mm (diameter; on rabbit retina)	300–1,500 cm^{-1}	3 s integration time (50 times)	RMSECV: 24.0mg/dl, R^2: 0.99	PLS analysis, EGA Analysis	Lambert et al. (2005)
C	785 nm diode laser	15	~0.002 mm (diameter; on mouse skin)	500–1800 cm^{-1}	15 s integration time (25 times)	MAE: 5.7%, R^2: 0.91	PLS analysis	Shao et al. (2012)
D	785 nm diode laser	400	~ 8 mm (diameter; on human skin)	541–1818 cm^{-1}	10 s integration time (10 times)	R^2: 0.83	PLS analysis, EMSC, EGA Analysis	Scholtes-Timmerman et al. (2014)
E	830 nm continuous-wave diode laser	300	0.005 mm^2 (area; on human skin)	300–1800 cm^{-1}	3 min integration time (1 time)	ISUP: 1.9 MARD: 25.8%, R^2: 0.69	ISUP parameter, 15-point Savitsky-Golay 1st order algorithm, EMSC	Lundsgaard-Nielsen et al. (2018)
F	830 nm diode laser (incidence angle of 60°)	250	~1.6 mm^2 (area; on swine ear skin)	810–1,650 cm^{-1}	4.75 min integration time (1 time)	Intrasubject R^2: 0.94 Intersubject R^2: 0.62	Savitzky-Golay filtering, polynomial baseline subtraction, MLR analysis	Kang et al. (2020)
G	830 nm diode laser	50	0.5 mm (diameter; on human skin)	400–1800 cm^{-1}	0.1 s integration time (6,000 times)	-	Estimation of power spectral density, Savitzky-Golay filtering	Wróbel et al. (2021)

PLS, partial least squares regression; EGA, clarke error grid; EMSC, extended multiplicative scatter correction; ISUP, Inter-subject unified performance; MAE, mean absolute error; MARD, mean absolute relative difference; MLR, multiple linear regression; RMSECV, root-mean-squared-error of cross validation.

Starting from that year, advanced data processing and analysis techniques, allowing the quantitative glucose detection in the combined Raman spectrum, have always been essential. Furthermore, several problems, such as transferring calibration models between patients due to changes in skin compositions, to turbidity-induced alterations in the Raman spectral intensities and peak widths, to the physiological lag between glucose level in blood and interstitial fluid (ISF) as well as to the millimolar detection limit of spontaneous Raman scattering combined with the low physiological concentration of glucose (4–10 mM), made of utmost importance the development of an accurate and robust chemometric (estimating the concentration) algorithm to be used in multiple human subjects or in the same subject at different times. The most commonly methods employed to build a multivariate calibration model were multiple linear regression (MLR), principal component regression (PCR) and partial least squares (PLS); however, they provided reasonable results on single subjects but they had poor predictivity across a cohort of people. Consequently, Barman et al. (2010a) proposed the first nonlinear calibration method for BGM. Construction of nonlinear calibration models has formed a cornerstone of the research efforts, enhancing the glucose prediction performance by almost 30% when compared to PLS-derived results (Barman et al., 2010b; 2010a).

In the same year, Chaiken and co-workers proposed the incorporation into the measurement device of an active tissue placement interface, useful also for modulating the relative optical coupling of mobile tissue components (blood, interstitial fluids) with respect to the one of static components, by impacting on blood circulation (Chaiken et al., 2010).

Dingari et al., in 2011, employed tissue phantom, animal and human subject experimental cases to investigate the impact of other analytes in the blood–tissue matrix, possibly with concentration changing with time, on the measures of BGL using RS (Dingari et al., 2011). Indeed, time-dependent physiological processes make the relation between glucose concentration and spectral data very complex. Amongst other results, these studies reported that Raman-spectra based calibration models were significantly more robust than similar models constructed from NIR absorption spectra when the concentration of the glucose was intentionally kept constant and the concentrations of other spectral interferents were varied randomly. In the same year, the same group analysed algorithms for determining optical properties of tissues using detection of diffuse light scattering; these can be used to correct the impact of a turbid medium, like skin, on Raman scattering signals collected simultaneously (Barman et al., 2011; Wróbel et al., 2021).

In 2012, Shao et al. proposed focusing lasers directly on dermal blood vessels (see Table 1 row C) in order to decrease the background signal, and using Raman measurement sequence within two physical state with and without occlusion of blood circulation in the measured region (Shao et al., 2012). While in the unpressed state, the laser irradiates the "free finger", thus the Raman signals come from both skin and blood, in the pressed state the measured Raman spectrum included contributions especially from skin constituents, since the pressure placed on the finger triggers the expulsion of most of the blood from the capillary bed. In this last condition, the measured Raman spectrum tends to show lower peaks, including from glucose signal. The most intense (best SNR) characteristic glucose Raman peak appears at 1,125 cm^{-1} and it was used to determine the glucose concentrations both in 1–400 mmol/dl glucose water solution, *in vitro*, and *in vivo* (mouse ear blood vessel). Although the authors state that they could not detect Raman signals at glucose concentrations below 500 mmol/L in water solution, even with very long exposure (10 min), they also state to have observed a clear linear relationship between Raman intensity and blood glucose concentration between ~50 and ~160 mmol/L *in vitro* and *in vivo*, after normalization of the glucose peak at 1,125 cm^{-1} using the haemoglobin one at 1,549 cm^{-1} (used as internal standard).

Scholtes-Timmerman group devised in 2014 a new Raman spectroscopic analysis system based on the subtraction of non-glucose-induced variable components from the spectra collected from a cohort of 111 hospitalized patients; the spectra were collected through the forearm skin of the patients, and the variable components where calculated starting from a principal component decomposition on spectra collected from patients grouped according to their glycaemia (see Table 1 row D for some information on the used setup) (Scholtes-Timmerman et al., 2014).

A radically different advancement was proposed in 2016 by the Polish M.S. Wróbel group, which suggested several promising improvement for a miniaturized Raman spectroscopy device: 1) a set-up simplification, in which only the Raman signals at the selected energies are detected by a set of photodetectors; 2) an analysis with Principal Component Analysis (PCA) as explorative analytical method, and a PLS-Regression or other advanced techniques (PLS-DA, SVM-regression) as more precise methods; 3) the detection of Raman signal from the dynamic components in transcutaneous spectroscopy, i.e., the moving blood (Wróbel, 2016). This can be done by exploiting the heartbeat, which modulates the quantity of blood present in the volume of observation. The detection of the dynamic component of the Raman signal varying with the heartbeat should eliminate the signals arising from the static components, such as solid tissues (skin, muscle, vessel walls, lipids, etc.). Steps toward the detection of the pulse frequency and the filtering of the periodical signal with suitable algorithms has further opened the door for the estimation of the pulse-correlated Raman signal by a Raman spectrometer equipped with a photopletysmographic detector (see Table 1 row G). There are several factors that may interfere in the final Raman spectra, such as turbidity-induced variations, changes in fluorescence of blood and/or of bulk tissue, red blood cells aggregation-disaggregation in capillaries, the differential nature of oxy- and deoxy-hemoglobin spectra or the hemodynamic pressure that induces expansion of the vessels; however, this approach has two main advantages. First, the achieved Raman spectra are less patient-specific, because optical parameters and chemical composition of blood are much more consistent over the human population of different races and ages than the ones of the surrounding solid tissue; second, measurements can be performed for a longer time utilizing natural blood pulse, with respect to techniques exploiting external occlusion of the blood flux, assuring better averaging and noise reduction.

An intriguing advance, proposed by Motz et al. (2004) and next developed by Kong et al. (2011), Ghenuche et al. (2012) and Pandey et al. (2017), concerns the development of tailored optical fiber probes for delivery and collection of light to and from the tissue interface. The ultimate achievement on optical fiber-probe based Raman instrument lead to measure reliably the Raman signal from a tissue spot in a lighted room (Motz et al., 2004; Kong et al., 2011; Ghenuche et al., 2012; Pandey et al., 2017).

Lundsgaard-Nielsen et al. (2018) introduced a new RS study of glucose sensing for non-invasive glucose detection in human skin (Lundsgaard-Nielsen et al., 2018). They employed a new table-top confocal Raman spectrometer on a cohort of 35 patients, obtaining highly correlated values between the measured glucose concentrations against the reference ones (see setup in Table 1 row E). The high reliability and accuracy of their device essentially come from two smart developed approaches. First, they presented the evidence that the optimal glucose-containing layer of the skin is below the stratum corneum: collecting the Raman signal from the interstitial fluid compartment at 250–300 μm of depth, they were able to note that the time lag (5 min) of changes in glucose concentration between the capillary and interstitial compartments was clearly lower than others reported in literature (almost 45 min). Moreover, Lundsgaard-Nielsen's group focused on the development of new spectral data processing: after spectra smoothing and corrections (15-point Savitsky-Golay 1st order algorithm and extended multiplicative scatter correction), they used PLS regression calibrated on 25 days for testing the setup in the last 5 days of the trial. Owing to the different behaviour amongst the PWDs concerning the quantification of BGL, they created, and relied on, an Inter-Subject Unified Performance (ISUP) parameter for comparing results amongst different patients, especially for understanding the optimum detection depth in human skin. The developed device is a small, user-friendly, but non-continuous, Raman-based glucometer, called GlucoBeam, which can operate for ~10 days without recalibration (Shang et al., 2022). Both calibration models and performance of GlucoBeam system were checked and assessed as comparable to the earlier scanning CGM FreeStyle Libre (Abbott Diabetes Care) system by a very recent report, performing the research on a cohort of 15 insulin-treated subjects with type 1 diabetes (Pleus et al., 2021). However, to date, this Danish device is still under development, probably to solve the need of continuous recalibration and/or for optimizing the reliability of the device.

In 2019, Li et al. employed another approach based on the Renishaw inVia confocal Raman spectrometer, enhanced by Optical Coherence Tomography (OCT) (Li et al., 2019). The measurement was performed by focusing the laser on the microvessels in the superficial layer of the extremely thin nailfold at 100–200 μm depths in the skin, reaching the stratum corneum and epidermis in order to avoid the background arising from the dermis and the physiological lag between blood glucose and ISF glucose. This approach, together with the use of sophisticated mathematical analyses based on PCA combined with back propagation artificial neural network (BP-ANN), enabled to establish high prediction accuracy for BGL estimation.

A radically different advancement was established in 2020 by Kang et al. by the construction of a high optical throughput noncontact vertical Raman system, equipped with an oblique angle (off-axis) laser, which overcome the result of a conventional endoscope-type Raman probe contacted to skin (Singh et al., 2018) and the limits of a conventional radiant angle (on-axis) Raman laser (see setup instrument Table 1 row F) (Kang et al., 2020). While this latter has a limited sampling volume and presses the skin during long measurements, the new oblique angle incidence device maximizes the effective sampling volume since more volume contribute to Raman scattering under the oblique angle illumination, decreases the collection of background signals and allows a stable long-term measurement without skin contact. Furthermore, this new Raman technology, combined with a robust spectral data processing method, allowed to achieve surprising results in terms of linearity between intensities of the glucose Raman peaks (911, 1,060, and 1,125 cm^{-1} glucose fingerprint peaks) and the reference glucose concentrations, especially when an additional Raman band at 1,450 cm^{-1}, arising from skin proteins and lipids, was considered for normalization.

4 Discussion

In this review, we elucidated the several available approaches for BGL assessment. Choosing the best technique requires to consider a number of factors crucial to its implementation, including invasiveness, continuity, long-term stability, reliability, and miniaturization. Indeed, the ideal glycaemia biosensor should be: 1) quantitative and accurate, at least within the glycaemia ranges discussed in the introduction; 2) reliable, and in particular it should give the value of BGL without delay; 3) cheap, small, and wearable, so that every diabetic patient can have one with or on them all the time; 4) user-friendly: it should be easy to be applied to patients; 5) non-invasive, i.e. it should not need anything inserted in or extracted from the body of the patients; 6) safe and not discomforting, e.g. not causing skin irritation; 7) continuous, or at least able to perform a measurement many times in an hour; 8) exempt from recalibration; this last point, actually, is related to several of the previous ones: (re)calibration is not user-friendly, needs another possibly invasive method for determining BGL, if needed it means that the sensor loses accuracy with time, and measurements are stopped during recalibration.

Regarding (ii), biofluids different from blood or interstitial fluid, like sweat, saliva, exhaled breath condensate, urine and tears, have been considered, since they can be obtained easily (Tang et al., 2020). However, 1) the biofluids glucose concentration is lower than that in blood (see concentrations in physiological fluids of healthy and diabetic patients in (Mohamad Yunos and Nordin, 2020)), therefore more sensitive techniques and a correlation calculation are required; 2) there is a delay in transmission of glucose levels from the blood to the other fluids, and this can represent a problem especially when BGL is rapidly changing, which is maybe the situation in which knowing the BGL and its trajectory is most needed.; 3) daily biofluids collection is sometimes inconvenient or not feasible, especially for elderly patients: e.g., urine cannot be used for continuous glucose-monitoring due to its intermittent nature, or sweat quantities are changing with the environmental situation or the activity of the PWD and there could be the need to extract it with electrophoresis or sonophoresis techniques; 4) the accuracy of the tests is significantly affected by biological parameters, including pH, temperature, mechanical/friction effects, and contamination. More research needs to be address to have an accurate relationship between glucose levels in blood and other fluids before they can be used with therapeutic intervention. As an example, glucose levels in sweat can be correlated, but not perfectly, with blood glucose levels although it lags by about 8 min the levels in blood. (Mohamad Yunos and Nordin, 2020). This did not stop researches for monitoring sweat glucose: we report wearable skin pads based on colorimetric fluorescent probes, a new user-friendly electrochemical sensor that however needs personalized precalibration; a self-powered smartwatch; and the already cited SERS-based wearable sensors (Zhao et al., 2019; Cui et al., 2020; Wang Y. et al., 2021, 2022; Sempionatto et al., 2021).

Minimally invasive devices (i.e. subcutaneous electrochemical sensors) partially decrease the discomfort of fingerstick testing, and are at the moment the most used ones for a continuous glucose monitoring (e.g., the Free Style Libre of Abbott Ltd., United States). However, a shift toward fully non-invasive prototypes would address several limitations of this category.

As stated in the introduction, the best (and maybe only) choice for truly non-invasive continuous blood glucose monitoring devices should be based on measurement where both excitation source and signal can pass through the patients' tissues, thus probably leaving only electromagnetic techniques and measurements of movements and/or sound/pressure. The developed medical devices should be based on glucose intrinsic molecular properties, such as its near-infrared or mid-infrared absorption coefficient, optical rotation, Raman shifts and photoacoustic properties, and these would allow in principle a direct BGL estimation. However, on humans it is difficult to obtain the best geometry for exploiting quantitatively many of these techniques, or (equivalently) to find a way for normalizing the glucose signal(s); moreover, the signals arising from other, possibly much more abundant, body components may affect the results, and these often depend on characteristics and physiological state of the subjects. Differently than for these devices based on direct measurements on the glucose molecules, indirect and nonspecific methods exploit the effect of glycaemia on the biological/chemical/physical properties of blood and tissues. Indeed, the effects of changing glycaemia on the various signals (e.g., spectra) could arise not only from the different impact of the ones arising from the glucose molecules, but also from variations in the relative abundance or from different chemical modifications of other moieties, e.g. the ones involved in cell metabolism. Of course, both factors (glucose fingerprints and indirect glycaemia-induced variations) are usually present at the same time, and other factors can similarly affect the signal, like changing device properties (sensor–skin interface, source fluctuation in terms of power or spectral characteristic, etc.) or differences due to people's intrinsic factors, both constant or slowly changing (age, gender, ethnicity, lifestyle, comorbidities, etc.), or fluctuating through the day (activity, hydration, blood supply and pressure, metabolic rate, environmental impacts, etc.).

All these factors must be considered in analysing the data: the spurious signals are often fully or at least partially eliminated through a calibration process, sometimes exploiting the fact that usually glycaemia is assumed to be more fluctuating than what is causing them. Many data analyses exploited advanced analysis techniques, often based on "artificial intelligence"/"machine learning", for separating the contributions in signals linked to BGL from the spurious ones. In these cases, the system requires a (possibly long) period of calibration in which the analysis algorithm is "trained" by correlating the measured signal/spectrum with the glycaemia measured by a standard method (e.g. finger pricking). A thorough discussion on the details of all the analysis algorithms is beyond the scope of this review; however, in general, the acquired signals are usually "fitted" as a (possibly linear) combination of components, and the "weight" of at least one of them is a function (often linear, but not always) of the BGL; the weight(s) of one or more of the other components can be used for normalization (e.g., signals arising from water, or from haemoglobin, etc.), and this can take into account at least the impact of the above mentioned device factors. This process can be carried out explicitly in data analysis, e.g. in methods based on PCA or simply by considering the heights of peaks specific to glucose and to blood or water, or can be hidden in the used algorithm (e.g. in "deep learning" based methods). The purpose of the calibration is to find the best "components" and the relation of the "weights" of these components with BGL. The calibration can be carried out in single individuals (personalized calibration), or on a cohort of people. The first case produces results that are more reliable, but can require long calibration times and recalibration is needed relatively often; in the second case, it is in principle possible to identify and then correct more interfering factors, and this could bring to a "universal" device, without, or with very short, personalized calibration. For this aim, we envision the production and use of libraries of the possible components of "signals," perhaps stratified for some characteristics like gender, ethnicity, age groups; these libraries could be uploaded in the BGM devices to be used in the data analysis without calibration, or at least as a starting point for the calibration procedure. Despite the possible use of "blind" AI algorithms for extracting BGL from various signals/spectra and for creating these "libraries," understanding the source of the various components can help in guiding the analysis process or for the pre-treatment of data.

We discussed above the advantages and the drawbacks of most of the technologies considered for continuous non-invasive quantitative glucose sensing. The most-used electromagnetic-radiation-based quantitative setups in laboratories (i.e., spectrophotometers) usually measure the extinction of light in a transmission configuration, with controlled optical path and a reference for the baseline. However, this is difficult to implement in wearable devices, also for the low transmissivity of the tissues in the spectral ranges of characteristic glucose absorption. Therefore, absorption of the tissues is usually measured in a back-scattering geometry, exploiting the random scattering of radiation from tissues, and this make a universal calibration more difficult.

Raman signals, instead, are per se collected at high angles with respect to the direction of the exciting laser, or even in back-scattering geometry. Raman spectra contains fingerprints of glucose and of other substances including water, and this can be used in principle to normalize the spectrum for calculating directly the concentrations. Moreover, by properly choosing the excitation light in the NIR region, both source and signal (Raman Stokes peaks) fall in the tissues transparency window (~650–1,350 nm), and this allow to reach deeper regions with more abundance of blood or at least of interstitial fluid. One of the most cited drawbacks for Raman spectroscopy is its low cross section, and therefore a weak signal. Increasing laser power can increase the SNR, but can be harmful, and the maximum permissible exposure (MPE) for skin laser irradiation must be considered. As a rule of thumb, at 788 nm the MPE raises (with the fourth root of time) from $3 \times 10–2$ J/cm^2 for times less than or equal to 10^{-7} s, up to 3 J/cm^2 for 10 s, and above this time the intensity must be below 0.3 W/cm^2 (Maini, 2013). Since the limits are on intensity or energy density, one possibility to increase the SNR is to increase the illuminated and observed area; however, some of the work discussed above considered instead focusing the laser in a region below the first layers of skin, in a region richer in ISF and/or in capillary blood.

In any case, also the Raman signal from the background is weaker, and this helps in obtaining a sufficient SNR, especially by choosing spectral regions where autofluorescence of tissues is low; moreover, glucose spectrum has features in regions where the background spectrum could be very small. Indeed, in some of the studies reviewed in §2.3 and §3, the height of just one or some of the glucose-fingerprint peaks are correlated to glycaemia (Shao et al., 2012; Kang et al., 2020). For example, in the above cited work by Shao et al. (Shao et al., 2012)., they correlated the height of the peak at 1,125 cm^{-1} with the glycaemia, normalizing the data using a characteristic peak of haemoglobin at 1,549 cm^{-1}. It is interesting to notice, however, that the height of the peak at 1,125 cm^{-1} did not tend to zero at very low BGLs (and this can explain why the authors could correlate his intensity to values below the minimum one at which they could discern, with the same setup, Raman spectra of glucose dissolved in water). The remaining non-negligible signal at very low glucose concentration in blood can have two components: 1) close Raman signals from other substances, e.g. the peak at 1,126 cm^{-1} due to a pyrrole half-ring stretching mode in haemoglobin; 2) Raman signal from glucose inside the cells, especially in non-circulating ones.

These two kinds of interference have to be considered in general. The first one can be solved by considering whole spectra and whole spectral components, as discussed above; this can also improve the uncertainty in the final measurement. Indeed, most of the devices being considered for commercialization use this method.

The second effect is subtler. Although the total glucose in the observation volume (the one from which the signal is collected) is correlated with the concentration of glucose in plasma, being able to discern the signal arising only from mobile fluids would allow a direct determination of the glycaemia, independent from or much less dependent on calibrations and corrections. As discussed above, one possibility is to consider the spectral differences in the same tissue when there are different amounts of liquids. This has been done, e.g., with occlusion spectroscopy, but maybe the most promising approach for continuous wearable devices is to exploit the differences in blood and interstitial fluid content caused by the heart pulse. It could be possible to consider just the periodically varying part in continuously-collected Raman signals, but extracting the changing component could be helped by considering the correlation between the cross correlation of the heartbeat, measured e.g. by gravitometry, pressure sensors, or PPG signal, with the Raman one. Data analysis should also consider that the spectral changes do not arise simply by increasing blood content in the tissue: the observation volume is approximately constant, so the amount of observed blood anticorrelates with the observed quantity of the remaining tissues, and these contain glucose, water, and other biomolecules as well. The idea of having other sensors integrated in a single device is interesting also because collecting other parameters together with the heartbeat (like temperature, blood pressure, blood oxygen level, etc.) can help analysing the spectra and correcting the measured glycaemia: e.g., it could be possible to correlate some "signal components" changes to some of these parameters, and this will help in determining their weight in the total detected spectra.

5 Conclusion and perspectives

A fully integrated and self-powered NIGM smartwatch or similar device is highly desirable in daily diabetes management. Several findings on the technical aspects of NIGM devices have matured over the last decades. In particular, Raman technology, together with sophisticated prediction algorithms, seems to have solid basis for further improvements in this field. As an example, the Raman-based GlucoBeam (RSP System A/S, Denmark) seems one of the best user-friendly device to provide self-monitoring glucose measurement, although it still suffers from poor reliability, poor long-term stability and unsolved issues with variations amongst patients (Lundsgaard-Nielsen et al., 2018; Pleus et al., 2021).

In order to expand the use of RS methodology, future efforts should aim at 1) maximizing the sensitivity in experiments 2) reducing the integration time (or exploiting changes in time of the signal) 3) miniaturizing the system and 4) improving the understanding of the factors affecting the inter-individual variations. Notably, we believe that a real-time and continuous RS device exploiting blood pulse (combined with the suitable detection algorithm) represents nowadays the best emergent technology for our purpose, even if the reliability of such device should be verified during both storing status and dynamic activities.

Author contributions

BT and SL wrote the manuscript, with discussion with and review by FB and FS; BT prepared the figures with contributions from SL. SL supervised the work. All Authors conceptualized the work. All authors read and approved the final manuscript.

Funding

This work has been supported by the Open Access Publishing Fund of the Scuola Normale Superiore. The authors declare that this study received funding from P.B.L. SRL. The funder was not involved in the study design, collection, analysis, interpretation of data, the writing of this article or the decision to submit it for publication.

Conflict of interest

Author FB and FS are employed by P.B.L. SRL, Italy, and by Omnidermal Biomedics SRL, Italy.

The remaining authors declare that the research was conducted in the absence of any commercial or financial relationships that could be construed as a potential conflict of interest.

Publisher's note

Supplementary material

The Supplementary Material for this article can be found online at: https://www.frontiersin.org/articles/10.3389/fchem.2022.994272/full#supplementary-material

References

Ahmadianyazdi, A., Nguyen, N. H. L., Xu, J., and Berry, V. (2022). Glucose measurement via Raman spectroscopy of graphene: Principles and operation. *Nano Res.* doi:10.1007/s12274-022-4587-9

Althobaiti, M., and Al-Naib, I. (2021). Optimization of dual-channel near-infrared non-invasive glucose level measurement sensors based on monte-carlo simulations. *IEEE Photonics J.* 13, 1–9. doi:10.1109/JPHOT.2021.3079408

Arakawa, T., Tomoto, K., Nitta, H., Toma, K., Takeuchi, S., Sekita, T., et al. (2020). A wearable cellulose acetate-coated mouthguard biosensor for *in vivo* salivary glucose measurement. *Anal. Chem.* 92, 12201–12207. doi:10.1021/acs.analchem.0c01201

Asharani, P. V., Lian Wu, Y., Gong, Z., and Valiyaveettil, S. (2008). Toxicity of silver nanoparticles in zebrafish models. *Nanotechnology* 19, 255102. doi:10.1088/0957-4484/19/25/255102

Atkins, C. G., Buckley, K., Blades, M. W., and Turner, R. F. B. (2017). Raman spectroscopy of blood and blood components. *Appl. Spectrosc.* 71, 767–793. doi:10.1177/0003702816686593

Badugu, R., Lakowicz, J. R., and Geddes, C. D. (2004). Ophthalmic glucose monitoring using disposable contact lenses—a review. *J. Fluoresc.* 14, 617–633. doi:10.1023/B:JOFL.0000039349.89929.da

Badugu, R., Reece, E. A., and Lakowicz, J. R. (2018). Glucose-sensitive silicone hydrogel contact lens toward tear glucose monitoring. *J. Biomed. Opt.* 23, 1. doi:10.1117/1.JBO.23.5.057005

Barman, I., Dingari, N. C., Rajaram, N., Tunnell, J. W., Dasari, R. R., and Feld, M. S. (2011). Rapid and accurate determination of tissue optical properties using least-squares support vector machines. *Biomed. Opt. Express* 2, 592. doi:10.1364/BOE.2.000592

Barman, I., Kong, C.-R., Dingari, N. C., Dasari, R. R., and Feld, M. S. (2010a). Development of robust calibration models using support vector machines for spectroscopic monitoring of blood glucose. *Anal. Chem.* 82, 9719–9726. doi:10.1021/ac101754n

Barman, I., Kong, C.-R., Singh, G. P., Dasari, R. R., and Feld, M. S. (2010b). Accurate spectroscopic calibration for noninvasive glucose monitoring by modeling the physiological glucose dynamics. *Anal. Chem.* 82, 6104–6114. doi:10.1021/ac100810e

Blood Sugar Level Ranges (2019). Diabetes.co.UK. Available at: https://www.diabetes.co.uk/diabetes_care/blood-sugar-level-ranges.html (Accessed January 15, 2019).

Blum, A. (2018). Freestyle Libre glucose monitoring system. *Clin. Diabetes* 36, 203–204. doi:10.2337/cd17-0130

Bolla, A. S., and Priefer, R. (2020). Blood glucose monitoring- an overview of current and future non-invasive devices. *Diabetes & Metabolic Syndrome Clin. Res. Rev.* 14, 739–751. doi:10.1016/j.dsx.2020.05.016

Boscari, F., Vettoretti, M., Amato, A. M. L., Vallone, V., Uliana, A., Iori, E., et al. (2021). Comparing the accuracy of transcutaneous sensor and 90-day implantable glucose sensor. *Nutr. Metab. Cardiovasc. Dis.* 31, 650–657. doi:10.1016/j.numecd.2020.09.006

Boscari, F., Vettoretti, M., Cavallin, F., Amato, A. M. L., Uliana, A., Vallone, V., et al. (2022). Implantable and transcutaneous continuous glucose monitoring system: A randomized cross over trial comparing accuracy, efficacy and acceptance. *J. Endocrinol. Invest.* 45, 115–124. doi:10.1007/s40618-021-01624-2

Cappon, G., Acciaroli, G., Vettoretti, M., Facchinetti, A., and Sparacino, G. (2017). Wearable continuous glucose monitoring sensors: A revolution in diabetes treatment. *Electronics* 6, 65. doi:10.3390/electronics6030065

Chaiken, J., Bussjager, R. J., Shaheen, G., Rice, D., Stehlik, D., and Fayos, J. (2010). Instrument for near infrared emission spectroscopic probing of human fingertips *in vivo*. *Rev. Sci. Instrum.* 81, 034301. doi:10.1063/1.3314290

Chen, L., Tse, W. H., Chen, Y., McDonald, M. W., Melling, J., and Zhang, J. (2017). Nanostructured biosensor for detecting glucose in tear by applying fluorescence resonance energy transfer quenching mechanism. *Biosens. Bioelectron. X.* 91, 393–399. doi:10.1016/j.bios.2016.12.044

Chen, T.-L., Lo, Y.-L., Liao, C.-C., and Phan, Q.-H. (2018). Noninvasive measurement of glucose concentration on human fingertip by optical coherence tomography. *J. Biomed. Opt.* 23, 1. doi:10.1117/1.JBO.23.4.047001

Choi, H., Luzio, S., Beutler, J., and Porch, A. (2017). Microwave noninvasive blood glucose monitoring sensor: Human clinical trial results, in 2017 IEEE MTT-S International Microwave Symposium (IMS), Honolulu, HI, USA, 04-09 June 2017, IEEE, 876–879. doi:10.1109/MWSYM.2017.8058721

Christiansen, M. P., Garg, S. K., Brazg, R., Bode, B. W., Bailey, T. S., Slover, R. H., et al. (2017). Accuracy of a fourth-generation subcutaneous continuous glucose sensor. *Diabetes Technol. Ther.* 19, 446–456. doi:10.1089/dia.2017.0087

Clarke, S. F., and Foster, J. R. (2012). A history of blood glucose meters and their role in self-monitoring of diabetes mellitus. *Br. J. Biomed. Sci.* 69, 83–93. doi:10.1080/09674845.2012.12002443

Cui, Y., Duan, W., Jin, Y., Wo, F., Xi, F., and Wu, J. (2020). Ratiometric fluorescent nanohybrid for noninvasive and visual monitoring of sweat glucose. *ACS Sens.* 5, 2096–2105. doi:10.1021/acssensors.0c00718

Dastoor, P., and Belcher, W. (2017). *Organic thin film transistors and the use thereof in sensing applications*. US patent US9766199B2, 12.

Delbeck, S., and Heise, H. M. (2021). Evaluation of opportunities and limitations of mid-infrared skin spectroscopy for noninvasive blood glucose monitoring. *J. Diabetes Sci. Technol.* 15, 19–27. doi:10.1177/1932296820936224

Delbeck, S., Vahlsing, T., Leonhardt, S., Steiner, G., and Heise, H. M. (2019). Non-invasive monitoring of blood glucose using optical methods for skin spectroscopy—Opportunities and recent advances. *Anal. Bioanal. Chem.* 411, 63–77. doi:10.1007/s00216-018-1395-x

DiaMonTech (2022). DiaMonTech: Non-Invasive blood glucose monitoring. Available at: https://www.diamontech.de/home (Accessed March 04, 2022).

Dingari, N. C., Barman, I., Singh, G. P., Kang, J. W., Dasari, R. R., and Feld, M. S. (2011). Investigation of the specificity of Raman spectroscopy in non-invasive blood glucose measurements. *Anal. Bioanal. Chem.* 400, 2871–2880. doi:10.1007/s00216-011-5004-5

Dixit, K., Fardindoost, S., Ravishankara, A., Tasnim, N., and Hoorfar, M. (2021). Exhaled breath analysis for diabetes diagnosis and monitoring: Relevance, challenges and possibilities. *Biosensors* 11, 476. doi:10.3390/bios11120476

Dziergowska, K., Łabowska, M. B., Gąsior-Głogowska, M., Kmiecik, B., and Detyna, J. (2019). Modern noninvasive methods for monitoring glucose levels in patients: A review. *Bio-Algorithms Med-Syst.* 15. doi:10.1515/bams-2019-0052

Enejder, A. M. K., Scecina, T. G., Oh, J., Hunter, M., Shih, W.-C., Sasic, S., et al. (2005). Raman spectroscopy for noninvasive glucose measurements. *J. Biomed. Opt.* 10, 031114. doi:10.1117/1.1920212

Galindo, R. J., Migdal, A. L., Davis, G. M., Urrutia, M. A., Albury, B., Zambrano, C., et al. (2020). Comparison of the FreeStyle Libre Pro flash continuous glucose monitoring (CGM) system and point-of-care capillary glucose testing in hospitalized patients with type 2 diabetes treated with basal-bolus insulin regimen. *Diabetes Care* 43, 2730–2735. doi:10.2337/dc19-2073

Gamsey, S., Suri, J. T., Wessling, R. A., and Singaram, B. (2006). Continuous glucose detection using boronic acid-substituted viologens in fluorescent hydrogels: Linker effects and extension to fiber optics. *Langmuir* 22, 9067–9074. doi:10.1021/la0617053

Ghenuche, P., Rammler, S., Joly, N. Y., Scharrer, M., Frosz, M., Wenger, J., et al. (2012). Kagome hollow-core photonic crystal fiber probe for Raman spectroscopy. *Opt. Lett.* 37, 4371. doi:10.1364/OL.37.004371

Hadar, E., Chen, R., Toledano, Y., Tenenbaum-Gavish, K., Atzmon, Y., and Hod, M. (2019). Noninvasive, continuous, real-time glucose measurements compared to reference laboratory venous plasma glucose values. *J. Maternal-Fetal Neonatal Med.* 32, 3393–3400. doi:10.1080/14767058.2018.1463987

Harman-Boehm, I., Gal, A., Raykhman, A. M., Zahn, J. D., Naidis, E., and Mayzel, Y. (2009). Noninvasive glucose monitoring: A novel approach. *J. Diabetes Sci. Technol.* 3, 253–260. doi:10.1177/193229680900300205

Heineman, W. R., and Jensen, W. B. (2006). Leland C. Clark Jr. (1918–2005). *Biosens. Bioelectron. X.* 21, 1403–1404. doi:10.1016/j.bios.2005.12.005

Heise, H. M., Delbeck, S., and Marbach, R. (2021). Noninvasive monitoring of glucose using near-infrared reflection spectroscopy of skin—constraints and effective novel strategy in multivariate calibration. *Biosensors* 11, 64. doi:10.3390/bios11030064

Hu, S., Jiang, Y., Wu, Y., Guo, X., Ying, Y., Wen, Y., et al. (2020). Enzyme-free tandem reaction strategy for surface-enhanced Raman scattering detection of glucose by using the composite of Au nanoparticles and porphyrin-based metal–organic framework. *ACS Appl. Mat. Interfaces* 12, 55324–55330. doi:10.1021/acsami.0c12988

Huang, H.-W., You, S. S., Di Tizio, L., Li, C., Raftery, E., Ehmke, C., et al. (2022). An automated all-in-one system for carbohydrate tracking, glucose monitoring, and insulin delivery. *J. Control. Release* 343, 31–42. doi:10.1016/j.jconrel.2022.01.001

Huang, J., Zhang, Y., and Wu, J. (2020). Review of non-invasive continuous glucose monitoring based on impedance spectroscopy. *Sensors Actuators A Phys.* 311, 112103. doi:10.1016/j.sna.2020.112103

IDF Diabetes Atlas (2019). IDF diabetes Atlas. Available at: https://diabetesatlas.org/atlas/ninth-edition/(Accessed December 16, 2021).

Indigo Diabets (2021). INDIGO Giving people with diabetes the extra sense for health. Available at: https://indigomed.com (Accessed December 21, 2021).

Jafri, R. Z., Balliro, C. A., El-Khatib, F., Maheno, M. M., Hillard, M. A., O'Donovan, A., et al. (2020). A three-way accuracy comparison of the Dexcom G5, Abbott Freestyle Libre Pro, and senseonics Eversense continuous glucose monitoring devices in a home-use study of subjects with type 1 diabetes. *Diabetes Technol. Ther.* 22, 846–852. doi:10.1089/dia.2019.0449

Ju, J., Hsieh, C.-M., Tian, Y., Kang, J., Chia, R., Chang, H., et al. (2020). Surface enhanced Raman spectroscopy based biosensor with a microneedle array for minimally invasive *in vivo* glucose measurements. *ACS Sens.* 5, 1777–1785. doi:10.1021/acssensors.0c00444

Kang, J. W., Park, Y. S., Chang, H., Lee, W., Singh, S. P., Choi, W., et al. (2020). Direct observation of glucose fingerprint using *in vivo* Raman spectroscopy. *Sci. Adv.* 6, eaay5206. doi:10.1126/sciadv.aay5206

Khalil, O. S. (2004). Non-invasive glucose measurement technologies: An update from 1999 to the dawn of the new millennium. *Diabetes Technol. Ther.* 6, 660–697. doi:10.1089/dia.2004.6.660

Kharroubi, A. T. (2015). Diabetes mellitus: The epidemic of the century. *World J. Diabetes* 6, 850. doi:10.4239/wjd.v6.i6.850

Kino, S., Omori, S., Katagiri, T., and Matsuura, Y. (2016). Hollow optical-fiber based infrared spectroscopy for measurement of blood glucose level by using multi-reflection prism. *Biomed. Opt. Express* 7, 701. doi:10.1364/BOE.7.000701

Kong, C.-R., Barman, I., Dingari, N. C., Kang, J. W., Galindo, L., Dasari, R. R., et al. (2011). A novel non-imaging optics based Raman spectroscopy device for transdermal blood analyte measurement. *AIP Adv.* 1, 032175. doi:10.1063/1.3646524

Kottmann, J., Rey, J., and Sigrist, M. (2016). Mid-infrared photoacoustic detection of glucose in human skin: Towards non-invasive diagnostics. *Sensors* 16, 1663. doi:10.3390/s16101663

Kownacka, A. E., Vegelyte, D., Joosse, M., Anton, N., Toebes, B. J., Lauko, J., et al. (2018). Clinical evidence for use of a noninvasive biosensor for tear glucose as an alternative to painful finger-prick for diabetes management utilizing a biopolymer coating. *Biomacromolecules* 19, 4504–4511. doi:10.1021/acs.biomac.8b01429

Lambert, J. L., Pelletier, C. C., and Borchert, M. (2005). Glucose determination in human aqueous humor with Raman spectroscopy. *J. Biomed. Opt.* 10, 031110. doi:10.1117/1.1914843

Lambert, J., Storrie-Lombardi, M., and Borchert, M. (1998). Measurement of physiologic glucose levels using Raman spectroscopy in a rabbit aqueous humor model. *IEEE Lasers Electro-Opt. Soc. U. S. A.* 6, 19095.

Lee, I., Probst, D., Klonoff, D., and Sode, K. (2021). Continuous glucose monitoring systems - current status and future perspectives of the flagship technologies in biosensor research -. *Biosens. Bioelectron. X.* 181, 113054. doi:10.1016/j.bios.2021.113054

Li, N., Zang, H., Sun, H., Jiao, X., Wang, K., Liu, T. C.-Y., et al. (2019). A noninvasive accurate measurement of blood glucose levels with Raman spectroscopy of blood in microvessels. *Molecules* 24, 1500. doi:10.3390/molecules24081500

Li, S., Zhou, Q., Chu, W., Zhao, W., and Zheng, J. (2015). Surface-enhanced Raman scattering behaviour of 4-mercaptophenyl boronic acid on assembled silver nanoparticles. *Phys. Chem. Chem. Phys.* 17, 17638–17645. doi:10.1039/C5CP02409A

Lipani, L., Dupont, B. G. R., Doungmene, F., Marken, F., Tyrrell, R. M., Guy, R. H., et al. (2018). Non-invasive, transdermal, path-selective and specific glucose monitoring via a graphene-based platform. *Nat. Nanotechnol.* 13, 504–511. doi:10.1038/s41565-018-0112-4

Lubinski, T., Plotka, B., Janik, S., Canini, L., and Mäntele, W. (2021). Evaluation of a novel noninvasive blood glucose monitor based on mid-infrared quantum cascade laser technology and photothermal detection. *J. Diabetes Sci. Technol.* 15, 6–10. doi:10.1177/1932296820936634

Lundsgaard-Nielsen, S. M., Pors, A., Banke, S. O., Henriksen, J. E., Hepp, D. K., and Weber, A. (2018). Critical-depth Raman spectroscopy enables home-use non-invasive glucose monitoring. *PLOS ONE* 13, e0197134. doi:10.1371/journal.pone.0197134

Ma, K., Yuen, J. M., Shah, N. C., Walsh, J. T., Glucksberg, M. R., and Van Duyne, R. P. (2011). *In vivo*, transcutaneous glucose sensing using surface-enhanced spatially offset Raman spectroscopy: Multiple rats, improved hypoglycemic accuracy, low incident power, and continuous monitoring for greater than 17 days. *Anal. Chem.* 83, 9146–9152. doi:10.1021/ac202343e

Maini, A. K. (2013). *Lasers and optoelectronics: Fundamentals, devices and applications*. Chichester, West Sussex, United Kingdom: John Wiley & Sons.

Meet Alertgy NICGM (2022). Blood glucose monitoring in the convenience of a wristband. Available at: https://www.alertgy.com (Accessed January 13, 2022).

MEET LIFELEAF (2022). The first non-invasive device for continuous, real-time remote patient monitoring. Available at: https://www.lifeplus.ai (Accessed June 26, 2022).

Mohamad Yunos, M. F. A., and Nordin, A. N. (2020). Non-invasive glucose monitoring devices: A review. *Bull. EEI.* 9, 2609–2618. doi:10.11591/eei.v9i6.2628

Monte-Moreno, E. (2011). Non-invasive estimate of blood glucose and blood pressure from a photoplethysmograph by means of machine learning techniques. *Artif. Intell. Med.* 53, 127–138. doi:10.1016/j.artmed.2011.05.001

Moore, B. (2009). The potential use of radio frequency identification devices for active monitoring of blood glucose levels. *J. Diabetes Sci. Technol.* 3, 180–183. doi:10.1177/193229680900300121

Moore, T., Moody, A., Payne, T., Sarabia, G., Daniel, A., and Sharma, B. (2018). *In vitro* and *in vivo* SERS biosensing for disease diagnosis. *Biosensors* 8, 46. doi:10.3390/bios8020046

Mosli, H. H., and Madani, B. M. (2021). Performance evaluation of egm1000^{TM} non-invasive glucose monitoring device in patients with type 2 diabetes and subjects with prediabetes. *Int. J. Med. Dev. Ctries.* 5 (4), 1020–1028. doi:10.24911/IJMDC.51-1611360395

Motz, J. T., Hunter, M., Galindo, L. H., Gardecki, J. A., Kramer, J. R., Dasari, R. R., et al. (2004). Optical fiber probe for biomedical Raman spectroscopy. *Appl. Opt.* 43, 542. doi:10.1364/AO.43.000542

Niedzwiecki, M. M., Samant, P., Walker, D. I., Tran, V., Jones, D. P., Prausnitz, M. R., et al. (2018). Human suction blister fluid composition determined using high-resolution metabolomics. *Anal. Chem.* 90, 3786–3792. doi:10.1021/acs.analchem.7b04073

Okura, T., Teramoto, K., Koshitani, R., Fujioka, Y., Endo, Y., Ueki, M., et al. (2018). A computer-based glucose management system reduces the incidence of forgotten glucose measurements: A retrospective observational study. *Diabetes Ther.* 9, 1143–1147. doi:10.1007/s13300-018-0427-z

Oliver, N. S., Toumazou, C., Cass, A. E. G., and Johnston, D. G. (2009). Glucose sensors: A review of current and emerging technology. *Diabet. Med.* 26, 197–210. doi:10.1111/j.1464-5491.2008.02642.x

Omer, A. E., Shaker, G., Safavi-Naeini, S., Kokabi, H., Alquié, G., Deshours, F., et al. (2020). Low-cost portable microwave sensor for non-invasive monitoring of blood glucose level: Novel design utilizing a four-cell CSRR hexagonal configuration. *Sci. Rep.* 10, 15200. doi:10.1038/s41598-020-72114-3

Pandey, R., Paidi, S. K., Valdez, T. A., Zhang, C., Spegazzini, N., Dasari, R. R., et al. (2017). Noninvasive monitoring of blood glucose with Raman spectroscopy. *Acc. Chem. Res.* 50, 264–272. doi:10.1021/acs.accounts.6b00472

Park, J. E., Yonet-Tanyeri, N., Vander Ende, E., Henry, A.-I., Perez White, B. E., Mrksich, M., et al. (2019). Plasmonic microneedle arrays for *in situ* sensing with surface-enhanced Raman spectroscopy (SERS). *Nano Lett.* 19, 6862–6868. doi:10.1021/acs.nanolett.9b02070

Park, J., Kim, J., Kim, S.-Y., Cheong, W. H., Jang, J., Park, Y.-G., et al. (2018). Soft, smart contact lenses with integrations of wireless circuits, glucose sensors, and displays. *Sci. Adv.* 4, eaap9841. doi:10.1126/sciadv.aap9841

Parlatan, U., Inanc, M. T., Ozgor, B. Y., Oral, E., Bastu, E., Unlu, M. B., et al. (2019). Raman spectroscopy as a non-invasive diagnostic technique for endometriosis. *Sci. Rep.* 9, 19795. doi:10.1038/s41598-019-56308-y

Pfützner, A., Strobl, S., Demircik, F., Redert, L., Pfützner, J., Pfützner, A. H., et al. (2018). Evaluation of a new noninvasive glucose monitoring device by means of standardized meal experiments. *J. Diabetes Sci. Technol.* 12, 1178–1183. doi:10.1177/1932296818758769

Pleus, S., Schauer, S., Jendrike, N., Zschornack, E., Link, M., Hepp, K. D., et al. (2021). Proof of concept for a new Raman-based prototype for noninvasive glucose monitoring. *J. Diabetes Sci. Technol.* 15, 11–18. doi:10.1177/1932296820947112

Pullano, S. A., Greco, M., Bianco, M. G., Foti, D., Brunetti, A., and Fiorillo, A. S. (2022). Glucose biosensors in clinical practice: Principles, limits and perspectives of currently used devices. *Theranostics* 12, 493–511. doi:10.7150/thno.64035

Ramasahayam, S., Koppuravuri, S. H., Arora, L., and Chowdhury, S. R. (2015). Noninvasive blood glucose sensing using near infra-red spectroscopy and artificial neural networks based on inverse delayed function model of neuron. *J. Med. Syst.* 39, 166. doi:10.1007/s10916-014-0166-2

Ribet, F., Stemme, G., and Roxhed, N. (2018). Real-time intradermal continuous glucose monitoring using a minimally invasive microneedle-based system. *Biomed. Microdevices* 20, 101. doi:10.1007/s10544-018-0349-6

Saha, S., Cano-Garcia, H., Sotiriou, I., Lipscombe, O., Gouzouasis, I., Koutsoupidou, M., et al. (2017). A glucose sensing system based on transmission measurements at millimetre waves using micro strip patch antennas. *Sci. Rep.* 7, 6855. doi:10.1038/s41598-017-06926-1

Scholtes-Timmerman, M. J., Bijlsma, S., Fokkert, M. J., Slingerland, R., and van Veen, S. J. F. (2014). Raman spectroscopy as a promising tool for noninvasive point-of-care glucose monitoring. *J. Diabetes Sci. Technol.* 8, 974–979. doi:10.1177/1932296814543104

Segman, Y. J. (2018). Device and method for noninvasive glucose assessment. *J. Diabetes Sci. Technol.* 12, 1159–1168. doi:10.1177/1932296818763457

Sempionatto, J. R., Moon, J.-M., and Wang, J. (2021). Touch-based fingertip blood-free reliable glucose monitoring: Personalized data processing for predicting blood glucose concentrations. *ACS Sens.* 6, 1875–1883. doi:10.1021/acssensors.1c00139

Shaker, G., Smith, K., Omer, A. E., Liu, S., Csech, C., Wadhwa, U., et al. (2018). Non-invasive monitoring of glucose level changes utilizing a mm-wave radar system. *Int. J. Mob. Hum. Comput. Interact.* 10, 10–29. doi:10.4018/IJMHCI.2018070102

Shang, T., Zhang, J. Y., Thomas, A., Arnold, M. A., Vetter, B. N., Heinemann, L., et al. (2022). Products for monitoring glucose levels in the human body with noninvasive optical, noninvasive fluid sampling, or minimally invasive technologies. *J. Diabetes Sci. Technol.* 16, 168–214. doi:10.1177/19322968211007212

Shao, J., Lin, M., Li, Y., Li, X., Liu, J., Liang, J., et al. (2012). *In vivo* blood glucose quantification using Raman spectroscopy. *PLoS ONE* 7, e48127. doi:10.1371/journal.pone.0048127

Shokrekhodaei, M., and Quinones, S. (2020). Review of non-invasive glucose sensing techniques: Optical, electrical and breath acetone. *Sensors* 20, 1251. doi:10.3390/s20051251

Sim, J. Y., Ahn, C.-G., Jeong, E.-J., and Kim, B. K. (2018). *In vivo* microscopic photoacoustic spectroscopy for non-invasive glucose monitoring invulnerable to skin secretion products. *Sci. Rep.* 8, 1059. doi:10.1038/s41598-018-19340-y

Singh, S. P., Mukherjee, S., Galindo, L. H., So, P. T. C., Dasari, R. R., Khan, U. Z., et al. (2018). Evaluation of accuracy dependence of Raman spectroscopic models on the ratio of calibration and validation points for non-invasive glucose sensing. *Anal. Bioanal. Chem.* 410, 6469–6475. doi:10.1007/s00216-018-1244-y

Smith, John L. (2021). *The pursuit of noninvasive glucose: "Hunting the deceitful Turkey*. 8th edition. https://www.nivglucose.com/The%20Pursuit%20of%20Noninvasive%20Glucose%208th%20Edition.pdf (Accessed September 5, 2022).

Song, C., Fan, W.-H., Ding, L., Chen, X., Chen, Z.-Y., and Wang, K. (2018). Terahertz and infrared characteristic absorption spectra of aqueous glucose and fructose solutions. *Sci. Rep.* 8, 8964. doi:10.1038/s41598-018-27310-7

Tang, L., Chang, S. J., Chen, C.-J., and Liu, J.-T. (2020). Non-invasive blood glucose monitoring technology: A review. *Sensors* 20, 6925. doi:10.3390/s20236925

Todaro, B., Moscardini, A., and Luin, S. (2022). Pioglitazone-loaded PLGA nanoparticles: Towards the most reliable synthesis method. *Int. J. Mol. Sci.* 20, 2522. doi:10.3390/ijms23052522

Torul, H., Çiftçi, H., Dudak, F. C., Adıgüzel, Y., Kulah, H., Boyacı, İ. H., et al. (2014). Glucose determination based on a two component self-assembled monolayer functionalized surface-enhanced Raman spectroscopy (SERS) probe. *Anal. Methods* 6, 5097–5104. doi:10.1039/C4AY00559G

Tozzini, V., and Luin, S. (2012). "Vibrational spectroscopy of fluorescent proteins: A tool to investigate the structure of the chromophore and its environment," in *Fluorescent proteins I: From understanding to design springer series on fluorescence*. Editor G. Jung (Berlin, Heidelberg: Springer), 133–169. doi:10.1007/4243_2011_31

UBAND-Know Labs (2021). Transforming non-invasive medical diagnostics. Available at: https://www.knowlabs.co.

Vahlsing, T., Delbeck, S., Leonhardt, S., and Heise, H. M. (2018). Noninvasive monitoring of blood glucose using color-coded photoplethysmographic images of the illuminated fingertip within the visible and near-infrared range: Opportunities and questions. *J. Diabetes Sci. Technol.* 12, 1169–1177. doi:10.1177/1932296818798347

Vega, K., Jiang, N., Liu, X., Kan, V., Barry, N., Maes, P., et al. (2017). Maui, Hawaii, USA: ACM, 138–145. doi:10.1145/3123021.3123039The dermal abyss: Interfacing with the skin by tattooing biosensorsProceedings of the 2017 ACM International Symposium on Wearable Computers:

Veiseh, O., Tang, B. C., Whitehead, K. A., Anderson, D. G., and Langer, R. (2015). Managing diabetes with nanomedicine: Challenges and opportunities. *Nat. Rev. Drug Discov.* 14, 45–57. doi:10.1038/nrd4477

Ventrelli, L., Marsilio Strambini, L., and Barillaro, G. (2015). Microneedles for transdermal biosensing: Current picture and future direction. *Adv. Healthc. Mat.* 4, 2606–2640. doi:10.1002/adhm.201500450

Villena Gonzales, W., Mobashsher, A., and Abbosh, A. (2019). The progress of glucose monitoring—a review of invasive to minimally and non-invasive techniques, devices and sensors. *Sensors* 19, 800. doi:10.3390/s19040800

Wang, D., Xu, G., Zhang, X., Gong, H., Jiang, L., Sun, G., et al. (2022). Dual-functional ultrathin wearable 3D particle-in-cavity SF-AAO-Au SERS sensors for effective sweat glucose and lab-on-glove pesticide detection. *Sensors Actuators B Chem.* 359, 131512. doi:10.1016/j.snb.2022.131512

Wang, Q., Wu, G., Pian, F., Shan, P., Li, Z., and Ma, Z. (2021a). Simultaneous detection of glucose, triglycerides, and total cholesterol in whole blood by Fourier-Transform Raman spectroscopy. *Spectrochimica Acta Part A Mol. Biomol. Spectrosc.* 260, 119906. doi:10.1016/j.saa.2021.119906

Wang, Y., Zhao, C., Wang, J., Luo, X., Xie, L., Zhan, S., et al. (2021b). Wearable plasmonic-metasurface sensor for noninvasive and universal molecular fingerprint detection on biointerfaces. *Sci. Adv.* 7, eabe4553. doi:10.1126/sciadv.abe4553

Weller, C., Linder, M., Macaulay, A., Ferrari, A., and Kessler, G. (1960). Continuous *in vivo* determination of blood glucose in human subjects. *Ann. N. Y. Acad. Sci.* 87, 658–668. doi:10.1111/j.1749-6632.1960.tb23229.x

WHO. Diabetes (2022). WHO. Diabetes. Available at: https://www.who.int/health-topics/diabetes#tab=tab_1.

Wróbel, M. S., Kim, J. H., Raj, P., Barman, I., and Smulko, J. (2021). Utilizing pulse dynamics for non-invasive Raman spectroscopy of blood analytes. *Biosens. Bioelectron. X.* 180, 113115. doi:10.1016/j.bios.2021.113115

Wróbel, M. S. (2016). Non-invasive blood glucose monitoring with Raman spectroscopy: Prospects for device miniaturization. *IOP Conf. Ser. Mat. Sci. Eng.* 104, 012036. doi:10.1088/1757-899X/104/1/012036

Yilmaz, T., Foster, R., and Hao, Y. (2019). Radio-frequency and microwave techniques for non-invasive measurement of blood glucose levels. *Diagnostics* 9, 6. doi:10.3390/diagnostics9010006

Yuen, C., and Liu, Q. (2014). Towards *in vivo* intradermal surface enhanced Raman scattering (SERS) measurements: Silver coated microneedle based SERS probe: Towards *in vivo* intradermal SERS measurements. *J. Biophot.* 7, 683–689. doi:10.1002/jbio.201300006

Yunos, M. F. A. M., Manczak, R., Guines, C., Mansor, A. F. M., Mak, W. C., Khan, S., et al. (2021). RF remote blood glucose sensor and a microfluidic vascular phantom for sensor validation. *Biosensors* 11, 494. doi:10.3390/bios11120494

Zhao, J., Lin, Y., Wu, J., Nyein, H. Y. Y., Bariya, M., Tai, L.-C., et al. (2019). A fully integrated and self-powered smartwatch for continuous sweat glucose monitoring. *ACS Sens.* 4, 1925–1933. doi:10.1021/acssensors.9b00891

Glossary

BGL Blood Glucose Level
BGM Blood Glucose Monitoring
Bio-RFID Body RadioFrequency Identification
BP-ANN Back Propagation Artificial Neural Network
BS Bioimpedance Spectroscopy
CGM Continuous Glucose Monitoring
EBA Exhaled Breath Analysis
EDT Enzymatic Detection Technology
EGA Clarke Error Grid
EMS ElectroMagnetic Sensing
EMSC Extended Multiplicative Scatter Correction
FDA Food and Drug Administration
FIR Far Infrared Radiation
FIRS Far Infrared Radiation Spectroscopy
FRET Fluorescence Resonance Energy Transfer
FT Fluorescence Technology
KB Ketone Breathalyzer;
ISF InterStitial Fluid
ISUP Inter-Subject Unified Performance
MHC Metabolic Heat Conformation
MLR Multiple Linear Regression
MI Minimally invasive
MIRS Mid Infrared Spectroscopy
MMS Millimetre and Microwave Sensing
MPE Maximum Permissible Exposure
MT MultiTechnologies
N/A Not Available
NCGM Non Continuous Glucose Monitoring
NI Non-invasive
NICBGL Non-Invasive Continuous Blood Glucose Level
NIRS Near Infrared Spectroscopy
NPT NanoPhotonics Technology
OCT Optical Coherence Tomography
OPT Optical Polarimetry Technology
OS Occlusion Spectroscopy
PAS PhotoAcoustic Spectroscopy
PCA Principal Component Analysis
PEG Parkes Error Grid
PLS Partial Least Squares
PLS-DA Partial Least Squares-Discriminant Analysis
PPG PhotoPlethysmoGraphy
PWD People With Diabetes
QCL Quantum Cascade Laser;
RFST RadioFrequency Sensor Technology
RI Reverse Iontophoresis
RS Raman Spectroscopy
SNR Signal to Noise Ratio
SPRT Surface Plasmon Resonance Technology
SSB Skin Suction Blister
ST Sonophoresis Technology
SVM Support Vector Machine
TOF Time of Flight
THz-TDS Terahertz Time-Domain Spectroscopy
UT Ultrasound Technology

Frontiers in Chemistry

Explores all fields of chemical science across the periodic table

Advances our understanding of how atoms, ions, and molecules come together and come apart. It explores the role of chemistry in our everyday lives - from electronic devices to health and wellbeing.

Discover the latest Research Topics

See more →

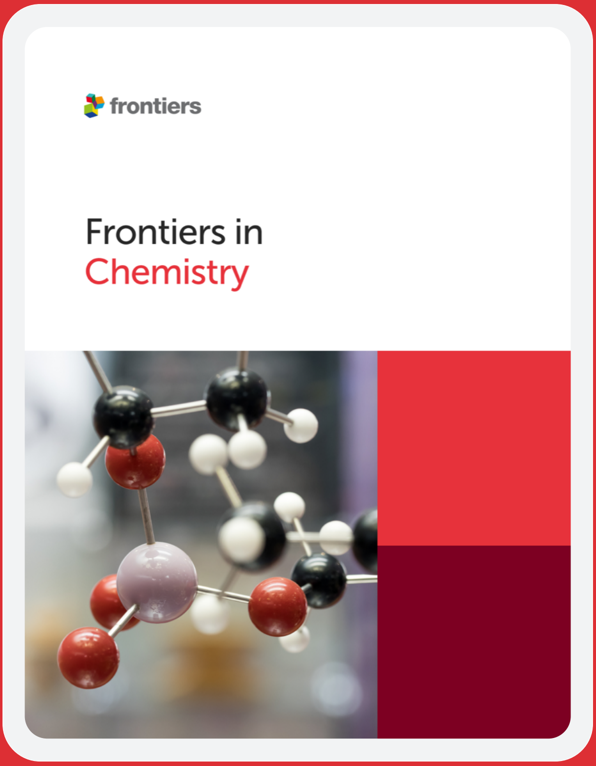
frontiers

Frontiers in
Chemistry

Frontiers

Avenue du Tribunal-Fédéral 34
1005 Lausanne, Switzerland
frontiersin.org

Contact us

+41 (0)21 510 17 00
frontiersin.org/about/contact